Characterization of Minerals, Metals, and Materials 2024:

Process–Structure–Property Relations and New Technologies

EDITED BY

Zhiwei Peng
Mingming Zhang
Jian Li
Bowen Li
Sergio Neves Monteiro
Rajiv Soman
Jiann-Yang Hwang
Yunus Eren Kalay
Juan P. Escobedo-Diaz
John S. Carpenter
Andrew D. Brown
Shadia Ikhmayies

TMS

Springer

The Minerals, Metals & Materials Series

Zhiwei Peng · Mingming Zhang · Jian Li ·
Bowen Li · Sergio Neves Monteiro · Rajiv Soman ·
Jiann-Yang Hwang · Yunus Eren Kalay ·
Juan P. Escobedo-Diaz · John S. Carpenter ·
Andrew D. Brown · Shadia Ikhmayies
Editors

Characterization of Minerals, Metals, and Materials 2024

Process–Structure–Property Relations and New Technologies

TMS

Springer

Editors
Zhiwei Peng
Central South University
Changsha, China

Jian Li
CanmetMATERIALS
Hamilton, ON, Canada

Sergio Neves Monteiro
Military Institute of Engineering
Rio de Janeiro, Brazil

Jiann-Yang Hwang
Michigan Technological University
Houghton, MI, USA

Juan P. Escobedo-Diaz
University of New South Wales
Canberra, ACT, Australia

Andrew D. Brown
Army Research Office
Durham, NC, USA

Mingming Zhang
Baowu Ouyeel Co. Ltd.
Shanghai, China

Bowen Li
Michigan Technological University
Houghton, MI, USA

Rajiv Soman
Chem Service Inc.
West Chester, PA, USA

Yunus Eren Kalay
Middle East Technical University
Ankara, Turkey

John S. Carpenter
Los Alamos National Laboratory
Los Alamos, NM, USA

Shadia Ikhmayies
Amman, Jordan

ISSN 2367-1181 ISSN 2367-1696 (electronic)
The Minerals, Metals & Materials Series
ISBN 978-3-031-50303-0 ISBN 978-3-031-50304-7 (eBook)
https://doi.org/10.1007/978-3-031-50304-7

This Springer imprint is published by the registered company Springer Nature Switzerland AG
The registered company address is: Gewerbestrasse 11, 6330 Cham, Switzerland

Paper in this product is recyclable.

Preface

This book is a compilation of selected papers from the symposium Characterization of Minerals, Metals, and Materials 2024: Process–Structure–Property Relations and New Technologies at the TMS 2024 153rd Annual Meeting & Exhibition held in Orlando, Florida, USA in 2024. The symposium aimed to provide an international intellectual platform for people to present the state-of-the-art research results in characterization of minerals, metals, and materials and applications of the results on the processing of these materials. It covered a broad range of areas, including, for example, novel methods and techniques for characterizing materials across a spectrum of systems and processes, characterization of mechanical, thermal, electrical, optical, dielectric, magnetic, physical, and other properties of metals, polymers, and ceramics, characterization of structural, morphological, and topographical natures of materials at micro- and nanoscales, characterization of extraction and processing including process development and analysis, and advances in instrument developments for microstructure analysis and performance evaluation of materials, such as computer tomography, X-ray and neutron diffraction, electron microscopy, spectroscopy, and modeling. At the TMS 2024 Annual Meeting & Exhibition, the symposium received 132 abstracts from all over the world, of which 67 abstracts were accepted for submitting manuscripts for publication in the book after peer reviewing.

This book provides a valuable guide and a collection of new and exciting insights for characterization of various minerals, metals, and materials. Scientists, engineers, educators, and students worldwide will enjoy the diverse topics that reflect the authors' brilliant achievements in clarifying the process-structure-property relations and developing novel characterization technologies.

The editors of this book wish to extend their sincere appreciation to all the authors and reviewers for their invaluable contributions. They would also like to thank the Materials Characterization Committee and Extraction and Processing Division of TMS for sponsoring the symposium and the publisher, Springer, for its great efforts in making this publication possible.

Zhiwei Peng
Mingming Zhang
Jian Li
Bowen Li
Sergio Neves Monteiro
Rajiv Soman
Jiann-Yang Hwang
Yunus Eren Kalay
Juan P. Escobedo-Diaz
John S. Carpenter
Andrew D. Brown
Shadia Ikhmayies

Contents

About the Editors

Zhiwei Peng is a professor in the School of Minerals Processing and Bioengineering at Central South University, China. He received his B.E. and M.S. degrees from Central South University in 2005 and 2008, respectively, and his Ph.D. degree in Materials Science and Engineering from Michigan Technological University, USA, in 2012. His research interests include dielectric characterization, ferrous metallurgy, microwave processing, comprehensive utilization of resources, waste valorization, powder agglomeration, low-carbon technology, process simulation, electromagnetic shielding, and synthesis of functional materials. Dr. Peng has published over 200 papers, including more than 150 peer-reviewed articles in journals such as *International Materials Reviews*; *Journal of Hazardous Materials*; *ACS Sustainable Chemistry & Engineering*; *Resources, Conservation & Recycling*; *Journal of Cleaner Production*; *Waste Management*; *Metallurgical and Materials Transactions A*; *Metallurgical and Materials Transactions B*; *JOM*; *Journal of Power Sources*; *Fuel Processing Technology*; *Energy & Fuels*; *IEEE Transactions on Magnetics*; *IEEE Transactions on Instrumentation and Measurement*; *Ceramics International*; *Powder Technology*; and *Separation and Purification Technology*. He holds 68 Chinese patents and has served as an associate editor for *Mining, Metallurgy & Exploration*, as a guest editor for *JOM* and *Metals*, and as an editor for *PLOS ONE*. He has also been a member of editorial boards of *Scientific Reports*, *Journal of Central South University*, and *Journal of Iron and Steel Research International*, and has served as a reviewer for more than 70 journals. Dr. Peng

is an active member of The Minerals, Metals & Materials Society (TMS). He has co-organized 13 TMS symposia and co-chaired 25 symposia sessions since 2012. He is a member of the Pyrometallurgy Committee and the chair of the Materials Characterization Committee. He was a winner of the TMS EPD Young Leaders Professional Development Award in 2014 and the TMS EPD Materials Characterization Award Best Paper—1st Place in 2020.

Mingming Zhang is currently a principal technical officer at Baowu Ouyeel Co. Ltd. in Shanghai, China. He has more than 20 years of experience in the field of mining, mineral processing, smelting, refining, and materials engineering. Before joining Baowu Ouyeel, Dr. Zhang held a principal consultant position at Wood Mackenzie in Chicago and the lead engineer position at ArcelorMittal Global R&D in East Chicago, Indiana. He obtained his Ph.D. in Metallurgical Engineering from The University of Alabama and his master's degree in Mineral Processing from the General Research Institute for Non-ferrous Metals in China. Prior to joining ArcelorMittal, he worked with Nucor Steel in Tuscaloosa, Alabama where he was a metallurgical engineer leading the development of models for simulating slab solidification and secondary cooling process. Dr. Zhang has conducted a number of research projects involving mineral beneficiation, thermodynamics and kinetics of metallurgical reactions, electrochemical processing of light metals, metal recycling, and energy-efficient and environmentally cleaner technologies. He has published more than 50 peer-reviewed research papers, and he is the recipient of several U.S. patents. Dr. Zhang also serves as editor and reviewer for a number of prestigious journals including *Metallurgical and Materials Transactions A* and *B*, *JOM*, *Journal of Phase Equilibria and Diffusion*, and *Mineral Processing and Extractive Metallurgy Review*.

Dr. Zhang has made more than 30 research presentations at national and international conferences including more than 10 keynote presentations. He was the recipient of the 2015 TMS Young Leaders Professional Development Award. He has served as conference/symposium organizer and technical committee chair in several international professional organizations including The

Minerals, Metals & Materials Society (TMS), the Association for Iron & Steel Technology (AIST), and the Society for Mining Metallurgy & Exploration (SME).

Jian Li is a senior research scientist and program manager at CanmetMATERIALS in Natural Resources Canada. He obtained his B.Sc. in Mechanical Engineering from Beijing Polytechnique University, M.Sc. in Metallurgical Engineering from Technical University of Nova Scotia, and Ph.D. in Materials and Metallurgical Engineering from Queen's University, Kingston, Ontario, Canada. He has broad experience in materials processing and characterization including alloys deformation, recrystallization, and micro-texture development. Dr. Li has experience in Focused Ion Beam (FIB) microscope techniques. He is also an expert in various aspects of SEM-EDS and EPMA techniques. Dr. Li has authored three book chapters and published more than 180 papers in scientific journals and conference proceedings.

Bowen Li is a research professor in the Department of Materials Science and Engineering and Institute of Materials Processing at Michigan Technological University. His research interests include materials characterization and analysis, metals extraction, ceramic process, antimicrobial additives and surface treatment, porous materials, applied mineralogy, and solid waste reuse. He has published more than 150 technical papers in peer-reviewed journals and conference proceedings, authored/co-authored 3 books, and edited/co-edited 15 books. He also holds 16 patents. Dr. Li received a Ph.D. degree in Mineralogy and Petrology from China University of Geosciences Beijing in 1998 and a Ph.D. degree in Materials Science and Engineering from Michigan Technological University in 2008. He has been an active member in The Minerals, Metals & Materials Society (TMS), Society for Mining, Metallurgy& Exploration (SME), and China Ceramic Society. At TMS, he has served as the chair of the Materials Characterization Committee and as a member of TMS CDDC Committee, Powder Materials Committee, Biomaterials Committee, and EPD Award Committee. He has also served as *JOM* subject advisor, and key reader for *Metallurgical and Materials Transactions A*. He has been organizer/co-organizer of a number

of international symposia and sessions. He also served as an editorial board member of the *Journal of Minerals and Materials Characterization and Engineering*. He is the recipient of the AIME Hal W. Hardinge Award (2022).

Sergio Neves Monteiro graduated as a Metallurgical Engineer (1966) at the Federal University of Rio de Janeiro (UFRJ). He received his M.Sc. (1967) and Ph.D. (1972) from the University of Florida, followed by a 1975 course in energy at the Brazilian War College, and a post doctorate (1976) at the University of Stuttgart. In 1968, he joined the Metallurgy Department of UFRJ as full professor of the postgraduation program in engineering (COPPE). He was elected as head of department (1978), coordinator of COPPE (1982), Under-Rector for Research (1983), and was invited as Under-Secretary of Science for the State of Rio de Janeiro (1985) and Under-Secretary of the College Education for the Federal Government (1989). He retired in 1993 from the UFRJ and joined the State University of North Rio de Janeiro (UENF), where he retired in 2012. He is now a professor at the Military Institute of Engineering (IME), Rio de Janeiro. Dr. Monteiro has published more than 2,000 articles in journals and conference proceedings and has been honored with several awards including the ASM Fellowship and several TMS awards. He is the top researcher (1A) of the Brazilian Council for Scientific and Technological Development (CNPq) and Emeritus Scientist of State of Rio de Janeiro (FAPERJ). He was president of the Superior Council of the State of Rio de Janeiro Research Foundation, FAPERJ (2012), and currently is coordinator of the Engineering Area of this foundation. He has also served as president of the Brazilian Association for Metallurgy, Materials and Mining (ABM, 2017–2019), as a consultant for the main Brazilian R&D agencies, and as a member of the editorial board of five international journals as well as Executive Editor of the *Journal of Materials Research and Technology*. He is the author of 150 patents and a top world researcher in “Natural Fiber Composites” and “Ballistic Armor”, Scopus 2022.

Rajiv Soman currently serves as Director of Operations, CHEM SERVICE Inc., and is a *Scientific Fellow* at AnalytiChem Group, USA. Prior to joining AnalytiChem Group, he served as Director, Purity Survey, Materials Science Division, Eurofins EAG Laboratories. He has over 33 years of professional experience in analytical chemistry and materials sciences. He earned a doctorate in Analytical Chemistry from Northeastern University, Boston, USA, and M.Sc. in Applied Chemistry from the Faculty of Technology & Engineering, Maharaja Sayajirao University of Baroda, India. He commenced his professional career as an Advanced Analytical Chemist in the Engineering Materials Technology Laboratories of General Electric Aircraft Engines. Dr. Soman served as Professor (Full) of Chemical Engineering, Chemistry, and Chemical Technology, and as a faculty member for 21 years. He also served as Department Head and Associate Dean. He has received numerous awards for excellence in teaching and twice has been listed in *Who's Who Among America's Teachers*. Dr. Soman's research interests are in the areas of atomic and mass spectrometry, with an emphasis on trace element determination and chemical speciation in a wide range of complex sample matrices. He was an invited guest scientist at the prestigious Forschungszentrum Jülich, Germany, where he conducted research in elemental mass spectrometry. He has co-authored several peer-reviewed publications in international journals and has made numerous presentations at national and international conferences. He holds two U.S. patents. Dr. Soman has been a member of the Society for Applied Spectroscopy (SAS) and the American Chemical Society (ACS) since 1986 and has served in numerous leadership positions in the Professional Societies. He is a member of TMS, where he serves as a member of the Materials Characterization Committee and as Chair of the Poster Awards Committee. He also served as co-organizer for several TMS Symposia and is a reviewer for the TMS proceedings volume *Characterization of Minerals, Metals, and Materials* and *JOM*.

Jiann-Yang Hwang is a professor in the Department of Materials Science and Engineering at Michigan Technological University. He is also the Chief Energy and Environment Advisor at the Wuhan Iron and Steel Group Company, a Fortune Global 500 company. He has been the editor-in-chief of the *Journal of Minerals and Materials Characterization and Engineering* since 2002. He has founded several enterprises in areas including water desalination and treatment equipment, microwave steel production, chemicals, fly ash processing, antimicrobial materials, and plating wastes treatment. Several universities have honored him as a guest professor, including the Central South University, University of Science and Technology Beijing, Chongqing University, Kunming University of Science and Technology, and Hebei United University. Dr. Hwang received his B.S. from National Cheng Kung University in 1974, M.S. in 1980 and Ph.D. in 1982, both from Purdue University. He joined Michigan Technological University in 1984 and served as its Director of the Institute of Materials Processing from 1992 to 2011 and the Chair of Mining Engineering Department in 1995. He has been a TMS member since 1985. His research interests include the characterization and processing of materials and their applications. He has been actively involved in the areas of separation technologies, pyrometallurgy, microwaves, hydrogen storage, ceramics, recycling, water treatment, environmental protection, biomaterials, and energy and fuels. He has more than 28 patents and has published more than 200 papers. He has chaired the Materials Characterization Committee and the Pyrometallurgy Committee in TMS and has organized several symposia. He is the recipient of the TMS Technology Award and of Michigan Tech's Bhakta Rath Research Award.

Yunus Eren Kalay is an associate professor in the Metallurgical and Materials Engineering Department and assistant to the president at Middle East Technical University (METU), Ankara, Turkey. Dr. Kalay received his Ph.D. with Research Excellence award from Iowa State University in 2009. His Ph.D. topic was related to the metallic glass formation in Al based metallic alloy systems. Following his Ph.D., he pursued post-doctoral research at Ames National Laboratory. In 2011, Dr. Kalay joined the Department of Metallurgical and Materials Engineering (METE) of METU as an assistant professor and in 2014 he was promoted to associate professor. His research interests span microstructural evolution in metallic alloys, rapid solidification of metallic alloys, nanostructured and amorphous alloys, high-entropy alloys, electronic packaging, and advanced characterization techniques such as scanning and transmission electron microscopy, electron and X-ray spectroscopy, atom probe tomography, and synchrotron X-ray scattering. Dr. Kalay was awarded the METU Prof. Dr. Mustafa Parlar Foundation Research Incentive Award, which is a very prestigious award that recognizes young scientists in Turkey with exceptional achievements and research productivity. He is also an active member of the TMS Materials Characterization Committee and served on organizing committees of three international and one national congress including IMMC, MS&T, and TMS. Dr. Kalay has also been involved in many synergistic activities such as being founding editor of Turkey's first undergraduate research journal, *MATTER*, and organizing the Materials Science Camps for K–12 students.

Juan P. Escobedo-Diaz is a senior lecturer in the School of Engineering and Technology (SEIT) at UNSW Canberra. He obtained his doctoral degree in Mechanical Engineering at Washington State University. Prior to taking up this academic appointment, he held research positions at the Institute for Shock Physics and at Los Alamos National Laboratory. His main research interests center on the dynamic behavior of materials under extreme conditions, in particular high pressure and high strain rate. His focus has been on investigating the effects of microstructural features on the dynamic fracture behavior of metals and metallic alloys. He has published

primarily in the fields of shock physics and materials science. He has been a member of The Minerals, Metals & Materials Society (TMS) since 2011. During this time, he has been a co-organizer of the symposium on Characterization of Minerals, Metals, and Materials since 2014. He was awarded a 2014 SMD Young Leaders Professional Development Award.

John S. Carpenters is a scientist within the manufacturing science and metallurgy division at Los Alamos National Laboratory. Dr. Carpenter received his Ph.D. in Materials Science and Engineering from The Ohio State University in 2010 after performing his undergraduate studies at Virginia Tech. Dr. Carpenter's research focuses on enabling advanced manufacturing concepts through experiments employing novel processing techniques, advanced characterization, and small-scale mechanical testing. Currently, he is working on projects related to the qualification of additively manufactured components, the development of new materials for high field magnets through severe plastic deformation and the use of high energy X-rays to study phase transformations during solidification in MIG cladding. Throughout his career he has utilized many characterization techniques including neutron scattering, X-ray synchrotron, XCT, PED, TEM, EBSD, and SEM. He has more than 75 journal publications and 50 invited technical talks to his credit. With regard to TMS service, Dr. Carpenter is a past chair for the Materials Characterization Committee, the Advanced Characterization, Testing & Simulation Committee, and the Joint Commission for *Metallurgical and Materials Transactions*. He is also the Program Committee Representative for the MS&T Conference and the current Vice Chair for the Extraction and Processing division. He is the 2021 recipient of the McKay-Helm Award from the American Welding Society and is the 2018 recipient of the Distinguished Mentor Award at Los Alamos National Laboratory.

Andrew D. Brown serves as Technical and Core Mission Support for the Sciences of Extreme Materials Competency Branch at the Army Research Office, a directorate of the U.S. Army Combat Capabilities Command Army Research Laboratory (ARL). Prior to joining ARO in 2022, Dr. Brown served in the Terminal Effects Division at ARL since 2018. Dr. Brown's research expertise is in the areas of advanced materials characterization, the mechanical response of structural materials subjected to high strain rate loading, and injury biomechanics. He obtained a B.S. in Mechanical Engineering at North Carolina State University (2009) and a doctoral degree in Mechanical Engineering at Arizona State University (2015). He then worked as a postdoctoral researcher in the Impact Dynamics Laboratory at the University of New South Wales Canberra at the Australian Defence Force Academy (2015–2018). He has been an active member of TMS since 2011, a co-organizer for the Characterization of Minerals, Metals, and Materials symposium (2018, 2020-present), and was the symposium's EPD Awards Representative from 2017–2022. Dr. Brown has published over 40 peer-reviewed articles in the fields of mechanical engineering, materials science, and biomechanics.

Shadia Ikhmayies received her B.Sc. and M.Sc. from the physics department in the University of Jordan in 1983 and 1987 respectively, and her Ph.D. in producing CdS/CdTe thin film solar cells from the same university in 2002. Her research is focused on producing and characterizing semiconductor thin films, and thin film CdS/CdTe solar cells. She works in characterizing quartz in Jordan for the extraction of silicon for solar cells and characterizing different materials by computation. Dr. Ikhmayies published 59 research papers in international scientific journals, 86 research papers in conference proceedings, and 3 chapters in books. She is the founder and editor of the book series "Advances in Material Research and Technology" published by Springer, and the editor in chief/editor of several books.

Dr. Ikhmayies is a member of The Minerals, Metals & Materials Society (TMS) where she was the chair of the Characterization Committee in 2016 and 2017, and the leading organizer of three symposiums; Solar Cell Silicon 2017-2020, Mechanical Characteristics

and Application Properties of Metals and Non-metals for Technology: An EPD Symposium in Honor of Donato Firrao, and Green Materials Engineering: An EPD Symposium in Honor of Sergio Monteiro. Dr. Ikhmayies is also a member of the World Renewable Energy Network/Congress (WREN/WREC) 2010-present. She is a member of the international organizing committee and the international scientific committee in the European Conference on Renewable Energy Systems (ECRES2015-ECRES2023). She is a guest editor and a member of the editorial board of several journals including *JOM* and the *Journal of Electronic Materials*. Dr. Ikhmayies has served as a reviewer for 24 international journals and several international conference proceedings. She has received several international awards including the TMS Frank Crossley Diversity Award 2018 and World Renewable Energy Congress 2018 Pioneering Award.

Part I
Advanced Characterization Methods I

Effect of Si on Microstructural and Magnetic Behaviour of Heat-Treated High Carbon Steel

Negin Sarmadi, Farshid Pahlevani, Sanjith Udayakumar, Smitirupa Biswal, Clemens Ulrich, and Veena Sahajwalla

Abstract Silicon (Si) is a versatile alloying element that can enhance the performance of high carbon steel by contributing to deoxidation, grain refinement, hardenability, strength, and toughness. The study investigates the influence of Si (0.8–3.6%) on the microstructural and magnetic properties of high carbon steel. The arrangement and density of magnetic moments, which are affected by the microstructure determines the saturation magnetisation of the material. Industrial-grade high carbon steel samples with varying silica were microstructurally tailored to obtain multiphase steel microstructures. The optical and SEM analyses revealed a combination of cementite and plate martensite, wherein the martensitic structures became finer with higher Si content. The evolution of martensitic microstructures along with mild oxidation of Si inclusions in the grain boundaries of the surface were observed using Confocal microscopy. An increase in the cementite with an accompanied decrease in the martensitic fraction was determined by the quantitative analysis of the X-ray diffractograms. The saturation magnetisation (M_S) of the samples witnessed a gradual decrease with increase in the Si content. Silicon's role in high carbon steel is quite notable, therefore, the nature of heat treatment and level of Si addition can be adjusted to limit the formation of cementite and increase the ferritic martensite or austenite in the microstructure.

Keywords High carbon steel · Heat treatment · Saturation magnetisation · Silicon · Martensite

N. Sarmadi (✉) · F. Pahlevani · S. Udayakumar · S. Biswal · V. Sahajwalla
Centre for Sustainable Materials Research and Technology, SMaRT@UNSW, School of Materials Science and Engineering, UNSW Sydney, Sydney, NSW 2052, Australia
e-mail: n.sarmadi@unsw.edu.au

C. Ulrich
School of Physics, UNSW Sydney, Sydney, NSW 2052, Australia

Z. Peng et al. (eds.), *Characterization of Minerals, Metals, and Materials 2024*, The Minerals, Metals & Materials Series, https://doi.org/10.1007/978-3-031-50304-7_1

Introduction

Steel stands as humanity's most vital structural resource, finding utility across all aspects of our daily existence and within the realms of industry. Its prevalence throughout various applications has led to its growing significance over time, establishing it as an indispensable alloy [1]. Dual-phase steels represent a recent category of steels. Their defining feature is a structure comprising tough martensite particles evenly spread within a pliable, soft matrix. The descriptor "dual phase" highlights the prevalence of two main components in the structure [2, 3]. High carbon dual-phase steel usually encompasses martensite and retained austenite phases, providing remarkable toughness, hardness, and resistance to abrasion. These characteristics make it well-suited for use in extreme operating conditions and environments [4].

Silicon (Si) is an important alloying element for the enhancement of properties in various grades of steel. Si generally enhances steel's strength and hardness, though it's less effective than manganese in this regard. It improves acid resistance, promotes larger grain sizes for higher magnetic permeability, aids crystal orientations in electrical steels, and bolsters oxidation resistance in high-temperature service steels [5]. High carbon steel with increased Si content can be quenched to form martensite more easily, resulting in greater hardness and wear resistance. Introducing Si raises the strength of dual-phase steels following annealing and gradual cooling, owing to the formation of a substantial amount of uniformly distributed, easily hardenable austenite. This process results in a significant presence of martensite within the final structure [6]. In recent advancements in high-strength steel development, a notable emphasis has been placed on incorporating retained austenite into the microstructure of martensitic steels. The objective is to elevate the ductility of the steel without excessively compromising its strength. Si is recognized for its capacity to hinder the development of cementite, likely attributed to its notably limited solubility within cementite. Theoretically, by impeding the precipitation of carbides, a greater quantity of carbon becomes accessible for allocation into retained austenite. Consequently, the introduction of Si has been documented to augment the ultimate proportions of retained austenite or elevate the carbon content within carbon and low-alloy steels [7–10]. However, high carbon steel typically contains cementite (Fe_3C) in its microstructure, which contributes to its hardness. Excessive Si can lead to the formation of excess cementite, which can affect the steel's properties. Moreover, Si is ineffective in retarding the precipitation of cementite if the parent phase is highly supersaturated with carbon [11]

The current work explores the effect of Si addition with variable amounts on the microstructural aspect of high carbon steel. The steel samples with varying Si content were subjected to heat treatment followed by quenching. Various characterisation techniques were employed to understand the evolution of microstructural phases along with magnetic behaviour with respect to Si content. Subsequently, the magnetic behaviour of the heat-treated steel was assessed, as the arrangement of magnetic moments within a material, and consequently, its saturation magnetization (M_S), can be significantly influenced by the microstructural characteristics of the material.

Materials and Methods

The study was conducted for industrial-grade high carbon steel with a chemical composition of 1.0%C–1.0%Mn–0.4%Cr (in wt.%) with three different concentrations of Si. The microstructure of these steels was initially a combination of martensite and a significant amount of retained austenite. The concentration of Si varied between 0.8 and 3.6 wt.%. The homogenised steel samples were subject to heat treatment, wherein the mode of heat treatment aimed to limit the microstructure to a dual-phase steel. The varying concentrations of Si in the high carbon steel may have both positive and negative effects on the desired microstructure. The sample composition, as determined using Laser-induced breakdown spectroscopy (LIBS) is provided in Table 1.

Heat Treatment Using High-Temperature Confocal Microscopy (HTCM)

The high carbon steel samples were first mirror polished and then subjected to heat treatment in an IR furnace SVF17-SP from Yonekura Corporation (Kanagawa, Japan) coupled with a confocal microscopy set-up—CSLM VL2000DX from Lasertec Corporation (Yokohama, Japan) for in-situ observations. To prevent the sample from undergoing oxidation at high temperatures during the experiment, the chamber was thoroughly purged of oxygen and moisture well in advance. This was accomplished by initially filling the chamber with purified argon gas, which had been filtered, for ~ 3 min. Subsequently, the chamber was evacuated for 3 min using an oil-sealed rotary vacuum pump. These procedures were iterated three times, resulting in oxygen and water concentrations of < 1.0 ppm. The samples were heated to 1100 °C in Ar atmosphere with a 15-min dwell period followed by rapid cooling with a rate of 50 °C/s. The confocal images of the steel during the heat treatment were recorded using a laser beam having a wavelength of 408 nm at a frame rate of 30 fps and a resolution of 1024 × 1024 pixels.

Table 1 High carbon steel: sample name and composition

Sample name	Percentage (%)			
	C	Cr	Mn	Si
Low-Si (L-Si)	1.1	0.4	1.0	0.8
Medium-Si (M-Si)				2.0
High-Si (H-Si)				3.6

Characterisation of Heat-Treated Samples

Semi-quantitative analysis of the sample's microstructure was conducted using X-ray diffraction. This involved using Co-K radiation at 45 kV and 40 mA current, employing a step size of $\Delta\theta = 0.0260°$, and scanning the diffraction angle from 30° to 130° for detection. To examine the surface morphology of the steel samples, we utilized a Hitachi S3400 scanning electron microscope equipped with energy-dispersive X-ray spectroscopy (EDS) [15]. The steel samples used for XRD analysis were prepared in accordance with standards for bulk solid analysis. For quantitative phase analysis, Rietveld refinement fits were carried out using PANalytical X'Pert High Score Plus software. This allowed us to determine the volume fractions of both the original and newly transformed phases in the specimens subjected to various test conditions. A series of automated wet grinding and polishing procedures were performed for the metallographic examination of the heat-treated samples using Optical and Scanning Electron Microscopy (SEM).

The magnetic characteristics (saturation magnetization, remanence, and coercivity) of the samples (1 mm × 5 mm) were assessed by advanced SQUID (Superconducting Quantum Interference Device) Quantum Design MPMS-3 magnetometer using the vibrating sample mode (VSM) to achieve highest sensitivity. The magnetic hysteresis loops were measured with a sensitivity control of magnetic field with $\leq 10^{-8}$ emu at ambient temperature.

Results and Discussion

The samples subjected to heat treatment were characterised using metallographic, microscopic, and diffraction analyses. During the austenitization and quenching processes in the heat treatment of high carbon steel, Si plays an important role in influencing the transformation of the steel's microstructure. The effects of Si addition in high carbon steel have been briefly discussed below.

Optical and SEM Analysis

The optical and SEM micrographs of the high carbon steel samples before and after heat treatment are shown in Figs. 1a, b and 2a, b. The optical micrographs of the Si-added samples before heat treatment were characterised by a pearlitic microstructure. Cementite grains were identified as dark black spots segregated at grain boundaries. A dominant martensitic microstructure was observed after heat treatment. The homogenised samples of Si-added steel exhibited mild surface oxidation, which increased with higher Si. From the SEM images, the sample morphology before

heat treatment showed lamellar ferritic structures and cementite. After heat treatment, the ferritic structures transformed into a combination of plate martensites. The martensitic structures evolved into a much finer structure with an increase in the Si content. The cementites were identified as small dark spots along the boundaries of the martensitic plates.

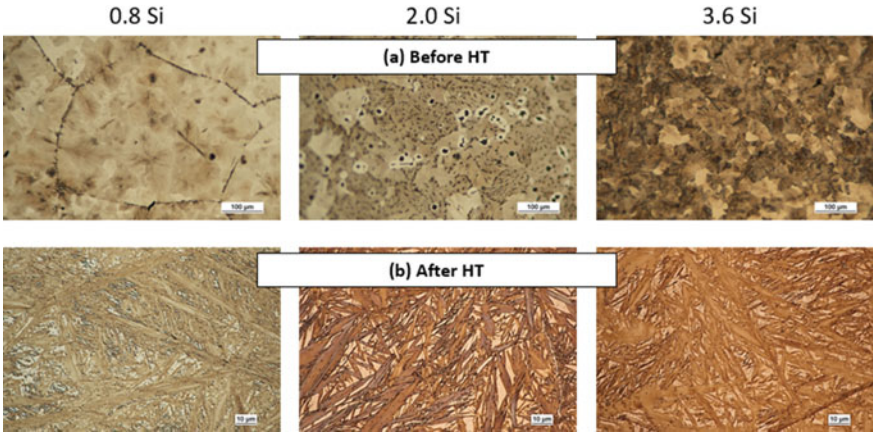

Fig. 1 Optical microscopy images of the steel samples with different Si concentrations before and after heat treatment

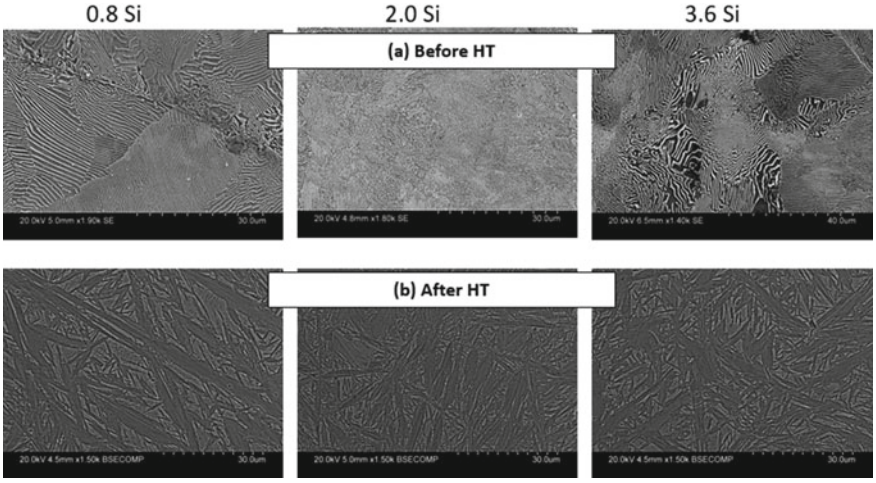

Fig. 2 SEM analysis of steel samples with different Si concentrations before and after heat treatment

Confocal Microscopy

The increase in Si content in high carbon steel typically does not directly increase the formation of cementite, ferrite, or austenite during the heat treatment process. Instead, its primary influence is on the microstructure, mechanical, electrical, and magnetic properties. Figure 3a–c present the confocal microscopic images, which provide in situ real-time studies of phase transformations during heat treatment of the steel. Figure 3 shows the evolution of microstructures of steel observed using a high temperature confocal microscope during the heat treatment. Si generally remains dissolved in the austenite phase during austenitization. It doesn't significantly affect the phase transformation and remains uniformly distributed within the austenite structure. However, during quenching, the high cooling rate prevents the carbon atoms and other alloying elements, including Si, from diffusing and forming new phases. As a result, the steel "freezes" in the high-temperature austenite phase, locking the carbon and Si atoms in their positions within the austenite lattice.

Silicon remains in solid solution within the martensite phase. It does not form separate Si-rich compounds or phases during quenching, but the formation of austenite in the Si-containing steel takes place through the nucleation process followed by limited growth, resulting in a refined microstructure with small islands of austenite with uniform carbon distribution [6]. On quenching, the low-Si steel displays a martensite-rich structure while higher Si contents favoured martensite and cementite structures. At lower Si concentrations the grain structure was larger in size and refinement of the grains was noticeable for higher Si contents. However, in the case

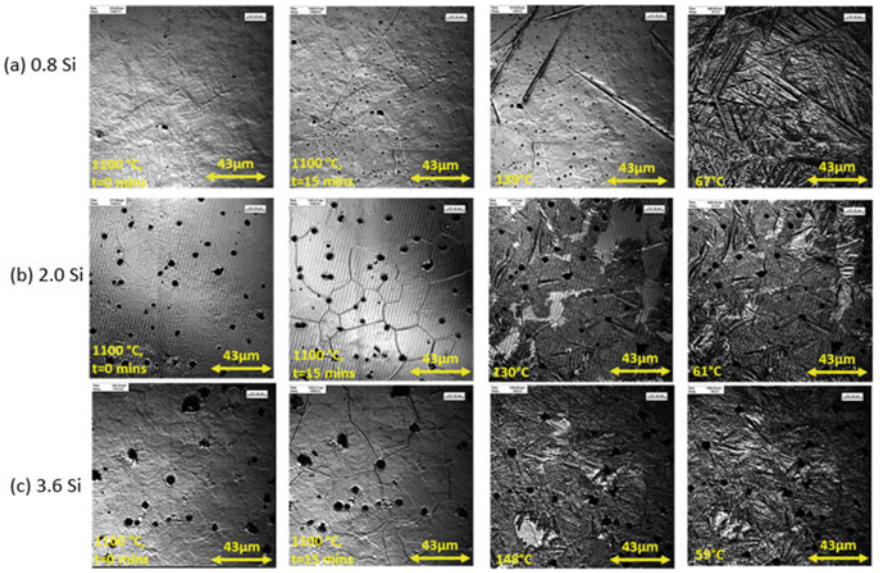

Fig. 3 Confocal microscopy images of Si-added high carbon steel samples

of high carbon steel, there were carbides produced in lower fractions which can pin the grain boundaries and impede grain growth [12]. The capacity to generate carbides increases with higher carbon in the steel, and effectively secures the grain boundaries. The pinning effect of precipitates on grain growth is caused by the reduction in grain boundary areas [13]. At high temperatures, Si also segregates at high temperatures towards the grain boundaries or interfaces forming mixed oxides.

XRD

Figure 4 shows the X-ray diffraction patterns before and after the heat treatment of the steel samples. The microstructural phase analyses of the samples after the heat treatment demonstrated α'-martensitic, α-ferrite, γ-retained austenite and cementite phases. From the quantification of phases using Rietveld analyses, it can be noticed that with increasing Si content, the martensitic fraction decreased while the cementite increased. On the other hand, there was a marginal increase in the ferrite fraction. It is normal for the ferrite fraction to increase, as Si favours the formation and strengthens ferrite and, to a lesser degree, austenite by solid solution hardening. While Si has a mild effect on hardenability of steel, it contributes to the hardening of the ferritic phase in steels [14]. Moreover, addition of Si also favours the formation of a homogeneous austenite of higher hardenability resulting in a higher volume of martensite in the final structure. In Si-containing steels, the austenite starts to form when the recrystallization of ferrite is mostly completed [15].

Si, in its dissolved form, remains in the austenite phase during the austenization process, and doesn't directly increase the formation of austenite, but rather it stays in solid solution within the austenite lattice. Generally, Si retards the precipitation of cementites from austenites, however at higher carbon content, when the parent phase is highly super saturated with carbon, Si becomes ineffective, and favours cementite formation. Also, the other reason is the low or near zero solubility of Si in cementite, which requires diffusion away from the growing carbide [16] or rejection into the surrounding ferrite [17].

Magnetic Characteristics

The addition of only small quantities of Si has considerable effect on the microstructure, leading to significant changes in the properties of the steel. The final microstructural composition that the steel holds determine its magnetic behaviour. Generally, at higher Si contents (~ 6.5wt.%), the electrical resistance is increased, the eddy current loss is reduced and the magnetostriction is almost zero. They also have the undesirable effects of decreasing the Curie temperature, reducing the saturation magnetization, and of embrittling the alloy when the Si exceeds about 2 wt.%. The embrittling effects of Si make it difficult to produce Si steels with more than about

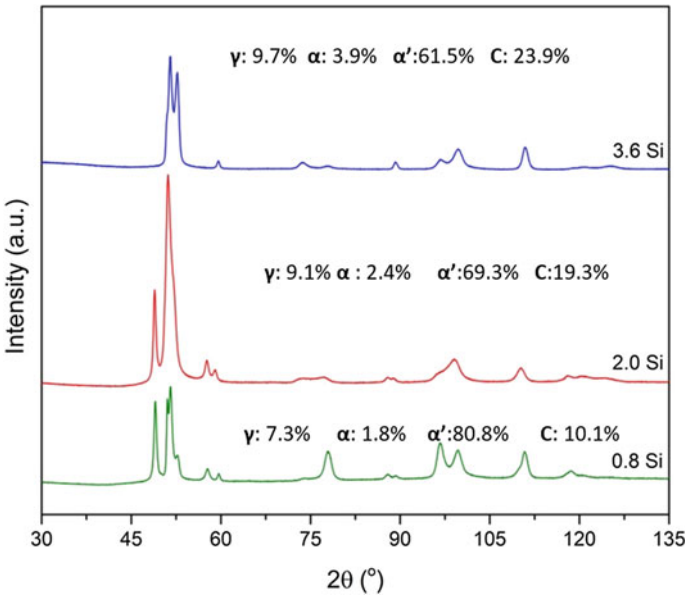

Fig. 4 XRD analyses of heat-treated high carbon steel samples (α—ferrite, α'—martensite, γ—austenite, and C—cementite)

3 wt.% Si. Thus, the microstructural distribution, determined by the amount of Si, plays a critical role in magnetic characteristics of the steel.

The Magnetic moment vs. Magnetic Field (Oe) curves at ambient temperature (300 K) for different Si steel samples subjected to heat treatment as measured by the SQUID-VSM magnetometer are shown in Fig. 5. The magnetisation curves corresponding to 0.8 and 2.0 Si did not vary much but were notably distinct compared to the 3.6 Si curve. It can be noticed that the saturation magnetisation (M_S) of the steels decreased with increasing Si contents. The magnetic properties of steel are strongly influenced by its microstructure, specifically the crystal structure and the presence of certain alloying elements [18]. The higher saturation magnetization of martensites is due to a combination of factors, including their unique crystal structure and the presence of iron atoms with unpaired spins [19]. However, note that the saturation magnetisation values are determined by the cumulative magnetic behaviour of the bulk steel sample, and not merely the martensitic fraction of the steel. The coercivity and remanence of the samples did not follow a similar trend as M_S. They seemed to be independent of the Si content in the steel samples.

Si does not form separate phases or compounds during these processes at the austenitization temperature; however, it contributes to the overall properties of the steel, including its hardenability and resistance to scaling. Addition of Si can improve the strength and toughness due to the refinement of grain size and its solution-hardening effect [20, 21]. Being a ferrite stabilising element, excessive addition of Si

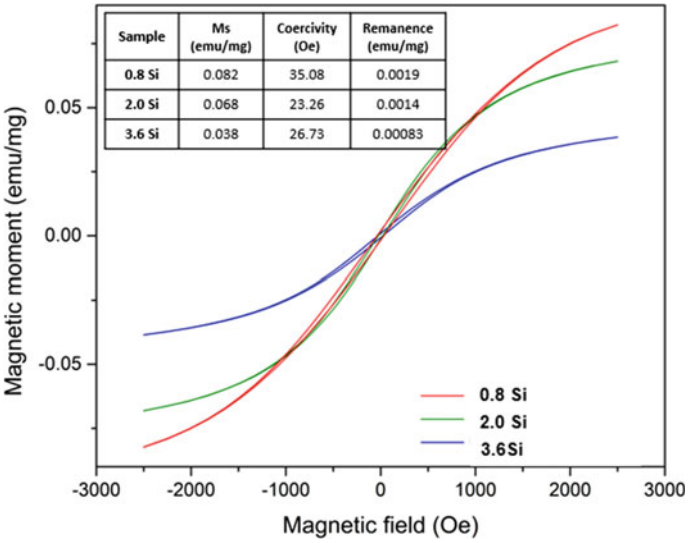

Fig. 5 Magnetization curves and characteristics of high carbon steel samples subject to heat treatment

may result in the increase of chromium equivalent and the decrease of nickel equivalent correspondingly, which will decrease the single-phase zone of austenite and form δ-ferrite easily in the process of austenitizing and further affect the microstructure and mechanical properties of the steels. Furthermore, Si addition has the tendency to improve the magnetic softness and increase the electrical resistivity, while decreasing the Curie temperature, and reducing the saturation magnetization, and demonstrated embrittlement of the alloy when exceeded above 2 wt.% [22]. Solid solution strengthening, grain refinement, phase transformation, and the interaction between Si and interstitial elements have been cited as the primary mechanisms responsible for altering the mechanical characteristics of Si-rich steel.

Conclusion

The industrial grade high carbon steel samples homogenised with different levels of Si (0.8–3.6 wt.%) were subjected to heat-treatment to obtain a multi-phase steel structure. The quantification of two phases, namely austenite and martensite in high carbon steels was investigated using quantitative X-ray diffraction. The optical and SEM analysis confirmed the presence of martensites and cementites as two dominant phases, with different densities of the martensitic fraction determined by the Si content. Quantitative XRD analysis suggested the presence of martensitic fractions

and cementites with lower quantities of retained austenite and ferrite. Magnetic characterisation of the samples denoted that the saturation magnetisation was higher for the samples with lower Si content, while coercivity and remanence was independent.

Acknowledgments This research was supported by the Australian Research Council's Industrial Transformation Research Hub funding scheme (Project IH190100009). The authors acknowledge the facilities and the scientific and technical assistance of Microscopy Australia at the Electron Microscope Unit (EMU) within the Mark Wainwright Analytical Centre (MWAC) at UNSW Sydney.

References

1. Islam T, Rashed HMMA (2019) Classification and application of plain carbon steels. In: Reference module in materials science and materials engineering. Elsevier, Amsterdam
2. Raabe D (2023) Dual phase steels. https://www.dierk-raabe.com/dual-phase-steels/
3. Speich GR, Committee AH (1990) Dual-phase steels. In: Properties and selection: irons, steels, and high-performance alloys. ASM International
4. Handoko W, Pahlevani F, Sahajwalla V (2017) Corrosion behaviour of dual-phase high carbon steel—microstructure influence. J Manuf Mater Process 1(2):21
5. Satyendra (2014) Silicon in steels. https://www.ispatguru.com/silicon-in-steels/
6. Drumond J et al (2012) Effect of silicon content on the microstructure and mechanical properties of dual-phase steels. Metallogr Microstruct Anal 1:217–223
7. Huang Q, et al. (2018) Influence of Si addition on the carbon partitioning process in martensitic-austenitic stainless steels. In: IOP conference series: materials science and engineering. IOP Publishing
8. Kim B, Sietsma J, Santofimia MJ (2017) The role of silicon in carbon partitioning processes in martensite/austenite microstructures. Mater Des 127:336–345
9. Mola J et al (2017) Tempering of martensite and subsequent redistribution of Cr, Mn, Ni, Mo, and Si between cementite and martensite studied by magnetic measurements. Metall Mater Trans A 48:5805–5812
10. Samanta S et al (2013) Development of multiphase microstructure with bainite, martensite, and retained austenite in a co-containing steel through quenching and partitioning (Q&P) treatment. Metall Mater Trans A 44:5653–5664
11. Kozeschnik E, Bhadeshia H (2008) Influence of silicon on cementite precipitation in steels. Mater Sci Technol 24(3):343–347
12. Zhou J et al (2020) Strengthening a fine-grained low activation martensitic steel by nanosized carbides. Mater Sci Eng A 769:138471
13. Gladman T (1966) On the theory of the effect of precipitate particles on grain growth in metals. Proc R Soc Lond Ser A Math Phys Sci 294(1438):298–309
14. Girault E et al (2001) Comparison of the effects of silicon and aluminium on the tensile behaviour of multiphase TRIP-assisted steels. Scrip Mater 44(6):885–892
15. Wu J et al (2003) Austenite formation and decomposition. Mater Sci Technol 19:291–309
16. Owen W (1954) The effect of silicon on the kinetics of tempering. Trans Am Soc Metals 46:812–829
17. Barnard S et al (1981) Advances in the physical metallurgy and applications of steels. Metals Soc Lond 33:32
18. Lashgari H et al (2014) Composition dependence of the microstructure and soft magnetic properties of Fe-based amorphous/nanocrystalline alloys: a review study. J Non-Cryst Solids 391:61–82
19. Pepperhoff W, Acet M (2001) Constitution and magnetism of iron and its alloys. Springer, New York

20. Anya C, Baker T (1989) The effect of silicon on the grain size and the tensile properties of low carbon steels. Mater Sci Eng A 118:197–206
21. Chen S, Rong L (2015) Effect of silicon on the microstructure and mechanical properties of reduced activation ferritic/martensitic steel. J Nucl Mater 459:13–19
22. Herzer G (1997) Nanocrystalline soft magnetic alloys. Handbook Magn Mater 10:415–462

Estimation Prediction of CaO–SiO_2–Fe_xO Slag System Based on Microstructure Analysis

Rui Zhang, Ting-an Zhang, Zhihe Dou, and Mao Chen

Abstract Understanding the transformation mechanism of the viscosity of the CaO–SiO_2–Fe_xO slag is of great significance for improving the quality of liquid steel and ensuring the smooth smelting process. In this study, the viscosity values of the CaO–SiO_2–Fe_xO system at different temperatures were measured, and its melt structure was analyzed by Raman spectroscopy. The microstructure analysis of the viscosity was then given from the perspective of melt structure. On this basis, a viscosity prediction model that depends on the concentration of oxygen bonds was established using the molar fractions of oxygen bonds calculated by structural analysis. By comparing the measured and calculated values of viscosity, it was found that the deviation of all data was within 0.1 Pa s, showing the higher accuracy and stability of the current model.

Keywords Model · Viscosity · Melt · Structure · Converter

Introduction

The standardization of converter steelmaking operations is one of the effective ways to reduce converter energy consumption. A reasonable slagging route is a key factor in formulating converter steelmaking regulations, which helps to avoid slag splashing, ensure smooth smelting, and improve the quality of liquid steel. The viscosity of molten slag, as a key physical parameter in the steelmaking process, is closely related to the formation and removal of inclusions in liquid steel, foaming operation of

R. Zhang (✉) · T. Zhang · Z. Dou
Key Laboratory for Ecological Metallurgy of Multimetallic Ores (Ministry of Education), Shenyang 110819, Liaoning, China
e-mail: zhangrneu@163.com

School of Metallurgy, Northeastern University, Shenyang 110819, Liaoning, China

M. Chen
State Key Laboratory of Vanadium and Titanium Resources Comprehensive Utilization, Panzhihua 617000, Sichuan, China

Z. Peng et al. (eds.), *Characterization of Minerals, Metals, and Materials 2024*, The Minerals, Metals & Materials Series, https://doi.org/10.1007/978-3-031-50304-7_2

molten slag, emulsification between liquid steel and molten slag, heat transfer and mass transfer among molten slag, liquid steel, and gas, etc. Accurate viscosity can provide powerful guidance for the design and optimization of slag composition. However, due to the complexity and vulnerability of the viscosity apparatus, and the difficulty and time consumption of high-temperature tests, numerous mathematical models of viscosity have attracted widespread attention in recent years.

The slag viscosity is very sensitive to its melt structure, and hence the prediction model of viscosity must take melt structure into account. With a deep understanding of slag, the bridging oxygen structure theory has been widely recognized. According to this theory, Zhang and Jahanshahi [1, 2] thought that viscosity of molten slag was related to the concentrations of bridging oxygen, non-bridging and free oxygen in melt, and utilized the Cell model formula to obtain various concentrations of oxygen bonds and derived a structure-related viscosity model. Subsequently, Nakamoto et al. [3] clarified the physical significance of the parameters in the activation energy equation, and deduced the viscosity model suitable for the $CaO–SiO_2–Al_2O_3$ system. It was noted that the values of oxygen bonds used in the model were indirectly obtained through the fitting formula of refractive index of glass or thermodynamic model.

In this paper, the typical steelmaking slag of the $CaO–SiO_2–Fe_xO$ system is focused on due to its significance in the process of basic oxygen steelmaking. To estimate the slag viscosity of this system, the types and the concentrations of different oxygen bonds are calculated by Raman analysis, and then the viscosity model depending on the concentration of oxygen bond is established. The calculated viscosities via the new model are compared with the experimental data to verify the accuracy and stability of this model.

Experimental Method

Preparation of Glassy Slags

A series of samples of the $CaO–SiO_2–Fe_xO$ system were determined according to the compositions of steelmaking slags. The samples were prepared with analytical reagent grade CaO, SiO_2, and $FeC_2O_4·2H_2O$ powders. FeO can be obtained from the decomposition of $FeC_2O_4·2H_2O$ when the temperature exceeds 850 °C. The well-mixed chemical reagents were placed in the Pt crucibles and were heated to 1600 °C and held at this temperature for one hour using the high-temperature quenching furnace. High-purity Ar gas was admitted in the furnace tube at a flow rate of 0.8 L min^{-1}. After the holding stage was completed, Pt crucibles were quickly quenched in ice water to obtain glassy slags. All the samples were ground to < 60 mesh for the following X-ray diffraction (XRD) and X-ray fluoroscopy (XRF). The XRD patterns of all the samples presented a broad peak around the diffraction angle 2θ of 30°, reflecting that the samples were amorphous and were homogeneous liquids

at 1600 °C. The analyzed values of experimental slags exhibited a good agreement between analyzed values and nominal values for CaO and SiO_2, and the Fe^{2+}/Fe^{3+} ratio is also maintained within 0.55 ~ 0.75.

Viscosity Measurement

The viscosities of experimental slags were analyzed by the rotating cylinder method. About 140 g of sample was put into the graphite crucible. The sample was heated to 1600 °C under an Ar atmosphere and kept for 30 min to fully melt. The Mo spindle was slowly lowered into the melt until submerged by the slag, and the speed of Mo spindle was 200 rpm. For continuous viscosity measurements, the furnace temperature decreased linearly at 3 °C min^{-1}. The viscosity and temperature were recorded continuously at intervals of 0.1 °C.

Results and Discussion

Model Establishment

The silicate melt is considered to be a network structure formed by [SiO_4]-tetrahedrons, and its schematic diagram is shown in Fig. 1. The movement of "cutting-off point" can cause the viscous flow of melt, and the increase in the number of non-bridging oxygen (NBO) and free oxygen (FO) can lead to a decrease in the activation energy of the viscous flow. Therefore, it is important to establish a viscosity prediction model from the perspective of oxygen bond. Based on the above theory, Nakamoto et al. [3] derived the viscosity prediction equation applicable to the ternary CaO–SiO_2–Al_2O_3 slag system, and the expression of the model is as follows:

$$\eta = A \cdot \exp(E_\eta / RT) \tag{1}$$

$$E_\eta = \mathrm{E_v} \Big/ \left(1 + \sum_i \boldsymbol{\alpha}_i \cdot n_{(\mathrm{NBO+FO})_i} + \sum_j \boldsymbol{\alpha}_{j\,\mathrm{in\ AlO_4}} \cdot n_{\mathrm{Al\text{-}BO}_j} \right) \tag{2}$$

where A is a pre-exponential factor, E_η (J mol^{-1}) is the viscous activation energy of a silicate melt, R (8.314 J mol^{-1} K^{-1}) is a gas constant, and T (K) is the temperature of molten slag. The studies of Bockris showed that the viscous activation energy of pure SiO_2, E_v, is 5.61 × 10^5 J mol^{-1}. α is a parameter of bond strength, i denotes the CaO and Al_2O_3, j denotes Ca^{2+}, and $n_{\mathrm{Al-BO}j}$ denotes the fractions of bridging oxygen connected by j in an [AlO_4]-tetrahedron.

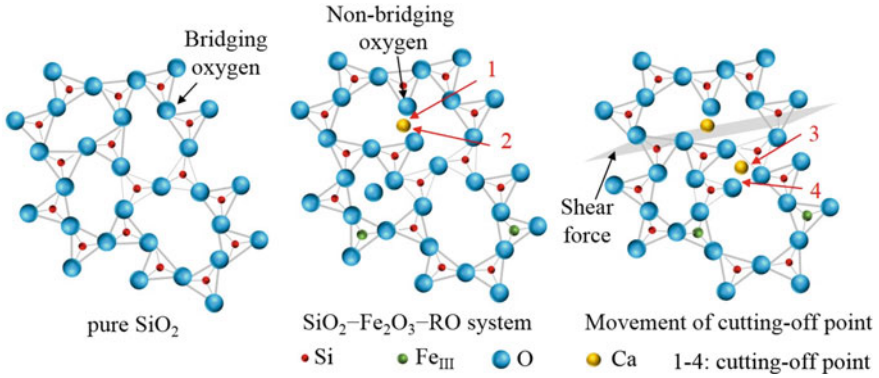

Fig. 1 Flow mechanism of silicate structure

From the previous results of melt structure [4], it is known that in the CaO–SiO_2–Fe_xO system slag, Fe_2O_3 is mainly used as a network former to form [FeO_4]-tetrahedron, and part of Fe_2O_3 is used as the network modifier to form [FeO_6]-octahedron. CaO and FeO can cut off the Si–O–Si bond and act as a charge compensator of [FeO_4]-tetrahedron. Therefore, Eq. (2) in the Nakamoto's model can be modified as follows:

$$E_{\eta} = \mathrm{E_v} \Big/ \left(1 + \sum_i \boldsymbol{\alpha}_i \cdot n_{(\mathrm{NBO+FO})_i} + \sum_j \boldsymbol{\alpha}_{j\,\mathrm{in\ AlO_4}} \cdot n_{\mathrm{Al\text{-}BO}_j} \right) \tag{3}$$

where i represents the oxides except SiO_2; j represents the modifying cation; the values of α_i, α_j are listed in Table 1.

Nakamoto et al. [3] indirectly obtained the molar fraction of oxygen bonds in the prediction model according to the fitting formula of the refractive index of glass. In the present model, the analysis of Raman spectra is used to directly calculate the concentration of oxygen bonds by Eqs. (4)–(8). Generally, NBO and FO are formed by adding oxides such as CaO, FeO, and Fe_2O_3 to pure SiO_2 melt. According to the formation mechanism, NBO + FO can be divided into $(\mathrm{NBO + FO})_{\mathrm{CaO}}$, $(\mathrm{NBO + FO})_{\mathrm{FeO}}$, and $(\mathrm{NBO + FO})_{\mathrm{Fe_2O_3}}$. The content of NBO and FO formed by different oxides can be calculated in terms of the molar ratio of oxides. Meanwhile, according to the types of modifying cations, the Fe–O–Fe bonds in [FeO_4]-tetrahedron can

Table 1 Values of α, a and b

Parameter	CaO	FeO	Fe_2O_3	Ca^{2+}	Fe^{2+}
α	2.98	3.80	1.00	1.48	3.15
a	4.5781	5.6834	9.8326	/	/
b	1.96×10^{-5}	1.94×10^{-5}	-1.92×10^{-5}	/	/

be divided into two types, Fe-O-$Fe_{Ca^{2+}}$ and Fe-O-$Fe_{Fe^{2+}}$. Then the molar fraction of bridging oxygen bonds in the [FeO_4]-tetrahedron compensated by the molar ratio of Ca^{2+} and Fe^{2+} are calculated by the following equations:

$$n_{(\mathrm{NBO+FO})} = n_{\mathrm{O}} - n_{\mathrm{Si-O-Si}} - n_{\mathrm{Fe-O-Fe}} \tag{4}$$

$$n_{\mathrm{Si-O-Si}} = 4n_{\mathrm{Q^4(Si)}} + 3n_{\mathrm{Q^3(Si)}} + 2n_{\mathrm{Q^2(Si)}} + n_{\mathrm{Q^1(Si)}} \tag{5}$$

$$n_{\mathrm{Fe-O-Fe}} \approx 2n_{\mathrm{FeO_4}} \tag{6}$$

$$n_{(\mathrm{NBO+FO})_i} = n_i \Big/ \sum n_i \cdot n_{(\mathrm{NBO+FO})} \tag{7}$$

$$n_{\mathrm{Fe-O-Fe}_j} = n_j \Big/ \sum n_j \cdot n_{\mathrm{Fe-O-Fe}} \tag{8}$$

where the molar fraction of Fe–O–Fe bond is assumed to be twice that of the tetrahedron due to the unknown types of [FeO_4]-tetrahedrons.

Due to the limited melt structure data measured in the present experiment, the Lagrange interpolation method is used to continuously interpolate the structure data, and the obtained data is called the "oxygen bond database". The oxygen bond content corresponding to different compositions in the database can be substituted into the viscosity prediction model by MATLAB software.

Model Verification

The present viscosity prediction model is evaluated via two evaluation indicators, average deviation (Δ) and root-mean-square-error (RMSE). The calculation formulas are shown in Eqs. (9) and (10). Average deviation reflects the model and root-mean-square-error reflects the model stability.

$$\Delta = 1/N \times \sum_{k=1}^{N} \left|\eta_{k,\mathrm{cal.}} - \eta_{k,\mathrm{exp.}}\right| \Big/ \eta_{k,\mathrm{exp}} \tag{9}$$

$$\mathrm{RMSE} = \sqrt{\sum_{k=1}^{N} \left(\eta_{k,\mathrm{cal.}} - \eta_{k,\mathrm{exp.}}\right)^2 / N} \tag{10}$$

where $\eta_{k,\,\mathrm{cal.}}$ represents the calculated viscosity of the kth experimental slag; $\eta_{k,\,\mathrm{exp.}}$ represents the measured viscosity of the kth experimental slag; N is the number of viscosity tests.

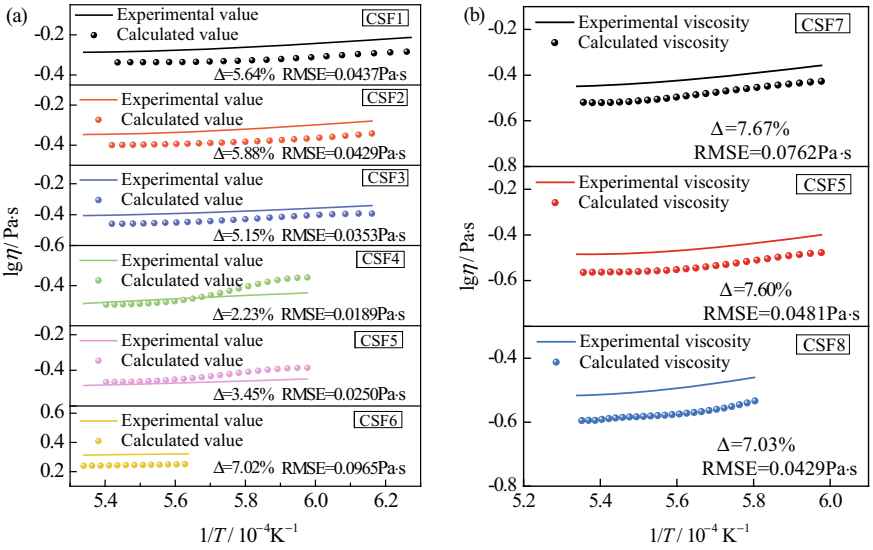

Fig. 2 Comparison of calculated and experimental viscosity curves of the CaO–SiO_2–Fe_xO slag systems. **a** Different CaO/Fe_xO. **b** Different CaO/SiO_2

Figure 2 shows the measured and predicted viscosity curves of the CaO–SiO_2–Fe_xO system slag. In Fig. 2a, the average deviations of experimental slags are respectively 5.64, 5.88, 5.15, 2.23, 3.45, and 7.02% and the root-mean-square-error is 0.0437, 0.0429, 0.0353, 0.0189, 0.0250, and 0.0965 Pa s, respectively. In Fig. 2b, the average deviations of experimental slags are 7.67, 7.60, and 7.03%, respectively, and the root-mean-square-errors are 0.0762, 0.0481, and 0.0429 Pa s, respectively. The present model predicts that the overall average deviation and root-mean-square-error are 5.75% and 0.0534 Pa s, respectively.

For the CaO–SiO_2–Fe_xO slag system, some scholars have proposed to use Urbain model, Nakamoto model, and QVC model to estimate the slag viscosity [3, 5, 6]. In order to further verify the accuracy of the present model, the calculated viscosity values of experimental slags using these models are compared with the measured and collected viscosities. The comparison results are shown in Fig. 3. The present model has a smaller average deviation and root-mean-square-error, showing higher accuracy and stability.

Conclusions

In this study, a structure-related viscosity prediction model depending on oxygen bond was developed for the CaO–SiO_2–Fe_xO system in order to accurately estimate the viscosities of steelmaking slags in the process of oxygen basic steelmaking. In

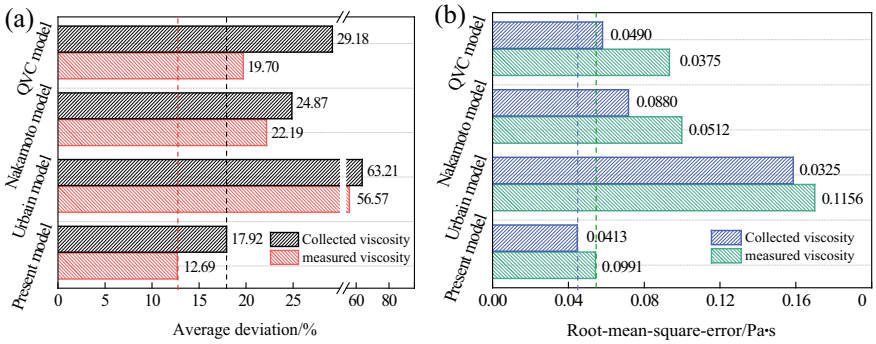

Fig. 3 Comparison of the CaO–SiO_2–Fe_xO slag systems by various models. **a** Average deviation. **b** Root-mean-square-error

melt, bridging oxygen bonds except Si–O–Si bonds can be classified into the Fe–O–Fe bonds modified by Ca^{2+} and Fe^{2+}. Non-bridging oxygen and free oxygen bonds can be also classified into the non-bridging oxygen and free bonds cut by CaO, FeO, and Fe_2O_3 due to the addition of oxides into pure SiO_2 melt. According to the deconvoluted results, the content of each structural unit is obtained, and the mole fraction of oxygen bonds is calculated in terms of structural units. Meanwhile, the database about different oxygen bonds has been established. The average deviation and root-mean-square-error of the new model were 5.75% and 0.0534 N m^{-1}, indicating that this model had higher accuracy and stability. Through the comparison with other models, the new model was more adequate to predict the viscosity of the ternary iron-containing system.

Acknowledgements This work was supported by the National Natural Science Foundation of China [Grant Numbers 52304323], the Open Fund of State Key Laboratory of Vanadium and Titanium Resources Comprehensive Utilization (Grand Number 2023P4FZG07A), the Fundamental Research Funds for the Central Universities (Grant Number N232405-06), and Northeast University Postdoctoral Foundation [Grant Number 20230309].

References

1. Zhang L, Jahanshahi S (1998) Review and modeling of viscosity of silicate melts: Part I. Viscosity of binary and ternary silicates containing CaO, MgO, and MnO. Metall Mater Trans B 29(1):177–186
2. Zhang L, Jahanshahi S (1998) Review and modeling of viscosity of silicate melts: Part II. Viscosity of melts containing iron oxide in the CaO–MgO–MnO–FeO–Fe_2O_3–SiO_2 system. Metall Mater Trans B 29(1):187–195
3. Nakamoto M, Miyabayashi Y, Holappa L (2007) A model for estimating viscosities of aluminosilicate melts containing alkali oxides. ISIJ Int 47(10):1409–1415
4. Zhang R, Min Y, Wang Y (2020) Structural evolution of molten slag during the early stage of basic oxygen steelmaking. ISIJ Int 60(2):212–219

5. Kondratiev A, Jak E (2005) A quasi-chemical viscosity model for fully liquid slags in the Al_2O_3–CaO–'FeO'–SiO_2 system. Metall Mater Trans B 36(5):623–638
6. Urbain G (1987) Viscosity estimation of slags. Steel Res 58(3):111–116

Optimization of Energy Efficiency of Electric Arc Furnace Steelmaking

A. Xu, R. Zhu, G. Wei, H. Zhang, and R. Zhao

Abstract To enhance the production efficiency of electric arc furnaces, conserve energy, and reduce consumption, a study was conducted to analyze the energy efficiency of electric arc furnace steelmaking. Through this analysis, an energy efficiency evaluation technology for electric arc furnace steelmaking was developed. The application of this technology enables the optimization of oxygen supply and power supply systems, leading to improved energy efficiency, reduced power supply time, shortened smelting cycles, and achieving cost reduction and efficiency enhancement in smelting processes. An industrial application test was conducted in a steel mill, comparing the results with the original working conditions. The outcomes demonstrated significant improvements. Under normal production conditions, the average values for various parameters are as follows: power supply time reduced by 2.12 min, smelting cycle shortened by 1.8 min, power consumption decreased by 37.3 kWh/t, power reduced by 0.4 MW, slag composition improved, metal recovery rate enhanced, and improvements in both energy efficiency and chemical energy efficiency were achieved.

Keywords Electric arc furnace steelmaking · Energy efficiency optimization · Smelting cycle · Energy saving

Introduction

The iron and steel industry stands as a vital pillar of China's national economy, playing a pivotal role in the country's industrialization and urbanization process. However, it is important to note that the steel industry is a high-energy, high-emission sector [1]. Among the prominent steelmaking methods globally, electric arc furnace steelmaking stands out due to its characteristics of a concise process, low energy

A. Xu · R. Zhu (✉) · G. Wei · H. Zhang · R. Zhao
Institute for Carbon Neutrality, University of Science and Technology Beijing, Beijing 100083, China
e-mail: zhurong@163.com

Z. Peng et al. (eds.), *Characterization of Minerals, Metals, and Materials 2024*, The Minerals, Metals & Materials Series, https://doi.org/10.1007/978-3-031-50304-7_3

consumption, and environmentally friendly practices. In the face of the dual challenges presented by the "double control" of total energy consumption and intensity, as well as the focus on carbon emissions reduction [2], major steel producers worldwide are increasingly prioritizing the short-process production technique of electric furnaces, utilizing scrap as the primary raw material [3, 4].

In recent years, the electric arc furnace steelmaking technology has been geared towards the principles of "high efficiency, low consumption, green, and intelligent" development. Steel mills have been actively pursuing high-efficiency and energy-saving technologies [5–7]. Regarding research methodologies concerning energy consumption and efficiency, Wu et al. [8] proposed the adoption of a systematic analysis approach to investigate energy issues within iron and steel enterprises. This method involves linking the energy production and usage of individual equipment, production processes, and entire facilities, enabling a comprehensive analysis of the entire energy consumption system. Elbling [9] emphasized that addressing energy challenges in iron and steel enterprises necessitates the utilization of energy system models to achieve optimal energy distribution.

Zhang et al. [10–12] employed the first and second laws of thermodynamics to establish methods for analyzing energy efficiency and models for waste heat and energy analysis. Through these models, they calculated the impact of various waste heat and energy technologies, process losses, and efficiency, thereby identifying the potential for energy conservation and emission reduction in the iron and steel industry. The requirements for high-efficiency production in electric arc furnace steelmaking have led to continuous increases in furnace capacity and the ongoing reduction of smelting cycles. This trend has heightened the demand for energy input intensity.

To meet these demands, enhancements are necessary not only in increasing main transformer capacity and improving electrical operation proficiency but also in augmenting the supply and recovery of other forms of chemical and physical energy [13]. The progress in science and technology within the realm of modern electric arc furnace steelmaking necessitates not only bolstering the energy supply but also enhancing energy utilization rates. This comprehensive approach is vital for improving production efficiency and curbing energy consumption effectively.

The article introduces a technique for energy efficiency analysis based on a relatively precise analysis of the supply of electrical equipment on the energy side. To validate this approach, an energy efficiency analysis and process optimization were conducted on a 60 ton electric arc furnace in a steel plant in China, operating under its existing conditions. After studying and analyzing the equipment condition, production data, and operation system of the 60 ton electric arc furnace, the optimized power supply and oxygen supply system was proposed, and the energy efficiency was improved by optimizing operation and the power supply time was shortened. Thus, the smelting effect of shortening the smelting cycle and increasing production capacity can be achieved.

Arc Furnace Main Equipment Process Parameters

The steel mill operates a 60 ton Consteel arc furnace with a nominal capacity of 60 tons. The average steel output is 65 tons, and the maximum steel output reaches 70 tons. The furnace is fed continuously with all scrap steel. The main transformer of the 60 ton Consteel EAF has a rated capacity of 45 MVA. The furnace is equipped with three main furnace walls KT oxygen guns, with the maximum flow rate of the main oxygen gun being 2500 m^3/h. Additionally, there is one water-cooled furnace door oxygen gun with a maximum flow rate of 3000 m^3/h.

Energy Efficiency Analysis Technology of Electric Arc Furnace

Based on the principles of mass conservation, energy conservation, and the electric arc furnace steelmaking process, a modern thermodynamic model for electric arc furnace steelmaking has been developed. This model incorporates specific conditions of electric arc furnace steelmaking and calculates material and energy balances by considering the composition of steelmaking raw materials. By determining the total energy required for smelting a batch of steel under the condition of using 100% scrap steel, including the chemical heat of the materials and auxiliary energy sources such as oxygen blowing, the model also calculates how much additional electrical energy supply is needed to ensure the smooth progress of the smelting process. The material balance model and the energy balance model for electric arc furnace steelmaking are illustrated in Figs. 1 and 2.

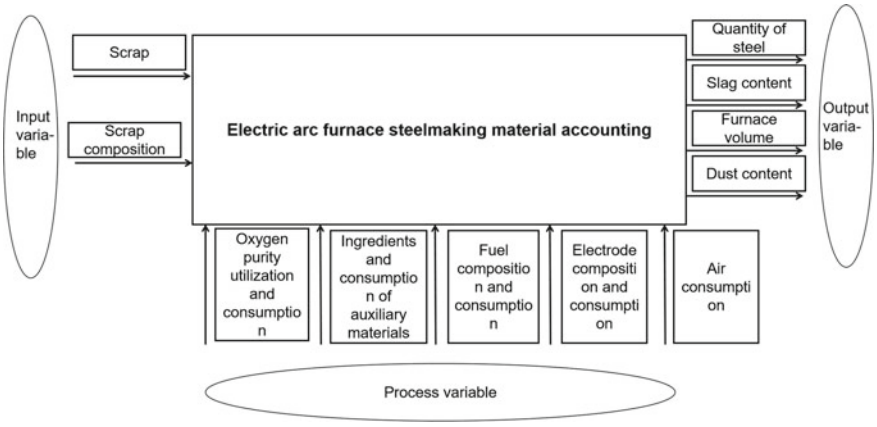

Fig. 1 Material balance model of electric arc furnace steelmaking

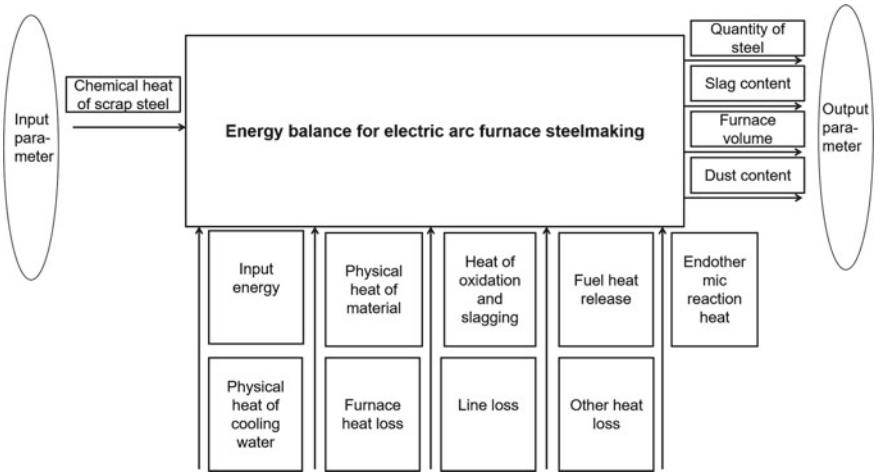

Fig. 2 Energy balance model of electric arc furnace steelmaking

On the basis of material balance and energy balance of electric arc furnace, the following energy efficiency of smelting furnace is calculated and analyzed.

The total efficiency of electric arc furnace η_Z refers to the energy efficiency of the whole electric arc furnace, excluding the circuit system. The total efficiency can be expressed using Formula 1.

$$\eta_Z = \frac{W_{GEZ}}{W_{SR} - W_{DS}} \tag{1}$$

where: W_{GEZ} represents the sum of heat taken away by liquid steel and slag, and heat absorbed by decomposition reactions in the furnace, measured in kilowatt-hours (kWh); W_{SR} represents the heat input into the furnace, measured in kilowatt-hours (kWh); W_{DS} represents transformer line loss and arc heat loss, measured in kilowatt-hours (kWh).

Energy efficiency η_{EL} is the proportion of the electric energy used for melting molten steel, steel slag, and heating in the total electric energy provided by the power supply line. Energy efficiency can be expressed using Formula 2.

$$\eta_{EL} = \eta_{SEC.C} \times \eta_{ARC} \tag{2}$$

where: $\eta_{SEC.C}$ represents the power efficiency coefficient of the secondary circuit, encompassing the transformer. This coefficient quantifies the electric energy consumed by the arc after accounting for the electric energy lost in the secondary circuit; η_{ARC} stands for the thermal efficiency coefficient of the arc. This coefficient characterizes the efficiency of the heat transfer process from the arc to the scrap steel or liquid metal.

Chemical energy efficiency η_{CH} is the ratio of the chemical energy used to melt molten steel, steel slag, and heating to the total energy provided by the reaction of each element in the electric arc furnace.

$$\eta_{CH} = \frac{W_{GEZ} - W_{EL} \times \eta_{EL}}{W_{CH}} \tag{3}$$

Formula: W_{EL} represents the total electrical energy input in kilowatt-hours (kWh); W_{CH} represents the theoretical supply of chemical heat in the furnace in kilowatt-hours (kWh).

Achieving higher energy efficiency in the smelting process is crucial, as it leads to reduced energy loss per unit time, shorter smelting cycles, and increased production capacity under the same energy consumption. The energy utilization and efficiency during the smelting period can be obtained through the established model. By combining these results with power supply parameters and the current operational processes, the current electric-oxygen matching degree can be analyzed. Finally, improving energy efficiency, reducing energy consumption, and increasing production capacity by optimizing the power supply and oxygen supply system. The specific concepts and steps of the energy efficiency analysis technology are shown in Fig. 3.

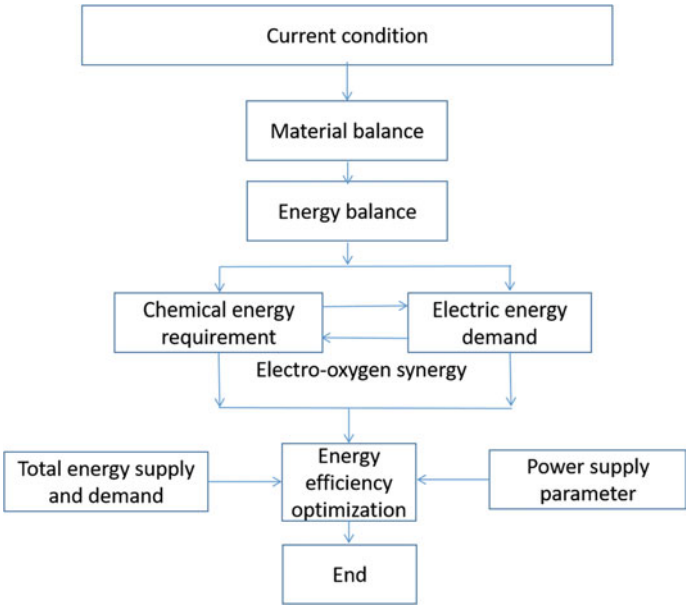

Fig. 3 Flow chart of energy efficiency analysis technology

Model Verification and Process Optimization

The production data from a 60 ton electric arc furnace in this steel plant serves as the benchmark calculation. The data is sourced from production log records predating the furnace operation. After excluding 36 instances where the furnace remained inactive for extended periods due to issues like record loss, failures, or thermal shutdowns, the statistically effective furnace count stands at 331. The production indicators are outlined below, as presented in Table 1.

Utilizing the aforementioned production data, material balance and energy balance models for scrap steel were formulated and subsequently validated. Using the existing production status as the initial condition, an energy balance analysis of the electric arc furnace was conducted. The outcomes of this analysis are depicted in Fig. 4.

The model assumes a furnace charge temperature of 250 °C, oxygen purity of 93%, oxygen utilization efficiency of 90%, and a 40% burn-off rate for carbon powder. The energy accounting calculation error of this model is 0.87%, which falls within an acceptable range, allowing for an accurate description of the energy utilization status of the electric arc furnace. Taking into account the factors of the materials and energy utilization rates mentioned above, and considering the current process operational procedures and energy input levels, an analysis has been conducted, leading to optimizations in the existing process conditions.

In the electrification process of smelting, due to the special feeding system of consteel furnace, the electrification time can be divided into two periods, namely, the melting period and the melting period. The main task of the melting period is to melt the scrap steel, which is characterized by the coexistence of solid charge and liquid charge, large arc fluctuation, as the average active power and power factors are lower, and the proportion of time is long, and the proportion of power consumption is high. The main task of the melting period is decarbonization and heating, which is characterized by the basic melting of the charge, the arc fluctuation is small at this time, and the arc can work stably because of the submerged arc action of the foam slag, the average active power is high, and the power factor is high.

In the smelting electrification process, the unique feeding system of the Consteel furnace divides the electrification time into two distinct periods: the melting period and the decarbonization and heating period. During the melting period, the primary objective is to melt the scrap steel. The notable characteristic of this period is the coexistence of solid and liquid materials in the furnace. The electric arc fluctuates significantly, resulting in lower average active power and power factor. This phase is characterized by a longer duration and higher energy consumption due to the presence of both solid and liquid materials in the furnace.

Conversely, the main focus of the decarbonization and heating period is to facilitate decarbonization and heating of the charge. At this stage, the furnace charge is mostly molten. The electric arc fluctuates less because of the stabilizing effect of foam slag, allowing the arc to work steadily. During this period, the average active power and power factor are higher due to the stable nature of the electric arc.

Table 1 Production index of 60 ton electric arc furnace in a steel plant

Indicators	Furnace count/(furnace)	Smelting cycle/(min)	Power supply time/(min)	Tapping temperature/(°C)	Electricity consumption/(kW h/t)	Oxygen consumption/(Nm^3/t)	Carbon powder consumption/(kg/t)	Steel tapping quantity/(*t*)	Average power/(MW)
	331	54.10	43.82	1617.1	431.7	38.4	10.01	65.0	38.1

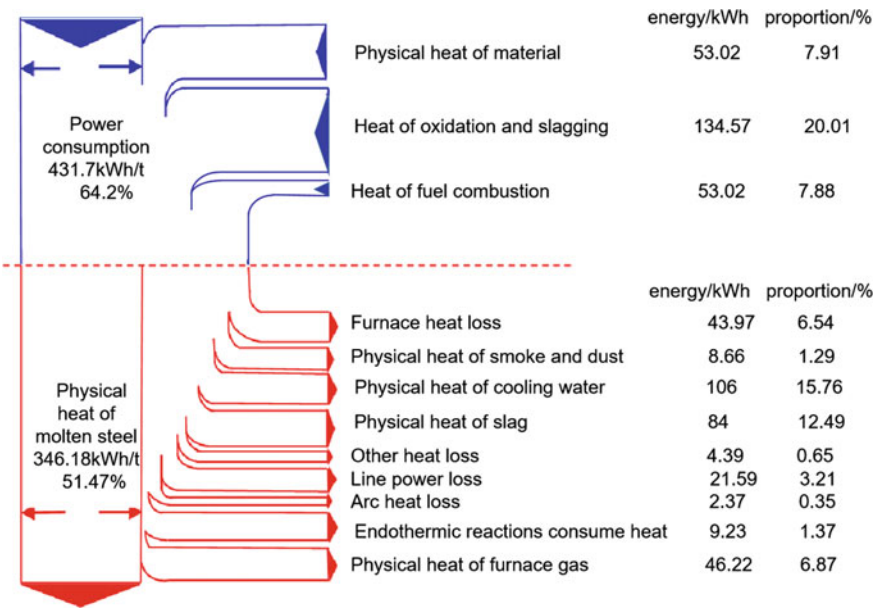

Fig. 4 Energy balance diagram of typical furnace under current condition

Based on the observations from the on-site smelting operations, it has been noted that the current usage of carbon powder is insufficient. There is a possibility to increase the quantities of both carbon powder and oxygen, which would augment the chemical energy and reduce electricity consumption. After determining the tasks for each stage of the smelting process, considering the power supply capacities at various levels, oxygen lance capacities, energy efficiency calculations, and optimization objectives, an optimized power supply and oxygen supply system has been devised, as illustrated in Fig. 5.

Process Practice and Analysis

After comparing partial data from the original process and the optimized process, and excluding abnormal data (such as prolonged non-electric periods caused by faults or operational pauses), an analysis was conducted. Data from 198 furnace count under the new process were used, excluding 10 furnace count with missing smelting time data and 9 furnace count with power outages lasting more than 20 min before electrification. Additionally, 20 furnace count were excluded due to mid-process power interruptions exceeding 20 min. This left a total of 159 furnace count for analysis. A comparison of production indicators before and after process optimization is detailed in Table 2.

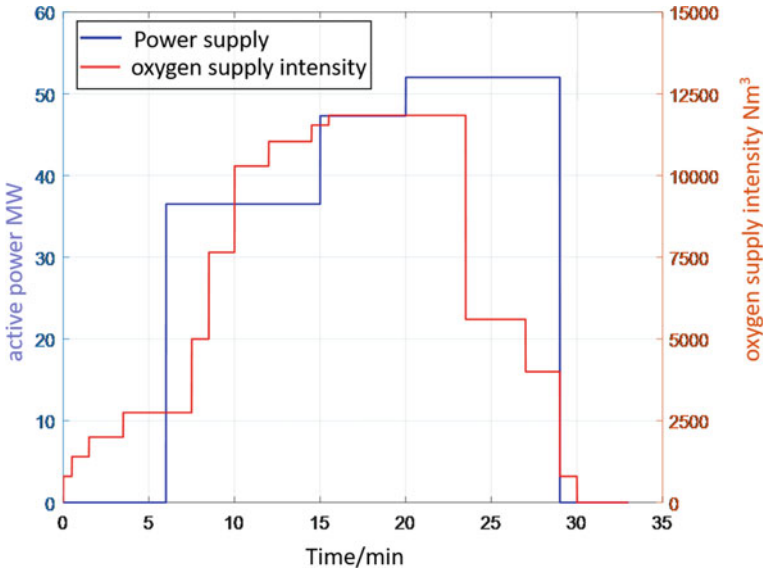

Fig. 5 Optimized power supply and oxygen supply system

Table 2 Comparison of production indicators

Indicators	Original technology	After process optimization
Furnace count/(furnace)	331	198
Average power consumption /(kWh t^{-1})	431.7	394.4
Average oxygen consumption /(m^3 t^{-1})	38.4	38
Average power supply time /(min)	43.82	41.7
Average smelting cycle /(min)	54.1	52.3
Average carbon powder consumption/(kg/t)	10.01	15.5
Average power/(MW)	38.1	37.7

Following the process optimization, the average power consumption was reduced by 37.3 kWh/t compared to the original smelting conditions, all while ensuring production stability. Oxygen consumption remained relatively constant, with a minor decrease of 0.4 m^3/t. The average power supply time saw a reduction of 2.12 min, and the average smelting cycle was shortened by 1.8 min, with non-energizing time remaining largely unchanged. There was a slight increase in the average carbon powder consumption by 5.49 kg, and the average power was reduced by 0.4 MW.

Table 3 Statistics of average slagging amount of some furnace times

Indicators	Slag weight/(t)
Original technology	12.54
After process optimization	11.64

Table 4 The result of composition test of partial furnace slag

Type	TFe/(%)	SiO_2/(%)	CaO/(%)	MgO/(%)	Al_2O_3/(%)	MnO/(%)	P_2O_5/(%)	S/(%)
Original technology	28.300	11.118	32.750	3.627	4.388	3.759	0.663	0.124
	32.802	10.650	25.986	4.246	4.050	3.861	0.502	0.170
After process optimization	24.523	12.956	31.185	5.612	4.196	5.592	0.682	0.153
	18.473	17.784	32.108	6.703	6.126	6.803	0.631	0.197

Slag Analysis

In the original process, the slag had a high iron content, coupled with a large amount of slag tapping, leading to high iron losses in the slag and reducing the metal recovery rate during steelmaking. Comparing the slag composition before and after the modification, it is evident that the iron content in the slag has decreased, leading to an improvement in the metal recovery rate (Tables 3 and 4).

Energy Efficiency

The energy efficiency of typical operation furnace after process optimization was analyzed. The total energy balance after optimization is shown in Fig. 6, and the comparison of energy efficiency before and after process application is shown in Table 5.

Compared with the original process, the thermal efficiency of electric energy is increased by 0.12%, the thermal efficiency of chemical energy is increased by 0.95%, and the total efficiency of EAF is increased by 1.77%. The optimized process mainly increases the use of carbon powder, helps to make foam slag, reduces arc phenomenon, reduces thermal radiation loss, and thus improves the thermal efficiency of electric energy;

Moreover, the increase in carbon powder intensifies the carbon–oxygen reactions, enhancing the chemical energy efficiency and reducing electricity consumption. The optimized power supply and oxygen supply system now adequately meet

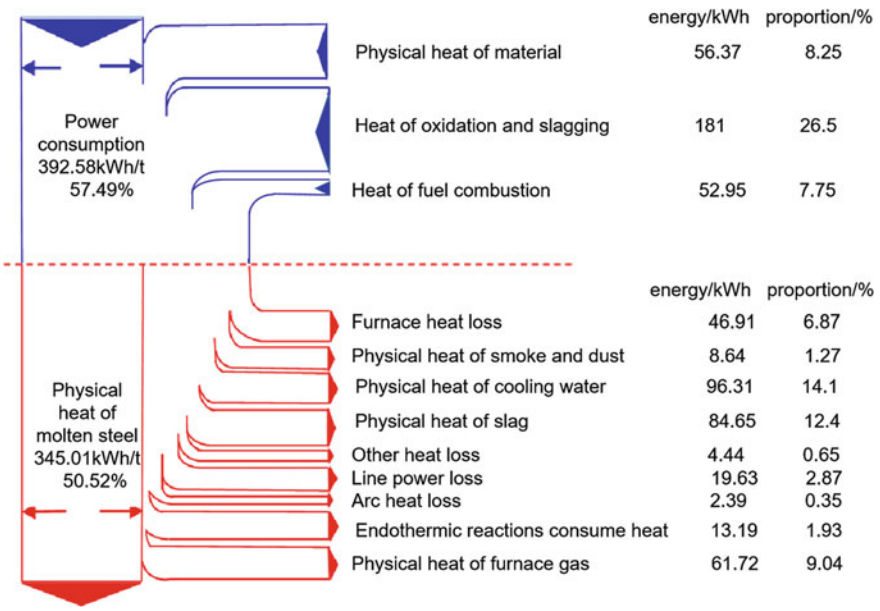

Fig. 6 Total energy balance diagram of typical heat after process optimization

Table 5 Comparison of energy efficiency for typical operation heats before and after process optimization

Indicators	Original technology	After process optimization
Electric energy thermal efficiency/(%)	67.16	67.28
Chemical energy thermal efficiency/(%)	70.3	71.25
Total efficiency of electric arc furnace/(%)	55.73	57.5

the electrical and oxygen requirements during smelting. This allows for standardization of on-site smelting operations, thereby reducing the electrification time, shortening the smelting cycle, and ultimately achieving metallurgical results that increase production capacity and save energy.

Conclusion

Based on real electric arc furnace steelmaking production, we have proposed a method for energy efficiency analysis and optimization. By optimizing the power supply of oxygen operation system, we have achieved effective coordination between electricity and oxygen supply. This optimization has not only optimized energy efficiency but also resulted in energy savings and cost reduction. The optimized process

has significantly improved production metrics: average smelting power consumption decreased by 37.3 kWh/t, average power supply time reduced by 2.12 min, average smelting cycle shortened by 1.8 min, and average power decreased by 0.4 MW. Following process optimization, the energy efficiency of typical operation furnaces has improved, with a 0.12% increase in electric energy thermal efficiency, a 0.95% boost in chemical energy thermal efficiency, and a substantial 1.77% increase in the total efficiency of electric arc furnaces.

References

1. Lu ZW, Cai JJ, Du T (2015) The macro-control on energy consumption, material consumption and waste emission of steel industry. Eng Sci 17(05):126–132
2. Shangguan FQ, Liu ZD, Yin RY (2021) Study on implementation path of "carbon peak" and "carbon neutrality" in steel industry in China. China Metall 31(9):15
3. Zhou TS (2020) Brief analysis on the development trend of short process steelmaking in electric furnace in China. China Steel 8:55
4. Duan WP, Yang SF, Li JS (2021) Development of rapid melting technology for steel scrap in modern electric arc furnace of China. China Metall 31(9):78
5. Memoli F, Grasselli A, Giavani C (2010) Consteel© EAF and conventional EAF: a comparison in maintenance practices. Metall Ital 7–8:9–13
6. Jurgis S (2006) Environmental process control: strategies and implementation. Bioautomation 4(1):30–40
7. Jiang ZH, Yao CL, Zhu HC (2020) Technology development trend in electric arc furnace steelmaking. Steel 55(07):1–12
8. Wu RH, Jung-Hsiang Y, Chen CY (1989) Energy analysis of an integrated steel mill: a process modeling approach. Energy 14(12):831–838
9. Elbling P (1975) Energy management systems metal industry perspective. In: Energy use and conservation in the metal industry. AIME Annual Meeting, New York
10. Zhang Q, Xu J, Zhao X (2018) Energy and exerge analyses of an integrated iron and steelmaking process. Int J Exergy 26(4):454
11. Zhang Q, Zhao X, Lu H (2017) Waste energy recovery and energy efficiency improvement in China's iron and steel industry. Appl Energy 191:502
12. Zhang Q, Xu J, Wang Y (2018) Comprehensive assessment of energy conservation and CO_2 emission smitigation in China's iron and steel industry based on dynamic material flows. Appl Energy 209:251
13. Schumacher K, Sands RD (2007) Where are the industrial technologies in energy-economy models? An innovative CGE approach for steel production in Germany. Energy Econ 29(4):799–825

Part II
Advanced Characterization Methods II

Numerical Multi-field Coupling Simulation of Multiple Slab Stacks Heated by Natural Gas Combustion in a Trolley Furnace

Bo Liu, Dong Yue, Jiulin Tang, and Liangying Wen

Abstract A multi-field coupling numerical simulation calculates the natural gas flow, combustion, and gas–solid heat transfer processes in a trolley furnace using a computational fluid dynamics (CFD) method, coupled with a turbulence model (Realizable k-ε model), a combustion model (EDC), and a radiation model (DO). This work has investigated the characteristics of components, temperature, and velocity along the axial course of a high-speed burner burning natural gas. The flow field and temperature distribution of the combustion flue gas in a trolley-type heating furnace are analyzed. The surface temperature distribution and its internal temperature deviation of a three-slab stack in a trolley furnace are studied and the heating uniformity of the slabs is evaluated.

Keywords Trolley furnace · Multi-field coupling numerical simulation · Combustion · Heat transfer

Introduction

Natural gas combustion is widely used as a heat source in a trolley-type furnace to heat stacked slabs or large workpieces in metallurgical, mechanical, chemical, and shipbuilding industries. The computational fluid dynamics (CFD) method is used to establish a simulation and calculation model with multi-field coupling of flow, combustion, and heat exchange [2, 3], and it is crucial to analyze the component concentration change, flow, heat transfer, and temperature distribution of the high-temperature flue gas generated by the natural gas combustion reaction process through numerical simulation for the regulation of the heating quality of the workpieces [1–3].

B. Liu · D. Yue · L. Wen (✉)
School of Materials Science and Engineering, Chongqing University, Chongqing 400044, China
e-mail: cquwen@cqu.edu.cn

J. Tang
Dongfang Electric Group Dongfang Boiler Co., Ltd. Equipment Department, Zigong 643000, China

Z. Peng et al. (eds.), *Characterization of Minerals, Metals, and Materials 2024*, The Minerals, Metals & Materials Series, https://doi.org/10.1007/978-3-031-50304-7_4

Oh et al. [4] used natural gas, air, and a separate oxygen inlet to the combustion chamber for numerical simulation and experimental study of the heating furnace temperature rising trend with the increase in oxygen molar concentration of the changing law; Prieler et al. [5] used numerical simulation methods, predicted the transient heating process temperature change of billets in industrial step heating furnace; Han et al. [6–9] used vortex dissipative combustion model simulation radiative heat transfer and billet heating characteristics in a non-steady state heating furnace, predicting the temperature distribution and thermal efficiency change rule in the furnace; Mayr et al. [10] proposed a semi-industrial gas-fired furnace combustion model that can be quickly calculated, which greatly reduced the calculation time compared with the simulation of the Eddy-Dissipation Model (EDM). Lewandowski et al. [11] adjusted some parameters to more accurately describe the EDC model; Wang et al. [12] examined the effect of burner position on the heating efficiency in the furnace by means of the model developed by Han et al. [7]. The simulation of the heating situation of multiple slab stacks in a combustion natural gas heated bogie furnace is more complicated as it involves the processes of natural gas combustion reaction flow, combustion, and gas–solid conjugate heat transfer. This study is intended for the production of the actual situation, taking into account the combustion of natural gas high-speed burner to produce high-temperature flue gas in the flow of multi-slab stacked trolley furnace, high-temperature radiation heat exchange process coupling, the study of high-speed burner axial along the course of the high-temperature flue gas of the changes in the components. Studied the flow field, and temperature field change law inside the cart furnace with multi-slab stacking, and analyzed the temperature offset condition on the surface and inside of the slab and the heating uniformity. Can provide a reference for optimizing the slab heating process and improving the heating quality.

Numerical Models

Turbulence Model

The flow in the trolley furnace is turbulent flow, and the turbulent kinetic energy and dissipation rate are described by the Realizable k-ε model to better predict the diffusion and flow of high-temperature flue gas in the furnace under strong turbulent motion, which can be expressed as [13]:

$$\frac{\partial k}{\partial t}+\frac{\partial (u_i k)}{\partial x_i}=\frac{\partial}{\partial x_j}\left[\left(v+\frac{v_t}{\sigma_k}\right)\frac{\partial k}{\partial x_j}\right]+\left(\frac{\partial u_i}{\partial x_j}+\frac{\partial u_j}{\partial x_i}\right)\frac{\partial u_i}{\partial x_j}-\varepsilon \tag{1}$$

$$\frac{\partial \varepsilon}{\partial t}+\frac{\partial (u_i \varepsilon)}{\partial x_i}=\frac{\partial}{\partial x_j}\left[\left(v+\frac{v_t}{\sigma_\varepsilon}\right)\frac{\partial \varepsilon}{\partial x_j}\right]+C_1 S_\varepsilon-C_2\frac{\varepsilon^2}{k+\sqrt{v\varepsilon}} \tag{2}$$

where k is turbulent kinetic energy, ε is dissipation rate; u_i, u_j are the velocity components in the i and j directions, respectively, v_t denotes the turbulent viscous coefficient, ν is the kinematic viscous coefficient, σ_k, and σ_ε are the turbulent Prandtl number of turbulence for turbulence kinetic energy and dissipation rate, which are 1.00, 1.20. C1 and C2 are the empirical parameters, which take the values of 1.44, 1.90, respectively. S_ε is the source term of the dissipation rate equation.

Combustion Modelling

Two types of models to describe the combustion process are Eddy-Dissipation Model (EDM) and Eddy-Dissipation Concept Model(EDC). The Eddy-Dissipation Model (EDM) does not take into account Arrhenius chemical kinetics calculations, which is low cost and fast, but has some errors with the actual combustion reaction [14]. In this study, the Eddy-Dissipation Conceptual Model (EDC) is used, which assumes that the chemical reaction occurs in a very small turbulent structure, called the "microstructure region", whose length scaling fractions and time scales are calculated by Eqs. (3) and (4), and the source term of species j during combustion, which is calculated by Eq. (5) [15].

$$\xi^* = C_\xi \left(\frac{v\varepsilon}{k^2}\right)^{1/4} \tag{3}$$

$$\tau^* = C_\tau \left(\frac{v}{\varepsilon}\right)^{1/2} \tag{4}$$

$$R_i = \frac{\rho(\xi^*)^2}{\tau^*\left[1-(\xi^*)^3\right]}\left(Y_i^* - Y_i\right) \tag{5}$$

where ξ^* is the length scale fraction occupied by the microstructured region, C_ξ is a volume fraction constant with a value of 2.1337, C_τ is a time scale constant with a value of 0.4082, Y_i^* is the small scale species mass fraction, τ^* is the chemical reaction time experienced within the microstructured region, R_i is the chemical reaction source term. Y_i is the average mass concentration of the component *i* within the cell.

The net production rate R_i of component i due to a chemical reaction is calculated as follows:

$$R_i = M_{w,i} \sum_{r=1}^{N_R} \hat{R}_{i,r} \tag{6}$$

where $M_{w,i}$ is the molecular weight of the component i, $\hat{R}_{i,r}$ is the rate of production or decomposition of the component i in the rth chemical reaction.

Radiation Modelling

The Discrete Ordinates method (DO) model is chosen as a radiation model and the solution model covers the entire optical thickness.

$$\nabla \cdot (I(r,s)s) + (a+\sigma_s)I(r,s) = an^2\frac{\sigma T^4}{\pi} + \frac{\sigma_s}{4\pi}\int_0^{4\pi} I\left(r,s'\right)\Phi\left(s\cdot s'\right)\mathrm{d}\Omega' \quad (7)$$

where r denotes the position vector, s is the direction vector, s' is the scattering direction vector, a is the absorption coefficient, n is the refractive index, σ_s is the scattering coefficient, σ is the Stefan-Boltzmann constant, I is the radiation intensity, Φ is the phase function, Ω' is the solid angle. The absorption coefficients were chosen from the weighted sum of gray gas model (WSGGM) proposed by Smith to calculate the radiation characteristics of the furnace.

Model Descriptions and Boundary Conditions

Model Descriptions

Model of a trolley furnace with natural gas combustion for heating multi-slab stacks, as shown in Fig. 1. The furnace length of 6.5 m, width 6.0 m and height 3.0 m. A total of 6 high-speed burners for natural gas combustion, staggered in the east and west sides of the trolley furnace. Figure 1 shows the natural gas inlet in red and the preheated air inlet in yellow. The flue gas outlet is located at the end of the trolley furnace end. There are 3 pad irons that support the slab and are placed to avoid areas where the hot flue gases from the combustion of natural gas are directly flushed. Three slabs heated simultaneously in the trolley furnace are stacked sequentially on top of a mat, with refractory bricks supporting each slab. The refractory bricks are five in total, one in the centre and one in the corners of each slab, as shown in Fig. 1.

Computational Grid

Geometric modeling of the trolley furnace shown in Fig. 1 is carried out using solidworks2019 software, and the geometric model is imported into ANSYS 2021R1 Meshing for meshing. Due to the complex structure of the geometric model, the computational domain mesh is a tetrahedral unstructured mesh, and the mesh encryption process is carried out in the position of the high-speed burner pipe for natural gas combustion, and the position of the pad iron in contact with the slab, as shown in Fig. 2.

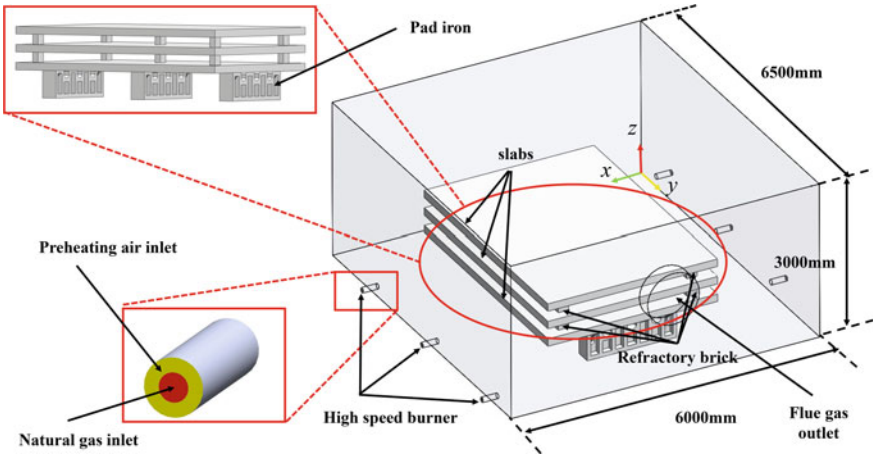

Fig. 1 Trolley furnace model of multi-slab stacking heated by natural gas combustion

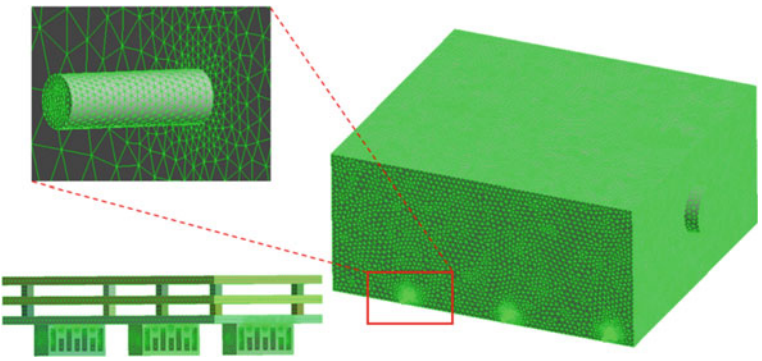

Fig. 2 The calculation grid division diagram of the trolley furnace model

The division and number of computational grids have a significant impact on the results of turbulent flow field calculations, in order to ensure the reasonableness of the calculation results, it is necessary to carry out an independence test of grid division. In this study, the slab temperature is a key control parameter, and the volume-averaged temperature of the slab is used as the index of the grid independence test. The results show that when the number of grids is greater than 1 million, the average temperature of the slab changes less, when the number of grids reaches 1.8 million, with the increase of the number of grids, the average temperature of the slab basically remains unchanged. In order to ensure the rationality and efficiency of the calculation at the same time, this simulation is carried out with a grid number of 1.8 million.

Boundary Conditions

The main component of natural gas is methane, in this simulation of the combustion reaction process selected methane-air two-step reaction model, the reaction mechanism parameters are shown in Table 1. combustion of natural gas, the high-speed burner inlet surface is set as the velocity inlet, post-combustion flue gas outlet set as pressure outlet, the specific selection of numerical values and the rest of the detailed boundary conditions are summarized in Table 2. The temperature change of the heated workpiece slab is a key parameter in the process operation, and the thermal conductivity and specific heat capacity of the slab are directly related to the temperature of the slab, and in the cyclic intermittent work of the trolley furnace heating process, the temperature varies from low to high in a wide range of changes, and taking into account the reasonableness of the results of the calculations, this study will be the thermal conductivity of the slab (λ) and the specific heat capacity (γ) is set as a linear function of the change in temperature as shown in Eq. (8). In addition, the thermal conductivity and specific heat capacity of the pad iron and refractory bricks supporting the slab as auxiliary parts are set as constants, as shown in Table 2. The surfaces of the slab, pad iron, and refractory bricks are set as coupled heat transfer surfaces.

$$\lambda = \begin{cases} 40 & 20\ ^\circ\text{C} \le t < 100\ ^\circ\text{C} \\ 41.25 - 0.0125t & 100\ ^\circ\text{C} \le t < 500\ ^\circ\text{C} \\ 35 & 500\ ^\circ\text{C} \le t < 700\ ^\circ\text{C} \\ 52.50 - 0.025t & 700\ ^\circ\text{C} \le t < 900\ ^\circ\text{C} \\ 30 & 900\ ^\circ\text{C} \le t < 1400\ ^\circ\text{C} \\ 0.3t - 390 & 1400\ ^\circ\text{C} \le t < 1500\ ^\circ\text{C} \\ 60 & 1500\ ^\circ\text{C} \le t \le 2100\ ^\circ\text{C} \end{cases}$$

$$\gamma = \begin{cases} 0.29t + 454.17 & 20\ ^\circ\text{C} \le t < 500\ ^\circ\text{C} \\ 0.625t + 287.50 & 500\ ^\circ\text{C} \le t < 900\ ^\circ\text{C} \\ 1390 - 0.60t & 900\ ^\circ\text{C} \le t < 1000\ ^\circ\text{C} \\ 790 & 1000\ ^\circ\text{C} \le t < 1100\ ^\circ\text{C} \\ 1670 - 0.80t & 1100\ ^\circ\text{C} \le t < 1200\ ^\circ\text{C} \\ 0.133t + 550 & 1200\ ^\circ\text{C} \le t < 1500\ ^\circ\text{C} \\ 750 & 1500\ ^\circ\text{C} \le t \le 2100\ ^\circ\text{C} \end{cases} \quad (8)$$

Table 1 Parameters of methane two-step reaction mechanism

	Reaction equation	Pre-exponential factor	Activation energy
1	$CH_4 + 1.5O_2 \rightarrow CO + 2H_2O$	5.012×10^{11}	2.0×10^8
2	$CO + 0.5O_2 \rightarrow CO_2$	2.239×10^{12}	1.7×10^8

Table 2 Setting the boundary condition

Parameters	Value
Natural gas inlet velocity	30.0 m/s
Preheated air inlet velocity	100.5 m/s
Methane volume fraction in natural gas	95%
Oxygen volume fraction in air	21%
Preheating air temperature	300 °C
Flue gas outlet pressure	− 20 Pa
Internal emissivity	0.5
Slab size	4500 × 3300 × 145 mm
Thermal conductivity of pad iron	44 W/(m·K)
Specific heat capacity of pad iron	480 J/(kg·K)
Thermal conductivity of refractory brick	0.35 W/(m·K)
Specific heat capacity of refractory brick	857 J/ (kg·K)

Results and Discussion

Parameter Laws Along the Axial Path of a High-Speed Burner

Figure 3a shows the characteristics of CO, O_2, CO_2, and H_2O component changes along the axial course of the high-speed burner when burning natural gas, and Fig. 3b shows the characteristics of CH_4 content changes. As can be seen in Fig. 3, with the combustion reaction between natural gas (methane) and oxygen in the combustion air, the CO content peaks near the exit of the high-speed burner, indicating that the natural gas combustion at the initial stage of sufficient methane reacts with oxygen to produce a large amount of CO is further consumed by the combustion to generate CO_2, and that the natural gas is burned to produce a large amount of CO, and that the natural gas is consumed by the combustion air. As the combustion reaction proceeds, the methane content decreases and the rate of CO production is less than the rate of consumption begins to decrease until combustion is complete, corresponding to the two-step methane-air combustion reaction mechanism. Along the high-speed burner axial journey, the oxygen content decreases rapidly, combustion produces CO_2, and H_2O increases rapidly, all in the distance from the high-speed burner outlet about 1 m tends to stabilise. Combined with the methane content, calculations show that about 97.38 per cent of methane is involved in the reaction, indicating that combustion is essentially complete, followed by a full combustion reaction of CO dispersed in the combustion flue gas with excess residual oxygen.

Figure 4 for the combustion of natural gas high-speed burner axial along the course of the temperature and speed change characteristics, methane in the gas and preheated air in contact with oxygen, rapid reaction, the release of a large amount of heat, resulting in along the course of the axial temperature rises, with the advancement

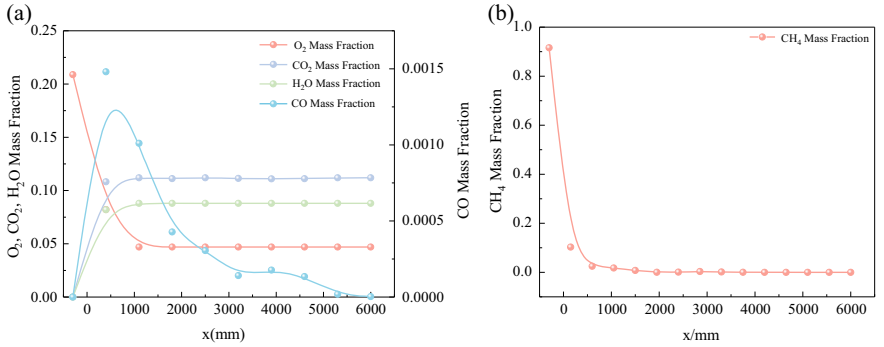

Fig. 3 Change characteristics of each component content along the burner axis

of the gas flow, the reaction is complete, the temperature began to remain stable, but due to the effect of coupled heat transfer, fluctuations slightly. The initial flow rate of natural gas is 30.0 m/s, while the flow rate of preheated air is 100.5 m/s. The two gas streams are mixed for the combustion reaction, which causes the natural gas flow rate to start to rise, and when the flue gas leaves the burner and enters the trolley furnace, the flow rate starts to decrease and gradually tends to stabilise due to the larger space range. This process, accompanied by high-temperature flue gas and pad irons, slabs for heat exchange.

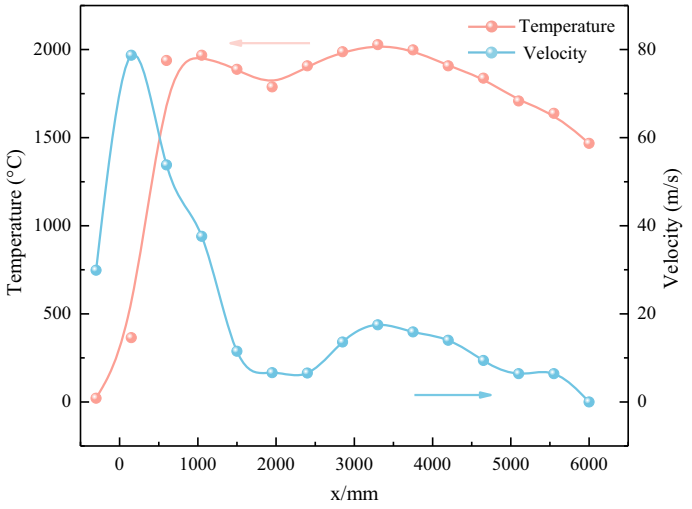

Fig. 4 Characteristics of temperature and velocity change along the axial direction of high-speed burner for burning natural gas

Changing Law of High-Temperature Flue Gas Flow Field and Temperature Field

Figure 5a–c for the three burner centre cross-section streamlines the diagram of the trolley furnace, due to the trolley being heated multi-slab stacking led to the three cross-sections in the furnace geometry differences, high-temperature flue gas flow is not the same, but there are obvious vortex, the vortex structure with size, scale, shape, speed and other different parameters of the characteristics of the natural gas diffusion and combustion efficiency of the impact of different degrees. When the combustion of high-temperature flue gas produced by nearly 100 m/s high-speed spray into the furnace, the vast majority of the flue gas flows directly through the lower slab, until the impact to the opposite wall, the direction of the gas flow changes, in the role of the surrounding airflow left and right mixing and interaction, and ultimately make the flue gas filled with the entire furnace space, including the gap between the multi-layer slabs. In addition, the flue gas velocity in the trolley furnace was eventually stabilised at 6 m/s.

Figure 5d and e shows the streamlines and vector diagram of the flue gas outlet cross-section. From Fig. 5d, it can be seen that the high-speed burner and its surrounding flow velocity are high, and it is easy to form a vortex under the synergistic effect of the gas flow and solid phase in the furnace. Figure 5e shows the velocity vector diagram, the gas-phase flow rate in the multi-slab stacking gap is low and the direction is variable. In addition, multi-slab stacking gap, the size of the arrow is not the same, indicating that the gas-phase flow rate is different, resulting in the surface of the slab having significant differences in heat transfer efficiency. At the

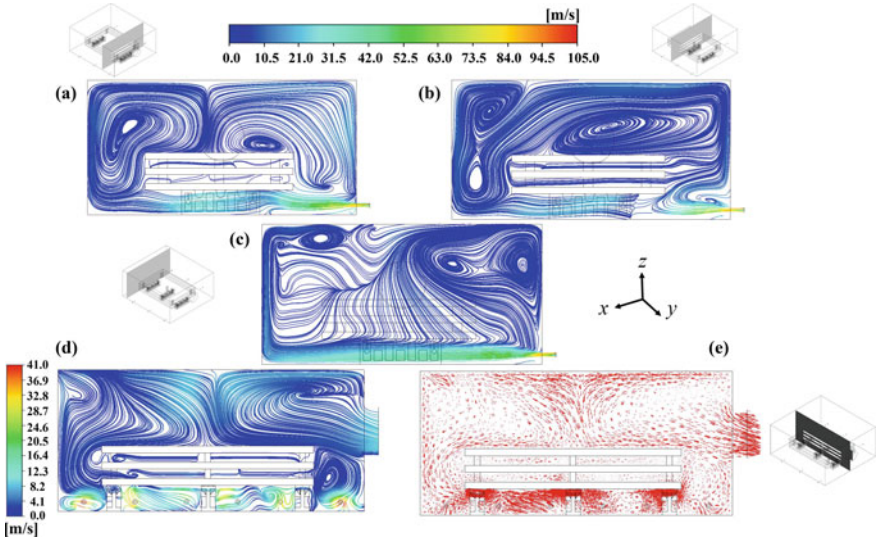

Fig. 5 Flue gas streamlines and velocity vector in the trolley furnace

exit position, the high-temperature flue gas flow rate increases, and high-temperature flue gas leaving the bogie furnace can be clearly observed.

Figure 6a–c shows the temperature contours of the three burner center sections of the trolley furnace, in which the section where Fig. 6a and b are located passes through the solid-phase region (the area where the pad irons and slabs are located), while the section in Fig. 6c is the pure gas-phase region. Combined with Fig. 5, it can be seen that when the gas phase passes through the region where the solid phase exists, its flow field is obviously more turbulent, and by the action of the solid phase, a part of the gas flow has a tendency to develop upward, so its high-temperature zone is characterised by the development of the direction of height, while the development of the length is hindered. On the contrary, in the pure gas-phase region, the length value of the high-temperature zone increases while the height value decreases, showing a flat shape. Figure 6d shows the temperature contour of the flue gas outlet cross-section, affected by the six high-speed burners on both sides, the bottom of the trolley furnace forms six corresponding high-temperature zones, and its shape is oval. The low-temperature zone is concentrated in the multi-slab stacking gap, mainly due to the low efficiency of radiation and convection heat transfer in this region, and the temperature is more uniform in the rest of the furnace.

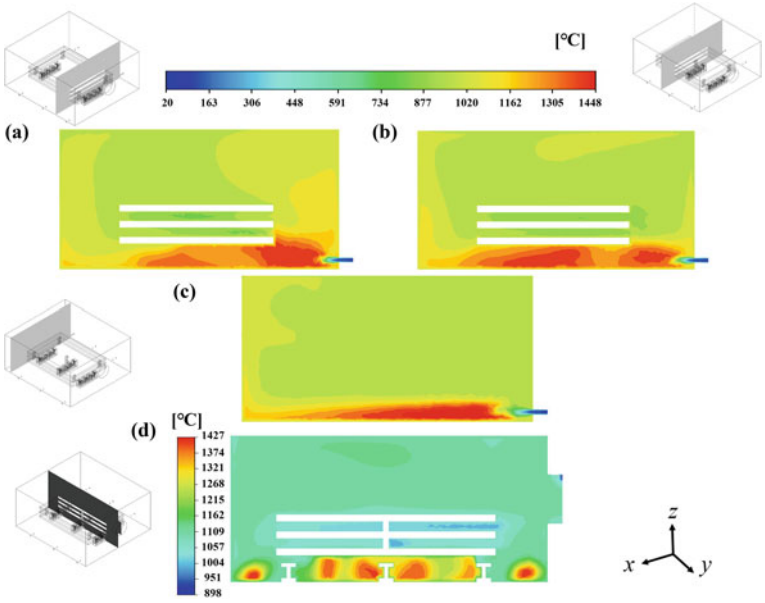

Fig. 6 Flue gas temperature distribution in the trolley furnace

Multi-slab Stacking Temperature Variation Characteristics

When the slab is heated, the deviation between the surface temperature and the internal temperature directly determines the temperature uniformity of the slab as a whole, so it has always been the most concerned issue in the heat treatment process, and the surface and internal temperature evolution laws of the three slabs are analyzed in this section.

Figure 7 shows the three slabs' upper and lower surfaces and internal centre section temperature contours, the slab in the top (Fig. 7a–c) and the slab in the middle (Fig. 7d–f) temperature change law is more consistent, the temperature cold zone is a long strip, and is not uniformly distributed along the centre of the slab position, Arkhazloo [14] article has a similar description, which is due to the result of the flow field around the slab is not uniform. In addition, the internal heat transfer of the slab mainly relies on heat conduction. At the edge of the slab, where the temperature is higher, there is not much difference between the temperature contours of the surface and the interior of the slab, whereas there is a significant difference in the shape of the contours in the region of lower temperatures, which indicates that the longitudinal heat conduction is more efficient when the temperature is higher, and it is easier to make the temperature of the inside and outside of the slab reach the same.

Figure 7g–i shows the temperature contours of upper and lower surfaces and internal centre section for the slab in the lower, a clear high-temperature zone is formed in the area passed by the burner airflow, while a low-temperature zone is formed in the upper left corner of the slab which is not directly passed by the burner, so the number of burners as well as the location of the burners have an extremely important influence on the temperature change of the slab.

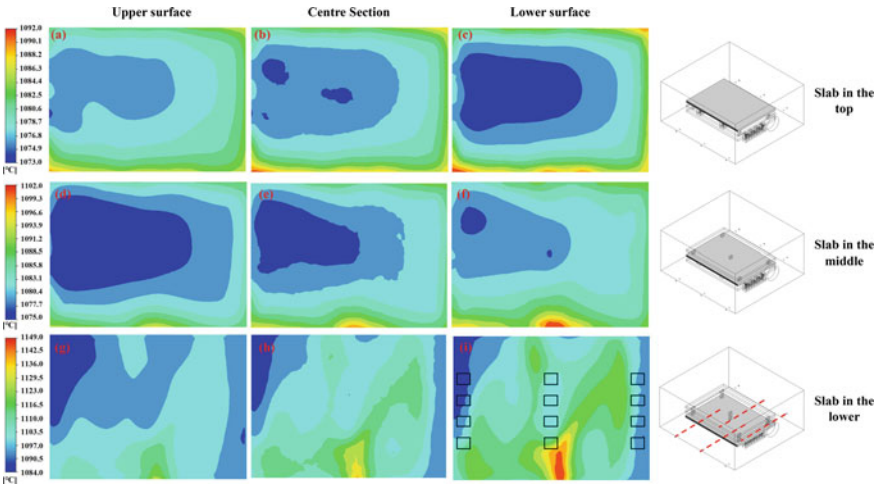

Fig. 7 Temperature contours of upper surface, centre section, and lower surface of three slabs

When the three slabs were analyzed together, the slab in the lower was more affected by the burner, while the slabs in the middle and top were less affected. The effect of the pad iron on the slab is mainly reflected in the lower surface of the slab in the lower in contact with it (Fig. 7i), where the black rectangle indicates the area where the pad iron is in contact with the slab, and the area covered by the pad iron blocks the active radiation and convection heat transfer from the furnace, so that the heat transfer in these areas relies only on thermal conduction, and it can be clearly found that the area where the pad iron is in contact with the slab is reduced due to the heat transfer efficiency, blocking the transfer of the high temperature zone, which makes the surface of the slab to form a significant temperature gradient on the surface of the slab and at the same time has an effect on the internal temperature distribution of the slab.

From Fig. 7, it can be seen that there are obvious differences in the surface temperature of the slab, in order to more accurately evaluate the temperature uniformity of the slab, the average temperature of a cross-section is obtained by using the area-weighted average formula, which is shown in Eq. 9. The temperature uniformity of the slab is evaluated by calculating the average temperature difference of the multi-layer cross-section of the comparative slab. In this paper, a slab is divided into five planes as shown in Fig. 8, where the five planes are numbered 1 to 5 from bottom to top.

$$\frac{1}{A}\int T\mathrm{d}A = \frac{1}{A}\sum_{i=1}^{n} T_i|A_i| \tag{9}$$

The weighted average temperature of each layer section of each slab is plotted to obtain a schematic diagram of the change rule of temperature in the direction of the height of the slab as shown in Fig. 9. Analyzed from slab temperature, the temperature of slab in the lower is the highest, the temperature of slab in the middle is the second highest, while the temperature of slab in the top is the lowest; in terms

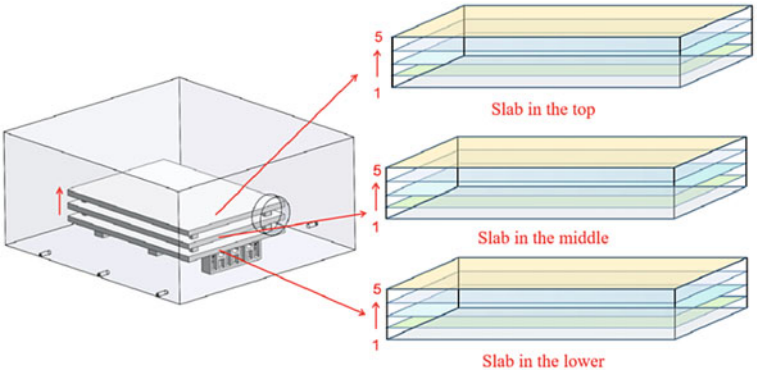

Fig. 8 Sections diagram of three slabs

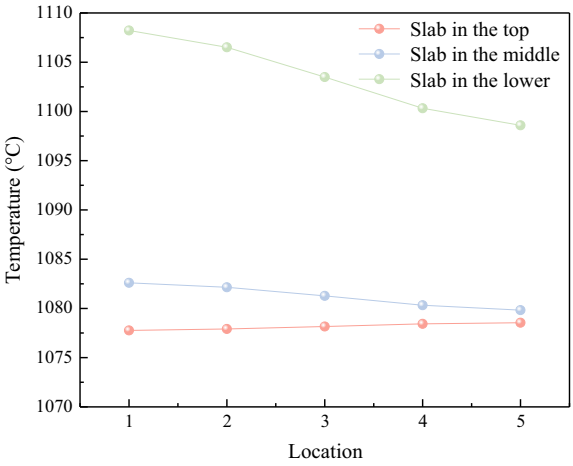

Fig. 9 The variation law of average temperature of slab sections at different heights

of slab heating uniformity, the slab in the top was optimal (temperature difference of 0.78 °C), the slab in the middle was the second highest (temperature difference of 2.78 °C), and the uniformity of the slab in the lower was the worst (temperature difference of 9.63 °C). The reason why the slab in the lower uniformity is the worst, is due to the lower surface of the slab in the lower and burner jets contact, is a heat exchange intense region, while its upper surface is located in the gap between the stack of slabs, heat exchange efficiency is low, resulting in poor uniformity. Overall the temperature of the three slabs is more uniform, and the heating effect of the slabs is better.

From Fig. 9, the slab in the lower has the highest overall temperature, which is due to the fact that the slab in the lower is closest to the gas burner high-temperature flue gas ejection area, the gas flow temperature is the highest, the slab coupling heat transfer effect is better. The slab height direction the higher up the lower temperature, this is due to the lower surface directly with the gas burner out of the high-temperature flue gas contact, intense convection heat transfer, so the lower surface can be rapidly warmed up, the upper and lower surfaces form a temperature difference, so that the height direction of the temperature shows a tendency to reduce.

From Fig. 9, the temperature of the slab in the middle gradually decreases in the height direction, which is due to the lower surface of the middle slab being closer to the burner, so it is affected by the thermal convection of the burner, and the temperature rises slightly faster than the upper surface, but this convection heating effect is much weaker than that of the slab in the lower, so the temperature difference between the upper and lower surfaces of the middle slab is small.

From Fig. 9, the temperature of the slab at the top in the height direction shows an increasing trend, and the temperature of its upper surface is the highest. This is due to the upper surface is not blocked, can better receive the furnace wall and high-temperature flue gas release of radiant energy, and the upper surface is closer to the exit of the flue gas, convective heat transfer effect is relatively better than

the lower surface, so the upper surface temperature is higher. At the same time, the lower surface is farther away from the burner, the convection heat transfer effect is weaker, and due to the influence of slabs stacking, the lower surface is blocked, the conditions for receiving radiation are weaker than the upper surface, so the lower surface temperature is lower.

Conclusions

In this paper, the conjugate heat transfer process of a large industrial bogie furnace containing turbulent combustion radiation is analysed based on CFD, and the main conclusions are summarised as follows:

(1) Optimisation of the slab heating process must take into account the geometric effect, the number of high-speed burners and spatial distribution, slab pads, and other arrangements will have a greater impact on the high-temperature flue gas flow in the furnace, resulting in significant changes in convective heat transfer, and ultimately become a direct source of uneven temperatures in the slab.
(2) The cold zones of the internal and surface temperatures of the slabs were not uniformly distributed along the centre of the slabs, but had a certain offset, in addition, the temperature uniformity of the slabs was evaluated based on the area-weighted average temperature, and the results showed that the slab in the top was optimal, and the slab in the lower had the worst uniformity. Overall the temperature uniformity of the three slabs is good.
(3) With the combustion reaction occurring, high-speed burner along the course of the axial O_2 content decreased rapidly and then tends to stabilise, CO_2 and H_2O content began to gradually increase and then tends to stabilise, CO content shows a trend of increasing and then decreasing. In addition, the high-speed burner axial direction along the course of the temperature by the reaction exothermic effect of the sudden rise, the high-temperature flue gas entering the furnace chamber is affected by the coupled heat transfer from the slab, and the temperature fluctuates but remains basically stable.

Acknowledgements The work is supported by the National Natural Science Foundation Project of China (51974046). The authors of this paper would also like to express their special thanks to Dongfang Electric Group Dongfang Boiler Co., Ltd. for providing the solid model for the project modelling calculations.

References

1. Han SH, Chang DJ (2012) Optimum residence time analysis for a walking beam typereheating furnace. Int J Heat Mass Transf 55(15–16):4079–4087
2. Yin CG, Yan JY (2016) Oxy-fuel combustion of pulverized fuels: combustion fundamentals and modelling. Appl Energy 162:742–762
3. Mayr B, Prieler R, Demuth M, Moderer L, Hochenauer C (2017) CFD analysis of a pusher type reheating furnace and the billet heating characteristic. Appl Therm Eng 115:986–994
4. Oh J, Lee E, Noh D (2015) Development of an oxygen-enhanced combustor for scrap preheating in an electric arc furnace. Appl Therm Eng 91:749–758
5. Prieler R, Mayr B, Demuth M, Holleis B, Hochenauer C (2016) Prediction of the heating characteristic of billets in a walking hearth type reheating furnace using CFD. Int J Heat Mass Transf 92:675–688
6. Han SH, Baek SW, Kim MY (2009) Transient radiative heating characteristics of slabs in a walking beam type reheating furnace. Int J Heat Mass Transf 52(3–4):1005–1011
7. Han SH, Chang DJ, Kim CY (2010) A numerical analysis of slab heating characteristics in a walking beam type reheating furnace. Int J Heat Mass Transf 53(19–20):3855–3861
8. Han SH, Chang DJ, Huh C (2011) Efficiency analysis of radiative slab heating in a walking-beam-type reheating furnace. Energy 36(2):1265–1272
9. Han SH, Chang DJ (2012) Radiative slab heating analysis for various fuel gas compositions in an axial-fired reheating furnace. Int J Heat Mass Transf 55(15–16):4029–4036
10. Mayr B, Prieler R, Demuth M, Potesser M, Hochenauer C (2017) Computational analysis of a semi-industrial furnace fired by a flat flame burner under different O_2/N_2 ratios using the steady laminar flamelet approach. J Energy Inst 90(4):602–612
11. Lewandowski MT, Ertesvag IS (2018) Analysis of the Eddy dissipation concept formulation for MILD combustion modelling. Fuel 224:687–700
12. Wang J, Liu YW, Sunden B, Yang R, Baleta J, Vujanovic M (2017) Analysis of slab heating characteristics in a reheating furnace. Energy Conver Manag 149:928–936
13. Shih TH, Liou WW, Shabbir A, Yang ZG, Zhu J (1995) A new K-epsilon eddy viscosity model for high Reynolds number turbulent flows: model development and validation. Comput Fluids 24(3):227–238
14. Arkhazloo NB, Bouissa Y, Bazdidi-Tehrani F, Jadidi M, Morin JB, Jahazi M (2019) Experimental and unsteady CFD analyses of the heating process of large size forgings in a gas-fired furnace. Case Stud Therm Eng 14:100428
15. Gao Q, Pang YH, Sun Q, Liu D, Zhang Z (2021) Numerical analysis of the heat transfer of radiant tubes and the slab heating characteristics in an industrial heat treatment furnace with pulse combustion. Int J Therm Sci 161:106757

Characterization of Mechanical Properties of Viscoelastic Materials Through Experimental Modal Tests Using an Inverse Technique

Jagesh Kumar Prusty and Sukesh Chandra Mohanty

Abstract Characterizing viscoelastic polymers is challenging due to their unique combination of elastic and viscous properties. Accurate identification of their mechanical properties is crucial for understanding their dynamic behaviour. Traditional methods like creep and stress relaxation tests are time-consuming and require specialized equipment. To address this, a novel inverse technique is proposed in this study for estimating the storage and loss moduli of viscoelastic materials using experimental modal test data. The technique considers a three-layered sandwich structure with isotropic face layers and a viscoelastic core layer. By integrating experimental measurements with mathematical modelling, an iterative process updates material parameters to minimize the difference between model and experimental results. Experimental case studies using dynamic mechanical analysis tests validate the technique, showing accurate estimation of frequency-dependent moduli with $< 3\%$ maximum error. This non-destructive and cost-effective approach enables improved material selection, design optimization, and enhanced performance in various engineering applications.

Keywords Characterization · Mechanical properties · Viscoelastic polymers · Modal analysis

Introduction

Sandwich structures incorporating viscoelastic damping layers are used in the design of lightweight and high-strength components in various engineering disciplines to dampen structural vibrations and reduce noise levels during operation. Viscoelastic

J. K. Prusty (✉) · S. C. Mohanty
Department of Mechanical Engineering, National Institute of Technology Rourkela, Odisha 769008, India
e-mail: jageshkumarprusty@gmail.com

S. C. Mohanty
e-mail: scmohanty@nitrkl.ac.in

Z. Peng et al. (eds.), *Characterization of Minerals, Metals, and Materials 2024*, The Minerals, Metals & Materials Series, https://doi.org/10.1007/978-3-031-50304-7_5

materials exhibit both elastic and viscous properties. Their mechanical behaviour can be described linearly through storage and loss moduli. To improve the dynamic performance of viscoelastic materials for specific applications, polymers are often combined with various reinforcements and fillers. However, these mechanical properties are not always readily available in materials handbooks, necessitating the development of novel methods for accurate identification. Conventional approaches, such as dynamic mechanical analysis (DMA) involving creep and stress relaxation tests, require specialized equipment and take considerable time. Vibration-based identification of material parameters has attracted the attention of many researchers as a promising non-destructive technique. Shi et al. [1] developed a method that employed the Nelder-Mead simplex optimization approach to determine the material properties of a sandwich beam by analyzing the observed resonance frequencies. Cortes and Elejabarrieta [2] conducted a study to establish the viscoelastic material characteristics of a cantilever beam in a free-layer damping configuration under seismic stimulation. The viscoelastic properties of 3 M damping polymer were calculated by Barkanov et al. [3] using the response surface method and the constrained optimization approach. Using a gradient-based optimization technique, Araujo et al. [4] developed an inverse method for predicting material properties in laminated plates of piezoelectric, elastic, and viscoelastic materials. Kim and Lee [5] determined the parameters of viscoelastic materials using measured frequency response functions (FRFs) obtained at various temperatures during impact testing of a beam with cantilever boundary conditions conducted in an environmental chamber. Martinez-Agirre and Elejabarrieta [6] developed an inverse method to determine the material characteristics of a high-damping viscoelastic material through a forced vibration test of a cantilever beam. Ledi et al. [7] developed an inverse technique based on the measurement of natural frequencies and modal loss coefficients to estimate the material parameters of a three-layer viscoelastic sandwich beam. Sun et al. [8] proposed an inverse methodology that relies on observed resonant frequencies and FRFs to characterize the mechanical behaviour of a damped cantilever plate. This comprehensive analysis covers both viscous and material damping, with the material parameters derived using the response surface method and a constrained optimization approach. Xie et al. [9] introduced a parametric model order reduction technique for the identification of viscoelastic material parameters. Kang et al. [10] used a genetic algorithm to fit an analytical solution to the FRFs of the beam under free-free boundary constraints, allowing the determination of the frequency-dependent complex modulus of the viscoelastic layer.

The primary goal of integrating viscoelastic materials into structures is to effectively reduce vibrations. The literature review discusses techniques for identifying viscoelastic material parameters by analyzing their structural vibration responses. One major limitation is the use of oversimplified models that do not accurately represent the complex behaviour of viscoelastic materials. It is evident that although several methods combining theory and experiment exist to identify these properties, there is still an ongoing search for more precise and efficient approaches. In pursuit of this research objective, an inverse identification method is proposed utilizing a neural network optimization (NNO) algorithm to determine the frequency-dependent

viscoelastic material parameters. To this end, a symmetric three-layered cylindrical sandwich shell is considered with aluminium as face layers and natural rubber as a core layer. Free vibration tests are performed on the structure using the impact hammer method under a clamped-free boundary condition. The theoretical model confirming the empirical scenario is developed utilizing a finite element technique in MATLAB programming language. The frequency-dependent viscoelastic material properties of natural rubber are identified by minimizing the error between corresponding experimental and numerical structural responses. To minimize the error function, the novel NNO algorithm is used. Besides, the elicited results are successfully validated with experimental results through the DMA test. The proposed inverse identification method offers a novel and powerful approach for the efficient exploration of the parameter space, reducing the computational cost and time required to identify the material parameters.

Experimental Analysis

Three-layered cylindrical sandwich shells with viscoelastic cores are fabricated using the hand lay-up method in line with Prusty et al. [11]. The sandwich shell specimens consist of two face layers made of aluminium, with a core layer composed of natural rubber. First, a cylindrical mould is prepared, and a release agent is applied to prevent sticking. The process begins by manually placing the first aluminium face layer inside the mould, ensuring proper alignment and eliminating air bubbles. A layer of araldite adhesive is then carefully applied to the aluminium surface. Subsequently, the core layer made of natural rubber is placed over the adhesive-coated face layer. Another layer of araldite is applied to the natural rubber core. Next, the second face layer of aluminium is hand-laid over the core and the entire assembly is carefully consolidated to ensure proper bonding and uniform thickness. The sandwich shell assembly is subjected to constant and uniform pressure to improve adhesion and eliminate any voids. After curing for 72 h at room temperature, the cylindrical sandwich shell is removed from the mould, and excess material is trimmed out. The specimen surfaces are cleaned with acetone to make them free from any impurities. The fabricated cylindrical sandwich shells are then subjected to modal testing employing the impact hammer method.

Experimental modal analysis, employing the impact hammer method, is a widely employed non-destructive vibration testing technique to establish structures' dynamic properties. Figure 1 illustrates the experimental configuration employed for conducting the free vibration test of the cylindrical sandwich shell subjected to a clamped-free boundary condition. In order to establish the clamped-free boundary condition, the test specimen is firmly clamped at one end to an iron frame using C-clamps. The Pulse Labshop and ME'scope modal analysis software tools are employed to perform modal analysis. For the vibration measurement, the roving hammer methodology is adopted, wherein the accelerometer is affixed at a designated location, and the test specimen is then excited by systematically moving the

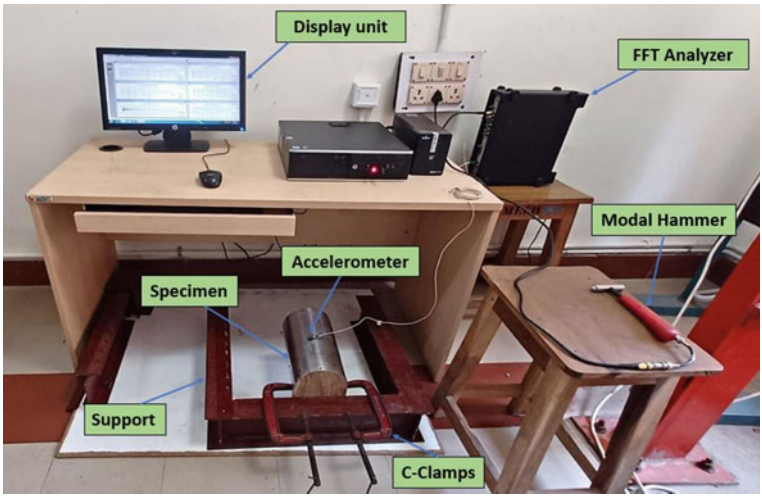

Fig. 1 Complete experimental set-up for modal testing of the cylindrical sandwich shell under a clamped-free boundary condition

modal hammer to various pre-marked points on the specimen. The modal hammer is used to apply a transient excitation to the structure. The accelerometer, affixed to the specimen, detects the response produced by the modal hammer. The FFT analyzer acquires a time-varying signal from the accelerometer, which is subsequently transformed into a frequency-based signal termed as the frequency response function (FRF). The FFT analyzer operates on the Pulse Labshop platform, generating input FRFs for modal analysis. ME'scope software is utilized for post-processing the recorded data to determine the modal characteristics of the sandwich shell specimens. To minimize the potential for experimental error, each sample is tested three times, and the average value of the vibration results is taken into consideration.

Numerical Analysis

The vibrational properties of the proposed sandwich shell are determined through the utilization of the finite element method (FEM), following the numerical simulation methodology outlined by Biswal et al. [12]. This approach involves several key steps in applying FEM to a three-layer sandwich shell with isotropic face layers and a viscoelastic core. First, the kinematic relationships between all layers in the shell are established, providing an accurate representation of its structure. Next, the sandwich shell structure is discretized into finite elements. These elements form a network of interconnected nodes and carry crucial material and section definitions for the shell. Following the discretization, the global stiffness and mass matrices are assembled. In conjunction with the boundary conditions specific to the sandwich

shell, these matrices constitute a system of equations that must be solved to obtain the shell's dynamic behaviour. Finally, the natural frequencies and modal loss factors are extracted from the FEM solutions and can be used to characterize the mechanical response of the three-layered sandwich shell.

In the present analysis, the rheological characteristics of the viscoelastic material are considered according to the complex modulus approach. Thus, for the core layer, the complex Young's modulus of the viscoelastic material can be represented as, $E_c = E_v(1 + i\beta_v)$ and the complex shear modulus can be defined as, $G_c = G_v(1 + i\beta_v)$, where E_v and G_v represents the storage modulus and β_v is the loss factor of the viscoelastic material.

Based on Hamilton's principle, the governing equation of motion is derived for the sandwich shell and can be presented as:

$$\int_{\tau 1}^{\tau 2} \delta(U - T)\mathrm{d}\tau = 0 \tag{1}$$

where, U is the total strain energy and T is the total kinetic energy of the sandwich shell, incorporating the energy contributions from the base layer, viscoelastic core layer, and constraining layer. The governing equation of motion for free vibration analysis of the sandwich shell can be expressed as:

$$(K - \lambda M)q = 0 \tag{2}$$

where, $[K]$ and $[M]$ are the sandwich shell's global stiffness and mass matrix, respectively and q stand for the global displacement vector. To find a substantial non-zero solution for the given expression, the following equation must hold:

$$|K - \lambda M| = 0 \tag{3}$$

Equation (3) is an eigenvalue problem that may be solved analytically to get the values λ. Due to the viscoelasticity of the core material, the value of λ is a complex number, which can be written as:

$$\lambda = \omega^2(1 + j\eta_s) \tag{4}$$

where, ω represents the natural frequency and η_s represents the modal loss factor for the sandwich shell. The natural frequency and the modal loss factor for the three-layered sandwich shell with a viscoelastic core can be given as:

$$\omega = \sqrt{\mathrm{Real}(\lambda)} \quad \text{and} \quad \eta_s = \frac{\mathrm{Imag}(\lambda)}{\mathrm{Real}(\lambda)} \tag{5}$$

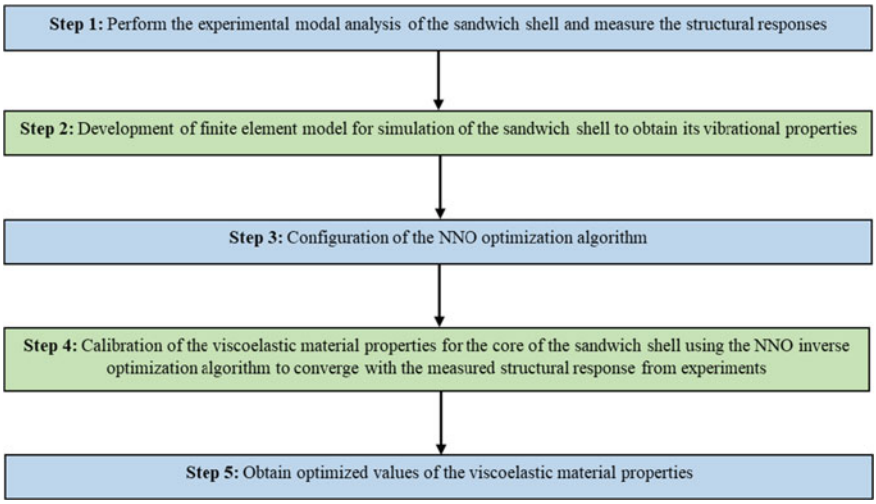

Fig. 2 Flow chart of the identification procedure

The Material Parameters Identification Procedure

The process of determining material parameters using inverse analysis is based on the integration of experimental test results with numerical analysis findings. Typically, the structural vibration responses of a system are determined by considering its geometric and material characteristics. Inversely, the material characteristics of the structure can be determined based on the observed structural responses. The inverse technique may be explained by considering the following proposition: the design variables, which need to be identified, must be iteratively updated inside a numerical model until the theoretical analysis outcomes align with the experimental findings. The material parameters identification procedure based on the present inverse method is described below in Fig. 2.

Results and Discussion

A generalized code using the finite element approach is developed using the MATLAB programming language. Convergence studies have been carried out with various mesh refinements to identify the optimum discretization of the finite element model. The proposed finite element formulation is validated with the existing works of literature within the equal testing domain. The resulting outcomes are represented in Table 1. It can be clearly observed that the results obtained from the present finite element analysis are in accordance with the literature results.

Table 1 Comparison of the first three natural frequencies and modal loss factors of a sandwich plate with viscoelastic core for all sides clamped boundary condition

Mode no	Natural frequency (Hz)		Modal loss factor	
	Present study	Araujo et al. [4]	Present study	Araujo et al. [4]
1	87.5752	87.66	0.1864	0.1886
2	152.4316	150.10	0.1606	0.1630
3	172.3108	170.99	0.1532	0.1527

The geometrical and material properties of the cylindrical sandwich shell considered in this study are presented in Table 2. The free vibration test is performed using the impact hammer technique at room temperature conditions. The first three modes of experimental natural frequencies and their corresponding modal loss factors of the sandwich shell are presented in Table 3.

Considering the viscoelastic material's shear storage modulus and loss factor as design variables and the difference between the sandwich shell's experimental and numerical natural frequencies and modal loss factors as the objective function, the NNO algorithm is applied. For this identification procedure, the upper and lower bounds for the shear storage modulus are set as 0.2–1.2 MPa and for the material loss factor as 0.1–0.2 for a frequency range of 1–500 Hz. From the proposed inverse method, the optimal values of shear storage modulus and material loss factor of the viscoelastic core are obtained as 0.94675 MPa and 0.12284, respectively. Figure 3 provides a visual representation of the NNO algorithm's evolution, showing the

Table 2 Geometrical and material properties of the cylindrical sandwich shell

Face layers (Aluminium, AL 6061)	Thickness, 1.485 mm Elastic modulus, 68.9 GPa Density, 2700 kg/m^3 Poisson's ratio, 0.33
Core layer (Natural rubber)	Thickness, 2.738 mm Density, 930 kg/m^3 Poisson's ratio, 0.49
Whole structure	Effective length, a = 285 mm Width, b = 145 mm Thickness, h = 5.708 mm Shalowness, R/b = 50

Table 3 Experimental natural frequencies and modal loss factors of the sandwich shell under a clamped-free boundary condition

Mode no	Natural frequency (Hz)	Modal loss factor
1	42	0.06538
2	102	0.04187
3	224	0.03659

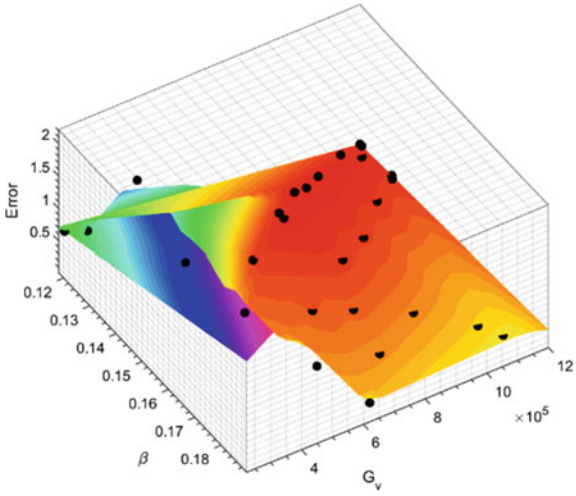

Fig. 3 Optimization space of the inverse problem considered in this study and points where the objective function is evaluated during the execution of the proposed NNO algorithm

optimization space and the points where objective function evaluations occurred until convergence.

The natural rubber's viscoelastic properties are determined experimentally using Dynamic Mechanical Analysis (DMA) tests. To prepare the samples of natural rubber, the ASTM-D4065 standard has been followed, specifying dimensions of 10 mm in width and 1 mm in thickness. The shear tests are conducted using a DMA-8000 instrument, and the dynamic behaviour of natural rubber is examined through a multi-frequency test while subjecting it to a temperature ramp. The summary of the DMA test results reveals that the shear storage modulus has an average value of 0.92439 MPa, and the associated material loss factor averages 0.12323. The comparison between the frequency-dependent material properties of natural rubber obtained by the inverse approach and the DMA test is shown in Fig. 4.

When compared to the outcomes obtained from the proposed NNO algorithm, the DMA test results exhibit a strong similarity. To quantify the error, it has been observed that the shear storage modulus and material loss factor have deviations of 2.36 and 0.32%, respectively. This high level of agreement clearly demonstrates the reliability of the proposed NNO algorithm.

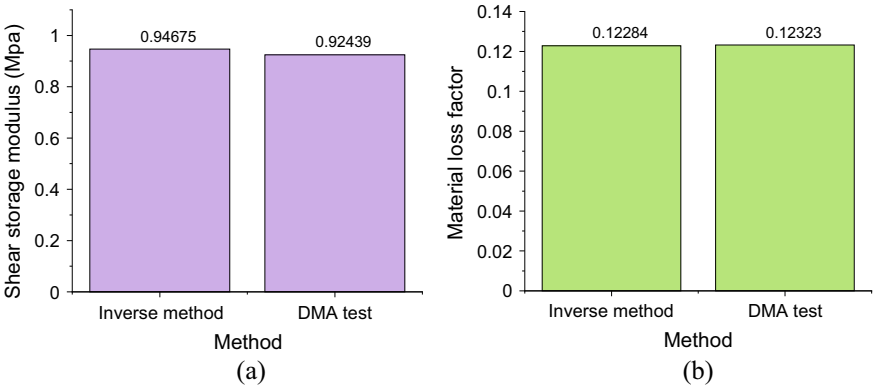

Fig. 4 Comparison of the proposed inverse method with the DMA test: **a** shear storage modulus, **b** material loss factor

Conclusion

This study aims to characterize the frequency-dependent material properties of a viscoelastic material by an inverse method. A three-layered cylindrical sandwich shell with face layers of aluminium and a core layer of natural rubber is considered. The experimental modal analysis is conducted using the impact hammer method, while the numerical simulations are performed using the finite element approach. To obtain the shear storage modulus and loss factor of natural rubber, an NNO algorithm is proposed based on the experimental modal analysis results of the sandwich shell.

As determined from the inverse approach, the frequency-dependent material properties of natural rubber show a high level of agreement with the experimental findings obtained with the DMA test. Thus, instead of performing costly and time-consuming DMA experiments, the proposed inverse approach may be utilized to estimate viscoelastic material properties utilizing structural responses. The accuracy of the current inverse method relies on the precision of physical experiments and precise theoretical modelling. In the context of reducing structural vibrations, having accurate knowledge of material parameters is essential for ensuring the safety and reliability of structural designs. The suggested inverse identification approach comes with notable benefits and practical uses in the fields of material science and engineering. The practical applications of this research are diverse and can have a significant impact on product design, performance optimization, and the development of safer and more efficient systems and structures in a variety of industries.

References

1. Shi Y, Sol H, Hua H (2006) Material parameter identification of sandwich beams by an inverse method. J Sou Vib 290:1234–1255. https://doi.org/10.1016/j.jsv.2005.05.026
2. Cortes F, Elejabarrieta MJ (2007) Viscoelastic materials characterisation using the seismic response. Mater Des 28:2054–2062. https://doi.org/10.1016/j.matdes.2006.05.032
3. Barkanov E, Skukis E, Petitjean B (2009) Characterisation of viscoelastic layers in sandwich panels via an inverse technique. J Sou Vib 327:402–412. https://doi.org/10.1016/j.jsv.2009.07.011
4. Araujo AL, Soares CM, Soares CA (2010) Finite element model for hybrid active-passive damping analysis of anisotropic laminated sandwich structures. J Sand Struct Mater 12:397–419. https://doi.org/10.1177/1099636209104534
5. Kim SY, Lee DH (2009) Identification of fractional-derivative-model parameters of viscoelastic materials from measured FRFs. J Sou Vib 324:570–586. https://doi.org/10.1016/j.jsv.2009.02.040
6. Martinez-Agirre M, Elejabarrieta MJ (2011) Dynamic characterization of high damping viscoelastic materials from vibration test data. J Sou Vib 330:3930–3943. https://doi.org/10.1016/j.jsv.2011.03.025
7. Ledi KS, Hamdaoui M, Robin G, Daya EM (2018) An identification method for frequency dependent material properties of viscoelastic sandwich structures. J Sou Vib 428:13–25. https://doi.org/10.1016/j.jsv.2018.04.031
8. Sun W, Wang Z, Yan X, Zhu M (2018) Inverse identification of the frequency-dependent mechanical parameters of viscoelastic materials based on the measured FRFs. Mech Syst Sign Proc 98:816–833. https://doi.org/10.1016/j.ymssp.2017.05.031
9. Xie X, Zheng H, Jonckheere S, Pluymers B, Desmet W (2019) A parametric model order reduction technique for inverse viscoelastic material identification. Comput Struct 212:188–198. https://doi.org/10.1016/j.compstruc.2018.10.013
10. Kang L, Sun C, Liu H, Liu B (2022) Determination of frequency-dependent shear modulus of viscoelastic layer via a constrained sandwich beam. Polymer 14(18):3751. https://doi.org/10.3390/polym14183751
11. Prusty JK, Papazafeiropoulos G, Mohanty SC (2023) Free vibration analysis of sandwich plates with cut-outs: an experimental and numerical study with artificial neural network modelling. Compos Struct 328:117328. https://doi.org/10.1016/j.compstruct.2023.117328
12. Biswal DK, Mohanty SC (2018) Free vibration and damping characteristics study of doubly curved sandwich shell panels with viscoelastic core and isotropic/laminated constraining layer. Eur J Mech A Solids 72:424–439. https://doi.org/10.1016/j.euromechsol.2018.06.008

Part III
Mineralogical Analysis and Process Improvement

Microwave and Conventional Carbothermic Reduction of Chromite Ore: A Comparison

Huimin Tang, Zhiwei Peng, Tianle Yin, Lei Ye, Qiang Zhong, and Mingjun Rao

Abstract The reduction of chromite ore is an important step in the production of ferrochromium alloy and stainless steel. The comparison between conventional and microwave reduction of chromite ore was investigated in this study with a focus on the effect of reduction time. Compared to conventional reduction, microwave reduction of chromite ore was more efficient by breaking the stable chromium-containing spinel structure, improving reduction performance of the ore with generation of large Fe–Cr particles. By fixing reduction temperature of 1100 °C and C/O molar ratio of 1.2, the metallization degrees of chromium and iron of the briquettes constituted by chromite ore and coke after microwave reduction increased from 91.57 and 83.03% to 93.53 and 85.78%, respectively, with increasing time from 0 to 120 min, which were higher than those obtained by conventional reduction for 4 h (7.00% for chromium and 67.26% for iron).

Keywords Microwave reduction · Conventional reduction · Chromite ore · Carbothermic reaction

Introduction

Chromite ore is the sole commercial source of chromium which is mainly present in the form of spinel containing multiple metal elements with the chemical formula of $(Mg,Fe)(Cr,Al,Fe)_2O_4$ [1–3]. Depending on its content of Cr_2O_3 and the mass ratio of Cr/Fe, chromite ore can be used in the fields of metallurgy, chemicals, and refractories. Currently, more than 90% of mined chromite ore is consumed to produce ferrochromium alloy for further stainless steel production owing to the excellent resistances of chromium to oxidation and erosion [4, 5]. High-carbon ferrochromium alloy is produced mostly by smelting chromite ore with the addition of coke and flux in the submerged arc furnace (SAF) [7, 8]. However, it is highly energy-intensive

H. Tang · Z. Peng (✉) · T. Yin · L. Ye · Q. Zhong · M. Rao
School of Minerals Processing and Bioengineering, Central South University, Changsha 410083, Hunan, China
e-mail: zwpeng@csu.edu.cn

Z. Peng et al. (eds.), *Characterization of Minerals, Metals, and Materials 2024*, The Minerals, Metals & Materials Series, https://doi.org/10.1007/978-3-031-50304-7_6

with a specific energy consumption of 2.4–4.8 MW·h/t of ferrochromium alloy [4, 6, 7]. It was reported that reducing chromite ore before smelting was an efficient approach for cutting energy consumption and operation costs [7].

Recently, microwave technology has been widely applied in the field of metallurgy [3, 8, 9] due to its high heating efficiency and environmental friendliness [10]. It was also used for the reduction of chromite ore based on silicothermic reduction [9]. In view of rare reports of microwave carbothermic reduction of chromite ore, the purpose of this study was to investigate microwave and conventional reduction of chromite ore by evaluating their reduction efficiencies, phase transformations, and microstructural evolutions, providing an efficient and green method for processing of chromite ore.

Materials and Methods

Materials

The chromite ore used in this study contained 40.98 wt% Cr_2O_3, 19.04 wt% FeO, 13.05 wt%Al_2O_3, and 3.35 wt% MgO with the mass ratio of Cr/Fe of 1.29, as shown in Table 1. The main phases of chromite ore were chromite ($(Mg,Fe)(Cr,Al,Fe)_2O_4$), and enstatite ($MgSiO_3$), as shown in Fig. 1. Coke having 84.81 wt% fixed carbon, 13.23 wt% ash, and 1.96 wt% volatile matter was used as reducing agent, as shown in Table 2. Figure 2 shows the scanning electron microscopy with energy dispersive X-ray spectrometry (SEM–EDS) analysis of chromite ore. The simultaneous enrichment of chromium, aluminum, iron, and magnesium from the EDS analyses of spots 1 and 2 indicated the presence of chromite [11, 12]. The atomic molar ratios of (Mg + Fe)/Si at spots 3 and 4 were close to 1 and 2, respectively, representing the occurrences of enstatite and forsterite, both of which contained chromium. The SEM–EDS analyses were consistent with the XRD analysis of chromite ore.

Table 1 Main chemical composition of chromite ore (wt%)

Item	Cr_2O_3	TFe	FeO	Al_2O_3	SiO_2	MgO	CaO	Na_2O
Content	40.98	21.75	19.04	13.05	4.04	3.35	0.36	0.04
Item	P	S	C	LOI	Cr/Fe			
Content	0.48	0.15	0.087	− 1.81	1.29			

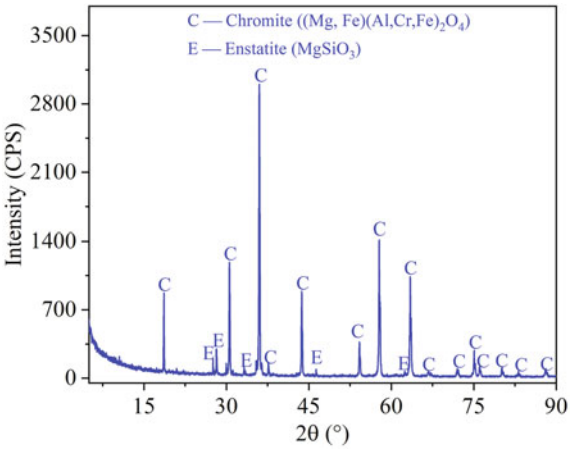

Fig. 1 XRD pattern of chromite ore

Table 2 Ultimate and proximate analyses of coke (wt%)

Proximate analysis			Chemical composition of ash						
F_{cad}	A_d	V_{dafc}	TFe	SiO_2	Al_2O_3	CaO	MgO	P	S
84.81	13.23	1.96	0.58	5.75	4.45	0.57	0.13	0.03	0.084

F_{cad}—fixed carbon content; A_d—ash content; V_{adf}—volatile content

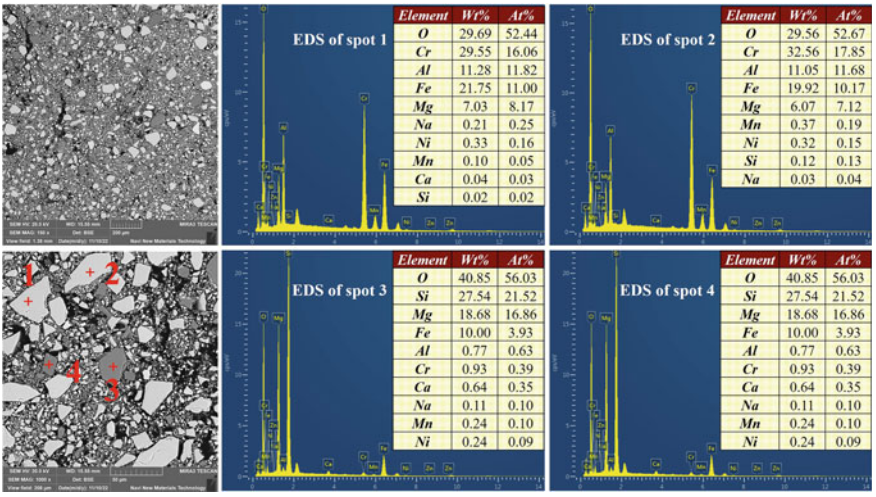

Fig. 2 SEM–EDS analysis of chromite ore

Methods

In the experiments, both chromite ore and coke were firstly ground until their particles were smaller than 74 μm. They were subsequently mixed for 20 min with the C/O molar ratio of 1.2 before being pressed into composite briquettes of 10 mm in diameter and 15 mm in height with the addition of water as a binder. After drying in a vacuum oven at 105 °C for 4 h, the briquettes were reduced in a horizontal tube furnace or in a microwave tube furnace (Hunan Huae Microwave Technology Co. Ltd., China) at 1100 °C for different time under the nitrogen atmosphere. After cooling, the reduction products were used for characterization.

Characterizations

The chemical compositions of the samples were determined using an inductively coupled plasma optical emission spectrometer (ICP-OES, ICAP7400 Radial, ThermoFisher Scientific, USA). The phase compositions of the samples were determined using an X-ray diffraction spectrometer (XRD; D8 Advance, Bruker, Karlsruhe, Germany). The microstructural evolutions of the samples were determined using a scanning electron microscope (SEM; Sigma HD, Zeiss, Oberkochen, Germany) equipped with an energy dispersive X-ray spectrometer (EDS; EDAX Inc., Mahwah, USA). The values of complex relative permittivity (ε_r) and permeability (μ_r) of the samples at room temperature were determined with the mass ratio of the sample powder to microwave-transparent paraffin of 7/3 by a vector network analyzer (E5071C, Agilent Technology Co., Ltd., Palo Alto, CA, USA) using the transmission line method in the frequency range 2–18 GHz. The total contents and zerovalent contents of iron and chromium were determined by chemical titration. The particle sizes were determined using the software Nano Measurer based on the SEM images.

Results and Discussion

Permittivity and Permeability

The reduction efficiency of chromite ore in the microwave field highly depends on its microwave absorption capability [8], which relies on its corresponding complex relative permittivity and permeability [10], as shown in Fig. 3. The relative dielectric constants (ε_r'), dielectric loss factors (ε_r''), magnetic constants (μ_r'), and magnetic loss factors (μ_r'') of chromite ore at 2–18 GHz fluctuated in the ranges 3.62–3.81, 0.10–0.42, 0.83–0.99, and 0.09–0.43, respectively. At 2.45 GHz, the values of ε_r', ε_r'', μ_r', and μ_r'' of chromite ore were 3.71, 0.38, 0.98, and 0.34, respectively, indicating

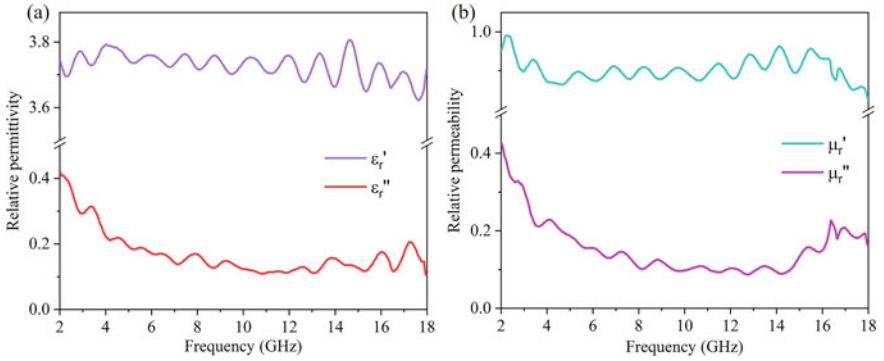

Fig. 3 Complex relative permittivities and permeabilities of chromite ore

similar contributions of dielectric loss and magnetic loss to the initial microwave heating of chromite ore [9].

Reduction Efficiency

The comparison of microwave and conventional reduction of chromite ore at 1100 °C for variable time is shown in Fig. 4. In both cases, increasing reduction time facilitated the reduction of chromite ore, thereby increasing the total contents of chromium (TCr) and iron (TFe), contents of zerovalent chromium (Cr^0) and iron (Fe^0), and metallization degrees of chromium (η_{Cr}) and iron (η_{Fe}). When conventional reduction time increased from 0 to 240 min, the values of η_{Cr} and η_{Fe} increased from 1.18 and 8.77% to 7.00 and 67.26%, respectively, as shown in Fig. 4a and b, indicating its strong time dependence. Compared to conventional reduction, the microwave reduction efficiency of chromite ore was obviously higher within a shorter reduction time, as shown in Fig. 4c and d. When the reduction time increased from 0 to 120 min, the values of η_{Cr} and η_{Fe} increased from 91.57 and 83.03% to 93.53 and 85.78%, respectively. It indicated that chromite ore could be mostly reduced at 1100 °C under microwave irradiation with a slight dependency on reduction time.

Phase Transformation

The comparison of phase composition between microwave reduction and conventional reduction of chromite ore for different periods of time is shown in Fig. 5. As shown in Fig. 5a, the main phases of the reduced briquettes obtained by conventional reduction at 1100 °C were $(Mg,Fe)(Cr,Al,Fe)_2O_4$, $Mg(Cr,Al)_2O_4$,

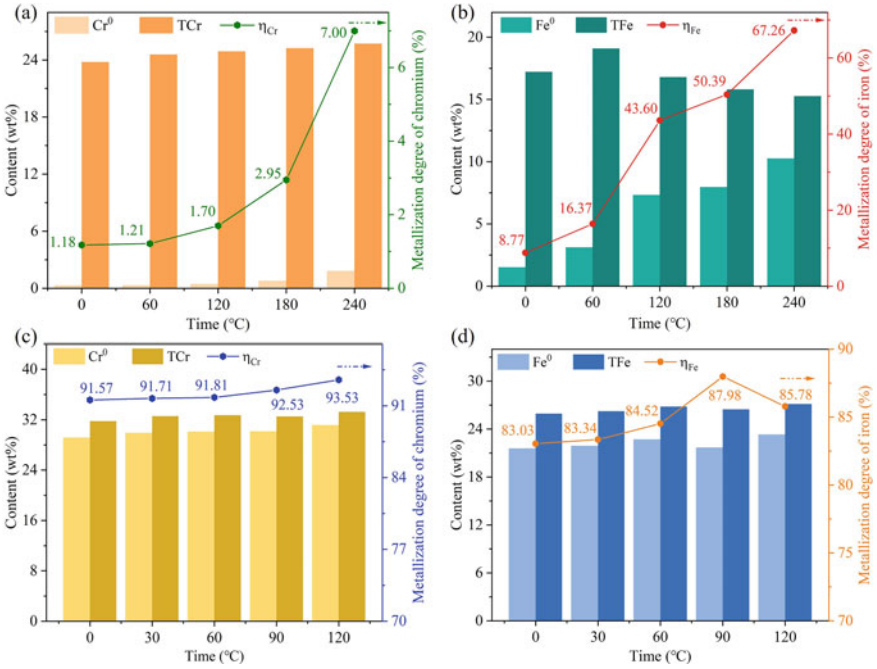

Fig. 4 Indexes of **a** and **b** conventional reduction and **c** and **d** microwave reduction of chromite ore

$(Mg,Fe)SiO_3$, and $(Fe,Cr)_7C_3$. With the extension of time, the intensity of diffraction peaks of $(Fe,Cr)_7C_3$ increased while the intensity of diffraction peaks of $(Mg,Fe)(Cr,Al,Fe)_2O_4$ and $Mg(Cr,Al)_2O_4$ decreased, which indicated the positive effect of increasing time on the reduction of chromite ore and the transformation of $(Mg,Fe)(Cr,Al,Fe)_2O_4$ to $Mg(Cr,Al)_2O_4$ and $(Fe,Cr)_7C_3$. Unlike those obtained in conventional reduction, the briquettes obtained after microwave reduction consisted of a few different phases, including $(Mg,Fe)(Cr,Al,Fe)_2O_4$, $(Fe,Cr)_7C_3$, $Mg(Cr,Al)_2O_4$, and $MgAl_2O_4$, as shown in Fig. 5b. The dominance of $Mg(Cr,Al)_2O_4$ and $MgAl_2O_4$ rather than $(Mg,Fe)(Cr,Al,Fe)_2O_4$ indicated the better reduction of chromite under microwave irradiation, which was probably associated with the stronger microwave response of spinel than other phases, such as silicates [13], enabling selective heating and rapid reduction of chromite under microwave irradiation. Besides, the phase composition had little changes with the increase of microwave reduction time. With the further extension of time, however, the intensity of diffraction peaks of $(Fe,Cr)_7C_3$ decreased while that of $MgAl_2O_4$ increased possibly attributed to further reduction of $Mg(Cr,Al)_2O_4$ to $MgAl_2O_4$ and more chromium in $(Fe,Cr)_7C_3$. Generally, due to the microwave selective heating of the spinel phases, including $(Mg,Fe)(Cr,Al,Fe)_2O_4$, $Mg(Cr,Al)_2O_4$, and $MgAl_2O_4$, $(Mg,Fe)(Cr,Al,Fe)_2O_4$ in the ore was initially reduced to $Mg(Cr,Al)_2O_4$ and finally

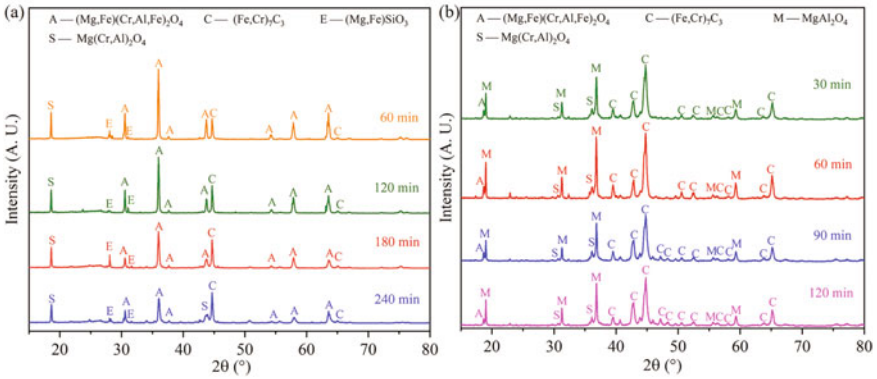

Fig. 5 XRD patterns of the briquettes **a** after conventional reduction and **b** microwave reduction

to $MgAl_2O_4$ under microwave irradiation, while $(Mg,Fe)(Cr,Al,Fe)_2O_4$ was only reduced to $Mg(Cr,Al)_2O_4$ by conventional reduction at 1100 °C.

Microstructural Evolution

The SEM–EDS analysis of the briquettes after conventional and microwave reduction at 1100 °C for different periods of time are shown in Fig. 6. After conventional reduction, the basic structure of chromite remained stable with the formation of a ring of small metallic particles around the surface of the spinel particles. The metallic particles, identified by corresponding EDS spectra which were absent for the sake of brevity, were iron and chromium carbides (Fe–Cr–C). Besides, enstatite particles $(Mg,Fe)SiO_3$ were also observed in the briquette. Increasing reduction time facilitated the reduction of spinel and thus the formation and growth of metallic particles. When the conventional reduction time increased from 60 (CR-60) to 240 min (CR-240), the average particle size of Fe–Cr–C phase increased from 0.94 to 2.20 μm, as shown in Fig. 7. Different from the conventional reduction of chromite ore, the reduced briquettes obtained by microwave reduction exhibited higher reduction efficiency by breaking the stable structure of chromite spinel, as revealed by the enrichment of iron in the spinel particle center and newly generated cracks. With the increase of microwave reduction time, the number and size of cracks in the sample increased, indicating the positive effect of microwave heating time on the reduction of chromite ore. Besides, the large Fe–Cr–C particles that were generated from chromite and connected by $Mg(Al,Cr)_2O_4$ phase also confirmed the better reduction of chromite ore under microwave irradiation. According to corresponding EDS spectra, the content of chromium in the Fe–Cr–C phase increased while the content of chromium in the $Mg(Al,Cr)_2O_4$ phase decreased with the extension of time, suggesting the reduction of chromium. In addition, as the microwave reduction time

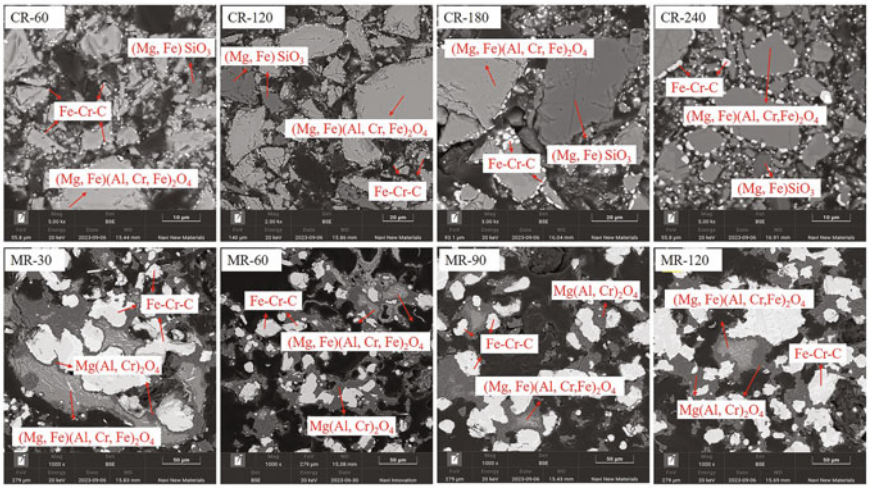

Fig. 6 SEM–EDS analysis of the briquettes after conventional and microwave reduction for different periods of time

increased, the average particle size of the Fe–Cr–C particles initially increased from 23.93 (MV-30) to 38.05 μm (MV-90) and then decreased to 24.49 μm (MV-120), as shown in Fig. 7.

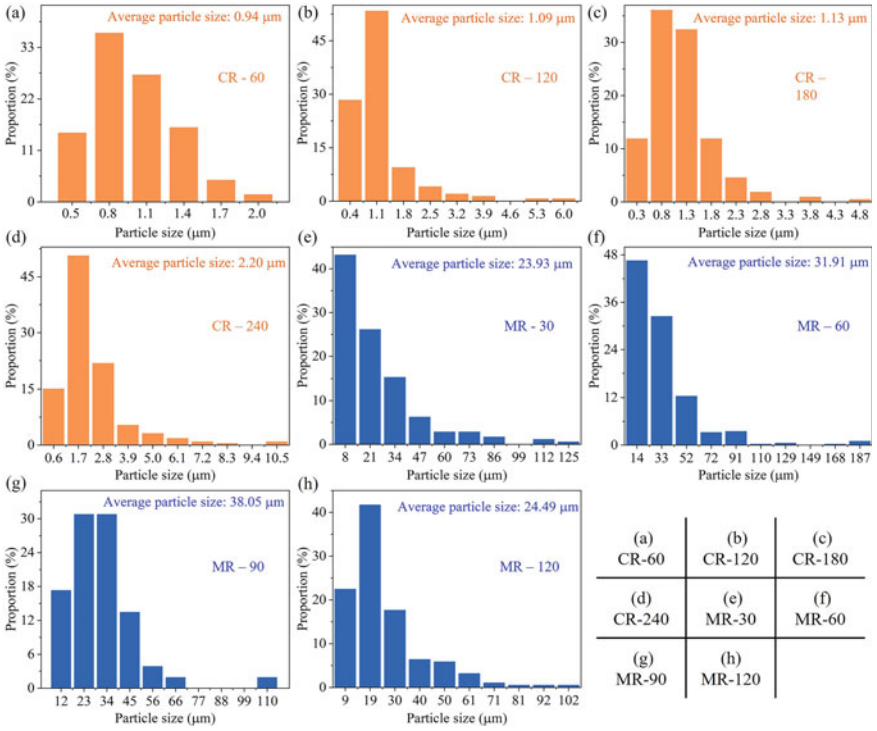

Fig. 7 Metallic particle sizes of the briquettes after conventional reduction and microwave reduction for different periods of time

Conclusion

The comparison between conventional and microwave reduction of chromite ore was investigated in this study with a focus on the effect of reduction time. Compared to conventional reduction, microwave reduction of chromite ore was more efficient by breaking the stable chromium-containing spinel structure, which was reported with better microwave response than silicates in chromite ore, enabling its rapid heating and reduction of spinel phases, including $(Mg,Fe)(Cr,Al,Fe)_2O_4$, $Mg(Cr,Al)_2O_4$, and $MgAl_2O_4$, under microwave irradiation. As a result, the metallization degrees of chromium and iron of the briquettes obtained after microwave reduction were higher than those after conventional reduction. By fixing reduction temperature of 1100 °C and C/O molar ratio of 1.2, the metallization degrees of chromium and iron of the briquettes constituted by chromite ore and coke under microwave irradiation increased from 91.57 and 83.03% to 93.53 and 85.78%, respectively, with increasing time from 0 to 120 min, which were higher than those obtained by conventional reduction for 4 h (7.00% for chromium and 67.26% for iron). In addition, the

average size of Fe–Cr–C particle in the briquettes after microwave reduction was 10–40 times larger than that of the briquettes after conventional reduction (23.93–38.05 vs. 0.94–2.2 μm).

Acknowledgements This work was partially supported by the National Natural Science Foundation of China under Grant 72088101.

References

1. Murthy YR, Tripathy SK, Kumar CR (2011) Chrome ore beneficiation challenges and opportunities: a review. Miner Eng 24:375–380
2. Nafziger RH (1984) A review of the deposits and beneficiation of lower-grade chromite. Metall Ore Dress Abroad 5:19–28
3. Tripathy SK, Murthy YR, Suresh N, Filippov LO (2021) Carbothermic reduction roasting for processing of ferruginous chromite ore using conventional and microwave heating. Adv Powder Technol 32:2234–2247
4. Kumar P, Patra SK, Tripathy SK, Sahu N (2021) Efficient utilization of nickel rich chromite ore processing tailings by carbothermic smelting. J Clean Prod 315:128046
5. Harsh R, Paswan DN, Jha SK (2016) Optimization of process parameter for smelting and reduction of ferrochrome. Int J Eng Res Technol 5:509–513
6. Zhang F, Zhu D, Pan J, Guo Z, Yang C (2019) Effect of basicity on the structure characteristics of chromium-nickel bearing iron ore pellets. Powder Technol 342:409–417
7. Yu D, Paktunc D (2019) Carbothermic reduction of chromite fluxed with aluminum spent potlining. Trans Nonferr Metal Soc 29:200–212
8. Ye Q, Peng Z, Li G, Liu Y, Liu M, Ye L, Wang L, Rao M, Jiang T (2021) Rapid microwave-assisted reduction of ferromanganese spinel with biochar: correlation between phase transformation and heating mechanism. J Clean Prod 286:124919
9. Hu T, Dai L, Guo Q, Liu B, Gui Q, Gang R, Ji H, Zhang L (2020) Dielectric properties of silicothermic reduction chromite in the microwave field. ACS Omega 5:12672–12681
10. Peng Z, Hwang J-Y (2015) Microwave-assisted metallurgy. Int Mater Rev 60:30–63
11. Parirenyatwa S, Escudero-Castejon L, Sanchez-Segado S, Hara Y, Jha A (2016) Comparative study of alkali roasting and leaching of chromite ores and titaniferous minerals. Hydrometallurgy 165:213–226
12. Xue Y, Zhu D, Pan J, Li G, Lv X (2023) Reduction of carbon footprint through hybrid sintering of low-grade limonitic nickel laterite and chromite ore. J Sustain Metall 9(2):648–664
13. Ma W, Wang J, Wu L (2018) Research on dielectric characterization of laterite ores under microwave radiation. J Microw Power Electromagn Energy 52:255–265

Upgrading Iron Ore by Microwave Desulfurization with Reduction of Harmful SO_2 Emission

Lei Ye, Ran Tian, Guanwen Luo, Huimin Tang, Jian Zhang, Mingjun Rao, and Zhiwei Peng

Abstract In this study, a novel method for simultaneously improving desulfurization of iron ore and lowering SO_2 emission in flue gas at low temperature by microwave roasting of the ore with the addition of urea was proposed. The results showed that the desulfurization percentage of iron ore increased significantly with lower SO_2 emission in flue gas when urea was added. By adding 1.5 wt% urea into iron ore and roasting the mixture at 250 °C for 60 min, the desulfurization percentage of roasted iron ore reached 67.37% and the SO_2 emission in flue gas decreased by 74.68%. After leaching of the roasted ore with water at room temperature for 30 min, the residual sulfur content of the leaching product decreased to 0.21 wt%. This study provided a good example for efficient, low-cost, and environmentally friendly desulfurization of iron ore.

Keywords Iron ore · Microwave irradiation · Urea · Desulfurization · SO_2 emissions · Water leaching

Introduction

With the rapid development of iron and steel industry, high-quality iron ore resources become gradually depleted [1]. The efficient utilization of refractory iron ore resources is of strategic significance for the industry [2, 3]. Among all refractory iron ores, sulfur-containing iron ore has attracted considerable attention owing to its abundant reserves [4, 5]. However, the strength of steel is negatively impacted by sulfur in iron ore. It is thus crucial to control the sulfur content in iron ore.

For desulfurization, various beneficiation methods have been employed [6] and their efficiency was limited by low iron grade, fine mineral distribution, and high gangue content in the iron ore [5, 7]. Thermal decomposition (roasting) is characterized as a simple and efficient desulfurization method because the sulfide minerals in

L. Ye · R. Tian · G. Luo · H. Tang · J. Zhang · M. Rao · Z. Peng (✉)
School of Minerals Processing and Bioengineering, Central South University, Changsha 410083, Hunan, China
e-mail: zwpeng@csu.edu.cn

Z. Peng et al. (eds.), *Characterization of Minerals, Metals, and Materials 2024*, The Minerals, Metals & Materials Series, https://doi.org/10.1007/978-3-031-50304-7_7

Table 1 Main chemical composition of iron ore (wt%)

Component	TFe	S	CaO	MgO	SiO_2	Al_2O_3	B_2O_3	P	Na_2O
Content	49.80	1.98	0.36	13.89	5.46	0.31	5.41	0.02	0.08

iron ore could be oxidized in the presence of oxidants and heat [8]. Compared with flotation processes and hydrometallurgical processes, however, roasting methods would release SO_2 to environment, causing harmful environmental impacts [9, 10]. It was reported that the desulfurization percentage of high-sulfur iron ore using conventional roasting method was relatively low even at 600 °C [11].

The sulfur in iron ore mainly exists in the form of iron sulfides, which are characterized as strong microwave absorbers (over 10 times than pure coal) [12, 13]. After oxidation in the roasting process, the SO_2 will emit into the flue gas, which should be purified. It was found that the SO_2 concentration in the flue gas would decrease sharply when it was injected through urea solution [14]. Therefore, it is anticipated that adding urea to iron ore can effectively desulfurize iron ore with reduction SO_2 emission in flue gas at low temperatures under microwave irradiation.

The purpose of this study was to develop a novel method for desulfurization of iron ore and flue gas at low temperature under microwave irradiation. The effect of urea addition on the desulfurization of iron ore and SO_2 emission in flue gas were determined.

Experimental

Materials

The iron ore used in this study was ludwigite ore, a typical sulfur-containing iron ore in China. The main chemical composition of iron ore is listed in Table 1. Figure 1 shows that the sulfur was mainly present in the form of pyrrhotite (Fe_7S_8). The average particle size of iron ore was 23.51 μm. Urea of analytical grade was used for reducing SO_2 emissions. The gas employed in this study consisted of 79% N_2 and 21% O_2.

Methods

Prior to the desulfurization test, urea was finely ground to particles smaller than 74 μm and mixed with iron ore at various mass ratios. Each mixture (mass: ~ 25 g) was then placed into a corundum crucible, which was subsequently transferred to a microwave tube furnace (maximum power: 1.4 kW, frequency: 2.45 GHz, Hunan Huae Microwave Technology Co. Ltd., China) for roasting at 250 °C for 60 min

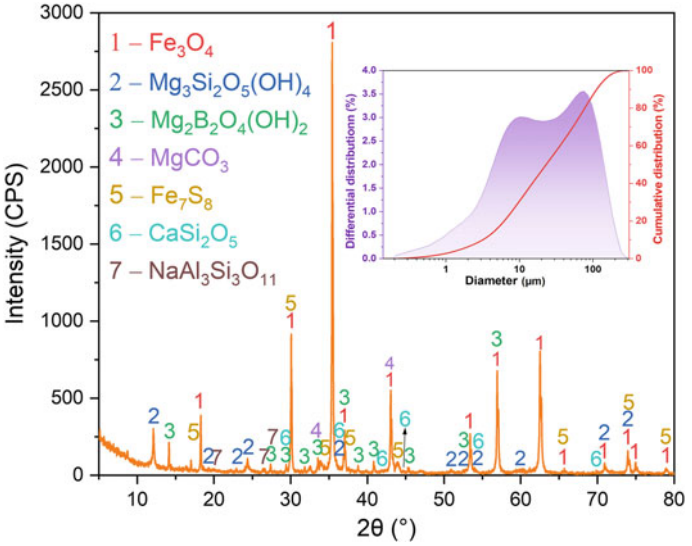

Fig. 1 XRD pattern and particle size distribution (inset) of iron ore

in the presence of an oxidizing gas flowing at a rate of 2.0 L/min. After cooling, the roasted ore was leached with water for 30 min at room temperature with a 20% solid-in-pulp concentration. The desulfurization percentage of the roasted ore (δ_R) was calculated based on Eq. (1).

$$\delta_R = \left(1 - \frac{m_1 \times \alpha_1}{m_0 \times \alpha_0}\right) \times 100\% \tag{1}$$

where m_0 is the mass of dried iron ore, g; α_0 is the sulfur content of dried iron ore, wt%; m_1 is the mass of roasted ore, g; α_1 is the sulfur content of roasted ore, wt%. The total mass of SO_2 (m_{SO_2}, mg) in the flue gas measured by flue gas analyzer can be calculated by Eq. (2) as follows:

$$m_{SO_2} = \int_0^t C_{SO_2} \times Q \times dt = Q \times \int_0^t C_{SO_2} dt \tag{2}$$

where C_{SO_2} is the SO_2 concentration in flue gas, mg/Nm^3; Q is the flow rate of flue gas equal to 2.0×10^{-3} Nm^3/min; t is the roasting time, min.

The relationship between standard Gibbs free energy changes of the relevant reactions and temperature was determined by calculation using the software FactSage 8.1 (Thermfact/CRCT, Montreal, QC, Canada; GTT-Technologies, Herzogenrath, Germany). The phase compositions of iron ore and roasted ore were determined by an X-ray diffraction spectrometer (XRD, D/max 2550PC, Rigaku Co., Ltd., Japan)

with a Cu anode having the wavelength of 1.54056 Å, step scan mode, and step length of 0.02°. The elemental distributions of the roasted ore and its leaching product were characterized using a scanning electron microscope (S4800, SIGMA HD, Nova 450, Japan). The SO_2 concentration in flue gas was detected using a specific flue gas analyzer (Photon, Madur Co., Austria).

Results and Discussion

Figure 2 shows the effect of urea addition on the desulfurization of iron ore. The standard Gibbs free energy changes of the main reactions involving the sulfur-containing component (i.e., Fe_7S_8) are given as equations (3)–(9).

$$4Fe_7S_8 + 21O_2 = 14Fe_2O_3 + 32S_2, \quad \triangle_r G_m^\theta = 0.75T - 3059.3\,\text{kJ/mol} \tag{3}$$

$$64CH_4N_2O + 4Fe_7S_8 + 85O_2 = 32(NH_4)_2SO_4 + 14Fe_2O_3 + 32N_2 + 64CO, \quad \triangle_r G_m^\theta = -4.68T - 3595.6\,\text{kJ/mol} \tag{4}$$

$$S_2 + 2O_2 = 2SO_2, \quad \triangle_r G_m^\theta = 0.016T - 305.3\,\text{kJ/mol} \tag{5}$$

$$2SO_2 + 2H_2O + O_2 = 2H_2SO_4, \quad \triangle_r G_m^\theta = 0.52T - 462.8\,\text{kJ/mol} \tag{6}$$

$$2SO_2 + O_2 + Mg_2SiO_4 = 2MgSO_4 + SiO_2, \quad \triangle_r G_m^\theta = 0.61T - 576.4\,\text{kJ/mol} \tag{7}$$

$$4NH_3 + 2H_2O + 2SO_2 + O_2 = 2(NH_4)_2SO_4, \quad \triangle_r G_m^\theta = 1.18T - 1013.2\,\text{kJ/mol} \tag{8}$$

$$2NH_3 + 2H_2O + 2SO_2 + O_2 = 2(NH_4)_2SO_4, \quad \triangle_r G_m^\theta = 1.10T - 792.5\,\text{kJ/mol} \tag{9}$$

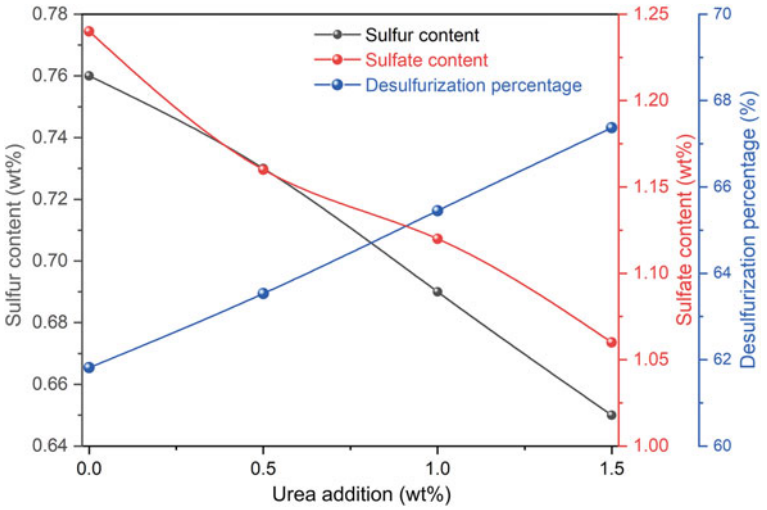

Fig. 2 Effect of urea addition on the desulfurization of iron ore

It can be concluded that all the above reactions are spontaneous below 400 °C according to thermodynamic analysis. It is generally known that compared with conventional heating, microwave heating can efficiently lower the needed temperature and dwell time of chemical reactions [15, 16]. The preliminary research suggested that the ideal desulfurization temperature for iron ore was 250 °C. As shown in Fig. 2, when the urea addition increased from 0 to 1.5 wt%, the sulfur content and sulfate content in the roasted ore decreased from 0.76 wt% and 1.24 wt% to 0.65 wt% and 1.06 wt%, respectively. It was reported that urea would decompose into biuret ($C_2H_5N_3O_2$) and ammonia (NH_3) when it was heated slowly [17]. The urea vapor and released NH_3 would react with SO_2 to form $(NH_4)_2SO_4$ or NH_4HSO_4, which could evaporate quickly under microwave irradiation. Figure 3 shows the XRD patterns of the roasted ore samples with different urea additions. As the urea addition increased, less $MgSO_4{\cdot}6H_2O$ and NH_4HSO_4 were observed, indicating that the presence of urea would compete with magnesium-containing phases to react with SO_2. Thus, the presence of urea not only decreased SO_2 emissions but also reduced the generation of sulfates of magnesium and other metals. Hence, there were considerable decreases of the sulfur content and sulfate content of the roasted ore.

Figure 4 shows the effect of urea addition on flue gas desulfurization. It was clear that the SO_2 concentration in flue gas presented triple-peak characteristics without the addition of urea. The initial peak of SO_2 created by Fe_7S_8 decomposition occurred at the roasting time of 8.37 min, with the peak value reaching 25,393.74 mg/Nm^3. With continuous roasting, lizardite in the iron ore began to decompose, releasing H_2O and forsterite (Mg_2SiO_4). Additionally, H_2O started to absorb SO_2 (i.e., $2SO_2 + 2H_2O + O_2 = 2H_2SO_4$), lowering the SO_2 concentration from 8.37 min to 20.37 min. It was consistent with the phase analysis of Mg_2SiO_4 in Fig. 3. The second peak

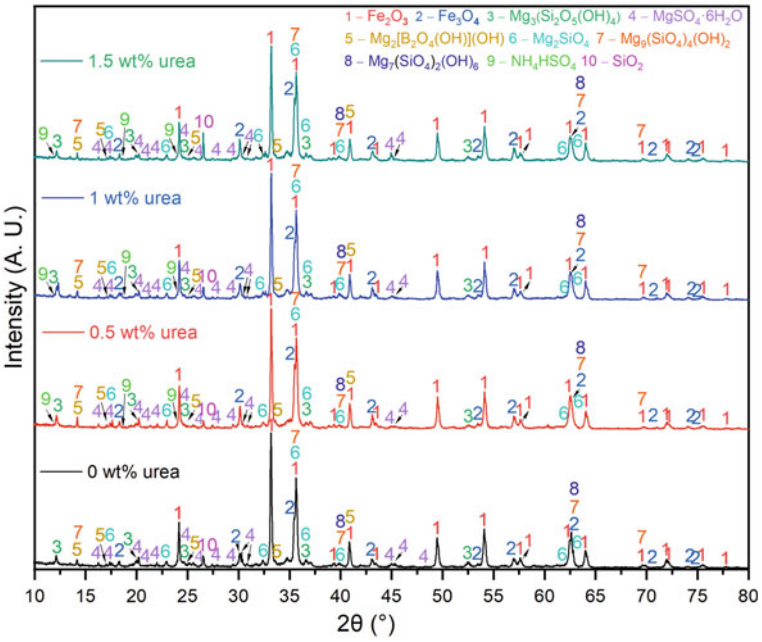

Fig. 3 XRD patterns of the roasted ore samples with different urea additions

of SO_2 occurred at 22.53 min, with the peak value reaching 15912.4 mg/Nm^3. It was attributed to the insufficient H_2O production from the gradual decomposition of lizardite. As the process continued, the temperature field in iron ore tended to be homogeneous due to thermal conduction. It was conducive to the chemical reaction between SO_2 and Mg_2SiO_4 with weaker microwave absorption capacity (i.e., $Mg_2SiO_4 + 2SO_2 + O_2 = SiO_2 + 2MgSO_4$). Consequently, the SO_2 concentration was further lowered until 32.9 min, also revealed by the phase analysis of SiO_2 in Fig. 3. The third peak occurred at 34.87 min with the value of 6162.21 mg/Nm^3, mainly caused by the insufficient metal oxides.

Compared with the SO_2 concentration in flue gas without addition of urea, roasting of the mixture of iron ore and urea significantly decreased the SO_2 emission in flue gas. The values of SO_2 concentration of the first peak were 8492.62 mg/Nm^3, 8505.42 mg/Nm^3, and 8330.10 mg/Nm^3 with the additions of 0.50 wt%, 1.0 wt%, and 1.5 wt% urea, respectively. As shown in Table 2, the SO_2 reduction percentages of flue gas were 24.72%, 66.91%, and 74.68%, respectively.

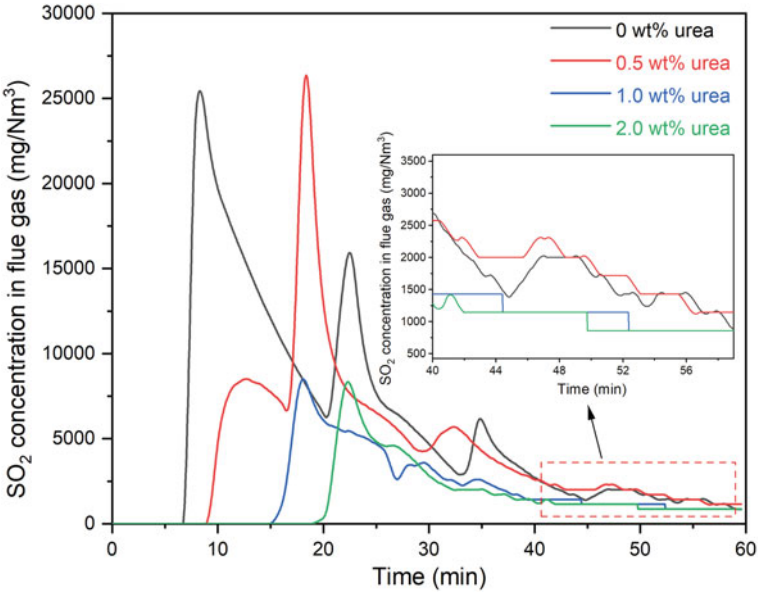

Fig. 4 Effect of urea addition on the flue gas desulfurization

Table 2 Effect of urea addition on the SO_2 reduction

Item	SO_2 mass (mg)	SO_2 reduction percentage (%)
No urea	684.81	–
0.5 wt% urea	515.52	24.72
1.0 wt% urea	226.61	66.91
1.5 wt% urea	173.37	74.68

To meet the requirements of iron ore in the steel industry, water leaching was carried out to further reduce the sulfur content in the roasted ore. According to Fig. 3, the main phase of sulfate in the roasted ore was water-soluble $MgSO_4{\cdot}6H_2O$ [18]. Table 3 shows the main chemical compositions of the roasted ore sample with 1.5 wt% urea addition (denoted by R_1) and its leaching product (denoted by R_2). Figure 5 shows their elemental distributions of O, S, and Mg. As can be seen from Fig. 5a–c, sulfur in to the roasted ore mainly existed in the form of $MgSO_4$. After water leaching at room temperature, the contents of S and Mg in leaching product, especially S, decreased significantly in Fig. 5e, f. Hence, iron ore containing 0.21 wt% S could be obtained by microwave roasting followed by water washing at room temperature. Meanwhile, the SO_2 emission in flue gas was effectively lowered.

Table 3 Main chemical compositions of the roasted ore and its water-leaching product (wt%)

Sample	TFe	S	CaO	MgO	SiO_2	Al_2O_3	B_2O_3	P	Na_2O
R_1	48.88	0.65	0.11	14.22	4.87	0.47	4.74	0.01	0.05
R_2	50.54	0.21	0.09	13.67	5.24	0.44	5.31	0.01	0.02

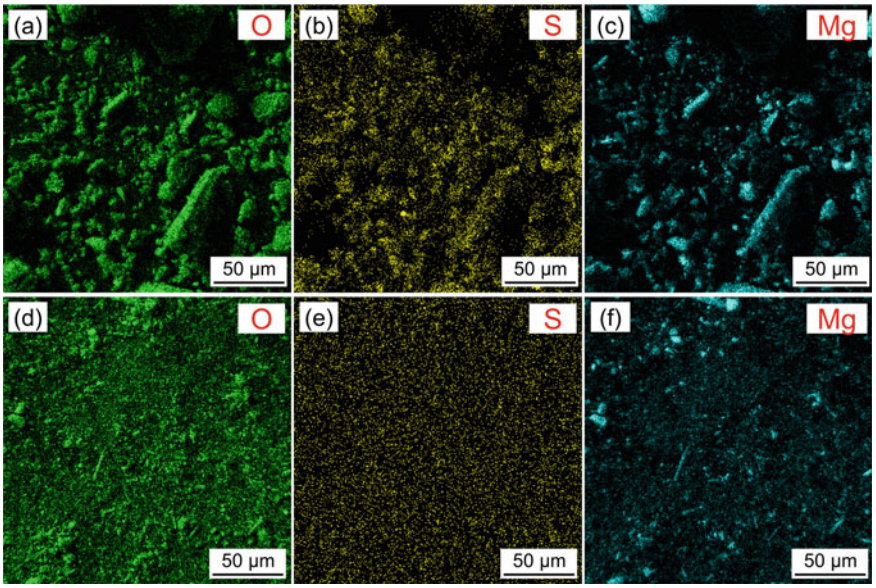

Fig. 5 EDS mapping analysis of **a**, **b**, and **c** the roasted ore and **d**, **e**, and **f** its leaching product showing the elemental distributions of O, S, and Mg

Conclusion

In this study, a novel method for simultaneously improving desulfurization of iron ore and lowering SO_2 emission in its flue gas by microwave roasting of the ore in the presence of urea. There were rapid SO_2 emissions from iron ore by microwave roasting at low temperatures, such as 250 °C. The addition of urea into iron ore was beneficial to desulfurization of both roasted ore and flue gas. Without the addition of urea, the SO_2 concentration in flue gas showed triple-peak characteristics due to the abundant lizardite in iron ore and the value of the first peak reached 25,393.74 mg/Nm^3 at 8.37 min. With the addition of 1.5 wt% urea, the value of the first peak only reached 8330.10 mg/Nm^3 at 22.33 min. By adding 1.5 wt% urea to iron ore and roasting the mixture at 250 °C for 60 min, the desulfurization percentage of the ore was 67.37% with the SO_2 emission in flue gas decreased by 74.68%. After leaching of the roasted ore with water at room temperature for 30 min, the residual sulfur content of the ore decreased to 0.21 wt%.

Acknowledgements This work was partially supported by the National Key Research and Development Program of China under Grant 2020YFC1909800 and the National Natural Science Foundation of China under Grant 72088101.

References

1. Sun W, Wang Q, Zhou Y, Wu J (2020) Material and energy flows of the iron and steel industry: Status quo, challenges and perspectives. Appl Energ 268:114946
2. Qin H, Guo X, Yu D, Tian Q, Li D, Zhang L (2023) Pyrite as an efficient reductant for magnetization roasting and its efficacy in iron recovery from iron-bearing tailing. Sep Purif Technol 305:122511
3. Yuan S, Zhou W, Han Y, Li Y (2019) Selective enrichment of iron from fine-grained complex limonite using suspension magnetization roasting followed by magnetic separation. Sep Sci Technol 55:3427–3437
4. Ye L, Peng Z, Tian R, Tang H, Zhang J, Rao M, Li G (2022) A novel process for highly efficient separation of boron and iron from ludwigite ore based on low-temperature microwave roasting. Powder Technol 410:117848
5. Yu J, Sun H, Li P, Han W, Li Y, Han Y (2023) A pilot study on recovery of iron from sulfur-bearing hematite ore using hydrogen-based mineral phase transformation followed by magnetic separation. J Environ Chem Eng 11(5):110630
6. Chandra AP, Gerson AR (2009) A review of the fundamental studies of the copper activation mechanisms for selective flotation of the sulfide minerals, sphalerite and pyrite. Adv Colloid Interf Sci 145(1–2):97–110
7. Liang Z, Yi L, Huang Z, Lu B, Jiang X, Cai W, Tian B, Jin Y (2019) Insight of iron ore-coal composite reduction in a pilot scale rotary kiln: a post-mortem study. Powder Technol 356:691–701
8. Rezvanipour H, Mostafavi A, Ahmadi A, Karimimobarakabadi M, Khezri M (2018) Desulfurization of iron ores: processes and challenges. Steel Res Int 89:1700568
9. Martin SC, Larivière C (2014) Community health risk assessment of primary aluminum smelter emissions. J Occup Environ Med 56(5):33–39
10. Chen R, Huang W, Wong CM, Wang Z, Thach TQ, Chen BH, Kan H (2012) Short-term exposure to sulfur dioxide and daily mortality in 17 Chinese cities: the China air pollution and health effects study (CAPES). Environ Res 118:101–106
11. Abzalov VM, Sudai AV, Yur'ev BP (2008) Desulfurization in roasting iron-ore pellets. Steel Transl 38(12):1003–1007
12. Marland S, Merchant A, Rowson N (2001) Dielectric properties of coal. Fuel 80(13):1839–1849
13. Tao X, Tang L, Xie M, He H, Xu N, Feng L, Yang Y, Luo L (2016) Dielectric properties analysis of sulfur-containing models in coal and energy evaluation of their sulfur-containing bond dissociation in microwave field. Fuel 181:1027–1033
14. Wang S, Bi X, Weng D (2013) Study on a new technology of flue gas desulfurization in sintering process. Adv Mater Res 726:2284–2290
15. Ye L, Peng Z, Tian R, Tang H, Anzulevich A, Rao M, Li G (2023) Efficient pre-reduction of chromite ore with biochar under microwave irradiation. Sustain Mater Technol 37:e00644
16. Li J, Guang M, Lu Y (2023) Effect of composition on low-temperature soda roasting of boron-rich blast furnace slag. J Sustain Metall 9:1215–1225
17. Chun T, Long H, Di Z, Zhang X, Wu X, Qian L (2017) Novel technology of reducing SO_2 emission in the iron ore sintering. Process Saf Environ 105:297–302
18. Zhang Y, Li Y, Guo H, Liu X, Cao J (2023) Experimental and calculated solubility isotherms of the quaternary NaBr–$MgBr_2$–Na_2SO_4–$MgSO_4$–H_2O system and its ternary subsystem at 298.15 K. J Chem Thermodyn 183:107040

Characterisation and Pre-concentration of a Pegmatite Columbite Ore for Niobium Extraction

Abraham Adeleke, Samson Adegbola, and Ayodele Daniyan

Abstract A columbite ore of pegmatite origin was characterised by subjecting it to energy dispersive X-ray fluorescence (XRF) and diffraction (XRD) analyses as well as scanning electron microscope-energy dispersive spectrometer (SEM–EDS) and Fourier Transform Infra-Red (FTIR) analysis. The sample was pre-concentrated with shaking table to upgrade its niobium content. The XRF analysis shows that the ore contains niobium and zirconium at 2.29 and 2.52 wt%, concentrations, respectively. The XRD chart gave prominent peaks at 2θ angles of 27.31, 30.38, 35.79, 38.07, 53.60, 55.92, and 63.70°, which indicate orthorhombic crystal structure of the columbite-iron ($FeNbO_4$) mineral phase. The SEM–EDS spot analyses showed points with Nb, Pt, Si, and Ta having 59.55, 34.03, 33.83, and 16.37 wt% concentrations, respectively. FTIR analysis reveals strong absorption band for Ta and Nb oxides in the regions 1100–1000 cm^{-1} and 900–800 cm^{-1}, respectively. Shaking tabling pre-concentration increased the Nb assay from 2.29 in the ore to 3.65 wt% in the concentrate.

Keywords Columbite · Tantalum · Pegmatite · Pre-concentration · Shaking table

Introduction

Niobium is a crucial component used in many high-tech products, including superconductors, electronics, and aerospace alloys, and its demand has increased significantly globally in recent years. Because the traditional supply chains for niobium are vulnerable to geopolitical disturbances, this increase in demand has motivated the exploration and development of alternate sources for niobium production. Due to their abundant presence in several geological formations globally and high niobium content, pegmatite columbite ores represent a viable supply of niobium [1]. The effective extraction of niobium from these ores, however, is a difficult and complex process that calls for the use of modern characterisation and pre-concentration procedures.

A. Adeleke (✉) · S. Adegbola · A. Daniyan
Department of Materials Science and Engineering, Obafemi Awolowo University, Ile-Ife, Nigeria
e-mail: adeadeleke@oauife.edu.ng

Z. Peng et al. (eds.), *Characterization of Minerals, Metals, and Materials 2024*, The Minerals, Metals & Materials Series, https://doi.org/10.1007/978-3-031-50304-7_8

Columbite is a mineral rich in tantalum and niobium, which accounts for a sizeable portion of the world's niobium reserves. Having a thorough understanding of the mineralogical and chemical properties of pegmatite columbite ores is essential to maximising their potential as a niobium resource. This entails thorough geochemical and mineralogical investigations, as well as the detection of related minerals and impurities that may have an impact on the effectiveness of niobium extraction [2].

The pre-concentration techniques are used to increase the ore's niobium content prior to the use of more advanced and expensive methods such as froth flotation to further upgrade the ore. By doing this, it is possible to greatly minimise the environmental effect and financial costs related to niobium mining, in addition to improving the overall recovery of niobium [3]. In order to optimise the niobium extraction procedures, this paper is primarily concerned with the characterization and pre-concentration of pegmatite columbite ores. To clarify the mineralogical composition and elemental distribution inside these ores, advanced analytical techniques such as X-ray diffraction (XRD), scanning electron microscopy (SEM), and chemical analysis will be used [4].

Experimental Procedures

Materials

The columbite ore used for this study was collected from three open pits within Edege-Mbeki, Nasarawa Local Government Area of Nasarawa State, north central Nigeria at latitude 08° 19′ 30″ N and longitude 70° 50′ 80″ E, with an area of about 400 km^2.

Instrumentation

Sieve analysis was used as a method of particle size distribution to obtain the particle distribution of the pulverized ore. The sieve size used for the analyses were 710, 500, 355, 250, 106, 75, 63, and 45 μm. The specific gravity of each sieve fraction was also determined to identify the particle size range with the highest concentration of mineral values.

The ore samples' mineralogical properties and phases were identified using GBC Difftech XRD with an X-ray generator operating at 0–60 kV and 0–80 mA. To identify the phases shown on the XRD chart, the diffraction peaks were analysed in relation to the JCPDS diffraction database. The scanning electron microscopy attached with (EDS) energy dispersive X-ray spectroscopy was used to determine the elements at random points on the pulverised columbite ore sample. The Fourier Transform Infra-Red spectroscopy (AGILENT) was used to confirm the absorption

band region of niobium and tantalum oxide. An energy-dispersive X-ray fluorescence (AMPTEK) was used to carry out the bulk chemical analysis of the columbite ore sample. Gravity pre-concentration of the ore was done using a Denver shaking table.

Results and Discussion

Chemical and Mineralogical Studies

The chemical analysis using ED-XRF shows that the mineral contains different minerals in their oxide forms. Niobium (Nb), which has a concentration of 2.29 wt%, as well as elements with significant concentrations such as Zr, which occurs as ZrO_2, and Fe, which occurs as Fe_2O_3, with wt% concentrations of 2.52 and 2.71, respectively. The elements Mn, Zr, Cr, and Si were also found in association with niobium and tantalum as reported in earlier literature [5]. Table 1 presents the results of the ED-XRF analysis.

Table 1 ED-XRF analysis of the columbite ore as-received in weight %

Elements	Compounds	Concentration (wt%)
K	K_2O	0.3936
Ca	CaO	0.0904
Ti	TiO_2	0.8897
V	V_2O_5	0.0419
Cr	Cr_2O_3	0.0243
Mn	MnO	0.2163
Fe	Fe_2O_3	2.712
Ni	NiO	0.0189
Cu	CuO	0.1127
Zn	ZnO	0.0297
Ga	Ga_2O_3	0.0541
As	As_2O_3	0.0532
Y	Y_2O_3	0.1238
Zr	ZrO_2	2.520
Nb	Nb_2O_5	2.288
Pb	PbO	0.0112

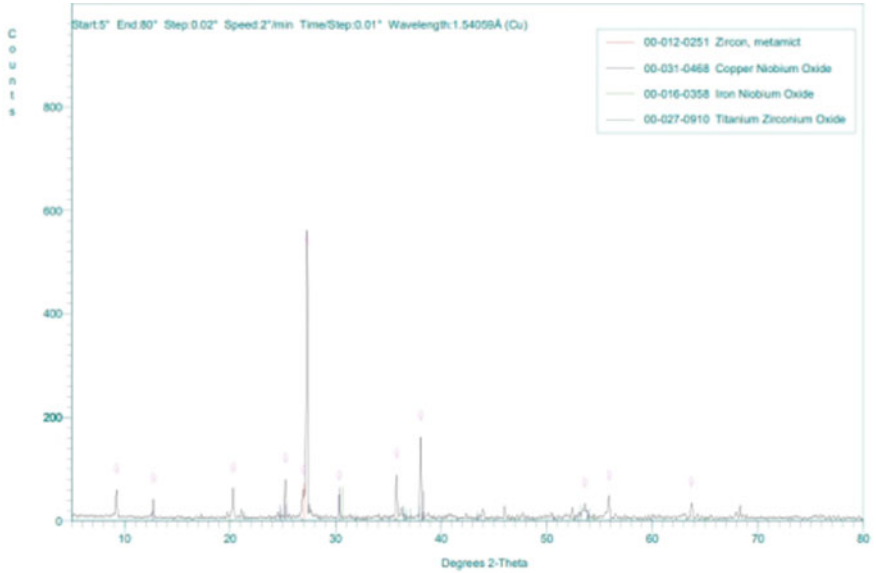

Fig. 1 X-ray diffractogram of the as-received columbite ore

XRD Analysis

Figure 1 shows the XRD diffractogram obtained for the columbite sample as received. It shows twelve distinct peaks that were not annotated. The most notable peak was found at 2θ angle 27.307 and it indicates an orthorhombic crystal structure phase. The remaining peaks at 2θ angles 30.38, 35.79, 38.07, 53.60, 55.92, and 63.70 show the $FeNbO_4$ phase. Since the phases at the peaks were not indicated by the diffractometer used, the sample's diffraction pattern was matched to those of known columbite patterns in the JCPDS database to determine the phases at the peak locations.

Scanning Electron Microscopy with Energy-Dispersive X-Ray Spectroscopy

The charts obtained (Fig. 2a–f) from SEM–EDS point analyses at six random points on the pulverised ore show the presence of different elements. The results show the presence of Nb at 23.62, 62.48, 54.29, and 59.55 wt% at spots 1, 2, 4, and 6, respectively. The element Pt was also found at points 1 and 4 at 34.03 and 10.89 wt%, respectively; while only point 6 gave Ta at 16.37 wt%. Spot 5 indicates a very high wt% concentration of Au at 36.87. This suggests that the ore contains few particles of gold-bearing minerals (Table 2).

Table 2 Summary of chemical compositions from SEM–EDS charts of selected spots on the pulverized columbite sample

Elements	Weights (%)					
	Spot 1	Spot 2	Spot 3	Spot 4	Spot 5	Spot 6
Al	12.89	–	18.58	–	12.43	–
Si	33.89	–	42.53	15.07	31.51	–
Fe	19.26	23.62	23.83	19.76	19.19	24.08
Pt	34.03	–	–	10.89	–	–
Nb	23.62	62.48	–	54.29	–	59.55
Ti	–	13.90	–	–	–	–
K	–	–	15.06	–	–	–
Au	–	–	–	–	36.87	–
Ta	–	–	–	–	–	16.37

FTIR

The FTIR chart shows significant absorption band in the regions of about 1100–1000 cm^{-1}, and 900–800 cm^{-1}, respectively. This indicates the existence of tantalum oxide and niobium oxide. The absorption is attributable to the stretching vibrations of the Ta–O and Nb–O bonds (Fig. 3).

Sieve Analysis

As presented in Table 3, the data were used to determine the particle size distribution of the columbite sample. From the cumulative weight percentage data, a cumulative particle size distribution curve was plotted. The curve provides a visual representation of the proportion of particles at different sizes.

Specific Gravity

The specific gravities of the ore and that of the different sieve fractions obtained from sieve analysis were determined. The highest specific gravity of 4.0 was obtained at the sieve fraction $-250 + 150$ μm. Since the major gangue mineral, silica, has a specific gravity of 2.65, which is substantially lower than this number, the result strongly suggests that value minerals of high specific gravities ṇare present in the size fraction.

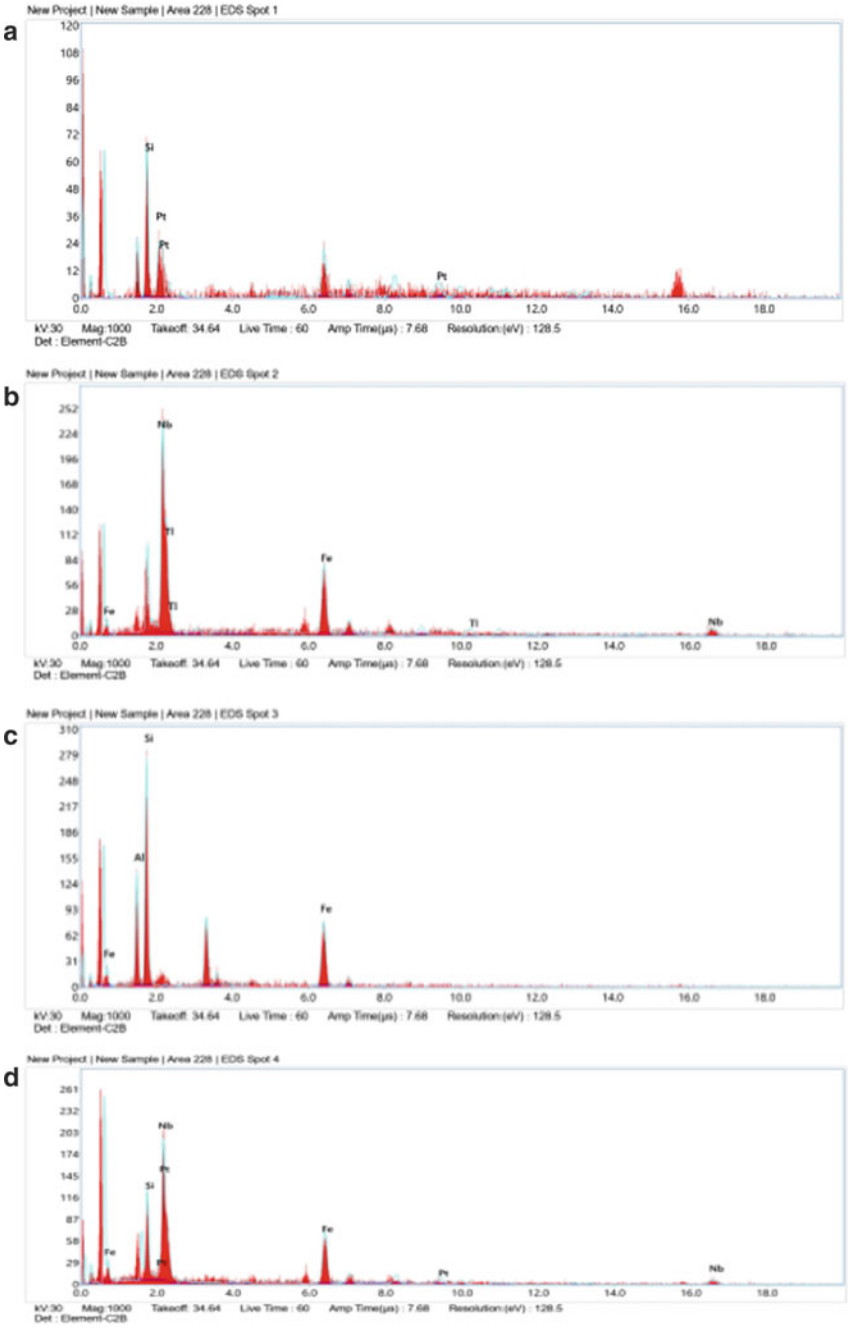

Fig. 2 **a** SEM–EDS of the columbite ore at point 1. **b** SEM–EDS of the columbite ore at point 2. **c** SEM–EDS of the columbite ore at point 3. **d** SEM–EDS of the columbite ore at point 4. **e** SEM–EDS of the columbite ore at point 5. **f** SEM–EDS of the columbite ore at point 6

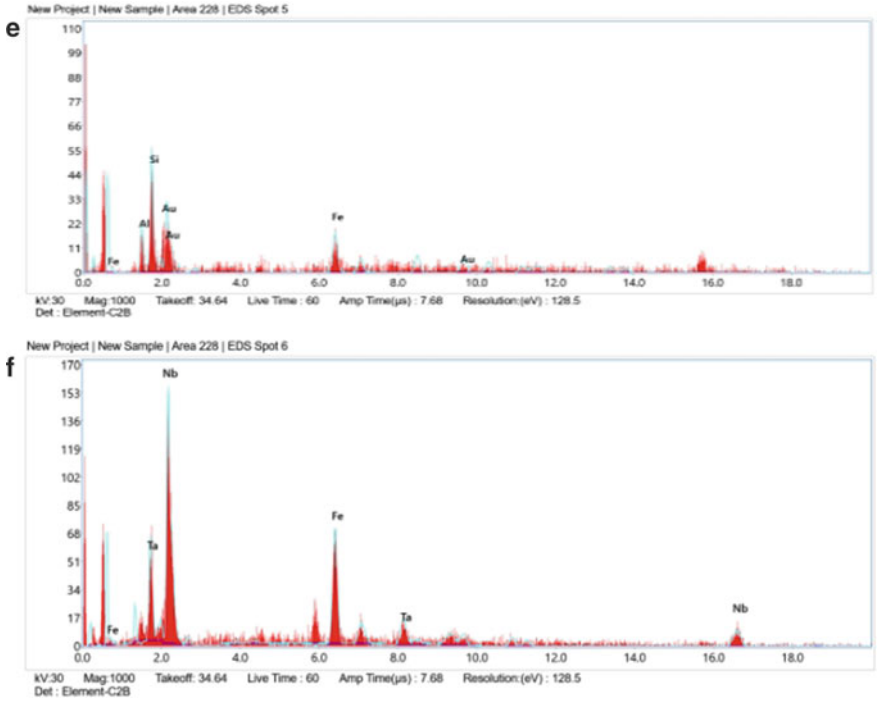

Fig. 2 (continued)

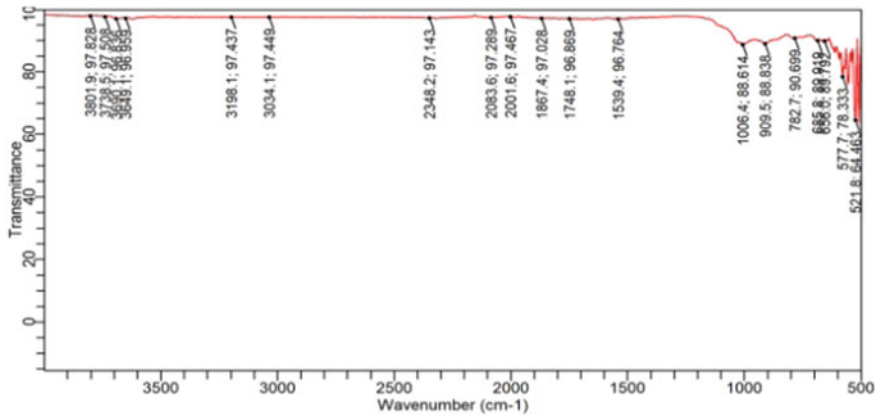

Fig. 3 FTIR of the columbite ore as-received

Table 3 Sieve analysis of the columbite ore

Sieve size (μm)	Nominal aperture size (μm)	Weight retained (g)	Weight retained (%)	Cumulative weight oversize (%)	Cumulative weight undersize (%)
+ 710	710	5.2	1.74	1.74	98.23
− 710 + 500	500	1.5	0.50	2.24	97.73
− 500 + 355	355	8.5	2.85	5.09	94.88
− 355 + 250	250	26.5	8.89	13.98	85.99
− 250 + 150	150	130.2	43.69	57.67	42.30
− 150 + 106	106	32.5	10.90	68.57	31.40
− 106 + 75	75	65.8	22.08	90.65	9.32
− 63	63	18.4	6.17	96.82	3.15
Pan	–	9.4	3.15	99.97	0
Total		298	99.97		

Gravity Separation Using Shaking Table

Changes in elemental composition concentration following gravity concentration using a shaking table show that niobium was successfully concentrated from other elements and enriched within the columbite sample. The XRF analysis of the shaking table concentrate is presented in Table 4.

The results obtained on the shaking table concentrate show that Nb, Ni, Zn, and Zr-bearing mineral particles were significantly concentrated by the gravity method. For example, Nb oxide content increased from 2.29 to about 3.66 wt%, while Zr oxide increased from 2.52 to 23.84 wt%. It was also observed that Ni oxide increased from 0.02 to 0.09 wt%, while Zn oxide was upgraded from 0.03 to 0.09 wt%.

Conclusions

The columbite ore was characterised and found to contain 2.29 wt% of Nb and various associated minerals of elements such as Fe, Sn, Zn, and Ti. The specific gravity of each of the size fractions of the sieve analysis was determined, and the − 250 + 150 μm size fraction that constitutes the largest proportion of particles gave the highest specific gravity of 4.0. Shaking tabling was performed as a method of gravity pre-concentration and the Nb content was upgraded from 2.29 to 3.66 wt%.

Table 4 XRF analysis of the columbite ore shaking table concentrate

Element	Compound	Concentration (wt%)
K	K_2O	0.1256
Ca	CaO	0.0148
Ti	TiO_2	0.0495
V	V_2O_5	0.0098
Cr	Cr_2O_3	0.0008
Mn	MnO	0.0619
Fe	Fe_2O_3	16.9443
Ni	NiO	0.0902
Cu	CuO	0.0511
Zn	ZnO	0.7951
W	WO_3	1.0095
As	As_2O_3	0.0000
Sn	SnO_2	3.1817
Cd	CdO	0.0000
Sb	Sb_2O_5	1.3346
Mo	MoO_2	0.1524
Nb	Nb_2O_5	3.6589
Rb	Rb_2O	0..2650
Pb	PbO	0.0000
Zr	ZrO_2	23.8422
Al	Al_2O_3	1.2332
Si	SiO_2	2.8778
P	P_2O_5	0.0275
S	S	0.0360

The research, therefore, indicates that the columbite ore is amenable to gravity pre-concentration prior to the application of more efficient beneficiation processes such as froth flotation and magnetic separation.

References

1. Alves A, Coutinho AR (2015) The evolution of the niobium production in Brazil. Mater Res 18:106–112. https://doi.org/10.1590/1516-1439.276414
2. Habinshuti JB, Munganyinka JP, Adetunji AR, Mishra B, Ofori-Sarpong G, Komadja GC, Onwualu AP (2021) Mineralogical and physical studies of low-grade tantalum-tin ores from selected areas of Rwanda. Results Eng 11:100248
3. Melcher F, Graupner T, Oberthür T, Schütte P (2017) Tantalum-(niobium-tin) mineralisation in pegmatites and rare-metal granites of Africa. S Afr J Geol 120:77–100. https://doi.org/10.25131/gssajg.120.1.77

4. Shikika A, Muvundja F, Mugumaoderha MC (2021) Extraction of Nb and Ta from a coltan ore from South Kivu in the DRC by alkaline roasting–thermodynamic and kinetic aspects. Miner Eng 163:106751
5. Guldris Leon L, Hogmalm KJ, Bengtsson M (2020) Understanding mineral liberation during crushing using grade-by-size analysis—a case study of the Penuota Sn–Ta mineralization, Spain. Minerals 10(2):164

Part IV
Metallurgical Processing Analysis and Characterization

Soda-Ash Roasting Behavior of Ludwigite Ore Under Different Oxygen Concentrations

Jinxiang You, Mingjun Rao, Zhiwei Peng, and Guanghui Li

Abstract Efficient and comprehensive utilization of the ludwigite ore in China has an important strategic significance. However, the significant challenge is the development of highly efficient boron and iron separation process. Soda-ash roasting proves to be a facile approach for boron activation and extraction, wherein magnetite frequently was converted to hematite, which affects the subsequent recovery of iron. This work investigated the phase transformations, microstructure evolution and magnetism changes of soda-ash roasted ludwigite ore under different O_2 concentrations at 1123 K. Results indicate that Fe_3O_4 was not obviously oxidized to Fe_2O_3 but reacted with MgO to form $Mg_xFe_{3-x}O_4$ and $Mg_yFe_{1-y}O$, when the O_2 concentration is not more than 5.0 vol%. As the O_2 concentration further increased, Fe_3O_4 was converted to Fe_2O_3 and $MgFe_2O_4$.

Keywords Ludwigite ore · Soda-ash roasting · Oxygen concentration · Spinel · Magnesiowüstite

Introduction

With the rapid development of Chinese industry, the boron demand has risen rapidly and is expected to continue to grow in future years [1]. Therefore, it is crucial to secure a guaranteed supply of boron. However, more than 75% of boron depends on imports currently. The ludwigite ore containing 5–8% B_2O_3, and other valuable components such as magnesia (MgO) and magnetite (Fe_3O_4), is a strategic and characteristic resource of boron with multiple-metal intergrowth of China [2]. It is therefore urgent to develop comprehensive and efficient utilization technology for the utilization of ludwigite ore.

Highly efficient separation of boron and iron from the ludwigite ore is the key challenge faced by scholars and industries. Many processes, including beneficiation,

J. You · M. Rao (✉) · Z. Peng · G. Li
School of Minerals Processing and Bioengineering, Central South University, Changsha 410083, Hunan, China
e-mail: mj.rao@csu.edu.cn

Z. Peng et al. (eds.), *Characterization of Minerals, Metals, and Materials 2024*, The Minerals, Metals & Materials Series, https://doi.org/10.1007/978-3-031-50304-7_9

pyrometallurgy, and hydrometallurgy, have been developed to treat the ludwigite ore [3–5]. Traditional beneficiation process is difficult to separate boron and iron entirely, due to the complex association between boron and iron minerals. Pyrometallurgical processes, including sintering-blast furnace method and pre-reduction-electric arc furnace melting method, are commonly employed to produce the hot metal. However, the existing problems hindered its industrial-scale application, such as the low capacity, large coke consumption, and low activity of the boron-rich slag. Hydrometallurgical processes face the issues of high consumption of acidic or alkaline leaching reagents and environmental pollution.

Soda-ash roasting followed by water leaching has emerged as an attractive way to active and extract of boron, which is regarded as one of the most efficient and facile approaches [6–9]. Boron-bearing minerals reacted with sodium carbonate to generate water-soluble sodium borate and simultaneously destroy the mineral structure. The activated boron and iron minerals can be separated by water leaching. However, the iron grade of leached residue did not increase, due to the low grade of B_2O_3. The iron grade after water leaching frequently failed to meet the requirement for the feed of blast furnace method. Hence, the leached ore needs further enrichment to improve the iron grade. On the premise of boron activation, efficient and facile enrichment of iron from ludwigite ore while ensuring considerable environmental, technical, and economic benefits would undoubtedly have market prospects and wide industrial appeal. A novel process of efficiently and selectively extracting boron and synchronous enrichment of iron concentrate from soda-ash roasted ludwigite ore has been proposed in our study.

In this work, the low-temperature (1123 K) soda-ash roasting behaviors of ludwigite ore under different O_2 concentrations were investigated. The effect of O_2 concentration on the phase transformations, microstructure evolution, and magnetism changes of roasted ores was studied to guide the comprehensive and efficient utilization of ludwigite ore.

Experimental

Materials

The ludwigite ore used in this study is derived from Liaoning Shougang Iron Born Co., Ltd., China. The ore contains 49.80% total iron, 5.41% B_2O_3, 13.89% MgO, and 5.46% SiO_2. The phase was composed of magnetite (Fe_3O_4), szaibelyite ($MgBO_2(OH)$), and lizardite ($Mg_3Si_2(OH)_4O_5$). The anhydrous sodium carbonate (Na_2CO_3) used in this study is an analytical reagent (AR) and the purity of gases, including N_2 and O_2 is higher than 99.99 vol%.

Methods

The ludwigite ore mixed with 20 wt% Na_2CO_3 was moisturized and briquetted. The furnace was heated to the target temperature and pure N_2 was introduced. Then the dry briquettes were loaded into a horizontal tube furnace for roasting, and the pure N_2 gas was replaced by the target mixture gases. After roasting, the samples were cooled to room temperature and collected for the tests.

Characterization

The chemical composition of the ludwigite ore was determined by chemical titration method and atomic absorption spectrum (AAS, Shimadzu, AA7000, Japan). The phase of the sample was analyzed by X-ray diffraction (XRD, D/Max 2500, RIGAKU, Japan) under the conditions of radiation: Cu Kα, scanning range: 10–80°/2θ, step size: 0.02°/2θ and scanning speed: 5°/min. The microstructure was characterized by a scanning electron microscopy (SEM, TESCAN, MIRA4, Czech) equipped with an EDAX energy dispersive X-ray spectroscopy (EDS). A vibrating sample magnetometer determined the saturation magnetization of roasted samples (VSM, LakeShore7404, USA). X-ray photoelectron spectroscopy (XPS) analysis was performed using a Thermo Fisher Scientific ESCALAB250Xi device. The iron species of roasted samples were determined by the chemical titration method.

Results and Discussion

Phase Transformations

According to the previous experimental results, the optimized roasting temperature and dosage of Na_2CO_3 for boron activation were 1123 K and 20 wt%, respectively. The effect of O_2 concentration (1.0–21.0 vol%) on the phase compositions of roasted samples was investigated. As shown in Fig. 1a, only magnetite was observed in the roasted ore, when the oxygen concentration was lower than 5.0 vol%, demonstrating that Fe_3O_4 was not oxidized to Fe_2O_3 under a low O_2 concentration. As the O_2 concentration increased to 5.0 vol%, the characteristic diffraction peaks of Fe_2O_3 and $MgFe_2O_4$ were found. With increasing O_2 concentration, the phase composition does not change, however, the intensity of diffraction peaks of Fe_2O_3 and $MgFe_2O_4$ was enhanced. Figure 1b shows that the diffraction peak attached to (311) plane was slightly shifted towards the small angle 2θ with the increase of O_2 concentration. This can be explained by the conversion of Fe_3O_4 to $MgFe_2O_4$ spinel. Figure 1c shows the MgO–Fe_3O_4 system binary phase diagram under different temperature and oxygen partial pressure with a MgO/(MgO + Fe_3O_4) molar ratio of 0.538 (calculated as raw

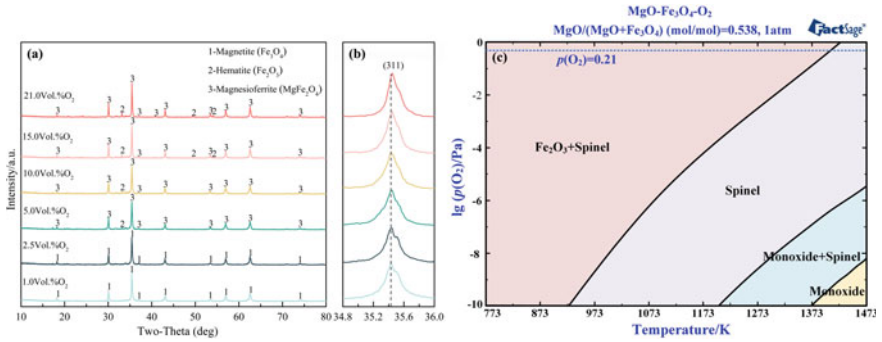

Fig. 1 **a** XRD patterns of roasted samples under different O_2 concentrations, **b** the large scale in the Miller index (311), and **c** MgO–Fe_3O_4 system binary phase diagram at different temperature and oxygen partial pressure with a MgO/(MgO + Fe_3O_4) molar ratio of 0.538

ore). With increasing oxygen partial pressure, the stable phase was transformed from spinel to Fe_2O_3 and spinel at 1123 K, which is consistent with the XRD results.

Microstructure Evolution

The microstructure evolution of roasted samples under different O_2 concentrations was investigated, and the results are shown in Fig. 2. SEM–EDS results in Fig. 2a, b and Table 1 show that the magnesiowüstite (Mg, Fe)O was observed (spot 2, 4), in addition of magnetite (Fe_3O_4). When the O_2 concentration is too low to oxidize Fe_3O_4 to Fe_2O_3, Fe_3O_4 would react with MgO to form $Mg_xFe_{3-x}O_4$ and $Mg_yFe_{1-y}O$. The EDAX results in Table 1 also indicate the presence of Mg in the magnetite phase (spot 1, 3). The possible chemical reactions are as follows:

$$Na_2CO_3 + Mg_2B_2O_5 = 2NaBO_2 + MgO + CO_2 \quad (1)$$

$$Na_2CO_3 + Mg_2SiO_4 = Na_2MgSiO_4 + MgO + CO_2 \quad (2)$$

$$Fe_3O_4 + MgO = Mg_xFe_{3-x}O_4 + Mg_yFe_{1-y}O \quad (x + y = 1) \quad (3)$$

SEM image in Fig. 2e shows the interface between magnetite and magnesiowüstite, and the line scanning spectrum in Fig. 2f shows that the Fe and Mg content sharply mutate with a vertically ascending or decreasing trend at the interface between $Mg_xFe_{3-x}O_4$ and $Mg_yFe_{1-y}O$. When the O_2 concentration increased to 10 vol%, the Fe_3O_4 was significantly oxidized to Fe_2O_3 and it presented a needle-like structure (spot 6). Meanwhile, the spinel phase ($MgFe_2O_4$) was observed (spot 5) (Fig. 2c). As the O_2 concentration further increased to 21 vol%, the reactions of

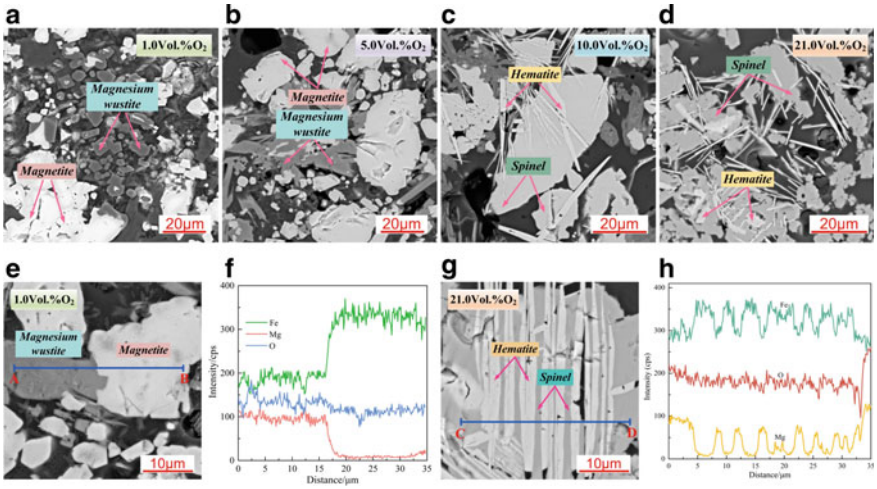

Fig. 2 SEM–EDS analysis of roasted samples under different O_2 concentrations. SEM images of roasted samples **a**, **e** 1.0 vol%, **b** 5.0 vol%, **c** 10.0 vol%, and **d**, **g** 10.0 vol% O_2. Elemental line scanning **f** 1.0 vol% and **h** 21 vol% O_2

Table 1 EDS composition analysis of spots is shown in Fig. 2

Spot	Element	Fe	Mg	O
1	wt/%	74.38	1.86	23.76
	at/%	46.03	2.64	51.33
2	wt/%	20.20	49.48	30.32
	at/%	8.43	47.42	44.15
3	wt/%	77.83	0.75	21.43
	at/%	50.43	1.11	48.46
4	wt/%	47.60	22.15	30.25
	at/%	23.33	24.94	51.74
5	wt/%	64.92	6.32	28.76
	at/%	36.10	8.07	55.83
6	wt/%	71.57	0.00	28.43
	at/%	41.91	0.00	58.09
7	wt/%	58.17	12.99	28.84
	at/%	30.83	15.82	53.36
8	wt/%	70.94	0.00	29.06
	at/%	41.42	0.00	58.58

oxidation of Fe_3O_4 to Fe_2O_3 and formation of $MgFe_2O_4$ forward more adequately (Fig. 2d). In addition, the interface between Fe_2O_3 and $MgFe_2O_4$ was observed (Fig. 2g), and line scanning was conducted, as shown in Fig. 2h. On the interface of hematite and spinel, the Fe content rapidly increased from the $MgFe_2O_4$ part to Fe_2O_3 part, however, the Mg content was just opposite to that of Fe. It is suggested that the Fe_3O_4 was first oxidized to Fe_2O_3, and then reacted with Mg-containing minerals to generate $MgFe_2O_4$ in the presence of Na_2CO_3 according to the following reactions.

$$Fe_3O_4 + O_2 = Fe_2O_3 \tag{4}$$

$$2Fe_2O_3 + Mg_2SiO_4 + Na_2CO_3 = 2MgFe_2O_4 + Na_2SiO_3 + CO_2 \tag{5}$$

$$2Fe_2O_3 + Mg_2B_2O_5 + Na_2CO_3 = 2MgFe_2O_4 + 2NaBO_2 + CO_2 \tag{6}$$

Magnetism Changes

Figure 3a shows the magnetic hysteresis loops of roasted samples under different O_2 concentrations. The magnetic hysteresis loops presented considerably small coercivity, which suggested that the samples exhibit soft magnetism. The saturation magnetization of roasted samples gradually decreased with the increase of O_2 concentration (Fig. 3b), of which the decline in magnetism is the fastest with the increase of O_2 concentration from 2.5 to 5.0 vol%. This can be explained by the abundant formation of $Mg_yFe_{1-y}O$ with poor magnetism. With the increase of O_2 concentration, more Fe_3O_4 was converted to Fe_2O_3 and $MgFe_2O_4$, resulting in the continued decrease in magnetism.

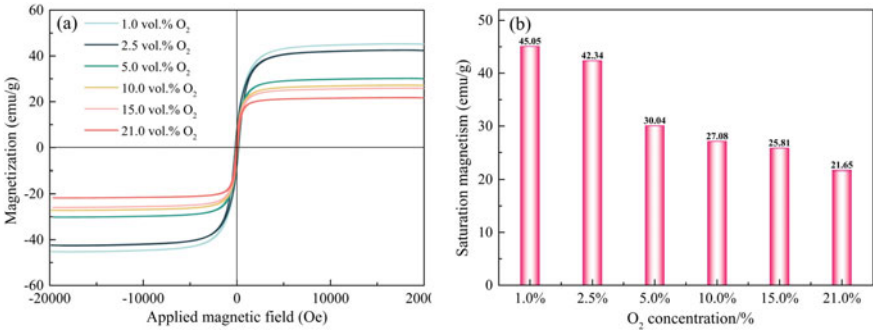

Fig. 3 Magnetic hysteresis loops (**a**) and saturation magnetism (**b**) of roasted samples under different O_2 concentrations

Chemical State

With increasing O_2 concentration, the Fe_3O_4 was gradually converted to Fe_2O_3 and $MgFe_2O_4$. The X-ray photoelectron spectroscopy (XPS) analyzer was conducted to check the chemical state of Fe and O on the sample surface. Figure 4a shows the variation of Fe 2p peak with the increasing O_2 concentration. According to the previous studies, the binding energies of Fe^{2+} and Fe^{3+} at Fe $2p^{3/2}$ are 709.6 eV and 710.8 eV, while those at $2p^{1/2}$ are 723.2 eV and 724.4 eV, respectively. The Fe 2p peak at Fe $2p^{3/2}$ became increasingly sharp with the increase of O_2 concentration, demonstrating the increase of Fe^{3+}/Fe^{2+} molar ratio in the roasted samples. The O 1 s spectra peak in Fig. 4b shows that the peak center was shifted towards the higher binding energy side with increasing O_2 concentration. Furthermore, the relative intensity of the fitted peak at 529 eV was significantly enhanced and shifted to the higher binding energy side, which indicates that the oxidation degree is gradually increasing.

Figure 5 shows the appearance of roasted ores under different O_2 concentrations. It was found that the presented color of roasted samples changed from black to reddish-brown with the increasing O_2 concentration.

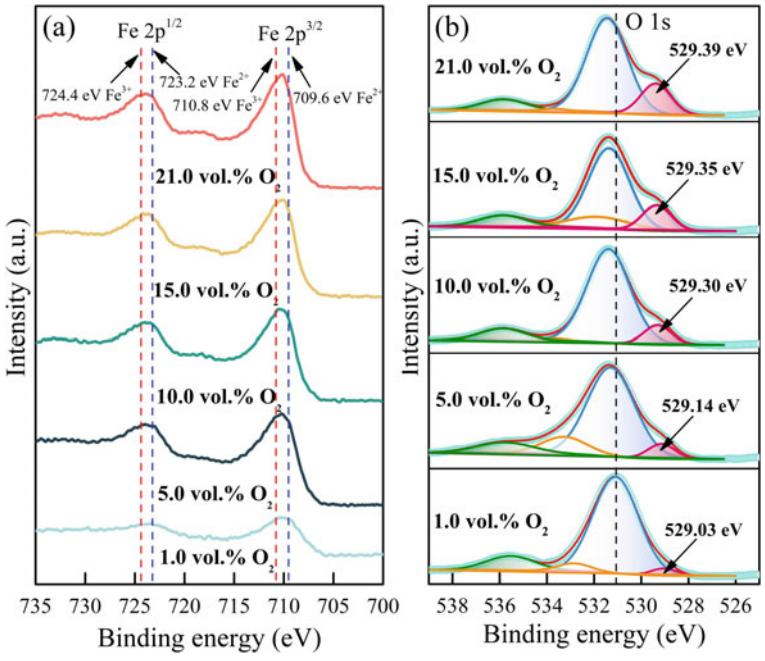

Fig. 4 XPS spectra of **a** Fe 2p and **b** O 1 s analysis of the roasted samples under different O_2 concentrations

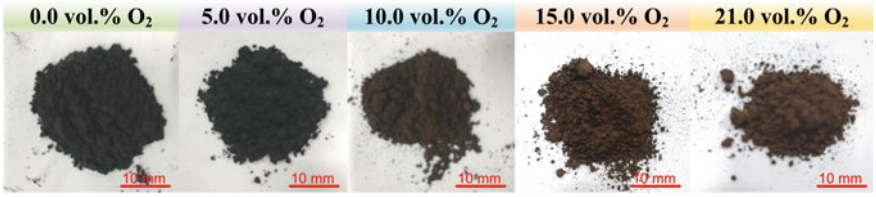

Fig. 5 Photographs of the roasted samples under different O_2 concentrations

Conclusions

The effect of O_2 concentration on the phase transformations, microstructure evolution, and magnetism changes of roasted ores was investigated. The conclusions are drawn as follows: XRD and SEM–EDS results indicate that when the O_2 concentration is not more than 5.0 vol%, Fe_3O_4 was not obviously oxidized to Fe_2O_3, and Fe_3O_4 reacted with MgO to form $Mg_xFe_{3-x}O_4$ and $Mg_yFe_{1-y}O$. As the O_2 concentration exceeded 5.0 vol%, Fe_3O_4 was evidently oxidized to Fe_2O_3, and then reacted with MgO to form $MgFe_2O_4$. VSM results suggest that the saturation magnetism decreased gradually with increasing O_2 concentration, and the decline in magnetism is the fastest with the increase of O_2 concentration from 2.5 to 5.0 vol%. XPS results show that the Fe^{3+}/Fe^{2+} molar ratio and oxidation level increased with the increase of O_2 concentration.

Acknowledgements This work was supported by the National Key Research and Development Program of China (2020YFC1909803), the Basic Science Center Project for the National Natural Science Foundation of China (Number 72088101), and the Graduate Research and Innovative Project of Central South University (506021739).

References

1. You J, Wang J, Luo J, Peng Z, Rao M, Li G (2022) A facile route to the value-added utilization of ludwigite ore: boron extraction and $M_xMg_{1-x}Fe_2O_4$ spinel ferrites preparation. J Clean Prod 375:134206. https://doi.org/10.1016/j.jclepro.2022.134206
2. Ye L, Peng Z, Tian R, Tang H, Zhang J, Rao M, Li G (2022) A novel process for highly efficient separation of boron and iron from ludwigite ore based on low-temperature microwave roasting. Powder Technol 410:117848. https://doi.org/10.1016/j.powtec.2022.117848
3. Wang G, Wang J, Ding Y, Ma S, Xue Q (2012) New separation method of boron and iron from ludwigite based on carbon bearing pellet reduction and melting technology. ISIJ Int 52(1):45–51. https://doi.org/10.2355/isijinternational.52.45
4. Liu S, Cui C, Zhang X (1998) Pyrometallurgical separation of boron from iron in ludwigite ore. ISIJ Int 38(10):1077–1079. https://doi.org/10.2355/isijinternational.38.1077
5. Fu X, Chu M, Gao L, Liu Z (2018) Stepwise recovery of magnesium from low-grade ludwigite ore based on innovative and clean technological route. Trans Nonferr Metal Soc 28(11):2383–2394. https://doi.org/10.1016/S1003-6326(18)64884-8

6. Li G, Liang B, Rao M, Zhang Y, Jiang T (2014) An innovative process for extracting boron and simultaneous recovering metallic iron from ludwigite ore. Miner Eng 56:57–60. https://doi.org/10.1016/j.mineng.2013.10.030
7. Liang B, Li G, Rao M, Peng Z, Zhang Y, Jiang T (2017) Water leaching of boron from soda-ash-activated ludwigite ore. Hydrometallurgy 167:101–106. https://doi.org/10.1016/j.hydromet.2016.11.004
8. Zhang X, Li G, You J, Wang J, Luo J, Duan J, Zhang T, Peng Z, Rao M, Jiang T (2019) Extraction of boron from ludwigite ore: mechanism of soda-ash roasting of lizardite and szaibelyite. Minerals 9(9):533. https://doi.org/10.3390/min9090533
9. Zhu Z, You J, Zhang X, Li G, Wang J, Luo J, Rao M, Peng Z, Jiang T (2020) Recycling excessive alkali from reductive soda ash roasted ludwigite ore: toward a zero-waste approach. ACS Sustain Chem Eng 8(13):5317–5327. https://doi.org/10.1021/acssuschemeng.0c00582

Effect of Pretreatment During Leaching of Chambishi Copper–Cobalt Air Roast–Leach Calcine Residue

Alexander Oniel Noel Old, Yotamu Rainford Stephen Hara, Phenny Mwaanga, Geshom Mwandila, Bawemi Sichinga Mtonga, and Emmanuel Chibwe

Abstract Copper–cobalt calcine leach tailings material from Chambishi township of Copperbelt province of Zambia is refractory in nature due to the presence of copper/cobalt silicate and residual sulphide minerals. With the aim of solubilizing copper and cobalt, the material was pre-treated by roasting in air alone and combination of air and elemental sulphur. As-received material was characterized by XRD and SEM techniques. Leaching without pre-treatment gave poor recoveries (< 45%) for copper and cobalt. Roasting of the feed material in air alone had no and little effect on improving leach efficiencies of copper and cobalt, respectively. On the other hand, copper and cobalt recoveries of 70 and 80% were obtained after roasting the feed material with elemental sulphur. The effects of roasting temperature and dosing of elemental sulphur were studied.

Keywords Copper · Cobalt · Chambishi · Zambia · Tailings

Introduction

Chambishi calcine leach tailings are rich in copper, cobalt, and gypsum. The tailings contain 1.0–1.8 weights % Cu, 0.1–0.4 weight % Co, and 25–30 weight gypsum with the balance being iron, silica, and aluminum oxide. The tailings dam covers an estimated area of 34 ha footprint containing about 2 million tons of tailings.

Since the tailings are from a calcine–leach process, it implies that copper is present as residual copper sulphide and/or acid insoluble phases such as silicate mineral phases. Froth flotation has been tried to upgrade copper and cobalt from this material but recoveries were very poor (less than 30%). The presence of high gypsum makes froth flotation a real challenge as it floats alongside copper sulphide. Furthermore, the tailings have an average particle size of about 68% passing 38 μm.

A. O. N. Old · Y. R. S. Hara (✉) · P. Mwaanga · G. Mwandila · B. S. Mtonga · E. Chibwe
The Copperbelt University, P.O. Box, 21692 Kitwe, Zambia
e-mail: yotamuhara@gmail.com

Z. Peng et al. (eds.), *Characterization of Minerals, Metals, and Materials 2024*, The Minerals, Metals & Materials Series, https://doi.org/10.1007/978-3-031-50304-7_10

It is important to investigate methods of processing these tailings owing to the following factors:

- The tailings are already ground and hence do not require comminution during processing.
- There is a worldwide demand for copper and cobalt [1–3].

As a result, this research focuses on extraction of copper and cobalt from Chambishi calcine leach tailings.

Sulphur may sulphate copper and cobalt silicates and ferrites according to reactions (1)–(4). Reactions (1)–(4) are thermodynamically feasible over a wide range of temperature.

$$CoFeSiO_4 + S + 1.5O_2 \rightarrow CoSO_4 + FeSiO_3 \quad (1)$$

$$CoFeO_2 + S + 2.5O_2 \rightarrow CoSO_4 + Fe_2O_3 \quad (2)$$

$$CuFeO_2 + S + 2.5O_2 \rightarrow CuSO_4 + Fe_2O_3 \quad (3)$$

$$CuFeSiO_4 + S + 1.5O_2 \rightarrow CuSO_4 + FeSiO_3 \quad (4)$$

Material and Methods

The material used was obtained from Chambishi calcine leach tailings. The material was collected from several different locations and levels of the tailings dump in order to obtain a representative sample. The individual samples obtained were combined and thoroughly homogenized using a riffle splitter. A sample from the bulk sample was obtained for the various test work and dried in an oven at 105 °C for 16 h in order to get rid of all the moisture present in the material. Screen analysis revealed that more than 99% of the material had a particle size of less than 0.425 mm. Furthermore, the total % moisture content and specific gravity of the material were found to be 18.17 and 2.78, respectively. The chemical analysis (by Rigaku Nex QC Quantez energy dispersive X-ray fluorescence and atomic absorption spectrometer) and the mineralogical characterization (by X-ray diffraction and scanning electron microscopy) of the tailings sample were determined prior to the concentration test works.

Roasting Tests

Pre-treatment roasting of the samples was carried out in air alone and the combination of air and elemental sulphur with the aim of solubilizing copper and cobalt [4–6]. For all roasting tests, sample particle size was kept constant at 100% passing 0.15 mm. Roasting in air alone was carried out at varying temperature (450–650 °C) at a step width of 50 °C and residence time of 1.5 h. Similarly, pretreatment roasting in air with the combination of elemental sulphur was conducted at a residence time of 1.5 h, however, the temperature was varied between 500 and 600 °C with a step width of 50 °C, this was as a result of the much higher recoveries of both copper and cobalt obtained in the temperature range between 500 and 600 °C as observed from pretreatment carried out in air alone. Upon completion of roasting, the samples were allowed to cool for about 30 min before being taken for leaching.

Leaching Tests

Leaching of the as-received tailings material was carried out at varying pH (1.0–2.2), while leaching after pre-treatment roasting was carried out at a constant pH of 1.8. However, the parameters' leaching temperature and pressure, residence time, and solid/liquid ratio were kept constant at room temperature and pressure (RTP), 1.5 h and 1:3, respectively. Flocculant was added to the leach slurry to promote solid/liquid separation. The leach solution was filtered off from the leach residue. The leach residues were washed in warm water to remove any entrained liquor and dried at 105 °C. The dried leach residues prepared for chemical analysis by digesting in concentrated acid. The analysis of all samples was done by atomic absorption spectrophotometer (AAS) and titration methods.

Chemical Analysis, Mineralogical Examination, and Sieve Analysis

For chemical analysis, a representative portion of the sample was dried at 105 °C then pulverized to 100% passing 75 μm and analyzed using a Rigaku Nex QC Quantez energy dispersive X-ray fluorescence for 4 min at a helium gas pressure of 100 kPa. The sample was further analyzed to confirm the composition of the trace elements by digesting in acid and analysis by atomic absorption spectrometer (Perkin Elmer Analyst 300).

Mineralogical examination of the samples was done by analysing the samples via X-ray diffraction and scanning electron microscopy techniques in order to understand the phases present in the material.

Table 1 Chemical analysis in weight % of the as-received Chambishi tailings

Cu_{Total}	ASCu	Co_{Total}	ASCo	Fe_2O_3	SO_3	CaO	SiO_2	Al_2O_3	TiO_2	As
1.60	0.52	0.28	0.13	30.92	31.46	22.11	11.66	1.44	0.31	0.01

X-ray diffraction analysis was carried out using Rigaku Miniflex bench top XRD with Cu Kα (0.15417 nm) radiation, at an acceleration voltage of 40 kV, current of 15 mA, and step size of $2\theta = 0.02°$. The samples were analyzed for 2θ between 5° and 80°. The phases present in the powder diffraction patterns were identified by using the X'Pert HighScore Plus software.

For characterization using scanning electron microscopy, the as-received sample was cold-mounted in epoxy resin. The mounted sample was ground and polished down to less than 1 μm. The sample was scanned under backscattered electron imaging in which the heavy and light phases (particles) appear bright and dark, respectively. The individual phases were quantified via SEM–EDX point analysis.

Results and Discussion

Characterisation of the Feed Material

Chemical Analysis

Chemical composition showing the major constituents of the tailings material is shown in Table 1. It can be observed from Table 1 that the material contains 1.60 weight % total copper (TCu) and 0.28 weight % total cobalt (TCo). More than 30% of the total copper and cobalt contained in the sample is acid soluble. The major gangue constituents are SiO_2, CaO, Al_2O_3, and Fe_2O_3.

Sieve Analysis

Screen analysis for the as-received tailings material is shown in Table 2. The following can be observed from Table 2 [7];

i. 99.37 wt% of the material has a particle size of less than 0.425 mm.
ii. Copper and cobalt are more concentrated in the finer size fractions (+ 0.038 and − 0.025 mm), while iron is more concentrated between + 0.075 and + 0.038 mm.
iii. More than 60 wt% of the tailings material has a particle size < 0.025 mm.

Table 2 Sieve analysis of the as-received Chambishi tailings

Screen size (mm)	Wt. retained	% Wt. retained	Cumm % retained	Cumm % passing	% Weight	
					Cu	Co
+ 0.425	5.48	0.63	0.63	99.37	0.447	0.138
− 0.425 + 0.300	5.93	0.68	1.31	98.69	0.587	0.160
− 0.300 + 0.212	12.34	1.42	2.73	97.27	0.936	0.185
− 0.212 + 0.150	32.32	3.71	6.44	93.56	1.320	0.202
− 0.150 + 0.106	11.70	1.34	7.78	92.22	1.430	0.199
− 0.106 + 0.075	88.76	10.19	17.97	82.03	1.470	0.199
− 0.075 + 0.053	39.18	4.50	22.47	77.53	1.660	0.244
− 0.053 + 0.038	76.55	8.79	31.26	68.74	2.520	0.372
− 0.038 + 0.025	65.85	7.56	38.82	61.18	2.120	0.309
− 0.025 (Pan)	532.90	61.18	100.00	0.00	1.740	0.329
Total	871.01	100.00	–	–	–	–

Mineralogical Characterization

XRD pattern for the as-received Chambishi tailings sample is shown in Fig. 1. It can be observed from XRD pattern in Fig. 1 that the major phases are quartz (SiO_2), anhydrite ($CaSO_4$), and Albite. The iron-bearing phases are hematite (Fe_2O_3) and magnetite (Fe_3O_4). On the other hand, the copper and cobalt-bearing phase peaks could not be detected in the sample because they are below the detection limit.

Scanning electron microscope images under backscattered electron imaging for the as-received tailings sample are shown in Fig. 2. Several phases can be observed in Fig. 2. Energy dispersive X-ray point analysis showed that most of the copper exists as a free mineral which is predominantly contained in the sulphide minerals (chalcocite and chalcopyrite) and partly in the phyllosilicate mineral (chrysocolla), iron–silicate phase (fayalite).

Leach of the As-Received Material

The results for leaching of the as-received material at various pH are shown in Fig. 3 from which the following important observations can be made:

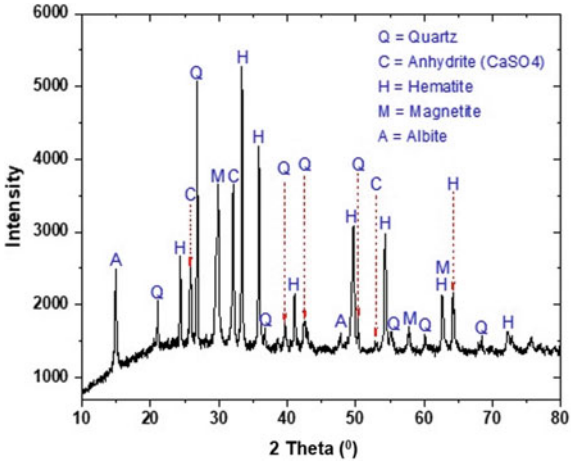

Fig. 1 XRD powder diffraction for the as-received Chambishi tailings sample

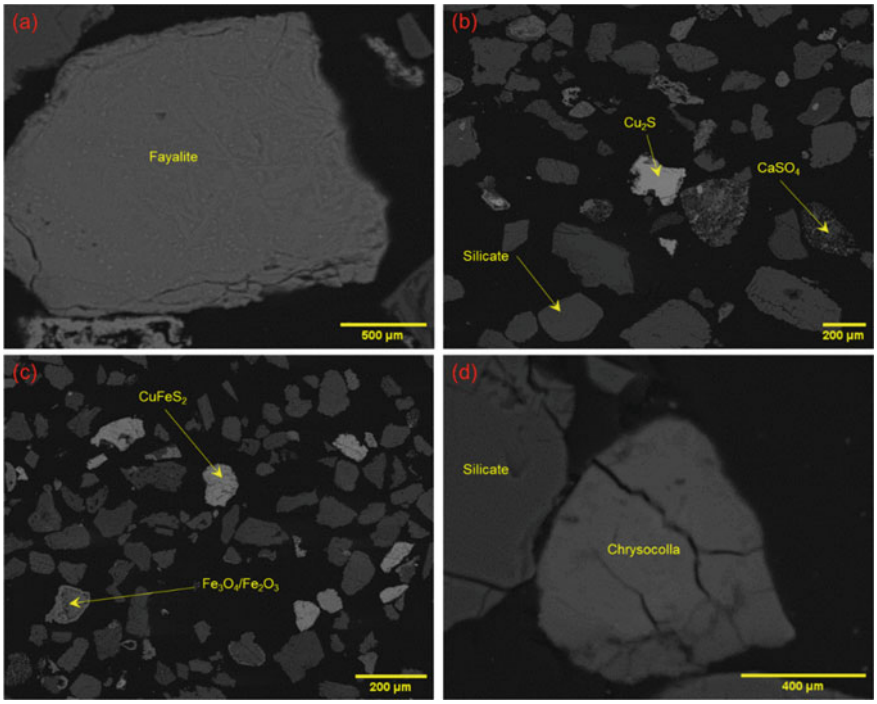

Fig. 2 Scanning electron microscope under backscattered electron imaging for the as-received tailings sample

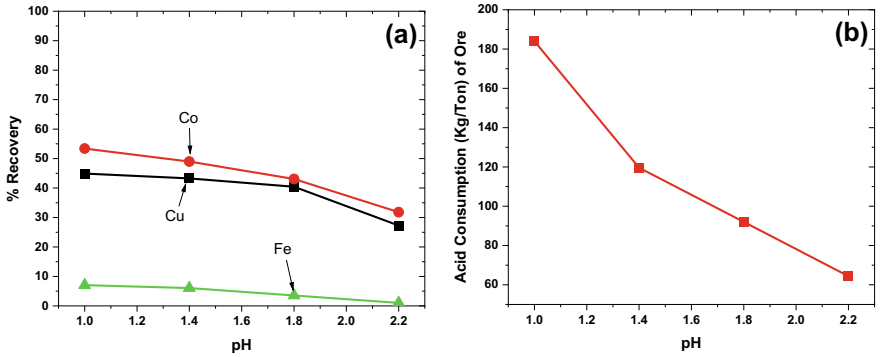

Fig. 3 Plot of **a** % recovery and **b** acid consumption (kg/ton) of ore against pH

i. The highest recovery for copper and cobalt attained at a pH of 1.0 was 44.92% and 53.40%, respectively.
ii. The recovery of iron was low for all leaching pH (< 10%) and this is because iron is present in complex forms.
iii. Recoveries of copper, cobalt, and iron decrease with increase in pH resulting in a corresponding decrease in acid consumption.
iv. Acid consumption was greater than 100 kgs per ton of material for pH below 1.4.

Based on the results in Fig. 3b, it can be concluded that the optimum leaching pH for the tailings is 1.0, however, the acid consumption was extremely high (> 100 kg/ton) of material.

Air Roasting of the Tailings Material

The results for leaching after pretreatment roasting in air alone at different temperatures are shown in Fig. 4 from which the following important observations can be made:

v. The highest recovery of copper was obtained at 550 °C where as the recovery of cobalt was highest at 450 °C. On the other hand, the recovery of copper and cobalt were comparable at 600 °C.
vi. The recovery of iron was extremely low for all roasting temperature (< 1%), this might have been due to the presence of complex mineral phases.
vii. Roasting temperature had no effect on the recovery of iron in the tailings material.
viii. Acid consumption increased as temperature increased from 450 to 600 °C and decreased as the temperature went beyond 600 °C.

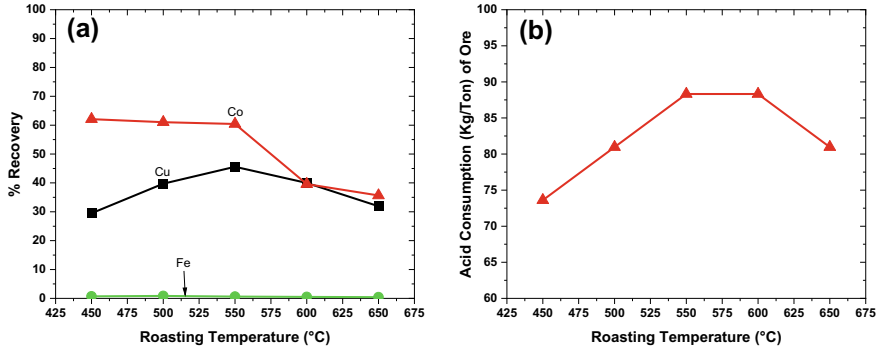

Fig. 4 Plot of **a** % recovery and **b** acid consumption (kg/ton) of ore against roasting temperature

Based on the results in Fig. 3, it can be concluded that the optimum roasting temperature for the recovery of both copper and cobalt lies between 500 and 600 °C.

Roasting of the Tailings with Elemental Sulphur Addition

In order to study the effect of elemental sulphur dosing, the tailings were subjected to pretreatment roasting at temperatures ranging from 500 to 600 °C at a step width of 50 °C, as established earlier. The elemental sulphur was pulverized to 100% passing 0.15 mm and combined with the tailings material in the following percent ratios (10, 20, 30, and 50%) and subjected to roasting. The results from leaching of calcine are graphically presented in Fig. 5. The following important observations can be based on the results in Fig. 5:

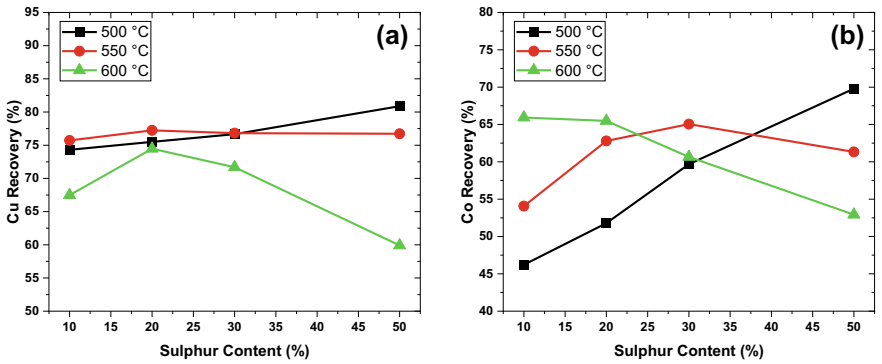

Fig. 5 Effect of sulphur addition during roasting of samples

1. The optimum temperature for the recovery of both copper and cobalt is 500 °C.
2. Recoveries of copper and cobalt generally increase with increase in sulphur addition at roasting temperatures of 500 and 550 °C.
3. Recoveries of copper and cobalt are maximum at 20 weight % elemental sulphur addition, decreases beyond this point.

Conclusions

1. As-received material has 1.6 and 0.28 weight % total and cobalt, respectively. More than 30% of the total Cu and Co are acid soluble.
2. Energy dispersive X-ray point analysis showed that most of the copper existed as free mineral, which was predominantly contained in the sulphide minerals (chalcocite and chalcopyrite) and partly in the phyllosilicate mineral (chrysocolla).
3. Sieve analysis revealed that copper and cobalt were more concentrated in the finer size fractions (+ 0.038 mm and − 0.025 mm), while iron was more concentrated between + 0.075 mm and + 0.038 mm.
4. The highest recovery for copper and cobalt for leaching of the tailings without any pre-treatment was 44.92% and 53.40%, respectively.
5. The optimum roasting temperature for the recovery of both copper and cobalt during pretreatment roasting in air was between 500 and 600 °C.
6. The optimum temperature for the recovery of both copper and cobalt for pretreatment roasting in air with the addition of elemental sulphur was established to be 500 °C.
7. Acid consumption was less than 40 kg per ton of material. This was a result of the sulphur added during pretreatment roasting, see Fig. 5.

Acknowledgements The authors would like to thank the National Science and Technology Council (NSTC) for the financial support.

References

1. Elshkaki A et al (2016) Copper demand, supply, and associated energy use to 2050. Glob Environ Chang 39:305–315
2. Hawkins M (2001) Why we need cobalt. Appl Earth Sci 110(2):66–70
3. Roberts S, Gunn G (2014) Cobalt. In: Critical metals handbook, pp 122–149
4. Bing L, Tongjiang P, Hongjuan S (2020) Innovative methodology for sulfur release from copper tailings by the oxidation roasting process. J Chem 11
5. Sánchez M et al (2004) Management of copper pyrometallurgical slags: giving additional value to copper mining industry. In: VII international conference on molten slags fluxes and salts. The South African Institute of Mining and Metallurgy
6. Ozer M (2019) Cobalt and copper recovery from the ancient flotation tailings by sulfation roast—leaching process. J Min Metall Sect B

7. Barry AW, Napier-Munn T (2006) Mineral processing technology: an introduction to the practical aspects of ore treatment and mineral recovery. Elsevier Science & Technology Books
8. Davila-Pulido G, Uribe-Salas A (2013) Effect of calcium, sulphate and gypsum on copper-activated and non-activated sphalerite surface properties. Miner Eng

Assessing MgO/Al_2O_3 Effect on Limonitic Laterite Sintering Process

Yikang Tu, Yuanbo Zhang, and Zijian Su

Abstract Sintering-blast furnace process is one of the most common methods for treating limonitic laterite. To reduce the negative impact of high aluminum content on the viscosity of blast furnace slag, adjusting the MgO/Al_2O_3 ratio of sinter is simple and effective. However, the effect of MgO/Al_2O_3 on the sintering process of limonitic laterite is still not clear. In this study, the effect of MgO/Al_2O_3 ratio on the output and quality indexes, phase compositions, and liquid phase content of sinter was investigated detailly. The results indicated that within the range of MgO/Al_2O_3 of 0.1–0.4, the output and quality indexes of the limonitic laterite sinter showed minimal fluctuations. While the value exceeded 0.4, the liquid phase content in the sinter significantly decreased, leading to a reduction of sinter strength. The MgO content in the liquid phase approached saturation after 0.4 MgO/Al_2O_3, further increasing the ratio would cause MgO to accumulate in spinel.

Keywords MgO/Al_2O_3 · Limonitic laterite · Sintering

Introduction

Pyrometallurgical smelting processes are regarded as the mainstream methods to treat limonitic laterite, in which sintering-blast furnace process is widely used for ores with low nickel and high iron on account of its lower energy consumption and cost [1–4]. As the amount of low aluminum limonitic laterite ($Al_2O_3 < 5\%$) decreased, the proportion of high Al_2O_3 ore in the sintering-blast furnace process continued to increase. Consequently, the Al_2O_3 content in the blast furnace slag rose, leading to an increase in slag viscosity and difficulties in the separation of slag and iron. Hence, it was common to promote the MgO content of sinter to improve the smelting of high Al_2O_3 furnace materials, thus enhancing the metallurgical performance of blast furnace slag [5–7].

Y. Tu · Y. Zhang (✉) · Z. Su
School of Minerals Processing and Bioengineering, Central South University, Changsha 410083, Hunan, China
e-mail: sintering@csu.edu.cn

Z. Peng et al. (eds.), *Characterization of Minerals, Metals, and Materials 2024*, The Minerals, Metals & Materials Series, https://doi.org/10.1007/978-3-031-50304-7_11

As the MgO content of sinter is closely related to Al_2O_3, the concept of MgO/Al2O3 has been proposed and widely recognized. The effect of MgO/Al_2O_3 on the microstructure of iron sinter had been studied. 1.22 was confirmed to be a suitable value for MgO/Al_2O_3, and an excessively high MgO/Al_2O_3 would cause acicular SFCA (composite calcium ferrite composed of SiO_2, Fe_2O_3, FeO, CaO, and Al_2O_3) to change to a plate shape, reducing the strength of the iron sinter [8]. Pure substance synthesis experiments indicated that $MgO/Al_2O_3 = 0.46–0.59$ facilitated the transformation of SFCA from an octahedral structure to a more stable tetrahedral structure, enhancing the microhardness of SFCA [9]. Despite some effects of MgO/Al_2O_3 on the iron sinter, the research on the impact on limonitic laterite sinter remained vacant. Furthermore, the Al_2O_3 content of limonitic laterite sinter (around 7%) was generally much higher than that of ordinary iron sinter (about 2%), so studying the impact of MgO/Al_2O_3 on the limonitic laterite sintering process was meaningful.

The effect of MgO/Al_2O_3 on the sintering performance of limonitic laterite had been studied systematically via sintering pot experiments. The influence of MgO/Al_2O_3 on the phase composition, yield, quality, and liquid phase components of limonitic laterite sinter was considered. The work was of great importance in strengthening the laterite sintering process.

Experimental

Materials

The limonitic laterite used in this study is derived from Philippines. The iron grade and alumina content were, respectively, 52.61 and 6.19%. In addition, the content of Ni_{total}, Cr_2O_3, FeO, CaO, SiO_2, and MgO in limonitic laterite was 0.69%, 3.45%, 2.51%, 0.06%, 2.22%, and 0.59%, respectively. The LOI reached up to 10.72% due to high crystal water. The iron concentrate was used for enhancing pelletization, whose iron grade and FeO contents were 67.84% and 28.75%, respectively. The flux used throughout this study was quicklime with 72.21% CaO content, and the dolomite contained 43.31% CaO and 28.41% MgO. The iron grade of the return ore was 50.92%, in which the FeO content was 23.25%. Besides, the content of Ni_{total}, Cr_2O_3, CaO, MgO, SiO_2, and Al_2O_3 in the return ore was 0.81%, 4.52%, 7.69%, 2.17%, 4.35%, and 6.82%, respectively. The determination of Fe_{total} and FeO depended on ISO 2597-1:2006 EN and ISO 9035:1989 EN, respectively. The content of other elements was obtained by ICP measurement after sample dissolution.

Methods

Experimental Procedure

The pilot-scale sintering tests were carried out in a laboratory sintering pot. Firstly, preparing mixture: limonitic laterite, iron concentrate, return ore, anthracite, flux, and water were weighed according to the designed parameters and mixed evenly. All samples were rotated for 5 min in a drum granulator with a diameter of 600 mm and a length of 300 mm, and the resulting granular sintering mixture was obtained. In the second step, sintering: the mixture was distributed to a sintering pot with a diameter of 100 mm and a height of 500 mm for ignition and exhaust sintering until the sintering process was finished, at which exhaust gas temperature reached the maximum value. The schematic diagram of the sintering pot is shown in Fig. 1. The ignition negative pressure and sintering negative pressure were 5 kPa and 7 kPa, respectively. After reaching the sintering end point, the negative pressure was adjusted to − 5 kPa and kept for 5 min to cool the sinter, then the sinter was poured out from the sintering pot and further cooled to the room temperature. At last, treatment of the sinter: the yield, tumble index, particle size distribution, and other properties of the sinter were measured after the sinter was cooled according to the previous literatures [10–14].

Characterization

The phases of the powder were tested by X-ray diffraction (XRD, D/Max 2500, RIGAKU, Japan). The chemical composition of the samples was determined by plasma emission spectrometer (ICP-AES, Icap7400 Radial, Thermo Fisher Scientific, USA) after dissolution.

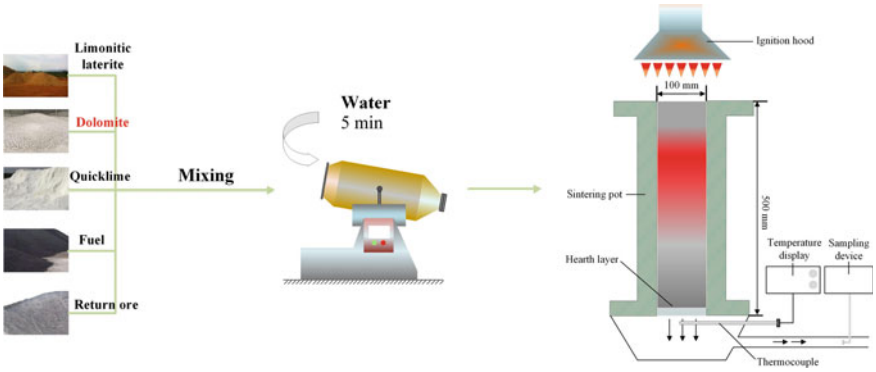

Fig. 1 Flowsheet of the limonitic laterite sintering process

Assessment Indexes

The productivity was calculated by Eq. (1). The tumbler index (TI) of the sinter was tested by 1/10 ISO 3271-2007, and calculated by Eq. (2). Sintering speed ($V_{\perp}$) was calculated by Eq. (3).

$$P = (m_1 - 0.25)/(m_0 - 0.25) \times 100\% \tag{1}$$

$$TI = M_1/M_0 \times 100\% \tag{2}$$

$$V_{\perp} = H/t \tag{3}$$

In Eq. (1), m_1 is the weight of the sinter with particle size greater than 5 mm (kg); m_0 is the total weight of sinter (kg); 0.25 is the weight of hearth layer (kg). In Eq. (2), M_0 is the total weight of sinter before tumbler (kg); M_1 is the weight of sinter with particle size greater than 5 mm after tumbler (kg). In Eq. (3), H is the height of sinter green bed (mm); t is the sintering time (min).

Results and Discussion

Effect of the Addition of Alloy Powder on Limonitic Laterite Sintering Performance

According to the preliminary experimental exploration, the optimized experimental conditions of 1.8 basicity and 19.5% moisture of the mixture were determined [15]. The influence of the MgO/Al_2O_3 ratio on yield and quality index of limonitic laterite sinter was systematically discussed. The dolomite was applied to adjust the MgO/Al_2O_3 of limonitic laterite sinter.

Figure 2 shows the impact of MgO/Al_2O_3 on the sintering performance of limonitic laterite. The initial MgO/Al_2O_3 of the sinter was 0.12 without dolomite addition. Within the range of $MgO/Al_2O_3 = 0.12$–0.4, the yield and tumble index of the sinter increased slowly. The yield and tumbling index respectively achieved their maximum values of 70.33 and 52.90% at 0.4 MgO/Al_2O_3. Meanwhile, the sintering speed continuously decreased, reaching the lowest value of 25.00 mm min^{-1} under 0.4 MgO/Al_2O_3. When MgO/Al_2O_3 exceeded 0.4, the yield and tumble index decreased, and the sintering speed increased. To ensure the output and quality indicators of the sinter, the suitable MgO/Al_2O_3 was found to be 0.12–0.4.

Two samples with different MgO/Al_2O_3 were chosen for phase analysis. The XRD analysis of Fig. 3 demonstrates that the main phases of the two samples were wustite and spinel containing Mg, Al, Cr, and Ni. Moreover, the diffraction peak intensities of 36.5° and 42.1° decreased while the MgO/Al_2O_3 exceeded 0.4, and it

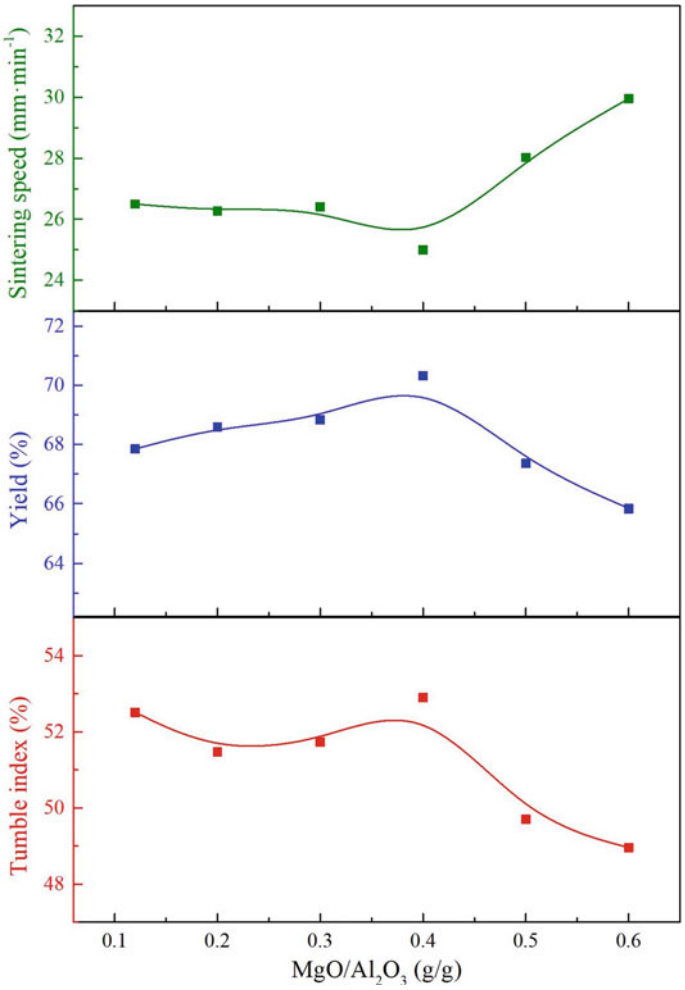

Fig. 2 Effect of MgO/Al_2O_3 on the limonitic laterite sintering performance

might be owing to the exorbitant MgO/Al_2O_3 made the sintering combustion zone narrow and the high temperature holding time shortened.

The reduction performance of two representative sinters is shown in Table 1. When the MgO/Al_2O_3 was 0.4 and 0.6, the reducibility index (RI) of sinter was close, which was 67.01% and 68.36%, respectively. In addition, the MgO/Al_2O_3 had no obvious effect on the low-temperature reduction index (RDI) of the two sinters, and the $RDI_{+6.3}$ and $RDI_{+3.15}$ both exceeded 96% and 98%, respectively.

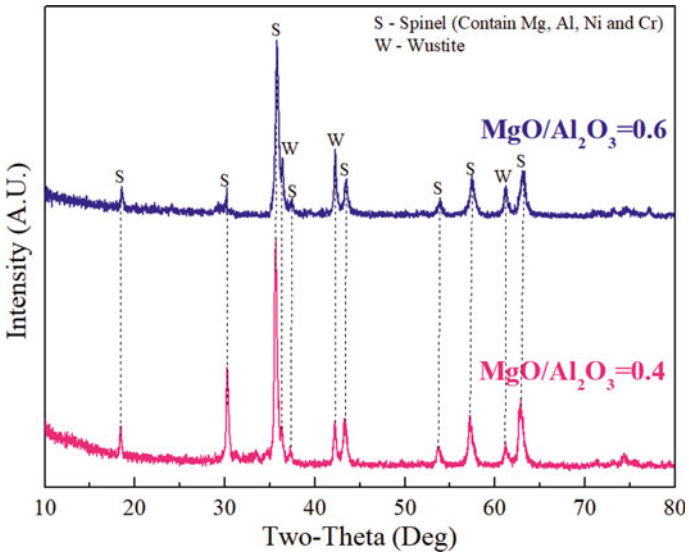

Fig. 3 XRD pattern of the representative limonitic laterite sinter

Table 1 Effect of MgO/Al_2O_3 on reduction performance of limonitic laterite sinter (%)

MgO/Al_2O_3	RI	RDI		
		+ 6.3 mm	+ 3.15 mm	− 0.5 mm
0.4	67.01	97.23	98.42	0.76
0.6	68.36	96.37	99.15	0.13

Thermodynamic Analysis of Phase Composition of Sinter Under Different MgO/Al_2O_3

Based on the chemical composition of limonitic laterite sinter (2.68% MgO, 6.70% Al_2O_3, 40.11% Fe_2O_3, 7.36% CaO, 4.40% SiO_2, 3.67% Cr_2O_3, 0.98% NiO, 29.10% FeO), the effect of MgO/Al_2O_3 on theoretical mineral composition of limonitic laterite sinter at different temperatures is shown in Fig. 4. The temperature range was chosen as 1250–1300 °C according to the high temperature zone during the sintering process. The theoretical mineral composition of the sinter was monoxide, spinel, bredigite, melilite, and liquid phase. As usual law, the content of liquid phase in sinter increased with the rise of temperature in the consistent MgO/Al_2O_3. As shown in Fig. 4a, the liquid phase content of sinter would be less than 1% after 0.4 MgO/Al_2O_3. In Fig. 4b, the amount of liquid phase increased from 32.0% to 38.3% as the MgO/Al_2O_3 rose from 0 to 0.4 at 1300 °C, and then gradually decreased. All in all, to ensure the liquid phase content of sinter, the suitable range was within 0.4.

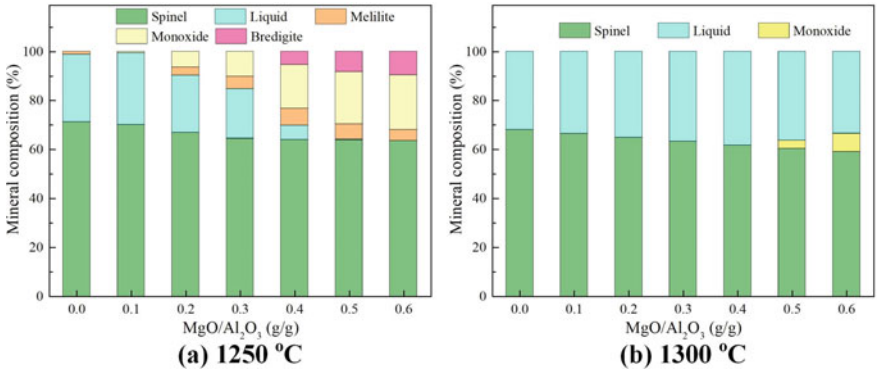

Fig. 4 Effect of MgO/Al_2O_3 on theoretical mineral composition of limonitic laterite sinter at different temperatures

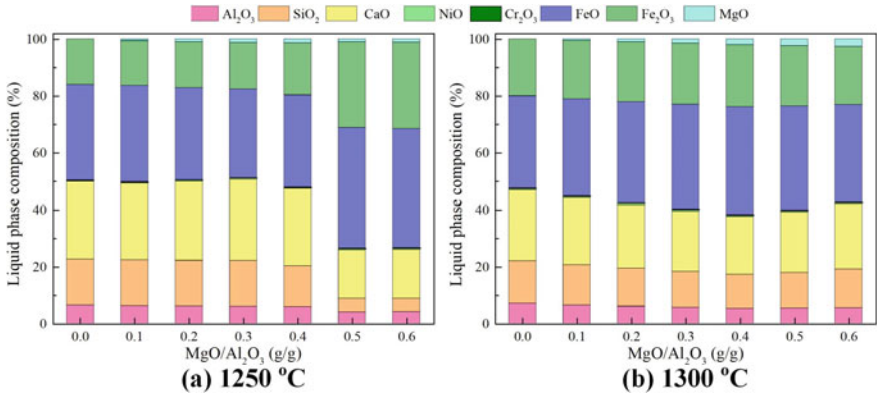

Fig. 5 Effect of MgO/Al_2O_3 on theoretical liquid phase composition of limonitic laterite sinter at different temperatures

The effect of MgO/Al_2O_3 on the theoretical liquid phase composition of limonitic laterite sinter at different temperatures was calculated based on the chemical composition of the same sample. The results in Fig. 5a showed that, as MgO/Al_2O_3 increased to 0.4, the MgO content in the liquid phase gradually increased and reached the maximum value of 1.3%. The MgO content began to decrease after 0.5 MgO/Al_2O_3. However, according to the results of Fig. 4a, the amount of the liquid phase in the sintered ore was too low to meet requirements. Therefore, the relationship between MgO and liquid phase could not be considered after 0.5 MgO/Al_2O_3 at 1250 °C. Figure 5b indicated that as MgO/Al_2O_3 rose from 0 to 0.6, the MgO content in the liquid phase continuously increased from 0 to 2.6% at 1300 °C. It was well known that the bonding phase of limonitic laterite sinter was SFCA. Within a certain range, an increase of MgO content in the sinter was beneficial for the transformation of

SFCA from octahedral structure to a more stable tetrahedral structure. Therefore, the yield and tumble index of the sinter at 0.4 MgO/Al_2O_3 in Fig. 4 reached their maximum values. Conversely, when the MgO content was too high, the bonding phase transformed into a free-state SFCA with a lower physical strength. Therefore, to ensure higher strength of SFCA, MgO/Al_2O_3 of the limonitic laterite sinter needed to be controlled within 0.4.

Conclusions

The effect of MgO/Al_2O_3 on phase compositions, yield, quality, and liquid phase compositions of limonitic laterite sinter was systematically investigated. The conclusions are drawn as follows:

1. With the 0.12–0.4 MgO/Al_2O_3, the yield and tumble index of limonitic laterite sinter increased slowly, reaching the highest values at 0.4 MgO/Al_2O_3, which were 70.33% and 52.90% respectively. Meanwhile, the sintering speed continuously decreased, reaching its lowest value of 25.00 mm min^{-1} at 0.4 MgO/Al_2O_3. To ensure the output and quality indicators of the sinter, the appropriate range for MgO/Al_2O_3 was 0.12–0.4. The main phases of the limonitic laterite sinter were wustite and spinel containing Mg, Al, Cr, and Ni, and MgO/Al_2O_3 did not change the phase composition of the sinter.
2. Thermodynamic results showed that the liquid phase amount of the sinter would be significantly lower after 0.4 MgO/Al_2O_3. As the MgO/Al_2O_3 increased, more MgO entered SFCA. When the MgO content was too high, the binder phase transformed into a free-state SFCA with lower physical strength. Therefore, MgO/Al_2O_3 in the limonitic laterite sinter needed to be controlled within 0.4.

Acknowledgements The authors would express their sincere thanks to National Natural Science Foundation of China (Number U1960114), The Science and Technology Innovation Program of Hunan Province (2023RC1025), and Xuchang Talent Plan (Number 2021-178).

References

1. Luo J, Li G, Rao M, Peng Z, Liang G, Jiang T, Guo X (2020) Control of slag formation in the electric furnace smelting of ferronickel for an energy-saving production. J Clean Prod 287:125082. https://doi.org/10.1016/j.jclepro.2020.125082
2. Uddin MH, Khajavi LT (2020) The effect of sulfur in rotary kiln fuels on nickel laterite calcination. Miner Eng 157:106563. https://doi.org/10.1016/j.mineng.2020.106563
3. Hang G, Xue Z, Wu Y (2020) Preparation of high-grade ferronickel from low-grade nickel laterite by self-reduction and selective oxidation with CO_2–CO gas. Miner Eng 151:106318. https://doi.org/10.1016/j.mineng.2020.106318

4. Chen J, Jak E, Hayes PC (2019) Investigation of the reduction roasting of saprolite ores in the caron process: microstructure evolution and phase transformations. Miner Process Exir Metall 130:148–159. https://doi.org/10.1080/25726641.2019.1699361
5. Zhu D, Xue Y, Pan J, Yang C, Guo Z, Tian H, Liao H, Pan L, Huang X (2020) An investigation into the distinctive sintering performance and consolidation mechanism of limonitic laterite ore. Powder Technol 367:616–631. https://doi.org/10.1016/j.powtec.2020.03.066
6. Xue Y, Zhu D, Pan J, Guo Z, Yang C, Tian H, Duan X, Huang Q, Pan L, Huang X (2020) Effective utilization of limonitic nickel laterite via pressurized densification process and its relevant mechanism. Minerals 10(9):750. https://doi.org/10.3390/min10090750
7. Zhu D, Xue Y, Pan J, Yang C, Guo Z, Tian H, Wang X, Huan Q, Pan L, Huang X (2020) Co-benefits of CO_2 emission reduction and sintering performance improvement of limonitic laterite via hot exhaust-gas recirculation sintering. Powder Technol 373:727–740. https://doi.org/10.1016/j.powtec.2020.07.018
8. Wang Z, Zhang J, Zuo H, Wang R, Huang K, Ban Y (2013) Influence of MgO/Al_2O_3 ratio on sinter mineral composition and metallurgical properties. Sinter Pellet 38(5):1–7. https://doi.org/10.13403/j.sjqt.2013.05.002
9. Hu C, Yan L, Zhang G, Zhao K, Shi X (2018) Effect of MgO/Al_2O_3 on microscopic structure and micro-hardness of silico-ferrite of calcium and aluminum (SFCA). Sinter Pellet 43(2):14–19. https://doi.org/10.13403/j.sjqt.2018.02.019
10. Fan X, Zhao Y, Ji Z, Li H, Gan M, Zhou H, Chen X, Huang X (2021) New understanding about the relationship between surface ignition and low-carbon iron ore sintering performance. Process Saf Environ 146:267–275. https://doi.org/10.1016/j.psep.2020.09.004
11. Wong G, Fan X, Gan M, Ji Z, Ye H, Zhou Z, Wang Z (2020) Resource utilization of municipal solid waste incineration fly ash in iron ore sintering process: a novel thermal treatment. J Clean Prod 263:121400. https://doi.org/10.1016/j.jclepro.2020.121400
12. Chun T, Long H, Di Z, Zhang X, Wu X, Qian L (2017) Novel technology of reducing SO_2 emission in the iron ore sintering. Process Saf Environ Prot 105:297–302. https://doi.org/10.1016/j.psep.2016.11.012
13. Liu Z, Cheng Q, Li K, Wang Y, Zhang J (2020) The interaction of nanoparticulate Fe_2O_3 in the sintering process: a molecular dynamics simulation. Powder Technol 367:97–104. https://doi.org/10.1016/j.powtec.2020.03.043
14. Zhang Y, Liu B, You Z, Su Z, Luo W, Li G, Jiang T (2016) Consolidation behavior of high-Fe manganese ore sinter with natural basicity. Miner Process Exir Metall Rev 37:333–341. https://doi.org/10.1080/08827508.2016.1218870
15. Tu Y, Zhang Y, Su Z, Jiang T (2022) Mineralization mechanism of limonitic laterite sinter under different fuel dosage: effect of FeO. Powder Technol 398:117064. https://doi.org/10.1016/j.powtec.2021.117064

Separation of Iron and Phosphorus from High-Phosphorus Oolitic Hematite Using Direct Reduction and Magnetic Separation

Guangheng Ji, Xu Gao, and Wanlin Wang

Abstract To efficiently utilize high-phosphorus oolitic hematite, phosphorus should be separated from iron, thus a process of direct reduction and magnetic separation was proposed. The physicochemical properties of oolitic hematite before and after treatment were characterized through analysis of the chemical composition, X-ray diffraction (XRD), scanning electron microscope (SEM), and energy-dispersive X-ray spectroscopy (EDS). The influence of various experimental parameters on the upgrading iron and phosphorus removal was investigated, including reduction temperature, reduction dose, and reduction time. Additionally, mass conservation was employed to determine the distribution and migration path of phosphorus from apatite to the slag, gas phase, and metallic iron. Results indicated that the optimal experimental conditions for achieving high recovery ratios of metallic iron and high removal ratios of phosphorus were the temperature of 1200 °C, reduction time of 120 min, and C/O molar ratio of 1.2. Under these conditions, 95.28% of iron was collected as metallic iron, while 70.02% of phosphorus remained in the slag residue. Therefore, the proposed method effectively restrained the reduction of apatite, which led to a good separation of iron from phosphorus.

Keywords Oolitic hematite · Direct reduction · Phosphorus removal · Magnetic separation

Introduction

China has large reserves of high-phosphorus iron ore resources, with reserves of 7.45 billion tons, accounting for 14.86% of the total reserves of iron ore resources [1]. These high-phosphorus iron ores are mainly distributed in Hubei, Hunan, Yunnan, Sichuan, Guizhou, Inner Mongolia, and other regions [2]. Due to the complex mineral

G. Ji · X. Gao (✉) · W. Wang
School of Metallurgy and Environment, Central South University, Changsha 410083, China
e-mail: xgao.sme@csu.edu.cn

National Center for International Cooperation of Clean Metallurgy, Changsha 410083, China

Z. Peng et al. (eds.), *Characterization of Minerals, Metals, and Materials 2024*, The Minerals, Metals & Materials Series, https://doi.org/10.1007/978-3-031-50304-7_12

composition of high-phosphorus iron ore, high phosphorus content, and fine particle size of phosphorus minerals, dephosphorization is very difficult. It has always been a technical problem in dressing and smelting at home and abroad [3, 4]. Since no ideal method for reducing phosphorus has been developed, this part of the iron ore resource has not been effectively developed and utilized as a "dull ore".

The dephosphorization process of high-phosphorus iron ore mainly includes roasting magnetic separation, strong magnetic separation, flotation process, selective agglomeration separation, combined process, and other methods [5]. In recent years, a lot of research has been done on the theory and technology of phosphorus reduction in high-phosphorus iron ore at home and abroad, and some progress has been made. There are still problems such as low removal ratio of phosphorus, large loss of iron, and high grinding cost [6–8]. The current research focuses on dephosphorization by reduction roasting-magnetic separation process [9, 10]. For example, Mansour et al. [11] conducted a coal-based direct reduction of high-phosphorus oolitic hematite assaying 53.20% TFe and 0.8% P. After roasting at 1250 °C for 30 min by adding 5% Na_2SO_4 to the mixed pellets, the iron grade of the final direct reduced powder can be upgraded to 96% with a recovery of 97.72%, the phosphorus content dropped to 0.16% after magnetic separation. Wu et al. [12] employed sodium salts to enhance the reduction of oolitic hematite prior to the recovery of iron by magnetic separation. They found that the dephosphorization ability of sodium salts was in the order of $Na_2SO_4 > Na_2CO_3 > NaCl >$ no sodium salts. However, adding a dephosphorization agent will cause a large amount of slag and increase the cost. How to dephosphorize without additives has attracted attention. In addition, not many researches focused on the migrating behavior of phosphorus among mineral phases during the reduction process, but which was important to effectively separate phosphorus from iron.

In this paper, the effect of temperature, C/O ratio, and reduction time on dephosphorization of high phosphorus oolitic hematite was investigated. In addition, the distribution and migration path of phosphorus during the reduction process was studied.

Experimental

Raw Materials

The oolitic hematite with 47.64% T. Fe and 0.93% P used in this study was collected from Hubei Province, China. Figure 1 shows the back-scattered (BSE) image of oolitic hematite and element maps for Fe, O, Ca, P, Si, and Al. Based on EDS analysis, it can be seen that the mineral phases contained hematite, chlorite, apatite, and quartz. The raw ore was composed of abundant ooids of varying sizes with concentric or eccentric layers of iron-bearing minerals and gangue minerals, forming the shell of the hematite, quartz, chlorite, and apatite. The ooids were very fine and in the range of 200–500 μm. Ca and P were associated closely in the form of apatite, which

was concentrated in the oolitic nucleus, oolitic ring, and the spaces between ooids. The reducing agent used was coke powder with a particle size of − 2 mm and its chemical analysis is shown in Table 1. It can be seen that the fixed carbon content in the reducing agent was 86.73%, and the contents of harmful elements such as phosphorus and sulfur were low, which was a good reducing agent.

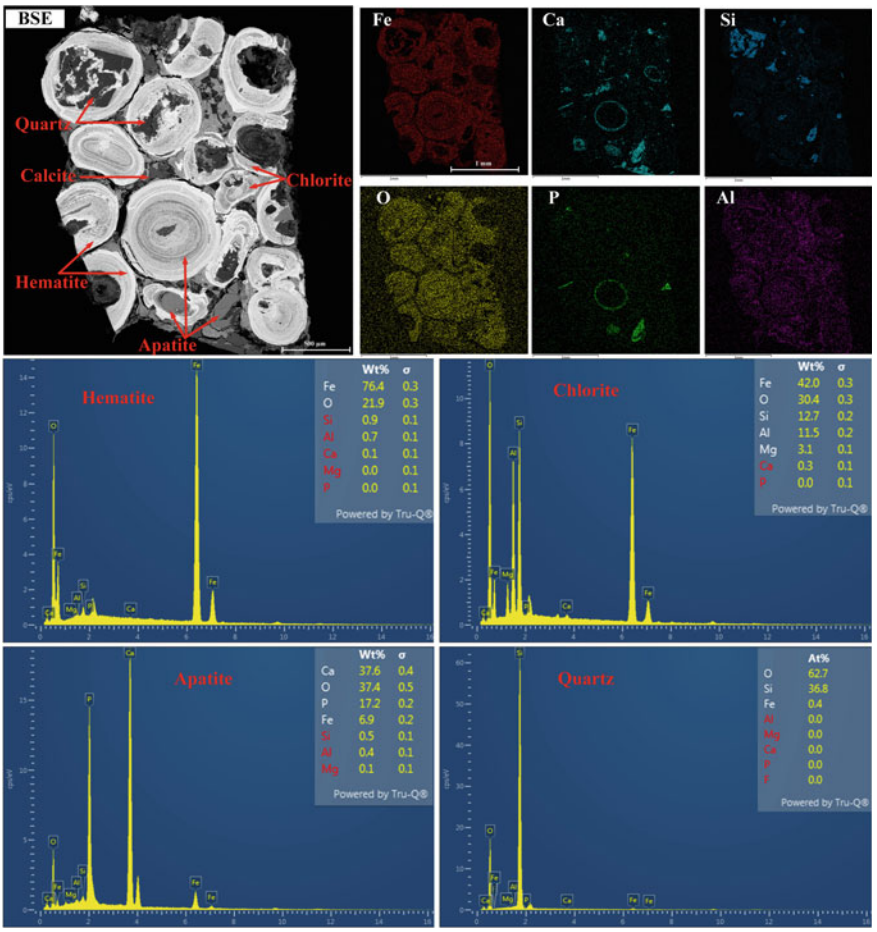

Fig. 1 Morphology and element distribution of the high-phosphorous oolitic hematite

Table 1 Chemical compositions of oolitic hematite and coke powder (wt%)

Raw	T. Fe	P	SiO_2	Al_2O_3	CaO	MgO	S	C
Ore	47.64	0.93	10.35	4.65	7.69	0.74	0.049	–
Coke	0.92	0.028	5.92	4.05	0.68	0.13	0.013	86.70

Experimental Procedure

To start with, the ore was crushed and sieved, ensuring that more than 80% of the particles were smaller than 0.074 mm. Simultaneously, the coke powder was ground to a particle size below 2 mm. Subsequently, the ore and coke powders were mixed according to a C/O ratio (molar ratio of carbon in coke to reducible oxygen in iron oxides) of 1.2. The mixture was then pressed into cylindrical briquettes with 10 mm in diameter and 10 mm in height. The briquettes were placed in an oven and heated to 120 °C for 2 h to dry. As illustrated schematically in Fig. 2, the samples were reduced within a Φ 60/50 × 750 mm tube electric furnace (SK-G06163-750F). Al_2O_3 crucibles were employed to hold the briquettes. Subsequently, the tube furnace was sealed and filled with a high-purity argon gas of 500 mL/min for 2 min to purge the internal atmosphere. Once the reduction temperatures of 1100, 1200, 1300 °C, or 1400 °C were attained, the crucibles were swiftly positioned at the central position of the furnace, and the timing commenced. The reduction time varied from 30 min, 60 min, and 120 min, respectively. Upon completion of the reaction, argon gas was allowed to eliminate residual CO and other reaction gases from the furnace. The crucibles were promptly pulled out in a water-cooled section of the furnace for rapid cooling, with a continuous stream of argon during the cooling process to prevent oxidation of the samples. This sequence of operations was repeated for different experimental groups with varying temperatures and times. Ultimately, after the experiments were concluded, the furnace was allowed to cool to room temperature. The samples were then extracted, crushed, and subjected to magnetic separation to isolate magnetic iron particles from non-magnetic slag.

Results and Discussion

Effect of Temperature on the Dephosphorization

Figure 3 presents the images of the reduced briquettes, SEM, and phosphorus mapping obtained at 60 min under different temperatures. Three types of reduced samples, identified as A, B, and C, maintained briquette shapes, corresponding to reduction temperatures of 1100, 1200, and 1300 °C. The morphology of the sample changed dramatically at 1400 °C. The reduction products consisted of two parts, namely non-magnetic slag and magnetic iron particles.

The EDS mapping of phosphorus in Fig. 3a–d demonstrates the apatite gradually decreased and disappeared with increasing temperature from 1100 to 1400 °C. Table 2 shows phosphorus contents of different phases in reduced samples by EDS analysis. At a low temperature of 1100 °C, fine and dispersed metallic iron was formed, but the amount of slag was very small. In addition, most of the phosphorus was still in the apatite. A small amount of phosphorus was in the slag, and no phosphorus was in the metallic iron. As the temperature increased to 1200 °C, there was a significant

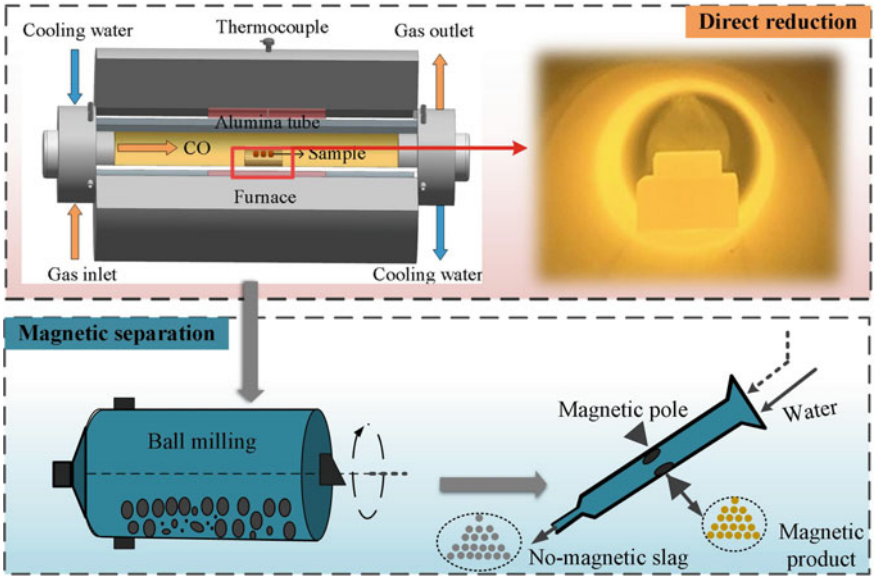

Fig. 2 Flow diagram of the experiment

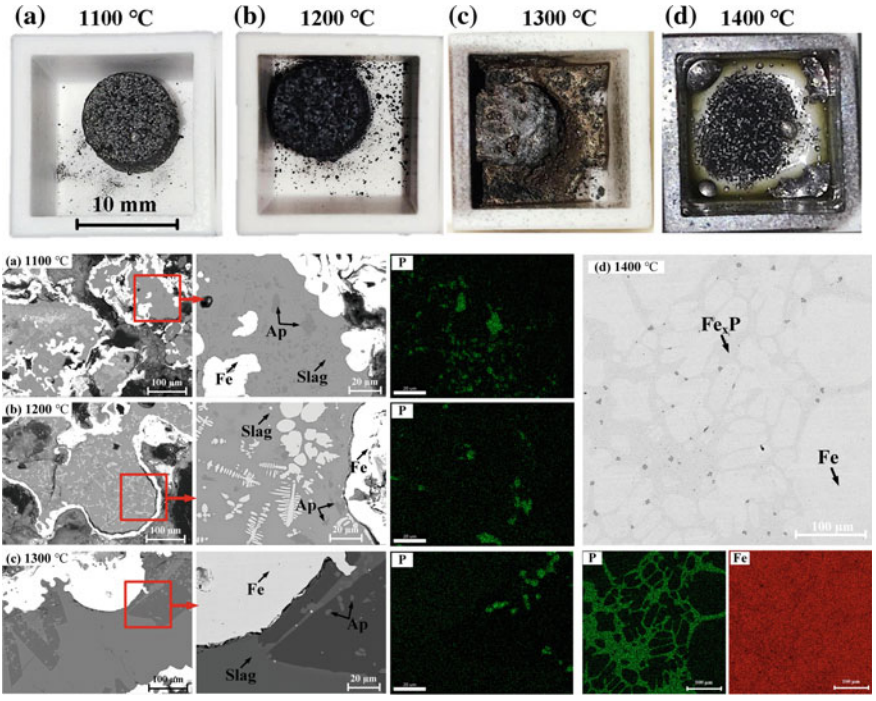

Fig. 3 Images and SEM–EDS of reduced samples at different temperatures, **a** 1100 °C, **b** 1200 °C, **c** 1300 °C, and **d** 1400 °C

increase of the phosphorus content in the slag phase, while no phosphorus content remained in the metallic iron, indicating it involved the melting of apatite in the slag. At 1300 °C, the phosphorus content in the slag decreased, and phosphorus appeared in the metallic iron. This demonstrates that the phosphate in the slag has been reduced. As the temperature was further increased to 1400 °C, it can be seen that the briquettes completely melted, which accelerated the reduction process of iron-bearing mineral and apatite due to the effective contact of the liquid phase (liquid iron and slag) with the carbon, especially its content in the iron phase increased to 12%, indicating a large amount of phosphorus was absorbed in the iron particles. After cooling, it was gathered into a network and precipitated in the formation of Fe_3P at the grain boundary in the iron particles. In summary, low temperatures limited the reduction of apatite, and phosphorus still existed in the apatite. On the contrary, a high temperature promoted the melting and reduction of phosphate in the slag, and the generated phosphorus dissolved in metallic iron, which was not conducive to dephosphorization.

Under the conditions of a C/O ratio of 1.2 and a reduction time of 60 min, the phase of the reduced products was presented in Fig. 4a across various temperatures ranging from 1100 to 1300 °C. At 1100 °C, the primary constituents of the reduction products were wustite (FeO), a small amount of metallic iron (Fe), fayalite (Fe_2SiO_4), hercynite ($FeAl_2O_4$), and apatite ($Ca_3(PO_4)_2$). As the temperature increased to 1300 °C, wustite, fayalite, and hercynite gradually vanished. Concurrently, the apatite content gradually diminished. In contrast, both the metallic iron and the precipitated anorthite ($CaAl_2Si_2O_8$) phase in the slag continuously increased.

Table 3 shows the iron and phosphorus contents of magnetic products and the phosphorus content of non-magnetic slag. The iron recovery rate (ε_{Fe}) and removal ratio of phosphorus (η_P) were derived by Eqs. (1) and (2). The results are depicted in Fig. 4b. It could be seen that as the temperature increased from 1100 to 1200 °C, the iron grade and dephosphorization ratio gradually increased, but the iron recovery declined. As shown in Fig. 4c, this is because the metallic iron size was small, and it was difficult to separate from slag and apatite at 1100 °C, but at 1200 °C, the size was greatly increased, and the slag and iron were better separated. In addition, the iron grade and the iron recovery exhibited an increment, but the removal ratio of phosphorus showed a sharp decrease from 1200 to 1400 °C. The metal iron continues to accumulate and grow into iron particles, but the phosphorus content in metal iron gradually increased, resulting in a decrease in the dephosphorization ratio.

Table 2 Phosphorus contents of the main phase in reduced samples by EDS analysis

Temperature (°C)	Phosphorus content (wt%)		
	Metallic iron	Slag	Apatite
(a) 1100	0.00	0.40	16.57
(b) 1200	0.00	0.96	15.81
(c) 1300	0.95	0.70	14.31
(d) 1400	12.00	0.00	0.00

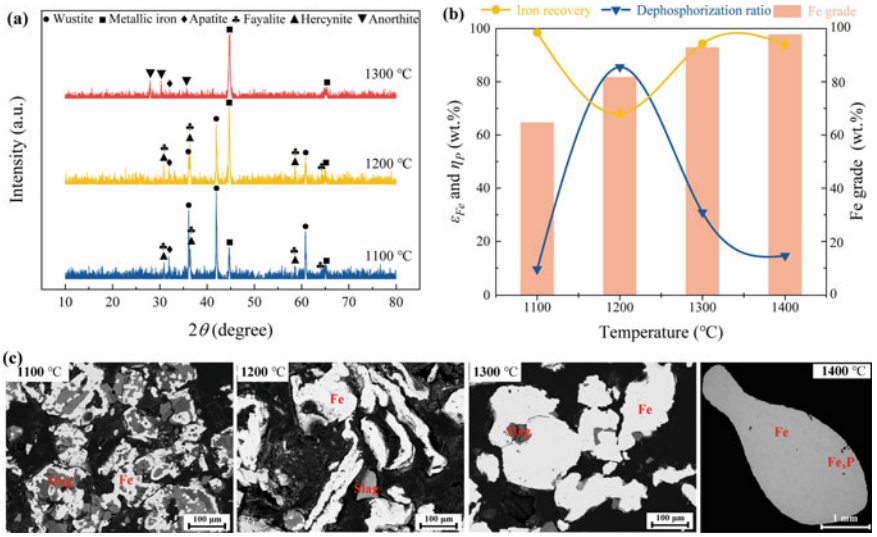

Fig. 4 **a** XRD results of reduced samples at different temperatures, **b** effect of temperature on iron and phosphorus recovery and iron grade in magnetic products, and **c** morphology of magnetic separation products at different temperatures

Table 3 Iron and phosphorus contents of magnetic products and phosphorus content of non-magnetic slag

Temperature (°C)	Magnetic products		Non-magnetic slag
	Fe	P	P
(a) 1100	64.66	1.07	0.24
(b) 1200	81.73	0.41	1.58
(c) 1300	92.94	1.33	0.68
(d) 1400	96.56	2.59	0

To summarize, when the temperature was 1200 °C, the removal ratio of phosphorus reached its peak at 85.52%. However, the iron recovery remained low at 68%, and it is still needed to improve the recovery of iron at 1200 °C.

$$\varepsilon_{\mathrm{Fe}} = \frac{\text{mass of magnetic product} \times \text{Fe content in magnetic procuct}}{\text{Initial mass of iron ore} \times \text{Fe content in iron ore}} \tag{1}$$

$$\eta_{\mathrm{P}} = 1 - \frac{\text{Final mass of product} \times \text{P content in procuct}}{\text{Initial mass of iron ore} \times \text{P content in iron ore}} \tag{2}$$

Effect of C/O Ratio and Reduction Time on Dephosphorization at 1200 °C

Figure 5 shows SEM images of reduced samples at 1200 °C under different conditions, (a) C/O = 0.8, t = 60 min, (b) C/O = 1.2, t = 60 min, and (c) C/O = 1.2, t = 120 min. Table 4 shows phosphorus contents of different phases in reduced samples by EDS analysis. With the increase of the C/O ratio and reduction time, the metallic iron gradually increased and aggregated. There was no phosphorus in the metallic iron, and the dissolved phosphorus in the slag gradually increased. Apatite still existed and was dispersed in the slag.

Figure 6a shows XRD results of reduced samples at different C/O ratios and reduction times. When the C/O was 0.8, the primary phases present in the reduction products were wustite, fayalite, and hercynite, along with minor amounts of metallic iron and apatite. As the C/O ratio was increased to 1.2, the metallic iron phase gradually increased. With a reduction time was 120 min, the dominant component of the reduced product was the metallic iron. There was a small quantity of fayalite and hercynite. During this period, the apatite phase gradually decreased. Similarly, the iron recovery ratio (ε_{Fe}) and removal ratio of phosphorus (η_P) were calculated by Eqs. (1) and (2) based on Table 5. As shown in Fig. 6b, with the increase of the C/O ratio and reduction time, the iron recovery increased significantly, but the removal ratio of phosphorus gradually decreased. This is attributed to the fact that with the enhancement of reduction conditions from Fig. 6c, the reduction of iron gradually increased, and the iron recovery increased, but the larger metallic iron would leave the slag in the gap, resulting in a lower dephosphorization ratio. On the whole, when

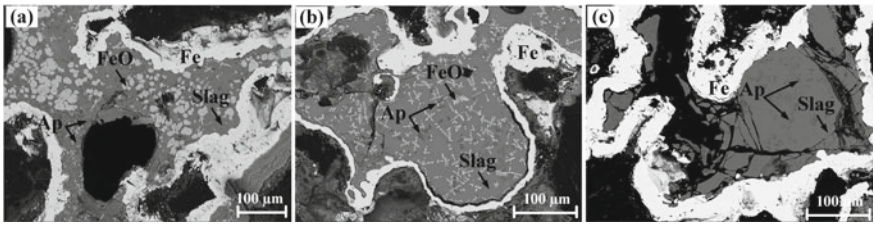

Fig. 5 SEM images of reduced samples at 1200 °C under different conditions, **a** C/O = 0.8, t = 60 min, **b** C/O = 1.2, t = 60 min, and **c** C/O = 1.2, t = 120 min

Table 4 Phosphorus contents of the main phase in reduced samples at 1200 °C under different conditions by EDS analysis

Conditions	Phosphorus content (wt%)		
	Metallic iron	Slag	Apatite
(a) C/O = 0.8, t = 60 min	0.00	0.58	15.07
(b) C/O = 1.2, t = 60 min	0.00	0.96	15.81
(c) C/O = 1.2, t = 120 min	0.00	1.01	14.95

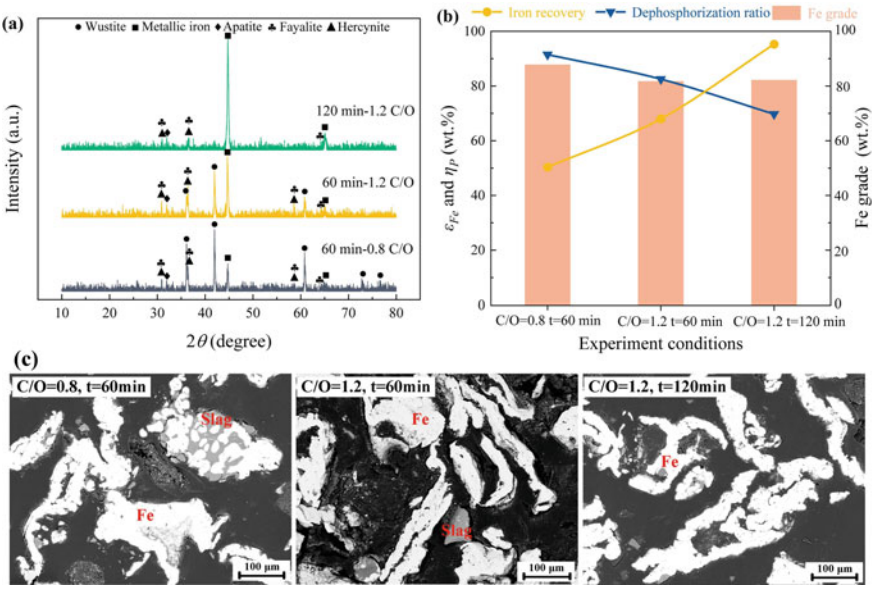

Fig. 6 **a** XRD results of reduced samples at different C/O ratios and reduction time, **b** effect of C/O ratios and reduction time on iron and phosphorus recovery in magnetic products, and **c** morphology of magnetic separation products at different C/O ratios and reduction time

Table 5 Iron and phosphorus contents of magnetic products and phosphorus content of non-magnetic slag at different C/O ratios and reduction time

Condition	Magnetic products		Non-magnetic slag
	Fe	P	P
(a) C/O = 0.8, t = 60 min	87.77	0.29	1.37
(b) C/O = 1.2, t = 60 min	81.73	0.41	1.58
(c) C/O = 1.2, t = 120 min	82.17	0.81	1.96

the temperature was 1200 °C, C/O ratio of 1.2, and reduction time of 120 min, the iron recovery reached 95.28% and the removal ratio of phosphorus was 70.02%.

Thermomechanical Analysis and Migration Path of Phosphorus During Reduction

Phosphorus exists as apatite in oolitic hematite. Based on thermodynamic calculation from Eq. (3), it is difficult to reduce solid apatite at experimental temperatures [13].

$$Ca_3(PO_4)_2(s) + 5C(s) \rightarrow 3CaO(g) + P_2(g) + 5CO(g) \quad (3)$$

$$\Delta G^0 = 3615500 - 1311.80T \text{ (J/mol)}$$

At equilibrium ΔG^0 of Eq. (3) = 0, therefore: $T = 2756$ K. However, the phosphorus would dissolve in the slag and exist in the form of P_2O_5, as shown in Eq. (4). Comparison of the thermodynamic data of reactions Eqs. (3) and (5) demonstrates that it is easier to reduce P_2O_5 in the slag than solid apatite [14].

$$Ca_3(PO_4)_2(s) \rightarrow P_2O_5(s) + 3CaO(s) \tag{4}$$

$$P_2O_5(s) + 5C(s) \rightarrow P_2(g) + 5CO(g) \tag{5}$$

$$\Delta G^0 = 1044980 - 974.9T \text{ (J/mol)}$$

At equilibrium ΔG^0 of Eq. (5) = 0, therefore: $T = 1072$ K.

$$P_2(g) \rightarrow 2[P] \tag{6}$$

$$\Delta G^0 = -315700 + 10.79T \text{ (J/mol)}$$

According to Eq. (6), the presence of P_2 is easily dissolved in the iron.

Figure 7 shows a schematic diagram of the distribution and the migration path of phosphorus during the reduction process. At 1100 and 1200 °C, a portion of the apatite gradually dissolved into the slag and existed in the form of P_2O_5. As the temperature rose to 1200 °C, most of the phosphorus was in the non-magnetic slag, and a small portion of the P_2O_5 in the slag was reduced to form the phosphorus gas phase. At 1300 °C, the phosphorus gas phase increased greatly, because a minor amount of phosphorus was absorbed by the metallic iron, resulting in an increase of phosphorus content in the magnetic products. When the temperature further increased to 1400 °C, phosphorus got enriched in the iron phase, gasified phosphorus decreased, and there was no phosphorus in the slag. Phosphorus was mainly distributed in the magnetic products (mainly in the metallic iron). While at 1200 °C, with an increase in C/O ratio and reduction time, the gasified phosphorus gradually increased, the phosphorus in the slag decreased steadily, and the phosphorus content in the magnetic product progressively increased.

Conclusion

(1) As the temperature increased from 1100 to 1200 °C, apatite gradually dissolved in the slag, and at 1300 °C, the dissolved phosphorus was reduced resulting in a substantial increase in the gasification of phosphorus. High temperature at 1400 °C promoted the reduction of dissolved phosphorus in the slag, and

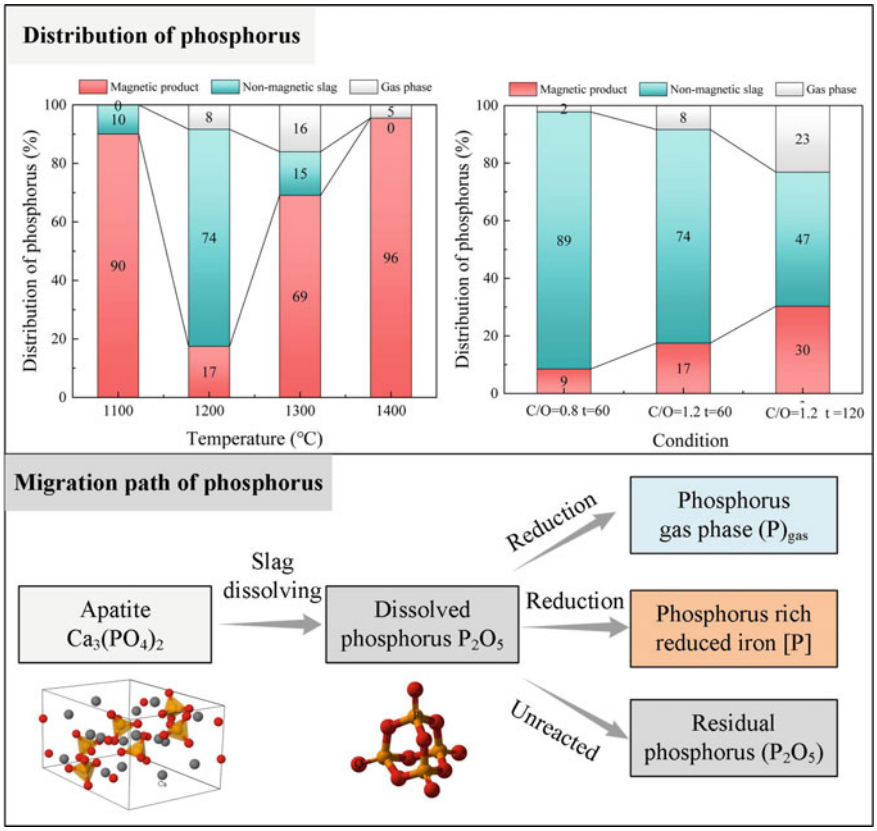

Fig. 7 Schematic diagram of the distribution and migration path of phosphorus during reduction process

the generated phosphorus dissolved in metallic iron to form phosphorus-rich metallic iron, which was not conducive for dephosphorization.

(2) When the temperature was 1200 °C, the removal ratio of phosphorus reached its peak at 85.52%. However, the iron recovery ratio was low at 68%. With the increase of the C/O ratio and reduction time, the iron recovery increased significantly, but the removal ratio of phosphorus gradually decreased.

(3) Migration route of phosphorus is indicated: apatite $Ca_3(PO_4)_2$ → dissolved phosphorus P_2O_5 in the slag → Phosphorus gas phase $(P)_{gas}$ and phosphorus-rich metallic iron [P] during the reduction process. The optimal experimental conditions for achieving a high iron recovery and removal ratio of phosphorus were a temperature of 1200 °C, reduction time of 120 min, and C/O ratio of 1.2. Under these conditions, the iron recovery and removal ratio of phosphorus of the magnetic products reached 95.28% and 70.02%, respectively.

Acknowledgements The authors would like to thank the financial support by the National Natural Science Foundation of China (Grant Number 52174326), the Hunan Scientific Technology Projects (Grant Number 2022SK2080), and the Postgraduate Scientific Research Innovation Project of Hunan Province (CX20230170).

Conflicts of Interest The authors declare no conflicts of interest.

References

1. Xiao JH, Zou K, Wang Z (2020) Studying on mineralogical characteristics of a refractory high-phosphorous oolitic iron ore. SN Appl Sci 2:1–12
2. Wang HH, Li GQ, Zhao D, Ma JH, Yang J (2017) Dephosphorization of high phosphorus oolitic hematite by acid leaching and the leaching kinetics. Hydrometallurgy 171:61–68
3. Wu SC, Sun TC, Kou J, Xu HD (2023) A new iron recovery and dephosphorization approach from high-phosphorus oolitic iron ore via oxidation roasting-gas-based reduction and magnetic separation process. Powder Technol 413:118043
4. Zhu DQ, Guo ZQ, Pan J, Zhang F (2016) Synchronous upgrading iron and phosphorus removal from high phosphorus Oolitic hematite ore by high temperature flash reduction. Metals 6(6):123
5. Keith Q (2018) A review on the characterisation and processing of oolitic iron ores. Miner Eng 126:89–100
6. Wu SC, Sun TC, Kou J, Gao EX (2023) Green and efficient separation of iron and phosphorus from high-phosphorus oolitic iron ore by reduction roasting without a dephosphorization agent. Process Saf Environ Prot. https://doi.org/10.1016/j.psep.2023.05.095
7. Roy SK, Nayak D, Rath SS (2020) A review on the enrichment of iron values of low-grade Iron ore resources using reduction roasting-magnetic separation. Powder Technol 367:796–808
8. Zhang J, Luo GP, Zhang H, Xin WB, Wang YC, Zhu JG (2023) Effect of the carbon mixing ratio on mineral evolution and gasification dephosphorization during the pre-reduction sintering process of bayan obo iron ore concentrate. ISIJ Int 63(3):455–465
9. Zhang HQ, Zhang PF, Zhou F, Lu MM (2022) Application of multi-stage dynamic magnetizing roasting technology on the utilization of cryptocrystalline oolitic hematite: a review. Int J Min Sci Technol 32(4):865–876
10. Pan J, Lu SH, Li SW, Zhu DQ, Guo ZQ, Shi Y, Dong T (2022) A new route to upgrading the high-phosphorus oolitic hematite ore by sodium magnetization roasting-magnetic separation-acid and slkaline leaching process. Minerals 12(5):568
11. Mansour FA, Ould-Hamou M, Merchichi A, Güven O (2021) Recovery of iron and phosphorus removal from Gara Djebilet iron ore (Algeria). Nat Hirn Univ Nauk Visn 4:82–88
12. Wu SC, Sun TC, Kou J, Li XH, Xu CY, Chen ZK (2022) Influence of sodium salts on reduction roasting of high-phosphorus oolitic iron ore. Miner Process Extr Metall Rev 43(8):947–953
13. Matinde E, Hino M (2011) Dephosphorization treatment of high phosphorus iron ore by pre-reduction, mechanical crushing and screening methods. ISIJ Int 51(2):220–227
14. Chiwandika EK, Jung SM (2023) Effect of H_2 on the distribution of phosphorus in the gaseous reduction of hematite ore. JOM. https://doi.org/10.1007/s11837-023-05990-5

Technology Development and Process Optimization of Bottom-Blowing O_2–CO_2–CaO in Dephosphorization Converter

Xin Ren, Kai Dong, Rong Zhu, and Lingzhi Yang

Abstract In the 300 t dephosphorization converter, the bottom-blowing O_2–CO_2–CaO technology has been developed and a range of tests executed to optimize the top-blowing parameters. A comprehensive analysis has been carried out on the effects of "tapping temperature T", "slag basicity R" and "slag T.Fe content" on the end-point P content, based on data gathered from nearly 2000 smelting operations, using single-factor analysis. Optimal thermodynamic conditions for dephosphorization were obtained, with a tapping temperature of T: 1290–1310 °C, slag basicity of $R > 1.3$, slag T, Fe content of 5–10%. The results indicate that dephosphorization rates have increased by nearly 12% under such conditions compared to the original process.

Keywords Bottom-blowing O_2–CO_2–CaO · Dephosphorization rate · Top-blowing parameters

Introduction

Converter steelmaking is currently one of the most important steelmaking methods in the world. Conventional converter generally adopts the blowing method of top-blowing supersonic oxygen jet, top-adding lump lime, and bottom-blowing inert gas with small flow rate [1]. Due to the slow slag formation of lump lime, small interface of slag-gold reaction, and low intensity of molten pool stirring, the metallurgical kinetic conditions of the conventional converter are still insufficient [2], which leads

X. Ren · K. Dong (✉) · R. Zhu
Institute for Carbon Neutrality, University of Science and Technology Beijing, Beijing 100083, China
e-mail: dkaiustb@163.com

L. Yang
School of Minerals Processing and Bioengineering, Central South University, Changsha 410083, China

Z. Peng et al. (eds.), *Characterization of Minerals, Metals, and Materials 2024*, The Minerals, Metals & Materials Series, https://doi.org/10.1007/978-3-031-50304-7_13

to the greater difficulties in treating the medium–high phosphorus molten iron or melting the ultra-low phosphorus molten steel [3–5].

Bottom-blowing O_2–CO_2–CaO process is an advanced steelmaking method to spray the lime required for dephosphorization directly from the bottom into the molten bath in the form of powder, which can achieve a larger dephosphorization reaction interface and higher stirring intensity of the molten bath [6]; the bottom-blowing O_2–CO_2–CaO process uses O_2–CO_2 as the carrier gas of the spray powder, which has good thermodynamic conditions for dephosphorization, and the phosphorus distribution ratio can be up to 2–4 times that of the conventional converter, and it can reduce the consumption of steelmaking raw materials and auxiliaries, while achieving an excellent dephosphorization effect [7].

The author's team has developed the bottom-blowing O_2–CO_2–CaO process, which has been tested and applied in the dephosphorization converter of a steel plant [8, 9], and has independently developed an advanced automated steelmaking model in which the processes of the powder spray system such as loading, pressure charging, blowing, and exhausting are all automated and controlled.

In industrial tests, it was found that after the application of the bottom-blowing O_2–CO_2–CaO process, the metallurgical reaction rate and reaction limit in the converter changed dramatically, which affected the process law and final results of the whole blowing process and resulted in the heat absorption and exotherm of the melt pool reaction. However, there are few studies on the adjustment of operating process regimes due to the changes in thermodynamic conditions for the bottom-blowing O_2–CO_2–CaO process. Therefore, based on the smelting data of nearly 2000 furnaces in industrial tests, this study comprehensively analyzed the effects of "tapping temperature", "slag basicity *R*", "slag T.Fe content" on the end-point P content to develop the optimal process system for bottom-blowing O_2–CO_2–CaO process.

Process Development and Introduction

The schematic diagram of the bottom-blowing O_2–CO_2–CaO process is shown in Fig. 1. All the lime required for melting can be sprayed in the form of powder from the bottom of the converter, and the maximum flow rate of powder spraying is designed to be 240 kg/min, and the amount of powder spraying can be up to 6–8 kg/t of steel for each furnace, which can satisfy the lime requirement of the dephosphorization furnace. The carrier gas for bottom-blowing powder spraying is O_2–CO_2 mixture, the flow rate of powder spraying carrier gas is 2700 Nm^3/h.

The author's team has independently developed an advanced automatic steelmaking model for bottom-blowing O_2–CO_2–CaO process, in which all the processes of loading, pressure charging, blowing, and exhausting of the powder spraying system are automated, and the process parameters are set independently according to the conditions of raw materials and the target state during the blowing process, which improves the stability and reliability of the bottom-blowing system.

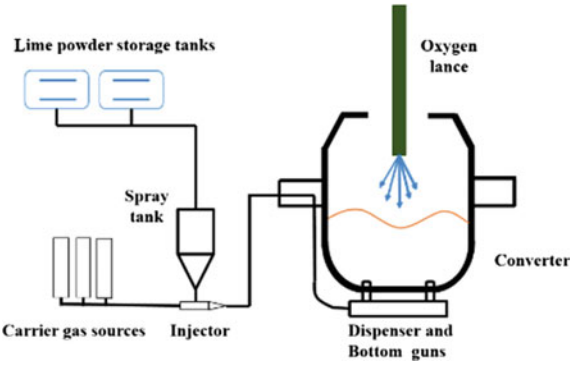

Fig. 1 Schematic diagram of converter bottom-blowing O_2–CO_2–CaO process [10]

Based on the results of previous research by the author's team [11], the dephosphorization reaction mechanism of the bottom-blowing O_2–CO_2–CaO process is proposed, as shown in Fig. 2. The excessive temperature within the fire-spot zone causes the CaO powder to melt, and the molten CaO reacts with (FeO) to form calcium ferrite (FeO–CaO) solid solution. The (FeO–CaO) solid solution has strong dephosphorization ability, it will react with P in the metal phase instantly to form ($3CaO{\cdot}P_2O_5$) and then float to the top slag, thus P is removed. The rest of the CaO powder will float into the top slag and continue to react in the slag phase. The dephosphorization reaction in the molten pool of steel-making can be expressed by Eq. (1) [12].

$$2[\mathrm{P}] + 5(\mathrm{FeO}) + 3(\mathrm{CaO}) = (3\mathrm{CaO} \cdot \mathrm{P_2O_5}) + 5[\mathrm{Fe}]$$

$$\Delta_r G = \Delta_r G^{\theta} + \mathrm{RT}\ \ln Q = -209{,}327 + 40.37\mathrm{T} + \mathrm{RT}\ \ln \frac{a_{\mathrm{Fe}}^5 \cdot a_{(\mathrm{P_2O_5})}^3}{a_{(\mathrm{FeO})}^5 \cdot a_{[\mathrm{P}]}^5} \quad (1)$$

Based on the above, the dephosphorization process model of the bottom-blowing O_2–CO_2–CaO converter is established [8]:

(1) Based on the above, the dephosphorization process model of the bottom-blowing O_2–CO_2–CaO converter is established.
(2) Ca–Ferrate particles oxidize P to form $3CaO{\cdot}P_2O_5$ initial slag particles during the floating process.
(3) The $3CaO{\cdot}P_2O_5$ initial slag particles continue to float and polymerize with low CaO/SiO_2 slag particles to form final slag particles.
(4) The $3CaO{\cdot}P_2O_5$ initial slag particles continue to float and polymerize with low CaO/SiO_2 slag particles to form final slag particles.
(5) Repeat the above four steps for continuous dephosphorization.

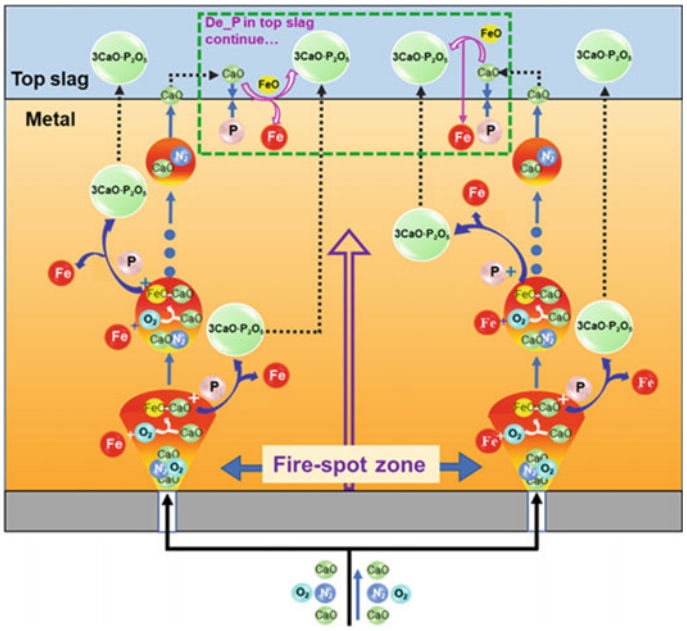

Fig. 2 Mechanism of dephosphorization in the bottom-blowing O_2–CO_2–CaO process

Analysis of Metallurgical Indicators

The bottom-blowing O_2–CO_2–CaO process for dephosphorization converter can be divided into three levels according to the powder spraying flow rate, which are defined as Model 1, Model 2, and Model 3, and the powder spraying flow rate is 120 kg/min, 180 kg/min, and 240 kg/min, respectively. Figure 3a compares lime consumption per tonne and the amount of lime blowed per furnance in origin process and different modes of the bottom-blowing O_2–CO_2–CaO process. Lime consumption of the dephosphorization converter is considerably reduced with the increase of the powder spraying amount. Figure 3b compares the slag T.Fe content and metal recovery rate of origin process and different modes of the bottom-blowing O_2–CO_2–CaO process. The bottom-blowing O_2–CO_2–CaO process significantly reduces the T.Fe content and dramatically improves the metal yield compared to the original process.

Figure 4 compares the end-point P and C contents of the original process and the bottom-blowing O_2–CO_2–CaO process. The average semi-steel end-point P content of the original process is 0.045%, and the average end-point P content of the different modes is 0.041%, 0.038%, and 0.035%, respectively. Compared with the original process, the bottom-blowing O_2–CO_2–CaO process mainly reduces the flow rate of the top lance, improves the position of the oxygen lance, extends the time of bottom powder spraying, improves the amount of powder spraying, and better solves the

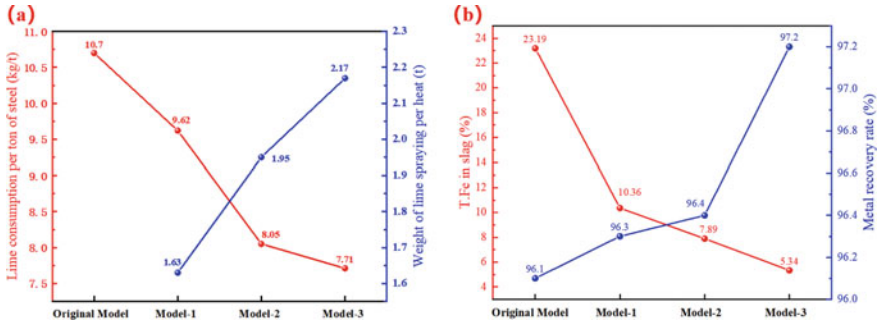

Fig. 3 Comparison of lime consumption and metal yield in different models

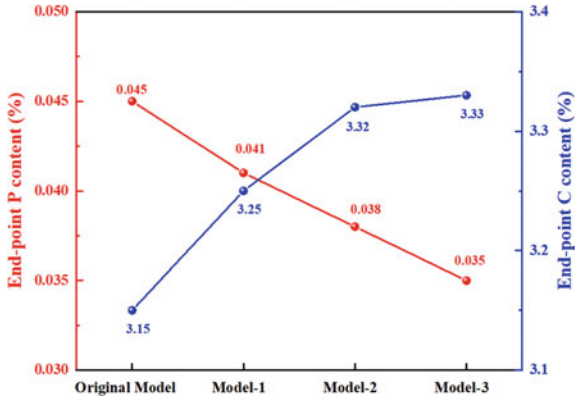

Fig. 4 Comparison of end-point P/C content in different models

problems of spraying and overflow of slag, etc., the melting process is smooth and stable, so the semi-steel end-point P content is significantly reduced.

From Fig. 4, it can be seen that after the application of the bottom-blowing O_2–CO_2–CaO process, the end-point C content of the semi-steel is noticeably improved, the actual average C content is higher than the target value of 3.25%, and the end-point C content of the bottom powder spraying process is increased by nearly 0.2% compared with the original process. Higher end-point C content of semi-steel means that in the subsequent melting process of the decarburization furnace, the use of temperature raising agent can be appropriately reduced to reduce production costs.

Through the above analysis, it can be seen that with the increase of bottom-blowing lime powder flow, the total lime consumption and steel material consumption are greatly reduced, the end-point P content is reduced from 0.040 to 0.037%, and the end-point C is increased from 3.15% to about 3.30%. However, due to the change of thermodynamic conditions, bottom-blowing O_2–CO_2–CaO process still has not played its best advantage.

Industrial Data Analysis and Optimization Directions

The thermodynamic conditions required for the de-P reaction are: higher slag basicity, higher slag T.Fe content, and lower molten pool temperature.

The traditional smelting process slagging system is different from that of the bottom-blowing O_2–CO_2–CaO process. After the application of bottom-blowing O_2–CO_2–CaO process, if the original process system is still used, it will lead to many problems, such as unstable De-P effect and spattering at the end of melting. Therefore, in order to achieve better metallurgical indictors, it is extremely necessary to develop a set of process system suitable for bottom-blowing O_2–CO_2–CaO process.

Influence of Tapping Temperature T *on De-P*

Figure 5a compares the semi-steel end-point P content with the tapping temperature. Segmented according to the steel-out temperature interval, the average of the end-point P content in the interval was taken. As can be seen from Fig. 5a, when the tapping temperature is lower than 1310 °C, the dephosphorization effect of the bottom-blowing O_2–CO_2–CaO process furnace is better than that of the original process furnace, and when the tapping temperature is higher than 1310°C, the dephosphorization effect of the original process furnace is better than that of the bottom-blowing O_2–CO_2–CaO process furnace.

The phosphorus partition between slag and hot metal L_P is defined as the ratio of P_2O_5 percentage in the slag to the end-point P concentration in the molten steel, the actual L_P is calculated as Eq. (2) [11]. It's an index of the phosphorus holding capacity of the slag, which determines the phosphorus content achievable in the finished steel. The larger L_P, the better dephosphorization effect.

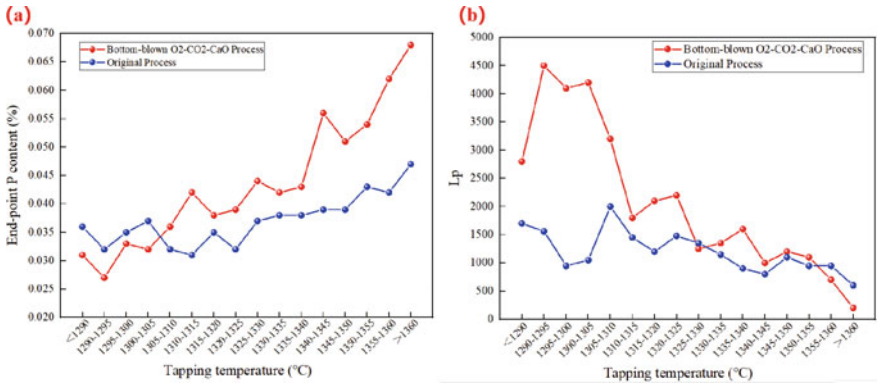

Fig. 5 Comparison of end-point P content/L_P in two processes

$$L_P = \frac{\omega(P_2O_5)}{\omega[P]^2} \tag{2}$$

where $\omega(P_2O_5)$ is the mass percentage of P_2O_5 in the slag [%].

Figure 5b compares the relationship between the L_P of semi-steel and the tapping temperature. From Fig. 5b, it can be seen that the L_P of the bottom-blowing O_2–CO_2–CaO process is larger than that of the original process, and the fluctuation with temperature change is wider. The lower the steel output temperature, the larger the L_P; while the original process L_P fluctuates less with temperature change, indicating that the temperature plays a crucial role in the bottom-blowing O_2–CO_2–CaO process.

The qualification rate of the bottom-blowing O_2–CO_2–CaO process and the original process to achieve the target P content ($P \leq 0.035\%$) in different temperature intervals are counted. For bottom-blowing O_2–CO_2–CaO process, when the tapping temperature > 1310 °C, the temperature increases, the target P qualification rate decreases rapidly; while for the original process, when the tapping temperature < 1330 °C, the effect of dephosphorization is relatively smooth, when the temperature > 1330 °C, the target P qualification rate decreases rapidly. If the target P qualification rate is assumed to be higher than 40% or more, the target tapping temperature of bottom-blowing O_2–CO_2–CaO process melting should be lower than 1320 °C. If the end-point P content is less than 0.030%, the target tapping temperature range is 1290–1310 °C.

Influence of Slag Basicity R *on De-P*

According to the slag basicity of the interval segmentation, the average value of the end-point P content in the same alkalinity interval is statistically presented in Fig. 6. The end-point P content decreases with the increase of the slag basicity, and when the bottom-blowing O_2–CO_2–CaO process is adopted, the average end-point P content is less than 0.035%,when the slag alkalinity $R > 1.25$. In order to achieve the end-point P content less than 0.030% in bottom-blowing O_2–CO_2–CaO process, the slag basicity $R \geq 1.3$.

Statistics on more than 2000 times of furnace data, it is found that for the top-adding lime process, to achieve the slag basicity $R > 1.25$, the average amount of top-added lime is 2.91 t. For the bottom-spraying lime powder process, to achieve the slag basicity $R > 1.25$, the average amount of bottom-sprayed lime powder is 2 t, to achieve the slag basicity $R > 1.3$, the average amount of bottom-sprayed lime powder is 2.13 t.

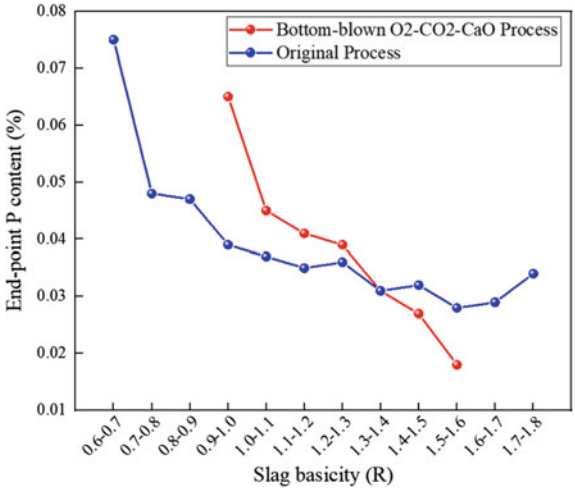

Fig. 6 Comparison of end-point P content

Influence of Slag T.Fe Content on De-P

The relationship between end-point P content and T.Fe in the slag is shown in Fig. 7. Comparing the bottom-blowing O_2–CO_2–CaO process with the original process, when the slag basicity is less than 1.2, both processes require a higher T.Fe content to achieve the desired dephosphorization effect.

When the slag basicity is similar, the T.Fe content in the slag required for bottom-blowing O_2–CO_2–CaO process is lower than that of the original process in order to achieve the same dephosphorization effect. Therefore, for the bottom-blowing O_2–CO_2–CaO process, the smelting process can reduce the T.Fe content by corresponding operation to achieve higher efficiency. However, too low T.Fe content is also

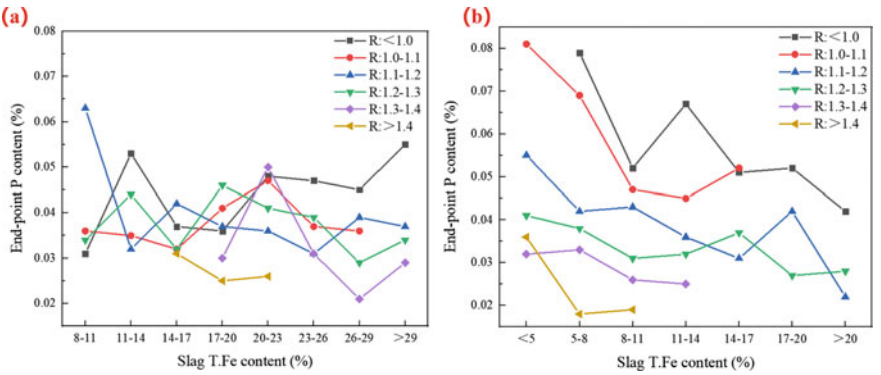

Fig. 7 Relationship between terminal P content and T.Fe in slag. **a** Original process; **b** bottom-blowing O_2–CO_2–CaO process

unfavourable for dephosphorization. As can be seen from Fig. 6, when the basicity $R > 1.2$, bottom blowing O_2–CO_2–CaO process can reach the target end-point P content by controlling the T.Fe in the slag at 5–15%, and too low or too high will affect the effect of dephosphorization. However, when the basicity is lower than 1.2, it is necessary to control the T.Fe content in the slag at more than 20% to achieve the target dephosphorization effect.

Optimization Effects

According to the analysis of the above data, it is concluded that the best thermodynamic conditions suitable for bottom-blowing O_2–CO_2–CaO process dephosphorization are: tapping temperature T: 1290–1310 °C, slag basicity: $R > 1.3$, slag T.Fe content: 5–10%. In order to achieve these thermodynamic conditions, the operating system of the bottom-blowing O_2–CO_2–CaO process is adjusted, including: reducing the oxygen lance flow, increasing the oxygen lance position, adjusting the bottom-blowing O_2, CO_2 mixture flow and ratio, improving the charging system of raw and auxiliary materials, and increasing the time of static stirring before tapping. After the optimization of 500 furnaces of the melting operation system, the best thermodynamic conditions suitable for bottom-blowing O_2–CO_2–CaO process dephosphorization were obtained. According to the statistics, after the optimization of the operating system, the average end-point P content of the bottom-blowing O_2–CO_2–CaO process was reduced to 0.029%, and the dephosphorization rate was increased by almost 12% compared to that before the optimization. After optimization, the metallurgical indicators are shown in Table 1.

Table 1 Metallurgical indicators of bottom-blowing O_2–CO_2–CaO process

Indicators	Original process	Bottom-blowing O_2–CO_2–CaO process	
		Before optimization	After optimization
Tapping temperature (°C)	1334	1315	1290–1310
Slag basicity	1.12	1.17	$\geq$ 1.3
T.Fe (%)	23.00	10.44	5–15%
Lime powder weight (t)	3.08	2.49	~ 2.1 t
End-point P content (%)	0.045	0.038	0.029
Dephosphorization rate (%)	43.75	51.5	63.75

Conclusion

This paper describes the application of the bottom-blowing O_2–CO_2–CaO process in a 300 t dephosphorization converter thoroughly and elaborates the dephosphorization mechanism of bottom-blowing O_2–CO_2–CaO process. Compared with the original process, the bottom-blowing O_2–CO_2–CaO process effectively reduces the lime consumption, decreases the slag T.Fe content, improves the metal yield, and increases the end-point C content. Based on the smelting data of nearly 2000 furnaces, by comprehensively analyzing the influence of "steel temperature", "slag alkalinity R", "slag T.Fe" on the end-point P content, it is concluded that the best thermodynamic conditions for dephosphorization: tapping temperature T: 1290–1310 °C, slag basicity: $R > 1.3$, slag T. Fe content: 5–10%. By reducing the oxygen lance flow, increasing the oxygen lance position, adjusting the bottom-blowing O_2, CO_2 mixture flow and ratio, improving the charging system of raw and auxiliary materials, and increasing the time of static stirring before tapping, the operating system under the optimum thermodynamic conditions suitable for the bottom-blowing O_2–CO_2–CaO dephosphorization process has been established. The results of the industrial test show that after the optimization of the operating system, the end-point P content is reduced to 0.029% and the dephosphorization rate is increased by almost 12%. According to calculations, the cost of a tonne of steel is reduced by $3.5 with bottom-blowing O_2–CO_2–CaO process.

References

1. Liu L (2004) Technical progress of oxygen converter steelmaking in China. China Metall 02:4–11
2. Wang X, Li J, Liu F (2017) Technological progress of BOF steelmaking in period of development mode transition. Steelmaking 33(01):1–11
3. Yang W, Gan Y, Wang M (2011) Steelmaking with high-phosphorus hot metal in BOF and the use of lron ore resources with high phosphorus. China Metall 21(03):4–10
4. Zhang X, Xie B, Li HY, Diao J, Ji CQ (2013) Coupled reaction kinetics of duplex steelmaking process for high phosphorus hot metal. Ironmak Steelmak 40(4):282–289
5. Wang Y, Yang SF, Li JS, Feng J (2018) Dephosphorization by double-slag process in converter steelmaking. High Temp Mater Processes (Lond) 37(7):625–633
6. Ohnishi M, Nagai J, Yamamoto T (1983) Metallurgical characteristics and operation of oxygen top and bottom blowing at Mizushima works. Iron Steelmak 10(8):28–34
7. Liao D S, Sun S, Waterfall S, Boylan K, Pyke N, Holdridge D (2015) Integrated KOBM steelmaking process control. In: International congress on the science and technology of steelmaking
8. Zhou Y, Zhu R, Hu S (2021) Study on metallurgical characteristics of the bottom-blown O2–CaO converter. Ironmak Steelmak 48(2):142–148
9. Li W, Zhu R, Dong K (2020) Physical simulation and industrial testing of bottom-blown O_2–CaO converter for steelmaking process. Metall Mater Trans B 51(3):1060–1069
10. Ren X, Dong K, Feng C, Zhu R, Wei G, Wang C (2023) Application of MLR, BP and PCA-BP neural network for predicting FeO in bottom-blowing O_2–CaO converter. Metals 13(4):782

11. Wang C, Zhu R, Dong K, Wei G, Ren X, Zhou Y, Xue Z, Feng C (2023) Research on mechanism change of temperature effect on dephosphorization in the bottom-blown O_2–CaO process of semi-steelmaking. J Mater Res Technol 24:8725–8735
12. Li W (2021) Basic research on dephosphorization by bottom blowing O_2–CO_2–CaO in converter steelmaking. Ph.D. thesis. University of Science and Technology Beijing, Beijing

Production of Zinc Oxide from Willemite Containing Ore from Kabwe Town in Zambia

Yotamu Rainford Stephen Hara, Daliso Tembo, Rainford Hara, Ronald Hara, Alexander Oniel Noel Old, and Stephen Parirenyatwa

Abstract High-purity zinc oxide (> 99 weight %) was obtained from complex zinc silicate ore of Kabwe town of the Central province of Zambia. The material was leached with sulphuric acid at varying pH to form zinc sulphate. There was partial dissolution of silica during leaching. The following parameters were studied; leaching temperature, pH, and solid to liquid ratio. Leach efficiency of 97% was obtained. Zinc was recovered from solution via precipitation with sodium hydroxide, magnesium oxide, and oxalic acid. Low-grade zinc oxide was obtained during precipitation with sodium hydroxide and magnesium oxide owing to co-precipitation of SiO_2. On the other hand, there was no co-precipitation of SiO_2 during precipitation with oxalic acid such that high-purity zinc oxalate was obtained. The precipitated zinc oxalate was heated up at 500 °C to obtain zinc oxide with purity of more than 99%.

Keywords Characterization · Hydrometallurgy

Introduction

Kabwe town of the Central province of Zambia has a large deposit of zinc. At present, the high-grade zinc ore (more than 35 weight % zinc) is sold overseas. It is worth noting that the high-grade zinc material is produced by either sorting of the mined ore or gravity separation technique. However, both methods are inefficient such that there is a lot of material with less than 28% zinc.

Y. R. S. Hara (✉) · D. Tembo · A. O. N. Old
Copperbelt University, Kitwe, Zambia
e-mail: yotamuhara@gmail.com

Y. R. S. Hara · R. Hara · R. Hara · S. Parirenyatwa
YCS Sustainable Solutions Limited, Kitwe, Zambia

Z. Peng et al. (eds.), *Characterization of Minerals, Metals, and Materials 2024*, The Minerals, Metals & Materials Series, https://doi.org/10.1007/978-3-031-50304-7_14

The production of zinc oxide incorporates a series of metallurgical and chemical processes, the two main metallurgical processes are; (I) Direct process; this involves the reduction of zinc ore in the presence of coal and, followed by vaporization and oxidation [1, 2], (II) Indirect process; involving the melting and vaporizing of zinc metal at 910 °C followed by the reaction with oxygen to produce zinc oxide particles [2]. Chemically, zinc oxide is produced via leaching in acidic media followed by precipitation with sodium hydroxide or sodium carbonate [2, 3]. The only downside of the leach-precipitation process is the co-precipitation of impurities with zinc oxide/hydroxide/carbonate. During controlled precipitation, zinc oxide is produced by altering pH and temperature of the solution to promote precipitation [4].

Applications of Zinc Oxide

Zinc oxide has wide applications in many industries as a result of its unique physical and chemical properties. It is utilized in the rubber industry to vulcanize rubber and fabricate many things such as shoe soles, tires, hockey pucks, etc. [5]. It is used with stearic acid during the process of vulcanization of rubber. In addition, the ceramic industry utilizes the high thermal conductivity, low expansion coefficient, and high thermal strength of ZnO particles to give a glossy surface and provide a matte finish touch to the products in moderate amounts. Furthermore, zinc oxide is used in the food industry because it is an essential micronutrient element, approved and regarded safe for consumption. The birth of nanotechnology led to zinc oxide developing many products with antimicrobial agent properties. ZnO nanoparticles have also presented many potential applications in food preservation and its industry. ZnO nanoparticles have been absorbed in polymeric patterns to provide an antimicrobial scheme to the packaging substance and improve some wrapping properties.

Owing to the availability of low-grade zinc oxide material and the demand for zinc oxide, this research focuses on production of zinc oxide from low-grade zinc ore material located in Kabwe town via leaching and precipitation.

Precipitation of Zinc from Sulphate Media

Owing to its limited solubility at pH of more than 4.0, zinc may be precipitated with different salts such as sodium carbonate (Na_2CO_3), sodium hydroxide (NaOH), magnesium oxide (MgO), lime (CaO), etc. [6] as shown in Eqs. (1)–(4). Reactions (1)–(3) yield respective soluble salts while reaction (4) yields an insoluble salt, which co-exist with zinc precipitate and hence undesirable. Even though reactions (1)–(3) yield soluble salts, other elements such as aluminum, silica, iron, manganese, etc. may co-precipitate with zinc.

$$ZnSO_4 + Na_2CO_4 = ZnCO_3 + Na_2SO_4 \quad (1)$$

$$ZnSO_4 + 2NaOH = Zn(OH)_2 + Na_2SO_4 \quad (2)$$

$$ZnSO_4 + MgO + H_2O = Zn(OH)_2 + MgSO_4 \quad (3)$$

$$ZnSO_4 + CaO + H_2O = Zn(OH)_2 + CaSO_4 \quad (4)$$

On the other hand, zinc may be precipitated from sulphate media with oxalic acid as shown in Eq. (5). The main advantages of precipitating zinc according to Eq. (5) are:

- Regeneration or production of sulphuric acid during precipitation may be recycled to the leaching step and hence reduce overall acid consumption.
- Selectivity of the process as precipitation is done in acidic environment and hence minimizes co-precipitation of other elements.

$$ZnSO_4 + C_2H_2O_4 \rightarrow ZnC_2O_4 + H_2SO_4 \quad (5)$$

Materials and Experimental Methods

Materials

As-received zinc ore was obtained from a named mine in Kabwe town of the Central province of Zambia. The material was sampled from 30 different locations in order to obtain good representation. The as-received material was further homogenized by crushing down to particle size of less than 2 mm. All leaching tests were carried out at particle size of less than 0.106 mm.

All leaching experiments were conducted in sulphuric acid media where pH was monitored. Analytical grade reagents (sodium hydroxide, sulphuric acid, oxalic acid etc.) were used in the experiments.

Chemical Analysis and Mineralogy

Chemical analysis was carried out by a combination of X-ray fluorescence (XRF), gravimetric, and atomic absorption spectroscopy (AAS). On the other hand, mineralogical examination was carried out using X-ray diffraction with a copper radiation.

Leaching

100 g of sample was used in each experiment. The samples were leached for 2 h at room temperature (25 °C) and at high temperature (70 °C). The leaching experiments were carried out at solid–liquid ratios of 1:5 and 1:8. Each sample was filtered after leaching and the leach residue was washed with warm water to remove entrained liquor. The washed leach residue was dried at 80 °C and the final weight was taken. The dried leach residue was analyzed for Zn using atomic absorption spectroscopy technique.

Precipitation of Zinc from Solution

Zinc was precipitated from solution by using either sodium hydroxide or oxalic acid at a solution strength of 10%. The sodium hydroxide solution was slowly added to the leach liquor until pH reached 6.5. On the other hand, precipitation of zinc with oxalic acid was carried out by following Eq. (5). Therefore, the concentration of zinc in solution was determined, and oxalic acid was added at 5% in excess of the stoichiometric requirement. The pH of the solution was monitored during precipitation in order to understand the regeneration of acid in Eq. (5). Zinc oxalate was further calcined at 500 °C to form zinc oxide.

Chemical Analysis

Chemical analysis was conducted by using atomic absorption spectrometer (Perkin Elmer Analysis 300 and X-ray fluorescence (XRF) techniques.

The steps that were taken for the production of high grade ZnO are summarised in Fig. 1.

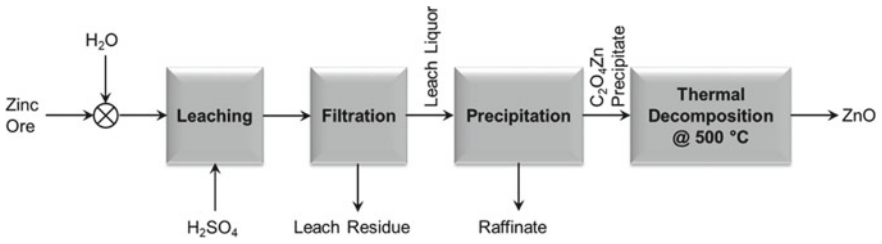

Fig. 1 Process flowsheet that was employed in the test works

Table 1 Chemical analysis of the as-received sample

Zn	Fe	Pb	Mn	SiO_2	Al_2O_3	CaO	MgO	P_2O_5	K_2O	V_2O_5
28.02	3.57	2.56	1.02	33.55	14.13	1.39	1.10	1.98	1.03	0.39

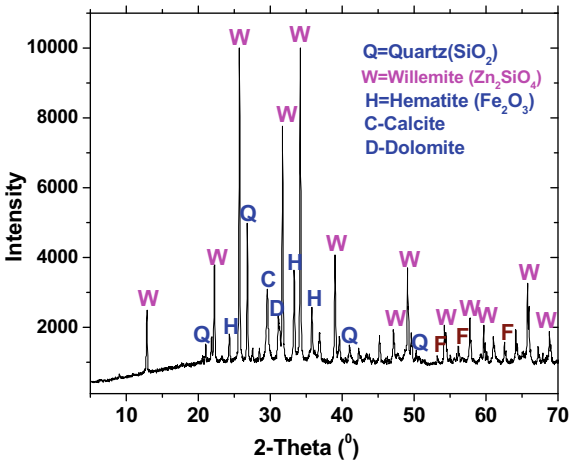

Fig. 2 XRD pattern for the as-received sample

Results and Discussion

Chemical Analysis and Mineralogical Examination

Chemical analysis of the as-received sample is shown in Table 1. It can be observed from Table 1 that the as-received sample contains 28.02 weight % zinc. The sample also contains 3.56, 2.56, and 1.02 weight % Fe, Pb, and Mn, respectively. The other impurities in the sample are SiO_2, Al_2O_3, CaO, P_2O_5, and K_2O in the decreasing order. XRD pattern for the as-received sample is shown in Fig. 2. Willemite (Zn_2SiO_4) is the main zinc-bearing mineral. Therefore, zinc is present in the silicate phase. The gangue phases in the samples are quartz (SiO_2), hematite (Fe_2O_3), calcite ($CaCO_3$), and dolomite ($CaMg(CO_3)_2$). Other phase phases that are not crystalline or amorphous could not be analysed from the material.

Leaching of the Samples

The results showing the effects of pH, leaching temperature, leaching time, and solid–liquid ratio are shown in Figs. 3 and 4. The results show that recovery of zinc decreases with increase in pH at both room temperature and high temperature (70 °C), and this is because of decrease in acidity as pH increases. The effect of pH is more

pronounced at pH of more than 1.4 as recovery decreases sharply with increase in pH. In general, the recovery of zinc increases slightly with increase in solid:liquid ratio.

The plot for acid consumption against pH is shown in Figs. 3b and 4b from which it can be observed that acid consumption is slightly higher at solid:liquid ratio of 1:8 than at 1:5, and this is why slightly higher recovery was obtained. Acid consumption increases at lower pH because of limited selectivity since other elements such as aluminum, potassium, iron, etc. that are present in the material either partially or completely leaches out lower pH.

Based on the leach test results in Figs. 3 and 4, it can be concluded that zinc leaches out from Kabwe ore as recovery of more than 90% was obtained at pH of less than 1.2. Acid consumption was slightly higher at high temperature (70 °C) than at room temperature and this is a result of increased dissolution of gangue elements at higher temperature.

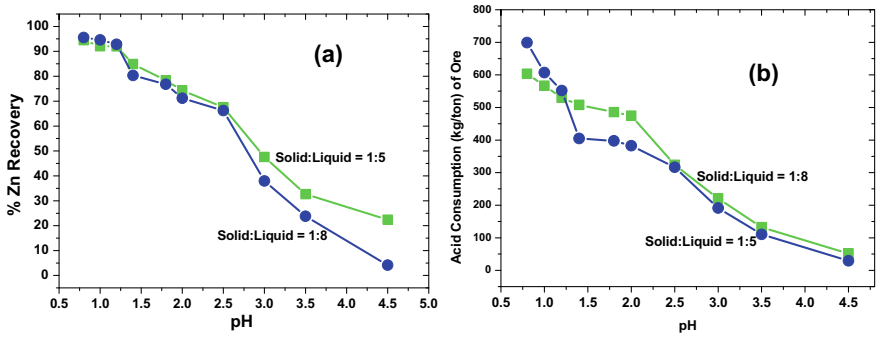

Fig. 3 Room temperature leach tests; **a** effect of pH on recovery of zinc at solid:liquid ratio of 1:5 and 1:8 and **b** effect of pH on consumption of acid

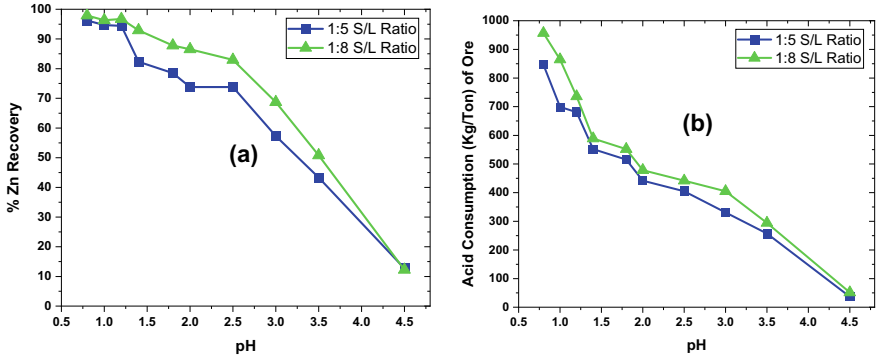

Fig. 4 High temperature (70 °C) leach tests; **a** effect of pH on recovery of zinc at solid:liquid ratio of 1:5 and 1:8 and **b** effect of pH on consumption of acid

Table 2 Leach analysis in grams per litre (gpl) for the leach liquors

	Zn	Fe	Pb	Mn	SiO_2	Al_2O_3	CaO	P_2O_5	K_2O	V_2O_5
Room temperature	23.1	0.61	< 0.01	0.07	11.05	0.69	0.96	0.75	< 0.01	0.27
High temperature	22.8	2.31	< 0.01	0.09	11.07	1.14	0.68	0.83	< 0.01	0.26

Table 3 Chemical analysis in weight % of the precipitates

Precipitant	ZnO	Fe	Pb	Mn	MgO	SiO_2	Al_2O_3	CaO	P_2O_5	K_2O	V_2O_5
MgO	81.18	0.09	< 0.01	0.02	7.16	8.40	2.14	0.18	< 0.01	< 0.01	0.23
NaOH	88.75	0.10	< 0.01	0.04	0.18	6.52	1.89	0.21	< 0.01	< 0.01	0.35

Results showing analysis of the two liquors that were leached at room and high temperature are shown in Table 2. The leach liquor contains high amount of SiO_2 implying that it leaches out and this is due to breaking down of the willemite matrix (Zn_2SiO_4) during leaching. It is worth noting that the dissolution of both iron and aluminum increases when samples are leached out at high temperature contrast to room temperature and hence higher acid consumption was observed at higher temperature. By comparison, lead does not leach out and this is because of its limited solubility in sulphuric acid media.

The results for the samples that were precipitated with oxalic acid are shown in Table 3. It is evident from the results in Table 3 that high-grade zinc oxide with 99.28 purity was obtained. The main impurity in the precipitate is vanadium oxide. The high-grade zinc oxide was obtained because iron, manganese, and silica did not precipitate alongside zinc oxide.

Precipitation of Zinc from Solution

As already stated, precipitation of zinc from leach solution was done with NaOH, MgO, and oxalic acid.

Precipitation with NaOH and MgO

Chemical analysis of the precipitates that were obtained with MgO and NaOH is shown in Table 3. It can be observed from the results that the precipitate that was obtained with NaOH has high-grade ZnO than the one with MgO, and this is because of the presence of residual MgO.

Table 4 Leach results for the samples that were precipitated with oxalic acid

	ZnO	Fe	Pb	Mn	SiO_2	Al_2O_3	CaO	P_2O_5	K_2O	V_2O_5
Room temperature	99.28	0.07	< 0.01	0.02	0.17	< 0.01	0.21	< 0.01	< 0.01	0.46
High temperature	97.75	0.07	< 0.01	0.03	1.65	0.29	0.30	< 0.01	< 0.01	0.45

Precipitation with Oxalic Acid

The results for the precipitates that were obtained with oxalic acid are shown in Table 4. It is evident from the results in Table 4 that high purity ZnO (more than 99 weight % ZnO) was obtained. As stated earlier, the production of high-purity ZnO is because oxalic acid is highly selective for zinc over other elements in solution. pH decreased to 0.6 during precipitation as a result of regeneration of acid.

Conclusions

1. Both chemical analysis and mineralogical examination of the as-received samples revealed that the major gangue phases in the samples are quartz (SiO_2), calcite ($CaCO_3$) and dolomite ($CaMg(CO_3)_2$, hematite (Fe_2O_3), and clay (aluminum silicate).
2. Mineralogical examination via X-ray powder diffraction showed that zinc is predominantly contained in willemite (Zn_2SiO_4) mineral phase.
3. Zinc readily leaches out from Kabwe ore as leach recovery of more than 90% was obtained at pH of less than 1.2. pH has a significant effect during leaching as leach recovery decreases with increase in pH.
4. Chemical analysis of the leach liquors revealed that SiO_2 partially leaches out and this is due to breakdown of willemite mineral (Zn_2SiO_4).
5. Acid consumption was slightly higher at 70 °C than at room temperature and this is a result of increased dissolution of gangue elements at higher temperature.
6. Precipitation of zinc from leach solution with sodium hydroxide produced poor-grade zinc oxide due to co-precipitation of SiO_2 and Al_2O_3.
7. A high-purity zinc oxide (more than 99 weight % ZnO) was produced via precipitation with oxalic acid followed by calcination. The major impurity in the precipitate is vanadium.

References

1. Vignes A (2011) Extractive metallurgy 2: metallurgical reaction processes. ISTE Ltd., Wiley, Great Britain, USA
2. Moezzi A, McDonagh AM, Cortie MB (2012) Zinc oxide particles: synthesis, properties and applications. Chem Eng J 185:1–22
3. Galvan C (2020) Zinc oxide production, properties and applications. Nova
4. Rodriguez PJE et al (2001) Controlled precipitation methods: formation mechanism of ZnO nanoparticles. European Ceramic Society, p 6
5. Gao J et al (2022) A new process of direct zinc oxide production by carbothermal reduction of zinc ash. Materials 15(15):5246
6. Kołodziejczak-Radzimska A, Jesionowski T (2014) Zinc oxide—from synthesis to application: a review. Materials 7(4):2833–2881

In Situ Method to Study the Dissolution of Ti(C,N) Inclusion in Molten Mold Flux

Li Zhang, Wanlin Wang, Lei Zhang, and Xu Gao

Abstract Mold flux plays a critical role in absorbing the inclusions floating from the liquid steel. However, this dissolution process is hard to observe in situ because the mold is a "black box". This paper used the in-situ single hot thermocouple technique (SHTT) combined with high definition microscope to investigate the dissolution behavior of Ti(C,N) inclusion in molten $CaO–SiO_2–B_2O_3$-based mold flux, as well as the dissolution mechanism was explored by scanning electron microscope (SEM) equipped with X-ray energy spectrometer (EDS) and X-ray photoelectron spectroscopy (XPS). The results suggest that Ti(C,N) inclusion was oxidized and then dissolved in molten slag as $[TiO_4]$ tetrahedra and $[TiO_6]$ octahedra, which is accompanied by the generation of N_2 and CO_2 gas. In addition, $CaTiO_3$ crystals tend to precipitate and stabilize in the molten slag, leading to the final solid–liquid mixed state of the melt. In addition, the precipitated $CaTiO_3$ crystals are greater in number but smaller in size because the dissolution of Ti(C,N) releases more gases that can provide more nucleation sites, thereby increasing the nucleation of the crystal.

Keywords Ti(C,N) inclusion · Mold flux · Fluorine-free · Continuous casting

Introduction

Titanium (Ti) as an alloying element is added into steel to improve its toughness and weldability. During the continuous casting process of Ti-containing steels, the Ti-bearing inclusions such as TiO_2, TiN, Ti(C,N), etc. will be preferentially precipitated and grow up in the liquid steel due to the strong affinity of Ti with O, N, and C [1]. The large particles of Ti-bearing inclusions will float on the surface of the liquid steel and gather in the submerged nozzle, thereby resulting in nozzle clogging [2]. However, partial inclusions floating up to the slag-steel interface will be absorbed by

L. Zhang · W. Wang · L. Zhang (✉) · X. Gao
School of Metallurgy and Environment, Central South University, Changsha 410083, China
e-mail: truth.zhang009@gmail.com

National Center for International Cooperation of Clean Metallurgy, Changsha 410083, China

Z. Peng et al. (eds.), *Characterization of Minerals, Metals, and Materials 2024*, The Minerals, Metals & Materials Series, https://doi.org/10.1007/978-3-031-50304-7_15

the molten mold flux covering the liquid steel surface [3]. The occurrence of the slag-steel reaction leads to the emulsion of slag-steel interface and the significant change in the composition of the mold flux, resulting in the deterioration of its properties, which in turn causes a series of casting quality defects [1, 4].

Researches indicated that the molten mold flux can effectively absorb floating TiO_2 inclusions due to their high solubility in molten slag [5]. However, TiN inclusions have a low solubility of less than 0.5wt% in the molten slag [3] and must first be oxidized to TiO_2 and then can be effectively absorbed [1, 6]. Meanwhile, the oxidation reaction will absorb a large amount of heat and release N_2, which leads to a decrease in the temperature of the liquid steel surface, so that the solidified steel will be covered with inclusions, bubbles, and slag. Ti(C,N) is also a common inclusion that will precipitate in the Ti-containing steels during the continuous casting process but so far the study on the dissolution of Ti(C,N) inclusions in molten slag is little.

B_2O_3 is an effective flux and it can significantly reduce the melting temperature and viscosity of mold flux [4, 7]. In addition, B_2O_3 can reduce the activation energy of Ti-bearing inclusions dissolved in the molten slag and effectively inhibit the precipitation of high-melting substances after the absorption of Ti-bearing inclusions [6, 8]. Therefore, a $CaO–SiO_2–B_2O_3$-based fluorine-free (F-free) mold flux was designed to effectively dissolve the Ti(C,N) inclusions, and this process was in situ observed and recorded using single hot thermocouple technology (SHTT), and their dissolution mechanism was explored by scanning electron microscope (SEM) equipped with X-ray energy spectrometer (EDS), and X-ray photoelectron spectroscopy (XPS) to analyze the fast-quenched sample from SHTT experiments.

Experimental

Sample Preparation

Table 1 shows the main chemical composition of the designed $CaO–SiO_2–B_2O_3$-based F-free mold flux with the basicity (CaO/SiO_2) of 1 and the B_2O_3 content of 6 wt%. The sample was prepared with analytical-grade reagents according to the designed composition. The weighed reagents were mixed well and poured into a graphite crucible. Then the reagents were heated up to 1500 °C in an induction furnace to melt, and held for 5 min to homogenize the composition and eliminate air bubbles. Afterwards, the melt was quenched in water to obtain a homogeneous glassy sample. Finally, the quenched sample was dried and ground into powder with particle size less than 10 μm for subsequent experiments. Prior to the experiments, the powder sample was examined by X-ray diffraction (XRD), and the result is shown in Fig. 1a. It can be seen that there are no obvious characteristic peaks in the pattern, indicating that the prepared sample is the glassy slag with uniform composition.

Furthermore, the morphology and crystal structure of the used Ti(C,N) inclusion were analyzed by SEM and XRD, respectively. The result (Fig. 1b) shows that the

Table 1 Main chemical compositions of the designed mold flux (mass%.)

CaO/SiO_2	CaO	SiO_2	Al_2O_3	Na_2O	B_2O_3
1.0	37.5	37.5	5	10	6

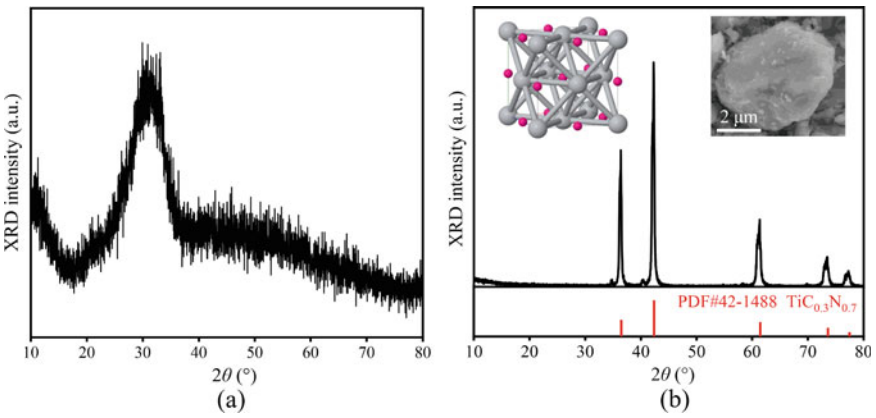

Fig. 1 **a** XRD result of quenched sample; **b** XRD and SEM results of the Ti(C,N) inclusion used in this study

XRD pattern of the Ti(C,N) inclusions matches well with the standard peak of the PDF #38-1420 card, i.e., $TiC_{0.3}N_{0.7}$, where the coordination number of the Ti atom is six, and each Ti atom is bonded to six C or N atoms to form a mixture of edge and corner-sharing octahedra [9]. The used Ti(C,N) inclusion is a dense particle as seen in the SEM image.

Inclusion Dissolution Experiment by SHTT

The dissolution experiment of Ti(C,N) inclusions in molten slag at 1500 °C was conducted using SHTT, and the temperature control profile is depicted in Fig. 2. The SHTT, equipped with a high-definition microscope, enables in-situ clear observation of the dissolution process of Ti(C,N) inclusions. The specific experimental procedure is as follows: First, about 40 mg of powder slag was placed on the B-type thermocouple and heated to 1500 °C at a rate of 10 °C/s to melt the sample, followed by holding for 180 s to eliminate air bubbles and homogenize the composition. Subsequently, a Ti(C,N) inclusion ball was held with a tweezer and placed directly over the molten slag, and dropped into the molten slag for gradual dissolution. At the end of the experiment, the sample was rapidly cooled to room temperature at a cooling rate of 30 °C/s. The entire experiment was conducted in an air atmosphere and the dissolution process was recorded in real time. In addition, in order to analyze the

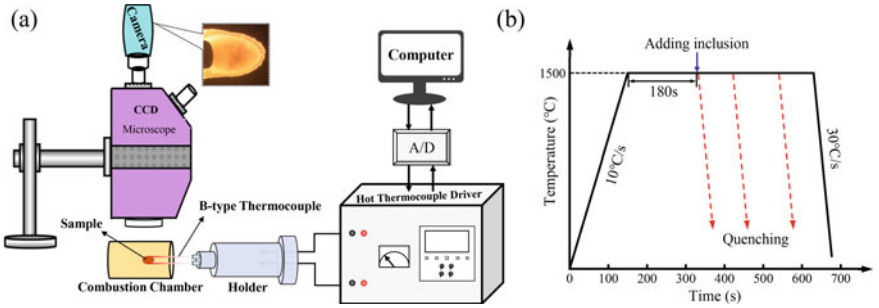

Fig. 2 Inclusion dissolution experiment: **a** The schematic of SHTT apparatus; **b** temperature control profile for inclusion dissolution experiment

state at different dissolution times, the corresponding sample at 1500 °C was rapidly quenched to room temperature at a maximum cooling rate of 30 °C/s, as shown by the red dashed line in Fig. 2b.

Analysis Method

The quenched samples at different times from the SHTT experiment were subjected to SEM and XPS analysis. For SEM analysis, the samples were first embedded in conductive resin, and then polished after being sanded with sandpaper. Microscopic observation can be performed with the accelerating voltage of 15 keV and the distance (less than 15 mm) between the samples and the electron beam gun by SEM (JSM-7900 F, Japanese Electronics Company, Japan), and elemental analysis was performed by EDS (APEX, EDAX, USA). In addition, the valence state and coordination information of the dissolved Ti were determined by X-ray photoelectron spectroscopy (XPS, Escalab 250Xi, Thermo Fisher Scientific, USA). The Ti 2p XPS fine spectrum of the quenched samples was recorded with an Al kα excitation ray source at a pass energy of 20.0 eV, and then corrected with a C1s peak at a reference binding energy of 284.8 eV.

Results

In-Situ Observation of the Dissolution Process by SHTT

Figure 3 shows the real-time image of the dissolution process of a Ti(C,N) inclusion in molten slag at 1500 °C. Bubbles are generated by the introduction of air at the moment the Ti(C,N) inclusion is added to the molten slag. As the dissolution proceeds, the

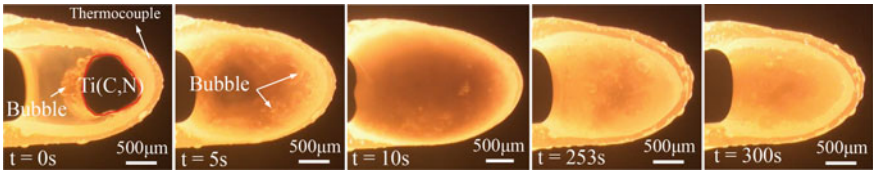

Fig. 3 The dissolution behavior of Ti(C,N) inclusion in molten slag at 1500 °C

Ti(C,N) inclusion is dispersed in the molten slag and slowly dissolved accompanied by a large number of bubbles. It can be seen that the Ti(C,N) inclusion is oxidized and then be dissolved in the molten slag because the bubbles generate such gases as N_2 and CO_2 gases. The reaction then gradually changes from violent to gentle, while solid aggregates begin to precipitate from the molten slag. At the dissolution time of 253 s, almost no bubbles are generated, indicating that the added Ti(C,N) inclusion has been completely oxidized. Subsequently, the solid aggregates are gradually dispersed in the melt and are difficult to be dissolved. Finally, the melt becomes a mixed solid–liquid state.

Microscopic Morphology and Elemental Analyses by SEM and EDS

Figure 4 shows the SEM and EDS results of the quenched samples at different dissolution times. In the sample with the dissolution time of 5 s (Fig. 4a), undissolved Ti(C,N) inclusion can be clearly seen, which are mainly concentrated at the edge of the slag, and there are a large number of small pores nearby, produced by the oxidation of the Ti(C,N) inclusion. For the samples at 120 s (Fig. 4b), it still contains pores, but the pores are significantly reduced in number, indicating that the oxidation of the Ti(C,N) inclusions is gradually weakening. In addition, the magnified observation reveals the aggregated particles (Point A) and dispersed precipitates (Point B), which are proven by EDS analysis to be the undissolved Ti(C,N) inclusion and the precipitated $CaTiO_3$ crystals, respectively. This is consistent with the phenomenon observed in Fig. 3, where the Ti(C,N) inclusion is slowly dissolved with the precipitation of some crystals. At the dissolution time of 300 s (Fig. 4c), the sample has no obvious Ti(C,N) inclusion and pores, but many $CaTiO_3$ crystals. This indicates that the Ti(C,N) inclusion can be dissolved in the $CaO–SiO_2–B_2O_3$-based F-free mold flux, but it will promote the precipitation of $CaTiO_3$ crystals and stabilize in the melt. Moreover, the precipitated $CaTiO_3$ crystals are greater in number and smaller in size than those in the dissolution of TiN inclusions in our previous study [10].

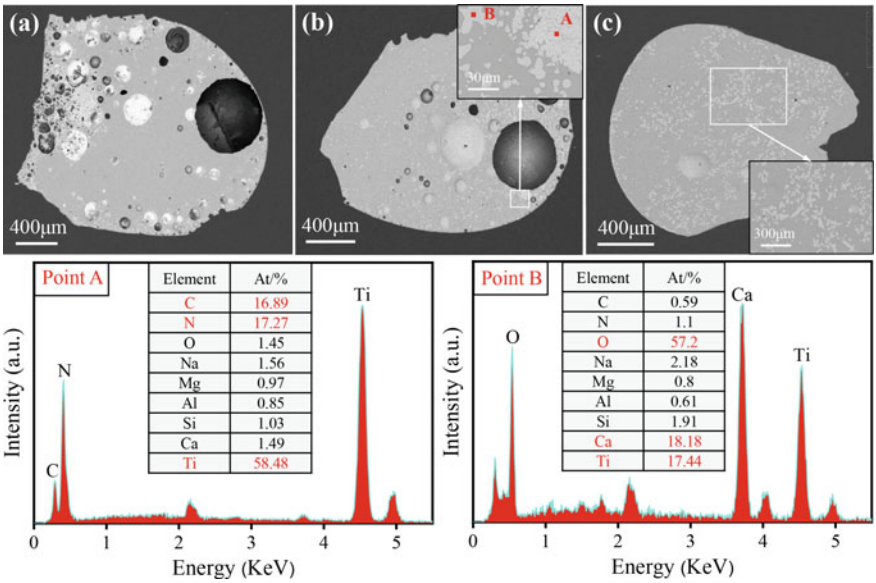

Fig. 4 SEM images and EDS results of the quenched samples that a Ti(C,N) inclusion was dissolved in molten slag at 1500 °C for different times: **a** 5 s; **b** 120 s; **c** 300 s

State Analysis of the Dissolved Ti by XPS

To understand the state of Ti dissolved in the slag, the quenched samples were analyzed by XPS. In general, Ti usually exists in two typical states in the melt, i.e., four-coordinated [TiO_4] tetrahedra and six-coordinated [TiO_6] octahedra, which can be obtained by fitting and deconvoluting the Ti 2p XPS fine spectrum within the binding energy of 454–468 eV. The primary peak Ti $2p_{3/2}$ is located at 458.3 eV while the secondary peak Ti $2p_{1/2}$ is located at 464.1 eV, and the primary peak Ti $2p_{3/2}$ is more intense and has less quantitative error. Therefore, the primary peak Ti 2p3/2 is usually fitted and deconvoluted, and then the two characteristic peaks are obtained, which are located at 458.05 and 458.81 eV for the [TiO_4] tetrahedra and [TiO_6] octahedra, respectively [11]. The relative mole fractions of the two structures can be obtained from their characteristic peak areas. The Ti 2p spectra of the quenched samples at different dissolution times and their deconvoluted results are shown in Fig. 5.

For the sample at the dissolution time of 5 and 120 s, the peak intensity in the Ti 2p XPS spectrum is very weak and the interference peaks are numerous. Therefore, it is not suitable for performing semi-quantitative fitting and deconvolution analysis. This is due to the low content of dissolved Ti in the melt at this time. The intensity of the primary peak is significantly enhanced for the sample at the dissolution time of 300 s, and the interference peaks are significantly reduced. The area proportions of the deconvoluted peaks assigned to [TiO_4] tetrahedra and [TiO_6] octahedra are about

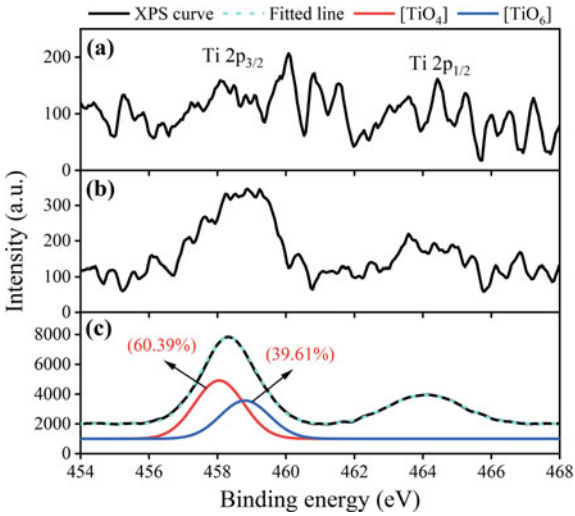

Fig. 5 Ti 2p XPS spectra and their fitting results for the samples in which a Ti(C,N) inclusion was dissolved in molten slag at 1500 °C for different times: **a** 5 s; **b** 120 s; **c** 300 s

60.39% and 39.61%, respectively. Although the coordination number of Ti atoms in the added Ti(C,N) inclusions is six, the oxidation of Ti(C,N) consumes a large number of O^{2-} ions during the dissolution process, which promotes the transformation of $[TiO_6]$ octahedra into $[TiO_4]$ tetrahedra to compensate for the consumed O^{2-}, as shown in Eq. (1) [12]. As a result, the proportion of $[TiO_4]$ tetrahedra in the melt is much higher than that of $[TiO_6]$ octahedra.

$$[TiO_6] \leftrightarrow [TiO_4] + 2O_2 \tag{1}$$

Discussion

Based on the above SHTT, SEM/EDS, and XPS analysis, the mechanism of the dissolution of Ti(C,N) inclusion in the $CaO–SiO_2–B_2O_3$-based F-free molten mold flux can be discussed as follows:

Ti(C,N) has a very low solubility in the molten slag and will be oxidized to form $[TiO_4]$ tetrahedra and $[TiO_6]$ octahedra structures accompanied by the generation of N_2 and CO_2 gases when added to the slag. The network-forming $[TiO_4]$ tetrahedra will combine with the existing $[SiO_4]$ and $[BO_4]$ tetrahedral structures in the melt to form stable titanosilicate and titanoborate network structures [12, 13], while the $[TiO_6]$ octahedra will exist primarily as monomers.

When the Ti(C,N) inclusion is added to the molten slag for 5 s, a very small amount of Ti(C,N) inclusion is oxidized but the reaction is violent. As the dissolution time increases to 120 s, the Ti(C,N) inclusion continues to be oxidized and dissolved [14], and the reaction becomes relatively less violent. Furthermore, the dissolved Ti(C,N)

introduces a certain amount of [TiO_6] octahedra, and the generated N_2 and CO_2 bubbles can act as nucleation points to lower the crystallization energy barriers and promote heterogeneous nucleation in the melt [15]. In addition, the movement of the bubbles accelerates the ion migration in the melt and reduces the crystallization incubation time. Thus, $CaTiO_3$ crystals easily nucleate and grow on the surface of bubbles with sufficient [TiO_6] octahedra monomers and Ca^{2+} ions in the melt. Meanwhile, the bubble grows until it bursts, and the precipitated $CaTiO_3$ crystals detach from the bubble surface and move in the melt. When the dissolution time is further extended to 300 s, the Ti(C,N) inclusion has been completely dissolved and no obvious bubbles are visible. The newly formed $CaTiO_3$ crystals are greatly reduced due to the lack of nucleation points for bubbles, but the precipitated $CaTiO_3$ crystals are stable in the molten slag and continue to grow.

It can be seen that the dissolution behavior of Ti(C,N) inclusions in the molten slag is similar to that of TiN inclusions due to their similar crystal structure, in which partial C atoms replace the N atoms and occupy their positions in the crystals [9, 16]. However, compared with TiN inclusions, the $CaTiO_3$ crystals in the sample with Ti(C,N) inclusion dissolved for 300 s are greater in number and smaller in size. This is because that the oxidation of a considerable amount of Ti(C,N) inclusion produces more gases, and the heterogeneous nucleation points in the melt increase correspondingly. Therefore, the nucleation rate of $CaTiO_3$ crystals increases and the crystal size decreases.

Conclusion

The dissolution behavior of Ti(C,N) inclusions in molten CaO–SiO_2–B_2O_3-based fluorine-free mold flux was investigated in situ by SHTT, and the dissolution mechanism was studied by XPS and SEM with EDS. It can be seen that Ti(C,N) inclusions are oxidized and then dissolved in the molten slag as [TiO_4] tetrahedra and [TiO_6] octahedra, which is accompanied by the generation of N_2 and CO_2 gas. Furthermore, $CaTiO_3$ crystals tend to precipitate and stabilize in the molten slag during the dissolution of Ti(C,N) inclusions, leading to the final solid–liquid mixed state of the melt. This is because the generated bubbles can act as nucleation sites to promote heterogeneous nucleation of [TiO_6] octahedra and Ca^{2+}. In addition, $CaTiO_3$ crystals precipitated from the Ti(C,N) dissolution process are greater in number and smaller in size than those from the TiN dissolution process. This is because the dissolution of Ti(C,N) releases more gases that can act as more nucleation sites, thereby increasing the nucleation of the crystal.

Acknowledgements The authors wish to acknowledge the financial support from the Fellowship of China National Postdoctoral Program for Innovative Talents (BX20220357) and the National Science Foundation of China (52130408).

Conflicts of Interest The authors declare that they have no known competing financial interests or personal relationships that could have appeared to influence the work reported in this paper.

References

1. Chen Z, Li M, Wang X, He SP, Wang Q (2019) Mechanism of floater formation in the mold during continuous casting of Ti-stabilized austenitic stainless steels. Metals 9(6):635. https://doi.org/10.3390/met9060635
2. Cheng LM, Zhang LF, Ren Y, Yang W (2021) Clogging behavior of a submerged entry nozzle for the casting of Ca-treated Al-killed Ti-bearing steel. Metall Mater Trans B 52:1186–1193. https://doi.org/10.1007/s11663-021-02110-z
3. Wang W, Cai D, Zhang L (2018) A review of fluorine-free mold flux development. ISIJ Int 58(11):1957–1964. https://doi.org/10.2355/isijinternational.ISIJINT-2018-232
4. Wang WL, Cai DX, Zhang L, Sohn IL (2021) Effect of TiO_2 and TiN on the viscosity, fluidity, and crystallization of fluorine-free mold fluxes for casting Ti-bearing steels. Steel Res Int 92(2):2000314. https://doi.org/10.1002/srin.202000314
5. Ren ZS, Hu XJ, Hou XM, Xue XX, Chou KC (2014) Dissolution and diffusion of TiO_2 in the CaO–Al_2O_3–SiO_2 slag. Int J Miner Metall Mater 21:345–352. https://doi.org/10.1007/s12613-014-0915-8
6. Zhou LJ, Pan ZH, Wang WL, Chen JY, Xue LW, Zhang TL, Lei Z (2020) Interfacial interactions between inclusions comprising TiO_2 or TiN and the mold flux during the casting of titanium-stabilized stainless steel. Metall Mater Trans B 51:85–94. https://doi.org/10.1007/s11663-019-01746-2
7. Zhang L, Wang WL, Sohn IL (2019) Crystallization behavior and structure analysis for molten CaO–SiO_2–B_2O_3 based fluorine-free mold fluxes. J Non-Cryst Solids 511:41–49. https://doi.org/10.1016/j.jnoncrysol.2019.01.035
8. Li BY, Geng X, Jiang ZH, Hou Y, Gong W (2021) Effects of BaO and B_2O_3 on the absorption of Ti inclusions for high titanium steel. Metals 11(1):165. https://doi.org/10.3390/met11010165
9. The Springer Materials (online database), Inorganic Solid Phases for $TiC_{0.3}N_{0.7}$ ($TiC_{0.5}N_{0.5}$) Crystal Structure. https://materials.springer.com/isp/crystallographic/docs/sd_1140134
10. Cai DW, Zhang L, Wang WL, Zhang L, Sohn IL (2023) Dissolution of TiO_2 and TiN inclusions in CaO–SiO_2–B_2O_3-based fluorine-free mold flux. Int J Miner Metall Mater 30:1740–1747. https://doi.org/10.1007/s12613-023-2622-9
11. Li JF, Huang JG, Feng H, Wang XY, Yin XC, Zhang ZT (2022) Effect of TiO_2/SiO_2 molar ratio on the structure, dielectric and crystallization properties of SiO_2–TiO_2–ZrO_2–RO–Al_2O_3 glasses. J Non-Cryst Solids 576:121243. https://doi.org/10.1016/j.jnoncrysol.2021.121243
12. Jin SQ, Wang ZD, Tao GJ, Zhang SL, Liu W, Fu WH, Zhang B, Sun HM, Wang YD, Yang WM (2017) UV resonance Raman spectroscopic insight into titanium species and structure-performance relationship in boron-free Ti-MWW zeolite. J Catal 353:305–314. https://doi.org/10.1016/j.jcat.2017.07.032
13. Wang Z, Shu QF, Chou KC (2011) Structure of CaO–B_2O_3–SiO_2–TiO_2 glasses: a Raman spectral study. ISIJ Int 51(7):1021–1027. https://doi.org/10.2355/isijinternational.51.1021
14. Monteverde F, Medri V, Bellosi A (2002) Microstructural evolution of titanium carbonitride based materials during oxidation. Microchim Acta 139:97–103. https://doi.org/10.1007/s006040200046
15. Yan K, Che DF (2010) A coupled model for simulation of the gas-liquid two-phase flow with complex flow patterns. Int J Multiph Flow 36(4):333–348. https://doi.org/10.1016/j.ijmultiphaseflow.2009.11.007
16. The Springer Materials (online database) Inorganic solid phases for TiN crystal structure. https://materials.springer.com/isp/crystallographic/docs/sd_0305677

Developing Bottom-Blowing O_2–CaO Control Model for Converter Steelmaking Process

Botao Xue, Kai Dong, Rong Zhu, Lingzhi Yang, and Hang Hu

Abstract As bottom-blowing O_2–CaO converter steelmaking process enables rapid slag formation, efficient phosphorus removal, and improved steel quality. It has significant strategic significance for the greening and high-quality development of the iron and steel industry. In this study, we collected field actual smelting data, established a mass and energy model, and developed a bottom-blowing O_2–CaO control model with Visual Studio.NET 2019 (VS2019) as the development tool. The application results indicated that bottom-blowing lime powder flow accuracy is ± 50 kg/min, time accuracy is ± 30 s, and the degree of automation reaches more than 90%. Real-time monitoring allows for dynamic adjustment of the converter's O_2–CaO bottom-blowing and accurate control, improving steelmaking production efficiency.

Keywords Converter steelmaking · Bottom-blowing O_2–CaO · Control model

Introduction

Converter steelmaking is one of the main steel smelting methods, which is carried out by adding hot metal and scrap into the furnace, melting, and tempering at high temperatures to produce steel with a qualified composition and temperature [1]. In the converter steelmaking process, slagging treatment is an essential step to remove tramp elements and improve the quality of molten steel. Bottom-blowing lime powder is an efficient slagging method [2]. However, its operation is complicated and affected

B. Xue · K. Dong (✉) · R. Zhu
Institute for Carbon Neutrality, University of Science and Technology Beijing, Beijing 100083, China
e-mail: dongkai@ustb.edu.cn

L. Yang · H. Hu
School of Minerals Processing and Bioengineering, Central South University, Changsha 410083, China

Z. Peng et al. (eds.), *Characterization of Minerals, Metals, and Materials 2024*, The Minerals, Metals & Materials Series, https://doi.org/10.1007/978-3-031-50304-7_16

by many factors, including parameters such as the amount and speed of lime powder blowing [3]. Therefore, quickly and accurately controlling the lime powder blowing parameters to achieve the best slagging effect has become a significant challenge for the steel industry.

To address this challenge, it is necessary to develop relevant control models to guide slagging operations. This includes real-time monitoring and adjustment of lime addition parameters to accurately control the slagging process and improve the slagging effect and quality. The reaction mechanism and blowing process of lime slagging in steelmaking have been thoroughly studied. Regarding reaction mechanisms, scholars have paid attention to lime and slag's reaction kinetics and thermodynamic properties. Ono et al. studied the kinetics of dephosphorization of lime powder in hot metal with oxygen injection and concluded that accelerating the lime slagging rate and increasing the oxygen potential is beneficial to the dephosphorization of the converter [4]. Maruoka et al. conducted an experimental study on the dissolution rate of various types of lime in steelmaking slag. They found that porous lime's dissolution rate was higher than dense lime [5]. Wang et al. discussed the effect of O_2–CaO blowing on the temperature of the fire point region in the converter steelmaking process and gave the optimum temperature range for the dephosphorization of molten steel [6].

In terms of the blowing process, top blowing can make slag quickly, but uneven distribution of lime needs to be avoided [7, 8]. The metallurgical technology of bottom blowing is highly efficient and can significantly improve the kinetic conditions in the molten pool. This process speeds up the reaction and homogenizes the composition and temperature of the bath. Additionally, it increases the hit rate of the smelting endpoint and has been proven [9, 10]. The amount of powder and the blowing speed are critical to the lime slagging operation, and deviations in the process can lead to poor slag performance. Protopopov et al. established a mathematical model of nozzle dispersion flow that the main factors affecting particle distribution are powder concentration, nozzle length, and particle size [11]. Tao et al. conducted a powder-blowing experiment on the top-blowing converter and achieved good results. The results show that the steel dephosphorization rate increases with an increase in the powder-blowing amount [12]. Wei et al. used the wrapped combustion flame to increase the O_2–CaO jet capacity. The results show that it can increase the impact of the jet, speed up the melting of CaO particles, and make it easier to use CaO [13]. Regarding modeling research, scholars have developed a series of slag-foaming models using mathematical modeling methods and computer network technology. Song et al. developed a static control model for converter steelmaking to guide the addition of lime according to the material balance and energy balance, which can effectively regulate the alkalinity of steel slag and reduce slagging material consumption [14]. Liu et al. designed the process control system for dephosphorization industrial furnaces to guide the charging operation, and the application of the system can effectively reduce material consumption and enhance the intelligence of industrial furnaces [15]. Zhan et al. developed a converter intelligent steelmaking

optimization model system, which calculates the amount of lime and other auxiliary materials added according to the distribution ratio of phosphorus and overcomes the shortcomings of the smelting process of manual experience dosing [16].

In summary, many studies on the reaction mechanism and blowing parameters in converter steelmaking have been studied. Nonetheless, the bottom-blowing O_2–CaO control models with real-time detection and adjustment features are even more scarce. Therefore, this paper has established a material balance and heat balance model based on the on-site process data of a 300-ton converter in a steel plant and develops an automatic control model of bottom-sprayed lime powder in the converter by using a SQL database and the Visual Studio.NET 2019 (VS2019) software development tool to realize the precise control of slagging process, which can help to improve the automation level of steelmaking and production efficiency.

Model Building and Data Collection

The bottom-blowing O_2–CaO control model was built based on mass and energy balance and cross-validated against each other using on-site production process data. The model calculates the parameters for lime powder blowing, including carrier gas flow, lime flow, and blowing time, based on the raw material conditions and the requirements of the target steel grade. Based on the trigger signal, the blowing parameters are automatically transmitted to the on-site programmable logic controller (PLC) to control the operation of the relevant powder-blowing equipment.

Mass and Energy Model

The material and energy balance model [see Eqs. (1) and (2)] is derived by analyzing the material and energy flows of the converter steelmaking process. According to the laws of mass and energy, the input mass and energy must equal the mass and energy output of the entire production process and of each zone [17]. These processes involve the consumption of scrap, hot metal, oxygen, flux, and other auxiliary materials (see Fig. 1).

$$\sum_{i=1}^{n} M_{\text{in},i} = \sum_{j=1}^{m} M_{\text{out},j} \tag{1}$$

$$\sum_{i=1}^{n} E_{\text{in},i} = \sum_{j=1}^{m} E_{\text{out},j} \tag{2}$$

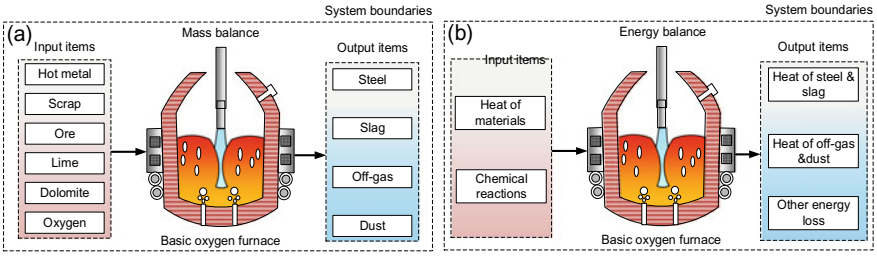

Fig. 1 Input and output items of the mass and energy model

where $\sum_{i=1}^{n} M_{\text{in},i}$ is the total raw material mass input terms, kg/ton; $\sum_{j=1}^{m} M_{\text{out},j}$ is the total raw material mass output terms, kg/ton; $\sum_{i=1}^{n} E_{\text{in},i}$ is the total energy input terms, kWh/ton; $\sum_{j=1}^{m} E_{\text{out},j}$ is the total energy output terms, kWh/ton.

Among them, many factors affect lime consumption, which need to be considered from the quality, composition, basicity, and operation technique. The consumption of bottom-blowing lime powder Q_{Lime} is determined by Eq. (3).

$$Q_{\text{Lime}} = \alpha \times \gamma_{\text{Lime}} \times \frac{\left(R \times \sum_{i=1}^{n} Q_{\text{SiO}_2}^{i} - \sum_{j=1}^{m} Q_{\text{CaO}}^{j}\right)}{\eta_{\text{Lime}}^{\text{CaO}} - R \times \eta_{\text{Lime}}^{\text{SiO}_2}} \tag{3}$$

where α is the effective utilization rate of lime,%; γ_{Lime} is the proportion of bottom-blown lime powder,%; R is the basicity of slag; $\sum_{i=1}^{n} Q_{\text{SiO}_2}^{i}$ is the SiO_2 mass of the input items, kg; $\sum_{j=1}^{m} Q_{\text{CaO}}^{j}$ is the CaO mass of the input items, kg; $\eta_{\text{Lime}}^{\text{CaO}}$ is the CaO content of lime powder, %; $\eta_{\text{Lime}}^{\text{SiO}_2}$ is the SiO_2 content of lime powder, %.

The bottom-blowing lime powder process requires a combination of oxygen and other gases as a carrier gas, in which oxygen provides the necessary heat [C, Si, Mn, P, and other elements of the oxidation reaction to release heat, see Eqs. (4)–(8)], to reduce in the outlet of the blowing equipment due to the overcooling of the accumulation, affecting its service life.

$$[\text{C}] + [\text{O}] = \{\text{CO}\} \tag{4}$$

$$[\text{C}] + 2[\text{O}] = \{\text{CO}_2\} \tag{5}$$

$$2[\text{P}] + \frac{5}{2}\text{O}_2 + 3(\text{CaO}) = (3\text{CaO}\cdot\text{P}_2\text{O}_5) \tag{6}$$

$$[\text{Si}] + 2[\text{O}] = (\text{SiO}_2) \tag{7}$$

$$[\text{Mn}] + [\text{O}] = (\text{MnO}) \tag{8}$$

The amount of oxygen blowing Q_{Oxy} at the bottom is calculated as shown in Eq. (9).

$$Q_{Oxy} = \gamma_{Oxy} \times \left(\sum_{p=1}^{q} \left(Q_P \times \frac{32}{M_P} \right) + \beta_{Dust} \times \left(\lambda_{FeO} \times \frac{16}{72} + \lambda_{Fe_2O_3} \times \frac{48}{160} \right) \right) \tag{9}$$

where γ_{Oxy} is the proportion of bottom-blown oxygen, %; Q_P is the mass of C, Si, Mn, P and other elements, kg; M_P is the relative molecular weight of C, Si, Mn, P and other elements, kg; β_{Dust} is the mass of dust, kg; λ_{FeO} is the proportion of FeO mass in the amount of dust, %; $\lambda_{Fe_2O_3}$ is the proportion of Fe_2O_3 mass in the amount of dust, %.

Data Collection

To verify the reliability of the balance model, it is necessary to include the actual data of steel enterprises. In this study, we take the 300-ton converter of a steel plant as an example and use KEPServerEX software as a third-party OPC server Kepware to build a data collection platform. The collected on-site process data are stored in Microsoft SQL Server 2012 database. The model synthesizes software and hardware model technology, consisting of application software, standardized software, and equipment servers. The collected data includes basic automation data (L1), process control data (L2), and production planning data (L3). The specific data are as follows:

(1) L1 information

The information on the converter steelmaking process mainly includes heat data (smelting time, oxygen supply time, bottom blowing time, gas flow data, weight data (hot metal, scrap), oxygen lance height, converter angle, trigger signal in the process of smelting, and other data directly reflecting the production status of the steelmaking process.

(2) L2 information

The process control data consist mainly of the rate and time of the multi-stage bottom-blowing of O_2–CaO, the type of gas, the flow rate of each gas involved in the blowing, and the duration of the blowing.

(3) L3 information

The information data acquired by the L3 system include production plan information (smelting furnace number, steel grade, route code, specification, etc.), task release, interruption operation record information (time, fault, solution, etc.), heat summary, and quality analysis data (HM composition data, scrap composition data, steel composition data, standard steel composition data, etc.).

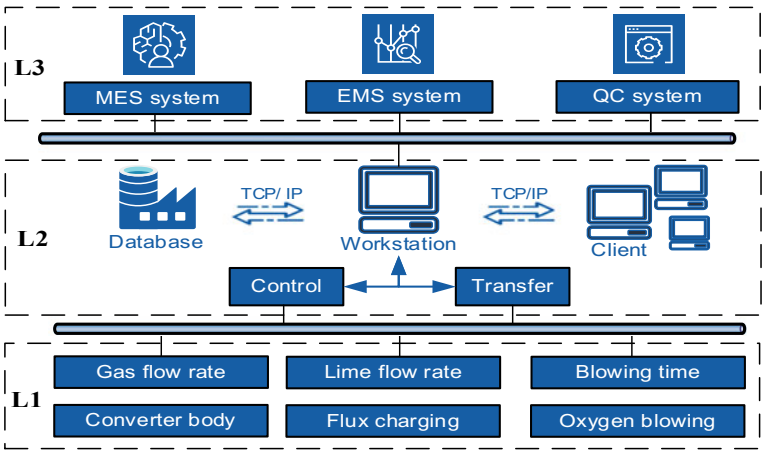

Fig. 2 Industrial network structure of a steel plant

Regarding hardware, we installed a well-performing server, which is responsible for real-time data collection and model operation and is the core component of the model. A client was also installed on-site to automatically control the model operation by bottom-blowing O_2–CaO powder. The server and the client are connected via industrial ethernet. The industrial network structure of a steel plant is shown in Fig. 2.

Model Interface and Function

The bottom-blowing O_2–CaO control model has been developed by Visual Studio.NET 2019 development tool, which calculates the bottom-blowing lime powder consumption, carrier gas consumption, and bottom-blowing time according to the target steel grade and raw material conditions and realizes the data communication with the on-site PLC to control the related valves and flow meters to complete the bottom-blowing lime powder operation. The specific functions of the model include data communication, process control, mode management, dynamic calculation, and data report. The functional structure diagram is shown in Fig. 3.

Figure 4 shows the main operation interface of the model, which integrates management, display, and operation and can dynamically display the current smelting information in real-time, such as basic data of process smelting (heat number, steel grade, blowing time, gas source information, etc.), composition and consumption of metal materials, bottom-blowing flow rate, pressure and consumption, and status records, and the interface can also adjust the blowing mode of the current furnace and the control status.

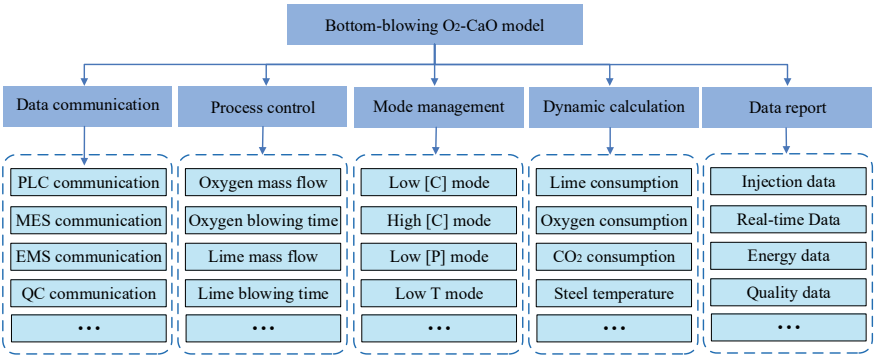

Fig. 3 Function structure diagram of bottom-blowing O_2–CaO model

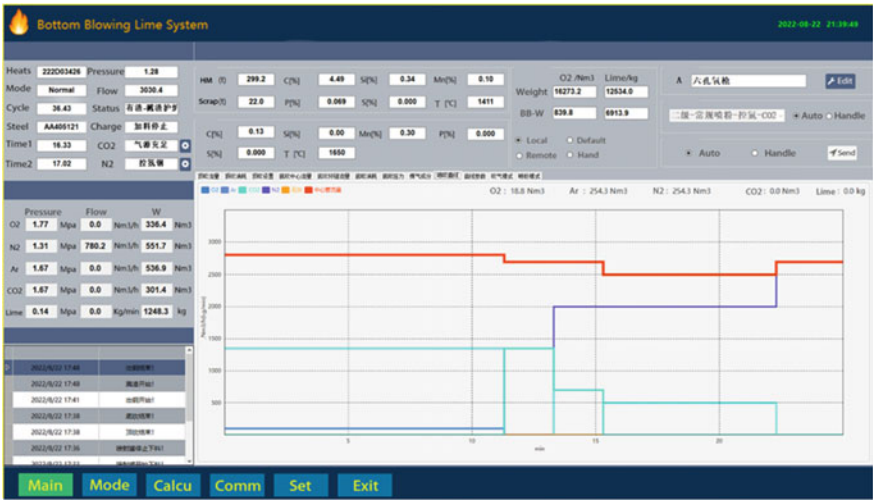

Fig. 4 Interface of bottom-blowing O_2–CaO control model

Model Application and Discussion

The developed converter bottom-blowing O_2–CaO control modeling system is applied to a steel plant 300-ton converter. This can improve the bottom-sprayed lime control accuracy and hit rate and optimize the slag-making process. Through computer control of steelmaking bottom blowing lime powder blowing speed precision control within ± 50 kg/min, blowing time control precision within ± 30 s, using the degree of automation is greater than 90%, compared with the hit rate of manual control has been dramatically improved. The model also has an advanced self-learning function, can accurately calculate the blowing parameters and continuously optimize them, which is more accurate compared with the rough calculation of

empirical steelmaking, and can adapt to the changes of melt and scrap raw materials and the changes of converter type, and control the amount of oxygen and lime dosage required for blowing in the optimal range.

By evaluating the application effect, a single component powder spraying intensity of up to 160 kg/min, lime powder to completely replace the top of the addition of chunks of lime, and compared with the unsprayed process, the consumption of lime per ton of semi-steel by 10 kg down to 7 kg; the endpoint of the average phosphorus quality fraction from 0.036% down to 0.029%; the endpoint of the average carbon quality fraction from 3.15% up to 3.25%, realizing green low-carbon clean steelmaking.

Nonetheless, there were some limitations in this study. A complicated interaction of parameters connected to data, model, and training influences the controlling accuracy of an established model. It's essential to carefully consider and experiment with these factors to optimize model accuracy for a specific problem. To adapt the model to changing data patterns and requirements, regular monitoring and updating may also be required to ensure that the bottom blow O_2–CaO system meets its control accuracy requirements and can effectively regulate the slagging process.

Conclusion

This study developed a control model for bottom-blowing O_2–CaO in converter steelmaking, using mass and energy balance principles, focusing on steel grades and raw material conditions. Using on-site smelting real-time data, the flow rate and time of blowing lime powder and carrier gas were calculated based on dynamic parameters and self-learning methods. These parameters were then automatically sent to the PLC control system, and the lime powder speed control accuracy reached $\pm$ 50 kg/min and the blowing time accuracy $\pm$ 30 s, with an automation degree of more than 90%, realizing accurate O_2–CaO blowing powder, completely replacing the need for top-added lime blocks, reducing the lime consumption per ton of semi-steel to 7 kg, lowering the average phosphorus content from 0.036 to 0.029%, increasing the average carbon content from 3.15 to 3.25%, improving the degree of automation and production efficiency of steelmaking, and providing valuable guidance for slag operation in converter steelmaking.

References

1. Jalkanen H, Holappa L (2014) Converter steelmaking. In: Treatise on process metallurgy. Elsevier, pp 223–270
2. Hu SY (2019) The application fundamental research on long-life bottom blowing O_2–CaO in converter steelmaking. Ph.D. thesis. University of Science and Technology, Beijing

3. Hu SY, Zhu R, Wang D, Li X, Wei GS (2021) Research on the gas–solid jet flow and erosion wear characteristics in bottom injecting lance used for oxygen–lime powder bottom blowing converter. Metall Mater Trans B 52:3875–3887
4. Ono H, Masui T, Mori H (1983) Dephosphorization kinetics of hot metal by lime injection with oxygen gas. Tetsu Hagané 69(15):1763–1770
5. Maruoka N, Ishikawa A, Shibata H, Kitamura SY (2013) Dissolution rate of various limes into steelmaking slag. High Temp Mater Process 32(1):15–24
6. Wang CY, Zhu R, Dong K, Wei GS, Ren X, Zhou Y, Feng C (2023) Research on mechanism change of temperature effect on dephosphorization in the bottom-blown O_2–CaO process of semi-steelmaking. J Mater Res Technol 24:8725–8734
7. Miyata M, Tamura T, Higuchi Y (2017) Development of hot metal dephosphorization with lime powder top blowing: part 1. Low blowing rate. ISIJ Int 57(10):1751–1755
8. Miyata M, Tamura T, Higuchi Y (2017) Development of hot metal dephosphorization with lime powder top blowing: part 2. high blowing rate. ISIJ Int 57(10):1756–1761
9. Dong K, Wang CY, Liu RZ, Ren X, Liu WJ (2017) Development status and prospects of bottom-blown O_2–CaO technology in converter steelmaking process. Iron Steel
10. Zhou Y, Zhu R, Hu S, Li WF (2021) Study on metallurgical characteristics of the bottom-blown O_2–CaO converter. Ironmak Steelmak 48(2):142–148
11. Protopopov EV, Galiullin TR, Chernyatevich AG, Kharlashin PS (2009) Powder injection into slag in a converter. Steel Transl 39(4):295–299
12. Tao QZ, Su TN, Liu KW (1983) Experiment on technique of dephosphorization with powder injection in LD converter. Iron Steel 03:51–54
13. Wei GS, Peng YH, Zhu R, Yang LZ, Wu XT (2020) Fluid dynamics analysis of O_2–CaO jet with a shrouding flame for EAF steelmaking. ISIJ Int 60(3):481–491
14. Song BM, Wang JJ, Shi SG (2021) Industry practice of smart steelmaking model. Henan Metall 04:40–43+56
15. Liu T (2022) Design of process control system for dephosphorization industrial furnace based on computer network technology. Ind Heat 51(08):50–53
16. Zhan XL, Zhang LQ, Zhang CJ, Fu KX, Song YQ, Zhao AN, Cheng JQ (2021) Research and application of intelligent smelting optimization model for converter. Metal World 02:23–28
17. Cullen JM, Cooper DR (2022) Material flows and efficiency. Annu Rev Mater Res 52:525–559

Emission Characteristics of SO_2 During Roasting of Iron Ore Pellets

Rongguang Xu, Yunqing Tian, Dawei Sun, Ruiqing Qian, Xiangjuan Dong, Wenwang Liu, Chengwei Ma, Xiaojiang Wu, Luyao Zhao, Tao Yang, and Li Ma

Abstract Baking cup experiments were carried out and emission characteristics of SO_2 during roasting of iron ore pellets were investigated. Concentration of SO_2 starts to increase when the temperature is about 800 °C, then reaches a peak when the temperature is just above 900 °C. Furthermore, emission characteristics of SO_2 during roasting of iron ore pellets in travelling grate machine were investigated. There are two peaks of concentration of SO_2, and the lower peak is in downdraft drying section, while the higher peak is in roasting section. Concentration of SO_2 is at a low level in preheat section, then begins to increase in roasting section, and reaches peak value in Number 11 wind boxes. Sulfur content in acid pellets is about only one fifth of that in alkaline ones, which might relate to calcium in iron ore pellets. Except for chemical compositions, temperature is another important factor for sulfur content in iron ore pellets. Sulfur in iron ore pellets made from roasting test was analyzed by XPS, and results show that there is mainly sulfate.

Keywords Iron ore pellet · SO_2 · Roasting · Baking cup experiment · Travelling grate machine

Introduction

China's crude steel production has exceeded one billion tons since 2020, exceeding 50% of the world production. At the same time, large amounts of pollutants are produced and more than 85% are gas pollutants [1, 2]. In recent years, China has

R. Xu (✉) · Y. Tian · L. Zhao · T. Yang · L. Ma
Beijing Key Laboratory of Green Recyclable Process for Iron & Steel Production Technology, Beijing 100043, China
e-mail: xrg1220@163.com

Research Institute of Technology, Shougang Group Co. Ltd., Beijing 100043, China

D. Sun · R. Qian · X. Dong · W. Liu · C. Ma · X. Wu
Shougang Jingtang United Iron & Steel Co. Ltd, Tangshan, Hebei 063200, China

Z. Peng et al. (eds.), *Characterization of Minerals, Metals, and Materials 2024*, The Minerals, Metals & Materials Series, https://doi.org/10.1007/978-3-031-50304-7_17

paid great attention to emission reduction in iron and steel industry, and issued a number of targeted policies. SO_2, NOx, and particulate matter are the main control targets. Until now, nearly 100 iron and steel enterprises have completed ultra-low emissions of pollutants, however, end treatment is widely carried out [3, 4].

In order to promote cleaner production in pelletizing plant, emission characteristics of SO_2 during oxidizing roasting of iron ore pellets should be made clear. Therefore, in this work, baking cup experiments of oxidized pellets were carried out, and emission characteristics of SO_2 during roasting of iron concentrate pellets were investigated. Moreover, SO_2 in flue gas in bellows at different zones of travelling grate machine was detected as well. At last, the effect of chemical compositions of iron ore pellets on sulfur content was studied.

Experimental

Raw Materials

Table 1 shows chemical compositions of raw materials. Iron concentrate A, iron concentrate B, and calcium-containing flux C were used in baking cup experiment, while iron concentrate D was the main raw material used in production. Iron concentrate A is a mixture of magnetite and hematite, while iron concentrate B and D are magnetite. X-ray diffraction (XRD) spectra of calcium-containing flux C are shown in Fig. 1. Result indicates that calcium-containing flux C is mainly portlandite (P) and also contains a small amount of calcite (Q).

Table 1 Chemical compositions of raw materials (wt%)

Raw materials	TFe	FeO	CaO	MgO	SiO_2	Al_2O_3	S	LOI
Iron concentrate A	66.52	17.78	0.24	0.44	3.07	0.56	0.05	− 0.53
Iron concentrate B	69.59	28.80	0.13	0.12	2.92	0.010	0.003	− 3.01
Calcium-containing flux C	–	–	68.43	0.56	0.99	0.35	–	27.58
Iron concentrate D	69.73	29.81	0.35	0.47	1.27	0.37	0.19	− 2.87

LOI loss on ignition

Apparatus and Instruments

Figure 2 shows baking cup equipment. The diameter of baking cup is 120 mm, and the height is 400 mm. The baking cup could be continuously heated up according to temperature procedure during experiment, which is shown in Table 2. The test

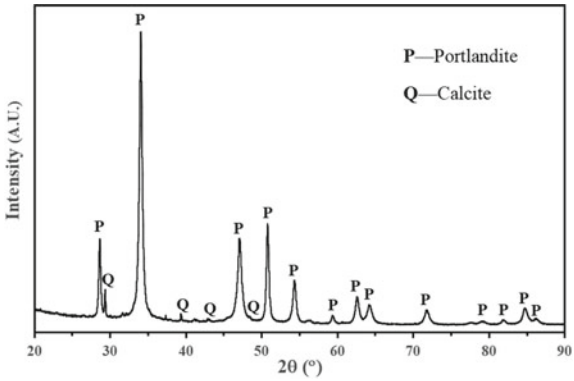

Fig. 1 XRD spectra of calcium-containing flux C

process includes drying, preheat, roasting, soaking, and cooling, which is consistent with travelling grate machine for iron ore pellets. Concentration of SO_2 in flue gas is obtained by gas analyzer testo 350.

Fig. 2 Baking cup equipment

Table 2 Temperature procedure of baking cup experiment

Section name	Drying	Preheat		Roasting		Soaking	Cooling
Temperature (°C)	450	700	1000	1200	1260	1100	25
Time (min)	8	5	7	4	8	3	15
Gas velocity (m/s)	1.8	1.7	1.6	1.5	1.5	1.2	2.0

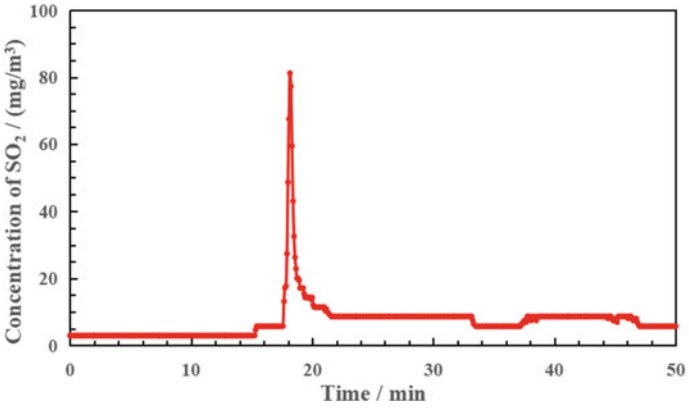

Fig. 3 Concentration of SO_2 in tail gas during baking cup experiment

Results and Discussion

Emission Characteristics of SO_2 During Baking Cup Experiment of Iron Ore Pellets

Baking cup experiment of iron ore pellets was carried out and charge mixture consisted of 48% iron concentrate A, 48% iron concentrate B, and 4% calcium-containing flux C. Compositions of tail gas during baking cup experiment of iron ore pellets were detected by gas analyzer testo-350. Concentration of SO_2 in tail gas is shown in Fig. 3, and result shows that concentration of SO_2 starts to increase at 15 min after start of experiment, when the temperature is about 800 °C; then there is a peak of concentration of SO_2 at 18 min, when the temperature is just above 900 °C.

Emission Characteristics of SO_2 at Different Sections of Travelling Grate Machine

Shougang Jingtang pelletizing plant currently has three sets of travelling grate machines of 504 m^2. Every device includes seven sections, as shown in Fig. 4 and Table 3. Figure 5 shows the process gas flows of travelling grate machine.

SO_2 in flue gas in bellows of travelling grate machine was detected continuously. As shown in Fig. 6, there are two peaks of concentration of SO_2, one of which is in downdraft drying section, and another is in roasting section. It is surprised that concentration of SO_2 in flue gas in downdraft drying section is higher than that in roasting section, which may be related to abnormal working conditions. In order to install gas analyzer, travelling grate machine stopped working temporarily, which would lead to abnormal working conditions and affect the detection at last.

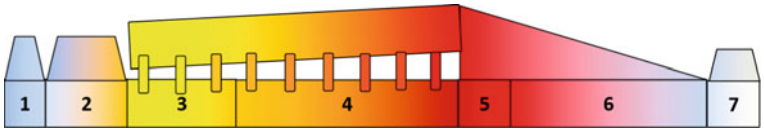

Fig. 4 Diagram of different sections of travelling grate machine

Table 3 Parameters of different sections of travelling grate machine

Section number	1	2	3	4	5	6	7
Section name	Updraft drying	Downdraft drying	Preheat	Roasting	Soaking	1st cooling	2nd cooling
Length (m)	9	15	15	33	9	33	12
Wind box number	1, 2A	2B, 3, 4	5–7	8–12	13, 14A	14B, 15–19	20, 21

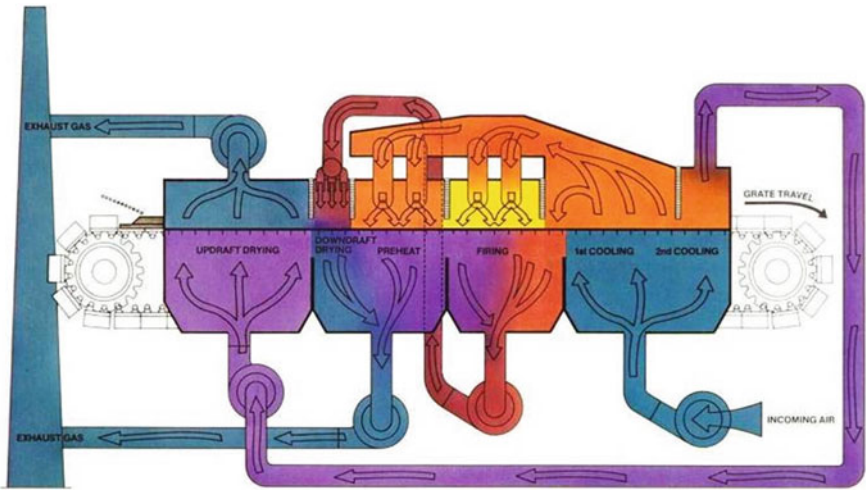

Fig. 5 Process gas flows

Concentration of SO_2 begins to increase in roasting section, where temperature rises gradually.

Moreover, SO_2 in flue gas in wind boxes of travelling grate machine was detected intermittently. As shown in Fig. 7, there are two peaks of concentration of SO_2 as well. One peak is in Number 3 and Number 4 wind boxes, which belong to downdraft drying section, while another peak is in Number 11 wind boxes, which is in roasting section. As gas in downdraft drying section comes from roasting section, as shown in Fig. 5. Therefore, it is reasonable that there is a lower peak of concentration of

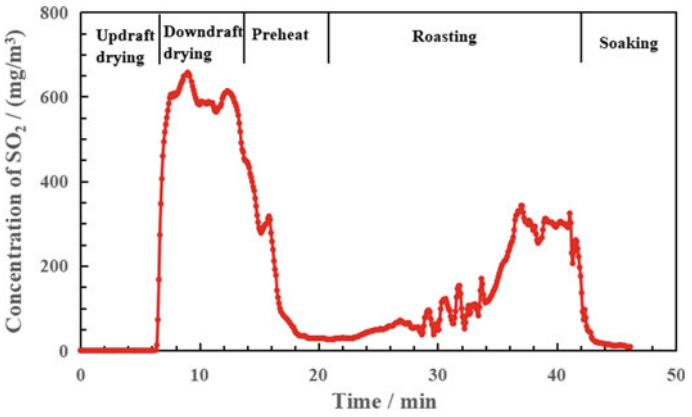

Fig. 6 Concentration of SO_2 in flue gas under trolley of travelling grate machine

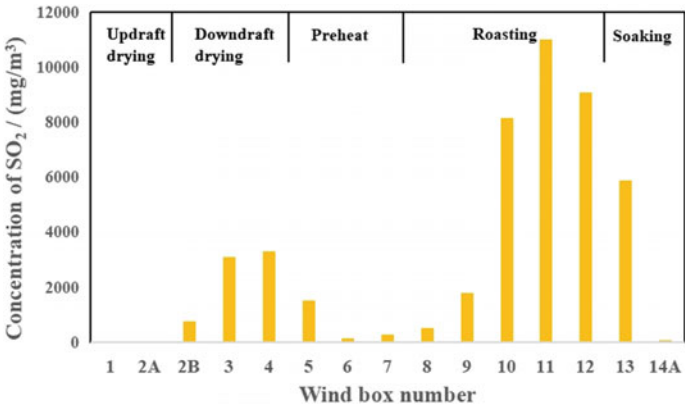

Fig. 7 Concentration of SO_2 in flue gas in wind boxes of travelling grate machine

SO_2 in downdraft drying section. Concentration of SO_2 is at a low level in preheat section, and begins to increase in roasting section, and reaches peak value in Number 10 and Number 11 and Number 12 wind boxes.

Effect of Chemical Compositions of Iron Ore Pellets on Sulfur Content

Using iron concentrate D as main material, acid pellets and alkaline ones were produced by travelling grate machines under similar process conditions. The average chemical compositions of acid pellets and alkaline ones in a month are shown in Table 4. It can be seen that sulfur content in acid pellets is about only one fifth of that

in alkaline ones, although other chemical compositions are similar except CaO and SiO_2. Calcium has sulfur retention [5–8], therefore, the difference of sulfur content in acid pellets and alkaline ones may relate to the difference of calcium content.

Compositions of acid pellets at different locations in rotary kiln, which belongs to Shougang Qian'an pelletizing plant, were studied. As shown in Table 5, it can be seen that all chemical compositions are similar except sulfur and FeO, and sulfur in pellets at kiln tail is the highest. Because heating temperature at kiln tail is lower than that at other locations of kiln, it can be inferred that temperature is an important factor for sulfur content in iron ore pellets.

X-ray photoelectron spectroscopy (XPS) spectra of iron ore pellets made from roasting test are shown in Fig. 8. The characteristic peaks of S2p in the XPS spectra of pellets are in range of 167.86–168.48 eV, indicating that sulfur in iron ore pellets exists in the form of sulfate [9].

Table 4 Compositions of acid pellets and alkaline ones (wt%)

Sample	TFe	FeO	CaO	SiO_2	MgO	Al_2O_3	NaO	K_2O	S
Acid pellets	65.45	0.69	0.98	3.51	0.72	0.70	0.077	0.056	0.005
Alkaline pellets	65.42	0.53	2.56	2.33	0.49	0.49	0.053	0.039	0.025

Table 5 Compositions of acid pellets at different locations in rotary kiln (wt%)

Sample	TFe	FeO	CaO	SiO_2	MgO	Al_2O_3	NaO	K_2O	S
Product pellets	65.05	1.42	0.38	4.70	0.51	0.73	0.13	0.063	0.005
Kiln head pellets	65.33	3.50	0.45	4.66	0.48	0.71	0.12	0.063	0.005
Kiln tail pellets	65.26	9.79	0.45	4.81	0.50	0.74	0.11	0.057	0.037

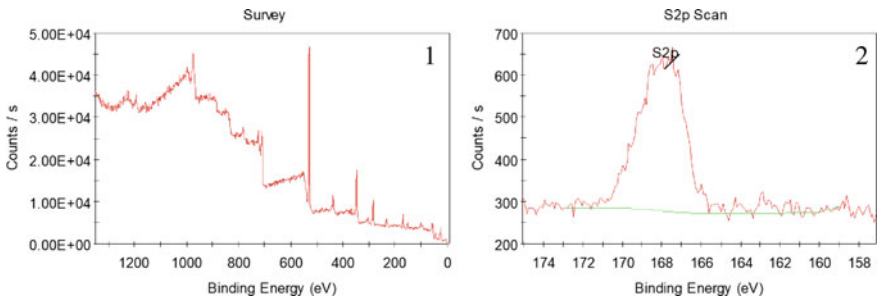

Fig. 8 XPS spectra of iron ore pellets

Comprehensive Discussion

Emission characteristics of SO_2 during baking cup experiments are different from those of travelling grate machine, which may relate to process conditions or existence state of sulfides. Extending oxidation time could change the presence of sulfur in pyrrhotite particles, converting the sulfides that have not been oxidized and removed into sulfates [10].

Calcium sulfate hardly decomposes below 1100 °C and starts to decompose between 1100 and 1300 °C, and range of mutation temperature of calcium sulfate decomposition is between 1300 and 1350 °C, however, reducing agents can reduce the decomposition temperature [11, 12]. The temperature of flue gas in roasting section is over 1250 °C. In addition, iron concentrate D is magnetite and heat would release during oxidizing roasting. Therefore, temperature of pellets may reach 1300 °C or higher. So, it is reasonable that concentration of SO_2 begins to increase in roasting section and reaches peak value in Number 10 and Number 11 and Number 12 wind boxes, where the temperature is highest in travelling grate machine.

Conclusions

Emission characteristics of SO_2 during roasting of iron ore pellets in baking cup experiment and travelling grate machine were investigated. In baking cup experiment, concentration of SO_2 starts to increase when the temperature is about 800 °C, then reaches a peak when the temperature is just above 900 °C. There are two peaks of concentration of SO_2 in travelling grate machine, and the lower peak is in downdraft drying section, while the higher peak is in roasting section. Sulfur content in acid pellets is about only one fifth of that in alkaline ones, which might relate to calcium in iron ore pellets. Except for chemical compositions, temperature is another important factor for sulfur content in iron ore pellets. Results of XPS show that sulfur in iron ore pellets exists in the form of sulfate.

References

1. Zhang JL, Yu JY, Liu ZJ, Xu RS (2021) Current situation and trend of air pollutant emission in China's steel industry. Iron Steel 56(12):1–9
2. Long YG, Pan JY, Farooq S, Boer H (2016) A sustainability assessment system for Chinese iron and steel firms. J Clean Prod 125:133–144
3. Liu JH, Fan ZY, Cheng H, Zhao SQ, Guo ZJ, Zhen L (2020) Integration and application of key technologies for ultra-low emission of flue gas in Qiangang pelletizing plant. Chin Metall 30(12):98–102
4. Zhang BL, Hong H, Wang TQ, Zhang XY, Wu BY, Liu B, Zhang SG (2023) Progress and prospects of flue gas deNOx technology for the iron and steel industry. Chin J Eng 45(9):1602–1612

5. Duan DP, Wan TJ, Guo ZC (2005) Decomposition and transformation behavior of sulfur in composite briquette/pellet of iron ore and coal. J Iron Steel Res 17(5):16–21
6. Chang KK, Ma ZB, Yang FL, Cheng FQ (2016) Transformation and performance of calcium-based sulfur retention agents during coal slime combustion. Clean Coal Technol 22(5):59–63
7. Yang YH, Zheng R, Zhu GJ (2018) Experimental study on sulfur capture efficiency of different calcium—based desulfurization agent. Energy Metall Ind 37(3):34–37
8. Meng JT, Wang J, Yang FL, Hao YH, Cheng FQ (2020) Effects of sulfur-fixing agent on coal combustion characteristics and S, N release law in condition of lean oxygen. Coal Convers 43(5):27–37
9. Chen P (1996) The application of XPS to studying the forms of organic sulfur in coal desulfurization. Clean Coal Technol 3(2):17–20
10. Yang DB, Zhang P, Li QK, Gan J, Zou C (2016) Study on pellet induration desulphurization mechanism of high sulphur and high basicity magnetite concentrate from Inner Mongolia. Sinter Pellet 41(2):41–46
11. Mei L, Li JH, Wang JC (2005) The influence of oxide and compound additives on the stability of $CaSO_4$ at high temperature. Acta Petrolo Mineral 24(6):587–590
12. Zhang XM, Xu RW, Sun SY, Song XF, Yu JG (2010) Study on the character of calcium sulfate reducing decomposition. Environ Sci Technol 33(12F):144–148

Reduction of Zn-Bearing Dust Using Biomass Char

Jianbo Zhao, Xiaohua Liu, Fupeng He, Yongjie Liu, and Zhixiong You

Abstract Biochar is a carbon-neutral fuel that can be used in the iron and steel industry. The reduction behavior of Zn-bearing dust using various reductants was compared. Thermodynamic analysis confirmed that the reduction of Fe and Zn followed the carbothermal reduction mechanism. The results indicated that regardless of the reductant used, the Fe metallization and Zn removal achieved a high level of approximately 95% and over 99%, respectively. However, the removal of K showed variability among the reductants, with removal ranging from 55.36 to 92.98%. The Na removal proved to be more challenging, with removal ratios of less than 20% achieved using all the reductants. CSC and BC exhibited higher volatile contents compared to other reductants, and biochar had a higher reactivity compared to CDQ and TC. The FC_{ad} contents of CDQ and TC were higher than other reductants, and FC_{ad} was proved beneficial for the removal of K and Na.

Keywords RHF · Zn-bearing dust · Biomass char · Carbothermal reduction

Introduction

With the development of the steel industry, global crude steel production has surpassed 1.8 billion tons. The steel production processes, including blast furnaces (BF), oxygen converters, electric arc furnaces, and other related processes, generate a substantial amount of Zn-bearing dust, which accounts for 3–4% of crude steel production [1–3]. Most of this dust is stored in steel plants, posing a significant risk of environmental pollution. Currently, the primary methods for treating Zn-bearing dust are pyrometallurgy and hydrometallurgy [4]. However, hydrometallurgical processes are complex, have a low zinc removal ratio, and generate large amounts of wastewater. Consequently, pyrometallurgical technology is considered an effective method for treating zinc-bearing dust, as it can efficiently remove zinc, lead, and alkali metals at high temperatures [5, 6]. Pyrometallurgical technology

J. Zhao · X. Liu · F. He · Y. Liu · Z. You (✉)
College of Materials Science and Engineering, Chongqing University, Chongqing 400044, China
e-mail: youzx@cqu.edu.cn

Z. Peng et al. (eds.), *Characterization of Minerals, Metals, and Materials 2024*, The Minerals, Metals & Materials Series, https://doi.org/10.1007/978-3-031-50304-7_18

includes direct reduction, smelting reduction, and microwave heating. The rotary hearth furnace (RHF) process is notable for its high degree of metallization achieved through the production of direct reduced iron (DRI). The DRI produced by this process exhibits excellent metallurgical quality and a high removal ratio of harmful elements. Consequently, iron and steel enterprises worldwide have widely adopted the RHF process for treating Zn-bearing dust [7–9].

However, the RHF process still has certain drawbacks, including high levels of CO_2 emissions, intensive energy consumption, low furnace space utilization ratio, and low heating efficiency [10]. Given the growing concern surrounding global warming, reducing greenhouse gas emissions, particularly in the steel industry, is essential [11, 12]. To reduce dependence on fossil fuels and alleviate CO_2 emissions, biomass is considered a promising alternative. Biomass can be processed into charcoal or coke, which can serve as reductants and fuels in iron and steel production [13, 14].

In this study, the utilization of biochar for the reduction of Zn-bearing dust in the simulated RHF process was explored. During the reducing process, zinc undergoes volatilization, and a metalized pellet can be obtained as a result. The possible reactions and thermodynamic calculations were analyzed using FactSage 8.1 software, which helped determine the thermodynamic conditions necessary for the reduction reaction in the Zn-bearing dust. To investigate the impact of different types of biochar on the Fe metallization and zinc volatilization of carbon-containing pellets, roasting experimental trials were conducted. Additionally, a thermogravimetric experiment was carried out to compare the differences among these various reductants.

Experimental

Materials

This study employed three types of dust as raw materials, namely, mixed ash of LT-OG (A), sample B from the BF taping procedure, and sample C of BF flue gas dust. Table 1 presents the main chemical composition of these dust samples, with samples A and C containing 4.38% and 6.54% zinc (Zn), respectively. Notably, sample C possesses a high carbon content of 20.31%, which must be considered as a reductant during the reduction process.

Table 1 Main chemical composition of Zn-bearing dust (wt.%)

Sample	TFe	FeO	C	Zn	SiO_2	MgO	Al_2O_3	CaO	K_2O	Na_2O	Cl
A	51.77	44.80	4.49	4.38	2.84	2.34	2.09	8.90	0.44	0.42	0.260
B	63.29	13.44	5.06	0.91	1.55	0.13	0.69	0.77	0.28	0.10	0.052
C	37.61	6.42	20.31	6.54	5.19	0.50	2.49	3.05	0.31	0.12	2.420

Table 2 Proximate and element analysis of the reducing agent (wt.%)

Reductant	V_{daf}	A_d	FC_{ad}	C	H	N	S
RHC	4.28	53.04	42.68	44.82	1.28	0.64	0.15
CSC	13.17	29.05	57.78	60.75	2.21	1.36	< 0.10
BC	9.80	37.25	52.95	53.73	1.87	0.75	< 0.10
TC	6.05	19.48	74.47	76.08	1.17	0.55	2.05
CDQ	1.20	12.45	84.40	–	–	–	0.62

As for the reducing agents, coke breeze (CDQ), tire charcoal residue (TC), and three types of biochar, including bamboo charcoal (BC), corn straw charcoal (CSC), and rice husk charcoal (RHC), were utilized. The reducing agents employed are ground to a particle size smaller than 0.074 mm. Table 2 displays the proximate and elemental analysis of these reducing agents. It can be observed that CDQ exhibits the highest fixed carbon (FC_{ad}) content. However, the biochar samples have a significantly higher volatile content compared to CDQ, and they also contain a certain amount of hydrogen that can potentially serve as a reductant.

Methods

In the experimental procedure, the dust samples were initially blended in specific proportions. Following that, the reductant was added while ensuring a fixed C/O molar ratio of 0.8, and the organic binder was maintained at a consistent level of 3.3%. Subsequently, the mixture was compacted into cylindrical pellets with dimensions of Φ20 mm × 10 mm using a powder tablet press machine, applying an absolute pressure of 20 MPa. Then the pellets were dried in an oven at 100 °C for 2 h.

The reduction process is carried out in a resistance furnace under argon atmosphere, with precise control over the roasting temperature within a range of ± 2 °C. A schematic diagram of the experimental setup can be found in Fig. 1. Prior to each experiment, the furnace was preheated to 800 °C. Following this, a corundum crucible containing the pellets was carefully placed in the hot zone of the furnace. Subsequently, the furnace was continuously heated in an argon atmosphere at a rate of 10 K/min. The heating schedule was designed to simulate the heating process in RHF. Once the specified temperature of 1250 °C was reached, the reduction roasting process was considered complete. The corundum crucible was then promptly removed from the furnace and rapidly quenched to the ambient temperature of 25 °C.

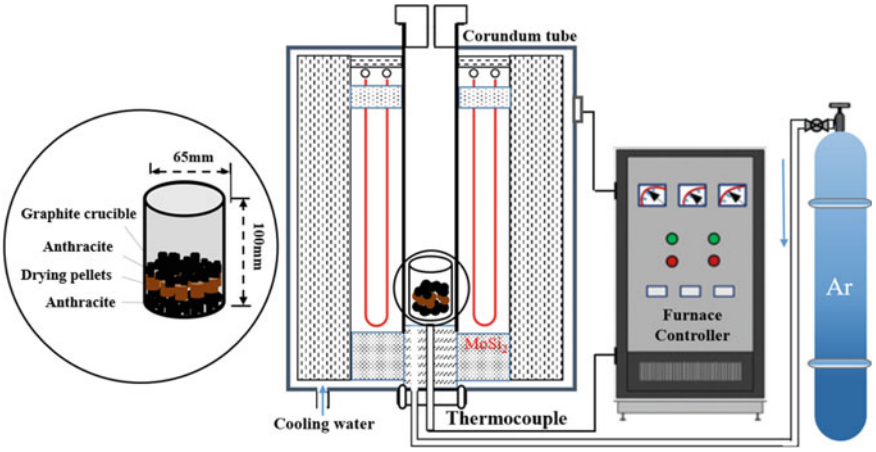

Fig. 1 Diagram of experimental apparatus

Results and Discussion

Thermodynamic Analysis

The thermodynamic equilibrium diagram for different oxides reduced by CO was calculated and shown in Fig. 2. The reduction of iron oxides has been extensively studied and widely accepted. When comparing the reducibility of K_2O and Na_2O, it is evident that K_2O is more easily reduced to gaseous potassium. This is primarily due to the lower CO concentration in the equilibrium of K_2O. Regarding the reduction of ZnO, the partial pressure of Zn(g) significantly affects the equilibrium CO content. Lowering Zn pressure aids in decreasing the necessary CO concentration for achieving equilibrium, thereby accelerating the dezincification process. Increasing the temperature will also increase the concentration of CO, thereby favoring the reduction process. The highest temperature achieved in an RHF is about 1250 °C. Based on theoretical deduction, it can be inferred that iron oxides would be reduced to metallic iron, while elements such as Zn, K, and Na would be converted into the gaseous state.

Reduction Roasting

Figures 3 and 4 illustrate the Fe metallization (MFe/TFe) and removal ratios of zinc (Zn), potassium (K), and sodium (Na) after the roasting process. From Fig. 3, it can be observed that the Fe metallization achieved by the five different reducing agents is nearly complete, reaching approximately 95%. Among the reducing agents, CSC

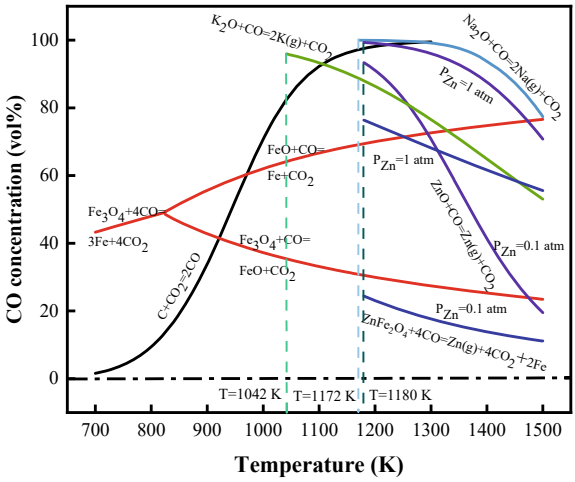

Fig. 2 Equilibrium diagram of different oxides reduced by CO

exhibits the highest metallization ratio of 97.16%, while CDQ showcases the lowest metallization value of 94.69%. Despite CDQ having the highest fixed carbon content among the five reducing agents, which is almost twice that of RHC possessing the lowest FC_{ad}, its metallization ratio after roasting is the lowest. This can be attributed to the production of hydrogen gas (H_2) by certain hydrocarbons present in the volatiles of the reducing agent. H_2 may act as an additional reducing agent with better performance than CO at high temperatures. CSC, having the highest hydrogen content, performs remarkably well in terms of metallization, whereas CDQ, with negligible hydrogen content, exhibits a lower metallization ratio.

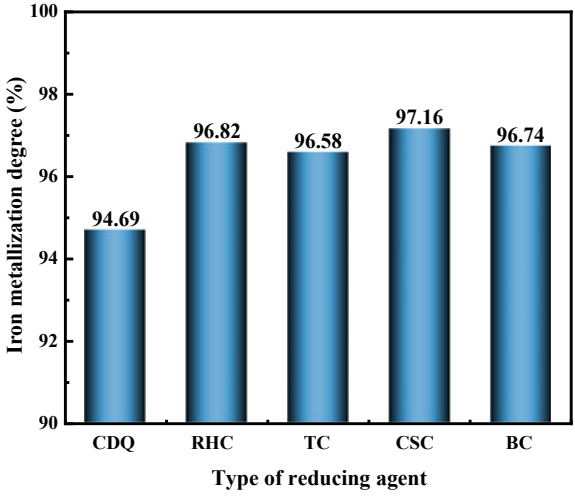

Fig. 3 Fe metallization of the pellets after roasting

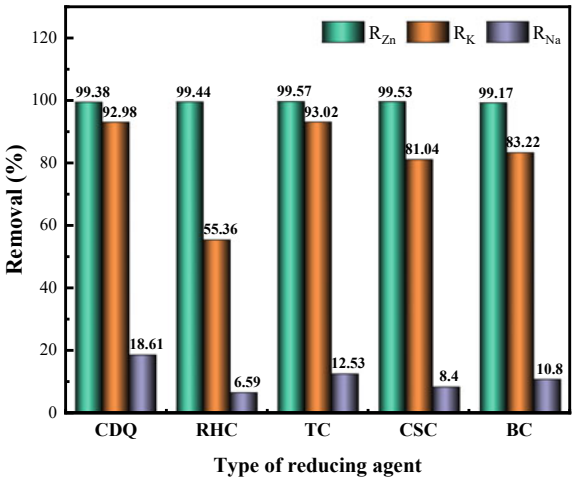

Fig. 4 Removal ratio of Zn, K, and Na after roasting

Based on Fig. 4, it is evident that the dezincification ratios of all the reducing agents are above 99%, indicating effective zinc removal with minimal variation observed among these agents. However, the removal of potassium (K) is significantly affected by the choice of reducing agent. RHC exhibits a K removal ratio of only 55.36%, while other reductants show K removal ratios above 80%. TC and CDQ demonstrate high K removal ratios of 93.02% and 92.98%, respectively. On the other hand, the removal of sodium (Na) proves to be more challenging, with removal ratios not exceeding 20%. CDQ achieves the highest Na removal of 18.61%, while RHC has the lowest ratio of only 6.59%. Previous thermodynamic analysis suggests that the reduction of Na is difficult due to the high temperature and CO concentration required. Notably, CDQ has a higher FC_{ad} content of 88.40% compared to RHC's 42.68%. From this, it can be inferred that a higher FC_{ad} content is beneficial for Na removal. Additionally, although the reduction of K is relatively easier, a high concentration of CO proves advantageous. Greater CO generation at high temperatures improves the porosity of the pellet, creating a more conducive environment for the removal of both K and Na [1].

Discussion on the Reaction Process

Thermogravimetric analysis (TGA) was conducted on five reducing agents under a CO_2 atmosphere, using a heating rate of 10 °C/min. The TGA results depicted in Fig. 5, experiments can provide insight into the reactivity and behavior of reducing agents in the process of carbothermal reduction. It is observed that CSC exhibits the earliest and most significant weight loss, which remains relatively stable below 1000 °C. This indicates that CSC has high reactivity and is favorable for the reduction process. Similarly, the biochars of BC and RHC also demonstrate relatively higher

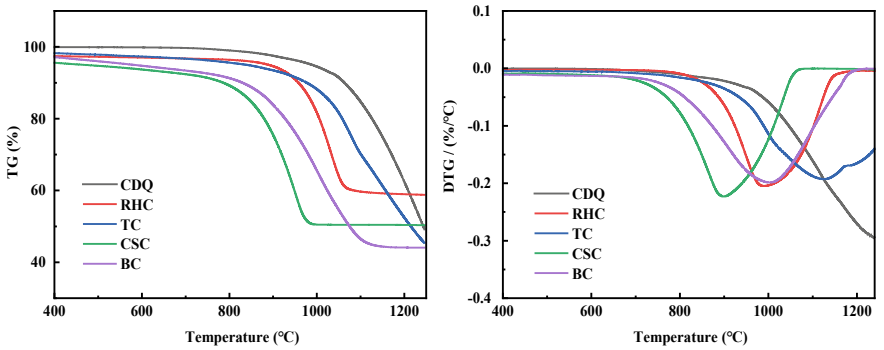

Fig. 5 TG and DTG curves of individual reductant under CO_2 atmosphere

reactivity, as evidenced by their weight loss patterns. TC and CDQ exhibit noticeable weight loss at approximately 1000 °C, suggesting that these reductants require higher temperatures for effective reduction. This behavior can be attributed to the higher FC_{ad} content and graphitization of carbon in TC and CDQ. The DTG curves further confirm this trend, with the temperature of rapid weight loss following the order: CSC < BC ≈ RHC < TC < CDQ. Notably, the results in Fig. 5 indicate that the weight loss of TC and CDQ at 1250 °C is not complete, suggesting that some carbon may remain, not fully participating in the reduction process.

The TG analysis of the mixture consisting of Zn-bearing dust and a reductant was conducted, and the results are presented in Fig. 6. The DTG curves reveal some important observations regarding the reduction process and the behavior of different reductants. The first peak in the DTG curves for CSC, BC, and CDQ reductants is observed at around 650 °C. This peak can be attributed to the volatilization of volatile compounds and the reduction of iron oxides, such as Fe_2O_3 and Fe_3O_4, occurring at lower temperatures. As the temperature increases to the range of 700–900 °C, the reduction of FeO and $ZnFe_2O_4$ is likely to take place. Additionally, beyond 900 °C, the reduction of ZnO and the volatilization of zinc become prominent since the boiling point of zinc is around 907 °C. Another peak in the DTG curves is observed at approximately 1000 °C, indicating the occurrence of the Boudouard reaction and intensification of the reduction process.

Analyzing the TG curves, it can be observed that the weight loss of samples using TC and RHC as reducing agents is around 18%, while the weight loss of other samples is approximately 25–30%. This difference can be attributed to the properties of these reducing agents. TC, known for its lower reactivity, contributes to a lesser extent to the reduction process. On the other hand, RHC, with a lower carbon content compared to other reductants, also results in less reduction agent available for the reduction reactions. As a result, the weight loss of these mixtures is lower compared to other samples.

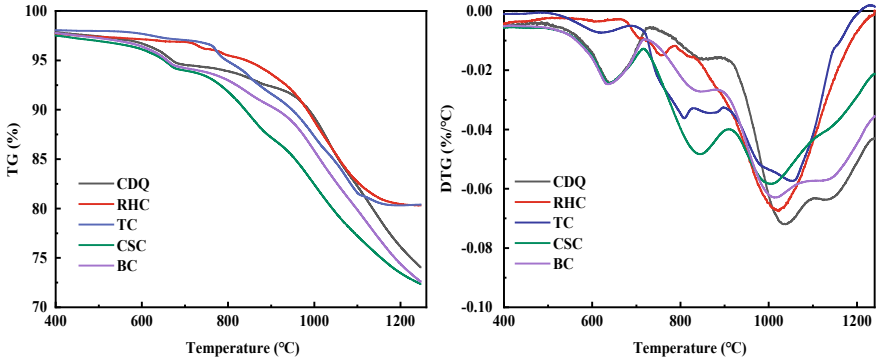

Fig. 6 TG and DTG curves of a mixture under Ar atmosphere

Conclusions

This study compared the reduction behavior of Zn-bearing dust using various reductants. The results indicated that regardless of the reductant used, the Fe metallization achieved a high level of approximately 95%. Similarly, the removal of Zn was highly efficient, with a removal ratio of over 99% under the same reduction conditions. Thermodynamic analysis confirmed that the reduction of Fe and Zn followed the carbothermal reduction mechanism. However, the removal of K showed variability among the different reductants, with removal ranging from 55.36 to 92.98%. The removal of Na proved to be more challenging, with removal ratios of less than 20% achieved using all the reductants. CSC and BC exhibited higher volatile contents compared to other reductants. This suggests that biochar had a higher reactivity with CO_2 compared to CDQ and TC. The reduction and removal of K and Na necessitated higher temperatures, indicating that a higher thermal energy input was required for their successful elimination. The FC_{ad} contents of CDQ and TC reductants were higher than those of other reductants. This higher FC_{ad} content proved beneficial for the removal of K and Na. It indicates that CDQ and TC reductants contained a higher proportion of FC_{ad}, which contributed to the higher removal of K and Na.

Acknowledgements The authors wish to express their thanks to the National Key R&D Program of China (2022YFC3901400) for the financial support of this research.

References

1. Chen Z, Zheng R, Ju D, Mao R, Ma H, Peng H, Du W (2022) Carbothermic kinetics and reaction mechanism of carbon-containing pellets: a combined treatment of chromium-containing sludge and zinc-bearing dust. J Sustain Metall 8(3):1001–1013. https://doi.org/10.1007/s40831-022-00549-1

2. Guo Z, Zhan R, Shi Y, Zhu D, Pan J, Yang C, Wang Y, Wang J (2023) Innovative and green utilization of zinc-bearing dust by hydrogen reduction: recovery of zinc and lead, and synergetic preparation of Fe/C micro-electrolysis materials. Chem Eng J 456:141–157. https://doi.org/10.1016/j.cej.2022.141157
3. KiranKuma T, Roy G (2022) A review on processing of electric arc furnace dust (EAFD) by pyro-metallurgical processes. Trans Indian Inst Met 75(5):1101–1112. https://doi.org/10.1007/s12666-021-02465-6
4. Lanzerstorfer C, Angerbauer A, Gaßlbauer M (2018) Feasibility of air classification in dust recycling in the iron and steel industry. Steel Res Int 89(7):180–197. https://doi.org/10.1002/srin.201800017
5. Omran M, Fabritius T (2019) Utilization of blast furnace sludge for the removal of zinc from steelmaking dusts using microwave heating. Sep Purif Technol 210:867–884. https://doi.org/10.1016/j.seppur.2018.09.010
6. Mombell D, Di Cecca C, Mapelli C, Barella S, Bondi E (2016) Experimental analysis on the use of BF-sludge for the reduction of BOF-powders to direct reduced iron (DRI) production. Process Saf Environ Prot 102:410–420. https://doi.org/10.1016/j.psep.2016.04.017
7. Andersso A, Gullberg A, Kullersted A, Ahmed H, Sundqvist-Ökvist L, Samuelsson C (2019) Upgrading of blast furnace sludge and recycling of the low-zinc fraction via cold-bonded briquettes. J Sustain Metall 5(3):350–361. https://doi.org/10.1007/s40831-019-00225-x
8. Antrekowitsch J, Rösler G, Steinacker S (2015) State of the art in steel mill dust recycling. Chem Ing Tech 87(11):1498–1503. https://doi.org/10.1002/cite.201500073
9. Chairaksa-Fujimot R, Inoue Y, Umeda N, Ito S, Nagasak T (2015) New pyrometallurgical process of EAF dust treatment with CaO addition. Int J Miner Metall Mater 22(8):788–797. https://doi.org/10.1007/s12613-015-1135-6
10. Hara Y, Ishiwata N, Itaya H, Matsumoto T (2000) Smelting reduction process with a coke packed bed for steelmaking dust recycling. ISIJ Int 40(3):231–237. https://doi.org/10.2355/isijinternational.40.231
11. Grimston MC, Karakoussis V, Fouquet R, van der Vorst R, Pearson P, Leach M (2001) The European and global potential of carbon dioxide sequestration in tackling climate change. Clim Policy 1(2):155–171. https://doi.org/10.3763/cpol.2001.0120
12. Archer D, Eby M, Brovkin V, Ridgwell A, Cao L, Mikolajewicz U, Caldeira K, Matsumoto K, Munhoven G, Montenegro A, Tokos K (2009) Atmospheric lifetime of fossil fuel carbon dioxide. Annu Rev Earth Planet Sci 37:117–134. https://doi.org/10.1146/annurev.earth.031208.100206
13. Fu JX, Zhang C, Hwang WS, Liau YT, Lin YT (2012) Exploration of biomass char for CO_2 reduction in RHF process for steel production. Int J Greenh Gas Control 8:143–149. https://doi.org/10.1016/j.ijggc.2012.02.012
14. Singh AK, Singh R, Sinha OP (2022) Characterization of charcoals produced from Acacia, Albizia and Leucaena for application in ironmaking. Fuel 320:123911. https://doi.org/10.1016/j.fuel.2022.123991

Part V
Materials Processing Analysis and Characterization

Boron Removal from Prepared Rice Hulls Ash Metallurgical-Grade Silicon via Solvent Refining Process

B. O. Ayomanor, C. Iyen, G. Ofualagba, J. Umukoro, O. Enamuotor, and E. Omughele

Abstract Metallurgical grade silicon (MG-Si) derived from an agricultural waste rice husk (RH) via metallothermic reduction of pulverized Mg and SiO_2 mixture at ratio 1:1 g was treated and purified by hydrometallurgical purification process. A low-cost silicon with high purity was produced by solvent refining process. In this work, silica of 98.03% has been prepared from rice hulls annealed at 700 °C for 6 h. Furthermore, the silica value was boosted by improved purification processes to yield 99.51% of silica. The X-ray fluorescence (XRF) showed that several metallic trace impurities were significantly reduced beyond its detection limit. The final process underwent centrifuge of solvent refined silicon with tin as a selected gettering metal. The X-ray mapping and energy-dispersive X-ray spectroscopy (EDS) quantitative analysis showed that B was eliminated. The XRF of final silicon powder showed purity > 98.5%.

Keywords Rice husk ash · Anneal · Mapping · Metallothermic · Leaching · Solvent refining

B. O. Ayomanor (✉) · J. Umukoro
Department of Physics, Federal University of Petroleum Resources, Effurun, Nigeria
e-mail: benorholor@yahoo.com

C. Iyen
Department of Pure and Applied Physics, Federal University Wukari, Wukari, Nigeria

G. Ofualagba
Department of Electrical and Electronics, Federal University of Petroleum Resources, Effurun, Nigeria

O. Enamuotor
Department of Environmental Management, Dennis Osadebay University, Asaba, Nigeria

E. Omughele
Department of Pharmacognosy and Traditional Medicine, Delta State University, Abraka, Nigeria

Z. Peng et al. (eds.), *Characterization of Minerals, Metals, and Materials 2024*, The Minerals, Metals & Materials Series, https://doi.org/10.1007/978-3-031-50304-7_19

Introduction

The green and renewable revolution has become one of the world dominating topics of interest today, following the gradual collapsing of traditional energy resources, the unsustainability of fossil fuels and upsurge attention in our environmental protection; the photovoltaic industry has in the past few years went through speedy development due to enormous need for solar-grade silicon (SoG-Si) [1]. The purification processes such as acid leaching [2], directional solidification [3], plasma treatment [4], vaporization refining [5], slagging [6], solvent refining [7], and reactive gas blowing [8]; having been used to overwhelm or lower the disadvantages of metallurgical-grade silicon (MG-Si) produced via the traditional Siemens process. However, this MG-Si is prepared commercially by heating silica and carbon in a furnace to about 2000 °C; thereby, making manufacturing of solar cells very expensive. The cost of manufacturing solar cell could be considerably reduced if a new and inexpensive source material is used. Presently, different methods are used to obtain silicon from various silicon compounds such as quartz (SiO_2). A metallurgical route combined with directional solidification successfully removed metallic impurities with low segregation coefficients from silicon. However, this route has been ineffective economically in removing high segregation impurities e.g. B, P, Al that are dopant elements, known to be very deleterious to the performance of solar cells; as is discussed in [9]. It is against this background that the potential of very rich silica obtained from rice husk that is agricultural waste product is being explored in this work for the production of solar grade silicon; as an alternative approach to the synthesis of low-cost solar grade silicon from rice hulls dominantly reactive silica [10–12]; the primary objective of this work is to produce highly pure silica that is feasible to metallothermically reduced silica to silicon for solvent refinement.

Materials and Methods

Rice Hulls (RH)

Rice hulls collected from rice milling industry are taken for thorough washing in a bowl with deionized water. The dirty water was descanted and refilled with fresh deionized water severally until water appears clean. The RH is dried in the open sun at 38 °C for 7 h and placed in a crucible for annealing.

Rice Hulls Ash (RHA)

Four crucibles were filled with rice hulls weighing 50 g each. The crucibles were loaded into an electric furnace and annealed in air at 350 °C for 2 h to burn-off all

Table 1 Chemical analysis of RHA using XRF

Compd.	SiO_2	MgO	Al_2O_3	P_2O_5	SO_3	K_2O	CaO	Na_2O	Fe_2O_3	B	Mn_3O_4
wt.%	94.98	1.01	0.44	0.75	0.24	0.30	0.40	0.30	0.14	0.30	0.05
Loss on ignition (wt.%)				1.09							

Table 2 Chemical analysis of treated RHA using XRF

Compd.	SiO_2	MgO	Al_2O_3	P_2O_5	SO_3	K_2O	CaO	Na_2O	Fe_2O_3	Mn_3O_4
wt.%	99.50	0.02	0.09	0.12	0.18	0.00	0.01	0.00	0.00	0.01

combustible gas and tar to yield a blackish ash with a lot of carbon known as char. The furnace was then allowed to heat steadily to a holding temperature of 700 °C with the char to anneal for 6 h. The char decarbonized to yield 41 g whitish RHA with low carbon content. The RHA silica specimen measuring 2.5 g was taken to laboratory for XRF analysis. The XRF results are tabulated in Table 1 and the remaining RHA sample was taken for hydrometallurgy treatment.

The hydrometallurgy treatment was done in a fume cupboard, following health regulation on chemical handlings. The leaching involved adding 1.5 cm^3 of 16 M HNO_3 to 25 g of RHA silica in a crucible; thereafter, transferred to an electric furnace to anneal at 700 °C for an hour. The product was then rinsed in 1000 ml beaker with deionized water, filtered, and dried in an oven for an hour at 110 °C. Its sample weighing 20 g then underwent digestion treatment using 5 M HCl acid in 1000 ml beaker for 120 min at 95 °C on a hot plate with constant agitation. The digested residue was filtered with Whitman paper; rinsed and descanted several times with deionized water until pH of water reads 7.3. The solid RHA silica was filtered, oven dried at 110 °C for an hour and 1.5 g of sample was taken for XRF analysis, and the results are tabulated in Table 2.

Metallothermic Reduction of Silica

The solid–liquid extracted RHA silica was pulverized and thoroughly mixed with magnesium powder at a ratio of RHAs: Mg (1.0 g:1.0 g) to form magnesium silicide. The mixtures of each sample weighing 10 g were transferred from the mortal to alumina crucibles for heating in an electric furnace with a controlled atmosphere at a temperature of 900 °C for 6 h before cooling down to room temperature. By heating the mixture, the magnesium reduced the oxygen atoms from the silica, leaving elemental silicon known as metallurgical-grade silicon. This was transferred to a desiccator and left to cool down for 72 h before leaching in HCl acid, filtered and the residues are oven dried for 1 h before thermally treated exclusively for minimizing residual carbon as shown in Eq. (1).

$$SiO_2 + 2Mg \rightarrow \underset{\text{Dissolved in acid}}{Si} + 2MgO \quad (1)$$

The sample thermally treated at 900 °C was powdered, preserved for XRF, and SEM quantitative and qualitative analysis.

Post-purification of Metallurgical-Grade Silicon by Alloying Process

The metallurgical-grade silicon derived from RHA silica was thoroughly mixed in a mortar with tin (Sn) powder. Tin powder weighing 29.58 g mixed with 4.0 g MG-Si was measured and transferred into a 20.71 cm^3 alumina crucible inside a fume hood. The crucible with its contents was introduced into a furnace programmed to holding temperature of 1200 °C at 3.5 °C/min heating rate for 3 h before it starts cooling down to room temperature at 2 °C/min. A solidified Si–Sn formed in the crucible is removed from furnace and crushed using a G-clamp as shown in Fig. 1.

The Si–Sn was separated from crushed crucible and ground to powder using Retsch vibratory disc Mill RS 200, German product grinding machine. Weighed 2 g of grind Si–Sn alloy powder was placed in a rotor plastic container with deionized water added and inserted into the rotor at room temperature for separation. The Sorvall RC6 centrifuge, UK product was regulated to 600 rpm rotation speed and held for 5 min. The Si particles were observed to separate from Sn particles and the separated Si fraction was taken for SEM and EDS analysis.

Fig. 1 Schematic of solidified Si–Sn alloy

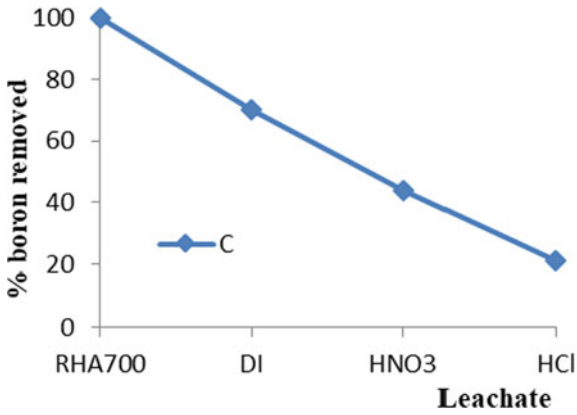

Fig. 2 Graph of boron impurity content leached out at each treatment step

Results and Discussion

X-ray Diffraction

The results of X-ray diffractogram obtained from a Philips X'Pert system indicate that the RHA heated at 700 °C for 6 h is amorphous, which is in agreement with Agrawal's findings.

Leaching Effect on RHA

The leaching results of Table 1 showed that RHA silica purity increased from 94.98 to 99.50% as shown in Table 2. It also showed that some trace impurities like K_2O, Na_2O, and Fe_2O_3 are leached out completely; CaO, Mn_3O_4, and MgO have over 90% purity; Al_2O_3, P_2O_5, and SO_3 are over 55% leached off. It is observed that hydrometallurgical leaching of RHA in deionized water (DI), HNO_3, and HCl can yield purity of up to 73% for B as shown in Fig. 2.

Metallurgical-Grade Silicon (MG-Si) Derived from RHA

The chemical analysis of MG-Si pyrolyzed in Xera Carb and analyzed in Sheffield Hallam University Research Laboratory of Material and Engineering Research Institute (MERI) in UK is tabulated in Table 3. The XRF analysis results for the derived MG-Si after leaching are presented in Table 3. The results indicate a Si yield of 98.82%, which is in agreement with the required value of metallurgical-grade silicon [13]. The impurities Al, Mg, P, S, Na, Fe, and Cl were observed using XRF. However,

Table 3 Chemical analysis of MG-Si using XRF and ICP-OES

Elements	Si	Mg	Al	P	S	Na	Fe	Cl
XRF results: wt.%	98.82	0.29	0.23	0.00	0.00	0.20	0.07	0.20
ICP-OES result for boron: wt.%				0.19				

due to the fact that B is too light to be detected by XRF, the inductive couple plasma optical emission spectrometry (ICP-OES) was used. The high amount of Al, Cl, and Mg observed are due to alumina crucible, excess Mg during silica reduction, and HCl use for leaching. It is observed that P was reduced below the detection limit of XRF. The micrograph results from transmission electron microscopy of the derived MG-Si showed tiny flakes up to 0.5 μm.

X-ray Mapping Using Energy Dispersive X-ray Spectrometer (EDS) on MG-Si

The X-ray mapping is used to understand the spatial distribution of specific elements in the derived MG-Si. The micrographs presented in Figs. 3 and 4 are EDX results used to generate composite maps for Mg, Si, Al, and O using the kα1 lines as shown below.

The EDS analysis of the derived MG-Si confirmed the presence of Al and Mg impurities. Hu et al. [14] reported Al, Mg, Ca, and P impurities were detected in the microstructure phase of their refined silicon after their refining process and that P

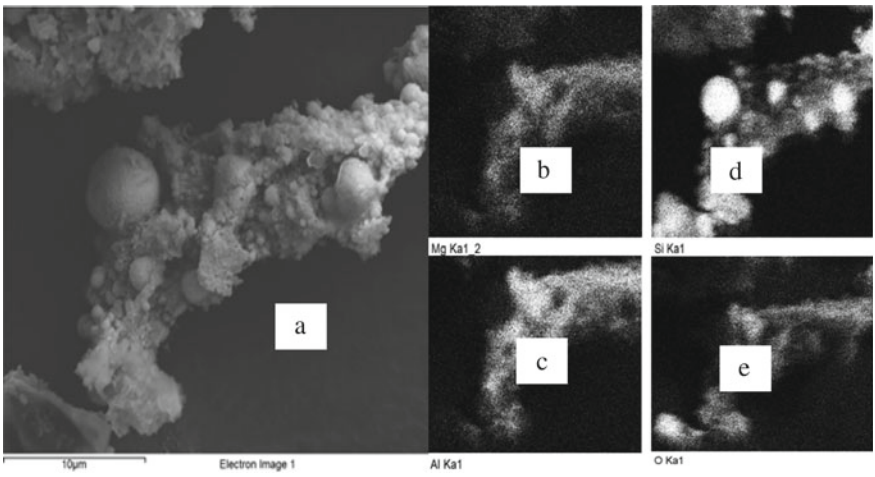

Fig. 3 X-ray mapping of MG-Si. **a** EDS micrograph of Si sample derived from RHA. **b** Mg mapping of Si sample. **c** Si mapping of Si sample. **d** Al mapping of Si sample. **e** O mapping of Si sample

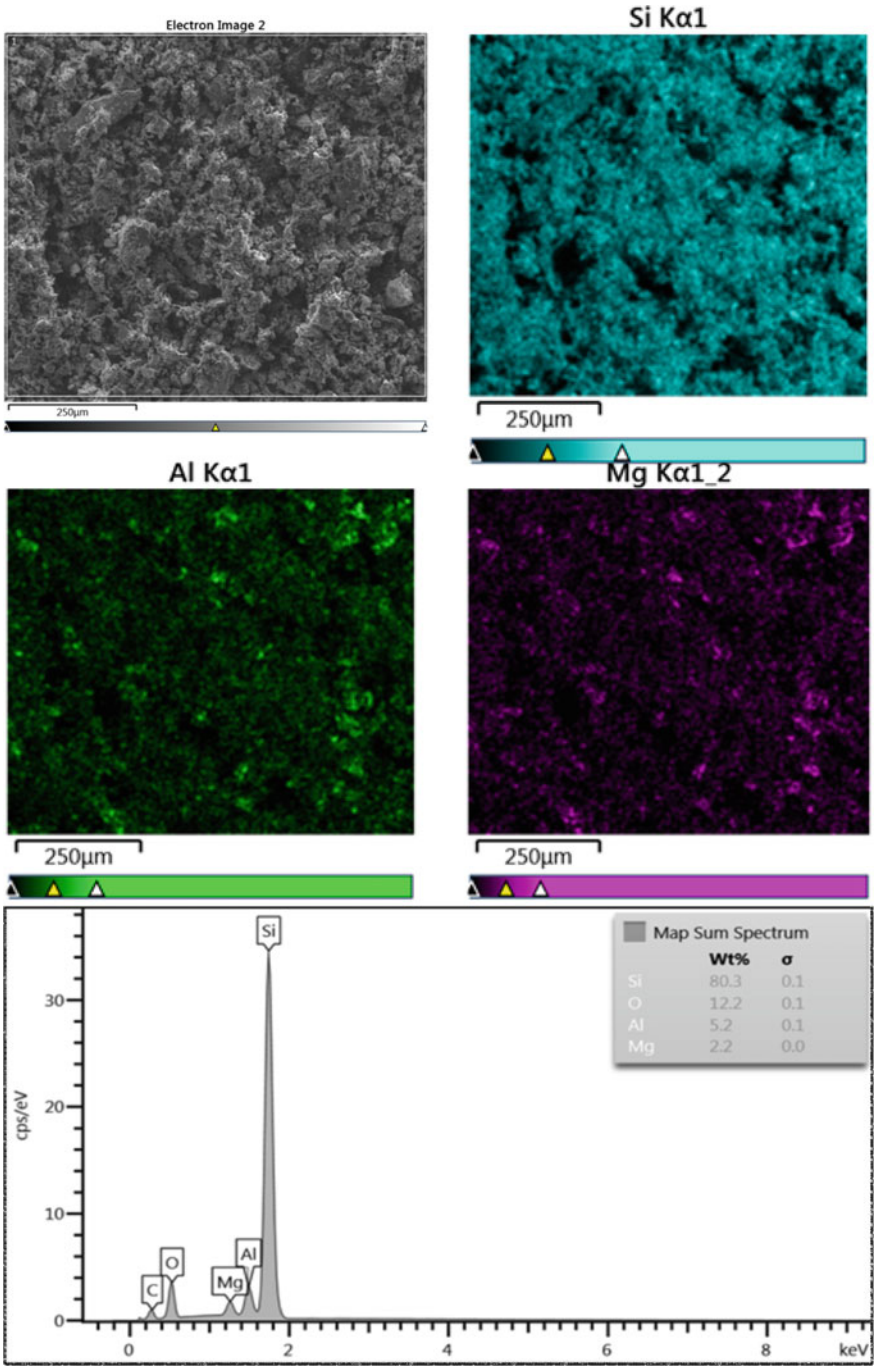

Fig. 4 X-ray mapping of an impurity phase in derived MG-Si (**a**, **b**, **c** and **d**) and EDS analysis

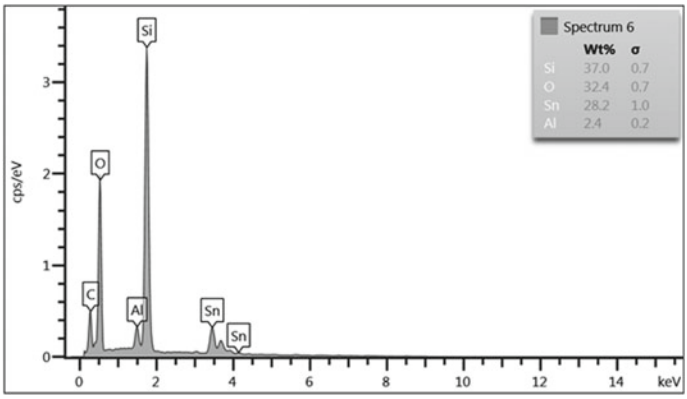

Fig. 5 The EDS analysis of impurities in Si–Sn refined alloy powder

was only removed at the microstructure phase of their refined work. The EDS result of this work further confirmed the XRF non-detection of P in the derived silicon. Zhao et al. [15] reported that the MG-Si impurities P and B are solidly dissolved inside the Si matrix, and even when crushed and acid leached, P cannot be removed except by solvent refining and B is too light to be detected by XRF. Contrary to Zhao et al. [15], none of EDS mapping impurity phase or analysis spectra for the derived silicon showed the presence of P in this work. This indicates that P impurity in MG-Si derived from rice hulls ash can be removed beyond SEM and EDS detection limit.

Refined Silicon Composition

The concentration of different impurities in ground refined Si–Sn powder and centrifuged sample was analyzed with SEM and EDS. The result for the ground refined Si–Sn powder shown in Figs. 5 and 6a indicates the presence of Sn in the alloyed powder sample; whereas, the result of the centrifuged alloyed powder presented in Fig. 6b indicated that Si was successfully separated from Sn.

Conclusions

The work shows that impurity B was reduced over 70% using hydrometallurgy process. The results from other works show that dopant elements P and B removal is not possible without solvent refining process. Furthermore, P impurity was shown to reduce beyond the limit of XRF detection with mere acid leaching; indicating it is feasible to eliminate B from MG-Si derived from rice husk ash.

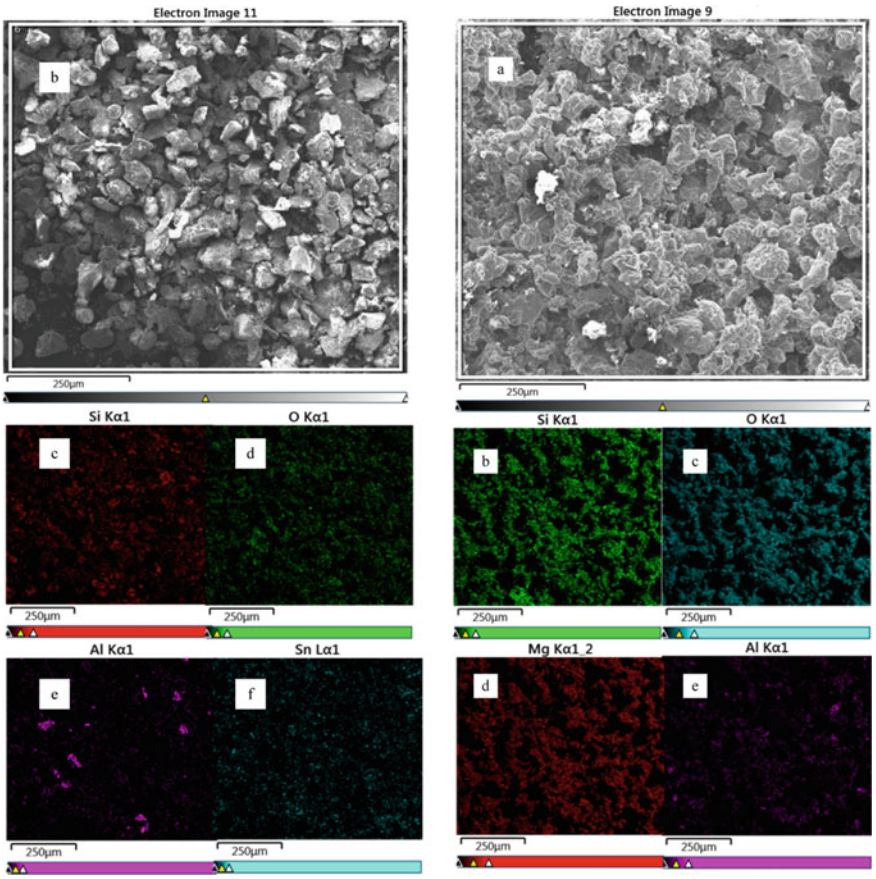

Fig. 6 The microstructure (left) is impurity phrases in refined Si–Sn alloyed powder and (right) is impurity phases in centrifuged refined Si–Sn alloyed powder

References

1. Woditsch P, Koch W (2002) Solar grade silicon feedstock supply for PV industry. Sol Energy Mater Sol Cells 72:11–26
2. He FL, Zheng SS, Chen C (2012) The effect of calcium oxide addition on the removal of metal impurities from metallurgical-grade silicon by acid leaching. Metall Mater Trans B 43:1011–1018
3. Liu T, Dong ZY, Zhao YW, Wang J, Chen T, Xie H, Li J, Ni HJ, Huo DX (2012) Purification of metallurgical grade silicon through directional solidification in large cold crucible. J Cryst Growth 355:145–150
4. Wang JT, Li XD, He YM, Feng N, An XY, Teng F, Gao CT, Zhao CH, Zhang ZX, Xie EQ (2015) Effects of slag refining in boron removal from metallurgical grade silicon using recycled slag with active component. Sep Sci Technol 50:2759-2766
5. Hanoka JI, Strock HB, Kotval PS (1981) 11% efficient single-crystal solar cells and 10% efficient polycrystalline cells made from refined metallurgical silicon. J Appl Phys 9:5829–5832

6. Yoshikawa T, Morita K (2012) An evolving method for solar-grade silicon production: solvent refining. JOM 64:946–951
7. Tang K, Anderson S, Nordstrand E, Tangstad M (2012) Removal of boron in silicon by H_2–H_2O gas mixtures. JOM 64:952–956
8. Barati M, Larbi KK, Roy R, Lakshmanan VI, Sridha R (2012) Process Research Ortech Inc. production of high purity silicon from amorphous silica. U.S. patent 8:337,795
9. Istratov AA, Buonassisi T, Pickett MD, Heuer M, Weber ER (2006) Control of metal impurities in "dirty" multicrystalline silicon for solar cells. Mater Sci Eng B 134(2–3):282–286
10. Agrawal BM (1989) Utilization of rice husk ash. Glass Ceram Bull 36:1–2
11. Farooque KN, Zaman M, Halim E, Islam S, Hossein M, Mollah YA, Mahmood AJ (2009) Characterization and utilization of rice husk ash (RHA) from rice mill of Bangladesh. Bangladesh J Sci Ind Res 44(2):157–162
12. Ayomanor BO, Vernon-Parry K (2016) Potential synthesis of solar-grade silicon from rice husk ash. Solid State Phenom 242:41–47
13. Pozzini S (1982) Solar grade silicon as a potential candidate material for low-cost terrestrial solar cells. Sol Energy Mater 6(3):253–297
14. Hu L, Wang Z, Gong X, Guo Z, Zhang H (2013) Impurity removal from metallurgical-grade silicon by combined Sn–Si and Al–Si refining processes. Metall Mater Trans B 44(4):828–836
15. Zhao LX, Wang Z, Guo ZC, Li CY (2011) Low-temperature purification process of metallurgical silicon. Trans Nonferrous Met Soc China 21(5):1185–1192

Purification of Rutile Ore by HCl and HF Leaching

Tong Zhang, Zhiwei Peng, and Shangyong Zuo

Abstract In this study, purification of rutile ore by leaching using 2–12 mol/L HCl and 2–12 wt% HF was investigated based on the thermodynamic analysis of the main involved reactions and experimental characterizations mainly using chemical titration, X-ray diffraction (XRD), and scanning electron microscopy (SEM). It was shown that compared with traditional HCl leaching, HF leaching could extract more impurities because of easier reactions between HF and impurity oxides, in spite of minor loss of TiO_2 caused by its reaction with the acid. The purification performance of both acids increased initially and then decreased with increasing acid concentration. When the ore was leached using HCl with concentration of 6 mol/L at 60 °C for 4 h, the TiO_2 content was enhanced from 95.39 to 97.31 wt% with the highest impurity removal percentage of 41.65%. For HF leaching, the proper acid concentration was 6 wt%. Under the same conditions as those in HCl leaching, the TiO_2 content in the ore could be elevated to 98.77 wt% with the impurity removal percentage of 73.32%.

Keywords Rutile ore · TiO_2 · Acid leaching · Purification

Introduction

The demand for medical titanium alloys is constantly increasing in the medical field due to their excellent performance [1, 2]. They are widely used in limb implantation, alternative functional materials, dentistry, and other related fields, owing to their good corrosion resistances, high specific strength, low elastic moduli, fatigue resistances, and good biocompatibilities [3, 4]. Titanium is usually extracted from natural titanium ores, including high-titanium rutile ore. For preparing titanium and titanium alloys, it is necessary to purify rutile ore for subsequent metallurgical processing [5].

T. Zhang · Z. Peng (✉) · S. Zuo
School of Minerals Processing and Bioengineering, Central South University, Changsha 410083, China
e-mail: zwpeng@csu.edu.cn

Z. Peng et al. (eds.), *Characterization of Minerals, Metals, and Materials 2024*, The Minerals, Metals & Materials Series, https://doi.org/10.1007/978-3-031-50304-7_20

Table 1 Main chemical composition of rutile ore (wt%)

Component	TiO_2	SiO_2	TFe	ZrO_2	Al_2O_3
Content	95.39	1.16	0.51	0.57	0.35
Component	V_2O_5	CaO	MgO	Nb_2O_5	Others
Content	0.45	0.03	0.04	0.52	0.98

For production of titanium dioxide from titanium-bearing raw materials, a number of methods based on H_2SO_4 leaching, chlorination, and HCl leaching are used [6, 7]. The H_2SO_4 leaching method has multiple steps and generates large amounts of sulfur-containing flue gas, waste acid, and residue. The chlorination method is simpler compared to the sulfuric acid leaching method [8, 9]. However, this method has high requirements for raw materials, technology, and equipment. The hydrochloric acid leaching method was first patented by Altair Company in the United States [10, 11]. It has less waste production and lower requirements for raw materials.

The aim of this study was to purify natural rutile ore using two types of acids, namely, HCl and HF. It was demonstrated that most of the impurities in the ore could be removed by the acids, depending on the acid concentration.

Experimental

Materials

The raw material used in this experiment was a natural rutile ore with high titanium oxide content. Table 1 shows the chemical composition of the sample. It had TiO_2 content of 95.39 wt%, SiO_2 content of 1.16 wt%, Al_2O_3 content of 0.35 wt%, ZrO_2 content of 0.57 wt%, iron content (TFe) of 0.51 wt%, and Nb_2O_5 content of 0.52 wt%. Other impurities, such as CaO and MgO, were also found. Its composition was also confirmed by the X-ray diffraction (XRD) analysis and energy dispersive X-ray spectroscopy (EDS) mapping, as shown in Figs. 1 and 2.

Methods

The temperature dependencies of standard Gibbs free energy changes of the reactions ($\Delta_r G_m^{\ominus} - T$) between the main components of rutile ore and HCl or HF were determined by calculation using the software Factsage 8.0 (Thermfact/CRCT, Montreal, Quebec, Canada; GTT Technologies, Herzogenrath, Germany). For leaching experiments, rutile ore was ground to ensure its particle size smaller than 0.074 mm. In each test, 15 g of the ore sample was used for acid leaching in a water bath under the conditions of solid–liquid ratio of 1/6, reaction temperature of 60 °C, reaction time

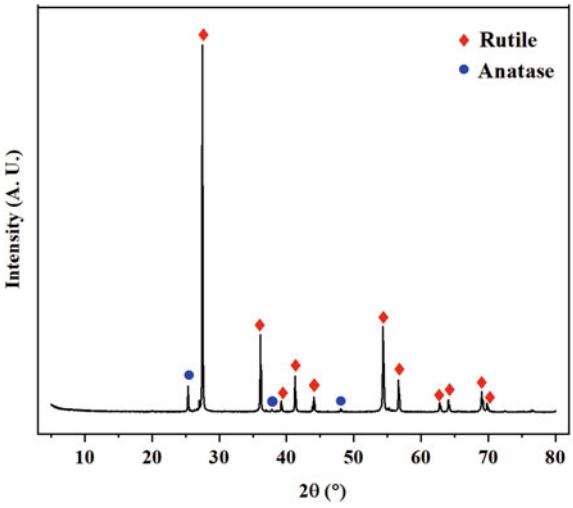

Fig. 1 XRD pattern of rutile ore

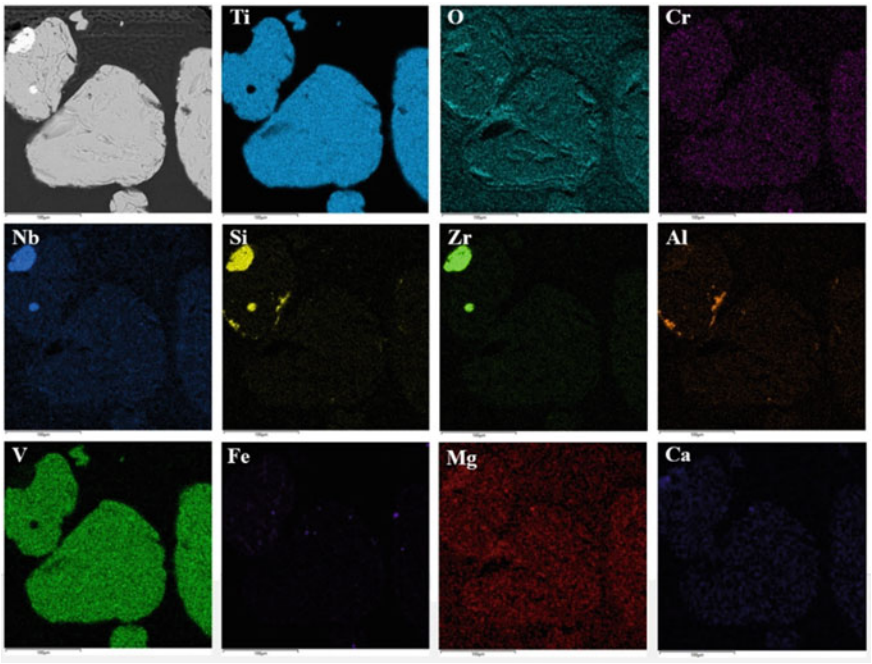

Fig. 2 EDS mapping analysis of rutile ore

of 4 h, and rotation speed of 500 r/min. After the reaction was completed, the sample was filtered and the solid product obtained was dried at 90 °C for 12 h for composition determination by chemical titration, XRD, and scanning electron microscopy (SEM).

Results and Discussion

The temperature dependencies of standard Gibbs free energy changes of the reactions between the main components of rutile ore and HCl or HF are shown in Tables 2 and 3 and Figs. 3 and 4.

Table 2 shows the expressions of temperature dependence of standard Gibbs free energy changes of the main reactions in HCl leaching. It indicated that Al_2O_3, ZrO_2, and TiO_2 hardly react with HCl. Conversely, Fe_2O_3, CaO, and MgO will react with HCl. These reactions are highly relied on the temperature which should be controlled as low as possible.

Table 3 shows the expressions of standard Gibbs free energy changes of the main reactions in HF leaching. From Fig. 4, it can be seen that the reactions between Al_2O_3, Fe_2O_3, Fe_3O_4, SiO_2, or ZrO_2 and HF are spontaneous. Considering the reaction between TiO_2 and HF, it is necessary to control the temperature to suppress the loss caused by HF leaching.

Table 2 Expressions of standard Gibbs free energy changes of the main reactions in HCl leaching

No.	Reaction equation	$\Delta_r G_m^\theta$ (kJ/mol)
(1)	$Al_2O_3(s) + 6HCl(l) = 2AlCl_3(l) + 3H_2O(l)$	168.123 + 0.6143 T
(2)	$Fe_2O_3(s) + 6HCl(l) = 2FeCl_3(l) + 3H_2O(l)$	− 76.601 + 0.58814 T
(3)	$CaO(s) + 2HCl(l) = CaCl_2(l) + H_2O(l)$	− 195.553 + 0.19452 T
(4)	$FeO(s) + 2HCl(l) = FeCl_2(l) + H_2O(l)$	− 108.569 + 0.20352 T
(5)	$MgO(s) + 2HCl(l) = MgCl_2(l) + H_2O(l)$	− 73.803 + 0.19808 T
(6)	$TiO_2(s) + 4HCl(l) = TiCl_4(l) + 2H_2O(l)$	52.7 + 0.30977 T
(7)	$ZrO_2(s) + 4HCl(l) = ZrCl_4(l) + 2H_2O(l)$	51.169 + 0.3907 T

Table 3 Expressions of standard Gibbs free energy changes of the main reactions in HF leaching

No.	Reaction equation	$\Delta_r G_m^\theta$ (kJ/mol)
(1)	$Al_2O_3(s) + 6HF(l) = 2AlF_3(l) + 3H_2O(l)$	− 354.78 + 0.6269 T
(2)	$Fe_2O_3(s) + 6HF(l) = 2FeF_3(l) + 3H_2O(l)$	− 277.47 + 0.5974 T
(3)	$Fe_3O_4(s) + 8HF(l) = 2FeF_3(l) + FeF_2(l) + 4H_2O(l)$	− 369.99 + 0.8052 T
(4)	$SiO_2(s) + 4HF(l) = SiF_4(g)\uparrow + 2H_2O(l)$	− 96.841 + 0.2342 T
(6)	$TiO_2(s) + 4HF(l) = TiF_4(s) + 2H_2O(l)$	− 53.953 + 0.3866 T
(7)	$ZrO_2(s) + 4HF(l) = ZrF_4(l) + 2H_2O(l)$	− 152.08 + 0.4173 T

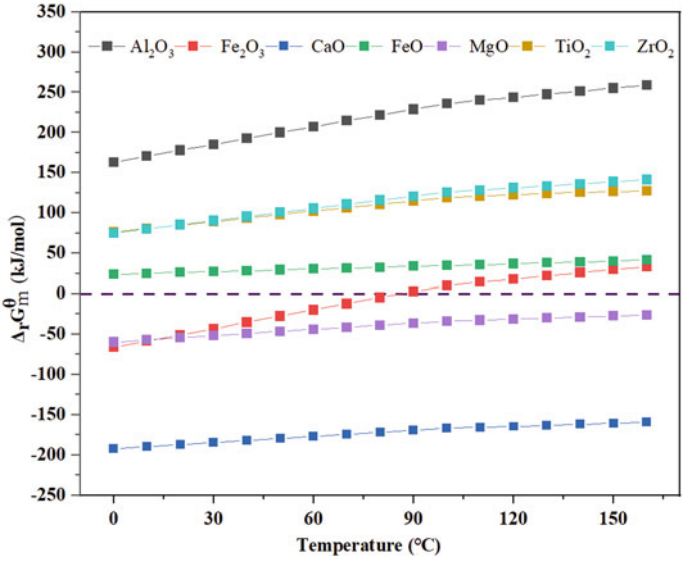

Fig. 3 Standard Gibbs free energy changes of the main reactions between various oxides and HCl

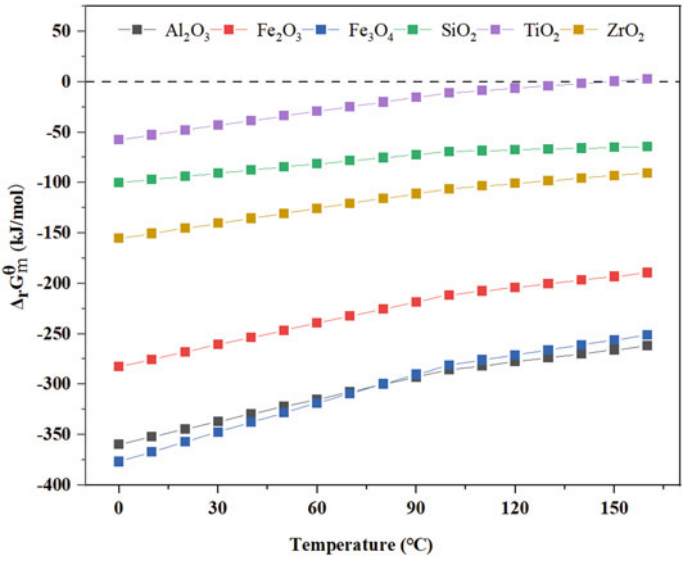

Fig. 4 Standard Gibbs free energy changes of the main reactions between various oxides and HF

It is expected that the acid concentration would play an important role in separation of impurities from rutile ore. As shown in Fig. 5, with increasing HCl concentrations, the TiO_2 content and impurity removal percentage increased initially and then decreased. The optimal purification performance was achieved when the acid concentration was 6 mol/L, with the TiO_2 content of 97.31 wt% and impurity removal percentage of 41.65%. For HF leaching, as shown in Fig. 6, the removal of impurities also depended on its concentration. The TiO_2 content and impurity removal percentage had the same changing trend as those in HCl leaching. It was obvious that the purification performance remained relatively stable when the HF concentration varied between 6 and 10 wt%. In other words, the proper HF concentration was 6 wt%. At this moment, the TiO_2 content and impurity removal percentage reached 98.77 wt% and 73.32%, respectively.

Figure 7 shows the XRD patterns of the rutile ore samples treated with 6 mol/L HCl and 6 wt% HF. Obviously, there was no significant change in the phase composition after leaching using both acids. The main phase composition of the ore was retained after purification. From Fig. 8, it compared with HCl leaching, the rutile ore became more porous and looser after HF leaching, agreeing with its better purification performance.

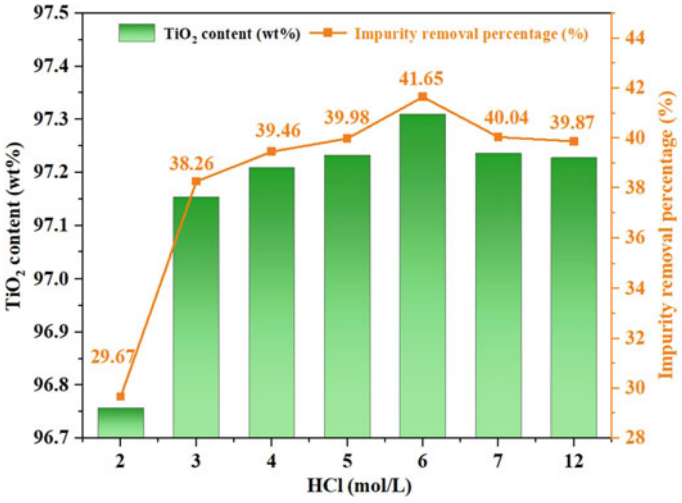

Fig. 5 Effect of HCl concentration on the TiO_2 content and impurity removal percentage of rutile ore

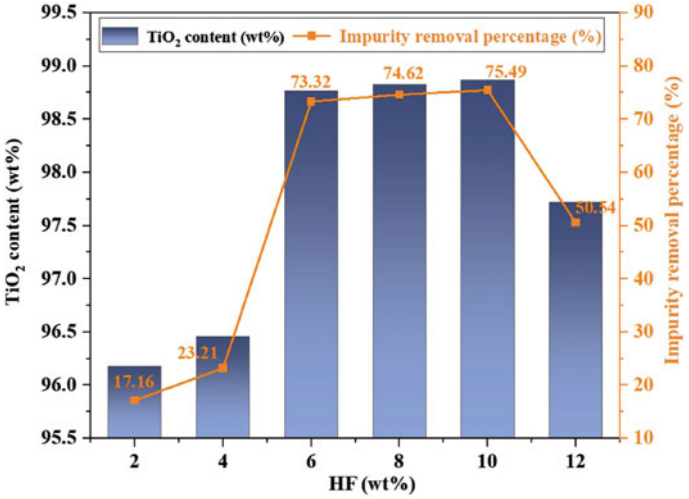

Fig. 6 Effect of HF concentration on the TiO_2 content and impurity removal percentage of rutile ore

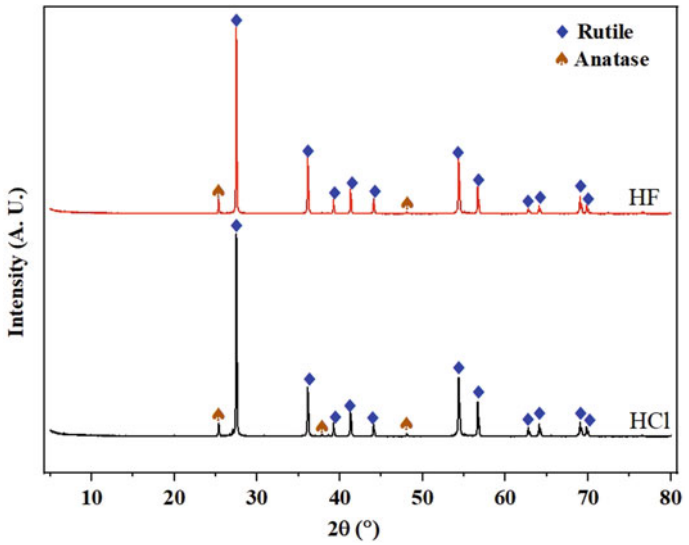

Fig. 7 XRD patterns of the rutile ore samples treated with 6 mol/L HCl and 6 wt% HF

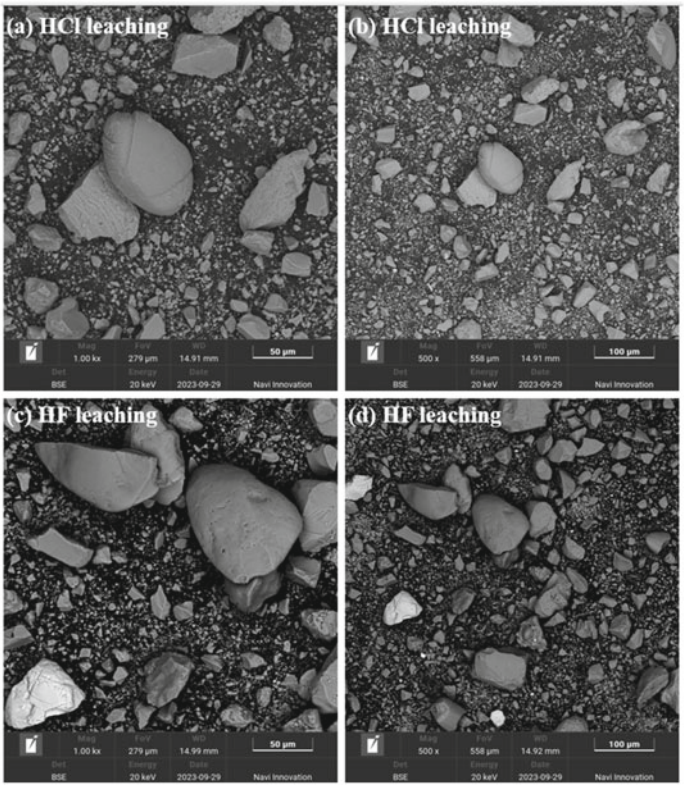

Fig. 8 SEM images of the rutile ore samples treated with 6 mol/L HCl and 6 wt% HF

Conclusions

In this study, the impurities in the natural rutile ore were removed by leaching using 2–12 mol/L HCl and 2–12 wt% HF, respectively. The thermodynamic and experimental analyses demonstrated that compared with HCl leaching, HF leaching could extract more impurities because of its easier reactions with impurity oxides, in spite of minor loss of TiO_2. Their purification performance increased initially and then decreased with increasing acid concentration. When the ore was leached by HCl with 6 mol/L at 60 °C for 4 h, the TiO_2 content could be enhanced from 95.39 to 97.31 wt%, with the optimal impurity removal percentage of 41.65%. For HF leaching, under the same conditions, the TiO_2 content was elevated to 98.77 wt% with the impurity removal percentage of 73.32% when the HF acid concentration was 6 wt%. The XRD and SEM analyses showed that leaching using both acids did not alter the phase composition of the ore evidently but caused changes of microstructure. For HF leaching, the product tended to be more porous and looser, in agreement with its better purification performance.

References

1. Basir A, Muhamad N, Sulong AB et al (2023) Recent advances in processing of titanium and titanium alloys through metal injection molding for biomedical applications: 2013–2022. Materials 16(11):3991
2. Alexander SB, Vladimirovich IO (2020) Open porous $\alpha + \beta$ titanium alloy by liquid metal dealloying for biomedical applications. Metals 10(11):1450
3. Mitsuo N, Yi L, Masaki N et al (2016) Biomedical titanium alloys with Young's moduli close to that of cortical bone. Regen Biomater 3(3):173–185
4. Oliveira DPD, Ottria L, Gargari M et al (2017) Surface modification of titanium alloys for biomedical application: from macro to nano scale. J Biol Reg Homeos Ag 31(2):221–232
5. Jung EJ, Kim J, Lee YR (2021) A comparative study on the chloride effectiveness of synthetic rutile and natural rutile manufactured from ilmenite ore. Sci Rep 11(1):4050
6. Muhammad N, Ahmad W, Khan M et al (2021) Purification and removal of hematite from talc by acid leaching assisted by chlorination techniques. Min Metall Explor 38(5):1–9
7. Hiraki T, Maruyama Y, Suzuki Y et al (2018) Up-grading of natural ilmenite ore by combining oxidation and acid leaching. Int J Miner Metall Mater 25(7):729–736
8. Serwale MR, Coetsee T, Fazluddin S (2020) Purification of crude titanium powder produced by metallothermic reduction by acid leaching. J South Afr Inst Min Metall 120(5):349–354
9. Vásquez R, Molina A (2012) Effects of thermal preoxidation on reductive leaching of ilmenite. Miner Eng 39:99–105
10. Wu Y, Lan G (2021) Preparation technology and progress analysis in the global three major titanium dioxide process by hydrochloric acid. Titanium Ind Prog 38(1):37–44
11. Mostafa NY, Mahmoud MHH, Heiba ZK et al (2013) Hydrolysis of $TiOCl_2$ leached and purified from low-grade ilmenite mineral. Hydrometallurgy 139:88–94

Quantitative Phase Analysis and Structural Investigation of Graphite Anode for Lithium-Ion Batteries

Hammad Farooq, Hilde Johnsen Venvik, and Sulalit Bandyopadhyay

Abstract Recycling of graphite anode from lithium-ion batteries (LIBs) has grown in recent years necessitating the development of advanced characterization methods. It is essential to establish a robust procedure to determine the changes in the crystalline structure, degree of graphitization, and the ratio of the 2H graphite phase to the 3R graphite phase. The distinction between graphite phases has crucial implications for the performance of LIBs. Using X-ray diffraction (XRD), quantitative and semi-quantitative phase analysis methods were employed to determine the structural parameters of graphite, the degree of graphitization, and the ratio of 2H to 3R phase based on the detection of diffraction lines within the 40 and 48° 2θ region. Quantitative XRD analysis of a natural graphite sample using the internal standard method revealed that the relative amount of the 3R phase is 27.18 wt.%. This insight can prove invaluable for industries aiming to optimize the recycling process and maintain high battery performance standards.

Keywords Graphite anode · Graphite XRD · 2H/3R quantification · Graphitization degree · Graphite *d*-spacing

H. Farooq · S. Bandyopadhyay (✉)
Department of Chemical Engineering, Particle Engineering Centre, Norwegian University of Science and Technology, 7034 Trondheim, Norway
e-mail: sulalit.bandyopadhyay@ntnu.no

H. Farooq
e-mail: hammadf@ntnu.no

H. J. Venvik
Department of Chemical Engineering, Norwegian University of Science and Technology, 7034 Trondheim, Norway
e-mail: hilde.j.venvik@ntnu.no

Z. Peng et al. (eds.), *Characterization of Minerals, Metals, and Materials 2024*, The Minerals, Metals & Materials Series, https://doi.org/10.1007/978-3-031-50304-7_21

Introduction

Graphite has long held prominence as an anode material in lithium-ion batteries (LIBs) due to its unique structural properties and characteristics [1]. During the charging and discharging of LIBs, lithium (Li) ions intercalate in and out of the layers of the graphite crystal structure, respectively. These properties make graphite a suitable anode material for the efficient and reliable operation of batteries. In end-of-life LIBs, the process of repeated intercalation and deintercalation of Li ions reversibly damages the graphite crystal structure by expanding the distance between graphite layers (called interlayer spacing). These structural changes can lead to increased electrode resistance, decreased lithium diffusion kinetics, and reduced cycling stability [2]. For the recycling reuse of graphite from end-of-life LIBs, it is essential to quantitatively analyze these structural changes to verify the requirement of any further treatment for this graphite to be suitable as an anode. This necessitates the development of a robust characterization and analysis method for the determination of interlayer spacing and related crystalline parameters such as crystal size along the *c*-axis and degree of graphitization.

The layered crystal structure of graphite is characterized by strong intralayer covalent bonds and weaker interlayer van der Waals interactions. This layered structure can be visualized with two distinct stacking sequences, ABAB stacking, and ABCABC stacking, as shown in Fig. 1. The ABAB stacking sequence involves every alternate layer having the same alignment and corresponds to the hexagonal (2H) phase. In the ABCABC sequence, the same alignment reappears every third layer and the assigned phase for such stacking sequence is the rhombohedral (3R) phase. These different stacking sequences give distinct electronic properties to graphite, affecting its crystal structure and electrochemical behavior [3]. The ABAB stacking sequence in the 2H graphite phase generally exhibits higher specific capacity, better rate capability, cyclability, and 1st cycle coulombic efficiency [4]. The ABCABC stacking sequence in 3R graphite results in higher discharge capacities, lower discharge potential, low 1st cycle coulombic efficiency, poor cyclability, and poor rate performance than the 2H graphite [4]. The 3R graphite phase selectively allows intercalation of unsolvated Li ions into the graphite layers while preventing co-intercalation of solvents [5].

Typically, the 2H phase is the more commonly observed graphite phase whereas the 3R phase is usually detected in natural graphite (NG) in varying amounts. Compared to NG, synthetic graphite (SG), produced through the high-temperature graphitization of carbon precursors, consists of the pure 2H phase [4]. However, during the recycling of graphite, mechanical treatments such as milling and attrition can introduce and increase the 3R phase amount [5]. Consequently, to clarify the electrochemical properties of recycled graphite, it is imperative to quantify the proportions of the 2H and 3R phases within the recycled graphite specimen. X-ray diffraction (XRD) is a robust characterization technique to investigate these important crystalline parameters i.e., interlayer spacing of graphite (d_c), crystal size along

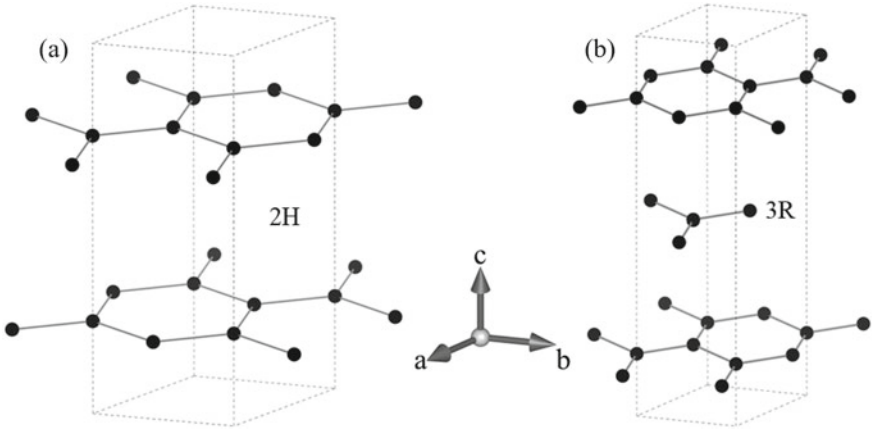

Fig. 1 Hexagonal layers of graphite crystal structure. **a** ABAB stacking in 2H phase, **b** ABCABC stacking 3R phase [ICDD PDF#00-056-0159, and PDF#01-075-2078]

the *c*-axis where Li ions intercalated and deintercalated (L_c), degree of graphitization (G), and the ratio of 2H and 3R phases. Previous studies have proposed different methods to semi-quantitatively analyze the 2H and 3R phases based on $I_{(101)2H}$ and $I_{(101)3R}$ peaks in the XRD diffraction pattern of natural graphite [6, 7]. In this investigation, the internal standard method is developed for quantitative phase analysis (QPA) of 2H and 3R phases, and the results are compared with the previously reported methods.

Materials and Methods

Materials and Chemicals

Table 1 lists the materials and chemicals used in this study along with the source and the assigned sample name. For the experimental work, graphite samples were provided by the industrial partners while other materials and chemicals were commercially purchased.

Table 1 Materials and chemicals used in this study, their sample name, and source

Material	Sample name	Source
Pristine synthetic graphite anode	SG	Provided by industrial partners
Pristine natural graphite anode	NG	Provided by industrial partners
Pure silicon used as a standard	Si	Purchased from Sigma-Aldrich (ref. 215619)

X-ray Diffraction (XRD) Experiments

XRD analysis was performed by a Bruker DaVinci1 diffractometer using Cu-Kα radiation ($\lambda = 1.54060$ Å). XRD diffraction experiments were carried out at a step size (2θ increment) of 0.01°, time/step of 3 s, fixed divergence slit (FDS) of 0.2° and a 2θ range of 20–60°. For XRD experiments of all samples, zero diffraction cavity type (10 mm diameter) sample holders were employed. Pristine graphite (SG and NG) powder samples were analyzed as obtained without any pre-treatment.

For internal standard quantitative phase analysis (QPA), pure silicon was used as the internal standard. Graphite powder and Si were weighed, mixed in a specific ratio, ground using a lab mortar, and then dispersed in Acetone (purchased from Sigma-Aldrich ref. 179124). The dispersed mixture was mixed for 5 min using a vortex and then placed inside a cabinet uncapped to dry. Once the acetone had completely evaporated, the graphite + Si mixture was again ground using a mortar and finally, the sample was prepared and placed in the above-mentioned XRD sample holder.

Results and Discussion

XRD Investigation of Pristine Graphite Anode

Figure 2a shows the XRD patterns of SG and NG for 2θ range 20–60°. An enlarged view between 2θ of 40 and 48° is displayed in Fig. 2b to distinctly show the peaks for 2H and 3R phases of graphite. SG shows two diffraction lines at 2θ of 42.4 and 44.4°, which correspond to $(100)_{2H}$ and $(101)_{2H}$, respectively [8]. While NG shows four diffraction lines, $(100)_{2H}$, $(101)_{3R}$, $(101)_{2H}$, and $(012)_{3R}$ at 42.4°, 43.5°, 44.4° and 46.2°, respectively [9–11]. This distinction between 2H and 3R phases within the 40–48° region is an important consideration to characterize the 2H and 3R phases since the other XRD peaks for these phases overlap including the main characteristic peak at $2\theta \approx 26°$ (Fig. 2a).

In SG, the main characteristic peak (002) at $2\theta \approx 26.4°$ has ABAB stacking sequence implying that every alternate layer has the same alignment. The XRD pattern of the 2H phase (SG sample) is matched with PDF entry 00-056-0159 from the ICDD PDF-4+ database [8].

Graphene layers in NG are a combination of ABAB and ABCABC stacking sequences due to the detection of 2H and 3R phase peaks within the 40–48° region (Fig. 2b). Previous studies have shown that the crystal structure for ABCABC stacking sequence in NG corresponds to space group 3R and the main characteristic peak is at $2\theta \approx 26°$ [9–11]. The main characteristic peak in NG at $2\theta \approx 26°$ is a combination of (002) and (003) since the peaks are so close together that they are completely convoluted. This is in agreement with the investigation, where the XRD pattern of NG (Fig. 2) matches with ICDD database entries for 2H (00-056-0159) and

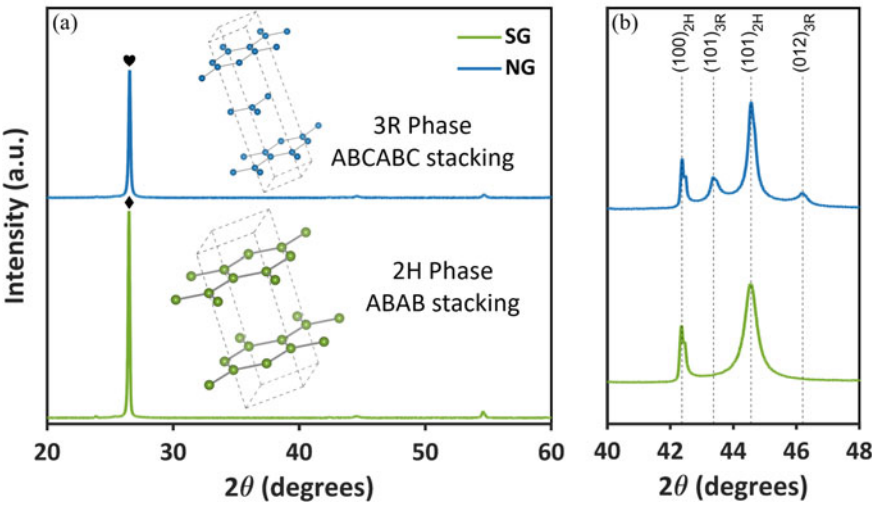

Fig. 2 *XRD* patterns of pristine synthetic graphite (SG) and natural graphite (NG) samples. **a** Plotted between 2θ values of 20 and 60°. ♦ shows main characteristic peak (002) of 2H graphite while ♥ represents main characteristic peak (003) of 3R phase of graphite. **b** XRD patterns plotted between 2θ values of 40 and 48°

Table 2 Crystalline parameter for 2H and 3R graphite phases

Crystalline parameters	2H graphite phase	3R graphite phase
PDF	00-056-0159	01-075-2078
Space group	P63/mmc (194)	R3 (166)
a (Å)	~ 2.4617	~ 2.4560
c (Å)	~ 6.7106	~ 10.0410
Characteristic peak (*hkl*)	002	003
Characteristic peak (2θ) (°)	~ 26.4	~ 26.6
Peak 101 (2θ) (°)	44.4	43.5

3R (01-075-2078) phases. Table 2 summarizes the crystalline parameters of pristine graphite anode samples, SG and NG.

Refinement and Analysis of XRD Patterns

For fitting and refinement of XRD patterns, the fundamental parameters' approach (FPA) in the TOPAS software is utilized. It works by combining several models that contribute to the instrument profile function and refining their parameters for an accurate representation of the experiment [12]. An essential benefit of the FPA method is

that it inherently corrects for instrument broadening [13]. The FPA method takes into account factors that influence the shape and intensity of diffraction peaks, including instrumental parameters, sample morphology, and crystallographic information. By considering these fundamental parameters, the FPA method allows for the refinement of diffraction patterns to obtain accurate structural and microstructural information about the sample [14].

Determination of Crystalline Parameters and Degree of Graphitization

Calculation of structural parameters of graphite requires an accurate peak position of the characteristic peak. Figure 3a, b show the fitting results of the characteristic peak at $2\theta \approx 26°$ for SG and NG, respectively, where the FPA method is applied to correct for instrumental parameters and instrumental broadening.

The small bump at $2\theta \approx 24°$ in both samples represents a contribution from the $CuK_{\beta}1$ wavelength of the Cu anode and has been accounted for in the refinement. A visual investigation of Fig. 3 shows a good fitting with a minute difference between the raw diffraction line and the fitted line.

The refined peak position of the main characteristic peak (shown in Table 3) is further employed for the calculation of crystal size (L_c), interlayer distance (d_c), and graphitization degree (G). Crystal size (L_c) is typically calculated using Eq. (1), called the Scherrer Equation, where K is the Scherrer constant, β_{FWHM} is the full width at half-maximum of the analyzed peak, λ is the $CuK_{\alpha}1$ wavelength (0.15406 nm), and θ is the Bragg's angle in radians (half of the peak position after FPA refinement).

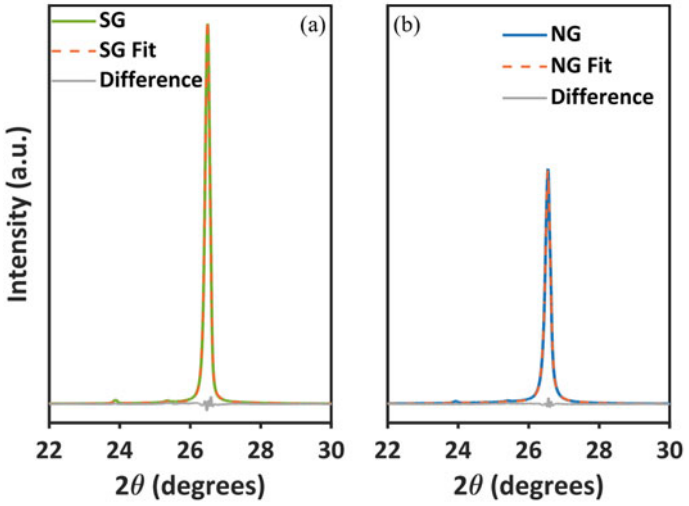

Fig. 3 Fitting of diffraction line near 2θ value of ~ 26°. The raw diffraction line and fitted line as well as the difference between these two lines are plotted **a** for SG, **b** for NG

Table 3 Structural parameters obtained from fitting the characteristic peak of SG and NG

Sample	Refined 2θ of (002)	d_c	L_c	G
	(°)	(nm)	(nm)	(%)
SG	26.51	0.336	83.05	92.9
NG	26.55	0.335	74.59	99.6

$$L_c = \frac{K\lambda}{\beta_{FWHM}\cos\theta} \tag{1}$$

The Scherrer constant K, which is related to the crystal shape, is usually unknown. For the determination of L_c in graphite, $K = 1$ is reported by previous studies, however, in this work, a different approach is taken for L_c determination by using a modified form of the Scherrer Equation where the (K/β_{FWHM}) factor is replaced by β_{IB} (Eq. 2) [15, 16]. It was reported that the value of K is not required when using β_{IB} (integral breadth) instead of FWHM.

$$L_c = \frac{\lambda}{\beta_{IB}\cos\theta} \tag{2}$$

$$d_c = \frac{\lambda}{2\sin\theta} \tag{3}$$

$$G(\%) = \frac{0.3440 - d_c}{0.3440 - 0.3354} \times 100\% \tag{4}$$

Bragg's law (Eq. 3), which relates the interlayer spacing (d_c) to the peak position, is employed to calculate the interlayer spacing, i.e., the distance between layers of graphite crystal structure (d_c). Based on the interlayer spacing of graphite samples (d_c), the degree of graphitization can be calculated by a semi-quantitative method. Equation (4) shows a semi-quantitative method to determine the degree of graphitization, where 0.3440 is the interlayer spacing of turbostratic graphite (in nm), 0.3354 is the interlayer spacing of single crystal graphite (in nm) and d_c is the interlayer spacing of the sample [16, 17]. Results show that the main characteristic peak of NG is slightly shifted towards the right (26.55°) compared to the main characteristic peak of SG (26.51°). Table 3 summarizes the results of this investigation, where Eqs. (2)–(4) are exercised for the calculation of crystallite size (L_c), interplanar distance (d_c), and graphitization degree (G).

Determination of 2H and 3R Phase Ratio in Graphite

The main characteristic graphite peak at $2\theta \approx 26°$ in NG cannot be used for differentiating between 2H and 3R graphite phases as the peak is a convoluted result of (002) and (003) peaks. However, within the 40 and 48° 2θ region, the 2H and 3R

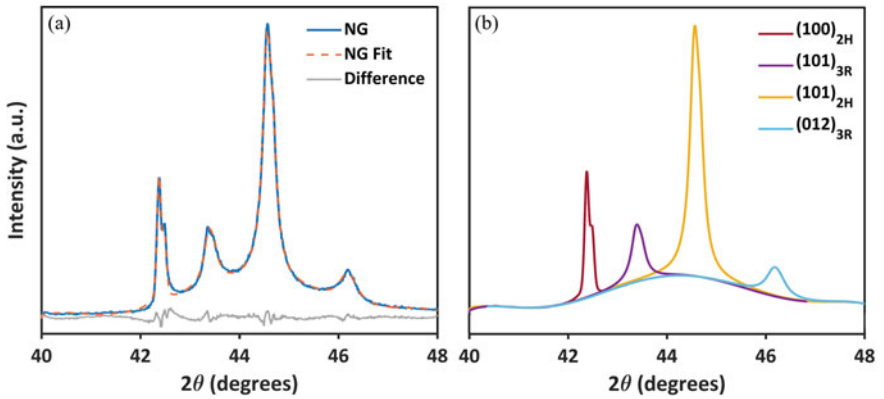

Fig. 4 XRD pattern of NG and refinement results within the 40 and 48° 2θ region. **a** The raw diffraction curves, the fitted curves, and the difference. **b** The de-convoluted $(100)_{2H}$, $(101)_{3R}$, $(101)_{2H}$, and $(012)_{3R}$ peaks

peaks are far apart enough to be analyzed, as shown by the XRD pattern of NG in Fig. 2b. A ratio between $I_{(101)2H}$ and $I_{(101)3R}$ peaks, located at 2θ values of ~ 44.4° and ~ 43.5°, respectively, can be used to calculate the relative wt. (%) of the 3R phase, as shown by the semi-quantitative Eq. (5) [6, 7]. Such an approach requires refinement of peaks between 2θ values of 40 and 48°, which is carried out using the FPA method and Voigt function.

$$3R(\%) = \frac{[101]_{3R} \times 15/12}{([101]_{3R} \times 15/12) + [101]_{2H}} \times 100\% \quad (5)$$

Figure 4a, b show the overall fitting of the XRD pattern and de-convoluted peaks of NG between 2θ values of 40° and 48°, respectively. The obtained $I_{(101)2H}$ and $I_{(101)3R}$ values from this refinement are employed to calculate the 3R wt.%, which is 21.94 wt.%.

A QPA method, specifically the internal standard method, is developed to quantify the 2H and 3R phases and compare the results with the previously explained semi-quantitative method. Figure 4a shows the NG raw diffraction curve, cumulative fit, Si fit, 2H phase fit, and 3R phase fit for 2θ range of 40–48°. An enlarged view is presented in Fig. 4b to better visualize the fitted curves for the 2H and 3R phases. For fitting of Si, 2H, and 3R phases in Fig. 4, the structure files obtained from the ICDD PDF-4+ database are 04-014-0362, 00-056-0159, and 01-075-2078, respectively.

The NG and Si mixture was prepared with 25.2 wt.% Si and the calculated weight of Si by the QPA method is 24.80 wt.% (Fig. 5b), i.e., the determined Si wt.% is in agreement with the Si wt.% in the prepared mixture of NG and Si. The determined weight of the 2H and 3R phases is 48.02% and 27.18%, respectively (Fig. 5b). There is a noticeable difference in the wt.% of the 3R phase between the semi-quantitative and the internal standard methods. This variance highlights the inherent

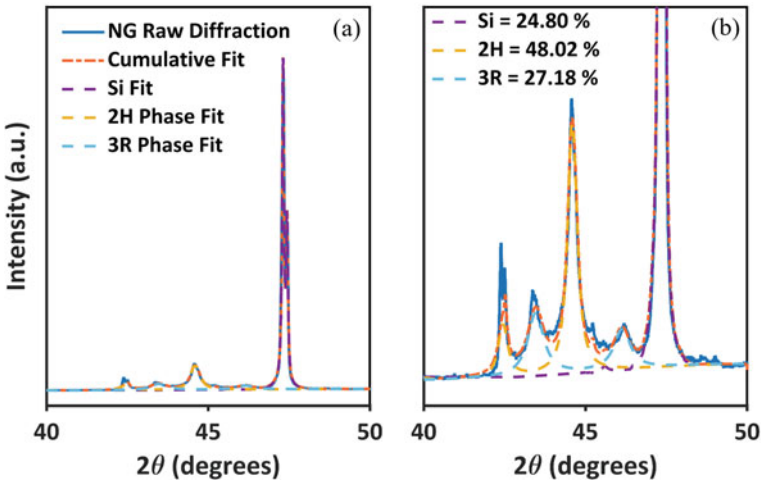

Fig. 5 Quantitative phase analysis (QPA) of NG by internal standard method using Si as the spike material where the GOF (goodness-of-fit) is 2.33. Structure files for Si (PDF 04-014-0362), 2H graphite phase (PDF 00-056-0159), and 3R graphite phase (PDF 01-075-2078) are obtained from ICDD PDF-4+ database. **a** NG diffraction data, cumulative fit, Si fit, 2H phase fit, and 3R phase fit curves are plotted from 2θ value of 40 to 50°. **b** Enhanced re-plotting to visualize the fit curves where QPA results show 2H phase wt. is 48.02%, 3R phase wt. is 27.18% and Si wt. is 24.80%

challenges associated with accurately quantifying the 3R phase. To ensure robust and definitive results, it is vital to carry out additional work and in-depth analysis. This might encompass improving the existing methodologies and exploring alternative refinement methods.

Conclusion

XRD analysis highlighted key distinctions between synthetic graphite (SG) and natural graphite (NG). SG predominantly exhibits the 2H graphite phase with a prominent characteristic peak (002). Conversely, NG displays both 2H and 3R graphite phases. The Fundamental Parameters Approach (FPA) is applied for the fitting and refinement of XRD patterns. Utilizing the FPA method, the exact graphite characteristic peak position was determined, enabling the derivation of crystalline parameters like crystallite size (L_c), interplanar distance (d_c), and graphitization degree (G).

The proximity of characteristic peaks (002 for 2H and 003 for 3R) at $2\theta \approx 26°$ complicates differentiation between these phases. However, distinctive patterns between 2θ values of 40 and 48° provide reliable grounds for analysis. Using the refined peaks between these 2θ values, semi-quantitative and quantitative methods are employed to measure the 2H and 3R phases. Quantitative Phase Analysis (QPA)

using an internal standard method provided clarity on the weight percentages of the 2H and 3R phases in NG. The determined weights of the 2H and 3R phases were found to be 48.02% and 27.18%, respectively, with Si content registering at 24.80%, closely matching its proportion in the prepared mixture (which was 25.2%).

In summary, this comprehensive XRD analysis draws attention to the crystal structure differences between SG and NG, offering insights into their phase compositions and crystalline characteristics. The methodologies investigated demonstrate accuracy and precision in determining the crystal structure parameters for different graphite phases, however, further work is required to validate the accuracy of methods for 2H and 3R phase quantification.

Acknowledgements This work was carried out as part of the SUMBAT (Sustainable Materials for the Battery Value Chain) project, funded by the Research Council of Norway, Innovation Norway, and SIVA (Industrial Development Corporation of Norway) under the Norwegian Green Platform Initiative.

References

1. Kulkarni S, Huang T-Y, Thapaliya BP, Luo H, Dai S, Zhao F (2022) Prospective life cycle assessment of synthetic graphite manufactured via electrochemical graphitization. ACS Sustain Chem Eng 10(41):13607–13618. https://doi.org/10.1021/acssuschemeng.2c02937
2. Zhang Y, Song N, He J, Chen R, Li X (2019) Lithiation-aided conversion of end-of-life lithium-ion battery anodes to high-quality graphene and graphene oxide. Nano Lett 19(1):512–519. https://doi.org/10.1021/acs.nanolett.8b04410
3. Liu YP, Goolaup S, Lew WS, Purnama I, Chandra Sekhar M, Zhou TJ, Wong SK (2013) Excitonic bandgap dependence on stacking configuration in four layer graphene. Appl Phys Lett 103(16):163108. https://doi.org/10.1063/1.4825263
4. Park T-H, Yeo J-S, Seo M-H, Miyawaki J, Mochida I, Yoon S-H (2013) Enhancing the rate performance of graphite anodes through addition of natural graphite/carbon nanofibers in lithium-ion batteries. Electrochim Acta 93:236–240. https://doi.org/10.1016/j.electacta.2012.12.124
5. Schaffer B, Hofer F, Kohs W, Besenhard J, Möller K-C, Winter M (2003) HREM study of hexagonal and rhombohedral graphites for use as anodes in lithium ion batteries. Microsc Microanal 9(S03):54–55. https://doi.org/10.1017/S1431927603012169
6. Seehra MS, Geddam UK, Schwegler-Berry D, Stefaniak AB (2015) Detection and quantification of 2H and 3R phases in commercial graphene-based materials. Carbon 95:818–823. https://doi.org/10.1016/j.carbon.2015.08.109
7. Flandrois S, Fevrier A, Biensan P, Simon B (1996) Carbon anode for a lithium rechargeable electrochemical cell and a process for its production. US patent 5554462, 10 Sept 1996
8. Singh PK, Singh PK, Sharma K (2022) Electrochemical synthesis and characterization of thermally reduced graphene oxide: influence of thermal annealing on microstructural features. Mater Today Commun 32:103950. https://doi.org/10.1016/j.mtcomm.2022.103950
9. Kosacki J, Dogan F (2021) The effect of expanded and natural flake graphite additives on positive active mass utilization of the lead-acid battery. J Electrochem Soc 168(12):120540. https://doi.org/10.1149/1945-7111/ac4188
10. Alharthi AI, Alotaibi MA, Din IU, Abdel-Fattah E, Bakht MA, Al-Fatesh AS, Alanazi AA (2021) Mg and Cu incorporated $CoFe_2O_4$ catalyst: characterization and methane cracking performance for hydrogen and nano-carbon production. Ceram Int 47(19):27201–27209. https://doi.org/10.1016/j.ceramint.2021.06.142

11. Pidaparthy S, Rodrigues M-TF, Zuo J-M, Abraham DP (2021) Increased disorder at graphite particle edges revealed by multi-length scale characterization of anodes from fast-charged lithium-ion cells. J Electrochem Soc 168(10):100509. https://doi.org/10.1149/1945-7111/ac2a7f
12. Cline JP, Black DR, Gil D, Henins A, Windover D (2010) The application of the fundamental parameters approach as implemented in TOPAS to divergent beam powder diffraction data. Mater Sci Forum 651:201–219. https://doi.org/10.4028/www.scientific.net/MSF.651.201
13. Cheary RW, Coelho AA, Cline JP (2004) Fundamental parameters line profile fitting in laboratory diffractometers. J Res Natl Inst Stand Technol 109(1):1–25. https://doi.org/10.6028/jres.109.002
14. Mendenhall MH, Mullen K, Cline JP (2015) An implementation of the fundamental parameters approach for analysis of X-ray powder diffraction line profiles. J Res Natl Inst Stand Technol 120:223–251. https://doi.org/10.6028/jres.120.014
15. Laue MV (1926) VI. Lorentz-Faktor und Intensitätsverteilung in Debye-Scherrer-Ringen. Z Kristallogr Cryst Mater 64(1–6):115–142. https://doi.org/10.1524/zkri.1926.64.1.115
16. Yu H, Dai H, Zhu Y, Hu H, Zhao R, Wu B, Chen D (2021) Mechanistic insights into the lattice reconfiguration of the anode graphite recycled from spent high-power lithium-ion batteries. J Power Sources 481:229159. https://doi.org/10.1016/j.jpowsour.2020.229159
17. Greene ML, Schwartz RW, Treleaven JW (2002) Short residence time graphitization of mesophase pitch-based carbon fibers. Carbon 40(8):1217–1226. https://doi.org/10.1016/S0008-6223(01)00301-3

Part VI
Characterization of Metals

New Method for the Production of Medium-Mn Steel with Micro-segregation Bands Induced by Sub-rapid Solidification

Hui Xu, Wanlin Wang, Peisheng Lyu, and Lankun Wang

Abstract Medium-Mn steel has important applications in the lightweight automotive industry due to its excellent comprehensive mechanical properties. However, the existence of cumbersome production steps, high energy consumption, and severe macro-segregation seriously limits its industrial development. Hence, this study proposed a green-short method for producing medium-Mn steel with micro-segregation bands using sub-rapid solidification technology. Exclusive components were designed, and OM, SEM, EPMA, and EBSD techniques were used to characterize the microstructure distribution, grain orientation, and elemental micro-segregation of the as-cast strips. The phase transformation behavior and formation mechanism of Mn micro-segregation during the sub-rapid solidification process were deeply discussed. This work innovatively utilized the sub-rapid solidification characteristics to effectively avoid the macro-segregation problem of Mn, and cleverly transformed it into micro-segregation bands that were beneficial for mechanical properties. Furthermore, the design of short process provides valuable idea for the industrial production and application of medium-Mn steels.

Keywords Medium-Mn steel · Sub-rapid solidification · Mn micro-segregation · Green industrial production

Introduction

Medium-Mn steel has important applications in the lightweight automotive industry due to its excellent comprehensive mechanical properties. Researchers have conducted extensive research on microstructure evolution and process design and

H. Xu · W. Wang (✉) · P. Lyu · L. Wang
School of Metallurgy and Environment, Central South University, Changsha 410083, Hunan, China
e-mail: wanlin.wang@gmail.com

National Center for International Research of Clean Metallurgy, Central South University, Changsha 410083, Hunan, China

Z. Peng et al. (eds.), *Characterization of Minerals, Metals, and Materials 2024*, The Minerals, Metals & Materials Series, https://doi.org/10.1007/978-3-031-50304-7_22

have achieved certain results [1–3]. At present, the mechanical properties of medium-Mn steel can basically meet the needs of the automotive industry for most parts, but there are still many problems that need to be solved before the large-scale industrial production. The high Mn content usually leads to severe Mn macro-segregation, and conventional production can only introduce a long-term and costly homogenization annealing process to regulate it. Liang et al. [4] introduced the pre-quenching process to eliminate the influence of Mn macro-segregation to achieve uniformity and optimize mechanical properties. The results showed that pre-quenching can effectively increase the contact region between ferrite and martensite, thereby improving the structural uniformity and mechanical properties of medium-Mn steel. Lee et al. [5] strictly controlled the composition, distribution, and morphology of the austenite in the rich and poor Mn regions to stimulate the favorable effect of Mn micro-segregation in medium-Mn steel. The results showed that the coarse austenite grown in the Mn-enriched region can effectively stimulate the TRIP effect during deformation, resulting in a good combination of mechanical properties with a strength of up to 1.6 GPa and an elongation of about 20%. Wang et al. [6] prepared medium-Mn steel with a composition of Fe–0.3C–4Mn–1.82Al–0.6Si using the "twin-roll strip casting—hot-rolling—critical annealing" processes. The results showed that there was Mn micro-segregation but no macro-segregation in the as-cast strip, which was a composite phase of martensite and austenite with obvious dendritic structure characteristics.

It is easy to produce Mn macro-segregation during the casting process of medium-Mn steel, resulting in uneven distribution of microstructure and ultimately degrading the overall mechanical properties. The several segregation control methods currently proposed (such as homogenization) generally take a long time and consume a huge amount of energy, which is not environmentally friendly. The sub-rapid solidification rate (10^3 ~ 10^4 k/s) during the strip casting process can effectively refine the dendrite spacing, suppress the macro-segregation tendency of alloy elements, which is expected to simplify the necessary homogenization treatment in the production of high alloy steel. In addition, the molten steel is directly cast into 1–5 mm strips during, which can greatly simplify the subsequent rolling process and reduce energy consumption. However, researchers on strip casting in the steel field mainly focused on low alloy steels. Although research has reported the micro-segregation behavior of Mn during strip casting [7], the formation mechanism, genetic characteristics, and impact on microstructure have not been clearly studied. This study used the strip casting technology to simulate the sub-rapid solidification process of medium-Mn steel, and deeply explored the micro-segregation behavior and microstructure evolution of Mn, providing new ideas for the process design of medium-Mn steel. Two different compositions of medium-Mn steel were designed, and the characteristics of microstructure distribution, grain orientation, and element micro-segregation of as-cast strip were studied. The phase transformation behavior and the formation mechanism of Mn micro-segregation during the sub-rapid solidification process of medium-Mn steel were also discussed.

Materials and Experimental Methods

The medium-Mn steel with compositions of Fe–0.1C–6Mn–0.5Al–2Si and Fe–0.1C–9Mn–0.5Al–2Si was designed, hereinafter referred to as 6Mn and 9Mn steel. To clarify the phase transformation patterns during solidification processes, the thermodynamic equilibrium phase diagrams were calculated as shown in Fig. 1. The dip tester simulator was used to conduct the sub-rapid solidification experiments, and the schematic diagram is shown in Fig. 2a. The simulator mainly includes a smelting system, an atmosphere control system, a temperature acquisition system, a water-cooled copper substrate, and a guide rail type motion system. The water-cooled copper substrate is the key to achieve sub-rapid solidification. Compared to other immersive strip casting thermal simulator, this system innovatively adopts a double-sided water-cooled copper substrate as the solidification crystallizer, which is closer to the twin-roll structure in actual industrial production. The water-cooled copper substrate is designed with a U-shaped water channel inside, which can better simulate the heat transfer behavior between liquid metal and crystallization roller in industrial production. Our previous research has demonstrated that this device can effectively simulate the strip casting process and obtain cast strips with similar properties to actual industrial production [8]. The specific experimental process and as-cast strip information are shown in Fig. 1b. The obtained as-cast strips are abbreviated as 6Mn strip and 9Mn strip, respectively.

Using wire cutting technology to cut the sample into 3 × 6 mm, and select the cross-section composed of rolling direction (RD) and normal direction (ND) as the observation surface. Metallographic sandpaper with roughness of 400#–1500# was used to sequentially polish the observation surface, followed by mechanical polishing treatment. The polished samples were chemically etched using 4 vol.% nitric acid alcohol solution. The microstructure of the corroded sample was observed using an optical microscope (OM, Olympus BX3M-LEDR) and a scanning electron microscope (SEM, JSM-7900F). The electron probe technique (EPMA, EPMA-1610) was used to characterize the elemental distribution in the samples. To avoid the impact of residual corrosion products on the surface of the sample on the accuracy of the results, samples observed by EPMA need to undergo ultrasonic vibration cleaning for 15 min.

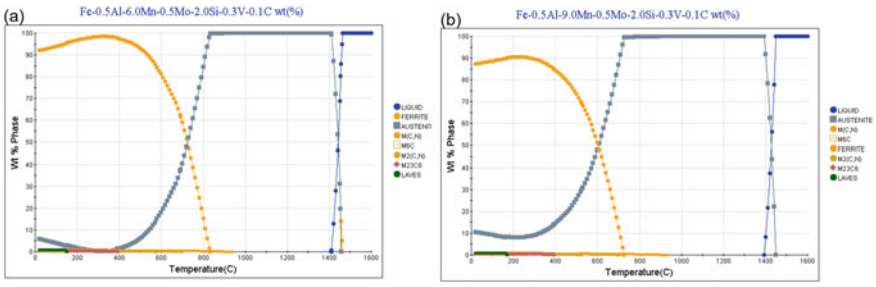

Fig. 1 Thermodynamic equilibrium phase diagrams of **a** 6Mn steel and **b** 9Mn steel

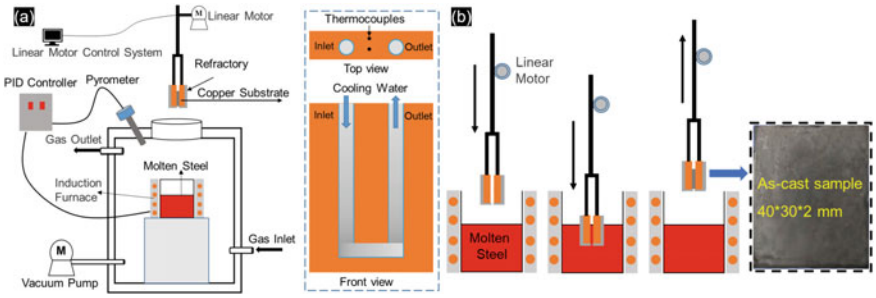

Fig. 2 Schematic diagrams of **a** strip casting simulator and water-cooling copper substrate, **b** experimental process and the corresponding as-cast strip information

Electron backscatter diffraction (EBSD) was used to characterize the grain boundary distribution, phase composition, texture orientation, and other aspects in the sample. The OIM data were processed using Channel 5.0 and MTEX software. The samples used for EBSD analyses were prepared using electrolytic polishing method using 10 vol.% ethanol perchlorate electrolyte to remove subsurface mechanical damage from mechanical polishing steps.

Results and Discussion

Mn Micro-segregation Behavior and Microstructural Characteristics of the As-Cast Samples

The results show that there is no Mn macro-segregation in both 6Mn and 9Mn as-cast strips, but there are different degrees of Mn micro-segregation (Fig. 3a, d). In the 6Mn as-cast strip, Mn is mainly enriched in the primary dendrite gap (primary dendrite spacing (PDS) about 13.7 μm) with the content ranging from 2.96 to 10.68 wt.%, and the Mn segregation bands are in the form of parallel bands. In the 9Mn as-cast strip, Mn is enriched in the primary and secondary dendrite interstices (PDS about 25.6 μm), with contents ranging from 5.67 to 14.55 wt.%, which is significantly higher than that in 6Mn as-cast strip. According to the relationship between PDS and cooling rate during solidification established by Jacobi and Schwerdtfeger [9], the dendrite spacing decreases with the increase of solidification cooling rate in strip casting, indicating that the sub-rapid solidification processes had taken place in both 6Mn and 9Mn steels [8]. The difference in PDS between the two samples may be related to the deterioration of the thermal conductivity due to the higher Mn content in the 9Mn steel.

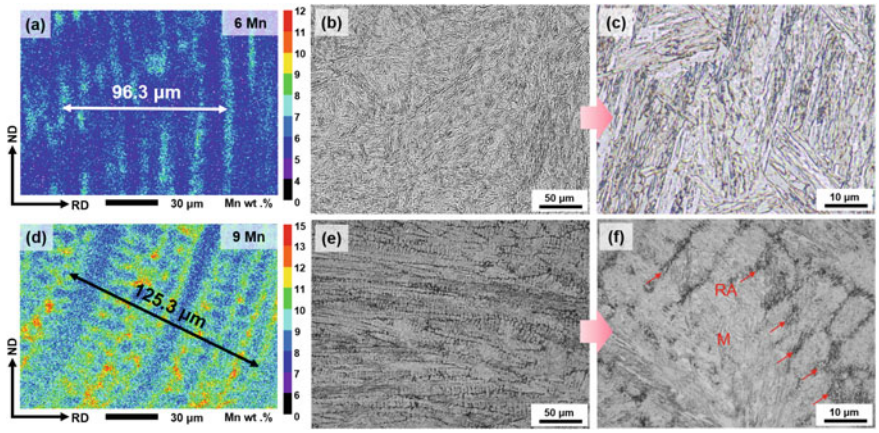

Fig. 3 EPMA Mn distribution maps: **a** 6Mn as-cast strip, **d** 9Mn as-cast strip; OM images of **b**, **c**: 6Mn as-cast strip, **e**, **f**: 9Mn as-cast strip

Optical microstructures show that the 6Mn as-cast strip is mainly composed of uniformly sized lath martensite (Fig. 3b, c), suggesting that the Mn micro-partitioning in the 6Mn as-cast sample has a relatively small effect on the distribution of retained austenite. Compared with 6Mn as-cast strip, the percentage of RA in the 9Mn as-cast strip is significantly increased, which is mainly distributed in the dendritic interstitials (Mn-enriched regions), indicating that the austenite distribution in the 9Mn as-cast sample is largely affected by the Mn micro-segregation in the steel. The results were consistent with the microstructural characteristics of the as-cast medium-Mn steel observed by Wang et al. [6]. Figure 4 shows the SEM and EBSD microstructures of the as-cast samples. There is a very small amount of RA uniformly distributed among the martensite laths in the 6Mn as-cast strip, and its distribution has little relationship with the Mn-enriched region indicating that the Mn micro-segregation does not affect the distribution of RA. For the 9Mn as-cast strip, RA is generally in the form of blocky morphology uniformly distributed in the interstices of primary and secondary dendrites, and martensite is in the shape of uniformly sized laths. It is noteworthy that no precipitated phases with micrometer size were found in both compositions of medium-Mn steel, indicating that the extremely fast cooling rate of the sub-rapid solidification can effectively inhibit the growth behavior of the precipitated phases during the solidification process.

Grain Orientation of the As-Cast Strip

Since it is difficult to retain the original austenite during the cooling process, it is not possible to directly observe the initial solidification phase morphology of the

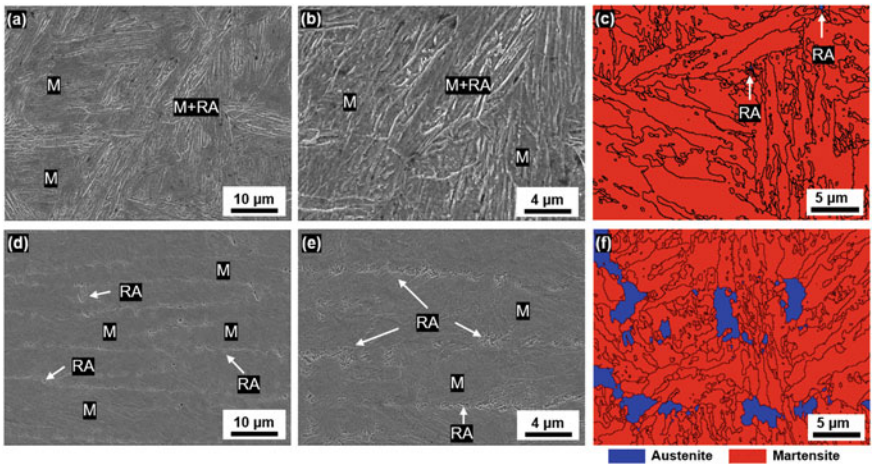

Fig. 4 The microstructure: **a**, **b** SEM images of 6Mn as-cast strip; **c** EBSD phase map

medium-Mn steel. Considering the tangential coherence of martensite transformation and the specific crystal orientation relationship between martensite and parent austenite, combining the orientation and morphology of the martensite can help us infer the morphology of the parent austenite. Figure 5a, b show the EBSD inverse pole figure (IPF) of each phase in 6Mn and 9Mn as-cast strips. The data iteration method proposed by Niessen et al. [10] was used to calculate the orientation of the parent austenite. For each martensite lath, this method can start from the initially predicted orientation relationship, iterate to the most practical orientation relationship, and finally accurately restore the original austenite orientation. By using the MTEX program on MatLab software, the original austenite grain morphology of martensitic grains in 6Mn and 9Mn as-cast strips were reconstructed.

Figure 5c, d shows the IPF diagram of the original austenite grains of the reconstructed 6Mn and 9Mn as-cast strips, with the black lines showing the large angle grain boundaries. It was found that the simulated original austenite orientation was consistent with the measured RA orientation, indicating that this method can effectively reflect the original austenite orientation during the solidification process. The white regions in Fig. 5c were the regions that were difficult to identify during austenite iterative back-calculation. According to the equilibrium phase diagram of 6Mn steel, δ Ferrite is only in a high-temperature state and then transforms into austenite during subsequent cooling, resulting in some small-grained original austenite transformed from δ-ferrite is present inside the coarser original austenite columnar crystals. The original austenite of both 6Mn and 9Mn steels are coarse columnar grains with certain orientation differences, which may be related to high-density defects caused by the faster cooling rate during the sub-rapid solidification process. Due to the influence of heat transfer direction, columnar crystals with an orientation of <001>//ND usually have the fastest growth rate during the solidification process. This results in a high proportion of <001>//ND oriented or nearly <001>//ND oriented austenite grains in

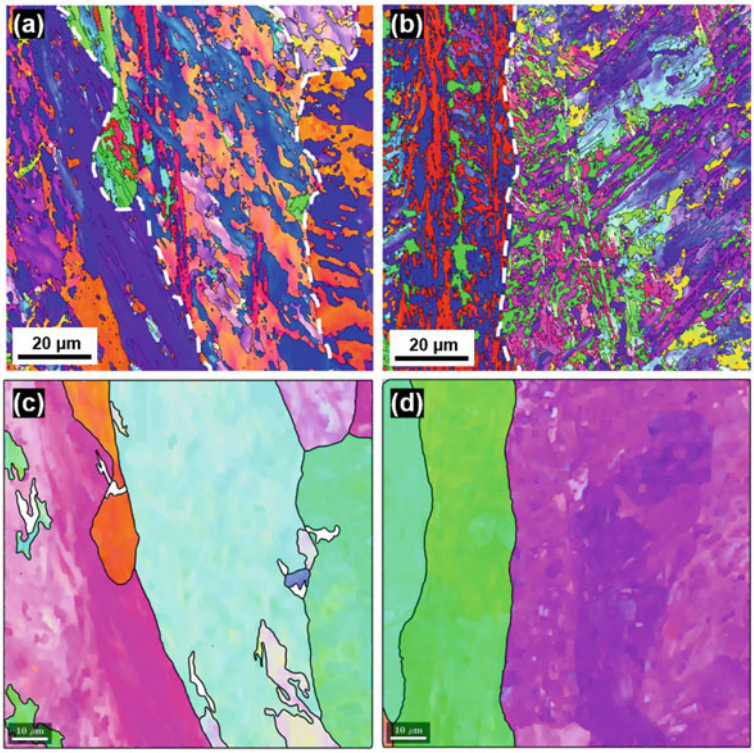

Fig. 5 EBSD IPF maps: **a** 6Mn as-cast strip; **b** 9Mn as-cast strip. The reconstructed primary austenite: **c** 6Mn as-cast strip, **d** 9Mn as-cast strip

both 6Mn and 9Mn steels, which is consistent with the austenite orientation observed by Hunter and Ferry [11] in strip casting austenitic stainless steel. However, due to the fact that the strip casting process is not a simple one-dimensional heat transfer model, there is a complex flow field between the crystallization rollers, and grain growth is also affected by various external forces represented by gravity, resulting in the formation of some other orientation austenite grains.

Microstructure Evolution of the As-Cast Strip During Sub-rapid Cooling Process

Mn can significantly improve the hardenability of steel, allowing medium-Mn steels to undergo almost no diffusive phase transformation during cooling. Due to the poor thermal stability of coarse original austenite, the vast majority of austenite in 6Mn as-cast strip and the austenite in the Mn-depleted region within the dendrites in 9Mn as-cast strip undergo martensitic transformation during the cooling process. The

microstructure of the 6Mn as-cast strip is almost entirely martensite, indicating that the austenite stability in the Mn-enriched region is still not sufficient to hinder the martensitic transformation. The 9Mn as-cast strip has a significantly higher degree of Mn-enriched, which enhances the thermal stability of austenite in the Mn-enriched region. During the cooling process of the 9Mn as-cast strip, martensitic transformation occurs in the Mn-depleted region, and the austenite in the Mn-enriched region between dendrites is retained, ultimately forming the as-cast structure with obvious dendritic characteristics. Comparing the morphology of martensite bundles in 6Mn and 9Mn as-cast strips, it can be found that the martensite laths in 9Mn as-cast strip are generally finer. The austenite that does not participate in the martensitic transformation in 9Mn as-cast strip plays a role in dividing the original austenite grain to a certain extent, reducing the grain size of the parent austenite, and finally refining the martensite laths in the matrix.

Conclusion

This study proposed a green-short method for producing medium-Mn steel with micro-segregation bands using sub-rapid solidification technology. The phase transformation behavior and formation mechanism of Mn micro-segregation during the sub-rapid solidification process were deeply discussed. This work innovatively utilized the sub-rapid solidification characteristics to effectively avoid the macro-segregation problem of Mn, and cleverly transformed it into micro-segregation bands that were beneficial for mechanical properties. Furthermore, the design of short process provides valuable idea for the industrial production and application of medium-Mn steels.

References

1. Liu H, Liu Z, Li C et al (2011) Solidification structure and crystallographic texture of strip casting 3wt.% Si non-oriented silicon steel. Mater Charact 5(62):463–468
2. Daamen M, Haase C, Dierdorf J et al (2015) Twin-roll strip casting: a competitive alternative for the production of high-manganese steels with advanced mechanical properties. Mater Sci Eng A 627:72–81
3. Shi J, Sun X, Wang M et al (2010) Enhanced work-hardening behavior and mechanical properties in ultrafine-grained steels with large-fractioned metastable austenite. Scr Mater 63(8):815–818
4. Liang J, Zhao Z, Tang D et al (2018) Improved microstructural homogeneity and mechanical property of medium manganese steel with Mn segregation banding by alternating lath matrix. Mater Sci Eng A 711:175–181
5. Lee H, Jo MC, Sohn SS et al (2018) Novel medium-Mn (austenite + martensite) duplex hot-rolled steel achieving 1.6 GPa strength with 20% ductility by Mn-segregation-induced TRIP mechanism. Acta Mater 147:247–260
6. Wang H, Zhang Y, Ran R et al (2019) A medium-Mn steel processed by novel twin-roll strip casting route. Mater Sci Technol 35(10):1227–1238

7. Zhang J, Huang M, Sun B et al (2021) Critical role of Lüders banding in hydrogen embrittlement susceptibility of medium Mn steels. Scr Mater 190:32–37
8. Lyu P, Wang W, Wang C et al (2021) Effect of sub-rapid solidification and secondary cooling on microstructure and properties of strip cast low-carbon bainitic–martensitic steel. Metall Mater Trans A 52(9):3945–3960
9. Jacobi H, Schwerdtfeger K (1976) Dendrite morphology of steady state unidirectionally solidified steel. Metall Trans A 7:811–820
10. Niessen F, Nyyssönen T, Gazder AA et al (2022) Parent grain reconstruction from partially or fully transformed microstructures in MTEX. J Appl Crystallogr 55(1):180–194
11. Hunter A, Ferry M (2002) Comparative study of texture development in strip-cast ferritic and austenitic stainless steels. Scr Mater 47(5):349–355

Part VII
Characterization of Polymers, Composites, Coatings and Ceramics

Preparation of Boronized Ti6Al4V/HA Composites by Powder Sintering for Dental Applications: Effect of Mixing Method

Shangyong Zuo, Qian Peng, Tong Zhang, Ting Luo, Yuehong Wang, and Zhiwei Peng

Abstract Three methods, namely, traditional one-step ball milling method, two-step ball milling method, and ball milling-resonant acoustic mixing method were used for mixing the powders of Ti6Al4V, hydroxyapatite (HA), and TiB_2 before sintering at 1050 °C for 30 min to prepare boronized Ti6Al4V/HA composites as dental implants. Their effects on the composition, microstructure, and mechanical properties of the composite were investigated. It was found that compared with traditional one-step ball milling and two-step ball milling method, the ball milling-resonant acoustic mixing method led to lower HA decomposition and better TiB_2 reactivity during subsequent sintering process, which contributed to better mechanical properties. When the powders were mixed by ball milling for 12 h, followed by resonant acoustic mixing for 20 min, the composite obtained after microwave sintering at 1050 °C for 30 min had good comprehensive properties, namely, compressive strength of 331.6 MPa, compressive modulus of 8.69 GPa, and Vickers microhardness of 286.0 HV.

Keywords Ti6Al4V · Hydroxyapatite · Ball milling · Resonant acoustic mixing · Mechanical properties

S. Zuo · T. Zhang · Z. Peng
School of Minerals Processing and Bioengineering, Central South University, Changsha 410083, China

Q. Peng (✉) · T. Luo · Y. Wang
Xiangya Stomatological Hospital, Central South University, Changsha 410008, China
e-mail: qqpeng@csu.edu.cn

Xiangya School of Stomatology, Central South University, Changsha 410008, China

Hunan Key Laboratory of Oral Health Research, Central South University, Changsha 410008, China

Z. Peng et al. (eds.), *Characterization of Minerals, Metals, and Materials 2024*, The Minerals, Metals & Materials Series, https://doi.org/10.1007/978-3-031-50304-7_23

Introduction

Ti6Al4V is a main type of dental implant material due to its outstanding mechanical properties and biocompatibility [1]. However, it has no bioactivity and a much higher elastic modulus than that of human bone which produces stress shielding after implantation and often leads to abnormal bone reconstruction [2, 3]. Synthetic hydroxyapatite (HA) is one of the bioactive ceramics with a chemical composition close to that of human bone [4]. It is popular to prepare composites of Ti6Al4V and HA [5]. However, HA decomposes during sintering at high temperature and hinders the diffusion between Ti6Al4V particles, resulting in significant decreases in the density and strength of the composite [6]. It was shown that adding TiB_2 into the mixture of Ti6Al4V and HA for microwave sintering could rapidly generate TiB, an in-situ reinforcing phase, in the composites at a low temperature, which strengthened the connection between Ti6Al4V particles [7]. However, in-situ reaction of TiB_2 occurred only in the surface layer [8]. It was because the fine needle-like HA particles acted as a buffer during the ball milling process [9, 10], inhibiting the deformation and fragmentation of Ti and TiB_2 particles, which was not conducive to their reactivity. In addition, the crystallinity of HA decreased during the long ball milling process, causing its further decomposition during the sintering process. Resonant acoustic mixing is a novel mixing technology with high efficiency and low energy consumption, whose paddle-less feature can avoid the destruction of powder lattice due to pressing force during the mixing process [11].

The aim of this study was to develop a novel two-step mixing method to enable easier activation of TiB_2 and higher crystallinity of HA in the mixed powders during the ensuing sintering process, thus inhibiting the decomposition of HA while promoting the in-situ conversion of TiB_2. The results showed that the composites obtained by the novel two-step mixing method had better mechanical properties and higher HA crystallinity, demonstrating their broad application prospects.

Experimental

Materials

Spherical Ti6Al4V powders (99.5% purity, ~ 17 μm) (Hebei Fengye Metal Materials Co. Ltd.) and acicular HA powders (99.5% purity, diameter: ~ 20 nm, length: ~ 100 nm) (Shanghai Hualan Chemical Technology Co. Ltd.), and TiB_2 powders (99.9%, ~ 202 nm) (Hebei Zhuotai New Materials Technology Co. Ltd.) were used as the main raw materials for production of the composites.

Methods

For comparison, 90 wt% Ti6Al4V, 5 wt% HA and 5 wt% TiB_2 powders with the addition of 3 wt% of stearic acid as binder were mixed by using different methods including the traditional one-step ball milling method and two-step mixing methods, including two-step ball milling method and ball milling-resonant acoustic mixing method. As shown in Fig. 1a, in the control group, the traditional one-step ball milling method was used. The powders and stainless-steel balls of 10 times the weight of the mixed powders were loaded into a ball milling jar for milling under argon atmosphere at 200 r/min for 12 h. In the experimental group, two-step mixing methods (Fig. 1b) were used. Ti6Al4V, TiB_2, stearic acid, and stainless-steel balls of 10 times the weight of the mixed powders were loaded into a ball milling jar for milling under argon atmosphere at 200 r/min for 12 h. The mixture was then supplemented with 5 wt% HA for ball milling for 20 min or transferred to a resonance acoustic mixer with accelerated rate at 50 g for 20 min.

The mixed powders were pressed into cylindrical briquettes with a diameter of 8 mm and a height of 10 mm using a hydraulic press with axial pressure of 900 MPa and dwell time of 45 s. The briquettes were then loaded in a conventional tube furnace with argon atmosphere and heated up to 380 °C at a ramp rate of 1.5 °C/min. They were then kept at 380 °C for 2 h to complete the debinding process. Finally, they were heated up to 1050 °C at a rate of 5 °C/min and kept for 30 min in a microwave tube furnace (frequency of 2.45 GHz, maximum power of 1.4 kW, Hunan Change Microwave Technology Co. Ltd., China) in argon atmosphere for preparing the composites.

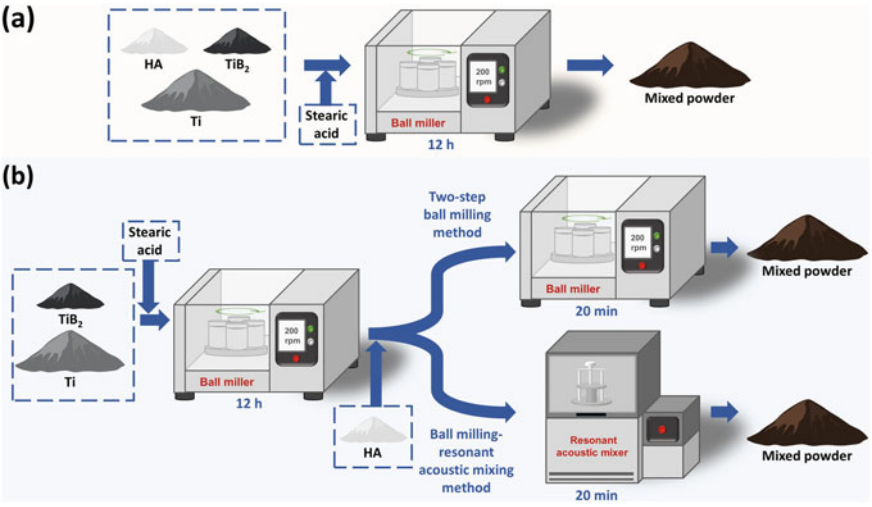

Fig. 1 Schematic illustration of the **a** traditional one-step ball milling method and **b** two-step mixing methods

Characterizations

The phase compositions of boronized Ti6Al4V/HA composites were examined using an X-ray diffraction spectrometer (XRD, Ultima IV). The microstructures and phase distributions of the mixed powders and boronized Ti6Al4V/HA composites were characterized using a field-emission scanning electron microscope (FESEM, Mira 3 LMH) equipped with an energy dispersive spectrometer (EDS, X-max 20). The bulk densities and porosities of the composites were determined according to the Archimedes' principle. The compressive stress–strain curves of the composites were examined using a universal mechanical testing machine according to the Chinese National Standard Test Method GB/T 7314-2005, from which the compressive strength and compressive moduli were calculated [8, 12]. The Vickers microhardness was measured using a Vickers hardness tester at a load of 10 N for 10 s.

Results and Discussion

Figure 2a shows the SEM images of the powders after traditional ball milling. Most of the Ti6Al4V particles were spherical and a part of the finer TiB_2 and HA powders were adhered on their surfaces. Figure 2b, c shows the SEM images of the powders obtained after mixing using the two-step ball milling method and ball milling-resonant acoustic mixing method, respectively. The results showed that their sphericity became worse. It indicated that the first step of the ball milling process of the two-step mixing methods played a different role from the traditional one-step ball milling method due to the absence of HA. It was attributed to the fact that the HA powders acted as a buffer between the Ti6Al4V and TiB_2 particles during ball milling, which inhibited the occurrence of deformation and fragmentation [9, 10].

The XRD patterns of the boronized Ti6Al4V/HA composites are shown in Fig. 3. The main phase of all the samples was α-Ti with a small amount of β-Ti. The presence of TiO in the samples was caused by oxidation reaction of titanium induced by the interstitial O atoms in the matrix and trace oxygen contained in the argon. Compared with the traditional one-step ball milling method, stronger diffraction peaks of HA

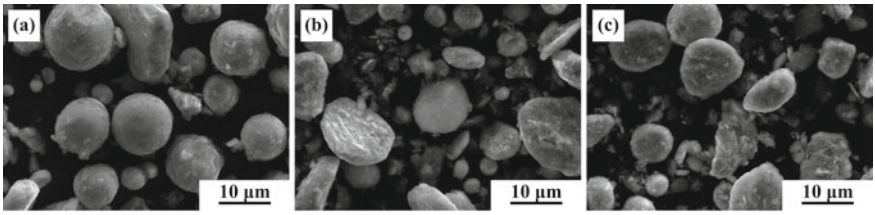

Fig. 2 SEM images of **a** traditional one-step ball-milled powders, **b** two-step ball-milled powders, and **c** ball milling-resonant acoustic mixed powders

were observed in the samples produced by two-step mixing methods. It indicated that two-step mixing methods enhanced the crystallinity of HA in the composites. This was because HA was involved in ball milling for a reduced period of time, which avoided serious decomposition of HA during the subsequent sintering process [13]. The absence of diffraction peaks of TiB_2 in all the samples demonstrated its good conversion to TiB. The diffraction peak intensity of TiB was higher in the samples produced by two-step mixing methods. Besides, the diffraction peaks of Ti_3B_4 were also observed attributed to the mutual extrusion of the powders in the first step of the ball milling process of the two-step mixing methods which improved the reactivity of Ti6Al4V and TiB_2. In addition, the samples produced by the two-step mixing methods had stronger Fe_2Ti_4O diffraction peaks, in which Fe was introduced owing to the wear of stainless-steel balls caused by the high-hardness TiB_2 during ball milling in the absence of HA buffer.

The SEM images of the boronized Ti6Al4V/HA composites are shown in Fig. 4. In general, Fe is a strong stabilizer of the β-Ti phase and can easily enter into the interstitial position of the body-centered cubic lattice, resulting in the distribution of Fe elements at locations where the β-Ti phase exists [14, 15]. In the composites prepared by the traditional one-step ball milling method, Fe was the main impurity in the Ti6Al4V particles, in which the stripe-like β-Ti phase was present. As mentioned earlier, Fe was introduced in the first step of the two-step mixing methods and solidly dissolved on the surface of the Ti6Al4V particles, so the β-Ti phase tended to be distributed at the edges of the particles. In addition, some of large or agglomerated TiB_2 particles in the samples prepared by the traditional one-step ball milling method underwent in situ reaction only at edges (Fig. 4a) with weak

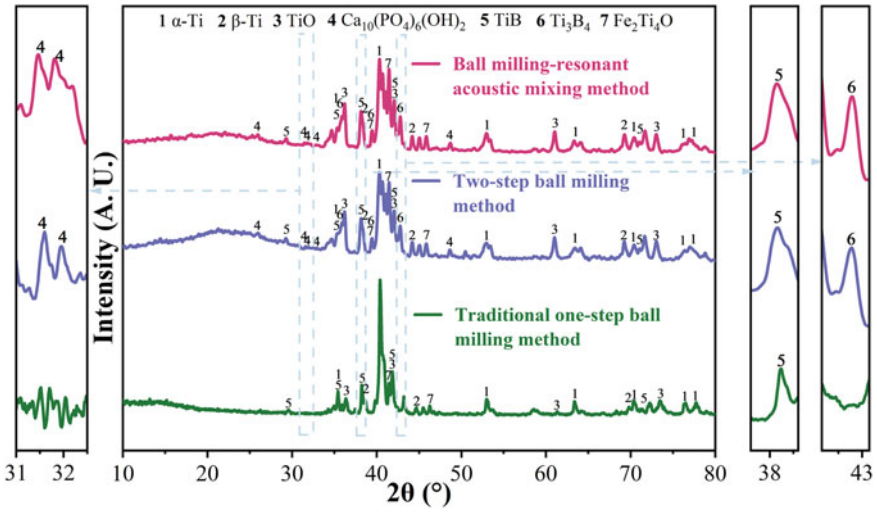

Fig. 3 XRD patterns of the composites prepared by mixing using different methods followed by sintering

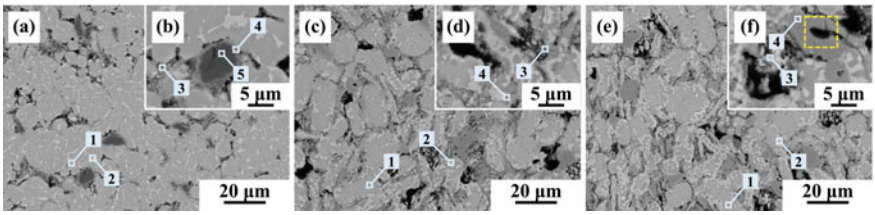

Fig. 4 SEM images of the boronized Ti6Al4V/HA composites using **a**, **b** the traditional one-step ball milling method, **c**, **d** the two-step ball milling method, **e**, **f** the ball milling-resonant acoustic mixing method, showing the phases identified by corresponding EDS spectra which were not provided for the sake of brevity, 1: α-Ti, 2: β-Ti, 3: HA, 4: TiB and Ti_3B_4, and 5: TiB_2

diffraction peaks of TiB according to the XRD results. Conversely, almost all of the TiB_2 particles underwent in situ transformation inside the samples prepared by the two-step mixing methods, leading to stronger diffraction peaks of TiB. Notably, as shown in Fig. 4f, a hole appeared in the center of the TiB_2 particles after the in-situ reaction. It confirmed that the interior TiB_2 particles were continuously consumed with the in-situ transformation during the microwave sintering. Therefore, there were different reactions.

Initially, the surface of TiB_2 particles reacted with Ti:

$$Ti + TiB_2 \rightarrow 2TiB \tag{1}$$

Then, the interior of TiB_2 particles reacted with the newly generated TiB in the surface to complete the in-situ transformation:

$$2TiB + TiB_2 \rightarrow Ti_3B_4 \tag{2}$$

No cracks due to non-uniform HA distribution or HA decomposition were observed in any of the composites, which would contribute to better mechanical properties [16]. There were many pores of several micrometers inside the samples produced by the two-step ball milling method (Fig. 4c), which were caused by the loss of undispersed HA particles when the samples were polished. There were less pores in the samples produced by the ball milling-resonant acoustic mixing method (Fig. 4e) which indicated that this method was more efficient in deagglomerating and mixing HA into the powders.

Figure 5 shows the effect of mixing method on the bulk density and porosity of the composite. Consistent with the SEM observations, the two-step mixing methods failed to completely deagglomerate HA due to its shorter mixing time, which restrained the densification of the composites, thus they had higher porosity than those produced by the traditional one-step ball milling mixing method. In particular, the ball milling-resonant acoustic mixing method showed a slightly lower porosity and a slightly higher density than the two-step ball milling method, which also proved

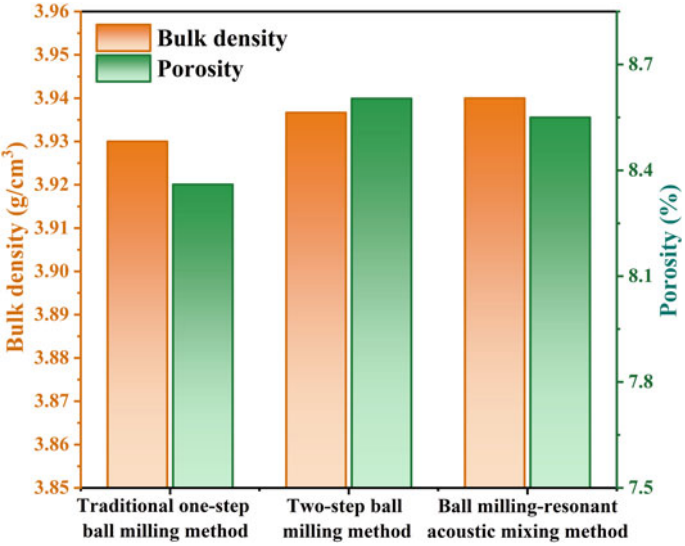

Fig. 5 Bulk densities and porosities of boronized Ti6Al4V/HA composites prepared by mixing using different methods followed by sintering

that the resonant acoustic mixing method possessed a higher mixing efficiency. Interestingly, the composites produced by the traditional one-step ball milling method had the lowest porosity and density, probably due to the different chemical compositions of the products.

Figure 6 shows the effect of mixing method on the compressive strength, compressive modulus, and Vickers microhardness of the composite. The Vickers microhardness of the composites produced by the two-step mixing methods was lower than that of the traditional one-step ball milling method, which was due to a greater degree of in-situ transformation of the harder TiB_2 phase. Among them, all these three parameters were higher for the composite produced by the ball milling-resonant acoustic mixing method compared with the two-step ball milling method, with compressive strength of 331.6 MPa, compressive modulus of 8.69 GPa, and Vickers microhardness of 286.0 HV, which were significantly better than those of the similar materials reported in previous studies [8, 17].

Conclusions

The boronized Ti6Al4V/HA composites with excellent mechanical properties were prepared by mixing Ti6Al4V, HA, and TiB_2 powders using two-step mixing methods followed by microwave sintering at 1050 °C for 30 min. The addition of HA before the second mixing step could promote the transformation of TiB_2 to TiB and Ti_3B_4

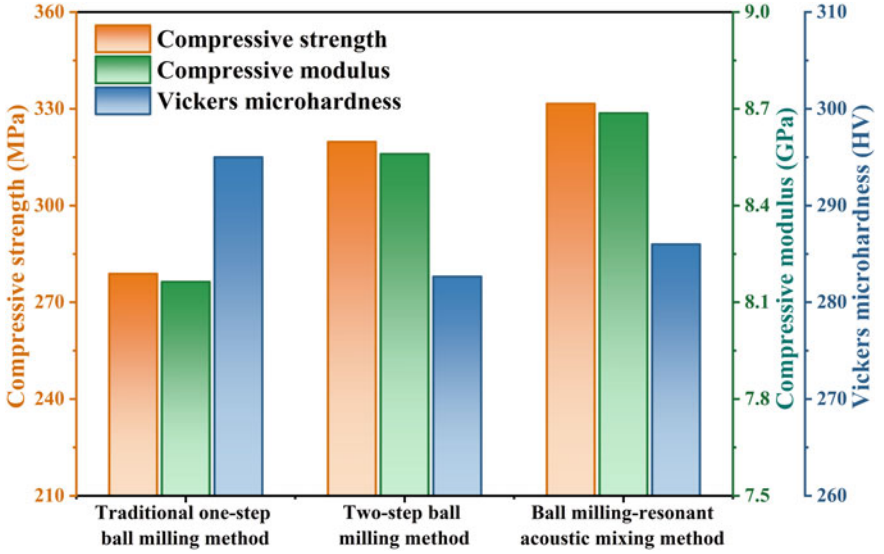

Fig. 6 Compressive strength, compressive moduli, and Vickers microhardness of boronized Ti6Al4V/HA composites prepared by mixing using different methods followed by sintering

in the subsequent sintering process and reduce the decomposition of HA. The results showed that due to the advantages of efficient mixing by resonance acoustic mixing, the boronized Ti6Al4V/HA composite prepared by the ball milling-resonant acoustic mixing method had the best mechanical performance, with compressive strength of 331.6 MPa, compressive modulus of 8.69 GPa, and Vickers microhardness of 286.0 HV, which were significantly better than those of the similar materials. The findings proved the good prospect of the new mixing method for clinical applications.

Acknowledgements The work was partially sponsored by the National Natural Science Foundation of China under Grant 82201113, the Hunan Provincial Natural Science Foundation of China under Grants 2023JJ20088 and 2021JJ40905, the Science and Technology Innovation Program of Hunan Province under Grant 2023RC3089, and the Graduate Student Research Innovation Program of Hunan Province under Grant CX20230209.

References

1. Huo WT, Zhao LZ, Zhang W, Lu JW, Zhao YQ, Zhang YS (2018) In vitro corrosion behavior and biocompatibility of nanostructured Ti6Al4V. Mater Sci Eng C Mater Biol Appl 92:268–279
2. Avila JD, Stenberg K, Bose S, Bandyopadhyay A (2021) Hydroxyapatite reinforced Ti6Al4V composites for load-bearing implants. Acta Biomater 123:379–392
3. Naghavi SA, Lin CR, Sun CN, Tamaddon M, Basiouny M, Garcia-Souto P, Taylor S, Hua J, Li DC, Wang L, Liu CZ (2022) Stress shielding and bone resorption of press-fit polyether-ether-ketone (PEEK) hip prosthesis: a sawbone model study. Polymers 14(21):4600

4. Szcześ A, Hołysz L, Chibowski E (2017) Synthesis of hydroxyapatite for biomedical applications. Adv Colloid Interface 249:321–330
5. Mahmud NN, Sulong A, Sharma B, Ameyama K (2021) Presintered titanium-hydroxyapatite composite fabricated via PIM route. Metals 11(2):318
6. Wei M, Ruys AJ, Swain MV, Milthorpe BK, Sorrell CC (2005) Hydroxyapatite-coated metals: interfacial reactions during sintering. J Mater Sci Mater Med 16(2):101–106
7. Peng Q, Tang ZG, Wang YH, Peng ZW (2019) Mechanical performance and in-vitro biological behaviors of boronized Ti6Al4V/HA composites synthesized by microwave sintering. Ceram Int 45(18):24684–24690
8. Peng Q, Bin X, Xuxing HY, Wang YH, Peng ZW, Tang ZG (2020) Facile fabrication of boronized Ti6Al4V/HA composites for load-bearing applications. J Alloy Compd 825:153102
9. Zhuman B, Saepurahman ASF, Hashaikeh R (2019) Obtaining high crystalline ball milled H-Y zeolite particles with carbon nanostructures as a damping material. Microporous Mesoporous Mater 273:19–25
10. Nassrullah H, Anis SF, Lalia BS, Hashaikeh R (2022) Cellulose nanofibrils as a damping material for the production of highly crystalline nanosized zeolite Y via ball milling. Materials 15(6):2258
11. Wan C, Guo ZQ, Zhang WZ, Chen SH, Qin Z, Xu KZ (2023) A new ternary high-energy composite based on nano titanium powder with low sensitivity and stable combustion. Combust Flame 247:112480
12. Sun WB, Ma YE, Zhang WH, Qian XD, Huang W, Wang ZH (2021) Effects of the build direction on mechanical performance of laser powder bed fusion additively manufactured Ti6Al4V under different loadings. Adv Eng Mater 23(12):2100611
13. Shao HL, Cao L, Sun DQ, Zhao ZK (2016) Low temperature spark plasma sintering of TC4/HA composites. Prog Nat Sci 26(2):192–196
14. Min J, Guo YH, Niu JZ, Cao JX, Sun ZG, Chang H (2021) The characteristic of Fe as a β-Ti stabilizer in Ti alloys. Materials 14(24):7516
15. Liu SY, Shin YC (2019) Additive manufacturing of Ti6Al4V alloy: a review. Mater Des 164:107552
16. Ou SF, Chiou SY, Ou KL (2013) Phase transformation on hydroxyapatite decomposition. Ceram Int 39(4):3809–3816
17. Peng Q, Bin X, Pan H, Wang YH, Peng ZW, Tang ZG (2020) Fabrication of boronized Ti6Al4V/HA composites by microwave sintering in mixed gases. ACS Omega 5(20):11629–11636

Mechanical Properties and EMI-Shielding Efficiencies of Graphite and Iron(II) Oxide-Filled Polypropylene and Polyethylene-Based Polymer Composites

Hülya Kaftelen-Odabaşı, Elshod Khakberdiev, Akın Odabaşı, and Selçuk Helhel

Abstract In this study, polypropylene (PP), polyethylene (PE), PP/PE blends containing graphite (1–3 wt.%) and FeO (10–30 wt.%) fillers were prepared using a melt mixing method. The effects of graphite and iron oxide amount on the mechanical properties and electromagnetic interference (EMI) shielding efficiency in the frequency range of 8–12 GHz (X-band) were investigated. The tensile strength value of the PP/graphite/FeO (1:10) sample increased from 26.09 to 32.47 MPa with the increase of the graphite/FeO amount to 3:30 in wt.%. Maximum total shielding efficiencies of SE_T ~ 39.35 dB and 38.31 dB could be observed respectively with a corresponding frequency value of 12.2 GHz for PE and PP polymer mixture filled with 3 wt.% graphite and 30 wt.% FeO with a thickness of 4 mm. The results obtained from the EMI shielding measurements showed that the total EMI SE increased synergistically with increasing FeO/graphite hybrid filler amount for each polymer composition.

Keywords Polymer blends · Polymer composites · Shielding efficiency · Mechanical properties

H. Kaftelen-Odabaşı (✉)
Department of Aircraft Maintenance and Repair, School of Civil Aviation, Fırat University, 23119 Elazığ, Turkey
e-mail: hkodabasi@firat.edu.tr

E. Khakberdiev
Institute of Polymer Chemistry and Physics, Uzbekistan Academy of Sciences, 7 B, Str A. Kadyri, Tashkent, Uzbekistan 100128

A. Odabaşı
Engineering Faculty, Department of Metallurgical and Materials Engineering, Fırat University, 23119 Elazığ, Turkey

S. Helhel
Engineering Faculty, Department of Electrical and Electronics Engineering, Akdeniz University, 07058 Antalya, Turkey

Z. Peng et al. (eds.), *Characterization of Minerals, Metals, and Materials 2024*, The Minerals, Metals & Materials Series, https://doi.org/10.1007/978-3-031-50304-7_24

Introduction

With the increasing usage of high-technology electronic and communication systems, studies to attenuate the harmful effects of electromagnetic interference are continuously increasing. In the material class developed to prevent electromagnetic wave interference by absorbing and transmitting EM waves, the investigation of polymer composites containing dielectric, magnetic, and conductive fillers has become increasingly important. The distinctive properties of polymer nanocomposites, such as high conductivity at low filler loads, low density (1–1.8 g/cm^3), structural flexibility, corrosion resistance, and ease of processing, compared to conventional metals, make them an accessible material for EMI shielding application [1]. The shielding efficiency of the polymer-based composites is affected by different parameters including (a) type, shape, amount, and distribution of the fillers, (b) electrical conductivity, dielectric and magnetic properties of the filler, (c) structure of the composites (3D, porous or multilayered, etc.), (d) immiscibility of polymer blends. For instance, combinations of metallic or metal oxide and carbon-based fillers in the CPC lead to synergy effects, which in turn higher EMI shielding efficiency than by using one type of filler [2]. Most of the prepared CPCs generally contain polyamide, polystyrene, polylactic acid, polycaprolactone, polycarbonate, polyurethane polymers [3]. Here, PP/PE blends were selected due to their wide range of use in polymeric materials, their cost advantages and unique properties such as chemical resistance and mechanical properties [4]. Moreover, blending PP with PE is important in terms of increasing its flexibility [5]. As far as we know, the research on EMI-shielding properties of PP/PE polymer composite blends is very rarely studied in the literature. Al-Saleh [6] investigated the EMI shielding properties of GNP:CNT filled 90/10 and 50/50 PP/PE composites and they found the highest EMI shielding value of approximately 26 dB for 90/10 PP/PE composite containing the 0:5 ratio of GNP:CNT hybrid filler. Tu et al. [7] examined PP/PE blends filled with 1.25 vol.% of graphene and investigated the effect of graphene localization on the electrical, mechanical, and rheological properties, but not EMI shielding properties. They found that [7] the selective localization of graphene sheets in the PE phase and the volume-exclusion effect of PP in the composite produces a networked structure at a lower graphene content, which significantly reduces the percolation threshold of composite. However, the combined effects of graphite/iron(II) oxide fillers on binary PP/PE polymer composites have yet to be investigated.

In this study, PE and PP were chosen as binary polymer matrices because of their immiscibility, which is expected to increase the shielding efficiency of the composites and cost advantages. For this purpose, we prepared graphite (Gr)/iron(II) oxide filled PP/PE (50/50) composites using an environmentally friendly and inexpensive processing method, i.e., melt compounding method. The influence of graphite and iron oxide amounts on the EMI shielding and mechanical properties of 50/50 (in wt.%) polypropylene and polyethylene (PP/PE) blends were investigated. In addition, the same amounts of graphite and iron oxide filled PP and PE were prepared in

order to understand the immiscibility effect on the EMI shielding properties as well as the mechanical properties.

Experimental Details

All composite blends are prepared by melt mixing using a batch mixer (Plastograph, Brabender, Germany). Prior mixing, Polypropylene ($\rho = 0.85$–0.95 g/cm^3) and linear low-density polyethylene (LLDPE, $\rho = 0.920$ g/cm^3), iron(II) oxide (> 99.5% purity, < 80 μm) and graphite powders (> 99.0% purity, < 80 μm) were dried under vacuum oven at 70 °C for 24 h. The melt mixing was conducted by a twin-screw laboratory plastograph at a rotation speed of 100 rpm and 180 °C for 10 min. Before graphite and iron(II) oxide powders were fed into the mixer, the polymers were melt-mixed for 3 min. Table 1 gives the prepared PE/PP blend compositions containing different amounts of graphite (1–3 wt.%) and iron(II) oxide (10–30 wt.%).

Tensile test of composite materials was carried out to determine the ultimate tensile strength using Schimadzu AG-X plus (Japan) tensile test instrument with a load cell of 10 kN in accordance with ASTM D638 standard. Each sample was measured three times at least to ensure the accuracy of the experiment. The EMI shielding effectiveness of the composites was measured according to the ASTM D4935-00 standards for planar materials with a dimension of 10 mm × 22 mm × 3 mm. The EMI shielding effectiveness (SE) in the frequency range of 8–12 GHz (X-band region) has been performed using a vector network analyzer (Agilent E4405B-ESA-E series) connected to a rectangular waveguide.

Table 1 Compositions of composite blends (in wt.%)

Sample code	PP	PE	Graphite (Gr)	FeO
PE(1:10)	0	100	1	10
PE(2:20)	0	100	2	20
PE(3:30)	0	100	3	30
PP(1:10)	100	0	1	10
PP(2:20)	100	0	2	20
PP(3:30)	100	0	3	30
PP/PE(1:10)	50	50	1	10
PP/PE(2:20)	50	50	2	20
PP/PE(3:30)	50	50	3	30

Results and Discussion

Shielding Properties of Composites

The EMI shielding performance of the PE, PP, and PP/PE:50/50 polymer matrix composites was investigated in the frequency range of 8.2–12.4 GHz (X-band). The total shielding efficiency (SE_T) of the PP and PE matrix composites as a function of Gr/FeO amounts are given in Fig. 1a, b, respectively. EMI SE_T showed stable fluctuations for each composition until at 10.5 GHz frequency value, and beyond this value, EMI SE_T increased with the increase of graphite/FeO amount. The irregular change of EMI SE_T in PP/PE:50/50 across the X-band indicates that the total shielding efficiencies of the composites are affected by filler amounts (Fig. 1c).

The maximum EMI SE_T achieved by Gr/FeO (3:30) fillers was 39.35 dB and 38.31 dB in PE and PP composites, respectively, at 12.2 GHz. Unlike Fig. 1a, b, EMI SE for PP/PE polymer blend composites nonlinearly changes against the frequency, this means that the shielding effectiveness fluctuates with frequency of the incident wave. This may be due to the disordered structure of conductive network that is

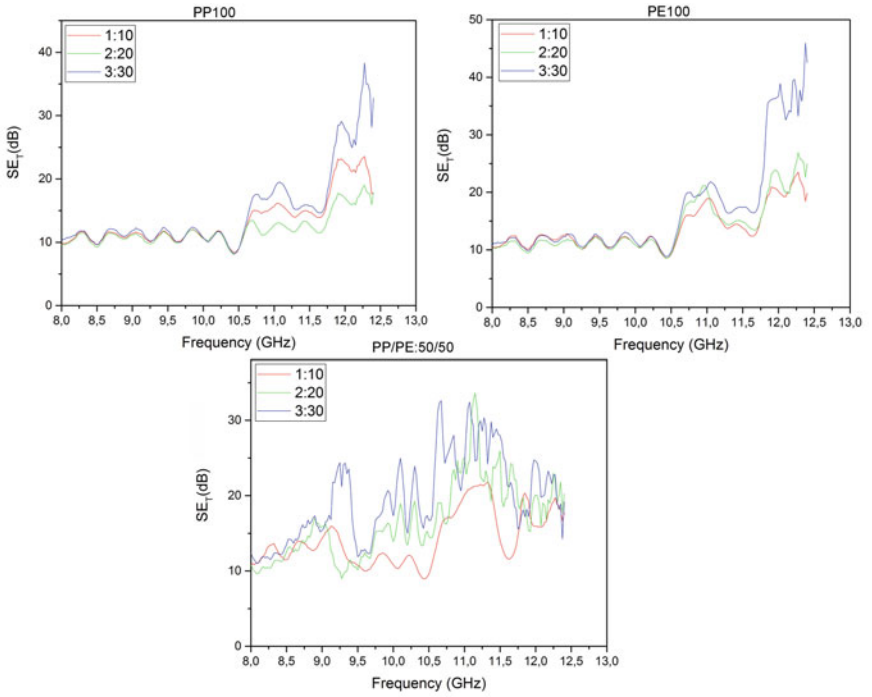

Fig. 1 Effect of graphite/FeO filler on the EMI SE_T of PP, PE, and PP/PE:50/50 polymer blend composites

formed in the matrix polymer blends. Similar fluctuations in EMI versus frequency graph were reported for carbon black-filled EVA/NBR:75/25 polymer blends [8].

Maximum EMI SE_T retained an almost similar value of about 33 dB for PP/PE:50/50 composite filled with (3:30) and (2:20) at 11 GHz (Fig. 1c). The results obtained from Fig. 1 showed that the total EMI SE increased synergistically with FeO/graphite hybrid filler loading at all frequencies over the frequency band of measurements for each polymer composition.

Tensile Properties

Tensile tests were employed to determine the mechanical properties including the elastic modulus, elongation at break, and tensile strength of the graphite FeO-reinforced polymer composites. The elastic modulus and tensile strength of the composite samples are given in Table 2. Note that the values given in this table represent the mean values with a standard deviation from measurements of at least three samples for each composite.

Based on the average values, it is clear that PP composites with graphite/FeO fillers show higher tensile strength values in the range of 26.09–32.89 MPa compared with the PE and PP/PE:50/50 matrix composites. As can be seen from Table 2, tensile strength of PE and PP/PE:50/50 matrix composites was not significantly dependent on the amount of filler, an improvement of about 20% was achieved by increasing the graphite/FeO weight percentages from 1:10 to 2:20 in PP matrix composites and reach the maximum value of 32.89 MPa. Dispersion and filler-matrix interaction are most likely responsible for the high strength [9] in the PP matrix composites while the moderate tensile values obtained for PP/PE:50/50 polymer matrix composites are likely caused by the lower miscibility between PE and PP polymers [6]. The standard deviations between PP(2:20) and PP(3:30) composites overlap, thus almost

Table 2 Tensile properties of composites

Sample code	Elastic modulus (MPa)	Tensile strength (MPa)
PE100	106.48 ± 12	19.75 ± 1.79
PP100	531.07 ± 42.97	44.44 ± 0.45
PE(1:10)	158.02 ± 10.95	18.34 ± 1.65
PE(2:20)	178.86 ± 14.11	17.72 ± 0.93
PE(3:30)	197.92 ± 9.07	16.96 ± 3.22
PP(1:10)	442.86 ± 33.57	26.09 ± 0.51
PP(2:20)	436.53 ± 46.67	32.89 ± 1.49
PP(3:30)	488.61 ± 83.50	32.47 ± 1.01
PP/PE(1:10)	354.41 ± 21.94	29.47 ± 1.29
PP/PE(2:20)	345.71 ± 27.66	27.92 ± 1.64
PP/PE(3:30)	388.78 ± 6.74	26.15 ± 2.11

remain the same level. Table 2 also lists the elastic modulus results taken from the composites. It is obvious from this table that PP matrix composites exhibit higher stiffness than PP/PE polymer blend ones, while the lowest stiffness is obtained for PE matrix composites. The blending of PE with PP polymers increased the elastic moduli values changing from the range of 158–197 to 354–388 MPa depending on the amount of the fillers. The elastic modulus reached a maximum value 488.6 MPa at 3:30 Gr/FeO/PP composites.

The incorporation of fillers, namely graphite and iron oxide, into both polypropylene (PP) and polyethylene (PE) had a significant impact on the mechanical properties of the resulting composites [10–14]. Figure 2 shows the stress–strain response of PP, PE, and PP/PE composites containing different weight percentages of graphite (Gr) and iron(II) oxide (FeO). Notably, there were distinct changes in mechanical strength (σ) as the filler content was varied in PP composites. Specifically, an increasing trend was observed in mechanical strength up to 3:30 Gr/FeO as the filler content increased. However, it is seen from stress–strain curve of PP/PE:50/50 composites that all filler amounts in PP/PE:50/50 have almost similar yield points in the range of 26–28 MPa. Unlike PP-based composites, it is clearly seen that the tensile strength in PP/PE:50/50 polymer blend composites was slightly reduced from 29.47 to 26.15 MPa with increasing the Gr/FeO fillers from (1:10) to (3:30).

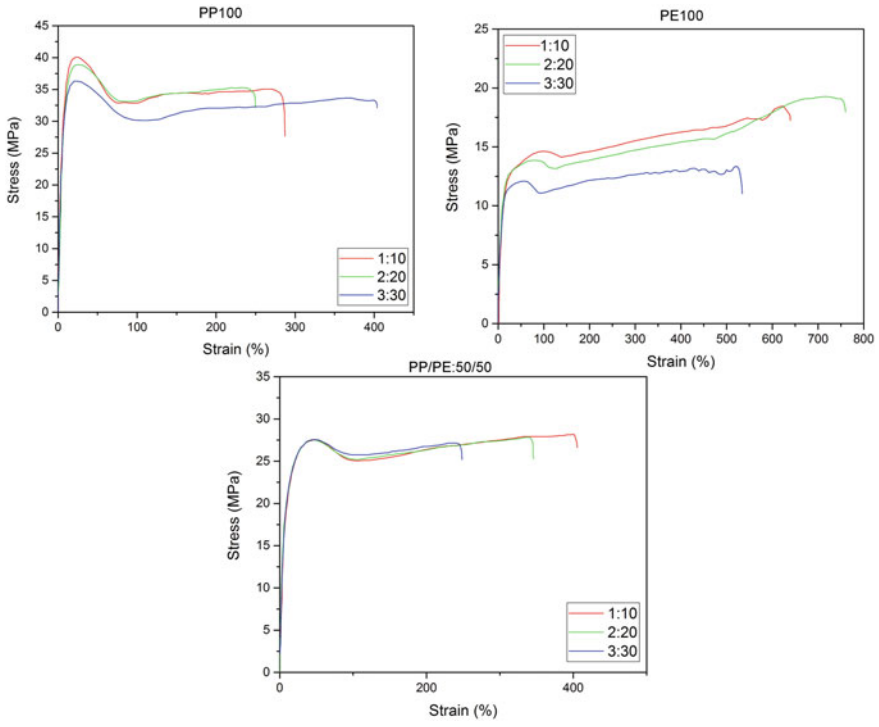

Fig. 2 Stress versus strain curves of polymer composites

In terms of the elongation (ε), contrasting trends were observed between the PP and PE-based composites (Fig. 2a, b). With the increase in the amount of Gr/FeO filler material, there was a noticeable increase in the relative elongation in PP-based composites, while a decrease was observed in PE-based composites. This divergence in behavior could potentially be attributed to the degradation of the crystal structure of PP or the nucleation effects induced by the fillers. Remarkably, PP/PE 50/50 samples appear to exceed that of pure PP, showing strain values in the range of 298–382%. This in turn affects the crystallization processes of the addition of PE to pure PP, leading to growth of crystallites and various other simultaneous processes. These multiple mechanisms collectively affect the flexibility of the final crystal structure as opposed to the α form, which may possibly require a transition to the β form [15].

Figure 3 represents the elongation at break (%) values of PE, PP, and PP/PE:50/50 blending polymer composites as a function of total amount of Gr/FeO fillers. For comparison, this graph also includes elongation at break values for the pure PP and PE without fillers. It appears from Table 2 and Fig. 3 that tensile properties of the PP, PE, and PP/PE composites with fillers show the opposite trend with elongation at break values. As expected, the elongation of PP was improved by adding the more ductile PE. The larger the content of PE, the higher is the strain at break compared to PP/Gr/FeO composites. As seen from Fig. 3, pure PE has a high elongation at break (707%) due to its low stiffness. Considering the standard deviations, no significant increase was observed with the addition of Gr/FeO (1:10) to pure PE without filler, while it slightly increased to 744% with the addition of Gr/FeO (2:20) and decreased to 595% with a further increase in filler amount.

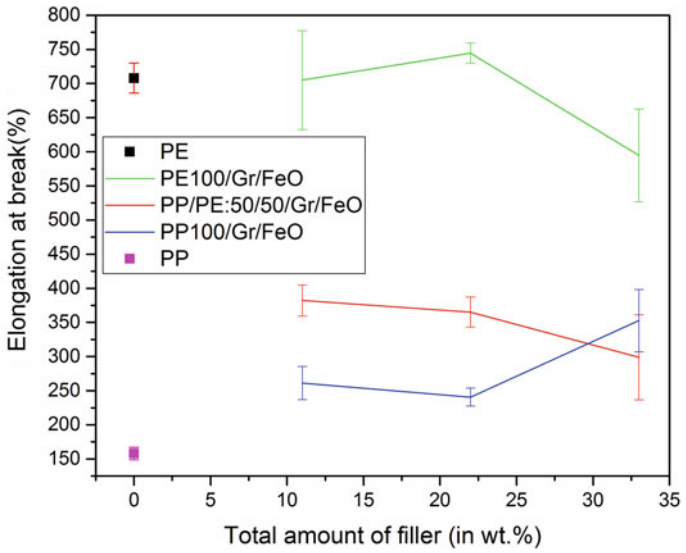

Fig. 3 Elongation at break as a function of total amount (in wt.%) of Gr/FeO fillers for PP, PE, and PP/PE:50/50 polymer composites

Conclusion

In this study, the effect of the graphite and Fe(II) oxide fillers with different amounts on the mechanical properties and EMI-shielding efficiencies of PP, PE, and 50/50 PP/PE polymer blends were investigated. PP composites with Gr/FeO (2:20) exhibit the highest tensile strength with a value of ~ 32.9 MPa compared with the PE and PP/PE:50/50 matrix composites. Blending PP with PE deteriorates the tensile strength values of composites and their strength values vary between 26.15 and 29.47 MPa depending on fillers. EMI shielding measurements obtained in the X-band region (8–12 GHz) indicated that total EMI SE increased synergistically with FeO/graphite hybrid filler loading at all frequencies over the frequency band of measurements for each polymer composition. In the EMI shielding versus frequency graph of PP/PE blending composites, the fluctuation of the PP/PE shielding efficiency values against the frequency of the incoming wave is most probably due to the irregular structure of the conductive network formed due to the matrix polymer blending effect.

References

1. Wu J, Chung DDL (2002) Increasing the electromagnetic interference shielding effectiveness of carbon fiber polymer–matrix composite by using activated carbon fibers. Carbon 40(3):445–447
2. Zhang H, Zhang G, Tang M, Zhou L, Li J, Fan X, Qin J (2018) Synergistic effect of carbon nanotube and graphene nanoplates on the mechanical, electrical and electromagnetic interference shielding properties of polymer composites and polymer composite foams. Chem Eng J 353:381–393
3. Anand J, Palaniappan S, Sathyanarayana DN (1998) Conducting polyaniline blends and composites. Prog Polym Sci 23(6):993–1018
4. Salih SE, Hamood AF, Alsabih AH (2013) Comparison of the characteristics of LDPE: PP and HDPE: PP polymer blends. Mod Appl Sci 7(3):33–42
5. Aumnate C, Rudolph N, Sarmadi M (2019) Recycling of polypropylene/polyethylene blends: effect of chain structure on the crystallization behaviors. Polymers 11(9):1456
6. Al-Saleh MH (2016) Electrical, EMI shielding and tensile properties of PP/PE blends filled with GNP: CNT hybrid nanofiller. Synth Met 217:322–330
7. Tu C, Nagata K, Yan S (2017) Influence of melt-mixing processing sequence on electrical conductivity of polyethylene/polypropylene blends filled with graphene. Polym Bull 74:1237–1252
8. Rahaman M, Chaki TK, Khastgir D (2011) Development of high performance EMI shielding material from EVA, NBR, and their blends: effect of carbon black structure. J Mater Sci 46:3989–3999
9. Bigg DM (1987) Mechanical properties of particulate filled polymers. Polym Compos 8(2):115–122
10. Tripathi SN, Rao GS, Mathur AB, Jasra R (2017) Polyolefin/graphene nanocomposites: a review. RSC Adv 7(38):23615–23632
11. Zaghloul MMY, Zaghloul MYM, Zaghloul MMY (2017) Experimental and modeling analysis of mechanical-electrical behaviors of polypropylene composites filled with graphite and MWCNT fillers. Polym Test 63:467–474
12. Osswald TA, Menges G (2012) Materials science of polymers for engineers. Carl Hanser Verlag GmbH & Co. KG
13. Ward Ian M, Sweeney J (2012) Mechanical properties of solid polymers. Wiley

14. Bartenev GM, Zuyev YS (2013) Strength and failure of visco-elastic materials. Elsevier
15. Bikiaris D (2010) Microstructure and properties of polypropylene/carbon nanotube nanocomposites. Materials 3(4):2884–2946

Phosphoric Acid Leaching of Ni–Co–Fe Powder Derived from Limonitic Laterite Ore

Jing Chen, Ding Xu, Zhongxiao Qin, Meishi Hu, Jun Luo, Guanghui Li, Tao Jiang, Xin Zhang, Zhiwei Peng, and Mingjun Rao

Abstract Efficient extraction of nickel and cobalt from laterite ores is essential for the rapid development of new energy vehicles (EVs). In this work, Ni–Co–Fe powder with nickel, cobalt, and iron grades of 11.98%, 1.18%, and 70.13%, respectively, was obtained from a limonitic laterite ore via rotary kiln reductive roasting followed by magnetic separation. The powdery alloy was readily dissolvable in the phosphoric acid solution at atmospheric pressure. From the leaching solution, amorphous $FePO_4 \cdot xH_2O$ was precipitated by adjusting pH, and the purified Ni–Co-rich solution could be used for Ni–Co sulfate.

Keywords Laterite ore · Solid-state reduction · Ni–Co–Fe powder · Phosphoric acid leaching · Iron phosphate

Introduction

Nickel and cobalt, as strategic metals, are indispensable parts in the development of the steel industry, and new energy industry [1–3]. Laterite ore is the principal source of nickel, accounting for 70% of global nickel land-based reserves and around 30% of overall cobalt reserves [4, 5]. With the increasing demand for nickel and cobalt resources in the new energy vehicles (EVs), efficient extraction and value-added usage of valuable components in laterite ore have become increasingly imperative [1, 6].

J. Chen · D. Xu · Z. Qin · M. Hu · J. Luo · G. Li · T. Jiang · X. Zhang · Z. Peng · M. Rao (✉)
School of Minerals Processing and Bioengineering, Central South University, Changsha 410083, Hunan, China
e-mail: mj.rao@csu.edu.cn

Z. Peng et al. (eds.), *Characterization of Minerals, Metals, and Materials 2024*, The Minerals, Metals & Materials Series, https://doi.org/10.1007/978-3-031-50304-7_25

Lateritic ores are classified into two types based on the distribution of ore layers: saprolitic ore (magnesium-rich, silicon-rich, and high-nickel-grade) and limonitic ore (iron-rich and low-nickel-grade). The limonitic ore, which accounts for 67% of the total, is a nickel and cobalt co-associated deposit as well as a high-quality iron ore resource. The high-pressure sulfuric acid leaching (HPAL) technique is now the most widely used method for processing limonitic laterite ore. Nickel and cobalt are leached into solution at an efficiency of over 95% during the leaching process [7]. Additionally, iron ions are initially dissolved, followed by a quick hydrolysis reaction, resulting in the generation of hematite in the residue, enabling the selective leaching of nickel and cobalt. However, the leaching process should be conducted under high pressures and temperatures (230–260 °C, 4–5 MPa) to achieve a high leaching efficiency, leading to higher equipment requirements and more considerable investment [8]. Moreover, the high-pressure acid-leaching residue is hard to dispose of [9].

In light of this, we have proposed using phosphoric acid leaching to extract nickel and value-added utilization of iron, efficiently utilizing iron resources by altering the iron precipitation to form iron phosphate [10, 11]. Moreover, we have also reported a technical route for the efficient enrichment Ni and Co by reduction roasting followed by magnetic separation and the enriched product was easy to leach under normal pressure with better leaching characteristics under atmospheric pressure [12, 13]. In this work, we prepared Ni–Co–Fe powder from limonite ore, as the feedstock for phosphoric acid atmospheric leaching, and then prepared iron phosphate from the solution. Ni^{2+} and Co^{2+} could be selectively extracted from the filtrate after iron precipitation.

Experimental

Materials

The limonite laterite ore sample was taken from Indonesia. Table 1 shows that the ore contains 42.53 wt.% of total iron Fe_{total}, 1.31 wt.% of Ni, 0.13 wt.% of Co, 3.44 wt.% Al_2O_3, 3.39 wt.% of Cr, 4.82 wt.% of MgO and 9.60 wt.% SiO_2. X-ray diffraction (XRD) results in Fig. 1 show that goethite, antigorite, lizardite, and quartz were the main phases. Sodium sulfate is an industrial-use sodium sulfate with a purity of 99 wt.%. Anthracite and semi-coke were used as a reducing agent, and their proximate analysis and ash composition are listed in Table 2. Anthracite (less than 3 mm) was used for briquetting and semi-coke (5–10 mm) was used for an additional reducing agent added directly to the rotary kiln.

Table 1 Chemical compositions of limonitic laterite (%)

Fe_{total}	Ni	Co	SiO_2	MgO	Al_2O_3	Cr_2O_3	MnO	CaO	S	LOI
42.53	1.31	0.13	9.60	4.82	3.44	3.39	1.10	0.75	0.20	13.02

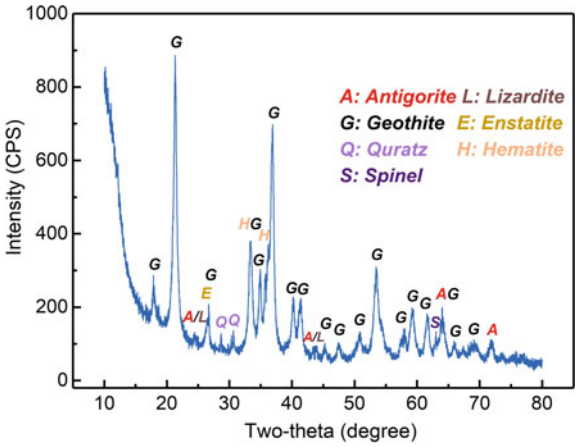

Fig. 1 XRD pattern of the limonitic laterite

Table 2 The proximate analysis and ash composition of anthracite and semi-coke (wt.%)

Samples	Proximate analysis				S	Ash composition				
	C_{ad}	V_{ad}	A_{ad}	M_{ad}		SiO_2	Al_2O_3	Fe_2O_3	CaO	MgO
Anthracite	83.80	5.23	11.19	1.19	0.36	52.48	24.06	9.45	1.43	1.31
Semi-coke	84.97	5.05	9.01	0.97	0.22	51.57	24.09	12.37	4.79	2.31

Methods

A rotary kiln with a diameter of 1.0 m and a length of 0.55 m was used for the reductive roasting trials. Briquetted laterite ore with sodium sulfate and fine anthracite using a briquetting machine at a pressure of 20 MPa. Initial experiments with reductive roasting in the muffle furnace have shown that the proper amounts of sodium sulfate and anthracite were 8–12 wt.% and 3–5 wt.%, respectively. Hence, sodium sulfate and reductive coal were fixed at 10 and 4 wt.% for the following tests. After heating the rotary kiln to the goal temperature, 15 kg of dry briquettes were added and heated for 25 ~ 30 min to the target temperature. To maintain the reductive atmosphere, semi-coke was occasionally injected to the kiln as an extra reducing agent during heating. After roasting, the roasted sample was discharged from the kiln and covered by coal to prevent reoxidation. The photographs of the rotary kiln, green briquettes, and roasted briquettes are depicted in Fig. 2. After cooling, the roasted ore was subjected to wet-grinding for 30 min with a pulp concentration of 1 g/mL. The magnetic separation

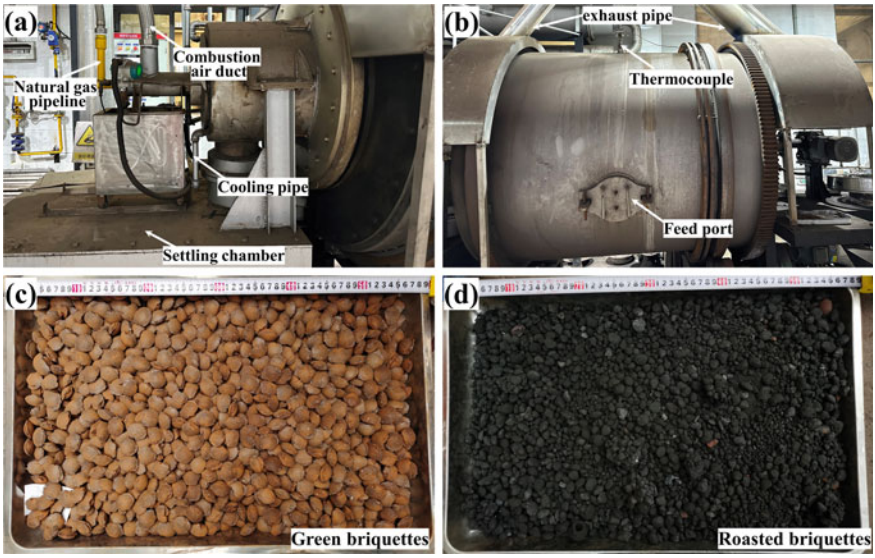

Fig. 2 Photographs of the rotary kiln (**a**, **b**), green briquettes (**c**), and roasted briquettes (**d**)

was conducted using a drum-type magnetic separator (XCRS74-Φ400 × 300) with a magnetic field intensity of 0.1 T.

The magnetic concentrate was performed in a 250 mL three-necked flask to leaching. A thermostatic water bath heated the slurry with mechanical stirring. The concentrations of elements in the leach liquor were determined by inductively coupled plasma optical emission spectrometry (ICP-OES). The leaching efficiency was calculated by Eq. (1):

$$\chi(\%) = \frac{c \times V}{m_0 \times w} \times 100\% \tag{1}$$

where χ (%) is the leaching efficiency of elements; c (mg L^{-1}) and V (L) are the concentration and volume of leach liquor, respectively, m_0 (g) and w (wt.%/100) represent the mass and elements mass fraction of the Ni–Co–Fe powder.

Characterization

The contents of Fe, Al, Si, Na, Mg, Ca, and Cr in the solid sample were determined by chemical titration. The phase compositions of laterite ore and Ni–Co–Fe powder were analyzed by X-ray diffraction using a Cu Kα source with a scanning rate of 5°/min (XRD, Rigaku, Ultima IV, Japan). The particle size of Ni–Co–Fe powders was determined using a laser particle size analyzer (Malvern Mastersizer 3000). The

SEM-EDS analysis was carried out using a scanning electron microscope (SEM, TESCAN, MIRA4) with EDAX energy dispersive X-ray spectroscopy (EDS). The concentrations of target elements in the leach liquor were measured by ICP-OES (PerkinElmer Optima, 5300 DV).

Results and Discussion

Solid-State Carbothermic Reduction Followed by Magnetic Separation

Under the parameters of mass of semi-coke of 2.5 kg and air–fuel ratio of 8, the impact of reductive temperature on the separation indices was assessed. With higher reductive temperatures, Ni and Fe grades and recoveries improved, and the optimal temperature ranged from 1050 to 1100 °C (Fig. 3a, b).

The chemical composition of the Ni–Co–Fe powder that was obtained after roasting and magnetic separation is shown in Table 3. The enriched levels of Ni, Co, and Fe were 11.84%, 1.18%, and 70.13%, respectively. And the recoveries of nickel, cobalt, and iron were 92.26%, 91.95%, and 16.68%, respectively. As shown in Fig. 4a, the primary constituents of the Ni–Co–Fe powder are kamacite (Fe–Ni), wustite (FeO), troilite (FeS), and nepheline ($NaAlSiO_4$). The concentrate has a homogeneous particle size distribution with an average particle size (D_{50}) of 38.2 μm (Fig. 4b).

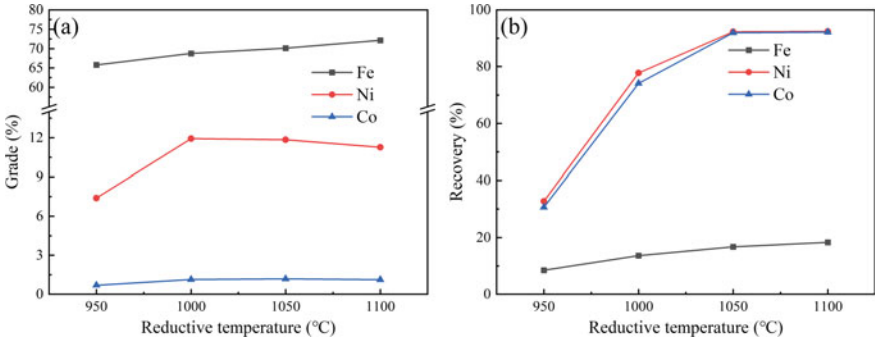

Fig. 3 Effects of the reductive temperature on the separation indices: **a** grade and **b** recovery

Table 3 Chemical composition of Ni–Co–Fe powder

Fe	Ni	Co	Al	Cr	Na	Mg	Si	Mn	S
70.13	11.84	1.18	0.47	0.49	0.35	0.94	1.71	0.62	1.63

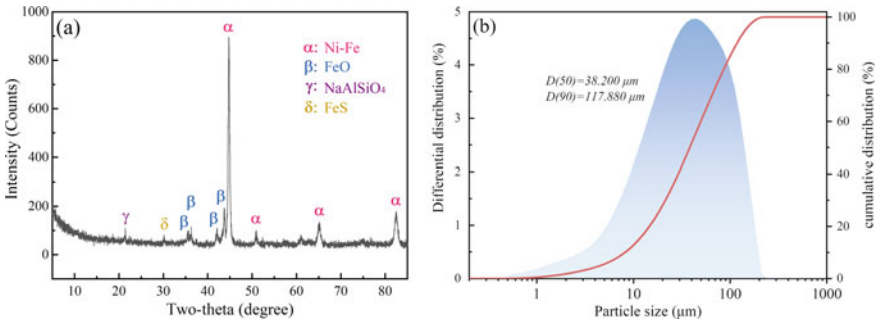

Fig. 4 XRD pattern (**a**) and particle size distribution (**b**) of the Ni–Co–Fe powder obtained by magnetic separation

Phosphoric Acid Leaching of Ni–Co–Fe Powder

Under the conditions of H_3PO_4 concentration of 3 mol/L, leaching time of 2 h and a liquid-to-solid ratio of 100 mL/g, the effects of leaching temperature on the extractions of varying metals were evaluated (Fig. 5a). The leaching efficiency of Fe, Ni, and Co all increased as the leaching temperature rose from 25 to 85 °C. At a leaching temperature of 85 °C, the extractions of Ni, Co, and Fe were 97.6%, 90.8%, and 92.3%, respectively. The decreased extraction of metals at 95 °C was due to the formation of iron hydrogen phosphate, as shown in Fig. 6. The initial acid concentration, liquid–solid ratio, and leaching time during the leaching process were also optimized, as shown in Fig. 5b–d. The extractions of Ni, Co, and Fe were 90.8%, 92.3%, and 97.6%, respectively, under the conditions of 4.5 mol/L H_3PO_4, 85 °C, 60 min, and *L*/*S* ratio of 12 mL/g.

Iron Precipitation of Leaching Solution for the Preparation of Iron Phosphorate

The initial precipitation pH_1 values of each elemental phosphate were calculated using the leachate fractions under optimal conditions (leaching temperature of 85 °C, H_3PO_4 concentration of 4.5 mol/L, leaching time of 120 min, liquid-to-solid ratio of 12 mL/g) based on the stepwise ionization properties of phosphoric acid and the precipitation product constants of each elemental phosphate, as shown in Table 4. The order in which each element initially precipitates out of the leaching solution is Fe > Al > Co > Ni > Mg > Cr > Mn. The liquid-phase co-precipitation for preparing $FePO_4$ precursor is generally controlled around 2, while the initial precipitation pH_1 of the other elements is greater than 2 [14]. Therefore, theoretically, by regulating the pH_1 of the precipitation endpoint, selective precipitation of iron can be accomplished.

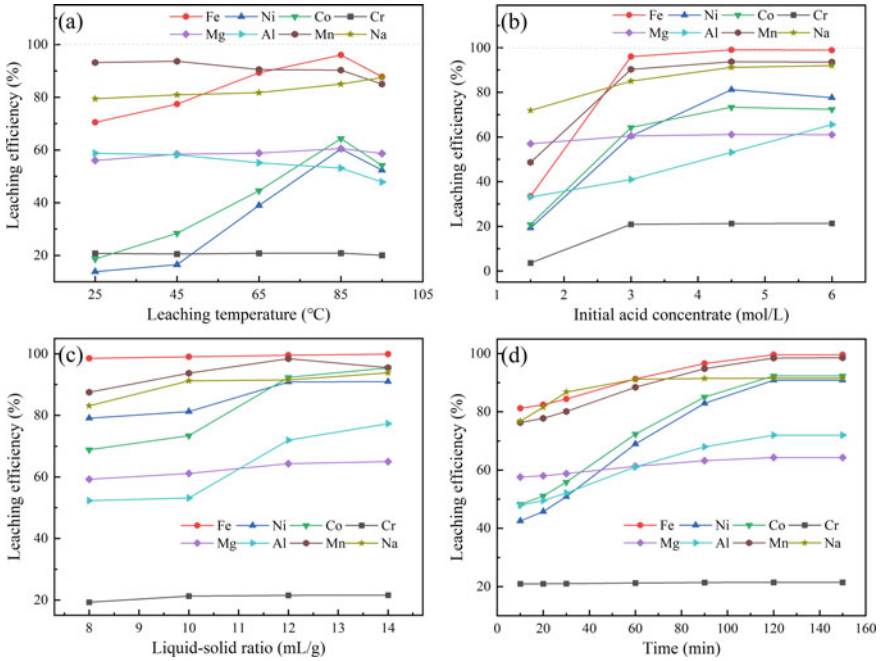

Fig. 5 Effects of leaching temperature (**a**), initial acid concentrate (**b**), liquid–solid ratio (**c**), and leaching temperature (**d**) on the leaching efficiency

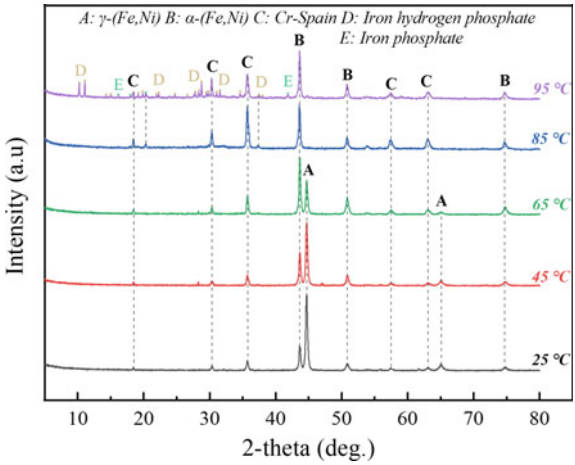

Fig. 6 XRD patterns of leaching residue at different temperatures

Table 4 Chemical composition of the leachate, solubility product (pK_{sp}), and theoretical initial precipitation pH_1

Ion	Fe^{3+}	Ni^{2+}	Co^{2+}	Al^{3+}	Mg^{2+}	Mn^{2+}	Cr^{3+}
Concentration ($g\ L^{-1}$)	5.820	0.896	0.091	0.036	0.050	0.051	0.0088
pK_{sp}	21.89	30.30	34.70	18.24	23.00	12.00	22.62
Initial precipitation pH_1	0.389	3.217	2.982	2.237	4.867	6.875	2.950

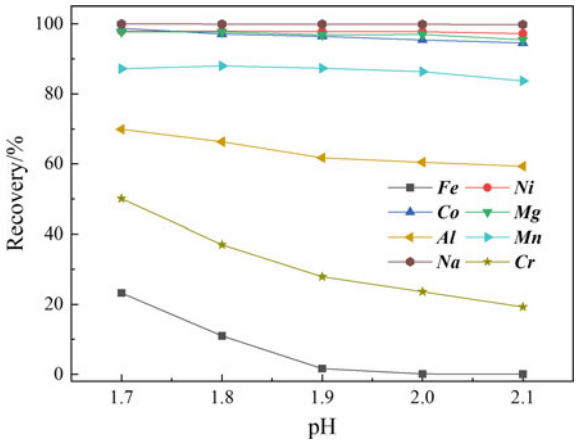

Fig. 7 Effect of pH on precipitation of varying metals

Figure 7 illustrates the impact of pH on elemental distribution during iron removal at 50 °C, 20 min, 700 rpm swirling, and H_2O_2(mol): Fe(mol) = 0.6. To ensure that the iron in the leach solution was completely precipitated as $FePO_4$, H_2O_2 was added to the leaching solution in order to convert Fe^{2+} into Fe^{3+}.

The recovery of the elements rapidly dropped as the pH value rose from 1.7 to 2.1 because the rise in pH value promoted the precipitation of varying elements. The formation of $Fe_3(PO_4)_2(OH)_2$, a flocculent precipitate with a high adsorption capacity that adsorbs metal ions, is the cause of the other side of the loss of metal ions [15]. The iron entirely precipitates when the pH hits 2.1, and the precipitate was characterized by XRD and SEM (Fig. 8). Only a broad hump was observed from the XRD pattern, indicating that the as-prepared iron phosphate crystallized poorly. After annealing at 700 °C for 2 h in the air, the diffraction peaks were well indexed to the reported phase of $FePO_4$ (PDF 29#0715). The SEM morphology validated a disc-shaped particle with size in the range of 200–500 nm. In addition, Ni^{2+} and Co^{2+} could be selectively extracted from the filtrate after iron precipitation through P204 and P507 [16].

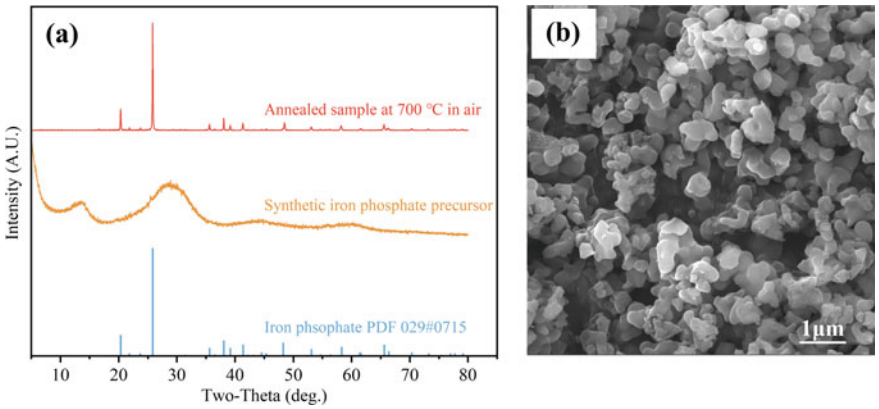

Fig. 8 XRD patterns (**a**) and SEM image (**b**) of iron phosphate precipitate

Conclusion

This work proposes and verifies an integrated process, which consists of reductive roasting, magnetic separation, and acid leaching, to the value-added utilization of laterite ore.

(1) Ni–Co–Fe powder was prepared from laterite via rotary kiln reductive roasting followed by magnetic separation under the conditions of the mass of semi-coke of 2.5 kg, the air–fuel ratio of 8, and reductive temperature of 1050 °C, with nickel, cobalt, and iron grades of 11.98%, 1.18%, and 70.13%, respectively, recoveries of 91.22%, 92.79%, and 16.68%, and selective recovery of Ni and Co in laterite nickel ore have been achieved.

(2) The obtained powdery alloy was readily dissolvable in the phosphoric acid solution at atmospheric pressure. Under the conditions of 4.5 mol/L H_3PO_4, 85 °C, 60 min, and *L*/*S* ratio of 12 mL/g, the Ni, Co, and Fe extractions were 90.8%, 92.3%, and 97.6%, respectively. After precipitating iron as amorphous $FePO_4 \cdot xH_2O$ from the leaching solution, Ni^{2+} and Co^{2+} could be further extracted either by P204 or P507.

Acknowledgements This work was supported by the National Natural Science Foundation of China (Grant Number 52174288).

References

1. Yin S, Deng W, Chen J, Gao X, Zou G, Hou H, Ji X (2021) Fundamental and solutions of microcrack in Ni-rich layered oxide cathode materials of lithium-ion batteries. Nano Energy 83
2. Shalom M, Ressnig D, Yang X, Clavel G, Fellinger T, Antonietti M (2015) Nickel nitride as an efficient electrocatalyst for water splitting. J Mater Chem A 3:8171–8177
3. Lv J, Shen H, Fu J (2021) A new phenomenon of Ni–Ti alloys and its application for fabricating thermally responsive microrobots. Adv Eng Mater 23
4. Ma B, Xing P, Yang W, Wang C, Chen Y, Wang H (2017) Solid-state metalized reduction of magnesium-rich low-nickel oxide ores using coal as the reductant based on thermodynamic analysis. Metall Mater Trans B 48:2037–2046
5. Nosrati A, Quast K, Xu D, Skinner W, Robinson D, Addai-Mensah J (2014) Agglomeration and column leaching behaviour of nickel laterite ores: effect of ore mineralogy and particle size distribution. Hydrometallurgy 146:29–39
6. Zhou D, Guo X, Zhang Q, Shi Y, Zhang H, Yu C, Pang H (2022) Nickel-based materials for advanced rechargeable batteries. Adv Funct Mater 32
7. Wang K, Li J, McDonald R, Browner R (2018) Iron, aluminium and chromium co-removal from atmospheric nickel laterite leach solutions. Miner Eng 116:35–45
8. Rubisov D, Papangelakis V (2000) Sulphuric acid pressure leaching of laterites—speciation and prediction of metal solubilities "at temperature." Hydrometallurgy 58:13–26
9. Tian Q, Dong B, Guo X, Wang Q, Xu Z, Li D (2023) Valuable metals substance flow analysis in high-pressure acid leaching process of laterites. J Cent South Univ 30:1776–1786
10. Luo J, Rao M, Li G, Zhou Q, Zhu Z, Jiang T, Guo X (2021) Self-driven and efficient leaching of limonitic laterite with phosphoric acid. Miner Eng 169
11. Li G, Zhou Q, Zhu Z, Luo J, Rao M, Peng Z, Jiang T (2018) Selective leaching of nickel and cobalt from limonitic laterite using phosphoric acid: an alternative for value-added processing of laterite. J Clean Prod 189:620–626
12. Rao M, Chen J, Zhang T, Hu M, You J, Luo J (2023) Atmospheric acid leaching of powdery Ni–Co–Fe alloy derived from reductive roasting of limonitic laterite ore and recovery of battery grade iron phosphate. Hydrometallurgy 218
13. Rao M, Li G, Zhang X, Luo J, Peng Z, Jiang T (2016) Reductive roasting of nickel laterite ore with sodium sulphate for Fe–Ni production. Part II: phase transformation and grain growth. Sep Sci Technol 51:1727–1735
14. Zhu Y, Ruan Z, Tang S, Thangadurai V (2014) Research status in preparation of $FePO_4$: a review. Ionics 20:1501–1510
15. Zheng J (2010) Synthesis and characterization of cathode materials $LiFePO_4$, $Li_3V_2(PO_4)_3$ and $xLiFePO_4 \cdot yLi_3V_2(PO_4)_3$ for lithium ion battery. Central South University, China
16. Rao M, Zhang T, Li G, Zhou Q, Luo J, Zhang X, Zhu Z, Peng Z, Jiang T (2020) Solvent extraction of Ni and Co from the phosphoric acid leaching solution of laterite ore by P204 and P507. Metals 10

Preparation of Forsterite-Spinel Refractory from MgO-Rich Residue Derived from Ludwigite Ore

Jing Wang, Tao Xiao, Jinxiang You, Jun Luo, Zhiwei Peng, and Mingjun Rao

Abstract MgO-rich residue, consisting of periclase, olivine, and forsterite, was generated from ludwigite ore. This study used MgO-rich residue as feed for preparing forsterite-spinel refractory. The phase transformation and physical properties as functions of sintering temperature and time were primarily investigated. Under optimized conditions of pre-roasting at 800 °C for 0.5 h and sintering at 1300 °C for 3 h, a high-quality refractory material with refractoriness of 1700 °C was obtained. This work provides ideas for the comprehensive utilization of ludwigite ore.

Keywords Ludwigite ore · MgO-rich residue · Forsterite · Spinel · Refractory material

Introduction

The ludwigite ore is characterized by high contents of boron, iron, and magnesium [1]. Various technologies have been explored for the comprehensive utilization of this ore [2], focusing on the recovery of boron and iron rather than magnesium [3–5]. Therefore, it's more advantageous to utilize the magnesium component to produce value-added products and retrieve boron and iron. An alternative process has demonstrated the potential and promising future of a coal-based direct reduction process for the stepwise recovery of metallic iron and borate from ludwigite ore [6]. After reductive roasting in the presence of soda ash, sodium metaborate and powdery metallic iron were obtained as the main products, with a high extraction efficiency of 72.1% for boron and 95.7% for iron [7]. Boron and iron were effectively recovered in this process, while large amounts of magnesium oxide (about 45 wt.% MgO) and silica were enriched in non-magnetic materials. Therefore, non-magnetic materials with high magnesium oxide and silicon dioxide content can be prepared into forsterite biphasic refractories [8].

J. Wang · T. Xiao · J. You · J. Luo · Z. Peng · M. Rao (✉)
School of Minerals Processing and Bioengineering, Central South University, Changsha 410083, Hunan, China
e-mail: mj.rao@csu.edu.cn

Z. Peng et al. (eds.), *Characterization of Minerals, Metals, and Materials 2024*, The Minerals, Metals & Materials Series, https://doi.org/10.1007/978-3-031-50304-7_26

Table 1 Main chemical compositions of the MgO-rich residue (wt.%)

MgO	SiO_2	TFe	B_2O_3	Al_2O_3	CaO	Na_2O	LOI
43.63	18.20	8.42	0.22	1.18	4.18	0.23	20.24

LOI mass loss upon ignition

This study aimed to investigate the impact of sintering temperature and time on the phase transformation, microstructural evolution, and properties of the refractory material, encompassing bulk density, compressive strength, apparent porosity, and refractoriness. The findings demonstrate that high-quality refractories can be produced from MgO-rich residue (MR) through appropriate sintering temperature and time.

Experimental

Materials

The MgO-rich residue (MR) was obtained from ludwigite ore after boron and iron extraction by coal-based reduction roasting, ball-mill grind-leaching, and magnetic separation [6]. The particle size of MR samples is all less than 74 μm. The primary composition of the MR is shown in Table 1, which was characterized by high magnesium (43.54 wt.% MgO) and silicon (16.07 wt.% SiO_2) contents. The X-ray diffraction (XRD) pattern (Fig. 1) indicates that the major components were periclase (MgO), olivine ($Mg_{1.98}Fe_{0.02}SiO_4$), forsterite (Mg_2SiO_4), lizardite ($Mg_3Si_2O_5(OH)_4$), and brucite ($Mg(OH_2)$).

Methods

Initially, the mixture of grounded MR was carefully mixed in a planetary ball mill for 20 min. Cylinders of 15 mm in diameter and 15 mm in height were briquetted by manual hydraulic pressing at 100 MPa using 5 wt.% of magnesium chloride solution (1.3 g/cm^3) as the binder. Then the briquettes were dried in a vacuum for 24 h at 110 °C. The dried briquettes were placed in a furnace for sintering. The samples were cooled to room temperature and taken out for the subsequent characterization tests. When testing the properties of refractories, five samples were tested to get an average value.

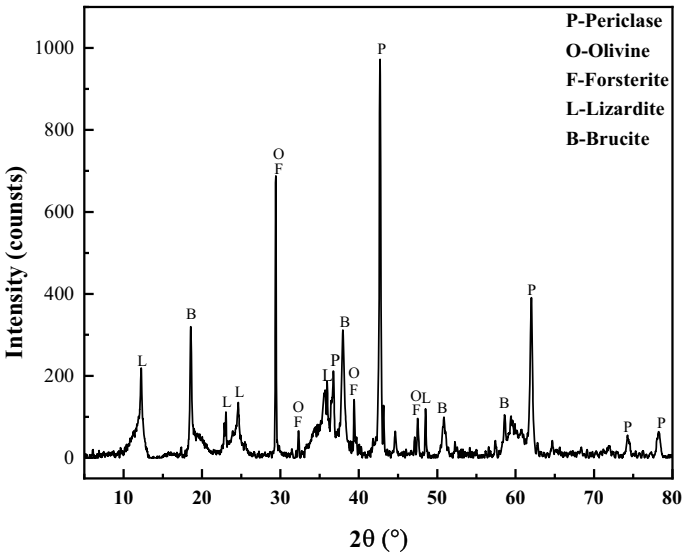

Fig. 1 XRD pattern of the MgO-rich residue

Characterization

The thermal stability of MR was determined using a thermal gravimetric analyzer (TG-DSC, TZSCH STA449C) by measuring the thermogravimetry and differential scanning calorimetry (TG-DSC) curves of the slag in air. The phase compositions of the resulting materials were determined using an X-ray diffraction spectrometer (XRD, BRUKER X'Pert PRO MPD). The microstructural changes of the materials were determined by using a scanning electron microscope (SEM; SIGMA Nova450) equipped with an energy-dispersive (EDS) detector. The values of bulk density/apparent porosity, compressive strength, and refractoriness of the materials were measured according to the Chinese National Standard Test Methods GBT 2997-2000, GBT 5072-2008, and GBT 7322-2007, respectively.

Results and Discussion

Pre-roasting of MgO-Rich Residue

The TG-DSC analysis determined the thermal stability of MR below 1400 °C, and the results are shown in Fig. 2. The TG curve presented a weight loss in three consecutive steps between 25–263, 263–433, 433–648, and 648–850 °C, corresponding to endothermic peaks at 92.8, 381.5, 553.5, and 728.0 °C. The first step is attributed

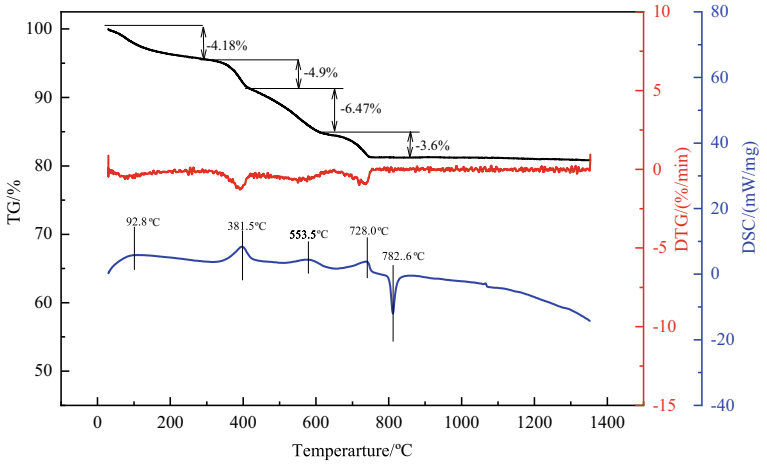

Fig. 2 TG-DSC results of the MgO-rich residue

to the removal of adsorbed water in MR; the second step is attributed to the thermal decomposition of brucite and the chemical reaction is shown as Eq. (1) [9]; the third step is attributed to the removal of lizardite interlayer water [10]; the fourth step is due to the dehydroxylation of lizardite and the chemical reaction is shown as Eq. (2) [11]. The DSC curve showed an endothermic peak at 782.6 °C and without a weight loss here. It's due to the decomposition of magnesia olivine to form magnesia olivine, iron oxide, and silicon dioxide.

$$\mathrm{Mg(OH)_2 = MgO + H_2O} \tag{1}$$

$$\mathrm{3MgO \cdot 2SiO_2 \cdot 2H_2O = 2MgO \cdot SiO_2 + MgO + 2H_2O} \tag{2}$$

As shown in Table 1 and Fig. 2, the LOI content reached 20 wt.% because lizardite and brucite contained a lot of crystal water. In preparing refractories from raw materials with high water content, the strength and densification of the refractories will be reduced due to the porosity generated by dehydration. Therefore, the MR was sintered at 800 °C for 0.5 h to dehydrate. Figure 3 shows XRD pattern after dehydration, indicating that the phase composition turned to periclase, forsterite, and magnesium iron spinel after sintering.

Phase Transformation During Sintering

Figure 3 shows the XRD patterns of refractory materials obtained by sintering of pre-sintering MR at 1100–1400 °C for 3 h. When the temperature reached 1100 °C,

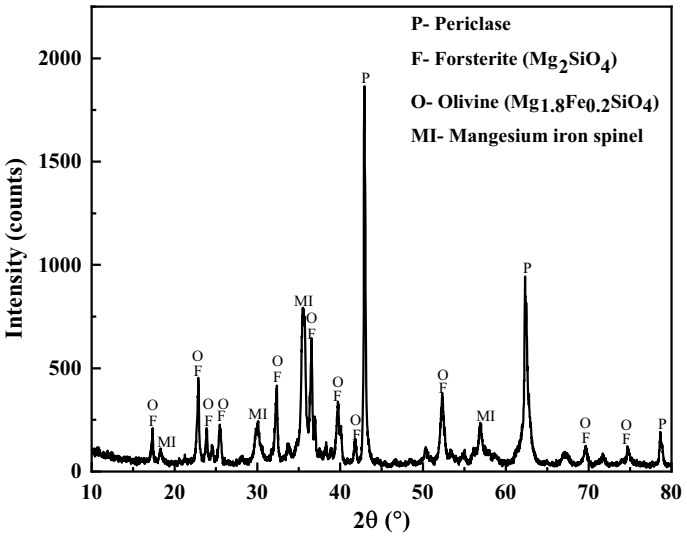

Fig. 3 XRD pattern of pre-roasted MgO-rich residue

the magnesia-ferritic olivine phase in the pre-sintering MR disappeared. At 1100–1400 °C, the main phase compositions of the samples were unchanged, including magnesia olivine, magnesia ferric spinel, and cubic magnesia. The diffraction peak intensity of magnesia olivine gradually increased with the rise of sintering temperature. It proves that the recrystallization of magnesia olivine occurs, and the strength of the diffraction peak of magnesia olivine increases due to grain growth with the increase of sintering temperature.

The intensity of the diffraction peak intensity of periclase exhibits a decrease with increasing roasting temperature. This phenomenon can be attributed to the thermal decomposition of ferric olivine into silicon dioxide and ferric oxide during the roasting process, resulting in MgO consumption through the formation of ferric olivine and ferric spinel [12, 13]. The equation is shown in Eqs. (3)–(5). Therefore, the increase in sintering temperature is favorable for the growth of magnesia ferric spinel and magnesia olivine, and the reaction is completed when the roasting temperature reaches 1300 °C (Fig. 4).

$$4\left[(\mathrm{Mg}\cdot\mathrm{Fe})\mathrm{O}\cdot\mathrm{SiO_2}\right] + 3\mathrm{O_2} = 4\mathrm{MgO}\cdot\mathrm{SiO_2} + 2\mathrm{SiO_2} + 2\mathrm{Fe_2O_3} \quad (3)$$

$$2\mathrm{MgO} + \mathrm{SiO_2} = 2\mathrm{MgO}\cdot\mathrm{SiO_2} \quad (4)$$

$$\mathrm{MgO} + \mathrm{Fe_2O_3} = \mathrm{MgO}\cdot\mathrm{Fe_2O_3} \quad (5)$$

Figure 5 shows the XRD patterns of refractory materials obtained by sintering of pre-sintering MR for 1–4 h at 1300 °C. Under different sintering time, the phase

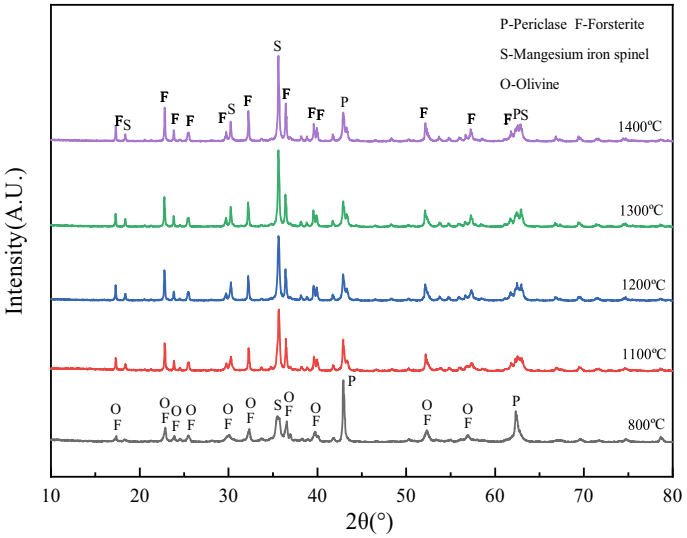

Fig. 4 XRD patterns of samples under different sintering temperatures

composition of the samples remained the same, and they were all magnesium olivine, periclase, and magnesia spinel. With the extension of the roasting time, the diffraction peak intensity of periclase and ferro-magnesia spinel gradually increased, and the diffraction peak intensity remained unchanged when the roasting time was greater than 2 h. It indicates that the phase transformation can be completed in 2 h.

Properties of the Refractory Materials

Figure 6 shows the effect of sintering temperature on the physical and mechanical properties of the refractory material when the time was 3 h. With the increase of sintering time, the apparent porosity of the sample decreased from 46.71 to 6.76%, the bulk density increased from 2.13 to 3.36 g/cm^3, and the compressive strength increased from 37.8 to 111.7 MPa. The compressive strength and bulk density increased with the increase of sintering temperature, contrary to the apparent porosity change. It was found that the properties changed in two different stages. The first stage was that when the temperature was less than 1300 °C, the bulk density and compressive strength increased sharply, and the apparent porosity decreased sharply. In the second stage, when the temperature was higher than 1300 °C, the bulk density, apparent porosity, and compressive strength were not changed. The increase in temperature promoted the formation of magnesia olivine and magnesia iron spinel, as well as the subsequent grain growth, resulting in an increased density of refractory

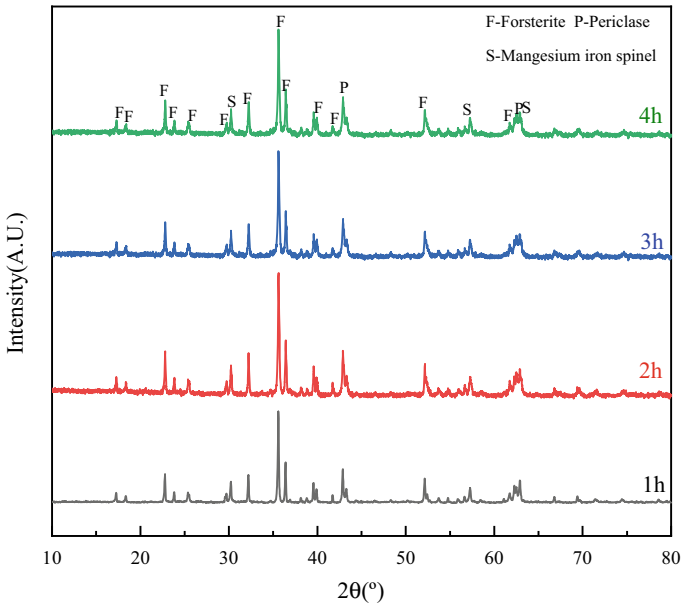

Fig. 5 XRD patterns of samples under different sintering time

materials and, consequently, an elevated volume density. Beyond 1300 °C, the grain formation and growth process reached its completion.

Figure 7 shows the effect of sintering time on physical and mechanical properties when the sintering temperature is 1300 °C. When the sintering time increased from 1

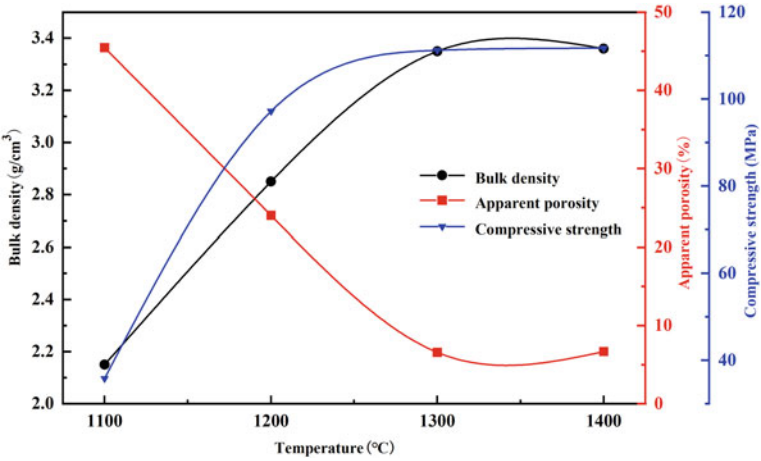

Fig. 6 Effect of sintering temperature on the compressive strength, bulk density, apparent porosity, and properties of refractories prepared by pre-sintering MR

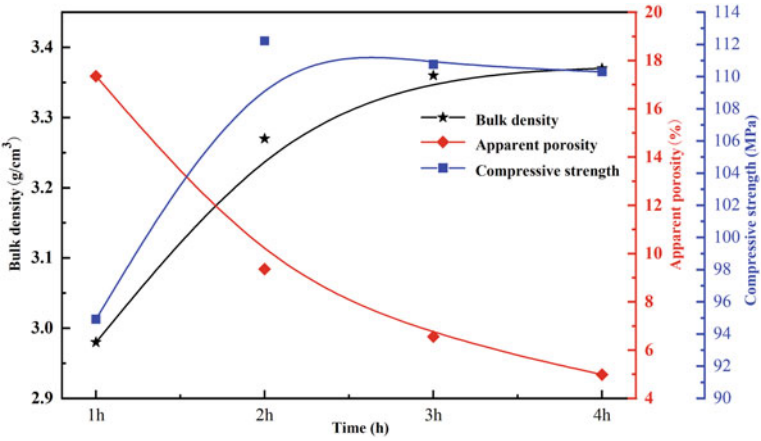

Fig. 7 Effect of sintering time on the compressive strength, bulk density, apparent porosity, and properties of refractories prepared by pre-sintering MR

to 3 h, the apparent porosity of the sample gradually decreased from 17.35 to 6.76%, the bulk density increased from 2.98 to 3.36 g/cm^3, and the compressive strength of the sample increased from 94.73 to 111.7 MPa. The prolonged firing time results in the infiltration of the generated liquid phase into the pores of the sample, thereby promoting material densification. With the increase of sintering time to 4 h, the bulk density of the sample basically remained unchanged.

The refractories obtained at the above sintering temperature and time were tested, and the term melt temperature was all 1700 °C.

Conclusion

In this study, the effects of sintering temperature and time on the preparation of refractories from MgO-rich slag were investigated. The increase in sintering temperature and time was conducive to the further formation of magnesia ferrospinel and magnesia olivine, as well as to the densification of the refractory material. Under conditions of pre-calcining at 800 °C for 0.5 h and sintering at 1300 °C for 3 h, the high-quality refractory material could be prepared, with a bulk density of 3.36 g/cm^3, apparent porosity of 6.56%, number of thermal shock resistance of 2, and term melt temperature higher than 1700 °C.

Acknowledgements This work was supported by the National Key Research and Development Program of China (2020YFC1909800).

References

1. Cheng G, Liu X, Yang H et al (2022) Sintering and smelting property investigations of ludwigite. Processes 10(1):159
2. Zhang X, Lang J, Cui C et al (1995) Comprehensive utilization of low grade ludwigite ore with blast furnace smelting. Ironmak Steelmak 30(12):9–11
3. Zhang J, Cheng J, Li Z (2009) Research on the new technology of flash roasting of ludwigite ore. Inorg-Salt Index 41:42–43
4. Huang W, Liu Y (2021) Effect of microwave radiation on the magnetic properties of ludwigite and iron-boron separation. J Microw Power Electromagn Energy 55:93–106
5. Liu Y, Jiang T, Wang J et al (2016) Formation of micro-fractures on ludwigite ore and its effect on grinding efficiency of ludwigite ore under microwave treatment. International Microwave Power Institute, pp 76–78
6. Liang B, Li G, Rao M et al (2017) Water leaching of boron from soda-ash-activated ludwigite ore. Hydrometallurgy 167:101–106
7. Li G, Liang B, Rao M et al (2014) An innovative process for extracting boron and simultaneous recovering metallic iron from ludwigite ore. Miner Eng 56:57–60
8. Jeon J, Kim S, Kim M et al (2019) A study on the interfacial reaction between liquid iron and MgO-based refractories containing TiO_2. Metall Mater Trans B 50(5):2251–2258
9. Ammar A, Rayson M, Geoff F et al (2019) Formation of magnesite and hydromagnesite from direct aqueous carbonation of thermally activated lizardite. Environ Prog Sustain Energy 38(3):13244
10. Cecilia V (2010) Serpentine minerals discrimination by thermal analysis. Am Mineral 95(4):631–638
11. Cheng W, Ding Y, Chi J (2002) A study of synthetic forsterite refractory materials using waste serpentine cutting. Miner Eng 15:271–275
12. Li J, Wang Q, Liu J et al (2002) Synthesis process of forsterite refractory by iron ore tailings. J Environ Sci 21:92–95
13. Mitchell M, Jackson D, James P (1998) Preparation and characterisation of forsterite (Mg_2SiO_4) xerogels. J Sol-Gel Sci Technol 13(1):359–364

Chemically Bonded Phosphate Ceramics and Their Composites

Henry A. Colorado and Mery Gomez-Marroquín

Abstract This research explores the chemically bonded ceramics and composites, their main advantages, limitations, applications, and structure-material property relations. Particularly, several case studies using calcium silicate and phosphoric acid are presented, mainly applied as a construction or building material, fire protection solution, radiation shielding, hazardous waste stabilization, and even electronics. Scanning electron microscopy (SEM) and X-ray diffraction (XRD) results are also shown to understand the microstructure of the cement. Results show an increasing trend to use these materials particularly for green construction of small houses, a wave that is expanding in many countries for clients interested in mitigating the pollution and decreasing their carbon footprint. Still, there are limitations in the materials developed, mainly in the durability and stability of the compositions under environmental conditions.

Keywords Ceramics · Chemical bonded ceramics · Phosphate · Cements

Introduction

Traditional ceramics typically require temperatures exceeding 1000 °C in their production process, leading to higher production costs and a negative impact on the environment. A solution to these challenges has been identified in a category of emerging materials that exhibit properties falling between those of Portland cement and ceramics. These materials are known as inorganic phosphate cements (PC), and also known as Chemically Ceramics (CBC) [1]. Among the applications with these materials are bone cements [2], nuclear cements for waste stabilization [3], construction materials for structural applications [4], and fire-resistant applications

H. A. Colorado (✉)
CCComposites Laboratory, Universidad de Antioquia UdeA, Calle 70 No. 52-21, Medellín, Colombia
e-mail: henry.colorado@udea.edu.co

M. Gomez-Marroquín
National University of Engineering, 210 Túpac Amaru Ave, Rímac, Lima 25, Peru

Z. Peng et al. (eds.), *Characterization of Minerals, Metals, and Materials 2024*, The Minerals, Metals & Materials Series, https://doi.org/10.1007/978-3-031-50304-7_27

[5]. Among the advantages of these materials are that usually can have much higher strength, lightweight, thermal stability, and neutral pH when compared with traditional Portland cement concrete, which usually has a pH bigger than 13. On the contrary, it is more expensive and their raw materials are sometimes now as available as those for concrete. However, tailoring the properties for the mentioned specific applications can give a solution for the limitations. These phosphates have been fabricated as composite [6] and nanocomposite materials as well [7]. Other applications including energy materials such as metal phosphates [8], phosphates in agriculture [9], food [10], and others are not explored in this research.

The current research presents the main phosphates for structural, fire resistant, and nuclear waste stabilization applications, presenting general aspects of their chemistry, microstructure, limitations, and applications.

Calcium Phosphate Cements (PCS)

Calcium-based phosphate cements (Ca-PC) are typically made of a mixture of calcium silicate, Wollastonite ($CaSiO_3$), a natural mineral, and phosphoric acid. The reaction can be very strong and fast, depending on factors such as powder size, humidity content, acid formulation temperature, and other processing parameters [11]. The crystalline phases found in the final set of cement are residual wollastonite ($CaSiO_3$), quartz (SiO_2), brushite ($CaHPO_4 \cdot 2H_2O$), and monetite ($CaHPO_4$). In addition, amorphous calcium phosphate and amorphous silica are present. Equations 1 and 2 describe the main products upon the acid and the calcium silicate reaction. The compressive strength in these materials typically runs from 70 to 150 MPa [11], depending on the raw materials and manufacturing processes.

$$CaSiO_3 + H_3PO_4 + H_2O = SiO_2 + CaHPO_4 \cdot 2H_2O \quad (1)$$

$$2CaHPO_4 \cdot 2H_2O \rightarrow 2CaHPO_4 + 4H_2O \quad (2)$$

Figure 1a shows the consistency of the inorganic paste after the mixing process of Wollastonite and phosphoric acid, while Fig. 1b shows an SEM image of the microstructure of these materials.

The process of formation has been represented in Fig. 2, with main steps after the mixing process being the sol–gel type reaction, and the polymerization leading to a solid material made at room temperature. This Ca-PC starts from the mixture of phosphoric acid and a raw calcium silicate powder, a metal oxide mineral known as Wollastonite, a triclinic ceramic material with many uses in engineering products. Upon the mixture, the acid produced the metal ion dissolution into the liquid, which starts an acid-based reaction thereby forming sol and gel steps until a crystallization leads into a solid material. This solid is typically composed of a new metal phosphate, in this case, calcium phosphate, and of residual grains from the raw ceramic powder.

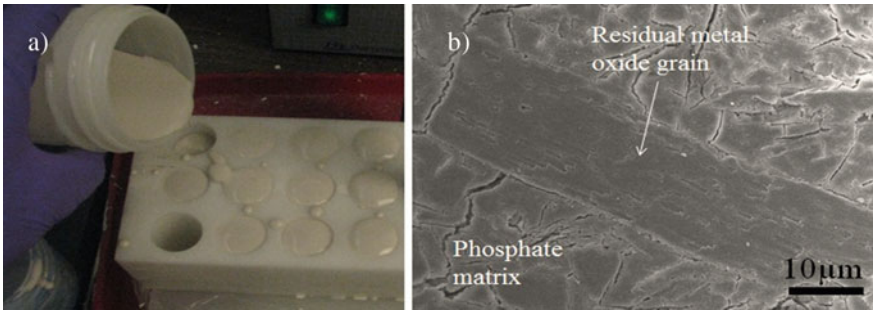

Fig. 1 **a** Inorganic PC resin, **b** SEM image showing the microstructure with a residual Wollastonite grain ($CaSiO_3$) and a phosphate-based matrix product of the chemical reactions

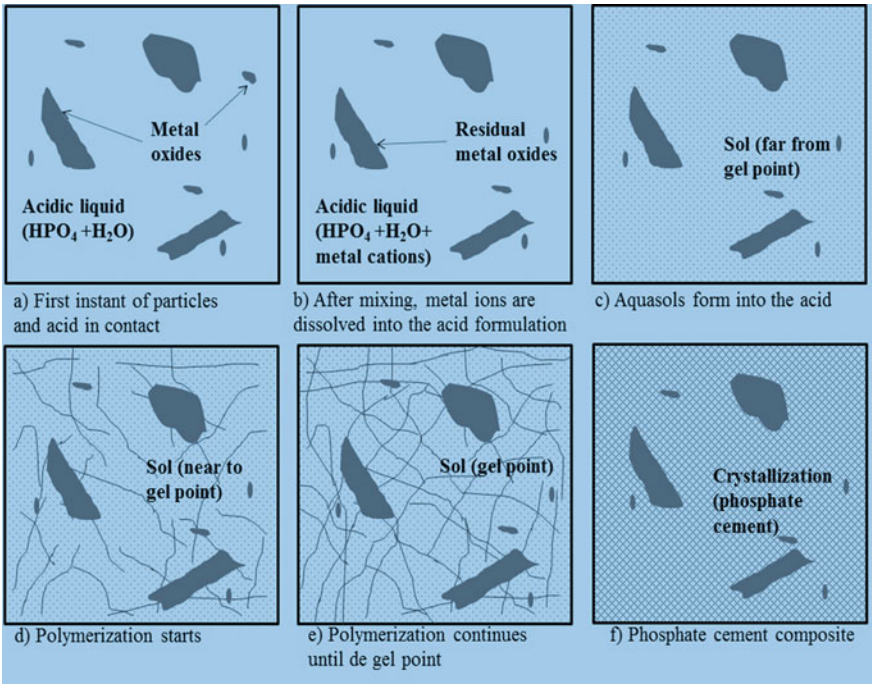

Fig. 2 Representation of Ca-PC formation

These materials have been successfully used as building and structural material [12], combined with other solid and liquid wastes for alternative green material [13], or as a hybrid composite material [14]. The typical microstructure of these Ca-PC is shown in Fig. 3. Figure 3a shows the SEM image that reveals the solid cement with some cracks generated during the solidification process. Figure 3b shows some of

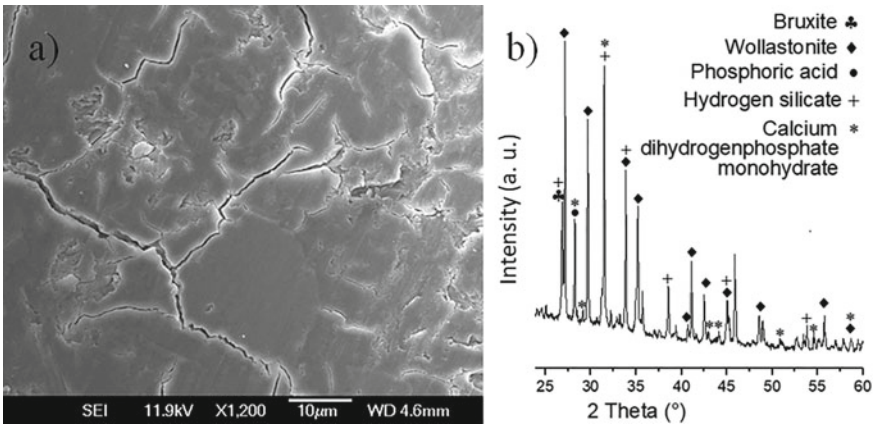

Fig. 3 Microstructure of Ca-PC, **a** SEM image, **b** XRD

the most representative phases that can appear in the cement formation, wollastonite as a residual raw material, and brushite, a calcium phosphate cement.

Ceramicrete Ceramics

Ceramicrete is a technology of PCs produced at Argonne National Laboratory (ANL) in the 1990s mainly but not limited for the encapsulation of low-level radioactive waste [7], currently used in many applications, that include construction materials [15], piezoelectrics [16], and radiation shielding [17]. It is based on an exothermic acid–base reaction, typically conducted at room temperature. One of the most common products is resulting in a solid material, a magnesium potassium phosphate cement (MKPC), $MgKPO_4 \cdot 6H_2O$ (Eq. 3). Typical compressive strength values range from 50 to 80 MPa.

$$MgO + KH_2PO_4 + 5H_2O \rightarrow MgKPO_4 \cdot 6H_2O \tag{3}$$

Figure 4 shows some of the modern architectures built today as demand of green technologies with low carbon footprint. The structures currently show limitations in the durability, waterproof, and efflorescence, a condition in which there is a formation of salt in the surface of the material, which is detrimental in properties and esthetics.

The nuclear waste stabilization via phosphate cements is a technology very adaptative to multiple chemistries of wastes, from acidic to alkaline pHs. From calcium-based PCs to mitigate irradiation [18], however, the possibilities now are open to new chemistries that partially replace traditional concrete, particularly in high-performance or extreme conditions applications, such as those parts under extreme

Fig. 4 Building applications now built with PCs, **a** large building structure, **b** glamping dome, **c** nuclear waste stabilization

irradiation, ultra-high pressure, high impact, or high temperature. Of course, additive manufacturing is now being used with PCs [19], enabling the manufacturing of complex geometries with also more sustainable manufacturing [12, 20].

Summary

PCs are modern materials that exhibit mechanical properties typically better than traditional cement concrete, but that normally some of the chemistries are limited by the largest costs and availability of the raw materials. The current needs and demands for more people who want to have green homes increased the demand on these materials, and thus more research is required to decrease their limitations and respond to the low carbon demand public.

References

1. Roy DM (1987) New strong cement materials: chemically bonded ceramics. Science 235(4789):651–658
2. Tamimi F, Sheikh Z, Barralet J (2012) Dicalcium phosphate cements: brushite and monetite. Acta Biomater 8(2):474–487
3. Wang Y, Liu Z, He F, Zhuo W, Yuan Q, Chen C, Yang J (2021) Study on water instability of magnesium potassium phosphate cement mortar based on low-field 1H nuclear magnetic resonance. Measurement 180:109523
4. Arora A, Singh B, Kaur P (2019) Novel material i.e. magnesium phosphate cement (MPC) as repairing material in roads and buildings. Mater Today Proc 17:70–76
5. Dai X, Qian J, Qin J, Yue Y, Zhao Y, Jia X (2022) Preparation and properties of magnesium phosphate cement-based fire retardant coating for steel. Materials 15(12):4134
6. Colorado HA, Hahn HT, Hiel C (2011) Pultruded glass fiber-and pultruded carbon fiber-reinforced chemically bonded phosphate ceramics. J Compos Mater 45(23):2391–2399
7. Colorado HA, Hiel C, Hahn HT (2011) Chemically bonded phosphate ceramics composites reinforced with graphite nanoplatelets. Compos Part A Appl Sci Manuf 42(4):376–384
8. Deniard P, Dulac AM, Rocquefelte X, Grigorova V, Lebacq O, Pasturel A, Jobic S (2004) High potential positive materials for lithium-ion batteries: transition metal phosphates. J Phys Chem Solids 65(2–3):229–233
9. Antoun H (2012) Beneficial microorganisms for the sustainable use of phosphates in agriculture. Procedia Eng 46:62–67
10. Ellinger RH (2018) Phosphates as food ingredients. CRC Press
11. Colorado HA, Hiel C, Hahn T, Yang JM (2011) Wollastonite-based chemically bonded phosphate ceramic composites. In: Metal, ceramic and polymeric composites for various uses, vol 13, pp 265–282
12. Revelo CF, Colorado HA (2021) A green composite material of calcium phosphate cement matrix with additions of car tire waste particles. Int J Appl Ceram Technol 18(1):182–191
13. Qin Z, Ma C, Zheng Z, Long G, Chen B (2020) Effects of metakaolin on properties and microstructure of magnesium phosphate cement. Constr Build Mater 234:117353
14. Revelo Huertas CF, Vieira CMF, Colorado HA (2021) A hybrid composite for structural applications made of rubber waste tires and calcium phosphate cement. Int J Appl Ceram Technol 18(4):1342–1353
15. Donahue PK, Aro MD (2010) Durable phosphate-bonded natural fiber composite products. Constr Build Mater 24(2):215–219
16. Ding W, Xu W, Dong Z, Liu Y, Wang Q, Shiotani T (2021) Piezoelectric properties and microstructure of ceramicrete-based piezoelectric composites. Ceram Int 47(21):29681–29687
17. Wagh AS, Sayenko SY, Dovbnya AN, Shkuropatenko VA, Tarasov RV, Rybka AV, Zakharchenko AA (2015) Durability and shielding performance of borated ceramicrete coatings in beta and gamma radiation fields. J Nucl Mater 462:165–172
18. Florez R, Loaiza A, Giraldo CHC, Colorado HA (2021) Calcium silicate phosphate cement with samarium oxide additions for neutron shielding applications in nuclear industry. Prog Nucl Energy 133:103650
19. Grossin D, Montón A, Navarrete-Segado P, Özmen E, Urruth G, Maury F, Maury D, Frances C, Tourbin M, Lenormand P, Bertrand G (2021) A review of additive manufacturing of ceramics by powder bed selective laser processing (sintering/melting): calcium phosphate, silicon carbide, zirconia, alumina, and their composites. Open Ceram 5:100073
20. Colorado HA, Velásquez EIG, Monteiro SN (2020) Sustainability of additive manufacturing: the circular economy of materials and environmental perspectives. J Mater Res Technol 9(4):8221–8234

Characterization and Modelling of Triply Periodic Minimum Surface (TPMS) Lattice Structures for Energy Absorption in Automotive Applications

N. D. Cresswell, A. A. H. Ameri, J. Wang, H. Wang, P. Hazell, and J. P. Escobedo-Diaz

Abstract The performance of triply periodic minimum surface (TPMS) lattice structures was evaluated for use as energy absorbers in automobile crash structures. Schoen's Gyroid TPMS lattice structures were manufactured from colorFabb carbon fibre reinforced nylon (PA-CF) filament using fusion deposition modelling (FDM) 3D printing. Compressive and energy absorption performance was quantified experimentally using quasi-static compression testing. Test samples were replicated at different gyroid cell size and continuous surface thickness combinations. Results were compared to published data from other lattice structures to assess relative performance, and analysed to develop a recommended gyroid TPMS geometry. It was determined that varying either the continuous surface thickness, or unit cell size influenced the performance of the structure. A gyroid TPMS structure with a cell size of 10 mm, and a continuous surface thickness of 2 mm was found to perform the best, achieving an impressively high specific energy absorption capacity of 13.06 J/g (± 0.15), significantly outperforming both 3D truss and traditional 2D lattice structures for use in the automotive industry.

Keywords Characterization · Modeling and simulation · Additive manufacturing

N. D. Cresswell · A. A. H. Ameri · J. Wang · H. Wang · P. Hazell · J. P. Escobedo-Diaz (✉)
University of New South Wales at the Australian Defence Force Academy, Canberra, ACT 2600, Australia
e-mail: j.escobedo-diaz@unsw.edu.au

Z. Peng et al. (eds.), *Characterization of Minerals, Metals, and Materials 2024*, The Minerals, Metals & Materials Series, https://doi.org/10.1007/978-3-031-50304-7_28

Introduction

The primary objective of a crash structure in an automobile is to provide a crumple zone to absorb kinetic energy and lower the acceleration pulse during an accident. Crash structures aim to control the paths of load transformation and energy dissipation throughout the vehicle. Optimising the stiffness and compressive characteristics of structures subject to impact is essential to increasing the survivability of passengers in the event of a collision [1].

Recent studies have investigated the performance potential of 3D truss lattice structures as energy absorbers in automobile crash structures. Niutta et al. [2] used numerical and experimental methods to investigate the performance potential of a bumper structure composed of 3D truss lattice structures of varying thickness manufactured by fused deposition modelling (FDM) 3D printing using carbon fibre reinforced nylon filament (PA-CF). It was determined that the 3D truss lattice structure performed better than an equivalent steel structure—it weighed 25% less than steel, yet it reduced intrusion by 7%.

It has also been determined that TPMS structures perform significantly better in compression and energy absorption metrics than 3D truss lattice structures, and traditional 2D lattice structures such as honeycomb [3–5]. TMPS structures are a class of lattice which have mathematically defined surfaces inspired by structures found in nature. The surfaces repeat periodically in three-dimensional (3D) cells. Advances in modelling and additive manufacturing techniques in recent years have enabled TPMS structures to be manufactured. The excellent energy absorption characteristics of TPMS structures present an opportunity for further application. There is a need to quantify the behaviour of different TPMS structures and to better understand how specific geometries effect their performance. TPMS cell size and surface thickness are two such characteristics which could be optimised. Automotive applications of TPMS structures have been identified as having high potential and further research and development is needed to quantify the performance and optimise the design of such structures [6]. Schoen's Gyroid TPMS geometries have been investigated in recent literature, and determined to perform extremely well in compressive and energy absorption experiments when manufactured using common additive manufacturing (AM) techniques such as fusion deposition modelling (FDM) and selective laser melting (SLM) 3D printing methods [4, 5].

The aim of this study is to investigate and analyse the applicability and performance potential of triply periodic minimum surface (TPMS) structures as energy absorbers in automobile crash structures. Gyroid TPMS structures were manufactured from carbon fibre reinforced nylon, samples varied in unit cell size, and in the thickness of the continuous surface of the structure. The energy absorption potential of these various sample geometries was characterised using quasi-static compression testing methods, and their relative performance was evaluated for application in automobile crash structures.

Methods

When determining the most suitable experimental procedure, the ISO 844:2021 and ATSM D1621-16 standards were consulted [7, 8]. For this study a sample size of 50 × 50 × 50 mm was used which is consistent with Miralbes et al. [9] and is a suitable choice when accounting for test equipment requirements, sample variability, ability to up-scale results, manufacturing time, and resources. Gyroid TPMS samples had unit cell sizes (Factor C) of 10 mm or 16.67 mm, each cell size was manufactured at a continuous surface thickness (Factor T) of 1, 2 or 3 mm These values were chosen to ensure that samples had sufficiently large internal voids to enable analysis of how the structure behaved before densification. Geometry combinations were compared as a 2 by 3 factorial. In quasi-static testing, 3 replicates of each unique geometry (treatment) were tested. Replicate numbers ensured that treatment effects were not obscured by experimental variability.

Samples were manufactured using a Prusa Bear MK3S + FDM 3D printer, from 1.75 mm diameter colorFabb PA-CF filament. It was fitted with a 0.4 mm diamond-coated hardened steel nozzle, and was used in conjunction with a EIBOS 3D Cyclopes filament dryer. This ensured that the filament did not absorb moisture during the manufacturing process, which can lead to printing defects [10]. To minimise dimensional inaccuracy and maximise consistency between samples, the x, y, and z axes of the machine were calibrated prior to manufacturing. The samples were 3D modelled, meshed (0.01 mm tolerance), and exported to PrusaSlicr 2.6.0 using the nTopology 3D generative design software package (nTop). PrusaSlicr 2.6.0 was used to slice the imported mesh and convert it to a .gcode file that the 3D printer could interpret. All samples were printed using the same settings within PrusaSlicr. The nozzle and print bed temperatures were set to 275 °C and 60 °C respectively. These values were chosen as they produced the most consistent layer adhesion, and minimised defects and other undesirable artifacts common with nylon-based filaments such as stringing or warping.

Quasi-static compression testing was conducted using a Shimadzu 100 kN universal testing machine. For these tests, samples were compressed at a speed of 0.05 mm/s until the force threshold of 80 kN was reached, or the sample had significantly surpassed its densification point. Results were recorded using the TRAPEZIUM X software package and analysed using MATLAB. High resolution video of each test was recorded using a Shimadzu TRViewX, and Canon EOS DSLR camera. Table 1 shows the outputs that were calculated from the measured data. Before testing, each sample was weighed (± 0.005 g), and its height, width, and depth were measured and recorded (± 0.005 mm). Table 1 includes the most important material parameters typically considered when determining the crashworthiness of a structure, to provide a clear understanding of the compressive behaviour of a sample [2, 4].

Table 1 Parameters calculated from quasi-static testing

Name (Abbreviation)	Units	Description
Peak Crushing Force (*PCF*)	N	The peak force experienced by the sample during compression, before the plateau region
Total Energy Absorption (*EA*)	J	The area under the force–displacement curve
Specific Energy Absorption (*SEA*)	J/g	The ratio of *EA* divided by the mass of the sample
Mean Crushing Force (*MCF*)	N	The mean force of the plateau (plastic deformation) region on the force–displacement curve
Crush Force Efficiency (*CFE*)	%	The ratio between the MCF and PCF. Higher efficiency translates to an impact response that is closer to optimal energy absorption

Table 2 Key for shorthand sample identification code

Level	1	2	3
Factor C: Cell size (mm)	16.67	10.00	–
Factor T: Surface thickness (mm)	1	2	3

Sample geometries will be represented by abbreviation in the form C*x*T*y*-*n*, using treatment factors C and T (Table 2). For example, the 2nd replicate of a sample that has a cell size of 16.67 mm, and a surface thickness of 3 mm will be represented by the code C1T3-2. Table 2 shows the shorthand key.

Results and Discussion

In this section, performance of gyroid TPMS structures in energy absorption will be discussed along with the visual failure mechanisms seen during testing. The experimental results from quasi-static testing are shown in Fig. 1. Table 3 displays the mean characterised energy absorption performance of the manufactured PA-CF gyroid TPMS structures.

An analysis of variance (ANOVA) was conducted to determine the influence of cell size (Factor C) and surface thickness (Factor T) treatments on the specific energy absorption (SEA) of the samples tested, and their interactions. The *p*-value shows if a treatment is statistically significant, a smaller value indicating that the treatment had a more significant effect ($p < 0.001$ is highly significant). Table 4 summarises the results of the ANOVA analysis.

As can be seen, the *p*-values for both cell size and surface thickness (Factor C and T) are very close to zero and therefore each treatment made a highly significant impact on the specific energy absorption capacity of the structure. In Table 4, *df* refers to degrees of freedom, *SS* to the sum of squares, and *MS* to the mean squared.

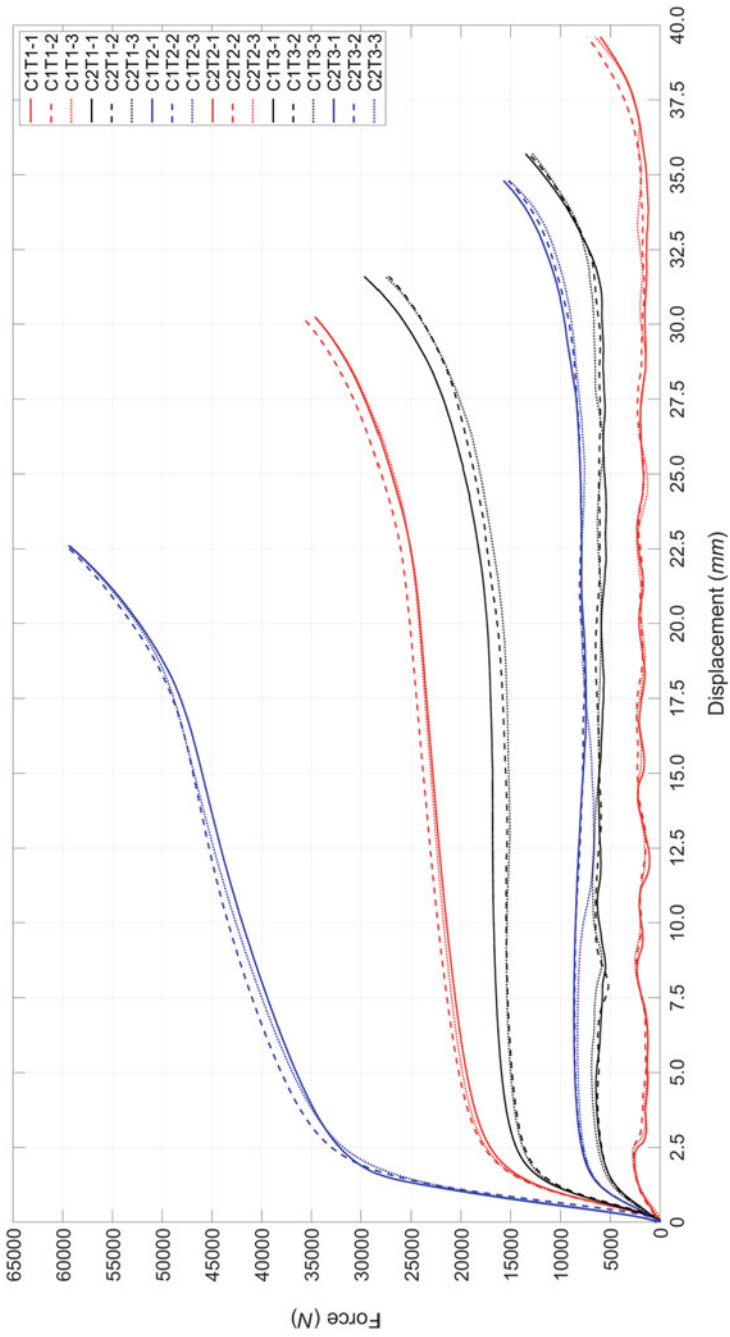

Fig. 1 Quasi-static force versus displacement curves of all treatments

Table 3 Parameters derived from quasi-static testing of gyroid TPMS structures

	Mean				
Treatment	PCF (N)	EA (J)	SEA (J/g)	MCF (N)	CFE (%)
C1T1	2673	79	5.11	2214	82.7
Std. Error	54.6	3.2	0.19	120.4	3.1
C2T1	6542	226	8.73	6368	97.3
Std. Error	179.6	4.2	0.13	200.9	1.1
C1T2	8509	288	9.16	8280	97.3
Std. Error	110.7	5.2	0.14	113.9	0.1
C2T2	20,563	698	13.06	> PCF	> 100
Std. Error	234.6	8.5	0.15	–	–
C1T3	15,856	531	11.18	≥ PCF	≥ 100
Std. Error	408.3	13.5	0.27	–	–
C2T3	36,420	951	11.70	> PCF	> 100
Std. Error	452.9	5.8	0.0	–	–

Table 4 ANOVA statistical analysis of SEA

Factors	*df*	*SS*	*MS*	*p*-value
C (Cell size)	1	32.34	32.34	0.000
T (Thickness)	2	76.10	38.05	0.000
Interaction between A and B	2	10.59	5.30	0.000
Error	12	1.00	0.08	
Total	17	120.03		

There are clear differences in performance between each treatment where only one factor varied, and the interaction between treatments was also highly significant. This is reflected in Fig. 1, and the characterised performance measures in Table 3.

Figure 1 shows that the three treatments C2T2, C1T3, and C2T3 exhibited foam-like behaviour when compressed [2, 11]. This is reflected by the MCF being greater than the PCF, resulting in a CFE exceeding 100% efficiency. All C1T3 replicates were between 100 and 102% efficiency. However, for the purpose of this study the MCF and CFE metrics will not be used as a performance comparison for the C2T2, C1T3, or C2T3 treatments.

It was observed in testing, and reflected in Fig. 1 that both T1 treatment sample sets (1 mm surface thickness) exhibited sequential layer collapse throughout compression, beginning with the top cell layer. This can be seen in the wave-like pulses in Fig. 1 for the relevant samples, caused by extensive buckling and associated print layer delamination. T1 treatment samples also experienced the least initial isotropic deformation, correlating with having the smallest elastic deformation region, shown by the small initial peak in Fig. 1. C1T2 samples exhibited similar behaviour, but to a

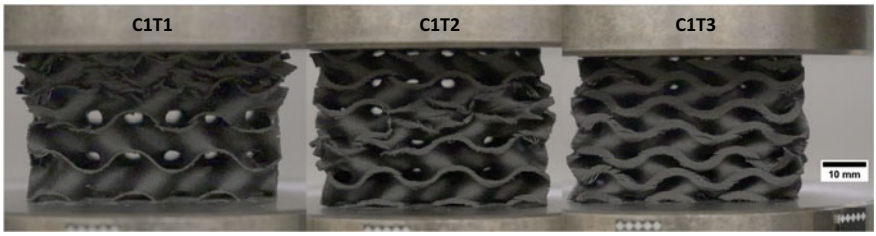

Fig. 2 C1T1-3, C1T2-3, and C1T3-3 samples under quasistatic compression

lesser extent as there was more initial isotropic deformation which instead progressed to diagonal shear failure through the central cell layers of the sample. This behaviour can be seen in Fig. 2 which shows a side-by-side comparison of all C1 treatments under compression. Shear failure behaviour across the width of the sample was not observed in any other treatments.

All other T2 and T3 treatment samples experienced isotropic deformation to collapse, and densification. It could be seen that this also correlated to an increased elastic deformation region, and a foam-like plastic deformation region. It was also observed that T2 and T3 treatments were much less prone to failure due to buckling, instead bulging outwards throughout compression, without ejecting fragments, unlike T1 treatments.

Initial print layer delamination began on the outer-most edges of the sample for all treatments. It should also be noted that only the outer face of the structure was able to be observed during testing, therefore making it impossible to observe exactly how the internal cells failed.

C1T1 samples had the lowest PCF, corresponding with a relatively small elastic deformation region. Print layer delamination was seen to begin at very small displacements, starting around the midpoint of the unit cell at the edges of the sample. The samples experienced sequential layer collapse, originating from brittle buckling failures in the top-most cell layer (Fig. 2), and localised shear failures through the midpoints of the outer edges of the continuous surface. Minor fragmentation was observed during collapse, once all layers were compressed to complete failure, the sample began to densify. This was consistent across all replicates. It can be seen in Table 3 that this treatment had the worst characterised performance, despite still having a relatively high SEA and CFE when compared to other high performing 3D lattice structures [2]. Buckling, and sequential layer collapse during quasistatic compression has also been reported for gyroid TPMS samples with a similar Factor C to Factor T ratio manufactured using a selective laser melting (SLM) printer from Ti–6Al–4V [12].

C2T1 samples performed significantly better than C1T1 treatments, despite exhibiting the same failure mechanisms. Samples with this treatment had noticeably more initial isotropic deformation, which corresponded with a PCF of ~ 2.5 times higher than C1T1 samples. Therefore, cell size has a large impact on the

energy absorption capability of gyroid TPMS structures. Initial print layer delamination was again seen at the edges of the structure at relatively low displacements, which progressed into buckling failure induced by localised shear failures in the outer continuous surface. This was followed by sequential cell layer collapse from top to bottom as the displacement increased. Due to the smaller cells, this behaviour was not as pronounced throughout the plastic region in Fig. 1 as it was for C1T1 samples. Once collapsed, the structure began to densify, which was consistent across all treatments.

Samples with the C1T2 treatment performed significantly better than C1T1 samples, outperforming C2T1 in all characterised performance measures. Samples experienced isotropic deformation until displacement exceeded ~ 8 mm. As discussed, C1T2 samples experienced diagonal shear failure through central cell layers. This was initiated by print layer delamination throughout the peaks and valleys of the outer continuous surface. This is likely due to these locations having the weakest print layer adhesion as there is no structure above or below to provide support during the printing process. Internal features, away from cell edges are self-supported and where higher stress concentrations are located in gyroid TPMS structures [4, 12].

C2T2 samples had the highest SEA of all measured treatments, significantly outperforming all equivalent PA-CF 3D truss lattice structure geometries explored by Niutta et al. [2]. Notably, they also outperformed C1T3 samples in all characterised performance measures. This suggests that increased cell count, and therefore higher areal density has a large effect on the energy absorption capacity of gyroid TPMS structures. As with other T2 and T3 treatments, the samples were seen to bulge outwards during isotropic compression (Fig. 2), and did not eject any fragments. The highest performing treatments C2T2, C1T3, and C2T3 consisted of the highest areal density, and all exhibited foam-like compression behaviour as shown in Fig. 1. This is when the CFE exceeds 100%, caused by the average force throughout plastic deformation region surpassing the PCF [11].

Figure 3 shows how the sample C2T3-2 behaved throughout quasi-static compression. At a displacement of ~ 10 mm, the cell layers can be seen compressing as the distance from peak to peak of the outer surface decreases, which is most apparent through the central cell layers. Print layer delamination through the outer surface is also apparent, concentrated around the outermost edges of the sample as they begin to bulge. At ~ 25 mm displacement, the sample has completely collapsed and is approaching maximum densification. This behaviour was consistent across all C2T3 replicates. C1T3 treatments followed an equivalent failure mechanism, however they exhibited more pronounced and widespread print layer delamination throughout the outer continuous surface.

Figure 4 shows a side-by-side comparison of C1T3 samples before and after quasi-static compression testing. The microscopic image is taken from above the sample, and focuses on the ‘trough’ between two outer continuous surface waves. The dashed arrows highlight the ‘valleys’ that contour downwards from the ‘trough’ on the left side of both images, whereas the solid arrows show the direction of the contour that rises up to the outer surface edges. It can be seen in Fig. 4 that the printed layers have significantly bulged throughout compression. This is notable as

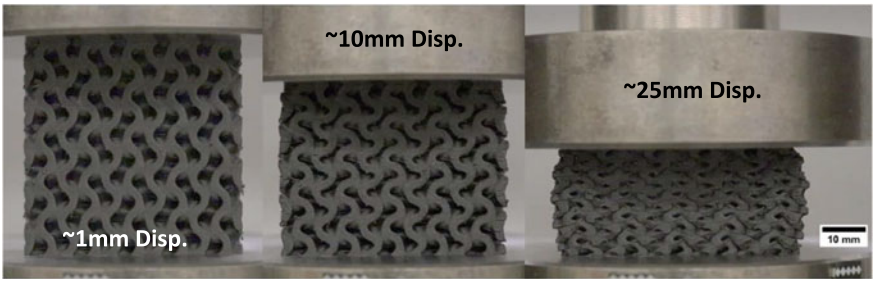

Fig. 3 C2T3-2 under quasistatic compression at varying displacements

it helps to understand how the colorFabb PA-CF polymer composite gyroid TPMS structure behaved, particularly for samples with greater surface thickness, such as T2 and T3 treatments. It also showed that given enough surrounding material, the printed layers deformed and bulged first, before any delamination occurred. It is this bulging behaviour that may promote isotropic deformation in the aforementioned treatments, as the continuous surface is predominately compressing not through print layer delamination and buckling failure, but instead by compacting the print layers which in turn causes the cell layers to deform and collapse. This also helps to explain why C2 treatments saw increased bulging during compression, as there were less internal voids to fill due to the reduced cell size, forcing material to the outer extremities of the sample.

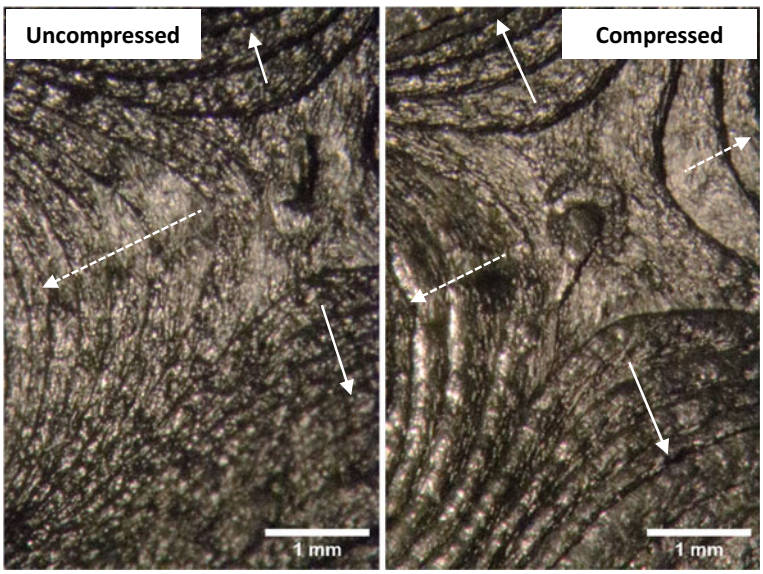

Fig. 4 Microscopic images of an uncompressed, and compressed C1T3 sample

Gyroid TPMS lattice structures manufactured from PA-CF carbon fibre reinforced nylon, with 10 mm cell size and 2 mm surface thickness (C2T2), yielded the best specific energy absorption (SEA) from the different geometries tested. The PA-CF 3D truss lattice structures explored by Niutta et al. [2] achieved a maximum SEA of 7.53 J/g, which significantly outperforms traditional 2D lattice structures. Yin et al. [4] reported an SEA value of 20.04 J/g for gyroid TPMS structures manufactured using a SLM 3D printer from 316 L stainless steel. The C2T2 treatment explored in the current study achieved an impressively high SEA value of 13.06 J/g ($\pm$ 0.15), outperforming PA-CF 3D truss structures, and approaching SEA values achieved by 316 L stainless steel gyroid samples.

The C2T2, and both T3 geometries were found to compress isotopically, and responded to quasi-static compression similarly to a foam. This characteristic is very desirable as it means that the structure exhibits behaviour similar to a spring, in which it requires an increasingly high amount of force to compress the structure throughout its plastic deformation region.

Gyroid TPMS lattice structures have considerable potential for application as energy absorbing structures in the automotive industry. For an automobile crash structure to function successfully, it must be able to provide a crumple zone to absorb kinetic energy and lower the acceleration pulse during an accident. It must also be compact, lightweight, and cost effective—to not adversely impact vehicle performance or affordability. To accommodate a wide range of collision scenarios, a crash structure should have zones designed to deal with different magnitudes of impact energy. It was seen in this study that varying the cell size, and/or continuous surface thickness, of PA-CF gyroid TPMS structures yielded highly efficient, lightweight energy absorbers capable of performing extremely well in a variety of impact scenarios. The self-supporting nature of the structure further enhances its applicability, as manufacturing difficulty and variability is reduced when using inexpensive FDM 3D printing methods.

Conclusion

Schoen's Gyroid TPMS lattice structures manufactured from carbon fibre reinforced nylon (PA-CF) were shown to have large specific energy absorption (SEA) capacity. Varying either the continuous surface thickness, or unit cell size, significantly influenced the performance of the structure. The interaction between surface thickness and cell size was also highly significant in affecting SEA. A gyroid TPMS structure with a cell size of 10 mm, and a continuous surface thickness of 2 mm was found to perform the best, achieving a SEA value of 13.06 J/g. This exceeds reported specific energy absorption capacity of both traditional 2D lattice structures and 3D truss geometries made from PA-CF and approaches that are of SLM printed 316 L stainless steel.

Some of the gyroid TPMS lattice geometries were shown to compress isotopically, and respond to quasi-static compression similarly to a foam, so that as the structure is compressed, more energy is required to compress it further. PA-CF was well suited to the application, yielding repeatable, high strength, yet lightweight samples that were easy to manufacture. The observed compressive behaviour means that gyroid TPMS lattice structures have considerable potential for application as energy absorbers in automobile crash structures.

Acknowledgements N. Cresswell would like to acknowledge the Australian Government Department of Defence for providing the Defence Civilian Undergraduate Scholarship program which supports his studies.

References

1. Vangi D (2020) Structural behavior of the vehicle during the impact. In: Vehicle collision dynamics—analysis and reconstruction. Butterworth-Heinemann, p 1–27
2. Niutta CB, Ciardiello R, Tridello A (2022) Experimental and numerical investigation of a lattice structure for energy absorption: application to the design of an automotive crash absorber. Polymers 14(6):11160. https://doi.org/10.3390/polym14061116
3. Sokollu B, Gülcan O, Konukseven EI (2022) Mechanical properties comparison of strut-based and triply periodic minimal surface lattice structures produced by electron beam melting. Addit Manuf 60:103199. https://doi.org/10.1016/j.addma.2022.103199
4. Yin H, Liu Z, Dai J, Wen G, Zhang C (2020) Crushing behavior and optimization of sheet-based 3D periodic cellular structures. Compos Part B 182:107565. https://doi.org/10.1016/j.compositesb.2019.107565
5. Peng C (2022) Novel lattice structures based on triply periodic minimal surfaces. Royal Melbourne Institute of Technology—Research Repository. https://researchrepository.rmit.edu.au/esploro/outputs/doctoral/Novel-lattice-structures-based-on-triply/9922198113301341. Accessed 5 Sept 2023
6. Yin H, Zhang W, Zhu L, Meng F, Liu J, Wen G (2023) Review on lattice structures for energy absorption properties. Compos Struct 304(1):116397. https://doi.org/10.1016/j.compstruct.2022.116397
7. ISO 844:2021: Rigid cellular plastics—determination of compression properties (2021). https://www.iso.org/standard/73560.html. Accessed 20 Aug 2023
8. ASTM D1621-16: Standard test method for compressive properties of rigid cellular plastics (2016). https://www.astm.org/d1621-16.html. Accessed 21 Aug 2023
9. Miralbes R, Ranz D, Pascual FJ, Zouzias D, Maza M (2020) Characterization of additively manufactured triply periodic minimal surface structures under compressive loading. Mech Adv Mater Struct 29(13):1841–1855. https://doi.org/10.1080/15376494.2020.1842948
10. Banjo AD, Agrawal V, Auad ML, Celestine A-DN (2022) Moisture-induced changes in the mechanical behavior of 3D printed polymers. Compos Part C 7:100243. https://doi.org/10.1016/j.jcomc.2022.100243
11. Xing Y, Sun D, Zhang M, Shu G (2023) Crushing responses of expanded polypropylene foam. Polymers 15(9):2059. https://doi.org/10.3390/polym15092059
12. Yang E, Leary M, Lozanovski B, Downing D, Mazur M, Sarker A, Khorasani AM, Jones A, Maconachie T, Bateman S, Easton M, Qian M, Choong P, Brandt M (2019) Effect of geometry on the mechanical properties of Ti-6Al-4V gyroid structures fabricated via SLM: a numerical study. Mater Des 184:108165. https://doi.org/10.1016/j.matdes.2019.108165

Microwave-Assisted Reduction Behaviors of Spent Cathode Material with Biochar

Zhongxiao Qin, Jinxiang You, Mingjun Rao, Xin Zhang, Jun Luo, and Zhiwei Peng

Abstract The production of spent lithium-ion batteries (LIBs) is expected to increase rapidly with the rapid development of new energy vehicles. Without proper disposal, the spent LIBs will cause a waste of resources and a threat to the environment. The route of carbothermal reduction followed by magnetic separation has been proven to be an efficient process to recover valuable metals from spent LIBs. This paper investigated the reductive roasting behaviors of the spent cathode material under microwave-assisted reduction using biochar as the reductant. Experimental results show that the chemical phases of spent cathode material were converted into Ni-Co alloy, MnO and Li_2CO_3, wherein Li_2CO_3 can be extracted by water leaching, and the Ni-Co alloy can be recovered by magnetic separation.

Keywords Spent cathode material · Microwave-assisted reduction · Biochar · Lithium

Introduction

Lithium-ion batteries (LIBs) are an excellent and efficient energy storage medium that have been widely used in many fields, such as consumer electronics, electric vehicles, and renewable energy. With the rapid expansion of the new energy vehicle market, the consumption and demand for lithium batteries are increasing yearly [1]. It is estimated that by 2025, China's discarded power lithium batteries will reach 134.5 GWh. Waste lithium-ion batteries contain metals such as Li, Ni, Co, Mn, etc. [2]. If not properly treated, they will cause pollution and damage to the natural environment, such as soil and water quality. Disposing and recycling of spent lithium batteries is becoming a crucial research topic. The valuable elements in spent LIBs are mainly concentrated in the positive electrode materials [3, 4].

Z. Qin · J. You · M. Rao (✉) · X. Zhang · J. Luo · Z. Peng
School of Minerals Processing and Bioengineering, Central South University, Changsha 410083, Hunan, China
e-mail: mj.rao@csu.edu.cn; raomingjun2003@126.com

Z. Peng et al. (eds.), *Characterization of Minerals, Metals, and Materials 2024*, The Minerals, Metals & Materials Series, https://doi.org/10.1007/978-3-031-50304-7_29

The current recycling methods mainly include pyrometallurgical, hydrometallurgical, and bioleaching processes. The pyrometallurgical process is conducted at high temperatures, where the material is melted as Cu, Co, Ni and Mn alloy, while Li and Al remain in the slag. The high temperature causes a large amount of Li to evaporate into the flue gas, wasting Li resources [5]. The hydrometallurgical process leaches all elements indiscriminately, and the subsequent separation and purification process consumes a large amount of acid, accompanying environmental issues. Bioleaching has the disadvantages of a long leaching cycle and being able to extract a target element.

As a high-frequency electromagnetic wave, the microwave has a wavelength of 1mm–1m and a frequency generally between 300 MHz and 300 GHz. Under microwave radiation, the direction of the external electric field, positive and negative poles, can change rapidly, thereby promoting the polarization of molecules between the media [6, 7]. Biochar is a common waste and the most promising renewable energy source with good absorption performance. It can be coupled with microwave heating to achieve low-temperature reduction [8]. In this study, the reduction behavior of biochar on the spent cathode material was investigated at different temperatures with microwave radiation, and the changes in phase and magnetism at different temperatures were investigated.

Materials and Methods

Materials

The pouch cell is discharged using a discharge module. Afterward, it is dismantled, and the cathode material electrolyte is washed with Dimethyl carbonate (DMC). The negative electrode material is separated from the battery separator and packaged separately. Finally, the positive electrode material on the aluminum current collector is scraped off. The chemical composition of the obtained positive electrode material is shown in Table 1.

Table 1 Elemental composition of cathode material (wt.%)

Li	Ni	Co	Mn	Al
7.39	29.70	12.21	16.79	0.15

Methods

The mixture of spent cathode material and 20% biochar was pressed into cylinders with a diameter of 5 mm and a height of 5 mm. The microwave furnace is heated to the target temperature and pure N_2 is introduced. The cylinders were put into a horizontal microwave tube furnace for roasting. After roasting, the roasted sample is cooled to room temperature and collected for XRD inspection and hysteresis loop testing.

Microwave Absorption Capability Analysis

The coaxial waveguide method determined the microwave absorption characteristic of the cathode material powder. The cathode material powder and paraffin were mixed with a mass ratio 7:3 and molded for the test. The parameters of complex relative permittivity and permeability were determined using a vector network analyzer. Based on the results, the microwave penetration depth D_p can be calculated from the following equation:

$$D_p = \frac{\lambda_0}{2\sqrt{2}\pi}\left\{\varepsilon_r''\mu_r'' - \varepsilon_r'\mu_r' + \left[(\varepsilon_r'\mu_r')^2 + (\varepsilon_r''\mu_r'')^2 + (\varepsilon_r'\mu_r'')^2 + (\varepsilon_r''\mu_r')^2\right]^{\frac{1}{2}}\right\}^{-\frac{1}{2}} \tag{1}$$

where λ_0 is the microwave wavelength in free space, m; ε_r' and ε_r'' are the real and imaginary parts of the complex relative permittivity of the sample; μ_r' and μ_r'' are magnetic loss and magnetic loss factors, respectively, indicating relative permeability

Characterization

The chemical composition of the cathode material is analyzed by an inductively coupled plasma optical emission spectrometer (ICP-OES, Optima, 5300 DV, USA). The mineral phases were analyzed by X-ray diffraction (XRD, D/Max 2500, RIGAKU, Japan). A vibrating sample magnetometer determined the saturation magnetization of roasted samples (VSM, LakeShore7404, USA). The electromagnetic properties were determined by vector network analyzers using the coaxial waveguide method.

Results and Discussion

Electromagnetic Properties

Generally, ε_r' and μ_r' represent the ability of a material to store microwave electric energy and magnetic energy, respectively, while ε_r'' and μ_r'' reflect the ability to convert electric and magnetic energy into thermal energy. Figure 1a–c shows the electromagnetic characteristics of the cathode material, biochar, and the mixture of the cathode material and biochar (cathode material and 20% biochar) varied with frequency, respectively. Compared with the cathode material, biochar presents an excellent microwave response. The relative permittivity is much higher than the relative permeability, suggesting the dominant contribution of dielectric loss in microwave heating. When the cathode material was mixed with 20% biochar, the electromagnetic properties of the mixture slightly changed. Figure 1d displays the penetration depth of the cathode material, biochar and the mix of the cathode material and biochar in the frequency range of 2–4 GHz. It is evident that the microwave penetration depth of the biochar changed slightly with the frequency and was only about 3 mm, due to its strong microwave absorbing property. The calculated microwave penetration depth of the cathode material generally decreased with the increase in frequency and was about 17 mm at the frequency of 2.45 GHz. When the cathode material was mixed with 20% biochar, the microwave penetration depth was much higher than that of the cathode material, but slightly lower than that of the biochar. The microwave penetration depth of the mixture was about 13 mm at the frequency of 2.45 GHz, demonstrating that the appropriate size of the sample was 13–15 mm.

Thermodynamic Analysis

Reduction roasting mainly involves the phase transformation of metal oxides. The possible chemical reactions and corresponding fitting $\Delta_r G^{\theta} - \mathrm{T}$ functions are shown in Table 2 and Fig. 2, respectively. There are currently no thermodynamic data for $LiNi_xCo_yMn_zO_2$. According to the literatures, ternary anode materials are first thermally decomposed into the corresponding metal oxides during the reduction roasting process, and the change of the standard Gibbs free energy with temperature of the chemical reaction (1)–(8) is calculated by the thermodynamic software FactSage 8.1. The standard Gibbs free energy of the reactions (1, 2, 3, 4, 5 and 8) is negative over the temperature range, indicating that the nickel oxide and cobalt oxides were reduced into metallic nickel and metallic cobalt, and the lithium would be converted into lithium carbonate. The standard Gibbs free energy change for the reaction (6 and 7) is positive over the temperature range, indicating that MnO and Li_2O are thermodynamically difficult to reduce into Mn and Li.

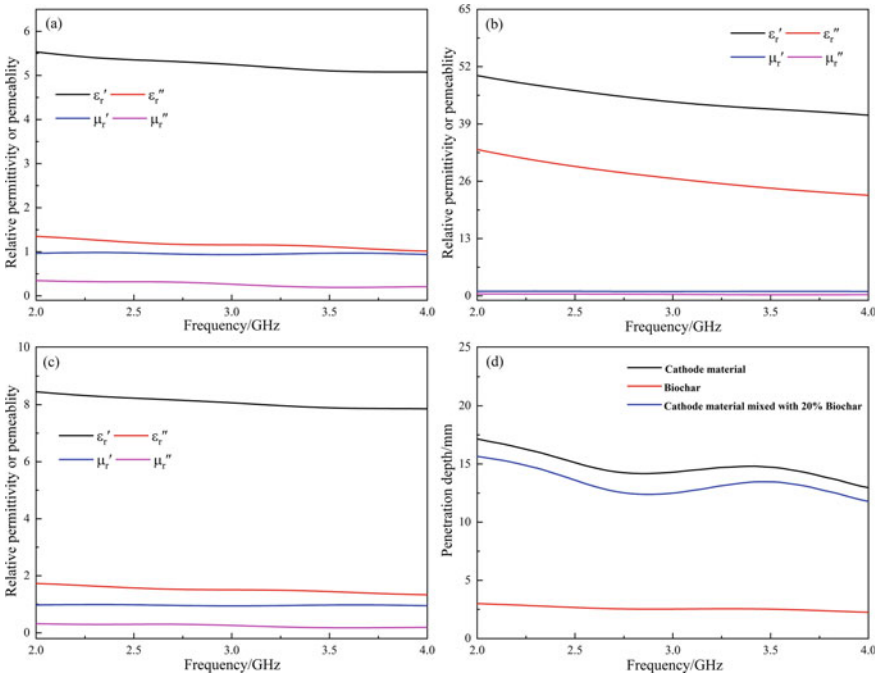

Fig. 1 Electromagnetic properties of the **a** cathode material, **b** biochar, **c** mixture of cathode material and 20% biochar, and **d** the calculated corresponding microwave penetration depth

Table 2 Possible chemical reactions and their corresponding $\Delta_r G^{\theta}{}_m$-T relations during reductive roasting

Eqs	Chemical reactions	$\Delta_r G^{\theta}{}_m - T$ (kJ/mol^{-1})
(1)	$2NiO + C{=}2Ni + CO_2(g)$	$79.62016 - 0.17523T$
(2)	$2Co_3O_4 + C{=}6CoO + CO_2(g)$	$10.01046 - 0.33332T$
(3)	$2CoO + C{=}2Co + CO_2(g)$	$75.47512 - 0.14396T$
(4)	$3MnO_2 + C{=}Mn_3O_4 + CO_2(g)$	$-232.15315 - 0.18968T$
(5)	$2Mn_3O_4 + C{=}6MnO + CO_2(g)$	$69.32207 - 0.25504T$
(6)	$2MnO + C{=}2Mn + CO_2(g)$	$375.13213 - 0.14828T$
(7)	$2Li_2O + C{=}4Li + CO_2(g)$	$812.10756 - 0.2743T$
(8)	$Li_2O + CO_2(g){=}Li_2CO_3$	$-257.63632 + 0.07712T$

Reductive Roasting Behavior

Figure 3 shows the XRD patterns of the roasted samples under different roasting temperatures. The roasted samples were composed of nickel (Ni), cobalt (Co),

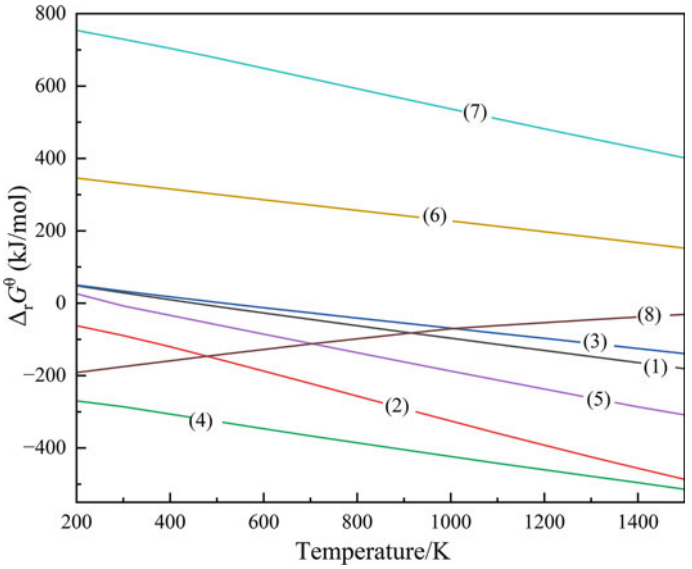

Fig. 2 The calculated standard Gibbs free energy variation with the temperature

manganosite (MnO), and zabuyelite (Li_2CO_3), which is consistent with the thermodynamic results. And the phase composition of the roasted samples slightly changed with the increasing roasting temperature.

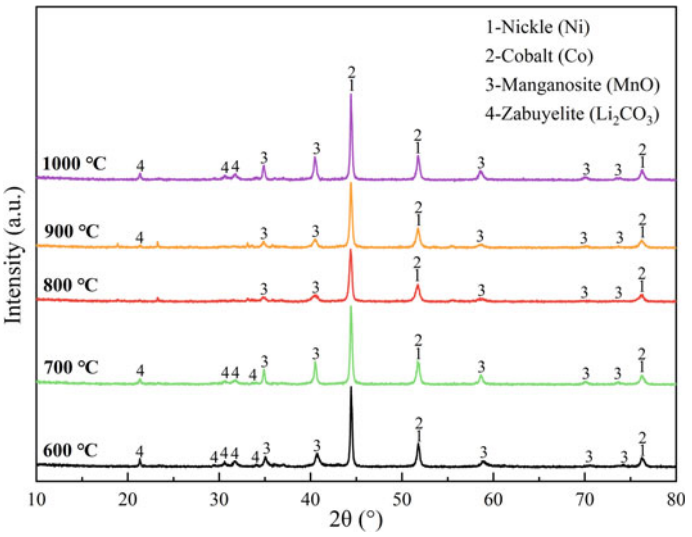

Fig. 3 XRD patterns of the roasted sample at different temperatures

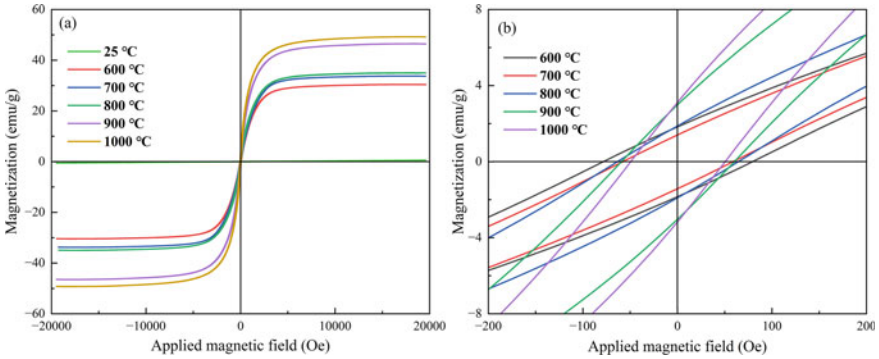

Fig. 4 Hysteresis loops (**a**) and coercivity (**b**) of the roasted sample at different temperatures

The magnetization property of the roasted samples at different roasting temperatures is shown in Fig. 4. Figure 4a shows the hysteresis loops of the roasted samples under different roasting temperatures. The hysteresis loops totally presented soft magnetic characteristics, high magnetic permeability and low coercivity. The saturation magnetism of roasted samples gradually increased with the roasting temperature. The saturation magnetism of the starting materials (cathode material and 20% biochar) at 2 °C is only 0.55 emu/g, indicating that the cathode material is almost non-magnetic. Then, the saturation magnetism rapidly increased to 30.37 emu/g, when roasting at 600 °C for 60 min. Since the nickel and cobalt oxides were reduced into Ni-Co alloy, the magnetism of the sample increased. The saturation magnetism of the roasted samples increased from 30.37 emu/g to 49.18 emu/g with the roasting temperature increasing from 500 to 1000 °C. The coercivity of the roasted samples decreased gradually with the increasing temperature (Fig. 4b).

Conclusions

Compared with the cathode material, biochar presents an excellent microwave absorbing property. When the spent cathode material was mixed with 20% biochar, the microwave penetration depth of the mixture was about 13 mm at a frequency of 2.45 GHz. Reductive roasting results display that the cathode material is converted into Ni–Co alloy, MnO and Li_2CO_3 after reduction, which is consistent with the results of thermodynamic analysis. The magnetism of the roasted samples gradually increased with the increasing temperatures, while the coercivity exhibited a downward trend. MnO and Ni–Co alloy could be well magnetically separated, and Li_2CO_3 could be extracted by water leaching.

Acknowledgements This work was financially supported by the National Natural Science Foundation of China (No. 52174288).

References

1. Yu W, Guo Y, Shang Z, Zhang Y, Xu S (2022) A review on comprehensive recycling of spent power lithium-ion battery in China. J Etran. 11:100155. https://doi.org/10.1016/j.etran.2022.100155
2. Zhao Y, Yuan X, Jiang L, Wen J, Wang H, Guan R, Zhang J, Zenga G (2020) Regeneration and reutilization of cathode materials from spent lithium-ion batteries 383:123089. https://doi.org/10.1016/j.cej.2019.123089
3. Leal VM, Ribeiro JS, Coelho ELD, Freitas MBJG (2023) Recycling of spent lithium-ion batteries as a sustainable solution to obtain raw materials for different applications 79:118–134. https://doi.org/10.1016/j.jechem.2022.08.005
4. Chen X, Wang Y, Li S, Jiang Y, Cao Y, Ma X (2022) Selective recycling of valuable metals from waste $LiCoO_2$ cathode material of spent lithium-ion batteries through low-temperature thermochemistry 434:13454. https://doi.org/10.1016/j.cej.2022.134542
5. Makuza B, Tian Q, Guo X, Chattopadhyay K, Yu D (2021) Pyrometallurgical options for recycling spent lithium-ion batteries: a comprehensive review 491:229622. https://doi.org/10.1016/j.jpowsour.2021.229622
6. Zhao Y, Liu B, Zhang L, Guo S (2020) Microwave-absorbing properties of cathode material during reduction roasting for spent lithium-ion battery recycling 384:121487. https://doi.org/10.1016/j.jhazmat.2019.121487
7. Liang GQ, Zhang JL, Liu H, Xu W, Yang C, Chen YQ, Wang CY (2023) Microwave-assisted sulfation method for lithium recovery from spent $LiNixCoyMnzO_2$ cathode material: process intensification and conversion mechanism. ACS Sustain Chem Eng 11(34):12484–12493. https://doi.org/10.1021/acssuschemeng.3c00343?urlappend=%3Fref%3DPDF&jav=VoR&rel=cite-as
8. Li Y, Xia G, Xia Y (2015) Recovery of Co, Mn, Ni, and Li from spent lithium ion batteries for the preparation of $LiNi_xCo_yMn_zO_2$ cathode materials 41:11498. https://doi.org/10.1016/j.ceramint.2015.05.115

Part VIII
Poster Session

Characterisation of 3D-Printed Auxetic Structures Under Low Velocity Blunt Force Impact for the Minimisation of Traumatic Brain Injury in Sport

Gracie Jeffrey, Jianshen Wang, Ali Ameri, Paul Hazell, Hongxu Wang, and Juan Pablo Escobedo-Diaz

Abstract The present study evaluates the suitability of 3D-printed PETG Double Arrowhead (DAH) auxetic structures for increased impact resistance of soft-shell headgear and decreased probability of Mild Traumatic Brain Injury (MTBI), during head-to-ground impacts in sport. A suitable structure should at minimum withstand 30 impacts at 100% likelihood of concussion and reliably absorb 15 J of energy from a 32 J impact to decrease the probability of MTBI from 100% to ~ 25% with less than 2% total plastic deformation. The peak force, peak acceleration, absorbed energy and cumulative damage of three distinct DAH auxetic structures were analysed by quasi-static compression and low velocity blunt force impact tests. The results of this experiment will aid the development of a new headgear technology which reduces the frequency of head trauma as a result of blunt force impact. This decreases the incidence of long-term effects induced by MBTIs.

Keywords Concussion · Auxetic structures · Additive manufacturing · PETG

Introduction

Prevailing soft-shell polyethylene foam headgear, developed for use in Rugby and Australian Rules Football (AFL) has been extensively proven to be ineffective in reducing the occurrence of Mild Traumatic Brain Injuries (MTBIs) [1–3]. With MTBIs accounting for approximately 25% and 23% of Rugby and AFL injuries, respectively [1, 4]. As a result, there are on average 3000 hospitalised MTBIs annually in Australia [1]. Despite this gap in commercially available technology, and the recent realisation on a global front of the long-term effects of repeated concussion, there has been limited visual progress in Australia to develop an improved device. In

G. Jeffrey · J. Wang · A. Ameri · P. Hazell · H. Wang · J. P. Escobedo-Diaz (✉)
School of Engineering and Information Technology, ZEIT4500/4501, The University of New South Wales at the Australian Defence Force Academy, Campbell ACT, Australia
e-mail: j.escobedo-diaz@unsw.edu.au

Z. Peng et al. (eds.), *Characterization of Minerals, Metals, and Materials 2024*, The Minerals, Metals & Materials Series, https://doi.org/10.1007/978-3-031-50304-7_30

2019 N-Pro Australia patented a new viscoelastic foam soft-shell headgear, which claims to absorb 75% more energy than existing polyethylene foam headgear [5]. Although, there is no publicly available experimental validation (as of May 2023). Literature attempts to bridge the performance gap by suggesting increased foam density and thickness, however, has succumbed to the conclusion that to solve the issue effectively and reliably, a different approach is required [2, 6].

The ground-breaking invention of auxetic structures in the early 1980s, exposed the possibility of designing structures with a Negative Poisons Ratio (NPR) [7] [8]. The manifestation of negative strain ratios causes auxetic structures to contract where conventional structures would otherwise expand under the same conditions. This gives auxetics exceptional stiffness per unit mass in addition to "high shear strength; high tensile strength; high compressive strength and high energy absorption" [9]. Due to their unique inherent mechanical response and intrinsic ability to attenuate impact, auxetics have thereafter been increasingly analysed for their application to personal protective equipment. Recent experiments focus on differentiating the inherent mechanical properties of the three most developed auxetics; re-entrant, arrowhead and anti-tetra chiral structures. NPR, energy absorption and compressive strength analysis in literature concluded that the arrowhead geometry has greatest potential for application to impact attenuating protective equipment at low velocities, due to its increased energy absorption in comparison to the re-entrant and anti-tetra chiral geometries [9].

The focus of existing auxetic literature is limited to the theoretical and finite element modelling of the strain behaviour of auxetic structures, with additional and modified ligaments. Some studies investigate the energy absorption capacity of cellular sandwich auxetics through destructive testing but fail to measure cumulative damage or verify the effects on performance of multiple impacts. Additionally, literature lacks experimental verification of the effects on energy absorption of scaling optimised geometry [10]. Furthermore, there is no known design for auxetic soft-shell headgear or any soft-shell headgear for that matter, which has been experimentally verified to reduce the probability of MTBI. The present study aims to bridge this gap by analysis of the cumulative damage of small scale auxetic structures and their ability to maintain peak energy absorption, with negligible plastic deformation ($< 2\%$) over repeated impact.

The biomechanics of concussion are crucial in defining the impact parameters and design specifications of the headgear. The definition of concussion varies greatly amongst biomedical literature, due to the wide range of symptoms and disparity in medical indicators of mild concussive injuries [11]. From this arises the capstone quandary in biomedical literature; identifying the principal variables which express the threshold for concussion, known as injury indices. These injury indices provide mathematical models which calculate when concussion will occur based on scenario dependent parameters such as, peak linear acceleration; peak angular acceleration; closing speed; impact power; impact energy; relative velocity and impact duration. The energy requirements for testing the performance of a headgear design are dictated by injury indices. Thus, it is crucial to the validity and accuracy of the experimental procedure, that the most accurate injury indices are chosen.

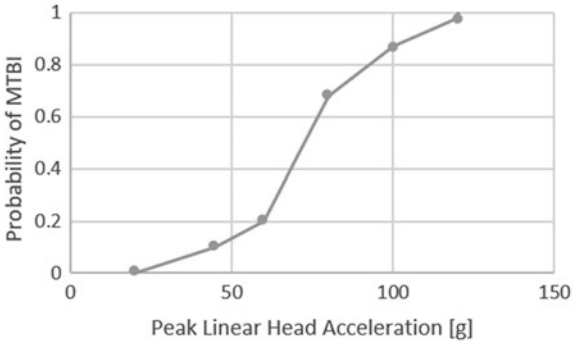

Fig. 1 Combined HIE data, probability of MTBI against peak linear acceleration

The most thoroughly developed injury indices are Head Impact Energy (HIE), Head Injury Criterion (HIC), Head Impact Telemetry System (HITS), and Head Impact Power (HIP) and have been thoroughly investigated in literature. Literature indicates no correlation between closing speed or change in linear head velocity and concussion and weak correlation for peak angular acceleration thus HIC was excluded from the present study as a viable injury index. There was disagreement among literature over the significance of impact duration and peak linear acceleration (Gadd Severity Index and HIE) until the establishment of the—2LLR model by Newman [12]. Whilst the model is still in development, it shows promising candidacy for prediction of MTBI, producing risk curves with close correlation to those produced by Kajatz [13], Funk [14] and Pellman [15]. Newman [12, 16] concluded that the injury indices with the highest significance are GAMBIT and HIP, both of which are described by angular and linear acceleration. Unfortunately, the present study is limited to linear acceleration tests by available testing facilities and resources, as a Hybrid III headform or similar would be required to run angular experiments of this nature, accurately and efficiently. Therefore, linear acceleration (HIE) will be used, which literature agrees [12, 16, 17] is the next most significant injury index. Injury index data for linear peak resultant acceleration was collated from multiple sources [12–15] yielding the risk curve in Fig. 1. From this, the energies at which headgear should protect against to decrease the likelihood of concussion can be derived.

Auxetic Structure Design

Current International Rugby Board (IRB) regulations limit the design of headgear by excluding the use of sandwich constructions and dictating a maximum foam thickness of 20 mm [19]. Additionally, it is stipulated that personal protective equipment may not be of 'rigid nature'. As such, the specimens are 16 mm ± 1 mm high with 2 mm thick polyethylene foam sheets on the top and bottom to comply with the thickness and rigidity restrictions. The specimens were designed with a 0.7 mm top and bottom flat plate to ensure the load is applied evenly and to allow a flat surface for the foam

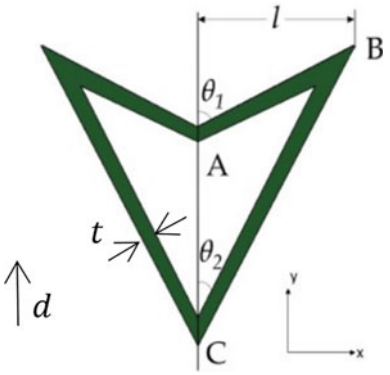

Fig. 2 Unit cell geometry of a DAH auxetic [18]. *Note* *d* is the depth into the page

sheeting to be adhered. It is noted that this will be a sandwich structure and as it stands, would not be readily accepted for use in Rugby or AFL without alteration to the rules [19].

The structure used in this study is a 2-Dimensional Double Arrowhead (DAH) auxetic with unit cell geometry described by Fig. 2. A 2D DAH structure will be used rather than a 3D DAH because it has been theoretically and experimentally validated to exhibit a favourable mechanical response and failure mechanism under low velocity impact. In contrast, the 3D DAH has increased complexity, is more prone to nodal failure and has limited experimental validation under similar conditions [20–22]. Of the studies which produced topological optimisation values, three with FEM and experimental validation were chosen for replication in the present study, DAH.1, DAH.2 and DAH.3. Where DAH.1 is analogous to the topological optimisation designed by Boopathi [23] with unit cell geometry at 5:3 scale of that proposed in the study (Table 1). DAH.2 is approximately 2:1 of the geometry proposed by the Francisco [18] optimisation and DAH.3 is a variation of the DAH.2 geometry with an increased wall thickness (Table 1). The overall geometry of each structure will be approximately 30 × 50 × 16 mm ± 5% which correlates to DAH.1, DAH.2 and DAH.3 having 6 × 2, 5 × 3 and 4 × 2 unit cells in the horizontal and vertical directions, respectively.

Material Selection and Properties

In line with literature, the specimens for this experiment were manufactured out of Polyethylene Terephthalate Glycol (PETG). PETG exhibits high ductility and high energy absorption capacity. Due to its ductility, PETG shows signs of plastic deformation after a greater strain rate in comparison to less ductile filaments such as PLA [24]. ABS shows comparable energy absorption however, PETG can withstand higher energy impact and a greater amount of cyclic loading than ABS without fracturing. Additionally, ABS is sensitive to FDM processing parameters which can

Table 1 Geometrical parameters of the double arrowhead specimens

	DAH.1	DAH.2	DAH.3
Optimised unit cell geometry from literature	Boopathi Optimisation [23]: $\theta_1 = 68.62°$ $\theta_2 = 26.60°$ $l = 6.60$ mm $t = 2.2$ mm	Francisco Optimisation [18]: $\theta_1 = 66.67°$ $\theta_2 = 33.61°$ $l = 6.60$ mm $t = 1.2$ mm	Adaptation of Francisco [18]: $\theta_1 = 66.67°$ $\theta_2 = 33.61°$ $l = 6.60$ mm $t = 1.6$ mm
Scaled geometry used in this study	Scale = 3:5 $d = 30.0$ mm $t = 1.342$ mm $l = 3.874$ mm $\theta_1 = 68.20°$ $\theta_2 = 26.87°$	Scale = 1:2 $d = 30.0$ mm $t = 0.470$ mm $l = 3.874$ mm $\theta_1 = 66.67°$ $\theta_2 = 33.61°$	Scale = 1:4 $d = 30.0$ mm $t = 1.264$ mm $l = 3.874$ mm $\theta_1 = 66.67°$ $\theta_2 = 34.81°$

cause warping and inconsistencies, adding complexity to the fabrication of specimens [25]. Black Prusament PETG was used which has a documented tensile yield strength of 30 ± 5 MPa, tensile modulus of 1.4 ± 0.1 GPa, elongation at yield of 2.5 ± 0.5% and a Charpy impact strength of 5 ± 1 kJ/m^2 [26]. Since the properties of PETG are well documented by literature the present study does not re-characterise the material through tensile or Charpy testing.

Fabrication

Eighteen initial specimens (6 × DAH.1, 6 × DAH.2, 6 × DAH.3) were fabricated using a Creality Ender V2 FDM 3D-printer. The printer was enclosed by a 0.3 mm flame retardant aluminium cloth to reduce the effects of natural convection on the heated bed. The optimal processing factors for Prusament PETG to achieve maximum energy absorption as defined by literature [27, 28] were used; nozzle temperature of 240 °C; layer thickness of 0.25 mm; printing speed of 35 mm/s; raster angle 0°; raster width 0.5 mm and 80% infill of 'grid' shape [27]. The specimens as received from the 3D printer are of overall dimensions approximately 30 × 50 × 16 mm ± 5% including 0.7mm top and bottom plates.

Quasi-static Experiment Design

Quasi-Static (QS) compression testing was conducted using a Shimadzu 100 kN Universal Testing Machine (UTM) to determine the suitability of a structure prior to impact testing. The specimens were tested at a strain rate of 10^{-3} s^{-1} and corresponding crosshead velocity of 0.02 mm/s. The energy absorption, peak force and maximum displacement was determined using the force–displacement data output

from the in-built load cell. The peak linear acceleration that the structure can withstand before critical failure was calculated by dividing the peak force by the 'head' mass (5.12 kg) and correlated to a probability of concussion using Fig. 1. The output of this phase of testing was an initial determination of the hypothetical maximum impact energy and probability of concussion the specimen could theoretically support before critical failure under impact. The energy absorbed in the elastic region was calculated by doing a definite integral of the force displacement curve for each structure over its elastic range (i.e. before yielding). A unit cell geometry was determined suitable for impact testing when it successfully sustained a peak force of 3.6 kN without failure which corresponds to a peak linear acceleration of 75 g and 50% probability of MTBI. An ideal sample would withstand a peak force of 5.5 kN (110 g) before failure, which corresponds to 100% probability of MTBI employing the risk curve in Fig. 1.

Impact Experiment Design

The results of the QS testing were used to find the theoretical peak linear acceleration and impact energy which correlated to 50% and 100% probability of concussion, as discussed above. Impact energy versus probability of MTBI was derived using peak acceleration and work energy (force times displacement) data from the QS compression tests to yield a new risk curve (Fig. 3) based on Fig. 1. The impact experiments in this study allow evaluation of transmitted energy through DAH structures under a finite number of low velocity, blunt force impacts. The planned obsolescence of the headgear, for the purpose of this study, is one season or one years' worth of use. The maximum number of head impacts per player sustained at the professional level in AFL and Rugby in one season was determined to be 25.5 [2, 4, 29]. Therefore, each specimen will be impacted 30 times per test, to provide a safety factor of ~ 1.2. Since approximately 50% of impacts result in concussion, the samples tested at 100% probability of concussion will have an inherent additional factor of safety of 1.5. This implies a total factor of safety of ~ 2.7 for the specimens tested at 100% probability of concussion and ~ 1.2 for the specimens tested at 50% probability of concussion.

The impact tests will be carried out using a CEAST 9350 (optional features) drop tower, with a 4.3 kg carriage, 0.665 kg AISI 4140 cylindrical steel impactor of diameter 70 mm. The total weight of the impact tests will be ~ 6.02 kg, since the average head mass is 5.12kg the impact energy will be slightly modified to adjust for the slightly heavier impact mass, as this study aims to replicate head-to-ground impact [2]. The design and use of an impactor which more closely resembles a compact soil surface was not within the scope of this study and as such it can be assumed that the results of the study will have some inherent error. DAH.1, DAH.2 and DAH.3 were tested under two different impact energies corresponding to 50% and 100% probability of MTBI and peak linear accelerations between 75 and 110 g, respectively. These accelerations and energies were determined based on the summarised risk

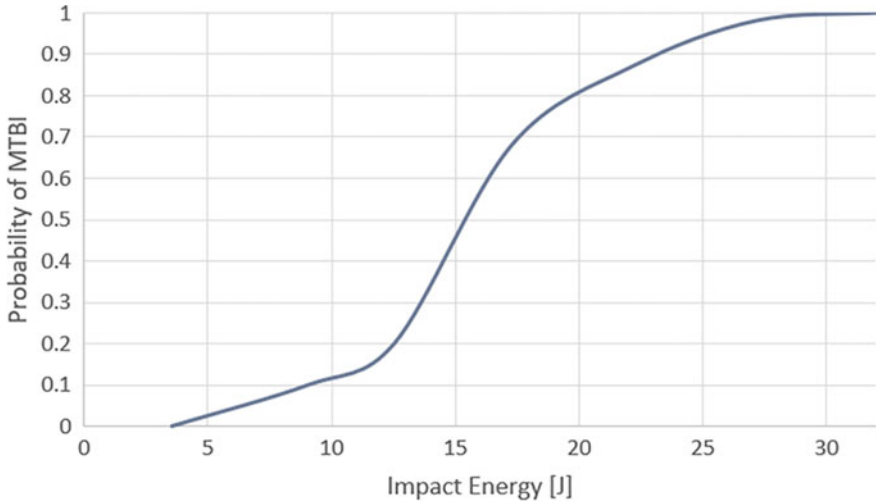

Fig. 3 Risk curve for impact energy versus the probability of MTBI derived from Fig. 8 and QS compression data

curve (Fig. 1) and the energies are extracted from QS compression data (Fig. 3) which align best with 50% and 100% likelihood of MTBI. These probabilities were determined to be optimal for testing the capacity of the auxetic to withstand the maximum and mean expected force over the expected number of impacts for a years' worth of use. It was assumed that head-to-ground impacts occur from a height of 1.75 m, the height of the average male [30] and that the average mass of head is 5.12 kg [2]. This yields a maximum impact energy of 87.9 J for a head-to-ground collision, using conservation of mechanical energy. The results of the QS testing were used to calculate specific impact energy to test at for 50% and 100% probability of MTBI. A suitable structure should at minimum withstand 30 impacts at 100% likelihood of concussion and reliably absorb 15 J of energy from a 32 J impact (Fig. 3) to decrease the probability of MTBI from 100% to ~ 25% with less than 2% plastic deformation.

Quasi-static Compression Results

DAH.1 withstood the largest average peak force of the three geometries in QS compression, with a peak force of approximately 10.5 kN ± 1% prior to plastic deformation. DAH.2 exhibited an average peak force of 1.1 kN ± 16% while DAH.3 had an average 9.4 kN ± 1%. DAH.1 absorbed an average of 11.4 J ± 8% of energy in the elastic region prior to failure while DAH.2 and DAH.3 absorbed 1.6 J ± 14% and 10 J ± 8%, respectively. Despite the decrease in absorbed energy between DAH.1 and DAH.3, DAH.3 was observed to have a slightly higher average peak displacement. DAH.3 had an average peak displacement of 5.6 mm ± 2% while

the average peak displacements for DAH.1 and DAH.2 were observed as 5.1 mm ± 4% and 4.2 mm ± 3%, respectively. The force versus crosshead displacement results from the QS compression tests for each of the three unit cell geometries, exhibit a similar non-linear elastic region prior to reaching yielding point, which was consistent for all nine samples tested. The mechanical response of DAH.1 and DAH.3 were similar however, DAH.1 displayed a larger plateau in force in the initial plastic region prior to densification (Fig. 4). Despite the fundamentally equivalent unit geometries of DAH.2 and DAH.3 the mechanical response of the two structures varied greatly. DAH.3 withstood considerably more force prior to plastic deformation (Fig. 4) where DAH.2 and DAH.3 consistently yielded at a peak force of 1.1 kN and 9.4 kN, respectively. Consistent with literature [10] there was minimal fracturing at any point of the specimens with the thicker ligaments; DAH.1 and DAH.3. The main cause of failure of DAH.1 and DAH.3 was elastic buckling at the midpoint between the nodes, see Fig. 5. This aligns with the hypothesis that PETG DAH structures are more prone to ductile failure over brittle failure in compression [27]. In contrast, the mode of failure for DAH.2 was brittle failure at the nodes (Fig. 6).

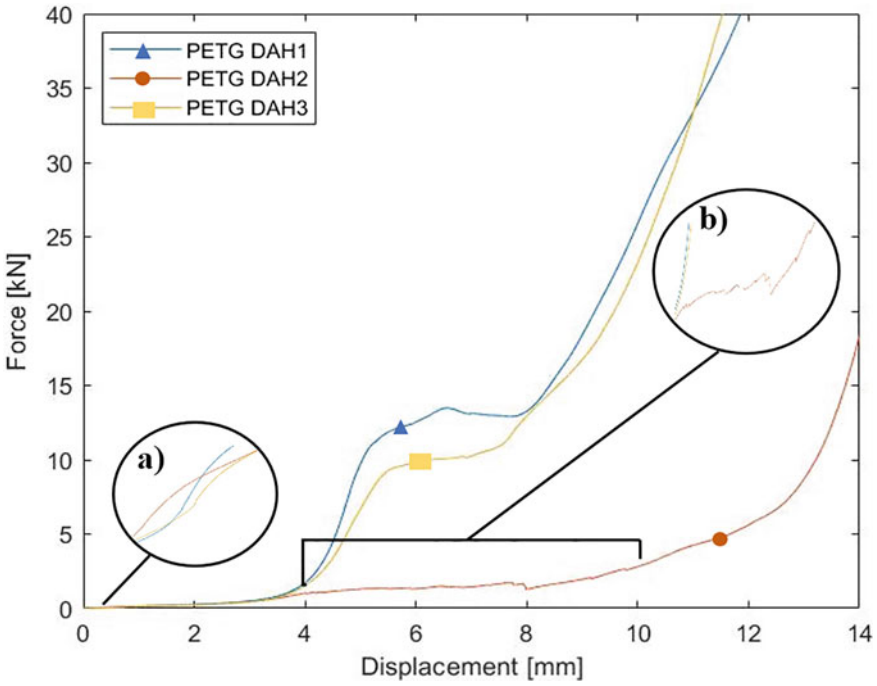

Fig. 4 QS compression average force versus average displacement for three data sets for each geometry (DAH.1-DAH.3). **a** Initial densification region of foam sheeting. **b** brittle fracture of DAH.2

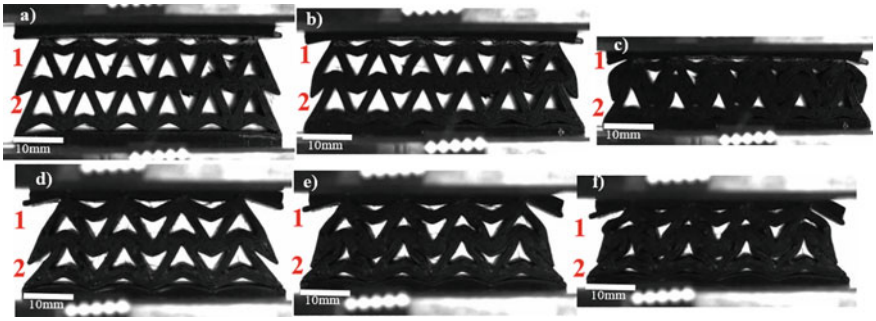

Fig. 5 DAH.1 (**a**–**c**) and DAH.3 (**d**–**f**) QS compression failure modes. **a**, **d** Initial compression, volume reduction in level 1 unit cells. **b**, **e** Volume reduction continues as level 1 unit cells compress over level 2 unit cells. **c**, **f** Densification begins after reaching yield

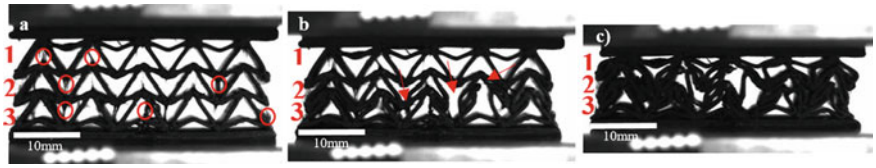

Fig. 6 DAH.1 QS compression failure modes. **a** Initial compression, volume reduction in level 1 and 2 unit cells. **b** Volume reduction continues stress concentration cause nodal failure (arrows). **c** Brittle failure at nodes continues until densification ensues. Note: circles indicate print inconsistencies (stringing)

It was observed that the 2 mm foam on the top and bottom of the specimens densified initially prior to elastic deformation of the auxetic. This can be seen in Fig. 4 as the initial slope which occurs at around 0.5mm displacement. The specimens were compressed until no gaps larger than 3 mm were visible. It was observed that there was limited elasticity in the PETG specimens as they did not appear to have any significant elastic recovery after unloading. There was a 12.4 mm ± 2%, 9.7 mm ± 4% and 6.8 mm + /2% reduction in height for DAH.1, DAH.2 and DAH.3 respectively. This was coupled with a 11.2 mm ± 2%, 4.5 mm ± 4% and 7.5 mm ± 2% increase in width for DAH.1, DAH.2 and DAH.3, respectively.

Impact Results

All three DAH structures exhibited significant plastic deformation for impacts of 32 J corresponding to 100% probability of concussion. DAH.1, DAH.2 and DAH.3 all consistently failed on the first impact at 32 J and as such no subsequent drop tests at 32 J were performed. DAH.1 experienced the largest maximum displacement at 32J (Fig. 7) measuring 9.63 mm ± 4% with DAH.3 closely following with a

maximum displacement of 8.16 mm ± 2%. DAH.2 had the smallest peak displacement measuring 5.35 mm ± 3% (Fig. 7). DAH.1, DAH.2 and DAH.3 exhibited brittle failure under 32 J with the main deformation localisation occurring at the nodes between unit cells (Figs. 8, 9 and 10). DAH.1 was observed to absorb the largest amount of energy prior to plastic deformation absorbing 6.7 J ± 8% of the 32 J impact. While DAH.3 elastically absorbed 3.1 J ± 8% and DAH.2 absorbed 0.9 J ± 14% of the 32J impact. The peak force and peak linear acceleration fluctuated between 8–12 kN and 175–200 g respectively for an impact energy of 32 J, corresponding to 100% probability of concussion. DAH.1 successfully withstood 30 impacts at 9.3 J without significant elastic buckling or brittle nodal fracture while DAH.3 experienced brittle failure at the nodes after 16 impacts and DAH.2 fractured on initial impact. With total lateral deformation of auxetic unit cells less than 1%. DAH.1 and DAH.3 both exhibited an initial increase in peak force and peak linear acceleration after the first impact, peaking at 10 impacts and then decreasing again and plateauing after 25 impacts (Fig. 11). The peak force and peak acceleration after 15 impacts at 9.3J was larger than the peak force on the initial impact for both DAH.1 and DAH.3 geometries (Fig. 11). It was observed that the number of impacts and maximum displacement were inversely proportional, as the number of impacts increased maximum displacement decreased until a threshold number of impacts was reached. This threshold was observed to occur after 10 impacts for DAH.3 and 20 impacts for DAH.1. After the threshold, the maximum displacement began to increase. However, the fracture displacement or displacement at conclusion of 30 impacts was consistently less than the displacement at first impact. DAH.1 was observed to have the highest average peak displacement (2.3 mm ± 5%). The peak force and peak linear acceleration for the three tested geometries fluctuated between 7–12 kN and 118–207 g respectively for an impact energy of 9.3J corresponding to an average probability of concussion of 100%. Where the highest peak force and peak acceleration was experienced by DAH.1 between the 5th and 25th impacts at ~ 12.2 kN ± 1%, DAH.3 had median peak force and DAH.2 experienced the lowest peak force, similar to the results of the 32J impact tests.

It was observed that keeping the impact energy constant and stimulating multiple impacts increased the peak force and probability of concussion as well as resulting in constant energy absorption for the DAH.1 geometry impacted at 5 J. Where the probability of concussion for DAH.1 was observed to increase from 20% on the 1st impact to 90% on the 30th impact at 5 J. This was coupled with drastic changes in peak force from 3 kN at impact 1 to 6 kN at impact 30 (Fig. 12). However, this was not reflected in the other geometries. Similar to DAH.1, DAH.3 also withstood 30 impacts at 5 J with negligible plastic deformation however no significant fluctuations in peak force was observed (Fig. 12). With total lateral deformation of auxetic unit cells less than 1%. DAH.3 maintained relatively constant maximum displacement of 1.7 mm ± 4%; peak force of 5.0 kN ± 2%; peak acceleration of 85 g ± 3%; absorbed energy of 4.8 J ± 0.3% and hence the probability of concussion remained at a constant 75% over the course of the 30 impacts. DAH.3 was observed to store a similar amount of elastic energy to DAH.1 (within 1J) while DAH.2 was seen to fracture on initial impact at 5 J (Fig. 12). The peak linear acceleration for DAH.1

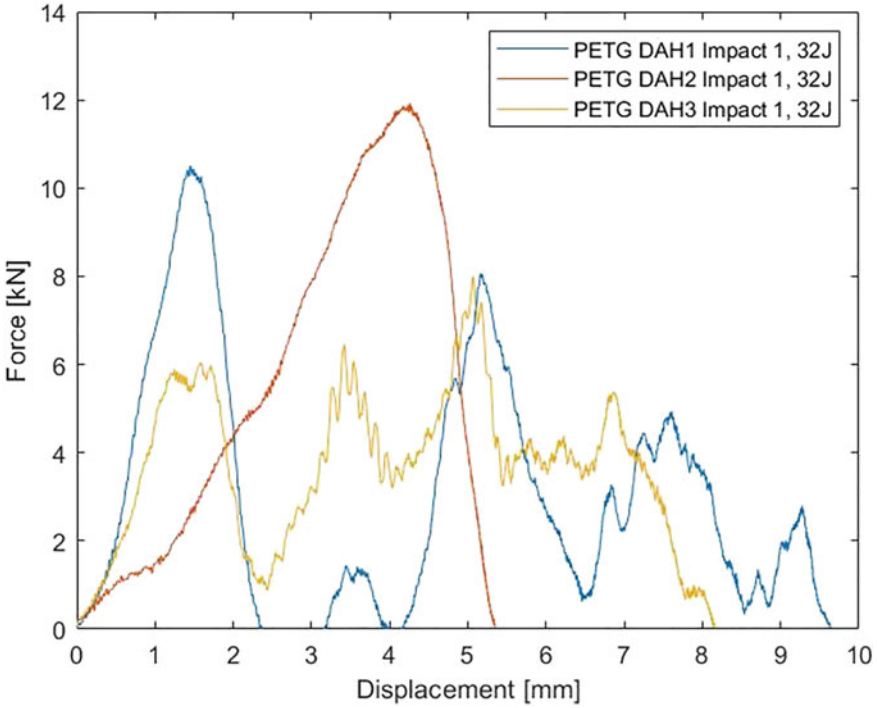

Fig. 7 Force versus displacement response of DAH.1, DAH.2, and DAH.3 under 32 J impact

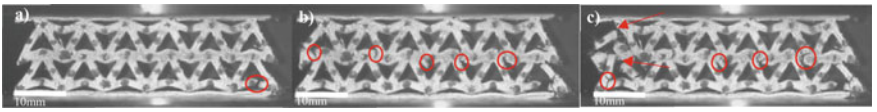

Fig. 8 DAH.1 failure on first drop tower impact at 32J. **a** Crack initiation at node of lower unit cell (circle). **b** Secondary failure phase initiated by crack propagation at the middle section of nodes (circles). **c** Further crack propagation at middles section of nodes (circles), brittle failure at nodes (arrows)

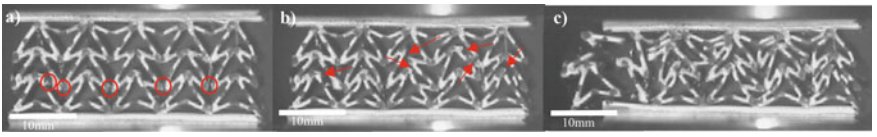

Fig. 9 DAH.2 failure on first drop tower impact at 32J. **a** Fracture at nodes of lower unit cell (circles). **b** Stress concentration builds as the second level of nodes fracture (arrows). **c** Complete brittle failure of the structure

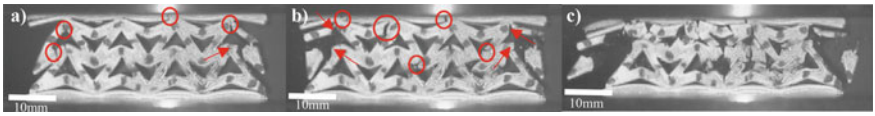

Fig. 10 DAH.3 failure on first drop tower impact at 32 J. **a** Fracture at nodes of upper unit cell (circles). **b** Stress concentration builds as the second level of nodes fracture occurs(arrows), crack propagation continues (circles). **c** Complete brittle failure of the structure

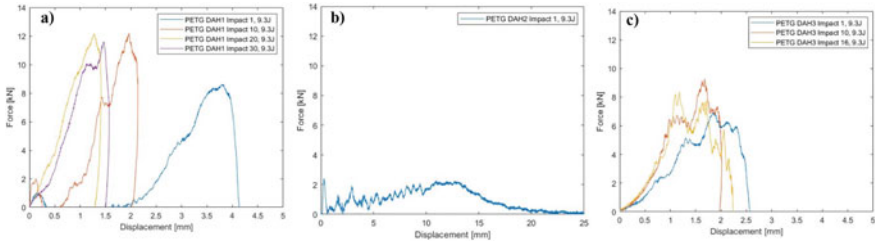

Fig. 11 Force–displacement response under repeated 9.3J impact. **a** DAH.1 response at impact 1, 10, 20 and 30 without fracture. **b** DAH.2 response at first impact (fracture). **c** DAH.3 response at impact 1, 10 and 16 (fracture). *Note* DAH.2 exhibited low stiffness in comparison to the other structures and as such a larger x-scale was used to display the significant features

increased from 60 to 90 g within the first 10 impacts, corresponding to a probability of MTBI of 20% and 80% respectively. By the 30th impact, DAH.1 reached a peak acceleration of 100 g's corresponding to a probability of concussion of 90%. The peak force experienced by DAH.1 under 5 J impact was also seen to increase from 3.4 kN to 5.7 kN over 30 impacts at 5 J. High speed videography revealed that there was limited volume reduction in the specimens prior to plastic deformation for the 32, 9.3 and 5 J impacts. Figures 9, 10 and 11 show the common modes of failure for the three geometries under impact was brittle failure at the nodes. This is seen in Figs. 12 and 13 as the sharp decrease in force known as the inertia effect when abrupt fracture occurs.

Discussion

A shallow non-linear section for QS compression was observed between 0.5mm and 1mm displacement for all samples (Fig. 4). This phenomenon was triggered by a combination of initial densification of the 2mm top and bottom sheets of foam and the plastic bending of the 0.7 mm PETG sheets on the top and bottom of each specimen. QS compression results revealed that the stiffest structure of the three was DAH.1 and this aligns with the literature [23] where the unit cell wall thickness, t, has a large effect on the impact and compressive strength of auxetics, particularly DAH geometries. This is further evidenced by the significant difference in energy

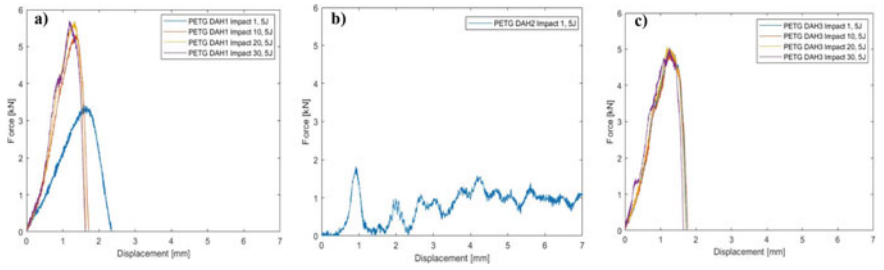

Fig. 12 Force–displacement response under repeated 5 J impact. **a** DAH.1 response at impact 1, 10, 20, and 30 without fracture. **b** DAH.2 response at first impact (fracture). **c** DAH.3 response at impact 1, 10, 20, and 30 without fracture

absorption capacity of DAH.2 and DAH.3 despite that other than their varied wall thickness, they are the same geometry. According to preliminary calculations in order for a geometry to be a suitable candidate for impact testing a peak force of greater than 3.5 kN is mandatory and greater than 5.5kN is desirable. The results indicate that only DAH.1 and DAH.3 were suitable structures and DAH.2 would require alterations prior to impact testing. This was further evidenced by the destructive failure of DAH.2 under all three impact energies 5, 9.3 and 32 J. This indicates that the PETG DAH.2 geometry would not provide sufficient impact attenuation at as low as 5J to prevent against even a 10% probability of MTBI according to the risk curve in Fig. 3. DAH.1 and DAH.3 far surpassed the 5.5 kN peak force threshold and were assumed to survive at minimum a single impact at 100% probability of concussion (32 J). However, both were consistently prone to brittle failure at the nodes during 32 J impacts. Analysis of the derived force data indicated that 32 J was a significant overestimate for the threshold energy for 100% probability of MTBI. It is well evidenced by literature that the threshold occurs at a peak acceleration of 110g. It was found that for an energy of 32 J the corresponding peak linear acceleration was between 175 and 200 g. It was found that the peak acceleration was dependent on the geometry and number of impacts. Typically, the stiffer the geometry the higher the peak acceleration. As such DAH.1 had the highest peak acceleration followed by DAH.3 and then DAH.2 for each impact energy.

As discussed in literature [24] QS testing can only accurately predict impact response up until an impact energy of 10 J. This was evidenced by the significant changes in peak acceleration, peak force and energy absorption capacity. The energy absorption capacity of DAH.1 extrapolated from QS data was 11.4 J however peaked at 6.7 J ± 8% and 9.2 J + /8% during 32 J and 9.3 J impact, respectively. This is evidence to support that the QS compression data cannot accurately predict the low velocity impact response of geometries. Additionally, the impact results should indicate less than 2% plastic deformation in both DAH.1 and DAH.3 for at least one impact of 9.3 J, as predicted by the QS compression tests where DAH.1 absorbed 11.4 J ± 8% and DAH.3 absorbed 10 J ± 8% before elastic–plastic transition. It is

noted that the steel impactor and baseplate used to conduct the quasit-static compression and impact experiments has some effect on the energy transmission through and absorption capacity of the specimens as in reality the ground in a head to ground impact would likely deform and absorb some energy. Since the steel is quite a lot stiffer than the auxetic specimens it undergoes little deformation at low energy levels meaning it imparts majority of the drop tower rig's potential energy through the specimen on impact.

DAH.2 was determined to be too inelastic for the intended purpose as a 50% reduction volume during compression resulted in brittle failure and consistently more than 2% plastic deformation. This implied that the structure could not function as an auxetic, as the inherent contraction resulted in failure. Contrastingly DAH.1 and DAH.2 were too stiff resulting in limited contraction before brittle failure. Thus, DAH.1, DAH.2 and DAH.3 are not suitable for application to soft shell headgear as they fail to absorb 18 J for a 32 J impact with negligible (< 2%) plastic deformation.

Conclusions

Quasi-static compression data indicated 32 J is sufficient to induce 100% probability of MTBI based on the assumption that peak linear acceleration would remain constant with constant impact energy, however it was found to vary with geometry and number of impact. It was determined from the impact results that 9.3 J would be sufficient to test 100% probability of MTBI and thus that the risk curve derived from QS testing is inaccurate to predict the impact energy and its corresponding risk of MTBI. Impact nor QS tests produced data which deemed any of the PETG specimens suitable for use in softshell headgear as DAH.2 was too brittle and DAH.1 and DAH.3 were too stiff and did not allow sufficient volume reduction on impact meaning that they could not absorb enough of the impact energy to reliably decrease the probability of MTBI from 100% to below 25%. It is recommended that the material is changed to one with higher ductility to allow greater deformation prior to fracture, thus increase energy absorbed in the elastic region.

References

1. Knouse CL, Gould TE, Caswell SV, Deivert RG (2003) Efficacy of Rugby headgear in attenuating repetitive linear impact forces. J Athl Train 38(4):330–335
2. Patton DA, McIntosh AS (2016) Considerations for the performance requirements and technical specifications of soft-shell padded headgear. Proc Inst Mech Eng Part P: J Sports Eng Technol 230(1):29–42
3. Withnall C, Shewchenko N, Wonnacott M, Dvorak J (2005) Effectiveness of headgear in football. Br J Sports Med 39(suppl 1):i40–i48

4. Convery S (2023) AFL Players' Association claims it has been kept in dark on League's Concussion Review Plan. The Guardian. https://www.theguardian.com/sport/2023/apr/19/afl-players-association-claims-it-has-been-kept-in-dark-on-leagues-concussion-review-plan#:~:text=Nearly%20a%20quarter%20of%20players,continuing%20to%20play%20or%20train. Accessed 17 May 2023
5. N-Pro (2023) AFL & Rugby helmets: N-pro, N-Pro. https://n-pro.com.au/. Accessed 17 May 2023
6. McIntosh AS, McCrory P, Comerford J et al. (2000) The dynamics of concussive head impacts in Rugby and Australian rules football. Med Sci Sports Exercise 32(12):1980–1984
7. Novak N, Vesenjak M, Ren Z (2016) Auxetic cellular materials-a review. Strojniški vestnik-J Mech Eng 62(9):485–493
8. Mustahsan F, Khan SZ, Zaidi AA, Alahmadi YH, Mahmoud ER, Almohamadi H (2022) Re-entrant honeycomb auxetic structure with enhanced directional properties. Materials 15(22):8022
9. Najafi M, Ahmadi H, Liaghat G (2021) Experimental investigation on energy absorption of auxetic structures. Mater Today: Proc 34:350–355
10. Lvov V, Senatov F, Korsunsky A, Salimon A (2020) Design and mechanical properties of 3D-printed auxetic honeycomb structure. Mater Today Commun 24:101173
11. Broglio SP, Sosnoff JJ, Shin S, He X, Alcaraz C, Zimmerman J (2009) Head impacts during high school football: a biomechanical assessment. J Athl Train 44(4):342–349
12. Newman JA, Shewchenko N (2000) A proposed new biomechanical head injury assessment function-the maximum power index. SAE Technical Paper, Techreport
13. Kajtaz M, Subic A (2015) Experimental investigation into suitability of smart polymers as an impact-absorbing material for an improved Rugby headgear
14. Funk JR, Duma S, Manoogian S, Rowson S (2007) Biomechanical risk estimates for mild traumatic brain injury. In: Annual Proceedings/Association for the advancement of automotive medicine, vol 51, p 343
15. Pellman EJ et al (2004) Concussion in professional football: epidemiological features of game injuries and review of the literature—part 3. Neurosurgery 54(1):81–96
16. Newman J et al (2000) A new biomechanical assessment of mild traumatic brain injury. Part 2: results and conclusions. In: Proceedings of the international research council on the biomechanics of injury conference, vol 28
17. Chuong P, Robbins J, Tsefrikas V, Whiteman M (1999) Analysis of indices relating to head impact
18. Francisco MB, Pereira JLJ, Vasconcelos GAVB, da Cunha Jr SS, Gomes GF (2022) Multiobjective design optimization of double arrowhead auxetic model using Lichtenberg algorithm based on metamodelling. Structures 45:1199–1211
19. WorldRugby.org. Regulations. World Rugby. https://www.world.Rugby/organisation/governance/regulations/reg-1. Accessed 17 May 2023
20. Guo M-F, Yang H, Ma L (2022) 3D lightweight double arrow-head plate-lattice auxetic structures with enhanced stiffness and energy absorption performance. Compos Struct 290:115484
21. Qiao J, Chen C (2015) Impact resistance of uniform and functionally graded auxetic double arrowhead honeycombs. Int J Impact Eng 83:47–58
22. Türkoğlu İK, Kasım H, Yazıcı M (2023) Experimental investigation of 3D-printed auxetic core sandwich structures under quasi-static and dynamic compression and bending loads. Int J Protective Struct 14(1):63–86
23. Boopathi B, Ponniah G, Burela RG (2020) Realizing the impact and compressive strengths of an arrowhead auxetic structure inspired by topology optimization. Int J Adv Eng Sci Appl Math 12:211–217
24. Santos F et al (2021) Low velocity impact response of 3D printed structures formed by cellular metamaterials and stiffening plates: PLA vs. PETG. Compos Struct 256:113128
25. Griffey J (2014) 3-D printers for libraries. American Library Association, pp 8–13

26. Prusament. Prusament.com. Prusament. https://prusament.com/media/2020/01/PETG_TechSheet_ENG.pdf. Accessed 21 May 2023
27. Srinivasan R, Kumar KN, Ibrahim AJ, Anandu K, Gurudhevan R (2020) Impact of fused deposition process parameter (infill pattern) on the strength of PETG part. Mater Today: Proc 27:1801–1805
28. Ambade MVV, Padole MV, Badole MB (2023) Effect of infill density, infill pattern and Extrusion temperature on mechanical properties of part produced by 3D printing FDM technology using ABS, PLA and PETG filament: a critical review
29. Meagher G (2023) Concussion rates in elite Rugby hit highest levels since records began. The Guardian. https://www.theguardian.com/sport/2022/jun/21/concussion-rates-in-elite-Rugby-hit-highest-levels-since-records-began#:~:text=The%202020%2D21%20season%20had,and%2017%20sustained%20in%20training. Accessed 17 May 2023
30. Roser M, Appel C, Ritchie H (2013) Human height. Our world in data

Characterization of a Zeolite Obtained by Means of a Hydrothermal Synthesis Process

F. R. Barrientos-Hernández, M. García-Ramírez, María I. Reyes-Valderrama, Julio Juárez-Tapia, M. Reyes-Pérez, X. Álvarez-Álvarez, and K. L. Fuentes-Trejo

Abstract Zeolites are aluminosilicates with porous structure. Due to their cation exchange properties, they are widely used for the treatment of water contaminated with metals. In this research a Mexican expanded perlite was used to obtain synthetic zeolite by the hydrothermal method, the material was characterized by XRF, XRD, FTIR, SEM techniques. A hydrothermal reactor with a 20 ml PTFE vessel, 1 g of material and 17 ml of NaOH solution were added, then placed in oven. The variables evaluated were NaOH concentration, maintained temperature and time of heating. The type of zeolites obtained were zeolite Na-P_1, cancrinite, sodalite, zeolite type A and zeolite type Y.

Keywords Expanded perlite · Zeolite · Hydrothermal synthesis

Introduction

Due to the increasing demand for inputs in the world and increasing pollutants to the environment, the disposal of waste from different industries containing heavy metals is a topic that nowadays occupies researchers. Several processes for the removal of such metals are applicable, such as reverse osmosis, ultrafiltration, electrolysis, ion exchange, among others [1]. The use of the method depends on environmental compatibility, costs, availability of materials and sustainability [2]. Ion exchange is an alternative for the removal of heavy metals, natural and synthetic zeolites are used for this purpose [2–4].

F. R. Barrientos-Hernández · M. García-Ramírez (✉) · M. I. Reyes-Valderrama · J. Juárez-Tapia · M. Reyes-Pérez · X. Álvarez-Álvarez · K. L. Fuentes-Trejo
Academic Area of Earth Sciences and Materials, Autonomous University of the State of Hidalgo, Pachuca-Tulancingo Km 4.5 Mineral de La Reforma, 42184 Hidalgo, México
e-mail: marcelino_garcia@uaeh.edu.mx

Z. Peng et al. (eds.), *Characterization of Minerals, Metals, and Materials 2024*, The Minerals, Metals & Materials Series, https://doi.org/10.1007/978-3-031-50304-7_31

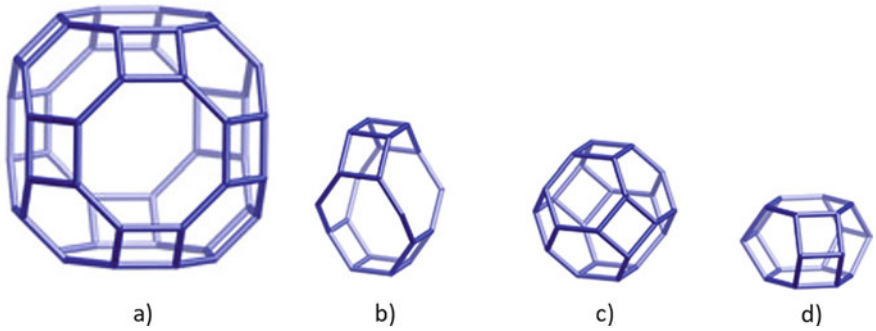

Fig. 1 Various cage: **a** LTA, **b** GIS, **c** SOD and **d** CAN, adopted and modified from the database of Zeolite structures [8]

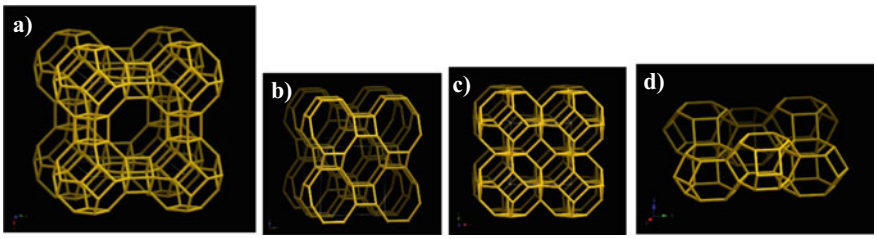

Fig. 2 Different framework structures: **a** LTA, **b** GIS, **c** SOD and **d** CAN, adopted and modified from the database of Zeolite structures [8]

In the case of synthetic zeolites, there are several materials that have been used as raw materials due to their low cost and availability, such as kaolinite [5], volcanic glasses (perlite, pumicite, perlite natura [6], coal fly ash [7]. The type of zeolite and quality to be obtained depends on the SiO_2/Al_2O_3 ratio, the purity of the precursors, concentration of the medium, temperature, time, and agitation. The zeolites most used for the removal of heavy metals are those with Framework GIS, SOD and LTA (see Fig. 1), metastable zeolites such as LTA type are larger cage (see Fig. 2) and have a higher cation exchange capacity of approximately 5.72 meq/g [4].

Experimental Methodology

For this study, a Mexican commercial perlite of the Agrolita brand was acquired. The chemical composition of the expanded perlite was obtained by X-ray fluorescence (XRF) using a RIGAKU ZSX Primus II spectrometer, and the results

obtained were as follows: SiO_2—75.14%, Al_2O_3—14.01%, Na_2O—4.276%, K_2O—4.147%, Fe_2O_3—0.70%, CaO—0.494%, TiO_2—0.17%, MnO—0.13%, MgO—0.123%, P_2O_5—0.05% and LOI—0.770%. The mineralogical species were detected by X-ray diffraction (XRD) with an INNEL Equinox 2000 diffractometer, with Co irradiation source ($\lambda = 1.789010$ Å). Functional groups were detected with a Perkin Elmer System 2000 FTIR spectrometer. Subsequently, a JEOL JSM-IT300 scanning electron microscope was used to determine the morphology.

The sample was reduced in size down to 147 μm, then dried at 80 °C for 24 h: The hydrothermal synthesis tests were performed in a reactor at autogenous pressure without agitation. As a first step, 1 g of expanded perlite was added to a PTFE vessel with a capacity of 20 ml, then 17 ml of a sodium hydroxide solution was added varying the concentration from 4 and 5 Molar, the reactor was placed in an oven at temperatures of 80 and 100 °C, with residence times of 6, 12, 18 and 24 h. The synthesis products were filtered and washed with distilled water until the pH of the drain was below 10, then dried at 80 °C for 6 h. The synthesis products were characterized by XRD, FTIR and SEM techniques.

Results and Discussion

XRF

The diffraction patterns and zeolites identified in the different working conditions are shown in Fig. 3 and Table 1 respectively. The diffractogram of the perlite shows a completely amorphous material. Zeolite Type A (38-0241), Type Y (40-1464), Na-P1 (40-1464), Sodalite (37-0476) and Cancrinite (70-5030) were detected. In the 6 h residence time tests, crystalline phases began to form, except for 5M–100 °C–6 h as sodalite and Na-P1 were detected. At 4M–80 °C–24 and 4M–80 °C–12 h metastable zeolite type A was formed, at 4M–80 °C–18 h zeolite type Y was detected, both zeolites coexist with Na-P1 and sodalite. The 4 Molar and 100 °C concentration tests showed cancrinite and Na-P1 as main and secondary phase, respectively. The 5 Molar and 80 °C experiments presented sodalite as major phase, 5M–80 °C–6 h also revealed type A zeolite. Finally, the 5 Molar and 100 °C tests show a transformation from sodalite to cancrinite with increasing time.

FTIR

The infrared spectra are observed in Fig. 4. All samples exhibit vibrational mode bands of stretching (3621–3415 cm^{-1}) [not shown in the Figure] and bending (1696–1637 cm^{-1}) of the O–H bond corresponding to water molecules contained in the perlite and zeolites. The pearlite show bands of asymmetric stretching vibrations

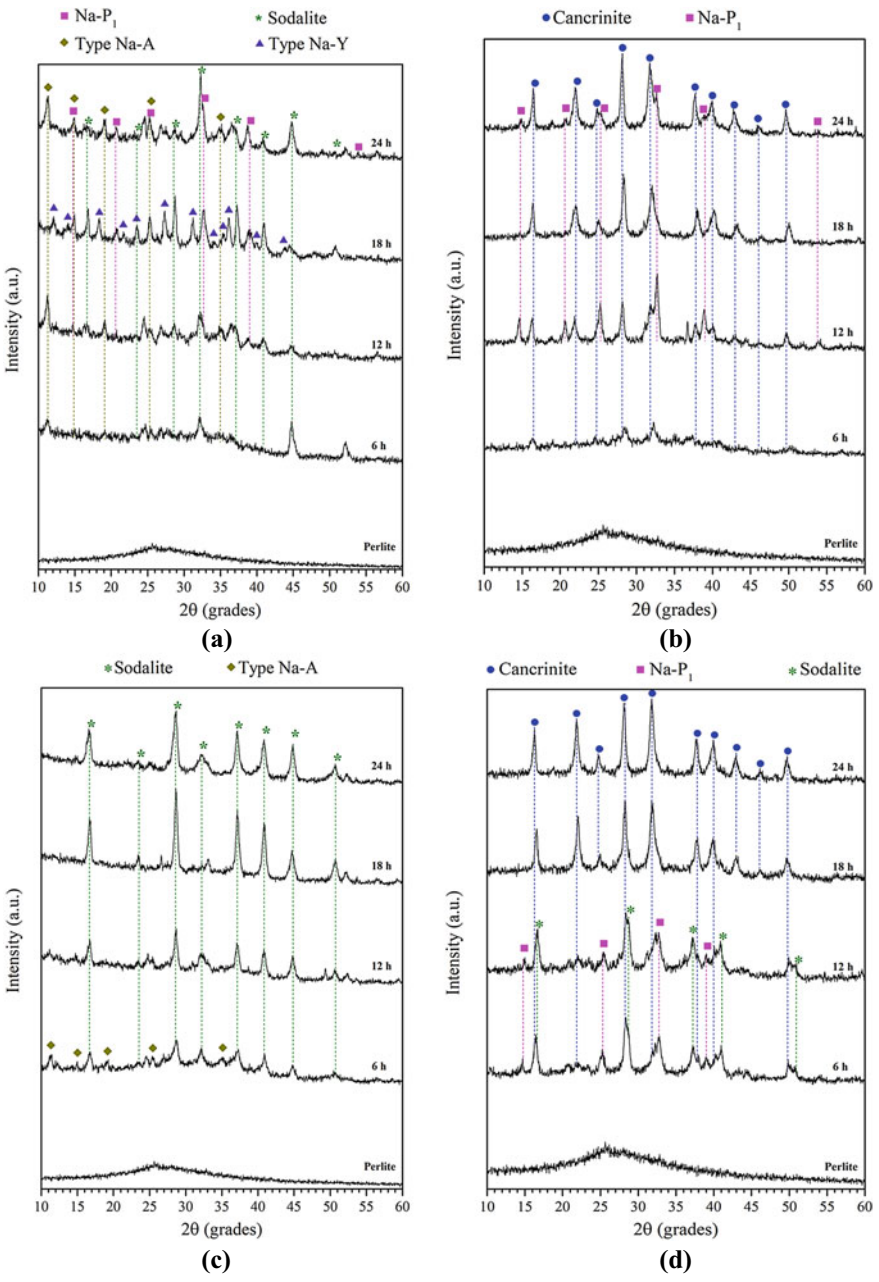

Fig. 3 Diffraction patterns of the samples obtained at: **a** 4M–80 °C, **b** 4M–100 °C, **c** 5M–80 °C and **d** 5M–100 °C

Table 1 Experimental conditions and type of zeolite obtained

Reagent			Hydrothermal treatment		Nomenclature	Type of zeolite
H_2O (ml)	Perlite (g)	NaOH (M)	Temperature (°C)	Time (h)		
17	1	4	80	6	4M–80 °C–6 h	Type A
				12	4M–80 °C–12 h	Type A, Na-P_1 and Sodalite
				18	4M–80 °C–18 h	Type Y, Na-P_1 and Sodalite
				24	4M–80 °C–24 h	Type A, Na-P_1 and Sodalite
			100	6	4M–100 °C–6 h	Cancrinite
				12	4M–100 °C–12 h	Na-P_1 and Cancrinite
				18	4M–100 °C–18 h	Cancrinite
				24	4M–100 °C–24 h	Cancrinite and Na-P_1
		5	80	6	5M–80 °C–6 h	Zeolite type A
				12	5M–80 °C–12 h	Sodalite
				18	5M–80 °C–18 h	Sodalite
				24	5M–80 °C–24 h	Sodalite
			100	6	5M–100 °C–6 h	Sodalite and Na-P_1
				12	5M–100 °C–12 h	Sodalite and Na-P_1
				18	5M–100 °C–18 h	Cancrinite
				24	5M–100 °C–24 h	Cancrinite

(1043 cm^{-1}), symmetric stretching vibrations (789 cm^{-1}) of the O–Si(Al) –O bond and bending stretching (443 cm^{-1}) of the Si–O–Si(Al) bond, the vibrational modes are typical of an expanded pearlite (1080–1055, 986 and 461 cm^{-1}) [9]. The bands in the 1500–1300 cm^{-1} region is assigned to the C–O bond of the CO_3^{2-} functional group [10].

During the synthesis Al displaces Si in the tetrahedra, therefore the initial 1043 cm^{-1} band of the pearlite moves to the right. There are tests where more than one zeolite coexists, therefore it is impossible to assign the functional group to the mineralogical species because of the band mixture. Sodalite could be detected with the bands 987, 463–458 and 434 cm^{-1}, which coincides with the bands 986, 466 and 437 cm^{-1} reported by Novembre and co-workers [11]. The 668 cm^{-1} band was assigned to the A-type zeolite with the Si–O–Al bond symmetric stretching vibrational mode [11]. The cancrinite was identified with the bands in the range of 560–570 and 624 cm^{-1} [12] corresponding to vibration of a 4-membered double ring (4D), the assignment bands were: 560–570 and 624 cm^{-1}[12].

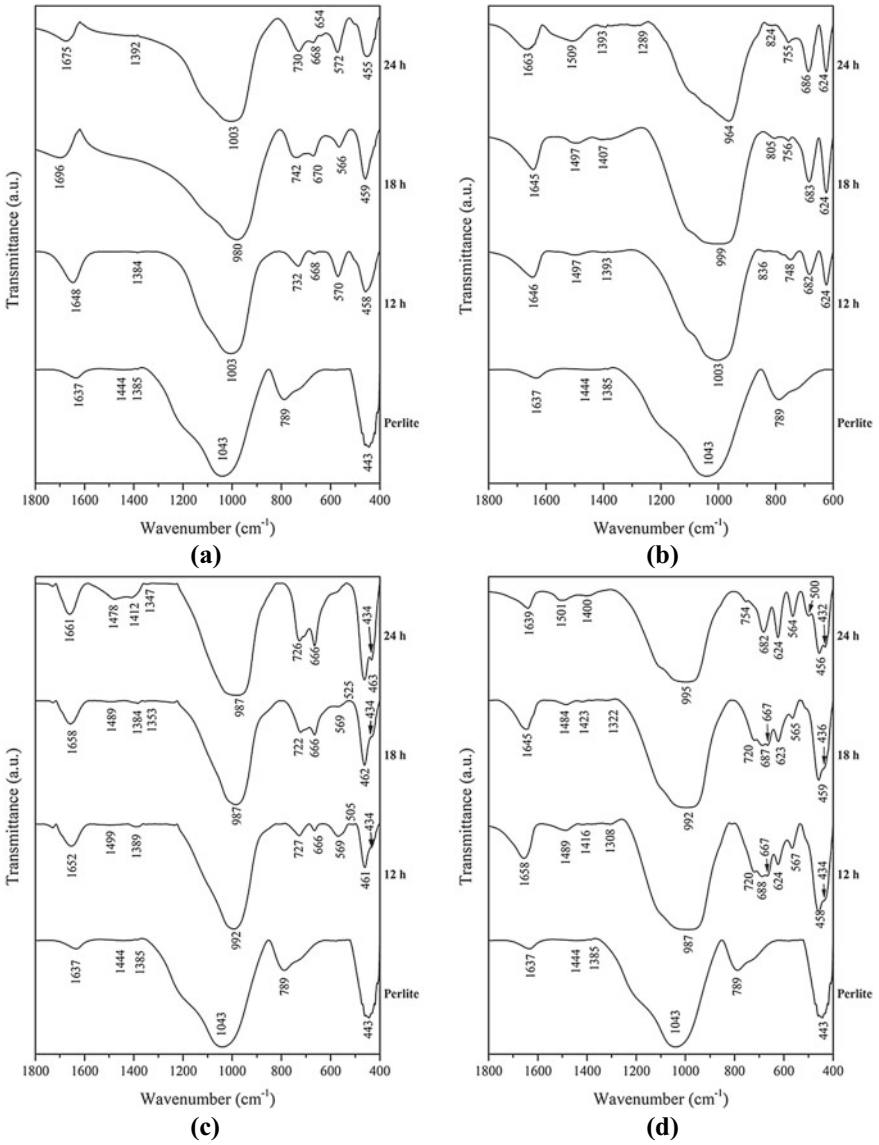

Fig. 4 FTIR spectra at different test conditions. **a** 4 Molar and 80 °C, **b** 4 Molar and 100 °C, **c** 5 Molar and 80 °C and **d** 5 Molar and 100 °C

SEM

The micrographs of the samples are shown in Fig. 5. The raw material before grinding (see Fig. 5a) presents a flake morphology, this is typical for a thermally expanded perlite, its real density is between 1.45 and 2.45 g/cm^3 [13]. Most of the zeolites obtained show an agglomerate of particles with sizes below 5 μm [see Fig. 5b, d)] without the presence of defined crystals in the order of microns. Only the sample 5 M–80 °C–24 h (see Fig. 5c) developed zeolite crystals with SOD structure, this shape coincides with Reyes et al. [5].

In this investigation, little amount of Na-P_1 zeolite is observed, for its formation low Na OH concentrations (1.0–3.0 M) are required [14]. Sodalite and cancrinite share the same formula Na_6 $[Al_6Si_6O_{24}]0.2NaX.$ $6H_2O$, where X can be OH^-, Cl^-, $NO_3{}^-$, ½ $CO_3{}^{2-}$ or ½ $SO_4{}^{2-}$ [5], FTIR spectra reveal that the anion present is $CO_3{}^{2-}$ due to $NaCO_3$ impurities from sodium hydroxide. On the other hand, when sodalite is present, there is a mechanism for the formation of cancrinite [12], time is required for a complete transformation from sodalite to cancrinite [5], such phenomenon is best observed in the 5 Molar NaOH and 100 °C temperature tests, where at 6 h of synthesis sodalite was formed and at 24 h 100% cancrinite was noticed.

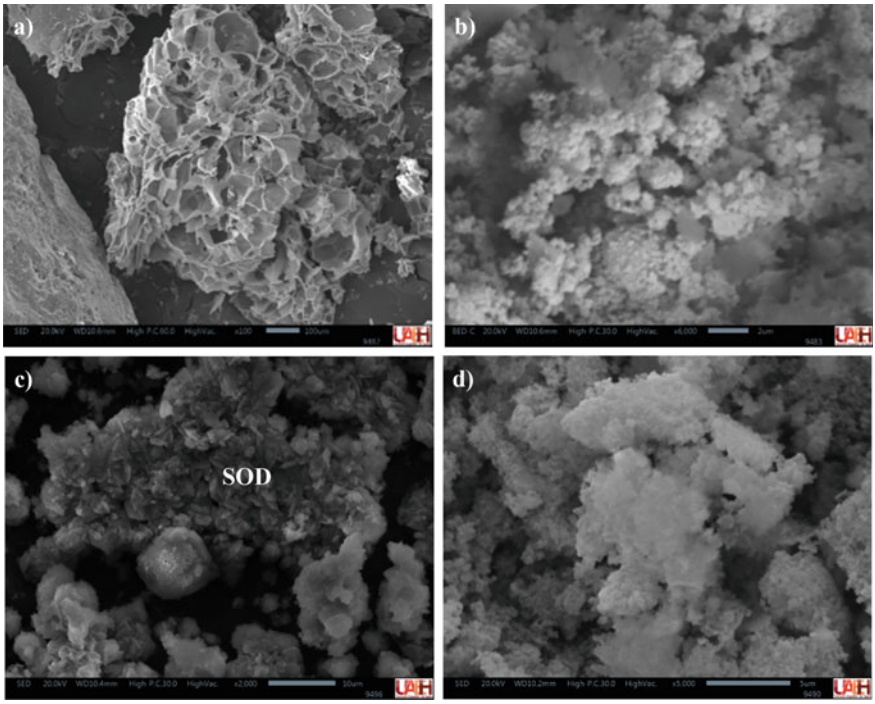

Fig. 5 Micrographs of samples analyzed by SEM, **a** Expanded perlite, **b** sample 4M–80 °C–18 h, **c** sample 5M–80 °C–24 h y **d** sample 5M–100 °C–24 h

Table 2 Comparative results table

Test conditions							Zeolite	References
Molar ratio SiO_2/Al_2O_3	S/L (gr/ml)	Na OH (M)	Time (hr)	Temperature (°C)	Pressure	Stir		
9.57	1:15	0.5–5	1–72	30–90	Atmospheric	No	Type X, ZSM-20, Na-P1, ZK-5, Type A and Sodalite	[6]
8.69	1:10	2 y 5	24	100	Autogenous	Yes	Na-P_1 and Sodalita	[2]
9.10	1:17	4 y 5	6–24	80 y 100	Autogenous	No	Type A, Type X, Type Y, Na-P_1, Sodalita and Cancrinite	This work

In Table 2 a comparison of similar studies in the synthesis was made, in conditions of 4 Molar, 80 °C and 24 h Króll and collaborators [6] obtained zeolite type X, Na-P_1 and ZK-5. In this work type A, Na-P_1 and sodalite were obtained. On the contrary, with the 5 Molar, 100 °C and 24 h test, Painer and collaborators produced sodalite as well as this research. This proves that agitation and pressure are variables that affect the results.

Conclusions

It is noted that at lower NaOH concentration and temperature, metastable zeolites (type A and type Y) are formed, with higher molarity of the solution, stable zeolites such as sodalite were obtained, and when the synthesis time is extended, sodalite is transformed into cancrinite. If zeolites are to be applied as ion exchangers, then it is desirable to produce zeolites with larger framework size, i.e., to search for parameters to obtain LTA type zeolites.

Acknowledgements The authors would like to thank Quim. Patricia Girón García for her support in the preparation and analysis of the samples by X-ray fluorescence belonging to the National Laboratory of Geochemistry and Mineralogy (LANGEM) of the Institute of Geology, UNAM.

References

1. Ibrahim HS, Jamil TS, Hegazy EZ (2010) Application of zeolite prepared from Egyptian kaolin for the removal of heavy metals: II. Isotherm models. J Hazard Mater 182:842–847
2. Painer F, Baldermann A, Gallien F, Eichinger S, Steindl F (2022) Synthesis of zeolite from fine-grained perlite and their application as sorbents
3. Babel S, Kurniawan TA (2003) Low-cost adsorbents for heavy metals uptake from contaminated water: a review. J Hazard Mater 97(1–3):219–243
4. Yuna Z (2016) Review of the natural, modified, and synthetic zeolites for heavy metals removal from wastewater. Environ Eng Sci 0(0)
5. Reyes CA, Williams C, Castellanos OM (2013) Nucleation and grow process of sodalite and cancrinite from kaolinite-rich clay under low-temperature hydrothermal conditions. Mater Res 16(2):424–438
6. Król M, Morawska J, Mozgawa W, Pichór W (2014) Low-temperature synthesis of zeolite from perlite waste part I: review of methods and phase compositions of resulting products. Mater Sci-Pol 32(3):503–513
7. Längaurer D, Čablíl V, Hredzák S, Zubrik A, Matik M (2021) Preparation of synthetic zeolites from coal ash by hydrothermal synthesis. Materials 14(5)
8. Baerlocher C, McCusker LB. Database of zeolite structures. Available online: http://www.iza-structure.org/databases/. Accessed 14 Sept 2023
9. Sodeyama K, Sakka Y, Kamino Y (1999) Preparation of fine expanded perlite. J Mater Sci 34:2461–2468
10. Della Ventura G, Gatta GD, Redhammer GJ, Bellatreccia F, Loose A, Parodi G (2009) Single-crystal polarized FTIR spectroscopy and neutron diffraction refinement of cancrinite. Phys Chem Miner 26:193–206
11. Novembre D, Di Sabatino B, Gimeno D, Pase C (2011) Synthesis and characterization of Na-X, Na-A and Na-P zeolites and hydroxysodalite from metakalonite. Clay Miner 46:339–354
12. Barnes MC, Addi-Mensah J, Gerson AR (1999) A methodology for quantifying sodalite and cancrinite phase mixtures and the kinetics of the sodalite to cancrinite. Microporous Mater 31:303–319
13. Aksoy Ö, Alyamaç E. Mocan M (2022) Characterization of perlite powders from Izmir, Türkie region. Physicochemical Probl Mineral Process 58(6)
14. Pichór W, Mozgawa W, Król M, Adamczyk A (2014) Synthesis of the zeolites on the lightweight aluminosilicate fillers. Mater Res Bull 49:210–215

Characterization of Bacterial Cellulose from Kombucha as a Potential Resource for Its Application on Biodegradable Films

R. N. Hernández-Hernández, R. A. Vázquez-García, J. R. Villagómez-Ibarra, R. Velasco Azorsa, N. Islas-Rodríguez, S. Vázquez-Rodríguez, and M. A. Veloz Rodríguez

Abstract The present study is centered on the biosynthesis of bacterial cellulose produced from kombucha inoculum, hereafter referred to as kombucha-derived bacterial cellulose (KBC). For KBC production, Green tea culture media was utilized. *Acetobacter xylinum* cultures were obtained from organic apple vinegar and unpasteurized commercial kombucha. The resulting KBC was characterized by scanning electron microscopy (SEM), thermogravimetric analysis (TGA), and Fourier-transform infrared spectroscopy (FT-IR) in order to verify its morphological characteristics, thermal resistance, and purity. Characterization aimed to evaluate the influence of isolation conditions in this region of the world on the physicochemical properties of KBC and determine its potential as a resource for producing biodegradable films.

Keywords Bacterial cellulose · Kombucha · SCOBY

R. N. Hernández-Hernández · R. A. Vázquez-García (✉) · N. Islas-Rodríguez · M. A. Veloz Rodríguez
Área Académica de Ciencias de la Tierra y Materiales, Mineral de la Reforma, Universidad Autónoma del Estado de Hidalgo, C. P. 42184 Hidalgo, México
e-mail: rosavg@uaeh.edu.mx

J. R. Villagómez-Ibarra · R. Velasco Azorsa
Área Académica de Química, Mineral de la Reforma, Universidad Autónoma del Estado de Hidalgo, C. P. 42184 Hidalgo, México

S. Vázquez-Rodríguez
Facultad de Ingeniería Mecánica y Eléctrica, Universidad Autónoma del Estado de Nuevo León, C. P. 66455 San Nicolás de los Garza, Nuevo León, México

Z. Peng et al. (eds.), *Characterization of Minerals, Metals, and Materials 2024*, The Minerals, Metals & Materials Series, https://doi.org/10.1007/978-3-031-50304-7_32

Introduction

Due to the growing demand for environmentally sustainable materials, biopolymers represent a viable replacement for synthetic polymers. Extensive research has aimed to obtain high-value-added products from natural polymers, including cellulose, starch, and chitin. Isolated primarily from plants, fungi, trees, and bacteria, cellulose is the most abundant biopolymer on Earth, with approximately 1.5 billion tons generated annually [1]. This material is of great value for producing food packaging, paper, textiles, nanofiber mats, pulp, construction, and fabric materials [2].

Moreover, kombucha is a traditional fermented Chinese beverage whose attributes were treasured by the Qin Dynasty as early as 220 BC. In 414 AD, Dr. Kombu brought kombucha tea from Korea to Japan. Over the following centuries, merchants popularized the drink in Russia, and during the nineteenth and twentieth centuries, it spread throughout Europe. During World War II, shortages of tea and sugar decreased kombucha consumption; however, after the war, it regained popularity in Germany, France, and Italy. Currently, kombucha is one of the most popular fermented drinks produced handcrafted on small scale, and commercial scales [3]; it was valued at 1.84 billion USD in 2019, and the kombucha market forecasts predict strong growth with projections of a 23.2% annual compound growth rate through 2027 [4]. The popularity of kombucha is attributed to its therapeutic effects, such as antimicrobial, antioxidant, anticancer, antidiabetic, detoxifying [5], antifungal, anti-inflammatory, antigenotoxic, and anti-stress properties [6]. It reduces cholesterol and blood pressure levels, promotes weight loss, improves glandular and gastric functions, reduces kidney calcification, combat acne, and inhibits cancer proliferation [7]. The preceding is because it contains different organic acids like gluconic and acetic; additionally, it comprises vitamins, lipids, proteins, polyphenols, minerals (manganese, copper, zinc, iron, cobalt, and cadmium), anions (chloride, fluoride, bromide, iodide, phosphate, and sulfate), etc. [8].

Kombucha is typically produced through the fermentation of sweetened green or black tea using a SCOBY (an acronym for "Symbiotic Culture of Bacteria and Yeast") as a starter culture [9]. The SCOBY is a cellulosic byproduct that forms at the liquid–air interface during fermentation [10]. It consists of a gelatinous membrane composed of pure cellulose [11], generally biosynthesized by *Gram-negative* bacterial strains, including *Acetobacter xylinum, Gluconacetobacter, Agrobacterium, Achromobacter, Sarcina*, etc. [12], whose function is to protect the medium from factors such as ultraviolet light, some fungi, and spores [13]; in the medium there is also yeast such as *Candida kefyr, Candida tropicalis, Dekkera anómala,* to name some of them [14].

Bacterial cellulose (BC) was first reported in 1886 by R. M. Brown, who described it as "a sort of moist skin, swollen, gelatinous and slippery" [15], and has become a valuable biomaterial due to its range of favorable properties; these include exceptional water retention capacity, high degree of polymerization (2000–8000), high crystallinity, mechanical strength, high purity (free from lignin, hemicellulose, and pectin), non-allergenicity, moldability, as well as excellent biocompatibility and biodegradability [16–18] rendering it suitable for applications in tissue engineering,

filtration, electronics, waste treatment, energy production [19], biomedicine, pharmaceuticals, fashion design (for the production of the so-called "vegan leather"), engineering, chemistry, environment; it was also categorized as GRAS (Generally Recognized As Safe) by the FDA (Food and Drug Administration) in 1992, being appropriate for food industry applications such as additive, stabilizer, and gelling in food, and packaging [20].

However, the characteristics, properties, and yield of BC are directly affected by numerous factors such as carbon source (sucrose, glucose, fructose, etc.) [21], incubation period (7–14 days), and temperature of fermentation (28–30 °C) [1]; oxygen pressure and, the amount supplied in the medium; pH (4–6), nitrogen source (yeast) [13]; agitated or static condition of the broth [22], even infusion times and geographical region in which kombucha is elaborated [3].

In this work, kombucha was prepared handcrafted employing a commercial starter inoculum. Then, KBC was characterized by SEM, TGA, and FT-IR to determine its thermal resistance, purity, and morphological characteristics. This is with the objective of obtaining a SCOBY for subsequent cultures, analyzing how these conditions influenced its properties, and determining KBC as a potential resource for its application in the preparation of biodegradable films in future works.

Materials and Methods

Kombucha culture (Vida Bebida), standard sugar, organic apple vinegar (Bragg), green tea, and black tea were purchased from a local market.

Kombucha Started Inoculum

The culture was prepared in a sterilized glass jar where 460 mL of organic vinegar, 235 mL of commercial unpasteurized kombucha, 1 L of water, 80 g of sugar, 2 mL of sugarcane alcohol, and one small homemade kombucha SCOBY were added, with an initial pH of 3. The glass jar was incubated statically at 30 °C for three days.

Preparation of the Infusion of Green Tea

20 g of green tea was boiled at 90 °C in 1 L of purified water and kept under infusion for 10 min, then sachets were removed and let the solution cool until room temperature (20 °C), following the best conditions described by Antolak et al., 2021 [3]. On the fourth day, green tea was added to the glass jar. It was kept incubated statically at 30 °C for 14 days.

Harvesting and Preparation of Kombucha BC

The KBC membrane formed at the liquid–air interface was carefully removed and washed with distilled water. A piece of the sample was placed on a Teflon sheet to dry at room temperature for three days and then cut into smaller pieces to be characterized.

Microbiological Analysis

Microbiological analysis of the kombucha and microscopic observations were conducted using Gram-staining fresh green tea preparation through a Carl Zeiss microscope.

Fourier Transform Infrared (FTIR) Spectrometry

The dried KBC film was characterized using a Perkin Elmer System 2000 Frontier FT-IR spectrophotometer over a wavenumber range of 400 to 4000 cm^{-1}.

Scattering Electron Microscopy (SEM)

The morphology of the BC samples was obtained using a scanning electron microscope (Jeol-IT300) with a voltage of 30 keV.

Thermogravimetric Analysis (TGA)

Thermogravimetric analysis was conducted utilizing a Mettler Toledo TGA/SDTA851 thermogravimetric analyzer under the N_2 atmosphere. The sample was heated from 25 to 750 °C at a constant heating rate.

Results and Discussion

A sample of 6 mL of KBC was taken to perform Gram staining and visually analyze the colonies. As observed in Fig. 1a, rod-shaped, reddish homogeneous forms are distinguished, indicating *Acetobacter xylinum,* a Gram-negative bacterium

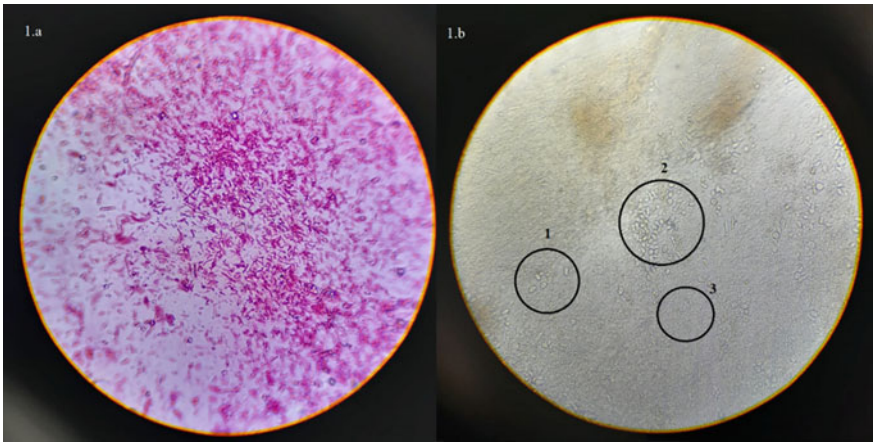

Fig. 1 **a** Gram-negative stain of KBC showing bacteria and **b** native visualization of bacteria and yeast in fresh KBC

that produces BC [23]. Likewise, a smear of the fresh KBC (Fig. 1a) was made, observing symbiosis between yeasts and bacteria (1.b.1), a yeast colony (1.b.2), and homogeneous bacteria (1.b.3) on the surface of the film.

Fourier Transform Infrared (FTIR) Spectrometry

Figure 2, shows the FTIR spectrum where the intensity and position of the absorption peaks are indicated, giving details about the functional groups found in the KBC film, which are similar to the literature and validate the structure of bacterial cellulose.

The band in 3286 cm^{-1} indicates the –OH stretching vibrations [24]. The signal at 2920 cm^{-1} is associated with the –CH stretching [24]. The band at 1645 cm^{-1} corresponds to the –OH bending of the absorbed moisture of the film [25]. Additionally, the signals at 1417 cm^{-1} and 1362 cm^{-1} match with the $-CH_2$ and CH bending, respectively [26, 27]; moreover, the band at 1034 cm^{-1} is associated with either C–O–C and C-O–H stretching vibration of the sugar ring in cellulose [27, 28].

Scattering Electron Microscopy (SEM-E/EDX)

SEM was utilized to analyze the morphological characteristics of the KBC film. As Fig. 3a shows, the SCOBY surface is formed of bacteria in a fibrous configuration and disordered clusters. In Fig. 3b, the bacteria comprising the clusters can be identified, which is consistent with the microbiological observations using optical microscopy. It can be seen that the KBC film presents a high microbial population, as Villarreal

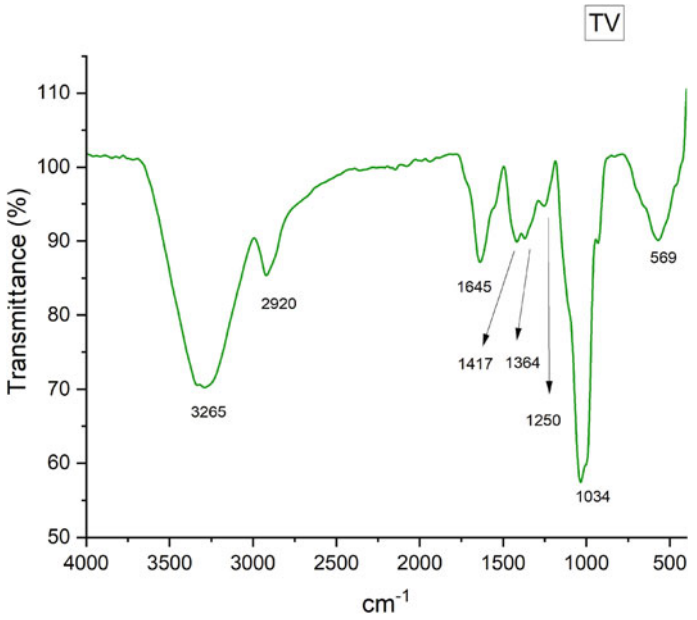

Fig. 2 FTIR spectrum of GTK SCOBY

et al., 2020 indicate, a substantial concentration of microbial cells can obstruct the interaction between fibrils in the network, leading to a decrease in the number of hydrogen bonds and consequently impacting the properties of the biofilm.

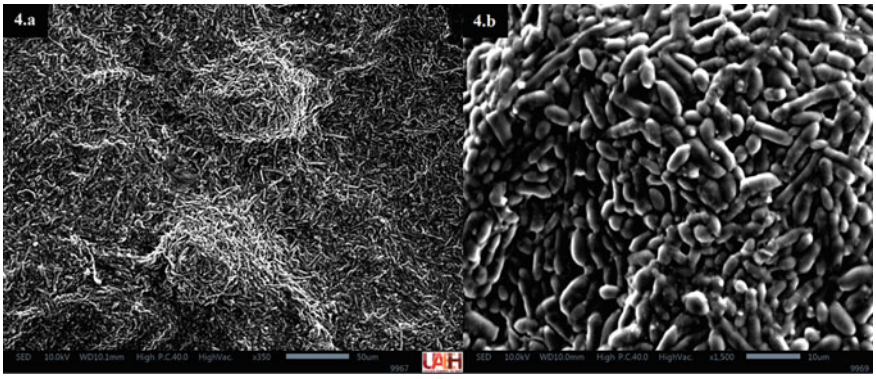

Fig. 3 Scanning electron microscopy (SEM), **a** GTK SCOBY surface (350×), **b** GTK SCOBY surface (1500×)

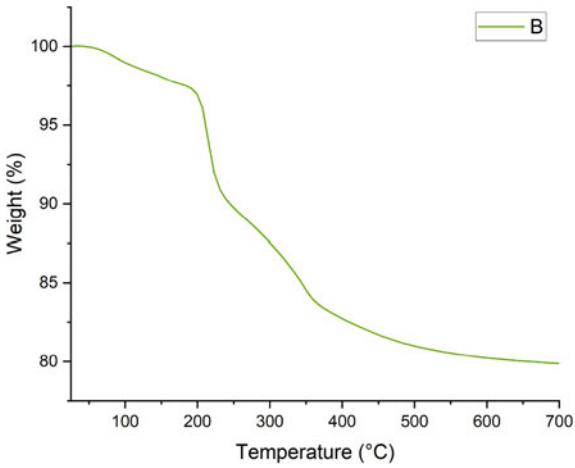

Fig. 4 Thermogram of TGA, KBC film evaluated from 25 to 700 °C under N atmosphere

Thermogravimetric Analysis (TGA)

In Fig. 4, a TGA thermogram is displayed, the first endothermic peak from 25 to 100 °C approximately, corresponds to the evaporation of moisture from the sample resulting in a weight loss of 1.04%, the second peak from 193 to 230 °C consists of the thermal degradation of the KBC sample losing a 15.84% of the weight. From 359 to 700 °C it is observed the decomposition of the KBC corresponds to 20.4% of the weight loss.

In Fig. 4, a TGA thermogram is displayed. The first endothermic peak, occurring approximately between 25 and 100 °C, corresponds to the evaporation of moisture from the sample, resulting in a weight loss of 1.04%. The second peak, ranging from 193 to 230 °C, consists of the thermal degradation of the KBC sample, resulting in a 15.84% weight loss. Between 359 and 700 °C, the decomposition of the KBC is observed, corresponding to a 20.4% weight loss. According to Villarreal et al., 2020, the decline in thermal stability might be associated with a higher crystallinity index.

Conclusions

The green tea kombucha SCOBY film analyzed by SEM shows a high concentration of bacteria, consistent with the microbiological observations, where Gram-negative, rod-shaped, reddish homogeneous forms are observed. As the literature indicates, the properties of the film such as its thermal behavior are influenced by this excess of bacteria on the surface of the SCOBY. Therefore, it is necessary to improve the conditions of the culture and prove other substrates to nourish kombucha, for example, black tea, and carbon sources, apart from improvising other variables such as time of fermentation, temperature, pH, and methods for cleaning the films. Currently, these

variables are under analysis and will be reported in the future; this initial experimentation phase allowed us to obtain the SCOBY, which was subsequently added to the new cultures.

Acknowledgements The authors would like to thank CONAHCYT for the support provided through scholarship 1034245 to R. N. Hernández Hernández in the Material Sciences Ph.D. program at the Universidad Autónoma del Estado de Hidalgo.

Conflict of Interest The authors declare that there are no conflicts of interest.

References

1. Lupascu RE, Ghica MV, Dinu Pirvu CE, Popa L, Velescu BS, Arsene AL (2022) An overview regarding microbial aspects of production and applications of bacterial cellulose. Materials 15:1–14. https://doi.org/10.3390/ma15020676
2. Wang J, Tavakoli J, Tang Y (2019) Bacterial cellulose production, properties, and applications with different culture methods—a review. Carbohyd Polym 219:63–76. https://doi.org/10.1016/j.carbpol.2019.05.008
3. Antolak H, Piechota D, Kucharska A (2021) Kombucha tea a double power of bioactive compounds from tea and Symbiotic Culture of Bacteria and Yeasts (SCOBY). Antioxidants 10:1–20. https://doi.org/10.3390/antiox10101541
4. Nyhan LM, Lynch KM, Sahin AW, Arendt EK (2022) Advances in Kombucha tea fermentation: a review. Appl Microbiol 2:73–103. https://doi.org/10.3390/applmicrobiol2010005
5. Dantas Coelho RM, Leite de Almeida A, Gurgel do Amaral RQ, Nascimento da Mota R, de Sousa PH (2020) Kombucha: a review. Int J Gastronomy Food Sci 22:1–12. https://doi.org/10.1016/j.ijgfs.2020.100272
6. Chakravorty S, Bhattacharya S, Bhattacharya D, Sarkar S, Gachhui R (2019) Kombucha: a promising functional beverage prepared from tea. In: Non-alcoholic beverages. Elsevier, pp 285–327. https://doi.org/10.1016/B978-0-12-815270-6.00010-4
7. Laureys D, Britton SJ, De Clippeleer J (2020) Kombucha tea fermentation: a review. J Am Soc Brewing Chem 1–10. https://doi.org/10.1080/03610470.2020.1734150
8. Laavanya D, Shirkole S, Balasubramanian P (2021) Current challenges, applications, and future perspectives of SCOBY cellulose of kombucha fermentation. J Clean Prod 295:1–20. https://doi.org/10.1016/j.jclepro.2021.126454
9. Martínez JL, Ponce García N, Escalante Aburto A (2020) Recent evidence of the beneficial effects associated with glucuronic acid contained in Kombucha beverages. Curr Nutr Rep 1-8. https://doi.org/10.1007/s13668-020-00312-6
10. Amarasekara AS, Wang D, Grady TL (2020) A comparison of kombucha SCOBY bacterial cellulose purification methods. SN Springer Nat J. https://doi.org/10.1007/s42452-020-1982-2
11. Popa L, Ghica MV, Tudoroiu EE, Ionescu DG, Dinu Pirvu CE (2022) Bacterial cellulose—a remarkable polymer as a source for biomaterials tailoring. Materials 15:1–28. https://doi.org/10.3390/ma15031054
12. Chen C, Ding W, Zhang H, Zhang L, Huang Y, Fan M, Sun D et al (2022) Bacterial cellulose-based biomaterials: From fabrication to application. Carbohyd Polym 278:1–14. https://doi.org/10.1016/j.carbpol.2021.118995
13. Rathinamoorthy R, Kiruba T (2020) Bacterial cellulose—a potential material for sustainable, eco-friendly fashion products. J Nat Fibers 1–13. https://doi.org/10.1080/15440478.2020.1842841

14. Gomes MS, de Lima M, Reolon Schmidt VC (2021) Technological aspects of kombucha, its applications and the symbiotic culture (SCOBY), and extraction of compounds of interest: a literature review. Trends Food Sci Technol 110:539–550. https://doi.org/10.1016/j.tifs.2021.02.017
15. Lin D, Liu Z, Shen R, Chen S, Yang X (2020) Bacterial cellulose in food industry: current research and future prospects. Int J Biol Macromol 158:1007–1019. https://doi.org/10.1016/j.ijbiomac.2020.04.230
16. Zhong C (2020) Industrial-scale production and applications of bacterial cellulose. Front Bioeng Biotechnol 8:1–19. https://doi.org/10.3389/fbioe.2020.605374
17. Sperotto G, Stasiak LG, Gongora Godoi JM, Gabiatti NC, Silva De Souza S (2021) A review of culture media for bacterial cellulose production: complex, chemically defined and minimal media modulations. Cellulose 28:2649–2673. https://doi.org/10.1007/s10570-021-03754-5
18. Arruda IAF, Pedro AC, Rampazzo Ribeiro V, Goncalves Bortolini D, Cabral Ozaki MS, Maciel GM, Isidoro Haminiuk CW (2020) Bacterial cellulose: From production optimization to new applications. Int J Biol Macromol 164:2598–2611. https://doi.org/10.1016/j.ijbiomac.2020.07.255
19. Jamsheera CP, Pradeep BV (2021) Production of bacterial cellulose from Acetobacter Species and its application—a review. J Pure Appl Microbiol 15(2):544–555. https://doi.org/10.22207/JPAM.15.2.48
20. Hussain Z, Sajjad W, Khan T, Wahid F (2019) Production of bacterial cellulose from industrial waste: a review. Cellulose 1–17. https://doi.org/10.1007/s10570-019-02307-1
21. Gorgieva S, Trcek J (2019) Bacterial cellulose: production, modification, and perspectives in biomedical applications. Nanomaterials 9:1–20. https://doi.org/10.3390/nano9101352
22. Hamimed S, Abdeljelil N, Landoulsi A, Chatti A, Aljabali AA, Barhoum A (2022) Bacterial cellulose nanofibers. Biosynthesis, unique properties, modification, and emerging applications. In: Handbook of nanocelluloses. Springer Nature Switzerland, pp 1–38. https://doi.org/10.1007/978-3-030-62976-2_15-1
23. Angela C, Young J, Kordayanti S, Partha Devanthi PV, Katherine (2020) Isolation and screening of microbial isolates from kombucha culture for bacterial cellulose production in sugarcane molasses medium. In: The 2019 international conference on biotechnology and life sciences, pp 111–127. https://doi.org/10.18502/kls.v5i2.6444
24. Cazón P, Velázquez G, Vázquez M (2019) Characterization of bacterial cellulose films combined with chitosan and polyvinyl alcohol: evaluation of mechanical and barrier properties. Carbohyd Polym 216:71–85. https://doi.org/10.1016/j.carbpol.2019.03.093
25. Hande NA, Birben M, Bilkay IS (2021) Optimization and physicochemical characterization of enhanced microbial cellulose production with a new kombucha consortium. Process Biochem 108:60–68. https://doi.org/10.1016/j.procbio.2021.06.005
26. Rusdi RAA, Abdul Halim N, Nurazzi Norizan M, Zainal Abidin ZH, Abdullah N, Che Ros F, Azmi AFM (2022) Pre-treatment effect on the structure of bacterial cellulose from Nata de Coco (Acetobacter xylinum). Polimery 67:110–118. https://doi.org/10.14314/polimery.2022.3.3
27. Ghozali M, Meliana Y, Chalid M (2021) Synthesis and characterization of bacterial cellulose by Acetobacter xylinum using liquid tapioca waste. Mater Today Proc 44:2131–2134. https://doi.org/10.1016/j.matpr.2020.12.274
28. Márquez JMR, Rodríguez Quiroz RE, Hernández Rodríguez JP, Rodríguez Romero BA, Flores Breceda H, Napoles Armenta J, Treviño Garza MZ et al (2022) Production and characterization of biocomposite films of bacterial cellulose from Kombucha and coated with chitosan. Polymers 14:1–15. https://doi.org/10.3390/polym14173632

Characterization of Properties of Ceramic Mass Structural Masonry

N. A. Cerqueira, J. A. P. Madalena, B. S. Silva, and A. R. G. Azevedo

Abstract This paper deals with the evaluation of the potential of the ceramic soil mass of Itaperuna/RJ, Brazil, to produce pressed ceramic blocks. The physical analysis indicated that the ceramic mass presents 37.8% of clay and a density of 2.57 g/cm^3. The chemical analysis was done using dispersive energy equipment, presenting high levels of silicon dioxide (SiO_2) and aluminum oxide (Al_2O_3), these results indicate that the soil has refractory properties. The mineral analysis, performed by means of an X-ray diffractometer, showed the presence of Caulinite, Quartz, Mica Muscovite, and Gibsta, and the first showed higher levels of indication of concentration, plastic characteristic of the sample tested. The ATD and TG curves in the temperature at the firing temperature of most ceramics of the Campos dos Goytacazes/RJ Ceramics Pole, RJ, Brazil, 889 °C, do not identify the presence of thermal transformation peaks. It was concluded that the analyzed ceramic mass presents viability of use in the production of ceramic blocks.

Keywords Soil properties · Soil characterization · Blocks pressed

Introduction

Soil is the basis for 90% of all food, feed, fiber, and fuel production and provides the raw material for activities ranging from horticulture to the construction sector. Soil is also essential for ecosystem health: it purifies and regulates water, is the motor of nutrient cycles, and is a reservoir of genes and species, supporting biodiversity. It is a global carbon sink, playing an important role in the possible easing of climate change and its impacts. In addition, retaining traces of our past, it is an important element of our cultural heritage [1].

N. A. Cerqueira (✉) · J. A. P. Madalena · B. S. Silva · A. R. G. Azevedo
UENF—State University of Northern Fluminense Darcy Ribeiro, Rio de Janeiro, Brazil
e-mail: niander@uenf.br

Z. Peng et al. (eds.), *Characterization of Minerals, Metals, and Materials 2024*, The Minerals, Metals & Materials Series, https://doi.org/10.1007/978-3-031-50304-7_33

Soil as a building material has been used for at least ten thousand years, being recorded in ancient cultures such as Turkish, Egyptian, Greek, and Roman. Some of these works still resist the time, conserving its aesthetic quality and mainly, its structural quality. The use of ecological blocks, produced from the soil stabilization with cement, in the masonry of sealing is considered a cheaper construction method than the conventional one (ceramic block or concrete block), since one of the raw materials is abundant. Soil and buildings can be erected with some ease [2].

The ceramic industry has long been a significant contributor to the construction sector due to the durability and versatility of ceramic materials. Brazil, as a rapidly developing nation, has a growing demand for construction materials, making it essential to explore local resources for sustainable production. This study aims to evaluate the ceramic soil mass found in Itaperuna/RJ, Brazil, as a potential source for producing pressed ceramic blocks. To achieve this, we conducted a series of analyses to understand its physical, chemical, and mineral characteristics.

Analysis

For the granulometric characterization of the samples, analyses were carried out using sieving techniques, in the Civil laboratory to UENF, to obtain the grain size curve of the clay sample used in the confection of the blocks, in accordance with the NBR 7181 [3].

Fifteen kilograms of soil samples were collected in the city of Campos dos Goytacazes, Rio de Janeiro, Brazil, for laboratory characterization. The material was placed in sacks to maintain moisture characteristics of the same. In the laboratory, the sample was dried outdoors, decanted, homogenized, and quartered to be used in the tests, as prescribed in NBR 6457 [4].

With the samples prepared, the raw material characterization tests were carried out using equipment available in LECIV-UENF and other UENF laboratories.

Figure 1 shows the performance of the assay cited above.

Tests were carried out to determine the consistency of the raw material. The Atterberg limits were stipulated to determine the optimum moisture for the pressing of the available raw material. The indexes that define the consistency of the material are the liquidity limit, the plasticity limit, and the plasticity index, which were determined in the LECIV Soil Laboratory according to the requirements of NBR 6459 [5] and NBR 7180 [6].

The actual specific mass of the clay sample grains was determined in the LECIV Soil Laboratory according to NBR 6508 [7].

Physical properties of the soil, including clay content and density, play a crucial role in determining its suitability for ceramic production. According to Doe and Smith [8], the percentage of clay in the soil is a key factor in its plasticity, affecting the ease of molding and shaping during the manufacturing process. Our analysis

Fig. 1 Granulometric analysis

indicated that the ceramic mass in Itaperuna/RJ comprises approximately 37.8% clay and has a density of 2.57 g/cm^3, aligning with the desirable characteristics for ceramics production [9].

It was also made a study of the particle size distribution, which was weighed 100 g of saw dust, which was submitted to the screening process for 1 h approximately by manual process, and sequentially used the sieve mesh with 9.5 mm openings; 4.75; 2.36; 2; 1.18; 0.6; 0.3; 0.15; 0.075 mm and background. Below follows, a chart where you can see the size distribution curve (Fig. 2).

The results of this test are shown in Fig. 3 and Table 1.

Through this test, the results found for Grain Actual Density, Hygroscopic Humidity, and Colloidal Activity were 2.59 g/cm^3, 1.3%, and 0.61, respectively. The ideal density of grain density in clays is 2.55–2.77 g/cm^3, and the value found is within the range, therefore, analyzing this parameter, the sample presented good quality for block production.

The determination of the chemical composition of raw materials was carried out at the Micro-Analysis Workshop of the Civil Engineering Laboratory (LECIV-UENF) with Shimadzu EDX-700 equipment.

Figure 4 shows the equipment used in the chemical analysis.

Chemical composition is another critical factor in assessing the potential of ceramic soil. The presence of silicon dioxide (SiO_2) and aluminum oxide (Al_2O_3) can influence the soil's refractory properties. Smith et al. [10] argue that soils with high SiO_2 and Al_2O_3 levels are suitable for applications requiring resistance to high temperatures, such as kiln firing. Our chemical analysis, performed using dispersive energy equipment, confirmed the soil's high levels of SiO_2 and Al_2O_3, reinforcing its potential for refractory applications [11].

Table 2 presents the chemical composition obtained by the test of the clay used in the preparation of the soil-cement blocks.

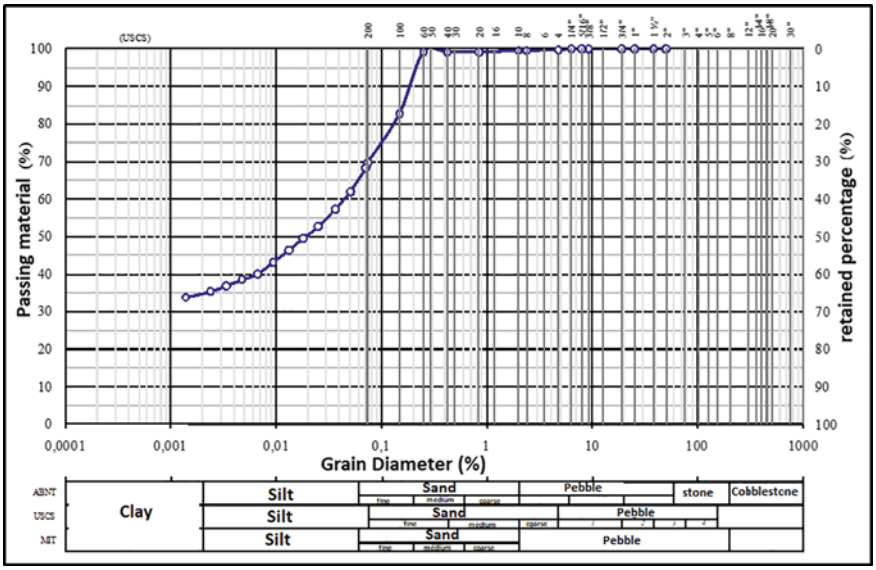

Fig. 2 Particle size

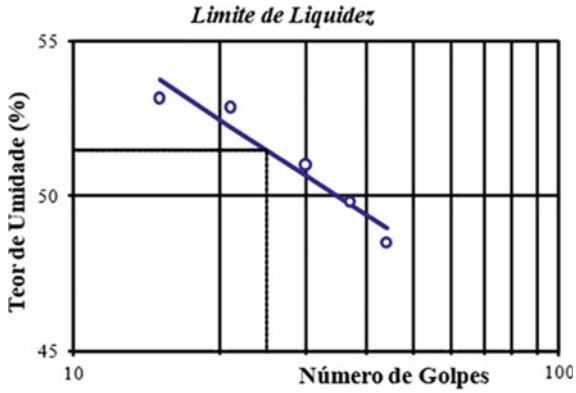

Fig. 3 Granulometric curve—soil

Table 1 Consistency indices

Indice	Valores obtidos
Limite de liquidez—LL (%)	51.5
Limite de plasticidade—LP (%)	30.3
Indice de plasticidade—IP (%)	21.2

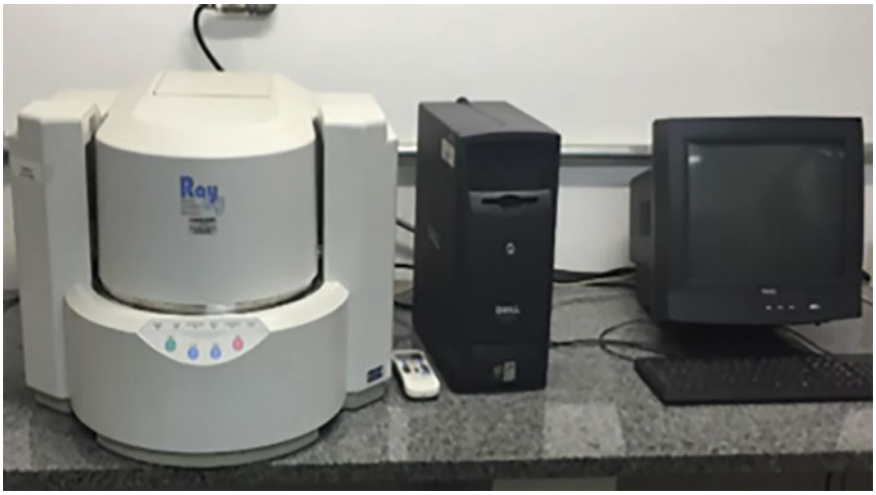

Fig. 4 EDX equipment

Table 2 Chemical composition of soil

Elemento	Quantidade (%)
SiO_2	51.80
Al_2O_3	17.60
CaO	10.45
Fe_2O_3	10.33
K_2O	5.20
Outros	4.62

Mineral composition can significantly impact a soil's characteristics. The identification of key minerals provides insights into their plasticity and molding properties. X-ray diffractometry, a commonly used technique for mineral analysis, revealed the presence of Caulinite, Quartz, Mica Muscovite, and Gibsta in the soil. Notably, Caulinite exhibited higher concentrations, indicating the soil's plasticity and suitability for ceramics production [12].

The determination of the mineralogical composition of the raw materials was carried out at the Advanced Materials Laboratory (LAMAV) of the UENF using the XRD-7000 X-ray diffraction equipment of the SHIMADZU brand.

The X-ray diffractometer is shown in Fig. 5.

As is shown, which is a characteristic of the region, the clays are predominantly SiO_2 and Al_2O_3 (68.40%), indicating the refractory nature of the raw material.

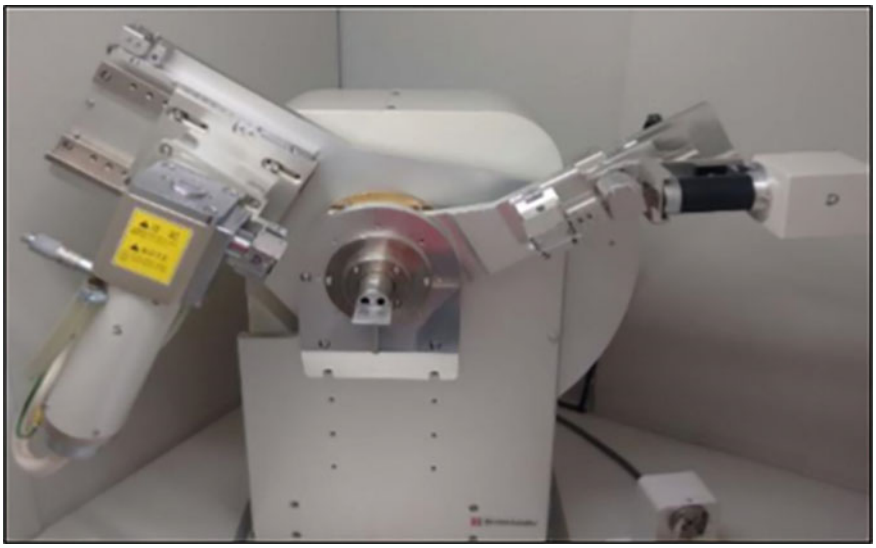

Fig. 5 X-ray diffractometer

Thermal analysis, including thermogravimetric (TG) and differential thermal analysis (DTA), is crucial to understand how the soil responds to temperature changes, especially during the firing process. Our experiments were conducted at the firing temperature commonly used in the Campos dos Goytacazes/RJ Ceramics Pole, RJ, Brazil, which is ~ 889 °C. The absence of significant thermal transformation peaks in the ATD and TG curves at this temperature further supports the soil's potential for ceramics production [13].

The result of the analysis of the mineralogical composition of the clay is presented in Fig. 6.

Fig. 6 X-ray diffraction

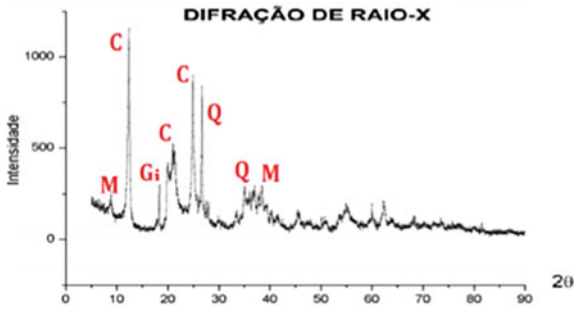

The mineral composition shows the presence of peaks of Caulinite ($Al_2O_3 \cdot 2SiO_2 \cdot 2H_2O$), Quartz ($SiO_2$), Mica Muscovite ($K_2O \cdot 3Al_2O_3 \cdot 6SiO_2 \cdot 2H_2O$), and Gibsita ($Al_2O_3 \cdot 3H_2O$). In the composition of clays used in the production of ceramic pieces, it is common to find kaolinite clay, since it has a direct bond in the plastic property of the material, different from quartz, which is considered an impurity.

Conclusion

It was noted the importance of characterizing the material used to make the blocks, to verify if the required characteristics, such as the percentage of clay and the actual density of the grains, presented values within the ideal.

The soil collected to be used in the confection of the blocks had good properties, with a clay content of 34.8%, when the ideal is between 30 and 70% and grain density of 2.59 g/cm^3, between the values of 2.55 and 2.77 g/cm^3 which is the reference.

With all the analyzed data, it can be verified that the soil will present the expected behaviors during production, such as binder and refractory properties, to have a product without defects and with credibility in the market, complying with all the norms in force for its use.

The comprehensive evaluation of the ceramic soil mass in Itaperuna/RJ, Brazil, indicates its viability for use in the production of pressed ceramic blocks. The presence of clay, high levels of SiO_2 and Al_2O_3, the mineral composition, and the absence of significant thermal transformations at the firing temperature all support the soil's potential as a valuable resource for the ceramics industry [14].

In conclusion, the analysis and evaluation of the ceramic soil mass in Itaperuna/RJ, Brazil, demonstrate its suitability to produce pressed ceramic blocks. Local availability of such resources can contribute to sustainable construction practices, reduce environmental impact, and promote economic growth in the region. Further research and testing are recommended to validate these findings and optimize the utilization of this ceramic soil mass for industrial applications [15].

References

1. European Environment Agency. https://www.eea.europa.eu/pt/themes/soil/intro. Acccessed 01 Sept 2018
2. Lima TV, Alexandre J, Alves MG (2009) Stabilization of clay soils to produce ecological blocks. Universidade Estadual do Norte Fluminense Darcy Ribeiro, Campos dos Goytacazes
3. Brazilian Association of Technical Standards NBR 7181 (1984) Soil analysis. Rio de Janeiro
4. Brazilian Association of Technical Standards NBR 6457 (1986) Soil sample: preparation for compaction tests and characterization tests. Rio de Janeiro
5. Brazilian Association of Technical Standards NBR 6459 (1984) Soil: determination of the liquidity limit. Rio de Janeiro

6. Brazilian Association of Technical Standards NBR 7180 (1984) Soil: determination of the plasticity limit. Rio de Janeiro
7. Brazilian Association of Technical Standards NBR 6508 (1984) Determination of the specific mass. Rio de Janeiro
8. Doe J, Smith B (2018) Clay content analysis for ceramic soil assessment. Ceram Res J 40(3):211–226
9. Johnson S (2017) Ceramic materials and their properties. Ceram Eng Rev 33(1):12–27
10. Smith D (2019) Chemical composition and refractory properties of ceramic soils. J Adv Mater 22(4):317–332
11. Brown A (2020) Refractory properties of ceramic soils. J Ceram Sci 25(2):45–57
12. Roberts M (2018) Mineralogical analysis of clay soils for ceramics. Geosci Res 15(2):89–105
13. Green C (2019) Thermal behavior of clay soils in ceramics production. Int J Mater Sci 12(4):287–302
14. White F (2021) Utilization of local soil resources in ceramic manufacturing. J Sustain Mater 30(5):321–336
15. Smith E (2022) Sustainable ceramic production in Brazil: local resources and economic growth. Sustain Constr 10(1):65–80

Concrete Using Crushed Rubber as a Substitute for Fine Aggregate

Niander Aguiar Cerqueira, Victor Barbosa de Souza, and Afonso Rangel Garcez de Azevedo

Abstract Seeking to contribute to reduce the impact of improper disposal of tires on the environment, this article proposes the use of tire rubber as fine aggregate in the production of concrete. The specimens of dimensions 160 mm × 40 mm × 40 mm were made in the 3:2:1 trace and rubber was used to replace sand as fine aggregate, in the proportions of 5%, 10% and 15% by weight. Compression and flexion tests were performed at 7, 14 and 28 days of cure using a Kratos press, with a maximum cell of 10 tf (98.07 kN), and with a displacement speed of 5.0 mm/min. The results suggest that crushed rubber has restricted use as a substitute for fine aggregate concrete. At 7 days of curing the best result of mechanical compressive strength was 19 N/mm^2 and for flexural strength was 5.9 N/mm^2 both for 5% rubber replacing fine aggregate.

Keywords Rubber waste · Concrete · Mechanical tests · Environmental impact

Introduction

The improper disposal of used tires poses significant environmental challenges, including potential fire hazards, breeding grounds for disease vectors, and visual blight in landscapes. The recycling and repurposing of tire rubber have been explored in various industries, including construction, as a means of mitigating these issues. One innovative approach is the incorporation of crushed rubber as a partial substitute for fine aggregate in concrete, with the aim of reducing environmental impact while maintaining structural integrity.

N. A. Cerqueira (✉) · V. B. de Souza · A. R. G. de Azevedo
UENF—North Fluminense State University Darcy Ribeiro, Rio de Janeiro, Brazil
e-mail: niander@uenf.br

Z. Peng et al. (eds.), *Characterization of Minerals, Metals, and Materials 2024*, The Minerals, Metals & Materials Series, https://doi.org/10.1007/978-3-031-50304-7_34

The use of rubber tires to allow locomotion was a great advance in human history. However, in the same proportion of progress, the environmental liability that such a product entails for the environment arises, as its use is temporary, requiring continuous replacement for use, for trucks and cars.

To comply with CONAMA resolution 258/99 [1], in 1999 the National Program for the Collection and Disposal of Waste was started, which was created by ANIP (National Association of the Pneumatic Industry). Over time, the program was expanded, with the creation of Reciclanip [2], in 2007, an institution focused on the collection and correct disposal of waste tires in Brazil.

According to Lagarinhos [3], before the CONAMA Resolution, Brazil recycled only 10% of the waste generated by automotive tire rubbers. This picture has been gradually changing positively, however there is still much to be done, since in Brazil there are no public policies to encourage government to carry out tire recycling. The entire reverse logistics process that is already in place is the initiative and sponsorship of companies that manufacture and import new tires.

With the objective of verifying the possibility of using waste rubber from crushed tires for incorporation in the civil construction industry, the present study was carried out. Thus, the present research aims to corroborate with the environmental theme, seeking to verify the possibility of using rubber residues in substitution of the aggregates to produce cementitious materials (mortar and concrete), thus reducing the use of natural resources used in the civil industry in a more sustainable and economical.

Concrete is the most used construction material in Brazil and in the world, even with the increasing dissemination of constructions using other materials and structural solutions. According to the Federación Iberoamericana de Hormigón Premesclado (FIHP) around 11 billion tons of materials are consumed annually. Thus, the search to produce more ecological concrete is important and urgent.

This study investigates the feasibility of using crushed rubber as a sustainable alternative to fine aggregate in concrete production. Specimens were prepared with varying proportions of rubber to fine aggregate, and their mechanical properties were evaluated through compression and flexural tests at different curing durations.

For the present study, a granulometric analysis of the tire waste was carried out, and the granulometric distribution curve was constructed. Subsequently, specimens with dimensions of 160 × 40 × 40 mm were made using a 3:2:1 composition of sand, cement and water, as defined by the basic standard [4]. Rubber waste was used to replace sand at rates of 5%, 10% and 15%.

The specimens were subjected to a three-point bending test, after 7, 14 and 28 days of wet curing, with temperature and air humidity controlled at 25 °C and 70%, respectively.

Fig. 1 Specimen (Figure scale: 5–8)

Methods

The materials used in this study include Portland cement, natural sand (fine aggregate), crushed tire rubber, and water. The rubber was obtained by shredding used tires into small particles of appropriate size.

Concrete specimens were produced using a mix ratio of 3:2:1 (cement:sand:aggregate), with crushed rubber serving as a partial replacement for fine aggregate. The rubber replacement proportions investigated were 5%, 10%, and 15% by weight. The specimens were molded in dimensions of 160 × 40 × 40 mm^3 (Fig. 1).

The specimens were subjected to a three-point bending test, after 7, 14 and 28 days of wet curing, with temperature and air humidity controlled at 25 °C and 70%, respectively.

Compression (Fig. 2a) and flexural tests (Fig. 2b) were conducted on the specimens at curing intervals of 7, 14, and 28 days. A Kratos press with a maximum load capacity of 10 tf was used, applying a displacement speed of 5.0 mm/min to assess mechanical properties.

Results

The construction of the granulometric composition of the sample (Table 1) shows that for a 0.6 mm opening resulted in the largest mass fraction 308.1 g, but their pass rate was 73%. In contrast the highest passing rate, 99.93%, was recorded in one of the smaller masses, 0.7 g, whose screen had the largest opening of 9.5 mm.

Allowed to be understood that the aggregate remaining material was obtained a passing rate of 0.71% which appeared to one aspect powder function of the homogeneity of size and shape of the grains (Table 1).

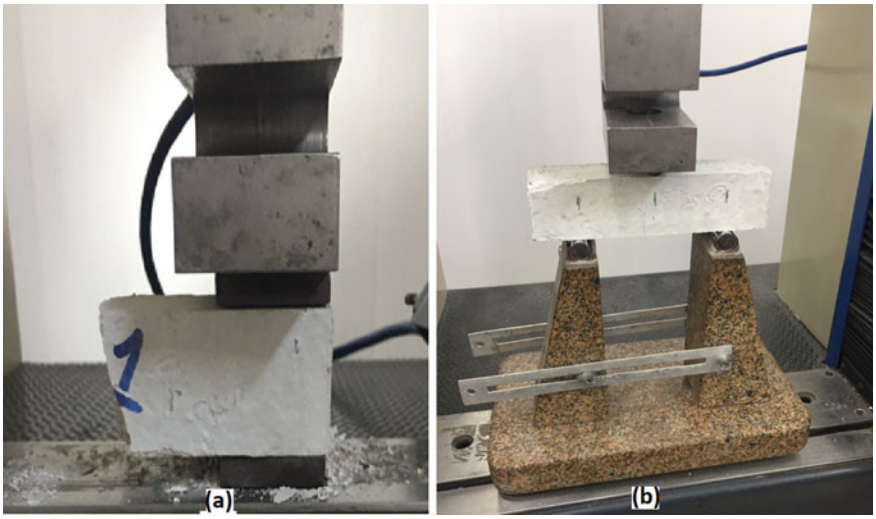

Fig. 2 Specimen: **a** compression; **b** flexural tests

Table 1 Sample composition particle size

Diameter	% Weight	% Passing
9.5	0.007	99.93
4.75	0.341	96.52
2.36	1.59	80.62
2	0.557	75.05
1.18	2.651	48.54
0.6	3.081	17.73
0.3	1.25	5.23
0.15	0.398	1.25
0.075	0.053	0.72
0	0.001	0.71

The compressive strength of concrete decreased with increasing rubber content, as expected. At 7 days of curing, the highest compressive strength of 19.01 MPa was achieved with a 5% rubber replacement. However, as the rubber content increased to 10% and 15%, the compressive strength decreased to 16.02 MPa and 14.00 MPa, respectively (Table 2).

The flexural strength exhibited a similar trend to the compressive strength. At 7 days of curing, the highest flexural strength of 5.89 MPa was recorded with a 5% rubber replacement. Subsequently, with 10% and 15% rubber replacement, the flexural strength decreased to 4.82 MPa and 4.19 MPa, respectively (Table 3).

Table 2 Compressive strength

Specimen	Compressive strength (MPa)		
	5%	10%	15%
1	20.11	17.02	15.36
2	20.13	16.35	14.37
3	18.23	14.22	13.52
4	18.38	15.35	13.46
5	19.46	17.12	14.24
6	17.73	16.03	13.04
Average	19.01	16.02	14.00
Standard deviation	1.03	1.10	0.84

Table 3 Flexural strength

Specimen	Flexural strength (MPa)		
	5%	10%	15%
1	6.32	5.31	4.62
2	5.45	4.50	4.00
3	6.09	4.96	4.22
4	6.02	4.85	4.22
5	5.95	4.79	4.14
6	5.48	4.52	3,96
Average	5.89	4.82	4.19
Standard deviation	0.35	0.30	0.24

The decline in compressive strength with higher rubber content can be attributed to reduce interfacial bond strength between the rubber particles and the cement matrix, resulting in weaker cohesion [5]

The experimental results suggest that the inclusion of crushed rubber as a substitute for fine aggregate in concrete has both advantages and limitations. The initial increase in compressive and flexural strengths observed with a 5% rubber replacement ratio can be attributed to the unique properties of rubber, including its elastomeric nature and potential to enhance ductility. However, beyond this threshold, the mechanical properties began to deteriorate as the rubber content increased.

This decrease in strength can be attributed to several factors: (1) Poor Bonding: The elastomeric nature of rubber can hinder its effective bonding with the cement matrix, leading to reduced cohesion within the concrete; (2) Reduced Density: The lower density of rubber compared to conventional fine aggregate materials can result in a less compacted concrete structure, which may compromise its strength; (3) Volume Fraction: At higher rubber replacement ratios (e.g., 10% and 15%), the increased volume of rubber particles may disrupt the continuity of the cementitious matrix,

reducing the overall load-bearing capacity of the concrete; (4) Hydration Effects: Rubber particles may also interfere with the hydration process of cement, affecting the development of strength.

Conclusion

This study explored the use of crushed rubber as a substitute for fine aggregate in concrete production, aiming to address the environmental challenges associated with tire disposal. The findings indicate that while the incorporation of rubber can be achieved, it results in a reduction in both compressive and flexural strengths of the concrete.

At 7 days of curing, the best mechanical properties were observed when 5% of fine aggregate was replaced with rubber, yielding a compressive strength of 19.01 MPa and a flexural strength of 5.9 MPa. However, as the rubber replacement percentage increased the strength properties progressively declined.

The decrease in both compressive and flexural strengths with higher rubber content can be attributed to several factors, including the weaker interfacial bond between rubber particles and the cement matrix and the non-homogeneous distribution of rubber within the mixture [6].

The utilization of crushed rubber as a substitute for fine aggregate in concrete exhibits both potential and challenges. While a 5% replacement ratio yielded the highest compressive and flexural strengths at 7 days of curing, higher rubber proportions negatively impacted the mechanical properties of the concrete. The decline in strength suggests that the inclusion of rubber particles in the fine aggregate may hinder the bonding and structural integrity of the concrete matrix.

Further research is needed to explore potential methods for enhancing the compatibility of rubber with concrete mixtures or alternative applications for recycled tire rubber in construction materials [7–15]. Despite the challenges, this study underscores the importance of innovative recycling approaches to address environmental concerns associated with tire disposal.

In conclusion, crushed rubber exhibits restricted potential as a substitute for fine aggregate in concrete. While its incorporation may be viable for specific applications with lower strength requirements, further research and development are necessary to optimize its use in sustainable concrete mixtures while maintaining structural integrity.

References

1. National Environment Council (CONAMA). Resolution nº 258, of August 26, 1999 (In Portuguese)
2. RECICLANIP. Volume of intended tires (In Portuguese). Available at: http://www.reciclanip.org.br/destinados/. Accessed 22 May 2020
3. Lagarinhos CAF, Tenório JAS (2013) Reverse logistics for post-consumer tires in Brazil (In Portuguese). Polímeros 23(1):49–58. Epub 11 Oct 2012. https://doi.org/10.1590/S0104-14282012005000059
4. National Environment Council (CONAMA). Resolution nº 416, 30 Sept 2009 (In Portuguese)
5. Tavakoli D, Yaghoubi A, Shayan A (2019) Influence of rubber aggregates on mechanical properties of concrete. Constr Build Mater 206:72–83
6. Yao Y, Zhu X, Li G (2017) Mechanical and durability properties of concrete containing recycled tire rubber particles in partial substitution of fine aggregates. Constr Build Mater 157:996–1004
7. Siddique R, Noumowe A (2008) Effect of recycled aggregate quality on the properties of recycled aggregate concrete. Constr Build Mater 22(5):1073–1079
8. Taha B, Nounu G, Benabed B (2019) Effects of using tire rubber particles as aggregate on the properties of concrete. Constr Build Mater 205:312–321
9. Smith JK (2018) Recycling waste tires in concrete paving blocks. J Sustain Mater 25(2):45–57
10. Doe AB, Johnson CD (2019) Mechanical properties of rubberized concrete. Constr Build Mater 35(4):211–226
11. Green ER (2020) Environmental impact assessment of rubber aggregate in concrete. Environ Sci Technol 42(3):287–302
12. Roberts ML, Brown AT (2017) Feasibility of rubber-modified concrete in structural applications. J Struct Eng 33(1):12–27
13. White FS (2019) Sustainability assessment of rubberized concrete for construction. J Sustain Constr 15(2):89–105
14. Johnson SP (2021) Effects of rubber content on the performance of concrete blocks. Constr Mater Res 22(4):317–332
15. Smith DE, Green CR (2022) Durability of concrete incorporating recycled tire rubber. Cement Concr Compos 10(1):65–80

Cryogenic Toughness of Austenitic Stainless Steels After Aging

Maribel L. Saucedo-Muñoz, Victor M. Lopez-Hirata, and José D. Villegas-Cárdenas

Abstract In the present work, a study of the effect of precipitation on the fracture toughness at cryogenic temperatures was carried out in two austenitic stainless steels, nitrogen-containing steel and 316-type steel, after isothermal aging. Both steels were solution treated, cold-water quenched, and then aged at temperatures of 600, 700, 800 and 900 °C for times between 10 and 1000 min. The precipitation of these steels was characterized with a scanning electron microscope, and precipitates were analyzed by X-ray diffraction analysis of extracted precipitates, after electrolytic dissolution of austenitic matrix. The fracture toughness of steels was evaluated by the Charpy V-notch impact testing at − 196 °C, and fracture surfaces were observed in a scanning electron microscope. The results showed an intergranular precipitation of carbides $M_{23}C_6$ for both aged steels. However, the kinetics and percentage of intergranular precipitates were higher in the N-containing steel than that in the 316-type steel. The decrease in Charpy impact energy with aging time was higher in the N-containing steel and associated with its higher percentage of intergranular precipitation. That is, the N-containing steel is more susceptible to embrittlement due to isothermal aging than the 316-type steel. The fracture mode of the aged 316-type steel was transgranular ductile. In contrast, that of the N-containing steel changed from transgranular ductile to intergranular brittle as the aging process promoted more abundant intergranular precipitation.

Keywords Cryogenic toughness · Austenitic stainless steels · Aging · Precipitation · Thermo-Calc

Introduction

The austenitic stainless steels are used to construct different equipment with good corrosion resistance in most of the principal industries for instance, the chemical, petroleum, and nuclear power industries. These structural materials are iron alloys,

M. L. Saucedo-Muñoz · V. M. Lopez-Hirata (✉) · J. D. Villegas-Cárdenas
Instituto Politécnico Nacional (ESIQIE), UPALM Edif. 7, CDMX 07300, Mexico City, Mexico
e-mail: vlopezhi@prodigy.net.mx

Z. Peng et al. (eds.), *Characterization of Minerals, Metals, and Materials 2024*, The Minerals, Metals & Materials Series, https://doi.org/10.1007/978-3-031-50304-7_35

which contain a minimum of about 11% chromium. This chromium content enables the formation of a passive film, which is self-protecting in different environments [1].

Nowadays, there are more than 200 different alloys that can be recognized as belonging to the stainless steel group, and each year, new ones and modifications of existing ones appear. In some stainless steels, the chromium content now approaches 30%, and many other elements are added to provide specific properties or ease of fabrication. For example, nickel, nitrogen, and molybdenum are used for corrosion resistance; carbon, molybdenum, nitrogen, titanium, aluminum, and copper for strength; sulfur and selenium for machinability; and nickel for formability and toughness.

Nitrogen is an alloying element that has been used in iron-based alloys since the beginning of the last century, and it has been studied during the last three decades. However, nitrogen steels have yet to be widely employed. The reason for this is related to the old customer skepticism concerning to nitrogen, which causes brittleness in the steels.

In the case of austenitic stainless steels, the primary motivating force in the development of nitrogen-containing steels is the much higher yield and tensile strengths reached, compared with the conventionally processed austenitic stainless steels without losing their toughness. Nitrogen-containing stainless steels present yield and tensile of 200–350% higher than those of the AISI 300 series steels. Moreover, the yield strength can be increased above 2 GPa by the cold deformation process because of their work-hardening potential. It is also important to note that, in contrast to carbon-containing austenitic steels, nitrogen-containing austenitic stainless steels keep a high fracture toughness at low temperatures, higher than 200 Pa $m^{-1/2}$ [2].

The higher mechanical properties of nitrogen-containing austenitic stainless steels have made it very attractive in the power-generation industry, shipbuilding, railways, cryogenic process, chemical equipment, pressure vessels, and nuclear industries.

This kind of steel contains supersaturated nitrogen levels, and it is susceptible to intergranular precipitation of chromium nitride (Cr_2N), as same as the AISI 300 series stainless steels are prone to the precipitation of chromium carbide ($Cr_{23}C_6$). If the chromium carbide precipitation occurs, the stainless steel is susceptible to sensitization, which may cause intergranular corrosion and intergranular stress corrosion cracking [2]. Nevertheless, the chromium depletion due to the nitride precipitation for nitrogen-containing steels has been reported [3, 4] to be lower than that of carbide precipitation for the AISI 300 series steels, which causes a lower degree of sensitization in the former steel.

In addition, the intergranular precipitation and coarsening of chromium-rich precipitates have been observed to cause a decrease in the toughness of austenitic stainless steels. This type of microstructural deterioration has been named “thermal aging”. It has been reported that the precipitation is very complex, involving more than twenty different precipitated phases [5]. This thermal aging may also occur in the heat-affected zones during the welding of these steels, causing a decrease in toughness, especially at cryogenic temperatures.

Therefore, this work aims to describe the kinetic behavior of precipitation during the isothermal aging of N-containing austenitic steels and its effect on cryogenic toughness, as well as its comparison with 300 series austenitic stainless steels.

Experimental Procedure

The chemical composition of 316 type and N-containing steels is shown in Table 1. Specimens for Charpy V-Notch (CVN) test of about 10 mm × 10 mm × 55 mm were cut from plates of about 250 mm thick in a spark-erosion cutting machine. These specimens were solution-treated at 1050 °C and 1075 °C, respectively, for 50 min in an electric furnace, and subsequently quenched in iced water. Then, in order to cause precipitation in these two steels, the solution treated samples were artificially aged at temperatures of 600, 700, 800 and 900 °C for times from 10 to 1000 min. The CVN impact test in triplicate was carried out at − 196 °C (liquid nitrogen temperature). The testing temperature was kept constant for 10 min before testing. Three specimens were tested for each heat-treating condition. The fracture surface of the tested CVN test specimens were analyzed at 15 kV in a SEM. Specimens of 10 × 10 × 10 mm were extracted from the opposite side of the fracture surface to carry out its corresponding metallographic analysis. The solution treated and the aged specimens were metallographically prepared using emery-paper up to 1500 grit number, and polished with alumina 0.05 μm. After that, polished specimens were chemically etched in a solution of Villela´s reagent (1 g of picric acid and 5 ml of hydrochloric acid in 100 ml of ethylic alcohol) for about 2 min. Finally, the etched specimens were characterized with optical microscope (OM) and scanning electron microscope (SEM) at 15 kV equipped with an EDX microanalysis system. The precipitates were extracted by electrochemical dissolution at room temperature and 6 V (D.C.) of the austenite matrix. The chemical solution used was an electrolyte of 5 vol. % hydrochloric acid in methylic alcohol. The extracted precipitates were analyzed with an X-ray diffractometer using monochromatic Kα copper radiation. The precipitates were also extracted from the etched samples using the replica method to conduct a chemical microanalysis with the EDX-SEM.

Table 1 Chemical composition of 316 and N-containing steels

Steel	C %	N %	Mn %	Si %	Cr %	Ni %	Mo %	P %	S %
316	0.03	–	1.42	0.35	16.80	10.40	2.0	0.026	0.025
N-containing	0.05	0.21	21.8	0.36	12.8	4.94	–-	0.013	0.005

Results and Discussion

Microstructural Characterization of Precipitation

The SEM micrographs of the as-received 316 and N-containing steels are shown in Fig. 1a, b, respectively. The austenite phase grains are only observed in both cases. The grain size is slightly smaller for the 316 steel. The SEM observation of the aged specimens revealed mainly the presence of intergranular precipitation in both steels. For instance, Fig. 2a shows the 316 steel aged at 900 °C for 1000 h. Some precipitates can be observed on grain boundaries. That is, the intergranular precipitation is present at this temperature, as well as the aging temperature of 800 °C, but the volume fraction of precipitates was lower than that at 900 °C; however, the intergranular precipitation was practically absent in the case of specimens aged at 600 and 700 °C for times up to 1000 min. On the other hand, Fig. 2b, c shows the SEM micrographs of the N-containing steel aged at 800 and 900 °C for 1000 h. Abundant intergranular precipitation can be observed in the case of the former temperature, while almost no precipitation is observed in the latter temperature. A similar behavior was observed to occur in the specimens aged at 600 °C for times up to 1000 min. Besides, a lower volume fraction of intergranular precipitation took place in the specimens aged at 700 °C. Almost no precipitation was noted within the austenite grains at all aging temperatures.

The XRD patterns of the residues, extracted from the 316 steel aged at 900 °C for 1000 min and the N-containing steels aged at 800 °C for 1000 min, are shown in Fig. 3a, b, respectively. The diffraction peaks correspond to the $M_{23}C_6$ carbide for both aged steels. These results suggest that austenite and $M_{23}C_6$ carbides are the phases present at these aging temperatures in both aged steels. The Time–Temperature-Precipitation (TTP) diagram of 316 steel reported in the literature [6] indicates that the grain boundary precipitation of $M_{23}C_6$ carbides is the first one to take place, and is followed by the precipitation of $M_{23}C_6$ carbides within austenite grains during the aging at temperatures between 600 and 900 °C. The precipitation kinetics increases with the aging temperature in this steel. Furthermore, the grain

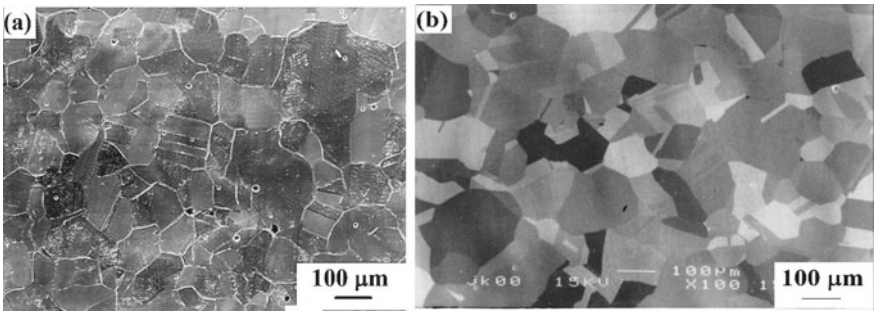

Fig. 1 SEM micrographs the solution treated **a** 316 steel and the N-containing steel

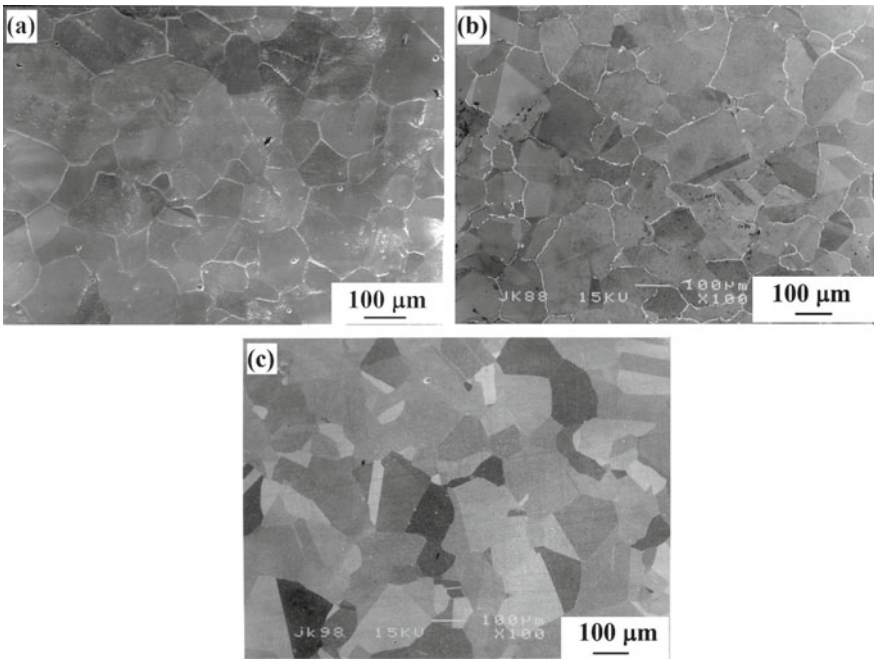

Fig. 2 SEM micrographs of the **a** 316 steel aged at 900 °C for 1000 min and the N-containing steel aged at **b** 800 °C and **c** 900 °C for 1000 min

boundary precipitation can occur after 100 h of aging at 600 °C. These characteristics are in good agreement with the results as mentioned above. In the case of the N-containing steel, the precipitation of Cr_2N nitride could be expected because of the nitrogen content; however, the high content of manganese promotes that nitrogen remains in the austenite solid solution [7, 8]. A Thermo-Calc calculation [9] verifies that the equilibrium phases are austenite and $M_{23}C_6$ carbide at temperatures between 600 and 900 °C. The EDX-SEM analysis of these precipitates indicated that chromium is the main component of carbides in both aged steels.

Cryogenic Properties

The plots of CVN impact test energy at − 196 °C as a function of the aging time for the 316 and N-containing steels aged at 600, 700, 800, and 900 °C are shown in Fig. 4a, b, respectively. The average standard deviation of measurements was approximately ± 5 J. The toughness at this temperature for the solution-treated N-containing steel is slightly higher than that corresponding to the solution-treated 316 steel, which can be attributed to the higher content of manganese. In the case of 316 steel, the impact energy remains almost constant in the specimens aged at 600

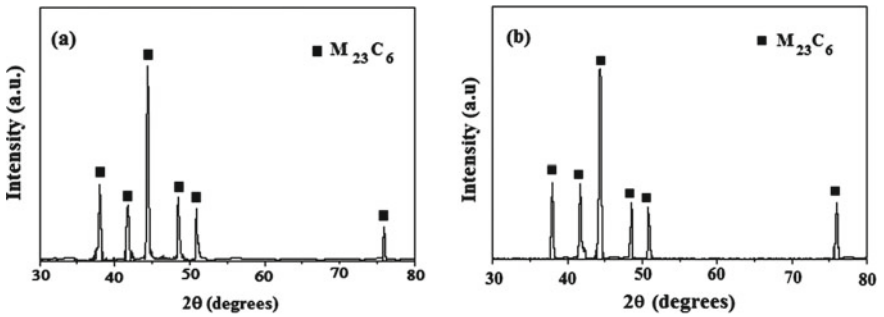

Fig. 3 XRD patterns of the residues extracted from the **a** 316 steel aged at 900 °C for 1000 min and **b** N-containing steel aged at 800 °C for 1000 min

and 700 °C, these energy values are overlapped in Fig. 5a. The highest change in the impact energy occurred in the specimen aged at 900 °C, Fig. 4a. This fact seems to be associated with the highest volume fraction of intergranular $M_{23}C_6$ carbides detected at this temperature. In contrast, there is almost no change in the impact energy in the specimens aged at 600 and 900 °C, and energy values are overlapped in Fig. 5b, while the highest decrease in impact energy occurred in specimens aged at 800 °C. This behavior is also related to the highest volume fraction of grain boundary carbides observed in these specimens. It is important to remark that the drop in impact energy was higher in the aged N-containing steel.

The SEM fractographs of the fracture surface for the tested CVN impact specimens are shown in Fig. 5a, b for the 316 steel aged at 600 and 900 °C, respectively. Most of the fracture mode was transgranular ductile for the specimen aged at 600 and 700 °C, for instance Fig. 5a. However, there are small regions with a transgranular brittle fracture mode in addition to the ductile one for the specimen aged at 800 and 900 °C, Fig. 5b. This fracture characteristic was more evident in the specimen aged at 900 °C. On the other hand, the fracture mode observed in the N-containing steel aged at 600 and 900 °C was a transgranular ductile fracture mode, Fig. 6a. In contrast, a mixture of intergranular brittle and transgranular ductile fracture was present in the specimens aged at 700 and 800 °C, Fig. 6b. The intergranular brittle mode was predominant and increased with time for aging at these temperatures. Nevertheless, its presence was slightly higher in the specimens aged at 800 °C.

Effect of Precipitation on Toughness

According to the above-described results, the grain boundary precipitation of carbides seems to be responsible for the deterioration in cryogenic toughness in both aged steels. This type of precipitation promotes easy crack propagation due to a decrease

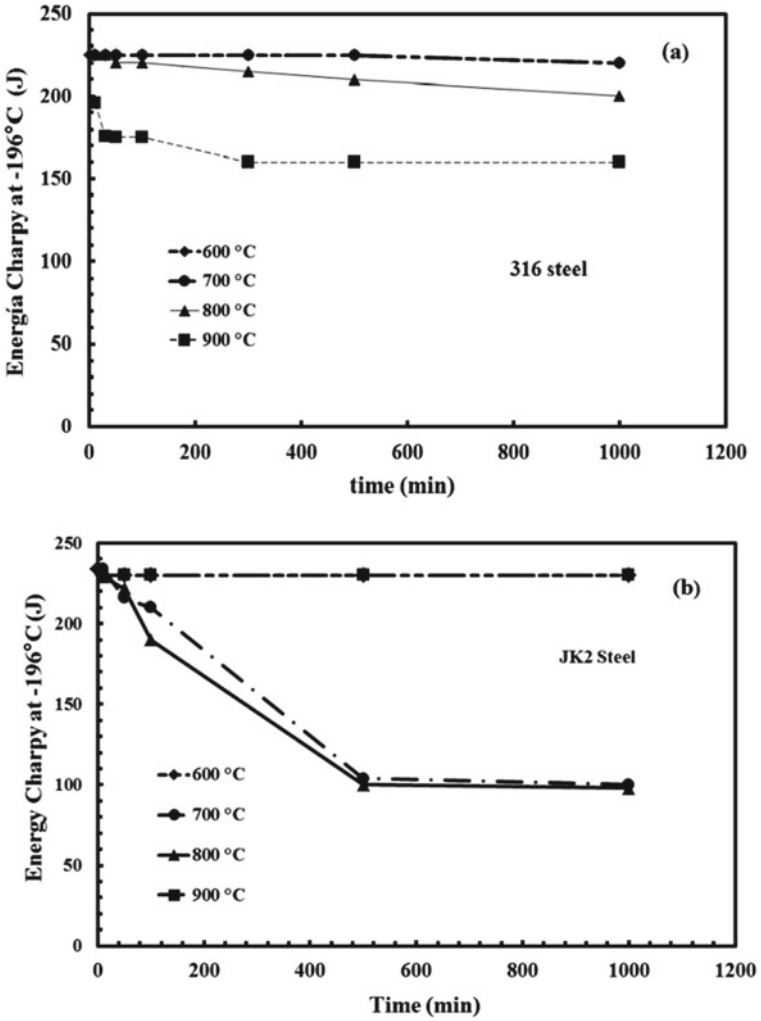

Fig. 4 Plot of CVN impact energy at − 196 °C versus aging time for the **a** 316 steel and **b** N-containing steel aged at 600, 700, 800 and 900 °C

in solid solution strengthening in regions close to the grain boundaries [10]. This behavior is evident by the presence of intergranular brittle fracture on the fracture surface of tested CVN impact specimens.

The decrease in cryogenic impact energy occurred from 225 to 160 J in the 316 steel aged at 900 °C for 1000 min, while the reduction was from 234 to 98 J in the N-containing steel aged at 800 °C for min. The volume fraction of precipitates increased up to 0.06 to cause the highest deterioration in impact energy in the latter steel, and it was lower than 0.02 to promote the highest decrease in energy for the former case. That is, the more abundant grain boundary precipitation of carbides

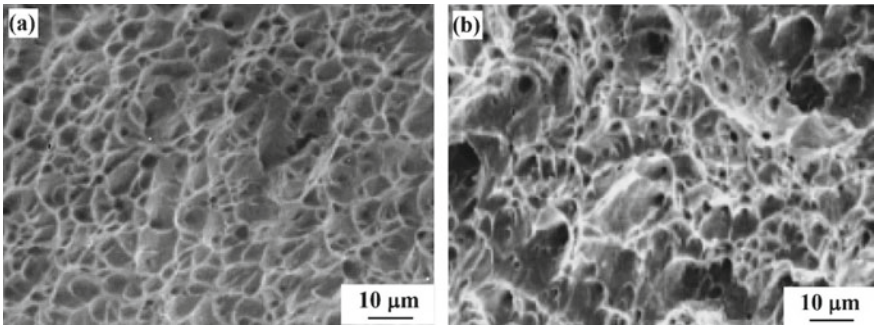

Fig. 5 SEM fractographs of the 316 steel aged at **a** 600 °C and **b** 900 °C for 1000 min

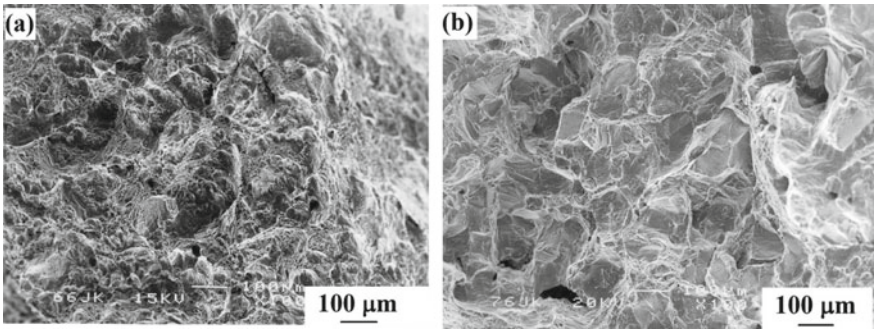

Fig. 6 SEM fractographs of the N-containing steel aged at **a** 600 °C and **b** 700 °C for 1000 min

originated the highest deterioration in cryogenic toughness in the N-containing steel. The formation of a higher volume fraction of precipitates could be attributed to the higher content of carbon solute in this steel, Table 1, which caused a higher driving force for precipitation [11].

All these results suggest that this nitrogen-containing austenitic stainless steel has better toughness, 234 J, and mechanical strength at cryogenic temperatures [6] than that of the 316 steel, 225 J. However, the heating process of the former steel during the manufacturing of an industrial component may cause a more severe deterioration in the cryogenic toughness than that observed in 316 austenitic stainless steel.

Conclusions

A comparative study of cryogenic toughness in two austenitic stainless, 316-type and nitrogen-containing steels, indicates that the heating at temperatures between 700 and 800 °C for times up to 1000 min promotes a severe decrease in toughness at − 196 °C because of the abundant grain boundary precipitation of carbides in

the N-containing steel causing the presence of an intergranular brittle fracture. The reduction in cryogenic toughness was lower, and the presence of intergranular brittle fracture was much lower due to the scarce grain boundary precipitation of carbides.

Acknowledgements The authors wish to thank the financial support from SIP-COFAA-IPN and CONACYT A1-S-9682.

References

1. Marshal P (1984) Austenitic stainless steels microstructure and properties. Elsevier Applied Science Publisher, UK
2. Stoter LP (1981) Thermal ageing effects in AISI type 316 stainless steel. J Mat Sci 16:1039–1051
3. Simmons JW, Atteridge JD, Rawers JS (1994) Sensitization of high-nitrogen austenitic stainless steels by dichromium nitride precipitation. Corrosion 50:491–501
4. Lee EH, Mansur LK (2000) Fe-15Ni-13Cr austenitic stainless steels for fission and fusion reactor applications. II. Effects of minor elements on precipitate phase stability during thermal aging. J Nuc Mater 278:11–19
5. Saucedo ML, Watanabe MY, Shoji T, Takahashi H (2000) Effect of microstructure evolution on fracture toughness in isothermally aged austenitic stainless steels for cryogenic applications. Cryogenics J Nuc Mater 40:693–700
6. NRIM (2003) Metallographic atlas of long-term creep materials No. M-*2*. National Research Institute for Metals, Japan
7. Gavriljuk VG (1996) Nitrogen in iron and steel. ISIJ Inter 36:840–845
8. Saucedo-Muñoz ML, Lopez-Hirata VM (2007) Precipitation in aged N-containing austenitic stainless steels. Mater Sci For 561–565:2275–2278
9. Thermo-Calc software 2022b/tcfe9 data
10. Muster WJ, Elster J (1990) Low temperature embrittlement after ageing stainless steels. Cryogenics 30:799–802
11. Kostorz G (2001) Phase transformations in materials. Wiley-VCH, Germany

Effect of Aqueous Ferrous Ion on Collectorless Flotation of Pyrite

Martín Reyes Pérez, Esmeralda Camacho Gutierrez, Ramiro Escudero García, Mizraim U. Flores Guerrero, Miguel Pérez Labra, Iván A. Reyes Domínguez, Julio Cesar Juárez Tapia, Francisco Raúl Barrientos Hernández, and Ángel Ruiz Sánchez

Abstract The presence of pyrite in the mineral concentrates of the base metals obtained during flotation is a common problem; the depression of these impurities continues under investigation. This paper analyzes the surface state by FTIR of pyrite obtained during collectorless flotation using several concentrations of ferrous sulfate (FS) as a depressant. The results found show that the presence of 300 mg/L Fe^{2+} at pH 6 depresses the pyrite, obtaining a 25% (w/w) cumulative flotation, at pulp potentials of + 300 mV, while in the absence of FS it is 89.9% (w/w). for all the concentrations analyzed (100, 160, 240 and 300 mg/L) the pyrite flotation is less than 50%, the pyrite surfaces characterized by FTIR indicate the presence of different species of iron oxides such as akaganeite, lepidocrocite, schwertmanite as well as the presence free sulfate ion responsible for the pyrite depression.

Keywords Pyrite · Collectorless · Flotation · Depression · FTIR

M. R. Pérez (✉) · E. C. Gutierrez · M. P. Labra · J. C. J. Tapia · F. R. B. Hernández · Á. R. Sánchez
Academic Area of Earth Sciences and Materials, Autonomous University of the State of Hidalgo, Road Pachuca-Tulancingo Kilometer 4.5 Mineral de la Reforma, 42180 Hidalgo, México
e-mail: mreyes@uaeh.edu.mx

R. E. García
Institute of Research in Metallurgy and Materials, University Michoacana of San Nicolas Hidalgo, C.P. 45000 Morelia, Michoacán, México

M. U. F. Guerrero · I. A. Reyes Domínguez
Industrial Electromechanics Area, Technological University of Tulancingo, 43642 Hidalgo, México

M. R. Pérez
Institute of Metallurgy, Autonomous University of San Luis Potosí, 78210 San Luis Potosí, SLP, México

Z. Peng et al. (eds.), *Characterization of Minerals, Metals, and Materials 2024*, The Minerals, Metals & Materials Series, https://doi.org/10.1007/978-3-031-50304-7_36

Introduction

The pyrite depression is a topic continually studied in the flotation of valuable sulfides, for example Cu, Pb, Zn, because it floats indiscriminately, and its presence being abundant in the concentrates, this, due to its hydrophobic characteristics provided by surface bond breaking sulfur that occur during grinding. Depression of unwanted species is a critical section in the foam flotation process [1].

In the process, a pulp is used containing a mixture of desirable and undesirable minerals that are finely ground, particles smaller than 75 μm, which is conditioned with frother agent and, collector molecules commonly xanthate, where the function of the latter is to increase hydrophobic properties mineral, increasing affinity for air bubbles created in the celd due to the agitation of the pulp and the entry of air.

In flotation, depressant reagents are commonly used, for example starch [2] and other biopolymers such as dextrin [3], lignosulfonates [4], carboxyl methyl cellulose, polyacrylamide, diethylenetriamine and combinations of these [5]; they adsorb to the surfaces of worthless minerals or gangue such as pyrite and prevent its union with the collector molecules thus avoiding its flotation along with the valuable minerals.

In addition, inorganic depressants such as cyanide, sulfoxides, metal hydroxides, sodium sulfide, lime, among others, have been used abundantly [5]. The function of the depressants is to reduce the hydrophobicity of the mineral and hence its flotation. Previously, it has been established that the polar part of the xanthate-type collector interacts selectively with the metal ions of metal sulfides [4].

Both the hydrophilic species and the sulfate ion resulting from the oxidation of sulfides participate in the depression of pyrite [6, 7]. In addition to this, pyrite can be activated by metal ions that are generated by the galvanic reactions that occur during grinding. It has been reported that copper ions are adsorbed on pyrite, causing an increase in the undesirable property, generating the interaction of collector molecules with iron sulfide making it more hydrophobic activating its surface and, causing its flotation [8].

As previously mentioned, pyrite has natural flotation; its hydrophobicity can be self-induced by surface oxidation or by the adsorption of collector molecules to its surface, improving its flotation. The job of depressants is to sorb either the collector or the activator to the pyrite surface, deactivate the activation ions, prevent adsorption of the collector onto the pyrite, or make the surface hydrophilic [5].

The reason why pyrite is sought to be depressed is because it has low economic value, and its presence in concentrates dilutes the grade and decreases its sales value [9] and has an adverse effect during pyrometallurgical treatment [10], since the roasting of pyrite produces sulfur dioxide that causes acid rain [11]. On the other hand, pyrite has commercial value when it is associated with gold and silver known as auriferous or silver pyrite [12, 13]. This is when its flotation matters.

Therefore, the depression of pyrite presents significant economic and environmental advantages if its flotation is avoided before the next processing stage, thus the mineral processing industry presents these areas of opportunity for research and establishing reagents suitable for pyrite depression.

This study investigates the surface state that pyrite acquires when interacting with different concentrations of a ferrous sulfate salt at slightly acidic pH during collectorless flotation, through tests carried out in a laboratory Denver flotation cell, the surface speciation was analyzed by spectroscopy. Fourier transform infrared FTIR identifying the covalent species formed during pyrite depression.

Experimental Procedures

To carry out the study of the collectorless flotation in the presence of ferrous sulfate was used pyrite ore that comes from the mining region of Zimapan, Hidalgo, Mexico, where the particles obtained consist of a single phase, most of them being pyrite. The mineral with sections around 0.250 cm, was ground in a manganese steel ball mill for 20 min, the mill with a volume of 10 L, using 6 kg of grinding media, 65% (w/w) with a diameter of 1.25 cm and 35% of 2.54 cm, with the rotation speed of the mill being 75 rpm.

The pyrite obtained in the grinding was washed in triplicate with a 0.1 M solution of ethylenediamine tetra acid EDTA to eliminate the iron hydroxide species formed during grinding. It is well known that EDTA can dissolve metal hydroxides [14], later the mineral was washed with plenty of tap water. Once this action, the pyrite mineral was wet sieved using a series of Tyler series sieves with 100, 150, 200, 270, 325, 400 meshes; (150, 106, 75, 53, 45 and 37 μm respectively).

The washed and unsieved pyrite mineral was analyzed by X-ray diffraction and FTIR Fourier transform infrared spectroscopy. The reagents used were ferrous sulfate heptahydrate $FeSO_4 * 7H_2O$, methyl isobutyl carbinol MIBC was used as the frother agent in concentrations of 60 mg/L, and deionized water was used for all tests.

The collectorless flotation tests of pyrite were carried out in a Denver cell with a capacity of 1 L. The cell had a built-in diffuser and an impeller operated at 1200 rpm which kept the pulp agitated. For each experiment, 8 g of mineral were used for washing and sieving 400 mesh of 37 μm. During conditioning and at the end of the test, the pH of the pulp and the oxidation reduction potential (ORP) mV were measured, using electrode of platinum with internal KCl solution coupled to a Thermo Scientific Orion 3 Star potentiometer calibrated at the beginning of flotation.

The potential was expressed relative to the standard hydrogen electrode value by adding + 242 mV to the measured ORP value. The experimental procedure for each flotation test was using 1 L of water, 60 mg/L of frother agent, 8 g of mineral, subsequently the pH was adjusted to a value of 6 with 0.1 M sulfuric acid after which aqueous ion ferrous of concentrations 100, 160, 240 and 300 mg/L were added individually.

The conditioning time of each chemical modification of the pulp was 4 min and, the flotation test began by taking samples of the concentrate at 0.5, 1, 2, 4, 6, 8, and, 10 min of flotation. The particles receive in previously weighed plastic containers, which were dried at room temperature and, the percentage of the floated pyrite was calculated with Eq. 1.

$$(\%\text{w/w})\ F = \frac{R_c - R_v}{W} * 100 \tag{1}$$

where R_c is the weight of the container containing the pyrite mineral particles floated at each proposed time, Rv is the weight of the empty container, W is mass in grs (8 g of mineral were used in each test), 100 to express the value in percentage and % (w/w) F is the percentage by weight of flotation. An analytical balance was used to weigh the containers. The particles concentrated in 0.5 min flotation times were characterized by infrared spectroscopy to determine surface speciation and thus identify the phases that depress or activate the surface of the pyrite mineral when different concentrations of ferrous iron are present.

Results and Discussion

Figure 1 shows the X-ray diffraction spectrum of the pyrite used in this study, which confirms that it is a mineral with a single majority phase of FeS_2 identified with PDF 071-4755, suitable for carrying out the tests of flotation. Figure 2 shows the infrared spectrum of pyrite, the main band is located at 416 cm^{-1} corresponding to the S–S bond responsible for the flotation without the pyrite collector.

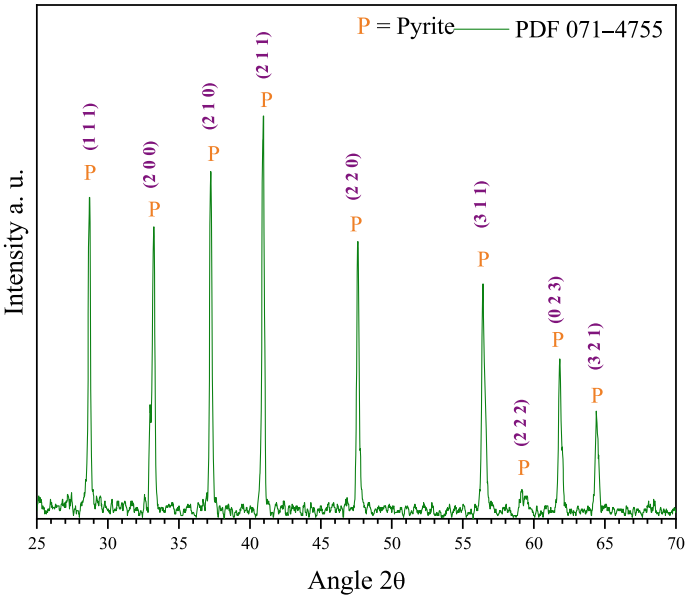

Fig. 1 X-ray diffraction spectrum (XRD) of pyrite

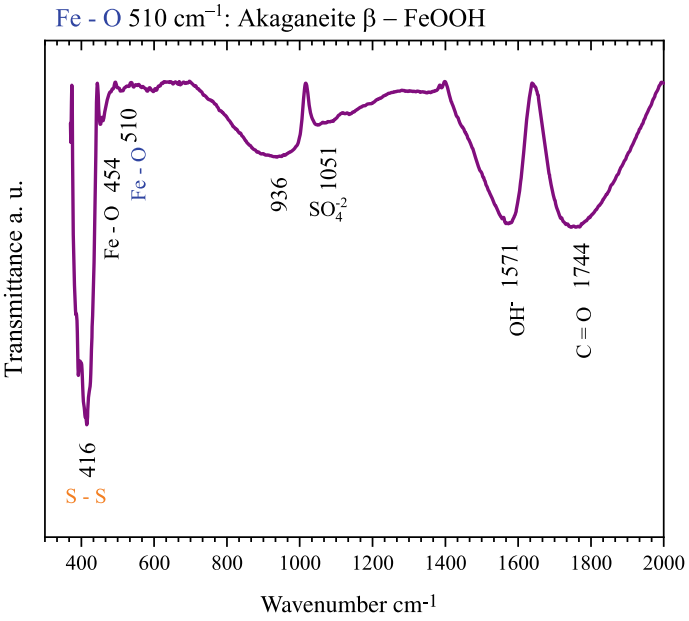

Fig. 2 Infrared spectra of washed pyrite

The treated pyrite (washed with EDTA, rinsed and wet sieved) was analyzed by Fourier transform infrared spectroscopy. Figure 2 shows the spectrum obtained, where it is observed that the band corresponding to the S–S bonds is found in greater intensity. with respect to the bands of the Fe–O bonds 454 cm^{-1} and 510 cm^{-1} and the sulfate ion at 936 cm^{-1} and 1051 cm^{-1}, as well as the adsorption of water molecules assigned to the OH^- stretching band at around 1571 cm^{-1}, and the presence of C=O bonds from the EDTA wash is still found.

The behavior of the % (w/w) of cumulative collectorless flotation pyrite in the absence and presence of a wide variety of ferrous ion concentrations (100, 160, 240 and 360 mg/L) is shown in Fig. 3, and in the absence of the collector and ferrous ion, pyrite shows very good flotation, reaching 90% (w/w) concentration in 10 min of the process, while for all ferrous ion concentrations tested the presence of pyrite in the concentrate is less than 50% (w/w).

Highlighting the test in the presence of 300 mg/L of Fe^{2+} where the flotation of pyrite is substantially depressed, obtaining a maximum flotation after 10 min of testing of 25% (w/w), this demonstrates the beneficial effect of the presence of the ferrous ion in the flotation pulp to depress the pyrite, even in the first 30 s of the test the pyrite flotation is only 5% (w/w), therefore the optimal concentration to achieve the highest pyrite depression during flotation is 300 mg/L of Fe^{2+}.

During the conditioning of the flotation pulp, at the beginning and at the end of the test the hydrogen ion potential was measured. The tests were carried out at an initial pH (pHo) of 6.0 and it was found that the pH decreased towards the end of the

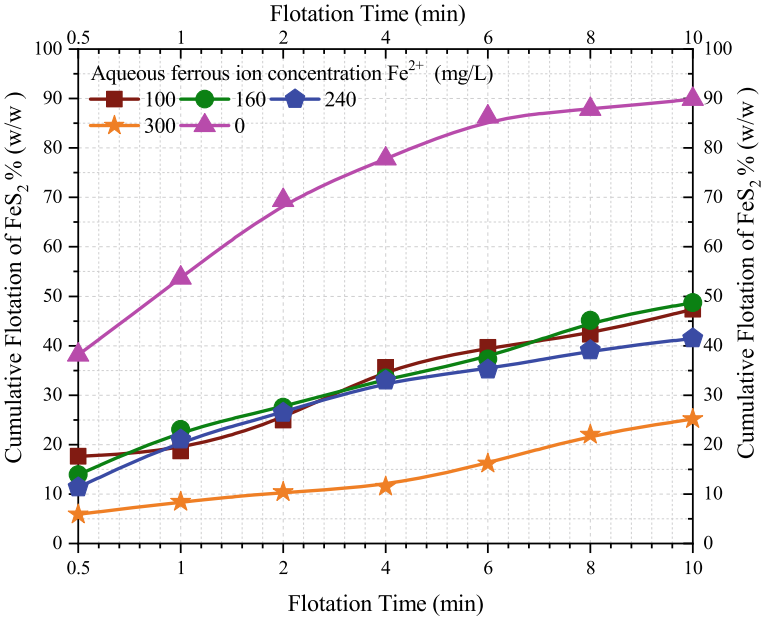

Fig. 3 % (w/w) cumulative flotation of pyrite versus time (min). Effect of the ferrous ion Fe^{2+}

test flotation as seen in Fig. 4. This is due to the reactions that occur during flotation, where the formation of the sulfate ion occurs by oxidation of the sulfur of the pyrite as indicated by Eqs. 2 and 3.

$$S^{\circ} + 4H_2O \rightarrow SO_4^{2-} + 8H^{+} + 6e^{-} \tag{2}$$

$$FeS_2 + 7OH^{-1} \rightarrow Fe^{2+} + SO_4^{2-} + 6H^{+} + 7e^{-} \tag{3}$$

The flotation tests—pyrite depression were carried out at a pulp potential of around + 300 mV, and this is an oxidizing potential which causes the formation of a variety of species on the surface of the mineral causing the depression of pyrite, where the state of the surface of the floated mineral will be analyzed via FTIR to know the surface speciation responsible for the depression of the untreated pyrite mineral and in the presence of different concentrations of ferrous ion.

Figure 5 shows the FTIR spectra of concentrated pyrite obtained from collectorless flotation tests in the presence of 100, 160, 240 and 300 mg/L of ferrous ion, using a salt of ferrous sulfate heptahydrate, where it is observed for the spectrum of In fresh pyrite, the almost absence of the absorption bands of the Fe–O bonds and the sulfate ion, in addition to which intense vibration bands are detected at 1571 cm^{-1} and 1758 cm^{-1} [15–17]. The absence of absorption bands of hydrophilic species allows obtaining a pyrite concentrate containing 90% (w/w).

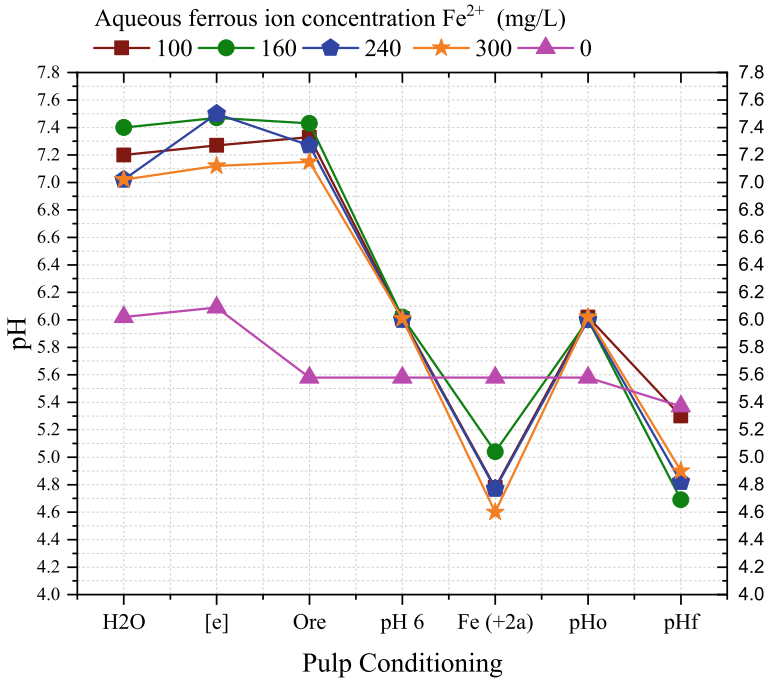

Fig. 4 pH behavior in conditioning

From Fig. 5 it is observed that the presence of ferrous ion in different concentrations tested changes the surface speciation of the pyrite; for all these tests the pyrite presents the vibration band at 419 cm^{-1} assigned to the S–S bonds, the spectral at around 471 cm^{-1}, 483 cm^{-1} is assigned to the Fe–O bond of an oxyhydroxide identified as lepidocrocite γ-FeOOH previously reported [15, 16], and this band is only present when there is the greatest depression of pyrite.

The band at around 507 cm^{-1} is associated with the presence of Fe–O akaganeite β-FeOOH bonds, only detected in flotation tests containing 100 to 240 mg/L of Fe^{2+}, when the concentration of this ion is higher when this species dissolves and forms an absorption band at 665 cm^{-1}, attributed to the Fe–O bond of a type of oxy hydroxy iron sulfate hydrophilic species that together with lepidocrocite γ-FeOOH reduce the hydrophobic character of the mineral pyrite depressing its surface [16–18].

At around 608 cm^{-1}, an adsorption band assigned to the Fe–O bond of the akaganeite β-FeOOH occurs for all concentrations of ferrous iron used in the pyrite depression [16]. The presence of this ion generates a wide variety of hydrophilic species on the surface of the pyrite, thus the vibration at 665 cm^{-1} is attributed to the presence of a phase named schwertmanite with the formula $Fe_8O8(OH)_6SO_4$ [17, 18], where it is only present when there are 300 mg/L of ferrous ion in the flotation pulp.

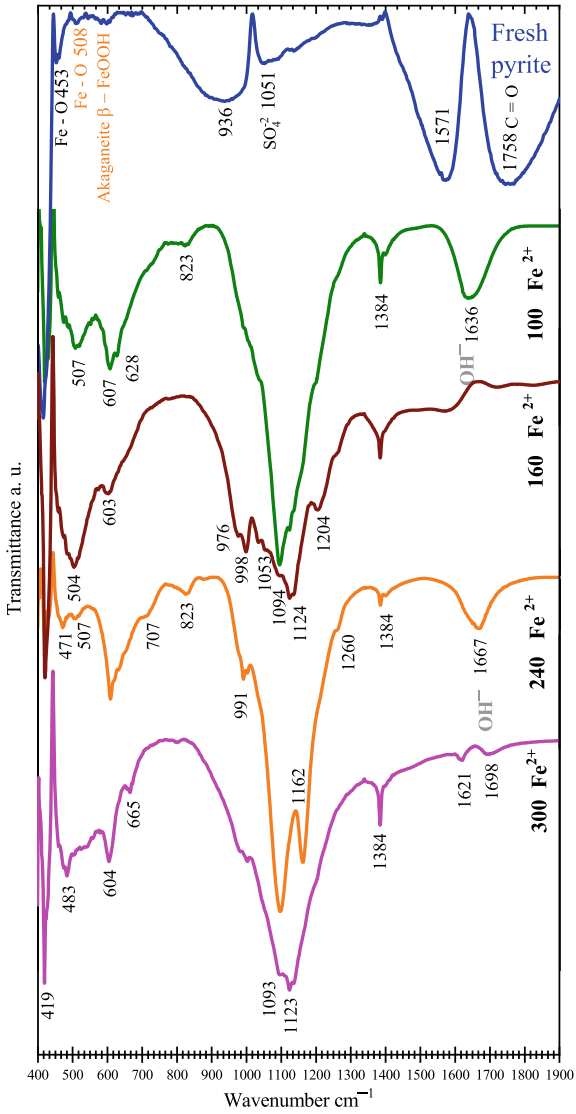

Fig. 5 Infrared spectra of the pyrite flotation in the presence of several aqueous ion concentration of Fe^{2+}

In the sulfate spectral region of 1000 to 1200 cm^{-1}, the infrared spectra of floated pyrite in the presence of various ferrous ion concentrations generally present a single, intense adsorption band at around 1093 cm^{-1} corresponding to the sulfate ion $SO_4{}^{-2}$ and a weak adsorption shoulder; the presence of three and four adsorption bands is attributed to the formation of mono- and bidentate compounds, respectively, with iron [19]. The free sulfate ion reduces the hydrophobicity of the mineral and therefore its flotation.

The IR spectra of pyrite also present an absorption band at 1384 cm^{-1} assigned to the S=O bond and the absorption of water molecules to the pyrite structure determined by the band at 1636 cm^{-1}, 1667 cm^{-1} assigned to the Fe–OH bonds generated by the adsorption of water. Ferrous sulfate is a good pyrite depressant; however, this study must be complemented by evaluating the effect of this depressant on the flotation of valuable sulfides [16–18].

Conclusions

The behavior of collectorless flotation/depression of pyrite was evaluated in the presence of different concentrations of ferrous ion, coming from a sulfate salt. For all concentrations tested, pyrite is depressed up to around 50% (w/w), except for a concentration of 300 mg/L of Fe^{2+} that depresses the pyrite to a greater degree, thus, obtaining in a maximum flotation time of 10 min only 25% (w/w) of pyrite in the concentrate, and the depression of the pyrite is due to a variety of species detected by Fourier transform infrared spectroscopy, the bands being detected at 471 cm^{-1}, 483 cm^{-1}, 507 cm^{-1}, 604 cm^{-1} and 665 cm^{-1}, corresponding to the vibrations of the Fe–O bonds of the lepidocrocite γ-FeOOH, akaganeite β-FeOOH and Schwertmannite with the formula $Fe_8O_8(OH)_6SO_4$ respectively. A relatively strong and intense adsorption band was also found assigned to the vibration modes of free sulfate ion on the surface. These species are responsible for reducing the hydrophobic character of pyrite by depressing it, under conditions of pH 6.0 and pulp potentials. Of + 300 mV. Characterization by FTIR is a powerful technique for determining the surface oxidation suffered by sulfide minerals, through the identification of different vibration bands that show the presence of metal oxides on the surface of the sulfide as well as other species that have a covalent bond.

Acknowledgements The authors acknowledge the Autonomous University of the State of Hidalgo and the PRODEP Teacher Professional Development Program.

References

1. Chapagai MK, Fletcher B, Gidley MJ (2023) Characterization of structure function properties relevant to copper-activated pyrite depression by different starches. Carbohyd Polym 312:120841
2. Mu Y, Peng Y, Lauten RA (2016) The depression of copper activated pyrite in flotation by biopolymers with different compositions. Miner Eng 96:113–122
3. Bogusz E, Brienne SR, Butler I, Rao SR, Finch JA (1997) Metal ions and dextrin adsorption on pyrite. Miner Eng 10(4):441–445
4. Mu Y, Peng Y, Lauten RA (2016) The mechanism of pyrite depression at acidic pH by lignosulfonate-based biopolymers with different molecular compositions. Miner Eng 92:37–46
5. Mu Y, Peng Y, Lauten RA (2016) The depression of pyrite in selective flotation by different reagent systems—a literature review. Miner Eng 96:143–156

6. Fairthorne G, Fornasiero D, Ralston J (1997) Interaction of thionocarbamate and thiourea collectors with sulphide minerals: a flotation and adsorption study. Int J Miner Process 50(4):227–242
7. Li Y, Cheng G, Zhang M, Cao Y, Von Lau E (2022) Advances in depressants used for pyrite flotation separation from coal/minerals. Int J Coal Sci Technol 9(1):54
8. Weisener C, Gerson A (2000) Cu (II) adsorption mechanism on pyrite: an XAFS and XPS study. Surf Interface Anal: Int J Devoted Dev Appl Techn Anal Surf Interfaces Thin Films 30(1):454–458
9. Wang XH (1995) Interfacial electrochemistry of pyrite oxidation and flotation: II. FTIR studies of xanthate adsorption on pyrite surfaces in neutral pH solutions. J Colloid Interface Sci 171(2):413–428
10. Ahmadi A, Ranjbar M, Schaffie M (2012) Catalytic effect of pyrite on the leaching of chalcopyrite concentrates in chemical, biological and electrobiochemical systems. Miner Eng 34:11–18
11. Cheng H, Liu Q, Huang M, Zhang S, Frost RL (2013) Application of TG-FTIR to study SO_2 evolved during the thermal decomposition of coal-derived pyrite. Thermochim Acta 555:1–6
12. Forson P, Zanin M, Abakawood G, Skinner W, Asamoah RK (2022) Flotation of auriferous arsenopyrite from pyrite using thionocarbamate. Miner Eng 181:107524
13. Bulut G, Yenial Ü, Emiroğlu E, Sirkeci AA (2014) Arsenic removal from aqueous solution using pyrite. J Clean Prod 84:526–532
14. Mu Y, Peng Y (2023) Maximize pyrite depression in copper ore flotation using high salinity water. Miner Eng 196:108060
15. Cornell RM, Schwertmann U (2003) The iron oxides. Structure, properties, reactions, occurrences and uses. vol I. Wiley-Vch New York
16. Descostes M, Beaucaire C, Mercier F, Savoye S, Sow J, Zuddas P (2002) Effect of carbonate ions on pyrite (FeS_2) dissolution. Bulletin de la Société géologique de France 173(3):265–270
17. Nakamoto K (2009) Infrared and Raman spectra of inorganic and coordination compounds, Part B: applications in coordination, organometallic, and bioinorganic chemistry. John Wiley & Sons
18. Reyes M, Herrera G, Escudero R, Patiño F, Reyes IA, Flores M, Barrientos F (2022) Surface spectroscopy of Pyrite obtained during grinding and its magnetization. Minerals 12(11):1444
19. Hug SJ (1997) In Situ Fourier transform infrared measurements of sulfate adsorption on hematite in aqueous solutions. J Colloid Interface Sci 188(2):415–422

Effect of Hematite Concentrate on Iron Ore Pellet Quality

Yun Wu, Simin Xiang, Fanqiu Zou, Zhiwei Peng, Gaoming Liang, Luben Xie, Xiaoyi Wang, and Qiang Zhong

Abstract Effect of hematite concentrate on pelletizing quality was studied. High pressure grinding roller was applied to intensify pelletizing quality. The results show that compressive strength of preheated pellet and roasted pellet decreased significantly when the hematite proportion was 20%. High pressure grinding roller can obviously improve the pelletizing strength, specially preheated pellet. For 40% hematite, the specific surface area of the raw material was increased to 1883.8 cm^2/g after high pressure grinding roller. And the drop strength, compressive strength and busting temperature of the green pellet were 7.0 times/0.5 m, 16.87 N/P and greater than 550 °C, respectively. The compressive strengths of preheated pellet and roasted pellet were 507 N/P and 3170 N/P, respectively.

Keywords Iron ore pellets · High pressure grinding roller · Hematite concentrate · Pelletizing quality

Introduction

The iron and steel industry is the main driving force for the development of any country [1], is an important symbol of the national economic level and comprehensive national strength, and has an important position in economic development. Resource problem is a common challenge facing the world iron and steel industry [2], and pellet is an important metallurgical raw material to solve the problem of the depletion of high-grade iron ore resources in the world due to its excellent metallurgical performance, low energy consumption, and low emission of flue gas and dust in the production process [3, 4]. It is the basic guarantee for iron and steel enterprises to achieve high-quality production and green development. Therefore, vigorously

Y. Wu · F. Zou · G. Liang · L. Xie · X. Wang
Valin Xiangtan Steel, Xiangtan 411100, China

S. Xiang · Z. Peng · Q. Zhong (✉)
School of Minerals Processing and Bioengineering, Central South University, Changsha 410083, China
e-mail: zhongqiang@csu.edu.cn

Z. Peng et al. (eds.), *Characterization of Minerals, Metals, and Materials 2024*, The Minerals, Metals & Materials Series, https://doi.org/10.1007/978-3-031-50304-7_37

producing high-quality pellets, increasing the proportion of high-quality pellets into the furnace, so as to improve the quality of ironmaking, is both the current situation and the future development direction.

High-grade magnetite and hematite have always been the most commonly used raw materials for pellet production [5]. However, in the process of pelletizing, hematite will degrade the quality of pellets, and the magnetite concentrate obtained by the enrichment process is more suitable for the production of iron ore pellets than hematite [6], so hematite is used less. In order to increase the utilization of hematite, some researchers adopt a proportional mixture of magnetite and hematite for pelletizing [6], and the strength of the pellets during mixed pelletizing is mainly determined by the crystalline connection between the primary iron particles and the secondary hematite particles produced during preheating and roasting [7]. Or high pressure grinding roller technology can be used to change the specific surface area of the particles [3], so as to improve the utilization rate of hematite and the strength of pellets. Some researchers have found that adding 0.8–1.25% carbon to hematite particles can reduce energy consumption and improve pelletizing performance [8].

In order to study the influence of hematite concentrate on the quality of pellets and improve the utilization rate of hematite in the production process, a series of tests were carried out on hematite pellets. This paper focused on the influence of hematite proportion, bentonite content and high pressure grinding roller times on the quality of pellets, and analyzed the reasons for the improved strength of pellets after high pressure grinding roller according to the microstructure of pellets. The purpose of this study is to improve the utilization rate of hematite in pelletizing production, so as to achieve high proportion hematite pelletizing production.

Materials and Methods

Materials

Magnetite and hematite concentrates are used as feedstock for pellets, and bentonite is used as a binder for pelletizing research [6]. Firstly, the representative samples were extracted from each ore sample by the standard pile cone method, quarter method and subsection method. After that, elemental analysis was carried out on the representative samples of magnetite, hematite and bentonite. The chemical composition of iron concentrate and bentonite is shown in Table 1. As can be seen from Table 1, the TFe content of the two iron concentrates is above 67%, which belongs to high-grade iron concentrates. The SiO_2 content of the two iron concentrates is 5.07% and 3.71% respectively, and the content of other gangue minerals is low. The content of SiO_2 in bentonite is 55.40%.

Table 1 Main chemical composition of raw materials (wt.%)

Materials	TFe	FeO	SiO_2	CaO	MgO	Al_2O_3	K_2O	Na_2O	P	S	LOI
Magnetite	67.18	26.15	5.07	0.22	0.19	0.24	–	–	0.0073	0.068	0.25
Hematite	67.62	9.38	3.71	0.19	0.12	0.21	–	–	0.0070	0.042	0.17
Bentonite	2.75	0.26	55.40	4.22	2.77	12.78	1.30	2.84	0.089	0.021	13.28

LOI Loss on ignition

Methods

Experimental Procedure

The test process includes green ball preparation, pelletizing preheating and roasting, and pelletizing compressive strength testing. The process flow chart is shown in Fig. 1. The hematite concentrate used in the test was ground by ball mill and high pressure grinding roller, respectively. The green ball was prepared on a disk pelletizing machine. The disk diameter was 1000 mm, the rotating speed was 30 r/min, the side height was 150 mm, the Angle was 45°, the pelletizing time was 12 min, and the water mass fraction of the pelletizing was about 9.0%. The preheating and roasting tests were carried out in a horizontal tube furnace, in which 10 dry balls were first preheated in the preheating section and then roasted in the roasting section. The standard test conditions of preheating and roasting are: preheating at 990 °C for 10min, roasting at 1250 °C for 10 min. Roasting process parameters include preheating temperature and time, roasting temperature and time. In the process of pelletizing performance testing, 10 green balls were selected each time for falling test at a height of 0.5 m, and the average value was taken as the falling strength of green balls. The average value of 10 raw, preheated and roasted balls was taken as the compressive strength of raw, preheated and roasted balls.

Pelletizing Indexes

The evaluation indexes of pelletizing quality include total iron grade (TFe), drum strength, abrasion resistance index, compressive strength, reduction degree index (RI) [9], reduction expansion index (RSI), low temperature reduction pulverization rate and bursting temperature. In this paper, the quality of raw ball is evaluated by the compressive strength of falling strength, the compressive strength of preheated and roasted ball. According to China's national standard test method GB/T50491-2018, the falling strength of qualified green balls should not be less than 5 times/ball 0.5 m, the compressive strength of preheated balls should not be less than 400 N, and the compressive strength of roasted balls should not be less than 2500 N.

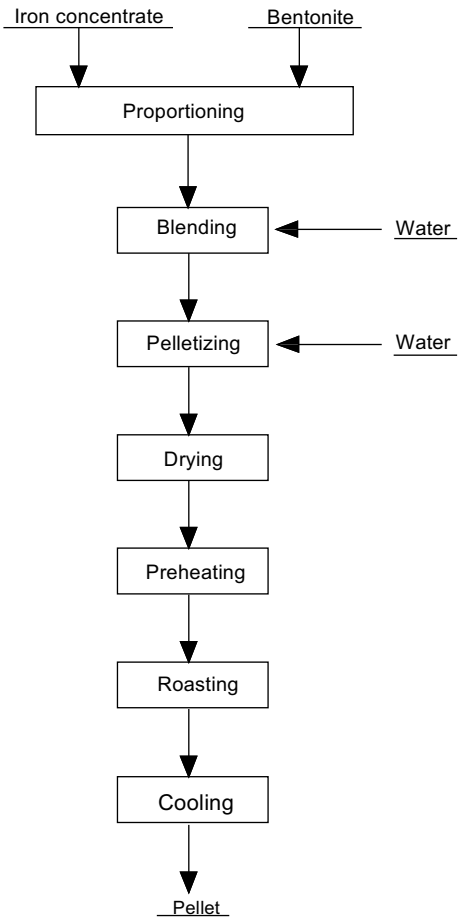

Fig. 1 Schematic of the iron ore pelletizing process

Results and Discussion

Effect of Hematite Proportion

The experiment first studied the effect of hematite ratio on pelletizing strength. Under the conditions of bentonite content of 1.2%, pelletizing moisture of 9.0%, pelletizing time of 12 min, preheating at 990 °C for 10 min and roasting at 1250 °C for 10 min, the pelletizing results of different hematite proportion are shown in Fig. 2. It is known that the bursting temperature of all pellets in the test is greater than 600 °C. In order to evaluate the effect of hematite ratio on the compressive strength of pellets, the lower limit of compressive strength of preheated pellets is greater than 400 N, and

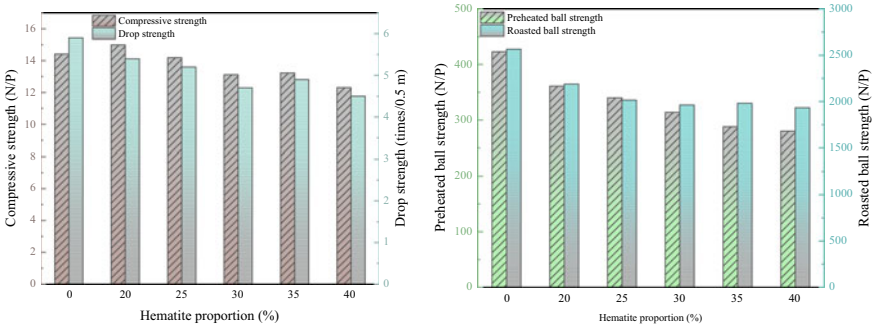

Fig. 2 Effect of hematite proportion on pelletizing indexes

the lower limit of compressive strength of calcined pellets is greater than 2500 N. It can be seen from Fig. 2 that compared with the benchmark (0% hematite), the strength of preheated and roasted pellets cannot meet the requirements when the proportion of hematite is greater than 20%. When the proportion of hematite reaches 40%, the compressive strength of preheated ball and roasted ball is 280 N and 1933 N, respectively. As the proportion of hematite increases, the compressive strength of the pellets decreases.

Effect of Bentonite Content

The effect of bentonite content on pelletizing strength was studied. Under the conditions of hematite proportion of 40%, pelletizing moisture of 9.0%, pelletizing time of 12 min, preheating at 990 °C for 10 min and roasting at 1250 °C for 10 min, the pelletizing results of different bentonites are shown in Fig. 3. As can be seen from Fig. 3, when the proportion of hematite is 40% and the bentonite content is increased, the compressive strength of the preheated ball and the roasted ball is higher than that when the content is 1.2%, but it still cannot meet the strength requirements. For example, when the bentonite content is increased to 1.8%, the compressive strength of the preheated ball and the fired ball is increased to 366 N and 2003 N, respectively, which does not meet the requirements. It can be seen that when the proportion of hematite is high, increasing the bentonite content can promote the improvement of the compressive strength of the pellets, but it cannot meet the strength requirements of high proportion hematite pellets.

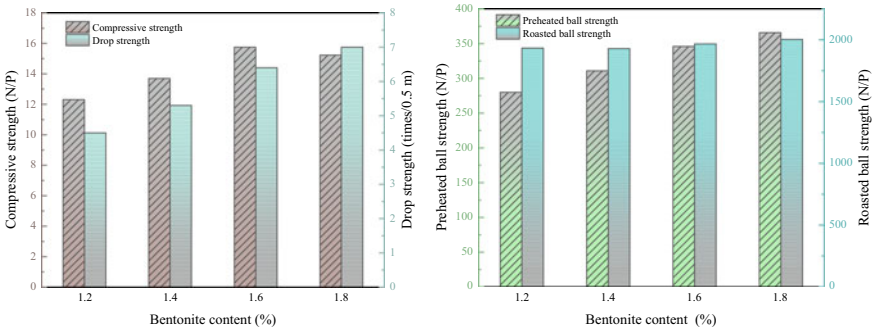

Fig. 3 Effect of bentonite content on pelletizing indexes

High Pressure Grinding Roller

Specific Surface Area

High pressure grinding roller can change the specific surface area of the particles, thereby improving the strength of the pellets. Therefore, the measure of high pressure grinding roller was adopted in the test. The size of high pressure grinding roller is Φ200 mm × 750 mm, the pressure is 0.67 N/mm^2 and its speed is 40 r/min. The number of roller grinding was changed to measure the specific surface area of the iron concentrate, and the results are shown in Fig. 4. It can be seen from the table that the specific surface area of the iron concentrate increases with the increase of roller grinding times, especially when the number of roller grinding times is 5, the specific surface area of the iron concentrate increases to 1883.8 cm^2/g.

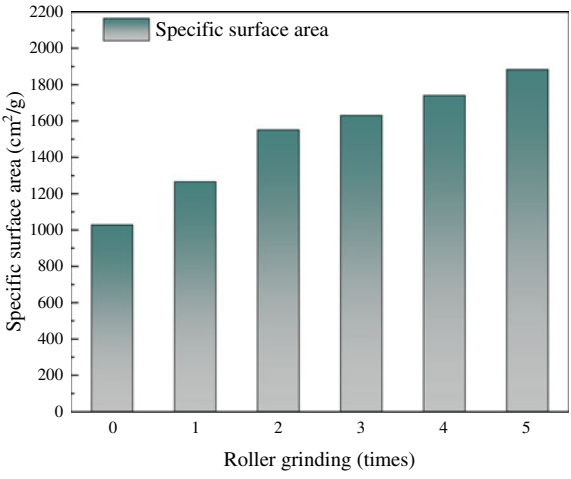

Fig. 4 Effect of roller grinding times on specific surface area of particles

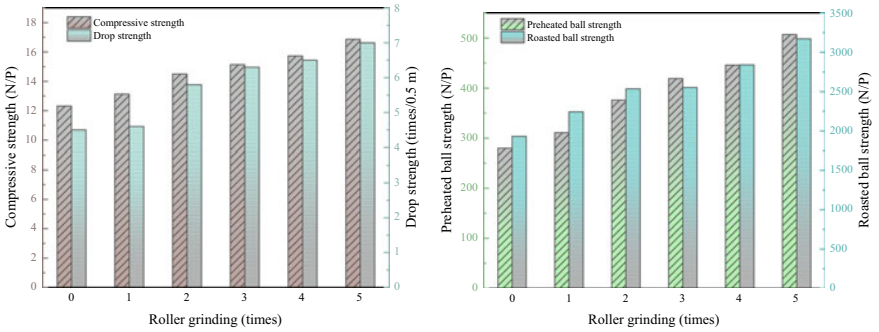

Fig. 5 Effect of roller grinding times on pelletizing indexes

Pelletizing Indexes

In order to determine the influence of high-pressure roller mill on the compressive strength of pellets, the experiment was carried out by changing the number of high pressure grinding roller. The effect of high-pressure roller mill is shown in Fig. 5. Under the conditions of hematite ratio of 40%, pelletizing water of 9.0%, pelletizing time of 12 min, preheating at 990 °C for 10 min, roasting at 1250 °C for 10 min. It can be seen from the table that with the increase of high pressure grinding roller times, the falling strength and compressive strength of green ball increase, especially the strength of preheated ball and roasted pellet increase significantly. Grinding roll 3 times, the quality of pellets basically meet the production requirements, roll grinding 5 times, the quality of pellets is much higher than the production requirements. It is confirmed that increasing the number of high pressure grinding roller to 3 times can significantly improve the strength of high proportion hematite pellets to meet the strength requirements.

Microstructure of Pellet

Microstructure of the pellet with 5 time high pressure grinding roller is shown in Fig. 6. It can be seen from Fig. 6 that the Fe_2O_3 grains in the calcined pellets show an interconnected crystal shape and are very closely connected, and there is sufficient oxidation inside the particles and almost no yellow Fe_3O_4, so the pelletizing strength is good. There is no large pore and thin wall phenomenon in the micro zone, the porosity distribution is more uniform, and the porosity in the grain is less and smaller. The pores between grains are more and larger.

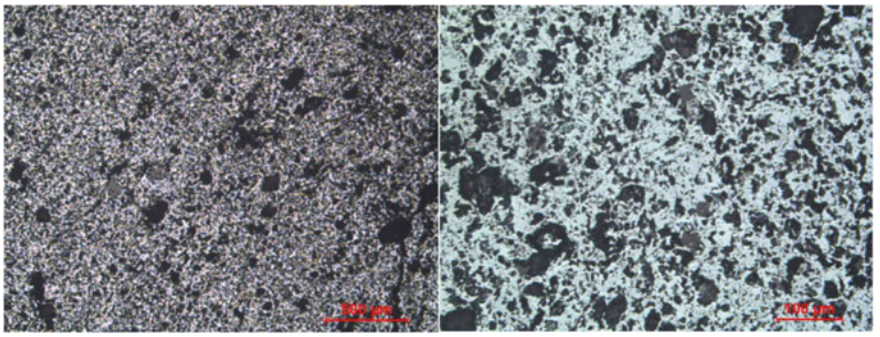

Fig. 6 Microstructure of pellet with 5 time high pressure grinding roller

Conclusion

(1) When the bentonite content is constant, the strength of pellets gradually decreases with the increase of hematite proportion and cannot meet the strength requirements.
(2) When the proportion of hematite is 40%, the pelletizing strength increases with the increase of bentonite content. However, it is still unable to meet the strength requirements of balls, and changing the amount of bentonite cannot solve the problem of poor strength of high proportion hematite pellets.
(3) High pressure grinding roller can significantly improve the strength of pellets, especially preheating pellets. When the high pressure grinding roller of iron concentrate reaches 3 times, it can still meet the production requirements of football under the condition of 40% hematite proportion, and the quality of the ball grinding 5 times is far higher than the production requirements.
(4) During 5 high-pressure roller grinding, the Fe_2O_3 grains in the calcined pellets show an interconnected crystal shape, and the connection is very close, and the Fe_3O_4 inside the particles is almost all oxidized to Fe_2O_3, so the pelletizing strength is good.

Acknowledgements This work was supported by the Basic Science Center Project for the National Natural Science Foundation of China (No. 72088101).

References

1. Kotta AB, Narsimhachary D, Karak SK (2020) Studies on the mechanical and physical properties of hematite iron ore pellets prepared under different conditions. Trans Indian Inst Metals 73(10):2561–2575
2. Lin L, Zeng J (2021) Consideration of green intelligent steel processes and narrow window stability control technology on steel quality. Int J Minerals Metall Mater 28(8):1264–1273

3. Elahidoost H, Sheibani S, Raygan S (2022) Mechanism of magnetite iron ore concentrate morphology affecting the pellet induration process. Adv Powder Technol
4. Zhao H, Zhou F, Ma C (2022) Bonding mechanism and process characteristics of special polymers applied in pelletizing binders. In: Coatings
5. Prusti P, Rath SS, Dash N (2021) Pelletization of hematite and synthesized magnetite concentrate from a banded hematite quartzite ore: a comparison study. Adv Powder Technol 32(10):3735–3745
6. Kumar PS, Ravi BP, Sivrikaya O (2021) The study of pelletizing of mixed hematite and magnetite ores. Sci Sintering 51(1):27–38
7. Umadevi T, Sridhara KS, Rameshwar S (2021) Optimization of induration cycle for magnetite concentrate and its usage in pellet-making process designed for hematite concentrate. Mining Metall Exploration 38(1):243–255
8. Ayyandurai A, Pal J (2022) Kinetics of carbon oxidation during induration of hematite ore pellet. Mining Metall Exploration 39(6):2551–2560
9. Gu F, Zhang Y, Li G (2020) Preparation of blast furnace burdens by composite agglomeration process: effect of distribution of magnetite and hematite concentrates in pelletized and matrix feed. J Iron Steel Res Int 27(12):1363–1371

Effect of Raw Material Size on Sintering Quality

Jie Liu, Xianguo Ma, Jizhong Tang, Qiang Zhong, Wenzheng Jiang, Hui Zhang, Libing Xv, and Jin Xun

Abstract In order to improve the output and quality of sinter, the influence of the particle size of the mixture on the quality of the sinter was studied. The results show that the change trend of the mixture size model is consistent with the actual mixture size change trend, and the original size distribution of iron ore directly affects the final mixture size. When the average particle size of the mixture is more than 4 mm, the drum strength and the yield both decrease. When the average particle size of the mixture is 3.86 mm, the sinter drum strength is the highest, and when the average particle size of the mixture is 4.08 mm, the sinter yield is the highest. Relying on the comprehensive technical improvement, by reducing the proportion of large-particle iron ore, the normal and high temperature performance of sinter are comprehensively improved after industrial application. And the sintering utilization Coefficient is stabilized at about 1.48 t/m^2 days, the daily output of the supplied blast furnace can reach 10,000 tons.

Keywords Particle · Mixture · Iron ore · Sinter quality · Quantitative research

Introduction

Angang Steel Company Limited Bayuquan Branch is located in Yingkou City, Liaoning Province, close to Yingkou Port, the second largest port in Northeast China, with two 4038 m^3 blast furnaces and two 405 m^2 sinter plants. The annual design capacity of the sintering system is 9.33 million tons, using 900 mm thick-layer sintering, 100% of the iron ore raw materials are purchased, of which the proportion of powder ore reaches more than 90%. The main iron ore varieties are Brazilian

J. Liu · X. Ma · J. Tang · H. Zhang · L. Xv · J. Xun
Iron and Steel Research Institute of Angang Group, Anshan 114009, China

J. Liu · Q. Zhong (✉) · W. Jiang
School of Minerals Processing and Bioengineering, Central South University, Changsha 410083, China
e-mail: zhongqiang@csu.edu.cn

Z. Peng et al. (eds.), *Characterization of Minerals, Metals, and Materials 2024*, The Minerals, Metals & Materials Series, https://doi.org/10.1007/978-3-031-50304-7_38

ore and Australian ore, and according to the cost demand with about 10% of cost-effective ore, the overall number of ore varieties is 6–8 kinds. Due to the influence of resource and market factors, the proportion of purchased ores and the variety of ores vary greatly. Also, due to the large fluctuation of the original particle size distribution of the ores, it has a large impact on the particle size distribution of the mixture after granulation, which in turn affects the permeability of the entire sinter layer, resulting in obvious changes in the sinter yield and quality.

Due to the many factors affecting the sintering granulation process, and the difficulty to quantify in the existing technical conditions and cannot realize the online monitoring of the particle size of the mixture, so the domestic and foreign has done a lot of research in this area [1–7], which mainly related to the nature of the raw material, mixing time, optimization of the rotary drum granulation parameters, rate and method of water addition, etc., but also developed a different predictive model and method of the final particle size, but most of the research results still favour laboratory research. And there is a large distance from industrial field applications. In order to effectively guide the Bayuquan Branch's iron ore sintering and ore blending optimization, improve the permeability of the sinter layer, based on the actual production process and equipment configuration, we carried out a study on the impact of the change of the mixture particle size on the quality of the sintering, to achieve a reasonable control of the size of purchased iron ore.

Experimental

Materials

Iron ore mixtures for the study were all taken from the production site. And the particle size distribution of the main iron-containing raw materials is listed in Table 1.

Table 1 Particle size distribution of ores

	Size distribution/%					Mean size
	> 8 mm	5–8 mm	3–5 mm	1–3 mm	< 1 mm	mm
Sinter feed carajas	22.70	17.90	15.00	19.40	25.00	4.50
Yandi iron ore	26.9	22.8	21.20	18.70	10.40	4.93
Newman iron ore	11.70	18.10	17.00	26.50	26.70	3.52
PB iron ore	8.71	6.02	18.21	30.79	36.28	2.70
Royhill iron ore	23.63	25.85	15.15	19.62	15.75	4.69
BF return ore	0	17.25	26.23	34.88	22.14	3.02
Miscellaneous materials	3.30	6.60	8.30	17.30	64.50	1.85
Concentrates	The proportion of those less than 0.074 mm are all above 80%, and the average particle size is calculated as 0.074 mm					

Methods

Sinter pot tests were carried out in the sintering laboratory of Ansteel, the dimensions of the sinter pot are 200 × 700 mm. The height of the mixture bed is 900 mm, the negative pressure of ignition is 8 kPa, the ignition time is 1.5 min, and the negative pressure of sintering is 12 kPa. After the sinter cake is cooled in the sinter pot, the dropping and ISO drum tests are carried out, and then samples are taken for chemical analysis and metallographic examination.

The granularity of the sinter mixture is divided into 5 grades: + 8, 5–8, 3–5, 1–3 and −1 mm. Dry sieving is to put the mixture in a 120° coven to dry for 2 h and then to sieve for 5 min, and then weigh it according to particle size. Wet sieving is to sieve the mixture containing water for 5 min, then to dry the sample in 120° coven for 2 h, and then to weigh it according to particle size.

Results and Discussion

Sintering Quality of Different Mixture Size

Relevant research shows that in the sintering of powder ore-based granulation, the core particles of the mixture are mainly iron ore-based, the formation of small ball particles of high strength, not easy to be destroyed, also will not be keep gathering and growing up. In two minutes time, 60% of the particles have reached the final diameter of the particles [8, 9], so that the size of the particles is restricted, the number of particles generated is relatively stable. Based on this theory, it can be seen that the original particle size of the iron ore plays the most critical role in the final particle size of the sinter mixture [10–13]. In order to further explore the influence of the mixture on the quality of sinter, for this reason, in the laboratory, according to the production site of a different stacking scheme after granulation of the actual mixture particle size and the corresponding sinter pot test indices were tested and analysed, and the average particle size of the mixture and the relationship between sinter tumbler strength and yield are shown in Figs. 1 and 2, respectively.

From Figs. 1 and 2, it is known that under the raw material conditions and process conditions of mackerel, the relationship equation between the average particle size of the sintered mixture and the tumbler strength is:

$$Y = -12.34X^2 + 95.34X - 117.7 \tag{1}$$

The relationship between the average size of the mix and the sinter yield is given by the equation:

$$Y = -22.07X^2 + 179.9X - 304.3 \tag{2}$$

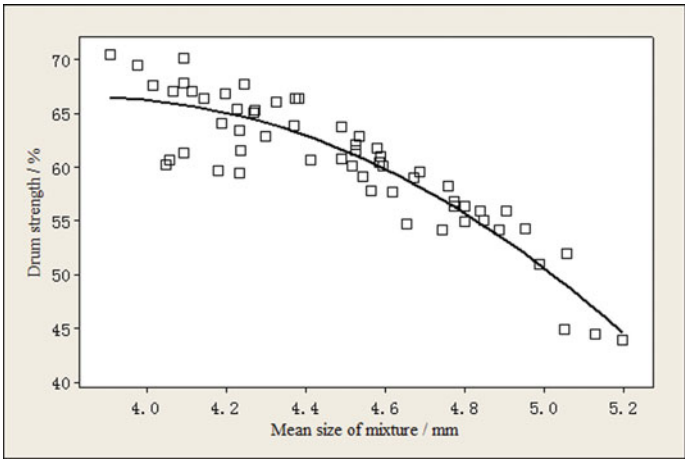

Fig. 1 Changes between mean size of mixture and drum strength of sinter

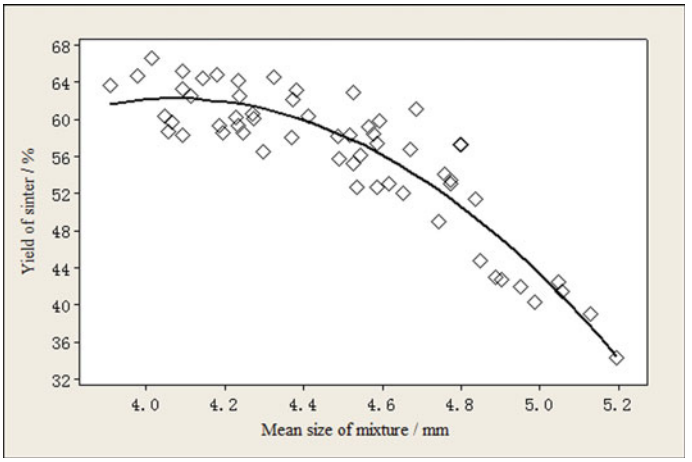

Fig. 2 Changes between mean size of mixture and yield of sinter

According to the above two equations, respectively, under the raw material and process conditions of the mackerel, when the average particle size of the mixture is 3.86 mm, the tumbler strength of the sinter is the highest, and when the average particle size of the mixture is 4.08 mm, the yield rate of the sinter product is at its peak, and after the average particle size of the mixture is more than 4 mm, the tumbler strength and the sinter yield are both in a decreasing trend. If the particle sizes of each batch of mixtures are arithmetically averaged, the average particle size of 4.486 mm, so appropriate to reduce the average size of the mixture to 4 mm or so, to improve the tumbler strength and yield of sinter is beneficial.

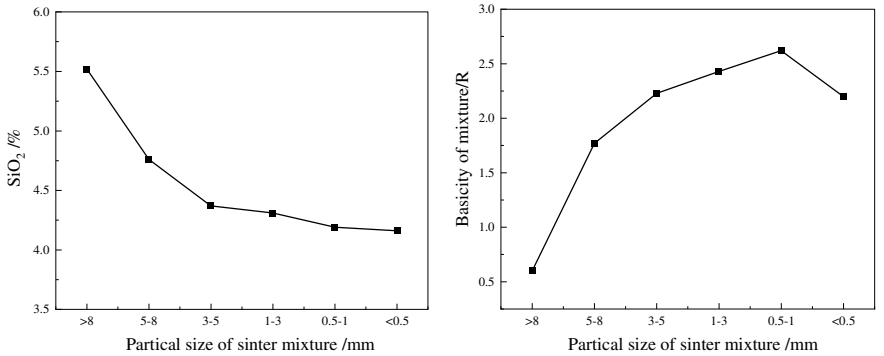

Fig. 3 SiO_2 and basicity changes in different size mixture

At the same time, the mixes were tested at the typical 2019 ore blending strategy and the variations in silica and alkalinity for different particle size classes are listed in Fig. 3.

It is known through Fig. 3 that, in the particle size composition of mackerel sinter feed mixtures, with the particle size level becoming finer, the overall trend of *R* is first increasing and then decreasing, while the SiO_2 content is generally decreasing. In the particle size below 3 mm, the difference of SiO_2 content is small, but the basicity is greater than 2.2, and the highest reaches 2.62, this part of the mixture will be sintering in the form of high basicity and ultra-high basicity, with sufficient liquid phase and high sinter quality. In the particle size above 3 mm, SiO_2 content is high, basicity is low, and the value changes are large, especially in the particle size composition larger than 8 mm, the mixture SiO_2 content reached 5.52%, corresponding to the SiO_2 content predicted to reach 6.30%, which directly affects the average content of sinter. At this time, the basicity of the mixture is only 0.60, so some of the large particles of high silica are not only difficult to form the liquid phase during the sintering process, but also difficult to be wrapped by other liquid phases due to the influence of segregation patterns, and mainly exist in the form of raw ore alone, which not only hampers the improvement of the sinter quality, but also affects the permeability of the blast furnace body after entering the blast furnace due to the small size compared with that of the natural lumps that are directly fed into the furnace.

Comprehensive study, it can be seen that the original particle size of iron ore has a direct impact on the final particle size of the sinter mixture, and the mixture particle size and the quality of the sinter product has a direct correlation.

Industrial Validation

In order to meet the requirements of blast furnace output and safe and smooth operation, the impact of mixed material particle size on sinter production is further verified in industry. On one hand, the previous ore blending strategy is changed, and the raw materials in each stockpile are tested for particle size and included in the sintering allocation plan as an optimization option, and the ratio of larger particles is intentionally reduced by the existing pre-screening process at the stockyard; on the other hand, in the procurement of ore, the accuracy of particle size and compositional indices becomes a mandatory criterion to achieve consistency and coherence between procurement and production. On the other hand, in ore procurement, the accuracy of particle size and compositional indices becomes a mandatory criterion, ensuring consistency and coherence between procurement and production. The particle sizes of sinter mixtures corresponding to different stacks in the mackerel sinter yard from March 2019 to March 2021 were examined, and the main results are listed in Fig. 4.

From the analysis of Fig. 4, it is known that before 2021 (before the dotted line), the fluctuation range of the particle size of the sinter mixture is large, and from the perspective of the wet sieve, the highest proportion of more than 8 mm can reach about 20%, and the dry sieve also reaches about 15%, and fluctuates between 5 and 20%, and this fluctuation range improves the permeability of the material layer to a certain extent, but the actual effective air flow into the material layer does not necessarily increase, and on the other hand, it brings a great deal of difficulties to the sinter layer and quality control brings great difficulties. After 2021, the maximum proportion of more than 8 mm is controlled at about 10%, fluctuating between 5 and 15%, with

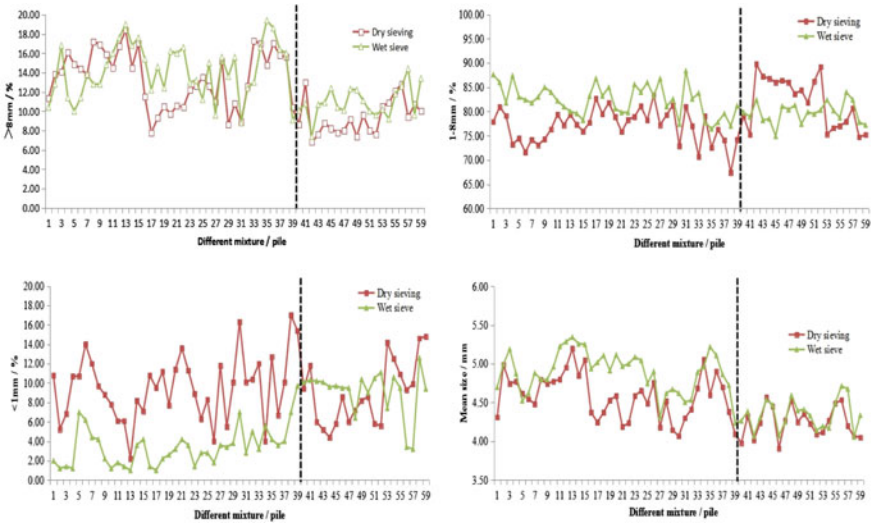

Fig. 4 Particle size distribution of mixture

the fluctuation amplitude significantly reduced. 1–8 mm mixed material particle size range accounted for more than 70% of both dry and wet sieve testing, and after 2021, it accounts for more than 75% of the total, and the dry sieve size accounted for more than a significant increase. The proportion of particles smaller than 1 mm in the mix is below 20%, and after 2021, the dry and wet sieves agree very well, the fluctuation decreases sharply, and the content of the fine-grained grades increases. The average particle size of the sinter mixture fluctuated between 4.0 and 5.5 mm before 2021, and the maximum size difference of the wet sieve reached 2.0 mm. After 2021, the average particle size of the mix had a significant downward process, and the average particle size decreased to 4.0–5.0 mm, and the maximum size difference of the wet sieve narrowed to about 1.2 mm. Mineralogical examinations of typical sinter before and after the change in particle size are listed in Figs. 5 and 6.

It is known that before the optimization of particle size, there are more large particles in the mixture, the pile density is small, and the permeability is better, but due to the fast cooling rate, there is more secondary hematite in the sinter mineral phase, with the presence of obvious skeleton crystalline hematite, and there are more holes, with a large amount of columnar calcium ferrate. After optimizing the particle

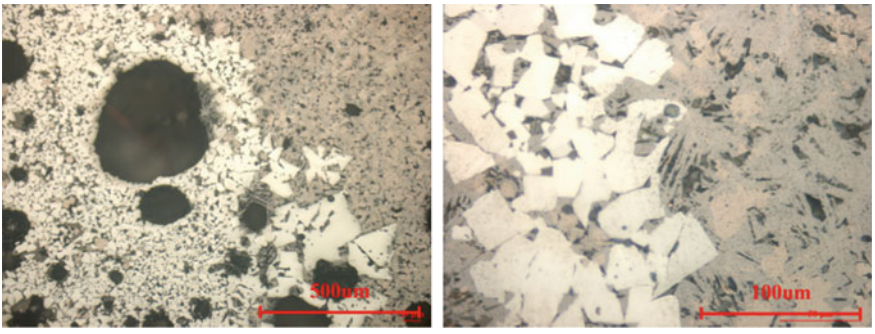

Fig. 5 Sinter microstructure before the optimization of particle size

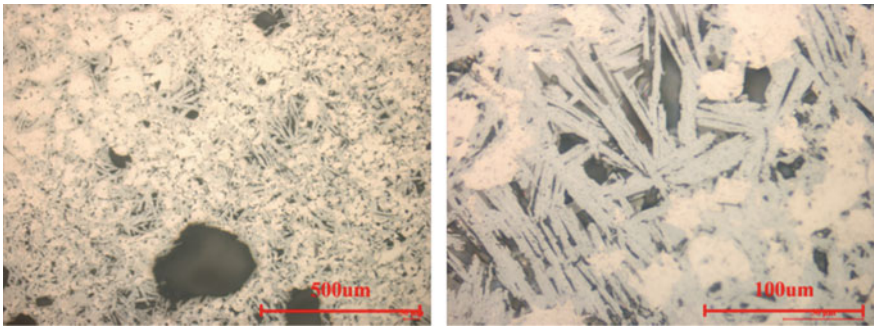

Fig. 6 Sinter microstructure after optimizing the particle size

Table 2 Sinter output and quality

	Yield/%	Drum strength/%	Mean size of sinter/mm	$RDI_{+3.15}$/%	Productivity/t/m^2 d
Before optimization	65.33	80.88	20.31	67.77	1.43
After optimization	69.86	81.21	21.86	71.21	1.48

size, the stack density of the mixture increases, the contact between particles and particles is more compact, thanks to the increase of the effective air volume of the material layer, the oxidation atmosphere is enhanced, the mineral crystallization is sufficient, there are a large number of needle-like calcium ferrate generation, the holes are obviously reduced, and the mineral structure is more uniform and compact.

While the average size of the mixture was reduced, the quality of sinter was also significantly improved, and the changes of the sintering indexes are listed in Table 2.

Considering the decrease of average particle size, it will definitely reduce the permeability of the whole thick material layer and affect the sinter output. For this reason, relying on the development and application of the Angang Iron & Steel's intelligent online air leakage monitoring system, the accurate detection and management of the sinter machine's air infiltration rate has been realized, and the air leakage rate has dropped from 50% in the past to about 40%, which has significantly improved the effective air volume of the entire material layer. Meanwhile, through the comprehensive measures of strengthening the management of the sintering process, checking the particle size of the fuel and flux, using high active lime to improve the granulation and raising the material temperature, etc., the yield of the sinter has increased by 4.56% points, the tumbler strength of the sinter has improved by 0.33% points, the low-temperature reduction chalking index has been improved by 3.44% points, and the utilization coefficient has been stabilized at 1.48 t/m^2 d, which is the leading level of the large-scale sintering machine in domestic and foreign countries. The utilization rate is consistently stable at 1.48t/m^3 d, reaching the leading level of domestic and foreign large-scale sinter plants, the quality indicators of the sinter are improved comprehensively. The permeability in the upper zone of the blast furnace is improved obviously, the operation is more stable, the utilization coefficient of the two blast furnaces is stable at more than 2.3 t/m d, the daily output of a single blast furnace can be up to 10,000 tons in the case of High-yield operation, and the average fuel ratio of the blast furnace decreases by more than 5 kg.

Conclusion

(1) In the production process conditions of Angang Steel Company Limited Bayuquan Branch, the average size of the mixture more than 4 mm, sinter tumbler strength and sinter yield are into a downward trend, the average size

of the mixture were 3.86 mm and 4.08 mm, respectively, the two achieved the maximum value of the mixture that is greater than 8 mm particle size mainly in the form of low alkalinity and high silica, to improve the quality of sinter which is unfavourable;

(2) By improving the ore allocation and procurement system, the fluctuation of the sinter mixture particle size is greatly reduced, the maximum difference of the average particle size is reduced from 2.0 to 1.2 mm, and the average particle size is reduced to 4–5 mm, the quality of sinter is comprehensively improved, and the utilization coefficient of sintering can be stabilized at 1.48 t/m^2 d, and the daily output of single blast furnace can be up to 10,000 tons or so.

References

1. Huang X, Xue, Z, Wang W et al (2017) Numerical simulation on packing behavior of iron ore granules. J Iron Steel Res 29(7):536–543
2. Waters AG et al (1989) A mathematical model for the prediction of granule size distribution for multicomponent sinter feed. ISIJ Int 29(4):274–283
3. Khosa J, Manuel J (2007) Predicting granulating behaviour of iron ores based on size distribution and composition. ISIJ Int 47(7):965–972
4. Knight P (2004) Challenges in granulation technology. Powder Technol 140:156–162
5. Guo X, Zhang L, He J et al (2019) Optimization of particle size of sintering mixture based on fuzzy PID control. Sinter Pelletzing 44(6):1–22
6. Wang Y, Du P, Ren L (2015) Influences of sintering mixture adhesive rate on performance indexes of sinter. Sinter Pelletzing 40(2):11–14
7. Xiong L, Mao X, Li J (2015) The study of the sinter mixture granulation process. In: Papers of the 10th China steel annual conference and the 6th Baosteel academic annual conference, pp 1–8
8. Ma X, Liu J, Wang X et al (2020) Research and application of sinter mixture's distribution characteristic in Ansteel. Angang Technol 424(4):38–49
9. Rankin WJ (1988) Granulation of mixture and its role in sintering. Sinter Pelletzing 4:55–66
10. Liang G, Tang W, Tang L et al (2013) Development and application of low water granulation technology of sintering in Xiangtan Steel. Metal Mter Metall Eng 4:24–29
11. He S, Feng H (2014) Analysis of the effects of high proportion iron concentrate on sinter quality and discussion of strengthening measures. China Metall 24(7):27–31
12. Sun Y, Lv Q, Li F (2011) The influence of moisture in mixture on sintering of V-Ti magnetite from Chenggang. China Metall 21(4):21–25
13. Venkatara R, Kapur PC, Gupta SS (2002) Modelling of granulation by a two-stage auto-layering mechanism in continuous industrial drums. Chem Eng Sci 57:1685–1693

Effects of the Rice Husk Ashes and Titanium Dioxide on Properties of ABS Composites Parts Obtained by 3D Printing

Gustavo F. Souza, Rene R. Oliveira, Durval Rodrigues Jr, Rita C. L. B. Rodrigues, and Esperidiana A. B. Moura

Abstract The purpose of this study was to evaluate the effects of incorporation of the rice husk ashes and titanium dioxide on properties of acrylonitrile butadiene styrene (ABS). The incorporation of rice husk ashes (RHA) (2.5 wt.%) and titanium dioxide (2.5; 5.0 wt.%) into ABS matrix was carried out by melting extrusion process using a twin-screw extruder. Neat ABS and its composites filaments for FDM 3D printing were produced using the melting extrusion process to obtain specimens for tests. The properties of ABS/RHA/TiO_2 composite samples were investigated by the properties of the ABS/RHA/TiO_2 composite samples were evaluated using tensile tests, SEM, XRD analysis, Charpy impact test, and water contact angle measurements. This study contributes to our understanding of the behavior of ABS composites containing RHA and TiO_2 for various industrial applications.

Keywords RHA · TiO_2 · ABS · Mechanical tests · SEM · DRX

G. F. Souza · E. A. B. Moura (✉)
Centro de Química e Meio Ambiente, Instituto de Pesquisas Energéticas e Nucleares, Av. Prof. Lineu Prestes, 2242, São Paulo, SP 05508-000, Brazil
e-mail: eabmoura@ipen.br

R. R. Oliveira
Centro de Ciências e Tecnologia de Materiais, Instituto de Pesquisas Energéticas e Nucleares, Av. Prof. Lineu Prestes, 2242, São Paulo, SP 05508-000, Brazil

D. Rodrigues Jr
Department of Material Engineering, Lorena Engineering School, University of Sao Paulo, Lorena, SP 12612-550, Brazil

R. C. L. B. Rodrigues
Department of Biotechnology, Lorena Engineering School, University of Sao Paulo, Lorena, SP 12602-810, Brazil

Z. Peng et al. (eds.), *Characterization of Minerals, Metals, and Materials 2024*, The Minerals, Metals & Materials Series, https://doi.org/10.1007/978-3-031-50304-7_39

Introduction

In recent years, the field of materials science and engineering has seen a surge in innovative research aimed at addressing pressing environmental and industrial challenges. ABS (acrylonitrile butadiene styrene) is a widely used thermoplastic in industries due to its excellent mechanical properties and processability [1, 2].

The use of fillers in polymeric composites has been gaining popularity in recent years due to the advantages they offer, such as improved mechanical, thermal, and electrical properties [3]. One type of filler that has attracted much attention is rice husk ash (RHA), which is a byproduct of the rice milling industry. RHA is a renewable and sustainable material that is abundant and low-cost. It is also a good reinforcing filler due to its high content of silica. Chaudhary et al. reviewed the performance of RHA in polymeric composites [4]. The authors emphasized the need for better characterization of RHA to obtain a better understanding of its behavior. The authors also proposed a new approach to RHA modification to improve its performance as a filler.

Among the different fillers used, such as clays, silicas, nanotubes, inorganics, etc., titanium dioxide (TiO_2) plays a special role in polymeric matrices, to synthesize high-performance and malleable polymer networks (e.g., improving viscosity, obtaining filaments for 3D printing) [5]. TiO_2 is found in many applications due to its good photocatalytic properties, hence it is used in antiseptic and antibacterial compositions, degrading organic contaminants and germs, as a UV-resistant material; this is due to its chemical inertness properties, non-toxicity, low cost, high refractive index, and other advantageous surface properties [6, 7].

Among these challenges, the treatment of oily water has gained significant attention, driven by the increasing offshore oil transportation activities and the unfortunate incidents of oil leakages. This study explores the pioneering work of Lei Han and his team, who have introduced a groundbreaking approach to tackle this issue. Their research revolves around the development of a functional TiO_2-ABS composite membrane, created through a cutting-edge three-dimensional (3D) printing strategy.

To enhance ABS for specific applications, additives such as rice husk ashes (RHA) and titanium dioxide have been investigated. The incorporation of RHA (2.5 wt.%) and titanium dioxide (2.5; 5.0 wt.%) was achieved using a twin-screw extruder in a melting extrusion process. Through this process, neat ABS and its composite filaments for Fused Deposition Modeling (FDM) 3D printing were produced, allowing the generation of test specimens. The properties of the ABS/RHA/TiO_2 composite samples were evaluated using tensile tests, SEM, DSC, XRD analysis, Charpy impact test, water absorbency test, and water contact angle measurements.

Materials and Methods

Materials

The materials used in this work to prepare the polymeric matrix was ABS (acrylonitrile butadiene styrene) from BASF, and as fillers, rice husk ashes (RHA) waste disposed by Brazilian Rice Industry and titanium dioxide (TiO_2) was purchased from Sigma Aldrich.

Methods

Rice Husk Ashes (RHA) and Titanium Dioxide (TiO_2) Preparation

Rice husk ashes (RHA) and titanium dioxide (TiO_2) powders were previously dried in an oven with air circulation at 60 °C for 24 h.

Composite Preparation

ABS was firstly dried in an oven with an air circulation system, at 80 °C for 24 h, to reduce moisture content to less than 2%. Polymeric composites were prepared in different compositions by weight: ABS with addition of rice husk ashes (RHA) (2.5 wt.%) and titanium dioxide (2.5 and 5.0 wt.%), according to composition presented in Table 1.

The compositions (ABS/RHA/TiO_2) were hand premixed and then processed in a Thermo Scientific HAAKE twin-screw co-rotating extruder, model Rheomex 332p, with 16 mm screw diameter and a length-diameter-ratio of 25. The biobased composites were processed in a two-step to better dispersion of RHA and TiO_2 into the ABS matrix. The compositions were processed in the temperature profile of 150/165/175/175/165/150 °C, and screw speed of 30 rpm. The extruded biobased composites were cooled down, pelletized, and dried again in an oven with an air circulation system at 80 °C for 4 h.

Table 1 ABS/RHA/TiO_2 biobased composites composition

Composition	Pure ABS (wt.%)	RHA (wt.%)	TiO_2(wt.%)
Neat ABS	100	0	0
ABS/RHA 2.5%/TiO_2 2.5%	95.0	2.5	2.5
ABS/RHA 2.5%/TiO_2 5.0%	88.0	2.5	5.0

Note The composite contained 5 wt.% silane

Filaments Preparation

The biobased composites, with different amount of TiO_2, were fed to a Thermo Scientific HAAKE twin-screw co-rotating extruder to produce the filaments for 3D FDM. The temperature profile was 145/160/175/175/165/145 °C, screw speed set to 30 rpm, temperature of cooling water of the filaments was 35 °C, and filament diameter of 1.75 ± 0.01 mm.

Fused Deposition Modeling (FDM) 3D Printing

The specimens for tensile and water absorption tests were manufactured using the FDM technique on a 3D printer, and they were pre-sliced using the Cura3D software, employing the following settings: 100% infill density, printed with a 0.4 mm nozzle, at a speed of 80 mm/s. The printing temperatures for all blends were set at 180 °C for the nozzle and 70 °C for the build platform to ensure adequate adhesion of the printed components. The components were produced using an Artillery Sidewinder X1 3D printer.

Characterization

X-ray Diffraction (XRD)

XRD patterns of ABS and the biobased composites were recorded with a Siemens-d5000 Diffractometer operated at 40 kV and 40 mA, with Cu–Kα radiation ($\lambda = 1.5406$ Å), over the 2θ range from 5° to 40°.

Scanning Electron Microscopy (SEM) Analysis

SEM analyses were conducted in a Model LX-30 Philips instrument operated at an electron acceleration voltage of 12 kV. The samples' cryofractured surfaces under liquid nitrogen were sputtered with a gold layer before SEM analyses of the morphology of the samples' surfaces.

Water Contact Angle Measurements

The absorption of water by a material's surface is related to the wetting process of water on the material's surface and, consequently, the hydrophilic/hydrophobic

character of the material's surface. A high degree of wettability between water and material means a greater contact area between them and a greater probability of absorption, making the material more hydrophilic. Wettability is commonly assessed by the contact angle of the liquid with the solid surface. In this phenomenon, the greater the contact angle, the lower the wettability, meaning that the material has a hydrophobic character when the liquid wets less the solid surface in contact. The surface wettability of composite samples was determined through water contact angle (WCA) measurements using a DSA 100 Kruss goniometer equipped with a camera to capture images of water droplets and then determine the contact angles. Deionized water was used to evaluate the wettability properties of these samples. Angle measurements were performed in triplicate, and the average values were taken [8].

Water Absorbency Test

Water absorbency measurements of the bionanocomposite film samples were conducted in triplicate, and the average values were recorded. The water absorption of the bionanocomposite films was assessed in terms of swelling. Each film sample was cut into a 2×2 cm^2 piece, dried at 45 ± 2 °C for 24 h in a circulating air oven, and pre-weighed. The pre-weighed samples were immersed in a Petri dish filled with 20 mL of deionized water and left undisturbed for 24 h at room temperature until equilibrium swelling was achieved. The samples were then removed from the deionized water, quickly dried with filter paper to remove surface droplets, and re-weighed. The samples were weighed at specific time intervals until equilibrium swelling was reached. The swelling ratio was calculated using the following expression, Eq. (3) [8, 9]:

$$\text{Swelling Ratio}\,(\%) = ((W_s - W_d)/(W_d) \times 100) \tag{3}$$

where W_s = weight of the swollen samples, W_d = weight of the dry samples in all three replicates.

Tensile Tests

Printed specimens from the neat ABS and the biobased composites were submitted to tensile tests using an Instron model 5564, according to ASTM D 638–99, at room temperature and with a cross-head speed of 50 mm/min. For each composition, five specimens were tested, and the average value of five specimens with the standard deviation was recorded.

Charpy Impact Test

The Charpy impact test involved striking a notched specimen with a pendulum hammer and measuring the energy absorbed by the specimen during fracture. The specimen was typically a rectangular bar with a V-shaped notch at its center. The specimen was placed on two supports, and the pendulum was released from a fixed height. The energy absorbed by the specimen was calculated by subtracting the final height of the pendulum from the initial height. The higher the energy absorbed, the tougher the material.

Results and Discussion

XRD Analysis Results

The XRD patterns of neat ABS and the biobased composites are shown in Fig. 1. For the neat ABS it can be seen the prevalence of the ABS characteristics, mainly amorphous, with peaks at around 15º, 22º and 42º. This behavior will be used for the comparison of all samples. For the composite with 2.5 wt.%TiO_2, these three peaks decreased intensities, showing the presence of crystalline material, as expected for the TiO_2, with peaks at 27º, 36º, 42º, 54º, and 56º, corresponding to the crystalline planes of TiO_2. Similar behavior can be seen for the sample prepared with 5.0 wt.%TiO_2, mainly showing only the peaks concerned to the crystalline phases. Increased amount of addition lead to the prevalence of characteristic diffraction peaks associated with TiO_2 in the X-ray diffraction (XRD) pattern. ABS, conversely, exhibits prominent peaks at 15º, 22º and 42º. It is noteworthy that the relative intensity of these peaks diminishes while their width increases for the samples containing increased amount of TiO_2.

SEM Analysis Results

The SEM images of cryogenic fracture surfaces of neat ABS and its biobased composites are shown in Fig. 3. It can be observed from Fig. 2a that neat ABS exhibits morphology characteristic of immiscible systems, with globular volumes. Upon the addition of TiO_2, the micrographs exhibit irregular particles embedded in the ABS matrix, indicating a low compatibility between ABS and TiO_2. Figures 2b, c show increasing amount of white spots, corresponding to the increased amount of TiO_2 (2.5 and 5.0 wt.%).

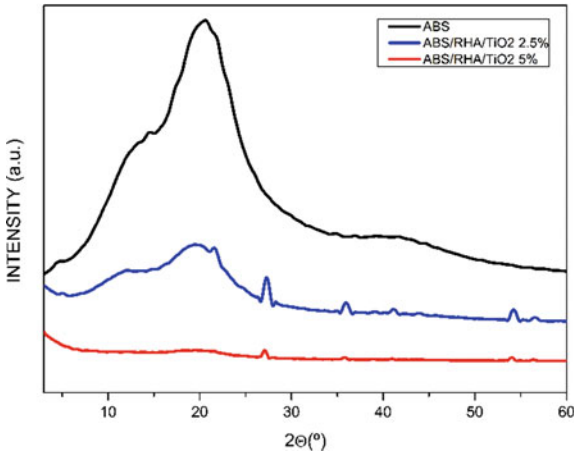

Fig. 1 XRD patterns of ABS matrix and its composites containing TiO_2

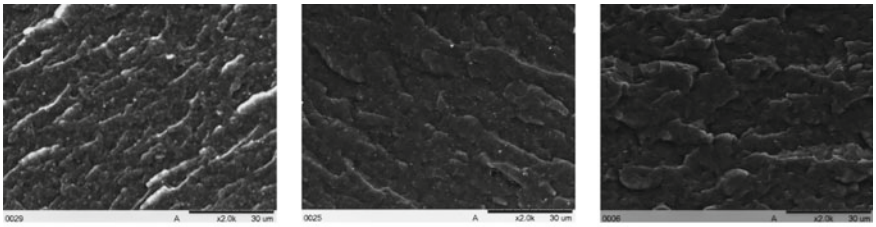

Fig. 2 SEM images of cryogenic fracture surfaces at 2000 X of magnification: **a** ABS; **b** ABS with 2.5 wt.%TiO_2; **c** ABS with 5.0 wt.%TiO_2

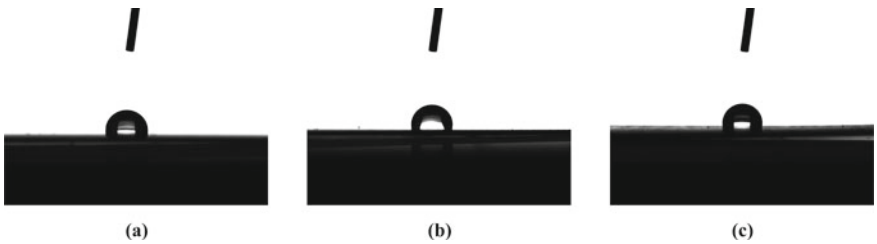

Fig. 3 Water contact angle (WCA) of samples: **a** ABS; **b** ABS with 2.5 wt.%TiO_2; **c** ABS with 5.0 wt.%TiO_2

Water Contact Angle (WCA) Measurements

The water droplet image on the composite film surfaces and the contact angle (WCA) measured for different TiO_2 content of 2.5 wt.% and 5.0 wt.% are shown in Fig. 3 and

Table 2 Water contact angle (WCA) degree of the ABS and the composite films

Composition	Water contact angle (°)	Swelling ratio (%)
Neat ABS	99.3 ± 1.22	0.48 ± 0.04
ABS/RHA 2.5%/TiO_2 2.5%	103.2 ± 1.01	0.65 ± 0.04
ABS/RHA 2.5%/TiO_2 5.0%	97.2 ± 0.87	0.45 ± 0.01

Table 2, respectively. The WCA of the composite sample surfaces were measured to evaluate the hydrophilic/hydrophobic character of the sample. The water contact angle of the composite samples remained approximately the same with or without TiO_2. The high contact angle values around 100º show that all the surfaces are highly hydrophobic, as expected for ABS. The addition of TiO_2 did not change this behavior, within the measure deviation. The surface hydrophobicity of ABS may explain these results, even with the dispersion of TiO_2 in the ABS matrix. The surface hydrophobicity of ABS reduces diffusion of water molecules on the surface. This behavior may also indicate the good homogeneity of the matrix obtained with the preparation procedure used for this work.

Water Absorbency Test

The results of swelling ratios (%) obtained in this study provide a profound understanding of the water absorbency characteristics of the different materials under investigation (Table 2). Firstly, the results revealed that neat ABS exhibited a swelling ratio of 0.48% ± 0.04. In contrast, the ABS/RHA 2.5%/TiO_2 2.5% composite displayed a swelling ratio of 0.65% ± 0.04. Finally, the ABS/RHA 2.5%/TiO_2 5.0% composite recorded a swelling ratio of 0.45% ± 0.01. Surprisingly, despite containing a higher concentration of TiO_2, this mixture showed a slightly lower water absorbency capacity compared to the composition containing only 2.5 wt.% TiO_2.

Tensile Test Results

Table 3 presents the dependence of tensile strength and elongation at break and at yield, and Young's modulus on the content of RHA and TiO_2 in the ABS composites. As shown in Table 3, the tensile strength at break and at yield have the same behavior, decreasing in values with the increase of the TiO_2 content, while the elongation increased for the ABS/RHA 2.5%/TiO_2 2.5% composites, which was to be expected since the material became more ductile. This declining trend in tensile strength showed in Table 3 could be related to the poor connectivity and low compatibility between the TiO_2 particles and the ABS matrix.

Table 3 Tensile test results of neat ABS and the composites

Composition	Tensile stress at break (MPa)	Tensile stress at yield (MPa)	Elongation at break (%)	Tensile extension at yield (mm)	Youngs' Modulus (MPa)
Neat ABS	46.6 ± 2.2	47.5 ± 1.3	16.9 ± 1.1	5.5 ± 0.4	869.4
ABS/RHA 2.5%/TiO_2 2.5%	37.0 ± 1.9	41.2 ± 2.8	23.4 ± 0.7	5.7 ± 0.5	712.4
ABS/RHA 2.5%/TiO_2 5.0%	33.4 ± 1.3	35.4 ± 1.3	17.3 ± 1.3	4.2 ± 0.2	852.8

In relation to ABS/RHA 2.5%/$TiO_2$5.0% composites, the increase in the amount of TiO_2 led to an increase in agglomerates, which act as a defect within the polymeric matrix, causing a non-uniform stress distribution in the ABS/RHA 2.5%/$TiO_2$5.0% composites capable of reducing the interaction between TiO_2 and the PBAT/PLA matrix and can also act as rupture sites and, consequently, reduce the tensile properties of the material. Regarding the values of Young's modulus for the samples with and without the addition of RHA and TiO_2, it is important to note that the Young's modulus of the composite material depends on the interfacial adhesion and the tension transferred between the matrix and the fillers. In cases where there is a lack of a strong connection or good interfacial adhesion between TiO_2 and ABS, the presence of TiO_2 tends to decrease the Young's modulus value. The decrease of the tensile properties of ABS when the filler amount increases has also been observed in composites of ABS with other fillers [10, 11].

Charpy Impact Test Results

Table 4 presents the results obtained with the Charpy impact tests for the samples with and without TiO_2 addition. The first behavior is the decrease of the necessary energy to fracture the composites with TiO_2, when compared to the neat ABS. This decreasing trend for the Charpy impact energy could again be related to the poor connectivity and low compatibility between the TiO_2 particles and the ABS matrix.

Table 4 Charpy impact test results of the ABS and the composite films

Composition	Charpy impact test (J)
Neat ABS	0.90 ± 0.15
ABS/RHA 2.5%/TiO_2 2.5%	0.36 ± 0.04
ABS/RHA 2.5%/TiO_2 5.0%	0.50 ± 0.06

Conclusion

This study successfully incorporated rice husk ashes (RHA) and titanium dioxide (TiO_2) into the acrylonitrile butadiene styrene (ABS) matrix using a melting extrusion process. Extensive testing and analysis were conducted to assess the influence of these additives on ABS composites. The addition of TiO_2 resulted in irregularly embedded particles within the ABS matrix, indicating some degree of incompatibility between ABS and TiO_2, which could impact mechanical properties. Tensile strength at break and yield decreased with the addition of TiO_2, indicating potential challenges related to the compatibility between TiO_2 particles and the ABS matrix. TiO_2-containing composites exhibited reduced impact energy compared to neat ABS, possibly due to limited compatibility between TiO_2 and ABS. However, the decrease in tensile strength and impact energy suggests the need for improved dispersion of TiO_2 to avoid compromising mechanical properties. These findings contribute to our understanding of enhancing ABS composites for various industrial applications. Based on this work, new studies must be carried out to develop more effective strategies to improve interfacial adhesion between RHA, TiO_2 and the ABS matrix, and consequently obtain composite materials with superior properties suitable for a wide range of applications.

Funding Sources The authors would like to thank the funding from FAPESP, Process number 2022/03904-7.

Acknowledgements The authors wish to thank FAPESP, CAPES, and CNPq for providing the financial support for this work.

References

1. Gong K, Liu H, Huang C, Cao Z, Fuenmayor E, Major I (2022) Hybrid manufacturing of acrylonitrile butadiene styrene (ABS) via the combination of material extrusion additive manufacturing and injection molding. Polymers (Basel) 14(23)
2. Almushaikeh AM, Alaswad SO, Alsuhybani MS, AlOtaibi BM, Alarifi IM, Alqahtani NB, Aldosari SM, Alsaleh SS, Haidyrah AS, Alolyan AA, Alshammari BA (2023) Manufacturing of carbon fiber reinforced thermoplastics and its recovery of carbon fiber: a review. Polym Test [Internet]. 122:108029. https://doi.org/10.1016/j.polymertesting.2023.108029
3. Anwajler B, Zdybel E, Tomaszewska-Ciosk E (2023) Innovative polymer composites with natural fillers produced by additive manufacturing (3D printing)—a literature review. Polymers 15(17):3534
4. Chaudhary DS, Jollands MC, Cser F (2004) Recycling rice hull ash: a filler material for polymeric composites? Adv Polym Technol 23(2):147–155
5. Vidakis N, Petousis M, Maniadi A, Koudoumas E, Liebscher M, Tzounis L (2020) Mechanical properties of 3D-printed acrylonitrile-butadiene-styrene TiO_2 and ATO nanocomposites. Polymers (Basel) 12(7):1–16
6. Anucha CB, Altin I, Bacaksiz E, Stathopoulos VN (2022) Titanium dioxide (TiO_2)-based photocatalyst materials activity enhancement for contaminants of emerging concern (CECs)

degradation: in the light of modification strategies. Chem Eng J Adv [Internet] 10(2):100262. https://doi.org/10.1016/j.ceja.2022.100262
7. Kamrannejad MM, Hasanzadeh A, Nosoudi N, Mai L, Babaluo AA, Ave H (2014) Aop267214.Pdf 17(4):1039–1046
8. Andrade MS, Ishikawa OH, Costa RS, Seixas MVS, Rodrigues RCLB, Moura EAB (2022) Development of sustainable food packaging material based on biodegradable polymer reinforced with cellulose nanocrystals. Food Packag Shelf Life 31
9. Yadav M, Chiu FC (2019) Cellulose nanocrystals reinforced κ-carrageenan based UV resistant transparent bionanocomposite films for sustainable packaging applications. Carbohydr Polym [Internet] 211:181–94. https://doi.org/10.1016/j.carbpol.2019.01.114
10. Al-Mazrouei N, Ismai A, Ahmed W, Al-Marzouqi AH (2022) ABS/silicon dioxide micro particulate composite from 3D printing polymeric waste. Polymers 14:509. https://doi.org/10.3390/polym14030509
11. Behera BK, Thirumurugan M (2022) A study on visco-elastic, thermal and mechanical characteristics of injection molded ABS/graphite composite. Mater Today Proc 56:2915–2922

Evaluation of Geopolymer Composites, Based on Red Mud and Metakaolin, for Building Application

Cássia Mirelly Milward de Souza, Beatryz Cardoso Mendes, Leonardo Gonçalves Pedroti, and Carlos Maurício Fontes Vieira

Abstract Portland cement is widely used in civil construction, although its production involves the emission of high amounts of carbon dioxide. Geopolymers have been studied as an alternative to replace Portland Cement. These materials can be produced using wastes and they are less aggressive to the environment. The aim of this work was the physical and mechanical evaluation of geopolymers composites based on red mud and metakaolin as precursors and sodium hydroxide (NaOH) as activator. Compressive strength tests were performed in ten mixtures with different percentages of the precursors and sand. The water absorption index and microstructural analysis were also determined. Furthermore, durability tests were performed on the composites, in order to allow complete characterization and suggestions of applicability in civil construction. The results showed that the composites have physical and mechanical characteristics that comply with the standards and good durability performance. Therefore, they can be used to produce construction bricks.

Keywords Geopolymer · Metakaolin · Red mud · Sustainability · Wastes

C. M. M. de Souza · L. G. Pedroti
DEC—Department of Civil Engineering, UFV—Federal University of Viçosa, Av. Peter Rolfs, s/n, Campus Universitário, Viçosa 36570-000, Brazil
e-mail: cassia.milward@ufv.br

L. G. Pedroti
e-mail: leonardo.pedroti@ufv.br

B. C. Mendes (✉)
DAU—Department of Architecture and Urbanism, UFV—Federal University of Viçosa, Av. Peter Rolfs, s/n, Campus Universitário, Viçosa 36570-000, Brazil
e-mail: beatryz.mendes@ufv.br

C. M. F. Vieira
LAMAV—Advanced Materials Laboratory, UFV—State University of the Northern Rio de Janeiro, Av. Alberto Lamego, Campos Dos Goytacazes 2000, 28013-602, Brazil
e-mail: vieira@uenf.br

Z. Peng et al. (eds.), *Characterization of Minerals, Metals, and Materials 2024*, The Minerals, Metals & Materials Series, https://doi.org/10.1007/978-3-031-50304-7_40

Introduction

The manufacture and application of one of the most used building materials in the world, Portland cement [1], is a serious environmental problem since it releases a large amount of carbon dioxide (CO_2) into the atmosphere. For this reason, new binder systems have been studied and, among them, alkali-activated ones stand out, which have properties similar to the traditional binder and can be applied in buildings [2, 3].

Alkali-activation is the name of the process derived from the combination of a precursor, which is generally mineralogically amorphous, and an activator, composed of alkaline metals dissolved in aqueous solution. The union of both creates a mass-like mixture and starts the setting time, hardening and mechanical strength reactions [4]. There is a class of binders originated by alkali-activation called geopolymer, a term that was mentioned for the first time in the 70's by the researcher Joseph Davidovits. Since then, it has been widely studied. Geopolymers consist of three-dimensional aluminosilicates and are synthesized by a high concentration alkaline solution, which can be hydroxides or silicates [5]. As a product of geopolymerization, three-dimensional structures of silica aluminates (N–A–S–H gel) are created.

Geopolymers have the advantage of being able to be obtained from industrialized compounds, such as metakaolin (MK), and even from by-products of industrial processes, such as red mud (RM). Metakaolin is a calcined clay and serves as a source of aluminosilicate [6], since it has high percentages of SiO_2 and Al_2O_3. Its activation can make materials more resistant and durable, which is why it is commonly used as an addition in concrete and mortar. Red mud, also called bauxite tailings, is a by-product of aluminum manufacturing, and it is produced in high quantities—it is estimated that annual production is approximately 160 million tons [7]. Therefore, the use of bauxite waste in geopolymers can be a viable alternative for its final destination, since they are disposed of in dams.

Considering that the red mud is originally in the crystalline and non-reactive phase, pre-calcination is necessary to make it suitable for geopolymerization. According to Ye et al. [8], when bauxite waste undergoes heat treatment and is mixed with another precursor, it can reach a satisfactory quality for synthesis. Thus, since done the calcination, this waste shows promising physical and chemical characteristics for using. Several authors have already investigated the use of metakaolin and red mud as precursors in geopolymers. Klaus [9] studied the use of materials for the production of geopolymer mortars, which offered results similar to traditional mortars. Brito et al. [10] reached values of mechanical strength even higher than those found in concrete from Portland cement when making geopolymers with both precursors. Therefore, it is possible to adopt this alternative for use in civil construction, being a more environmentally and economically correct option, since it makes use of waste obtained at low cost.

Given the above, the present research aims to characterize the red mud, as well as to evaluate the mechanical behavior and water absorption of the geopolymeric binder produced from bauxite waste and metakaolin as precursors, jundu sand (JS)

as the small aggregate and sodium hydroxide (NaOH) as the activating solution. Then, 10 compositions were generated with different percentages of addition, statistically evaluating the results and thus defining an optimal mixture, which was used in a durability test by drying and wetting. From these analyses, it was possible to characterize the geopolymer and suggest uses in civil construction.

Materials and Methods

The materials used in this research were red mud, metakaolin, jundu sand, sodium hydroxide and distilled water. Red mud was supplied by a company located at Miraí, Brazil. The metakaolin bought was industrialized and jundu sand was obtained from Piranga River, Brazil. The alkaline solutions were produced with the addition of NaOH pellets (CRQ P.A., 99% purity).

The red mud was characterized by particle size distribution, chemical and mineralogical composition. The particle size was determined by means of Bettersize 2000 laser particle size analyzer, in a range of 0.02–2000 μm. The chemical analysis was obtained by X-ray fluorescence technique, using a Shimadzu Micro-EDX-1300 spectrometer. The mineral phases were assessed by X-ray diffraction (XRD), through the D8—Discover with radiation Cu-Kα ($\lambda = 15418$ Å). Analysis of the morphology of the red mud powder was obtained by means of three-dimensional micrographs obtained through Scanning Electron Microscopy (SEM), using the microscope Leo 1430VP.

Using Minitab® software, 10 compositions were generated with different proportions of solid inputs. The experimental design was carried out in a simplex network, with three components and with the following addition intervals: jundu sand (20–70%); red mud (20–70%) and metakaolin (10–60%). Then, 6 specimens of each mixture were carried out, 3 for compressive strength test at 7 days of curing, 3 for 28 days of curing. The pressing load, of 3 ton-force (tf), and the water/binder ratio (w/b), set at 0.30, were two parameters obtained after extensive bibliographical research [11]. Before application, the red mud was pre-calcined at 800 °C for 3 h, at a growth rate of 5 °C per minute.

First, the mixture was carried out with the solid materials, dry. Subsequently, the necessary alkaline solution and water were added, then pressed with a cylindrical metallic mold in a manual hydraulic press. The weights and dimensions of the specimens were taken, which were approximately (3.0 × 4.5) cm. During the first 24 h, the specimens underwent hydrothermal curing in containers with water at 60 °C, after which time they remained in a humid chamber until the performance of mechanical tests.

After the mechanical resistance test, the results were statistically treated once more in the software, generating a new composition called optimal mixture (OPM) which supposedly would provide the best resistance. Another mixture was also generated that contained the highest possible amount of red mud (MRM) without reaching resistance below the standard. The optimal mixture and the one with the highest red

Table 1 Composition of OPM and MRM in percentages

Mixture	Red mud	Metakaolin	Jundu sand
OPM	20	51	29
MRM	63	16	21

mud content were obtained experimentally and its composition is shown in Table 1. Both underwent curing for 28 days and were tested for mechanical strength and water absorption. Finally, the optimal mixture was subjected to the wetting and drying durability test, going through 5 cycles, namely: dried in an oven (105 °C ± 5) for 24 h and weighed, submerged in a container with water for 24 h and weighed. The durability analysis was performed by means of visual observation and monitoring of mass loss.

Results and Discussion

Characterization of Red Mud

The particle size distribution of red mud is shown in Fig. 1. The red mud has an average diameter (D50) of 8.0 μm, so it can be classified as silty material and has about 20% of clay fraction in its composition. The greater fineness of the material is an interesting characteristic for the reactivity and geopolymerization potential.

Table 2 shows the chemical composition of red mud. One can notice that bauxite residue is largely composed by Al_2O_3 (39.70%), SiO_2 (28.80%) and Fe_2O_3 (21.60%). Although silica appears among the largest compounds and this was a favorable characteristic, the value found in the silica/alumina ratio was 0.72, which is considered low for the performance of the geopolymer binder to be reinforced in terms of mechanical resistance [12].

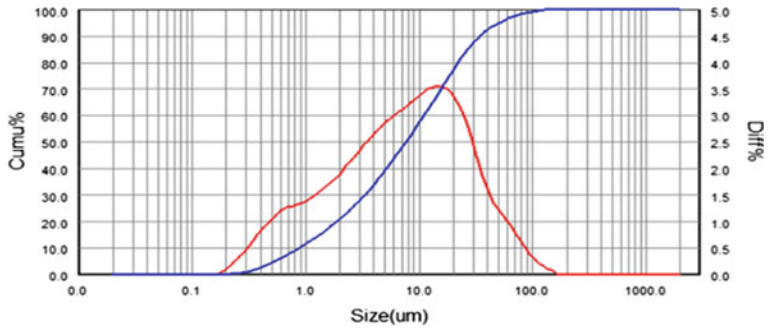

Fig. 1 Particle size distribution of red mud

Table 2 Chemical composition of red mud

Raw material	Chemical composition (%)								
	SiO_2	Al_2O_3	Fe_2O_3	CaO	K_2O	MgO	Ti_2O	Na_2O	Other
Red mud	28.80	39.70	21.60	0.00	0.20	0.00	1.40	0.00	0.40

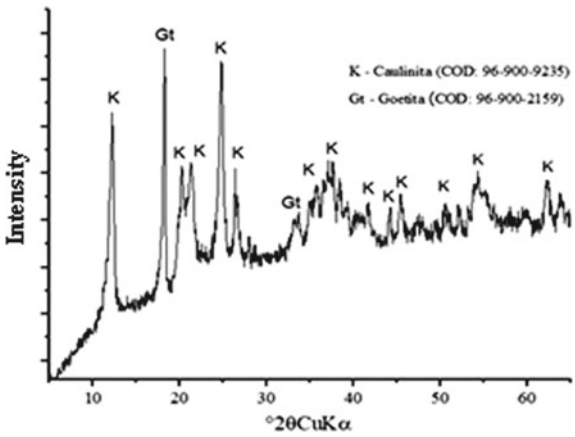

Fig. 2 XRD patterns of red mud (K—kaolinite; Gt—Goethite)

Figure 2 shows the XRD patterns of red mud. The XRD test detected peaks of clay minerals such as kaolinite and goethite with a well-defined appearance, suggesting that the silica and alumina present are not in their reactive state, making it difficult for these species to be solubilized in an alkaline medium. For this reason, pre-calcination proved to be a good solution to make the bauxite residue applicable in geopolymers.

Figure 3 shows the result of the red mud morphology analysis. It was noticed that the material is made up of particles of various shapes, some rounded and smaller, others in agglomerates with porous flakes. This variation in sizes and shapes may be due to the composition of the bauxite waste, which has several minerals in their composition.

Characterization of Geopolymeric Composites

Figures 4 shows the compressive strength of the ten mixtures. One can notice that the increase of mechanical strength from 7 to 28 days was very significant in virtually all specimen. The mixture that presented the highest mechanical resistance was the M7, which is formed mainly by metakaolin. The one that achieved the lowest resistance value was the M9, which contours with only 10% metakaolin. Therefore, it is inferred that this material has a great influence on obtaining resistance by the specimens, probably due to the predominance of silica in its composition [13].

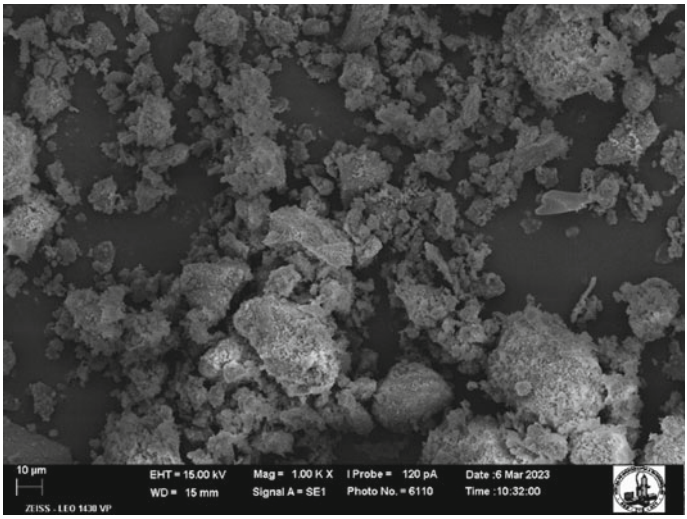

Fig. 3 SEM of red mud

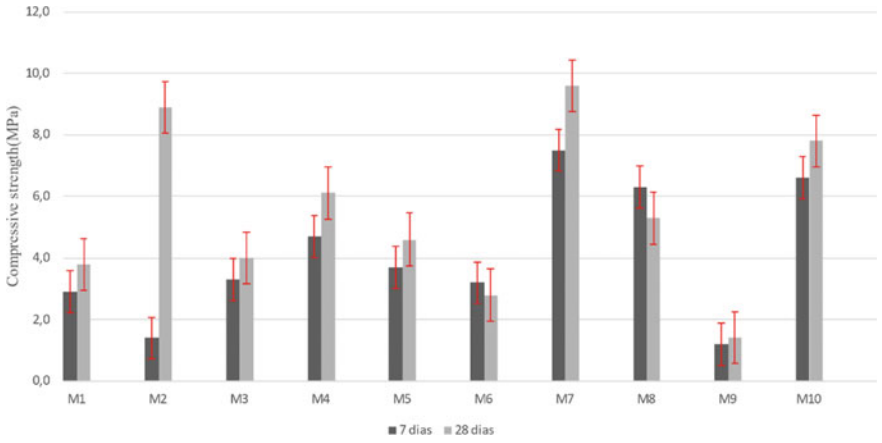

Fig. 4 Compressive strength of pastes at 7 and 28 days

The geopolymer composites obtained with a higher red mud content showed less resistance—which is explained by the fact that the red mud has a lower geopolymer potential. Since the waste has larger particles compared to jundu sand and metakaolin, it contributes to reducing its specific surface area, making it less reactive than other products. However, even the jundu sand presenting fine granulometry, the packing was not the main factor to define the result of the final resistance of the obtained

product, but the geopolymerization matrices. Therefore, it is possible to infer that increasing the amount of sand will not add resistance to the geopolymer produced, since the material enters inertly.

Among the mechanical resistance results obtained, 80% of the specimens presented average values equal to or above 4 MPa, which is the minimum established for clay bricks [14]. Furthermore, the results obtained fit those found in other studies, such as the study by Ascensão et al. [15] which reached, in 28 days, 5.48 MPa for mixtures with 25% red mud, while the current work for 26.7% replacement reached 6.1 MPa. In that case, it can be said that satisfactory results were reached in terms of mechanical strength. Figure 5 shows the result of the experimental analysis by the software, in which the darker areas are the composition regions with greater mechanical resistance.

Figure 6 shows the results of the compression test of the optimal mix (OPM) and mix with higher addition of red mud (MRM). The optimal mixture reached about 65% of the mechanical strength predicted by the software, while the one with the largest addition of waste reached 57%. This variation in the value achieved is related to the term *R-sq(pred)*, which predicts how much the equation fits the assumption—given that the value found for the parameter was 86%, it can be assumed that the difference is due to the uncertainty related to the equation. The optimal mixture

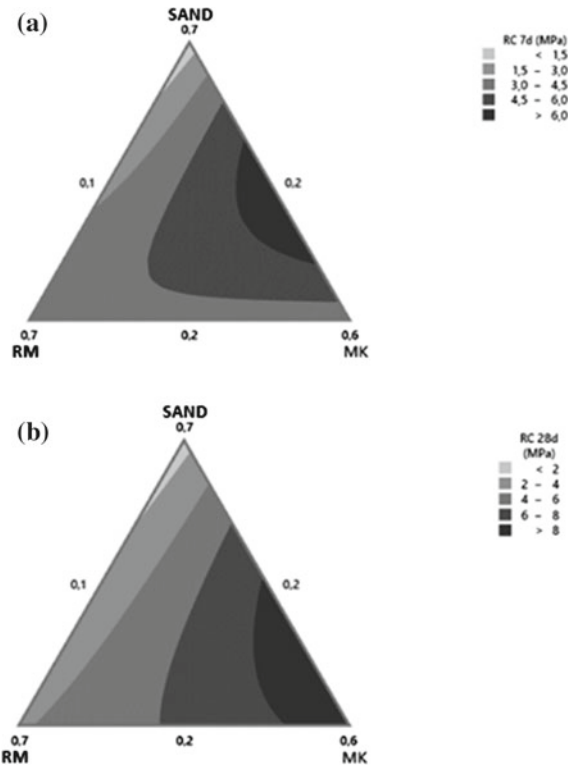

Fig. 5 Mixture contour plot: **a** 7 days; **b** 28 days

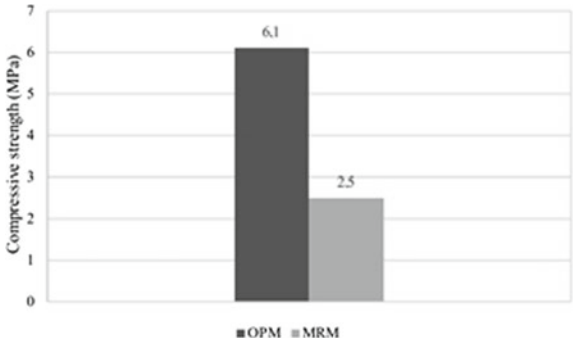

Fig. 6 Compressive strength of pastes at 28 days

achieved satisfactory mechanical strength results, while the other did not, remaining below the standardized minimum. Regarding the water absorption test, the mixture with the highest amount of red mud was better in packing factor, reaching only 16.4% of absorption, while the other one had 22.4%. Both mixtures showed lower indices than the maximum suggested by NBR 15,270 standard [14], equal to 25%.

The following figures show the wear on the specimens during the cycles. Initially, small cracks appeared, which increased throughout the test. At the end of the cycles, the materials were not in complete ruin, however, they were weakened due to the loss of mass they went through. It was possible to observe that at each cycle new cracks appeared due to wear, making the material more porous and more susceptible to absorbing water. Subsequently, due to the loss of mass, the value of the dry mass reduces again as the specimen begins to break down. It was possible to notice a small and constant loss of mass in all specimens, which is a satisfactory result of durability. However, the values found by the drying and wetting method must be evaluated by greater and more in-depth criteria, so that the importance of the results achieved and their real connection with the durability of the geopolymers can be truly evaluated (Fig. 7).

Conclusions

This study aimed to evaluate the mechanical behavior and microstructure of geopolymeric pastes produced from red mud and metakaolin-based alkaline solutions. According to the experimental program and the statistical tools applied, one can conclude the following:

- Both red mud and metakaolin presented suitable characteristics for their application in the production of geopolymeric materials, such as appropriate contents of SiO_2 and Al_2O_3 and reach of amorphous phase.
- The curing time impacts on the mechanical resistance gain, since most of the specimens reached greater resistances at 28 days than at 7 days.

Fig. 7 Durability test on specimens

- The precursor that had the most positive impact on compressive strength was metakaolin, due to its high concentration of silicates. The addition of jundu sand does not promote gain in mechanical resistance since it is an inert material.
- The microstructural analyses showed that the red mud does indeed need heat treatment prior to application. Thus, after pre-calcination, the results of its application in geopolymers proved a good performance as a precursor.
- Considering the mechanical results, red mud and metakaolin have potential to be applied in geopolymer products. The suggested use are products that do not request higher values of compressive strength, such as coating mortars. The mixtures that underwent the absorption test reached satisfactory values for this parameter.
- The specimens had a reasonable performance in the wetting and drying tests, not reaching complete ruin. Therefore, further studies are needed to reach concrete conclusions about its durability.

Acknowledgements This study was financed in part by the Coordenação de Aperfeiçoamento Pessoal de Nível Superior—Brasil (CAPES)—Finance Code 001. The authors also want to thank the CNPq agency for the financial support provided and the Sustainable and Innovative Construction Research Group (SICon) for the technical assistance.

References

1. da Silva RJ (1994) Energy analysis of Portland cement production plants. UNICAMP, Campinas
2. Feuchard, LM et al (2020) Microestrutura e propriedades físicas e mecânicas de cimento Portland tipo II álcali-ativado. Braz J Dev 6(11):84929–84951

3. Langaro, EA et al (2017) The influence of chemical composition and fineness on the performance of activated alkali cements obtained with blast furnace slag. Matter (Rio de Janeiro) 22. https://doi.org/10.1590/S1517-707620170001.0124
4. Assi LN, Eddie Deaver E, Ziehl P (2018) Effect of source and particle size distribution on the mechanical and microstructural properties of fly ash-based geopolymer concrete. Construct Build Mater 167:372–380. https://doi.org/10.1016/j.conbuildmat.2018.01.193
5. Cardoso BM (2020) Development of geopolymer mortars produced with industrial residues in the precursor and activator phases
6. Maccarini HS et al (2015) Development of geopolymer from the use of metakaolin
7. International Aluminium Institute. Opportunities for use of bauxite residue in special cements [s.l: s.n.]. Disponível em: https://international-aluminium.org/media/filer_public/2020/03/16/opportunities_for_use_of_bauxite_resid
8. Ye N et al (2016) Synthesis and strength optimization of one-part geopolymer based on red mud. Construct Build Mater 111:317–325. https://doi.org/10.1016/j.conbuildmat.2016.02.099
9. Andrade IKR (2022) Development of "one-part" geopolymers based on metakaolin and red mud
10. Brito WS, Racanelli LD, Souza JA (2020) Geopolymerization of red mud: influence of naoh concentration on synthesis at room temperature. Matter (Rio de Janeiro) 25. https://doi.org/10.1590/S1517-707620200001.0923
11. Milward C, Mendes BC, Pedroti LG (2022) Application of ceramic residues for the production of pressed geopolymers. Nat Meet Technol Built Environ 19:1–12. https://doi.org/10.46421/entac.v19i1.1975
12. Silva SM, Freire CB (2022) Methodology for geopolymer synthesis aiming at the treatment of organic radioactive waste methodology for geopolymer synthesis for the treatment of organic radioactive waste. Braz J Dev 8(5):33457–33474. https://doi.org/10.34117/bjdv8n5-055
13. De Souza Vassalo EA (2013) Obtaining geopolymer from activated metakaolin
14. Brazilian Association of Technical Standards (2017) NBR 15270-2: ceramic components—blocks and bricks for masonry. Part 2: test methods. Rio de Janeiro
15. Ascensao G et al (2017) Red mud-based geopolymers with tailored alkali diffusion properties and pH buffering ability. J Clean Prod 148:23–30

Evaluation of the Mechanical Properties of Geopolymers Manufactured in Molds of Different Sizes

J. A. T. Linhares Jr, L. B. Oliveira, D. V. André Jr, T. P. R. de Mello, M. T. Marvila, C. M. Vieria, S. N. Monteiro, and A. G. de Azevedo

Abstract Geopolymeric materials have been extensively studied in science due to their properties similar to Portland cement. These materials offer ecological and energy advantages due to their production processes. However, there are costly components that are involved, such as those in the activating solution. Another challenge regarding studies involving geopolymers is the absence of standards, in many cases, an adaptation of those used in Portland cement is made. In this context, the objective of this work is to produce geopolymeric metakaolin mortars and investigate the influence of the volumetric reduction of standardized prismatic and cylindrical specimens compared to cement. The goal is to determine whether there is a statistical difference in the properties of mechanical resistance to flexion and compression when using smaller and more economical molds. The molds have proven to be efficient and have resulted in significant material savings.

Keywords Compressive strength · Geopolymer · Flexural strength · Molds

Introduction

Geopolymers have gained prominence in studies aiming to find ecological binders as alternatives to Portland cement. These materials possess desirable properties and characteristics, including low CO_2 emissions, good durability, and excellent thermal,

J. A. T. Linhares Jr · L. B. Oliveira · D. V. André Jr · C. M. Vieria · A. G. de Azevedo
LAMAV—Advanced Materials Laboratory, UENF—State University of the Northern Rio de Janeiro, Av. Alberto Lamego, 2000, Campos dos Goytacazes, Rio De Janeiro 28013-602, Brazil

T. P. R. de Mello · S. N. Monteiro
Department of Materials Science, IME—Military Institute of Engineering, Square General Tibúrcio, 80, Rio de Janeiro 22290-270, Brazil

M. T. Marvila (✉)
UFV—Federal University of Viçosa Campus Rio Paranaíba (UFV-CRP), Rodovia BR 230 KM 7, Rio Paranaíba 38810-000, Brazil
e-mail: markssuel.marvila@ufv.br

Z. Peng et al. (eds.), *Characterization of Minerals, Metals, and Materials 2024*, The Minerals, Metals & Materials Series, https://doi.org/10.1007/978-3-031-50304-7_41

chemical, and mechanical resistance [1]. The technological properties of geopolymers are of great importance, as they provide essential information for the application of these materials. Among these properties, mechanical resistance to flexion and compression stands out as crucial for the civil construction industry, and it has been evaluated in various studies [2, 3].

In order to guide the resistance tests of geopolymers, several standards are used, adapted from Portland cement so that there is a standard. The NBR 7215 standard [4] determines the guidelines for carrying out compressive strength tests, requiring specimens with cylindrical geometry with a diameter of 50 ± 0.1 mm by 100 ± 0.2 mm in height. The NBR 13,279:2005 standard [5] establishes a specimen of prismatic geometry, with a square section of 40 × 40 (± 0.4) mm and a length of 160 ± 0.8 mm.

In this context, the objective of this study is to analyze the mechanical properties of compression and flexion in relation to the reduction in prismatic and cylindrical molds, aiming to determine if there are significant differences in the results. The reductions in size were in accordance with the standards, resulting in specimens of 20 × 20 × 160 mm (prismatic) and 20 × 30 mm (cylindrical). The same geopolymer mortar, based on metakaolin activated with sodium hydroxide (NaOH), was used to create the test specimens.

Materials and Methods

In conducting this study, geopolymeric mortars were prepared using the following materials and their respective mass proportions: metakaolin (1210.5 g); sand (1815.75 g); NaOH (81 g); Na_2SiO_3 (396 g); distilled water (684 g).

The activating solution was initially prepared 24 h in advance to allow for the dissipation of any residual heat from the dissolution process. The reagents NaOH and silicate (Na_2SiO_3) were dissolved using a magnetic mixer with heating at 80 °C. The precursor and the sand (sieved to 10 Mesh) were dry homogenized. In the next step, the activator solution was added, and the entire mixture was homogenized using a benchtop mortar.

For molding, we utilized large prismatic molds standardized by NBR 13,279:2005 [5], with a square section of 40 × 40 mm and a length of 160 mm (BP), as well as molds with half the dimensions (SP). Cylindrical molds for compression with a diameter of 50 mm and a height of 100 mm were also employed, following the NBR 7215 standard [4], alongside reduced molds measuring 20 mm in diameter and 30 mm in height. The curing process was conducted at ambient conditions for a duration of 7 days.

To perform the tests, a universal mechanical testing machine from the INSTRON brand, model 34FM-100-SA, was used, with a loading speed set at 0.25 ± 0.05 MPa/s. For the statistical analysis, an analysis of variance (ANOVA) and the Tukey test were applied to assess the statistical differences between the sample groups, with a significance level of 5%.

Results and Discussion

Figure 1 shows the results of the compression test at 7 days for metakaolin geopolymeric mortars cured at 25 °C. Tables 1 and 2 present, respectively, the statistical analysis CRD ANOVA ($p \leq 0.05$) and the Tukey test. For ANOVA, varied repetitions were used according to the different dimensions of the specimens or treatments (LP, SP, LC, SC).

Statistical analysis performed by CRD—ANOVA ($p \leq 0.05$) shows that $F_{cal} > F_{tab}$. Thus, it is inferred that the results are significant and that there are at least two different means. Subsequently, Tukey's test was performed as a complementary analysis to compare means. Thus, it is observed that the prismatic specimens (SP and LP) are statistically equal. However, when comparing the other averages with cylindrical specimens (LC and SC) they had statistically different results, that is, the dimensions of the specimens were significant for the compressive strength results. A possible explanation for this is that the cylindrical specimens (LC and SC) do not

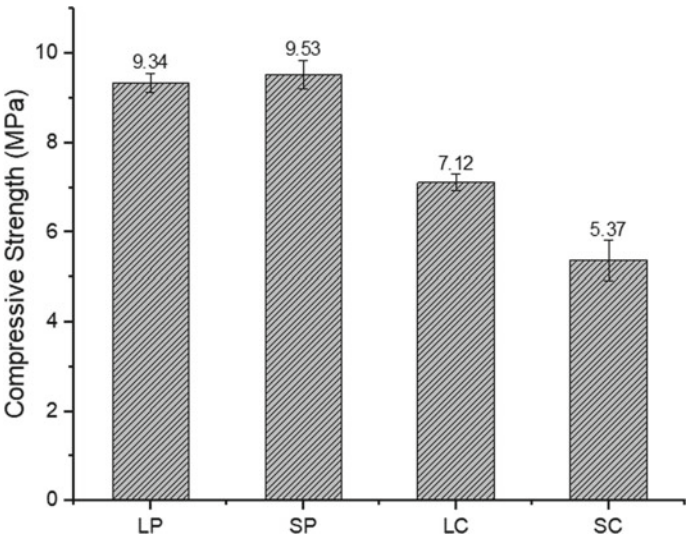

Fig. 1 Compressive strength at 7 days according to the dimensions of the specimens (large prism (LP), small prism (SP), large cylinder (LC), small cylinder (SC))

Table 1 CRD-ANOVA ($p \leq 0.05$) for compressive strength at 7 days varying according to the dimensions of the specimens

SV	GL	SQ	MQ	F_{calc}	F_{tab}
Treatment	3	46.08	15.36	163.38	3.49
Error	12	1.13	0.09	–	–
Total	15	47.21	–	–	–

Table 2 Tukey test for contrasting mean compressive strength at 7 days

Treatment	Mean (MPa)	Tukey
LP	9.34	A
SP	9.54	A
LC	7.12	B
SC	5.37	C

show proportional decreases. In addition, the SC do not present the H/D = 2 ratio, which is a possible cause for the discrepancy in the results.

Figure 2 shows the results of the flexural test at 7 days for metakaolin geopolymer mortars cured at 25 °C. Table 3 present the CRD ANOVA statistical analysis ($p \leq 0.05$). For ANOVA, varied repetitions were used according to the different dimensions of the specimens or treatments (LP, SP).

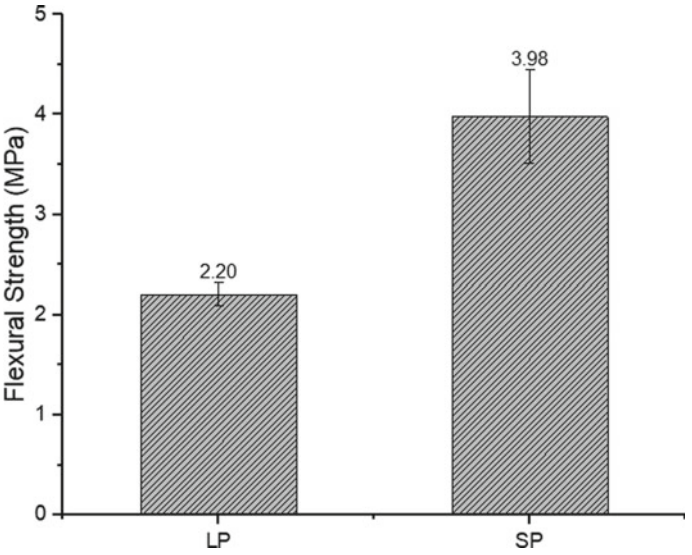

Fig. 2 Flexural strength at 7 days according to the dimensions of the specimens (large prism (LP), small prism (SP))

Table 3 CRD-ANOVA ($p \leq 0.05$) for flexural strength at 7 days varying according to the dimensions of the specimens

SV	GL	SQ	MQ	F_{calc}	F_{tab}
Treatment	1	6.30	6.30	39.41	5.59
Error	7	1.12	0.16	–	–
Total	8	7.42	–	–	–

Statistical analysis performed by CRD—ANOVA ($p \leq 0.05$) shows that $F_{cal} > F_{tab}$. Thus, it appears that the results are significant and that the two averages are different. However, other reasons may be related to the significant differences in the results. As it is a ceramic material prepared in the laboratory, the way of densifying, compacting and unmolding the test specimens may be relevant to the results. In addition, the small number of specimens tested can also cause this difference.

Conclusions

After evaluating the results, the study concluded that, in relation to prismatic specimens of different dimensions, there were no significant differences when tested for compressive strength, presenting 9.34 and 9.54 MPa, for LP and SP respectively. However, when compared in terms of flexural strength, there was a significant difference, with the samples presenting 2.20 MPa (LP) and 3.98 MPa (SP). Therefore, it is concluded in relation to this geometry that the specification test is viable with the reduction of dimensions. In relation to cylindrical specimens, a statistical difference was found for the samples. Therefore, it is concluded that the reduction of cylindrical molds for compression tests is not recommended. Probably due to the non-maintenance of the proportion in the reduction.

References

1. Ye H, Asante B, Schmidt G, Krause A, Zhang Y, Yu Z (2023) Eco-friendly geopolymer-wood building materials: interactions between geopolymer and wood cell wall. J Clean Prod 420. https://doi.org/10.1016/j.jclepro.2023.138381
2. Naenudon S, Anousit V, Yuwadee Z, Weerachart T, Ampol W, Vanchai S, Prinya C (2022) High flexural strength lightweight fly ash geopolymer mortar containing waste fiber cement. C S Construct Mater 16. https://doi.org/10.1016/j.cscm.2022.e01121
3. Linhares Jr JA, Azevedo ARG, Marvila MT, Teixeira SR, Fediuk R, Vieira CMF (2022) Influence of processing parameters variation on the development of geopolymeric ceramic blocks with calcined kaolinite clay. Case Stud Construct Mater 16. https://doi.org/10.1016/j.cscm.2022.e00897
4. Brazilian Association of Norms Technical (1996) NBR 7215. Cimento Portland—Determinação da resistência à compressão. Rio de Janeiro (In Portuguese)
5. Brazilian Association of Norms Technical (2005) NBR 13279. Argamassa para revestimento de paredes e tetos – Determinação da resistência à tração na flexão e à compressão. Rio de Janeiro (In Portuguese)

Evaluation of the Performance of Sustainable Paints Using Red Mud

Jean Carlos Bernardes Dias, Leonardo Gonçalves Pedroti, Márcia Maria Salgado Lopes, Hellen Regina de Carvalho Veloso Moura, and Júlia Lopes Figueiredo

Abstract Red mud is a residue generated in the processing of bauxite for aluminum production and its improper disposal causes significant environmental damage. This study assesses the potential use of red mud as a pigment in sustainable paint production. The residue underwent deagglomeration, mechanical dispersion, and particle sieving, and was characterized physically, chemically, and morphologically. An experimental mixture design was employed to evaluate paint performance by varying the proportions of red mud, water, and resin. Statistical analysis determined the optimal composition as 33% residue, 55% water, and 12% resin. This paint demonstrated an abrasion resistance of 126 cycles and a hiding power of 4 m^2/L, meeting the requirements for economic paints. These findings present a sustainable alternative for utilizing red mud, contributing to the reduction of environmental harm caused by this residue.

Keywords Paints · Red mud · Waste · Sustainability · Environment

Introduction

The use of paint dates to prehistoric times, when hominids used it in cave paintings depicting the animals and habits of the time. They used blood, clay, earth, plants, stones, and ground bones to paint. As humanity advanced and new civilizations emerged, such as the Egyptians and Chinese, paints began to be used as a decorative material to adorn temples, palaces, and tombs. Over the years, new techniques have been developed to ensure better durability and performance, such as the use of minerals as pigments and even the use of egg white as a binding vehicle [1].

According to Castro [2], with the advance of the Industrial Revolution in the seventeenth century, new equipment emerged that enabled the technical development

J. C. B. Dias (✉) · L. G. Pedroti · M. M. S. Lopes · H. R. de Carvalho Veloso Moura · J. L. Figueiredo
DEC—Civil Engineering Department, UFV—Federal University of Viçosa, Av. Peter Rolfs, s/n, Campus Universitário, Viçosa 36570-000, Brazil
e-mail: jean.dias@ufv.br

Z. Peng et al. (eds.), *Characterization of Minerals, Metals, and Materials 2024*, The Minerals, Metals & Materials Series, https://doi.org/10.1007/978-3-031-50304-7_42

of paints, as well as their production, which became large-scale, reaching many people who previously had no access to this material due to its high cost and difficult formulation.

With the advent of technology, paints underwent new improvement processes and began to be used in various applications, such as painting houses, cars, furniture, among others. However, as a result of this technological advance, paints are now composed of organic solvents that release volatile organic compounds (VOCs) and pigments that contain heavy metals [3].

These components are considered potential contaminants of the environment and of the indoor air quality of buildings, and they also affect the health of human beings, especially during the construction phase of the building [4]. Faced with this scenario, the real estate paint industry is looking for solutions to reduce the environmental impacts caused by the products used in real estate paints. Among these is the use of red mud as a pigment to produce real estate paints.

According to the Associação Brasileira de Alumínio [5], Brazil has one of the largest bauxite reserves in the world, located especially in the states of Pará and Minas Gerais. Brazil's reserves total 2.6 billion tons and, according to the Anuário Mineral Brasileiro [6], its annual production exceeds 46 million tons. According to Babisk et al. [7], Brazil is the eleventh largest producer of primary aluminum and the third largest in both alumina production and bauxite extraction, representing an important economic and employment opportunity for the country. This implies great concern about the waste generated in this industrial sector, as the quantity is significant and can cause numerous impacts on the environment.

Bauxite is made up of aluminum hydroxide and some iron and silicon impurities. 92% of the world's bauxite production is used to extract alumina, mainly through the Bayer process, which is then used to manufacture aluminum metal. The Bayer process begins by mixing crushed bauxite with a solution of sodium hydroxide in reactors (digesters). The bauxite dissolves to form a sodium aluminate solution that is used to produce alumina. The iron oxide residues and other compounds present in the bauxite are separated, generating an insoluble, highly alkaline residue called red mud [8].

In Brazil, the amount of red mud generated varies from 10 to 25 million tons/year and its disposal usually occurs in tailings dams, generating high financial and environmental costs, as well as the risk of flooding, underground contamination or dam failure [9]. It is therefore proposed that red mud be used in sustainable, low-cost paints for the construction industry. This proposal aims to minimize the problem of the lack of paint that occurs in most Brazilian peri-urban buildings, due to the high cost of finishing products, as well as being an alternative that contributes to the sustainable development of construction.

The aim of this study is therefore to produce and evaluate the performance and durability of sustainable, low-cost paints using red mud.

Materials and Methods

For this work, red mud generated after the Bayer process was used. Initially, the red mud collected was subjected to a process of deagglomeration and mechanical dispersion of the particles in an aqueous medium, using a Cowles disk coupled to a mechanical agitator. The material was then wet sieved using a 0.15 mm sieve.

According to Merten et al. [10], solvent-based real estate paints contain significant amounts of VOCs and emissions of these solvents have negative consequences for human health. In this sense, the solvent chosen was water, since it is more readily available and, in addition, its harmful character is not harmful compared to organic solvents. This solvent had a specific mass of 1.00 g/cm^3 and an average pH of 6.62.

The binder used in the mixtures was *Cascorez* polyvinyl acetate (PVA) resin, extra grade, with a density of 1.05 g/cm^3, a pH of between 4.0 and 5.0 and a solids content of 46%. According to Cardoso et al. [11], the use of this resin shows favorable results when mixed with certain types of soil pigments, in addition to its availability on the market.

According to Donádio [12], the use of additives in paints gives them special characteristics and improves their properties, such as biocides, dispersants, drying agents, defoamers, among others. However, they were not used in this work due to the difficult access to these materials, meaning that the reapplication of this work would be difficult in social and economic terms.

The red mud was characterized by particle size distribution, chemical and mineralogical composition. The particle size was determined by means of Bettersize 2000 laser particle size analyzer, in a range of 0.02–2000 μm. The chemical analysis was obtained by X-ray fluorescence technique, using a Shimadzu Micro-EDX-1300 spectrometer. The mineral phases were assessed by X-ray diffraction (XRD), through the D8—Discover with radiation Cu–Kα ($\lambda = 15418$ Å). Analysis of the morphology of the red mud powder was obtained by means of three-dimensional micrographs obtained through Scanning Electron Microscopy (SEM), using the microscope Leo 1430VP.

The independent variables in the mixing plan were red mud pigments varying from 25 to 35%, resin varying from 10 to 15% and water varying from 55 to 70%. These variation ranges were defined based on the pigment and resin contents of the commercial PVA latex paints studied by Silva and Uemoto [13]. Table 1 shows the experimental design generated using Minitab®.

Based on the proportions obtained, a quantity, in grams, of red mud dispersed in water and PVA resin was mixed. The mixture was then stirred with the *Cowles* disk attached to the mechanical stirrer for 15 min at a speed of 500 rpm.

The viscosity tests were then carried out using a Ford number 4 orifice cup. In addition, the solids content of each mixture was determined, and the pH was measured using the MS TECNOPON pH meter model mPA-210.

To determine the performance of the paints, the hiding power and abrasion resistance tests without abrasive paste were carried out.

Table 1 Proportions of paints designed in the Minitab® statistical analysis software

Mixture	Red mud	Water	Resin
1	0.2750	0.5750	0.150
2	0.2875	0.5875	0.125
3	0.3250	0.5500	0.125
4	0.2500	0.6250	0.125
5	0.2500	0.6000	0.150
6	0.3500	0.5500	0.100
7	0.2500	0.6500	0.100
8	0.3000	0.6000	0.100
9	0.3000	0.5500	0.150

NBR 14942:2016 [14] establishes a method for determining the hiding power and yield of a dry film of paint for civil construction. According to this standard, the hiding power of a dry paint film corresponds to the maximum area applied, in m^2, per unit volume, in liters, with a contrast ratio of 98.5%, which indicates the paint's ability to hide the substrate after drying. The contrast ratio corresponds to the ratio between the respective intensities of reflected light, i.e., the ratio of the reflectance value in the black area of the card to the value in the white area of the card.

To analyze the contrast ratio, the cards were scanned after drying, in each coat, and a comparison was made using the *B* factor (brightness) of the HSB color standard, using Photoshop® software. According to Lopes [15], by measuring the *B* factor on the black and white areas, it is possible to check how much black and white are still able to pass through the dry paint film.

According to NBR 15078:2006 [16], in the abrasion resistance test without abrasive paste, the number of cycles (one round trip of the brush) is defined based on the cycles required to remove 80% of the paint film applied to the PVC card. The support used in the test was the washability machine [15].

Once the hiding power and abrasion resistance results had been obtained, a statistical analysis was carried out in order to obtain the optimum regions for the performance parameters, using the statistical desirability function in the Minitab® software. According to Lopes [15], each response variable is transformed into an individual desirability value, ranging from 0 to 1, indicating an unacceptable value and a desirable value, respectively. The target values were defined according to ABNT NBR 15079-1:202 [17], following the minimum requirements for economical latex paint, so that the dry paint coverage power is 4 m^2/L and the resistance to wet abrasion without abrasive paste is 100 cycles.

Results and Discussion

Characterization of Raw Materials

The particle size distribution of red mud is shown in Fig. 1. The red mud has an average diameter (D50) of 8.0 μm, so it can be classified as the silty material and has about 20% of clay fraction in its composition. According to Dumitru and Jitaru [18], both the fineness and dispersion of mineral fillers in paints play an important role in their formulation, resulting in good hiding power and chemical stability. Therefore, the finer the mineral filler, the better the properties obtained.

Table 2 shows the chemical composition of red mud. One can notice that bauxite residue is largely composed by Al_2O_3 (44,473%), SiO_2 (31,534%) and Fe_2O_3 (21.526%).

Figure 2 shows the XRD patterns of red mud. The XRD test detected peaks of clay minerals such as kaolinite and goethite.

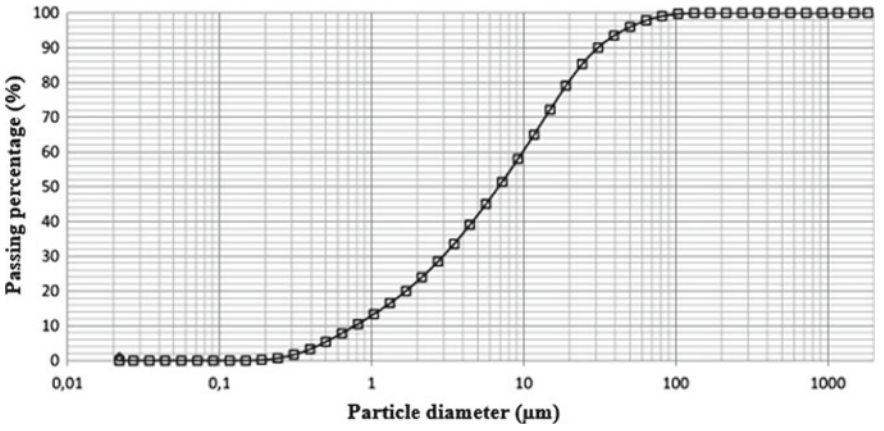

Fig. 1 Particle size distribution of red mud

Table 2 Chemical composition of red mud

Raw material	Chemical composition (%)								
	Al_2O_3	SiO_2	Fe_2O_3	TiO_2	CaO	K_2O	SO_3	P_2O_5	Others
Red mud	44.473	31.534	21.526	1.435	0.256	0.233	0.186	0.113	0.244

Al_2O_3 aluminum oxide, SiO_2 silicon dioxide, Fe_2O_3 iron III oxide, TiO_2 titanium dioxide, CaO calcium oxide, K_2O potassium oxide, SO_3 sulfuric oxide, P_2O_5 phosphorus pentoxide

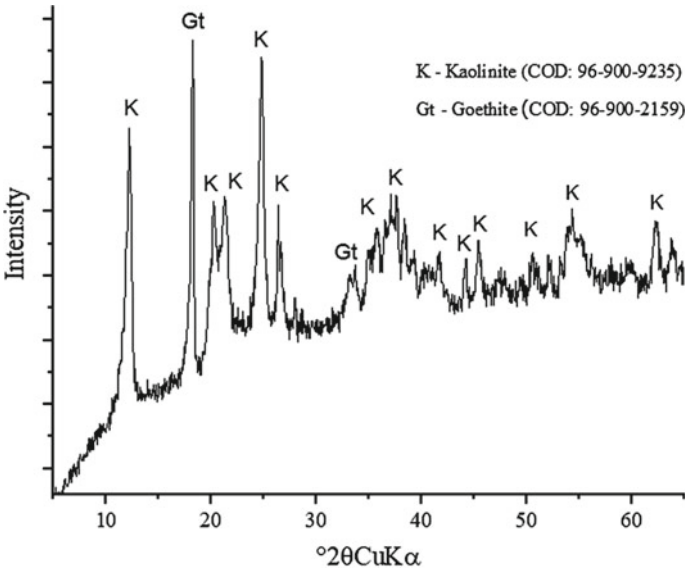

Fig. 2 XRD patterns of red mud (K—kaolinite; Gt—Goethite)

Characterization and Performance of Paints

Table 3 shows the results of the characterization of the paint samples produced, solids content (SC), viscosity and pH, and the performance results, such as hiding power (HP) and abrasion resistance (AR). The desirability values (DSB), obtained using Minitab® software, are also shown.

About the solids content, for samples with lower proportions of red mud and higher proportions of water, the solids content obtained was below 35.6%. Similarly,

Table 3 Characteristics and properties of red mud-based paint mixtures

Mixture	TS (%)	Viscosity (s)	pH	HP (m^2/L)	AR (cycles)	DSB
1	0.35	12.40	4.59	3.07	264	0.88
2	0.34	15.62	4.88	3.30	137	0.91
3	0.38	9.77	4.92	3.33	128	0.91
4	0.31	14.90	4.81	3.27	181	0.90
5	0.32	14.73	4.8	2.38	214	0.77
6	0.38	11.03	5.02	4.80	36	0.60
7	0.30	13.09	4.88	3.43	94	0.86
8	0.34	15.07	5.01	4.65	77	0.88
9	0.37	9.65	4.81	3.10	286	0.88

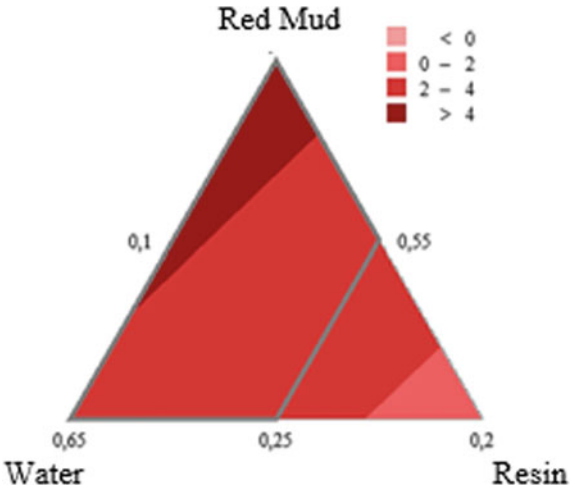

Fig. 3 Graph of the hiding power, ranging from 0 to 4 m^2/L, as a function of the proportions of the components in the mixtures

for higher proportions of red mud, the solids content tended to be higher, indicating the contribution of red mud to this result.

In terms of the viscosity times measured, it is possible to observe a variation from 9 to 16 s. This variation is related to the proportion of water added to the mixtures, i.e., as the proportion of water in the mixture increased, the lower the value obtained when measuring the fluid flow time, obtained from the Ford orifice cup number 4.

According to Dumitru and Jitaru [18], a pH between 8.0 and 9.0 provides safe stability for the paint and prevents the formation of bacteria and fungi that develop in aqueous media at a pH below 8.0. All the samples have a pH below 8.0, which can contribute to the development of fungi and bacteria.

In addition, response surfaces were generated for hiding power and abrasion resistance. Figure 3 shows the hiding power graphs for the paints produced with red mud. The hiding power values were divided into a scale of 0–4 m^2/L.

It was observed that for the paints produced with red mud, the higher the proportion of red mud, the greater the hiding power of the paint film. It was also noted that only samples 6 and 8 met the minimum standard specification of 4 m^2/L, indicating that the proposed paints have considerable coverage.

Figure 4 shows the abrasion resistance response surfaces for the paints produced. The values have been divided into a scale of 50–300.

From Fig. 4 and Table 3, within the delimited study area there were mixtures with values above 100 cycles, i.e., they met the minimum requirement demanded by the standard. The possible explanation for the high abrasion resistance value of the paint film is related to the properties of red mud, which is predominantly composed of aluminum oxide, which has high tenacity and hardness, providing protection against paint wear [19].

Similarly, red mud is composed of silicon dioxide, which provides wear resistance and hardness properties [20]. In addition, the use of a greater amount of resin is in line

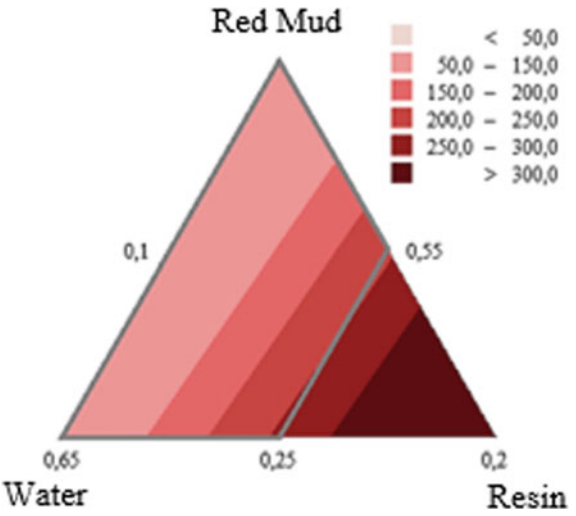

Fig. 4 Graph of the abrasion resistance values, ranging from 50 to 300 cycles, as a function of the proportions of the mixture components

with the results presented by Galvão et al. [21], indicating that abrasion resistance increases as a result of the increase in binder content.

About desirability, calculated from the specifications for the hiding power of the dry paint and the resistance abrasion without abrasive paste, the mixtures showed high desirability values (Table 3). However, no mixture simultaneously met the specifications for hiding power and resistance to abrasion prescribed by ABNT NBR 15079-1:2021 [17]. It is known that in order to meet the minimum requirements for an economical latex paint, the hiding power of the dry paint must be 4 m^2/L and the resistance to wet abrasion without abrasive paste 100 cycles. Therefore, using Minitab® software, the results were optimized based on the target values of 4 m^2/L and 100 cycles and it was found that the best performing red sludge paint is composed of 33% red mud, 55% water and 12% resin, resulting in an abrasion resistance of 126 cycles and a hiding power of 4 m^2/L.

Conclusions

The aim of this study was to produce and evaluate the performance of sustainable paints for the construction industry made from water, PVA resin, and red mud. According to the experimental program and the statistical tools applied, one can conclude the following:

- The production of paints with red sludge, based on a statistical mixing plan, made it possible to determine the formulation with the best performance in terms of hiding power and resistance to abrasion.

- The hiding power was positively influenced by the type and amount of pigment used in the mixture, while resin content positively influenced abrasion resistance. In addition, the larger particle size of the residue increases the roughness of the paint film, which also contributes to a decrease in abrasion resistance.
- The use of red mud in the production of low-cost, low-environmental-impact paints is an alternative with the potential to guarantee the use of waste.

Acknowledgements This study was financed in part by the Coordenação de Aperfeiçoamento Pessoal de Nível Superior—Brasil (CAPES)—Finance Code 001. The authors also want to thank the FAPEMIG agency for the financial support provided and the Sustainable and Innovative Construction Research Group (SICon) for the technical assistance.

References

1. Mello VM, Suarez PAZ (2012) As formulações de tintas expressivas através da história. Revista Virtual de Química 4(1):2–12
2. Castro CD (2009) Estudo da influência das propriedades de diferentes cargas minerais no poder de cobertura de um filme de tinta. 2009. 134f. Tese (Doutorado em Engenharia) - Programa de Pós-Graduação em Engenharia de Minas, Metalurgia e Materiais, Escola de Engenharia, Universidade Federal do Rio Grande do Sul, Porto Alegre
3. CETESB (2006) Companhia de Tecnologia de Saneamento Ambiental. Guia técnico ambiental tintas e vernizes – série P+L. São Paulo 70p
4. Schieweck A, Bock MC (2015) Emissions from low-VOC and zero-VOC paints-valuable alternatives to conventional formulations also for use in sensitive environments? Build Environ 85:243–252
5. Associação Brasileira de Alumínio (2017) Bauxita no Brasil—Mineração responsável e competitividade. São Paulo
6. Anuário Mineral Brasileiro: principais substâncias metálicas (2022) Brasília: ANM, 23p. Disponível em: https://www.gov.br/anm/pt-br/centrais-de-conteudo/publicacoes/serie-estatisticas-e-economia-mineral/anuario-mineral/anuario-mineral-brasileiro/PreviaAMB2022.pdf. Acesso em: 10 ago 2023
7. Babisk MP et al (2020) Evaluation and application of sintered red mud and its incorporated clay ceramics as materials for building construction. J Mater Res Technol 9:2186–2195. https://doi.org/10.1016/j.jmrt.2019.12.049
8. Alves, Álvaro Antônio de Moreira (2017) EXTRAÇÃO DE ALUMINA—UMA AVALIAÇÃO DOS PARÂMETROS INFLUENTES. 2017. Dissertação (Mestrado em Engenharia de Processos) - Universidade Federal do Pará, Belém
9. Antunes MLP, Conceição FT, Navarro GRB, Fernandes AM, Durrant SF (2021) Use of red mud activated at different temperatures as a low cost adsorbent of reactive dye. Eng Sanit e Ambient 26:805–811. https://doi.org/10.1590/s1413-415220180180
10. Merten HO et al (2017) Compostos Orgânicos Voláteis de Tintas imobiliárias e certificações ambientais: estudo de caso para subsolos. REEC-Revista Eletrônica de Engenharia Civil 13(1)
11. Cardoso FP, Alvarenga RCSS, Carvalho AF, Fontes MPF (2016) Processos de produção e avaliação de requisitos de desempenho de tintas para a construção civil com pigmentos de solos. Ambiente Construído 16(4):109–125
12. Donádio PA (2011) ABRAFATI (Associação Brasileira de Fabricantes de Tintas). Manual Básico sobre Tintas, Águia Química

13. Silva JM, Uemoto KL (2005) Caracterização de tintas látex para construção civil: diagnóstico do mercado do estado de São Paulo. Escola Politécnica da Universidade de São Paulo, Boletim Técnico. SP
14. Associação Brasileira de Normas Técnicas (2012) NBR 14942: Tintas para construção civil. Método para avaliação de desempenho de tintas para edificações não industriais. Determinação do poder de cobertura de tinta seca. ABNT, Rio de Janeiro, 8p
15. Lopes MMS (2018) Utilização do resíduo de granito como carga mineral em tinta látex econômica para construção civil. 2018. 69 f. Dissertação (Mestrado em Engenharia Civil) - Universidade Federal de Viçosa, Viçosa
16. Associação Brasileira de Normas Técnicas (2004) NBR 15078: Tintas para construção civil. Método para avaliação de desempenho de tintas para edificações não industriais. Determinação da resistência à abrasão úmida sem pasta abrasiva. ABNT, Rio de Janeiro, 5p
17. Associação Brasileira de Normas Técnicas (2021) NBR 15079-1: Tintas para construção civil— Requisitos mínimos de desempenho - Parte 1: Tinta látex fosca nas cores claras. ABNT, Rio de Janeiro, 5p
18. Dumitru P, Jitaru I (2010) Improving hiding power obtained by variation of fillers for interior emulsion paints. Rev Chim (Bucharest) 61(5):479–482
19. Milak P, Minatto FD, Noni Jr A, Montedo ORK (2015) Wear performance of alumina-based ceramics—a review of the influence of microstructure on erosive wear. CERÂMICA 61:88–103
20. Kouam J et al (2022) Characterization of Si and SiO_2 in dust emitted during granite polishing as a function of cutting conditions. Materials 15(11):3965
21. Galvão JLB, Andrade HD, Brigolini GJ, Peixoto RAF, Mendes JC (2018) Reuse of iron ore tailings from tailings dams as pigment for sustainable paints. J Clean Prod 200:412–422

Evaluation of the Properties in the Fresh and Hardened State of a Metakaolin Geopolymeric Mortar Reinforced with Açaí Fibers

L. B. Oliveira, E. R. G. Júnior, D. V. A. Júnior, J. A. T. L. Júnior, M. T. Marvila, S. N. Monteiro, C. M. F. Vieira, and A. R. G. Azevedo

Abstract The use of agro-industrial residues in the production of geopolymeric mortars has been a point of growing scientific interest not only for gains in mechanical properties, but also for sustainability. In this context, natural fibers stand out for being biodegradable and having lower energy consumption, availability, low density and low cost when compared to synthetic fibers. The natural fiber from açaí is an example of agro-industrial waste generated in large quantities whose disposal is a major environmental problem. Thus, the objective of this work was to produce a metakaolin geopolymeric mortar with the addition of açaí fibers at 1 and 2% in relation to the mass of the precursor, with fibers not treated and treated with 5 and 10% of NaOH. Then, the samples were tested in the hardened state with resistance to flexion and compression tests and in the fresh state by the Vicat and dropping-ball tests.

Keywords Geopolymer · Mortar · Metakaolin · Açaí · Natural fiber

L. B. Oliveira · E. R. G. Júnior · D. V. A. Júnior · J. A. T. L. Júnior · C. M. F. Vieira
LAMAV—Advanced Materials Laboratory, UENF—State University of the Northern Rio de Janeiro, Av. Alberto Lamego, 2000, Campos dos Goytacazes, Rio De Janeiro 28013-602, Brazil
e-mail: vieira@uenf.br

M. T. Marvila
UFV—Federal University of Viçosa, CRP—Rio Paranaíba Campus, Rodovia BR 230 KM 7, Rio Paranaíba, MG 38810-000, Brazil
e-mail: markssuel.marvila@ufv.br

S. N. Monteiro
Department of Materials Science, Square General Tibúrcio, IME—Military Institute of Engineering, 80, Rio de Janeiro 22290-270, Brazil

A. R. G. Azevedo (✉)
LECIV—Civil Engineering Laboratory, UENF—State University of the Northern Rio de Janeiro, Av. Alberto Lamego, 2000, Campos dos Goytacazes, Rio De Janeiro 28013-602, Brazil
e-mail: afonso@uenf.br

Z. Peng et al. (eds.), *Characterization of Minerals, Metals, and Materials 2024*, The Minerals, Metals & Materials Series, https://doi.org/10.1007/978-3-031-50304-7_43

Introduction

Portland cement (CP) is a material widely used in civil construction as a binder in the production of concrete, mortar and pastes and generates a harmful environmental impact [1]. It is estimated that the production of 1 ton of CP results in the release of 0.9 ton of CO_2, representing around 9% of total global greenhouse gas emissions. Therefore, there is a need to develop alternative construction materials that are more sustainable and less polluting. [2].

Geopolymers emerge as one of these possibilities, being defined as inorganic polymers made through the chemical reaction between an aluminosilicate source and an alkaline solution [3]. According to recent research, this material manages to reduce CO_2 emissions from 10 to 60%, depending on the production processes of the untreated materials. In addition, it has the advantage of using industrial waste, which would be discarded in landfills, in its production [4].

Geopolymers have important properties to be applied in the civil construction industry, such as high initial strength and fire resistance [1]. However, these materials are more susceptible to cracking when compared to PC [5]. Propagation of these microcracks leads to brittle failure. Thus, it is necessary to improve some properties of this product such as toughness, tensile strength and flexural strength. This advance can contribute to the use of the geopolymer as a construction material and one of the ways to achieve this result is with the addition of fibers [6].

In this context, açaí fiber stands out as one of the main residues generated by the Brazilian agroindustry, which presents a rich source of lignocellulosic biomass [7]. In view of this, producing geopolymeric composites reinforced with açaí fibers proves to be a possibility for improving the mechanical properties of geopolymeric composites and also reducing the impact of carbon dioxide emissions that promote sustainability in the construction industry.

Thus, the objective of this work is to analyze the incorporation of açaí fiber at 1 and 2% in a metakaolin geopolymer mortar. The fibers were treated with 5 and 10% NaOH and the samples were tested in the fresh and hardened state.

Materials and Methods

The materials used were metakaolin ULTRA, from Metacaulim do Brasil company, sodium hydroxide and sodium silicate powder solubilized in water. The sand used was natural, extracted from the Paraíba do Sul, river, in the city of Campos dos Goytacazes, RJ. The açaí residues were collected in an açaí industry, located in the city of Rio Novo do Sul, in the state of Espírito Santo, Brazil. After being collected, the residues were properly separated manually, with the fibers being removed from the seeds.

To mitigate fiber/matrix interface problems, alkaline surface treatments were performed on all fibers used. The high pH solution was prepared with sodium

hydroxide (NaOH) 24 h in advance and the concentration was 5–10% by weight. After preparation, the fibers were completely immersed in the solution for a period of 1 h. After the established time, they were washed in running water until all impurities or traces of solution were removed and then dried in an oven at 60 °C until constant mass. The mortar dosages are shown in Table 1.

Thus, after preparing the geopolymeric mortars, the samples were tested in an untreated situation and in a solution of 5 and 10% NaOH and with the addition of 1 and 2% açaí fibers in relation to the weight of the metakaolin mass. Subsequently, the samples were cured at room temperature (25 °C). In the hardened state, tests were carried out for 7 days with flexural strength and compressive strength tests in accordance with NBR 13,279. The dropping ball test adapted from BS 4551—Part 1:1998 was also performed.

Metakaolin was chemically characterized by the XRF analysis (Table 2) and mineralogically by the XRD analysis (Fig. 1). By chemical analysis, it was found that metakaolin is rich in silica and alumina, essential components for the formation of N–A–S–H gel. Through mineralogy analysis, it was observed that there are essentially amorphous regions in the metakaolin and crystalline peaks of quartz and kaolinite, the latter being an indication that the clay did not undergo total calcination for the formation of metakaolinite.

Table 1 Dosage of geopolymers with incorporation of açaí fiber

Samples	Metakaolin (g)	Fiber (g)	NaOH (g)	Na_2SiO_3 (g)	H_2O (g)
Reference	120	0	9	44	76
1% fiber	120	1.2	9	44	76
2% fiber	120	2.4	9	44	76
1% fiber 5 NaOH	120	1.2	9	44	76
2% fiber 5 NaOH	120	2.4	9	44	76
1% fiber 10 NaOH	120	1.2	9	44	76
2% fiber 10 NaOH	120	2.4	9	44	76

Table 2 Chemical composition of metakaolin

Metakaolin	SiO_2	Al_2O_3	TiO_2	Fe_2O_3	SO_3	K_2O	CaO	Others
Percentage	61.85	32.81	1.77	1.52	1.46	0.39	0.1	0.1

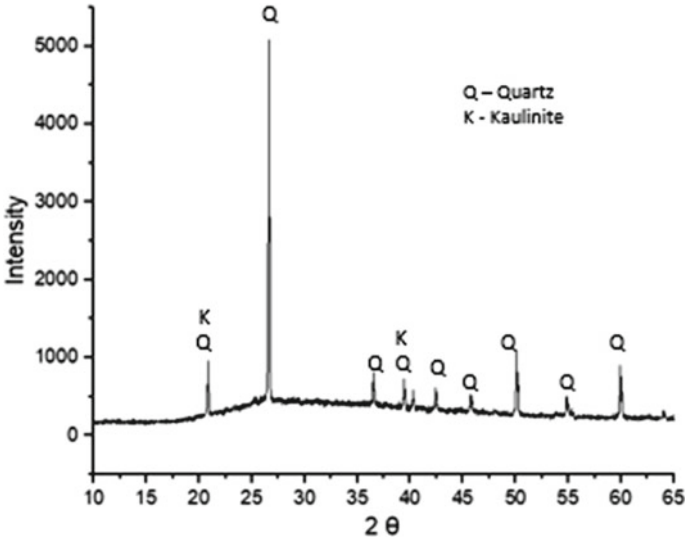

Fig. 1 Mineralogical composition of metakaolin

Results and Discussion

Figure 2 shows the result of flexural strength for metakaolin geopolymeric mortars with the incorporation of treated and untreated açaí fibers after 7 days. Tables 2 and 3 present, respectively, the DIC ANOVA statistical analysis ($p \leq 0.05$) and the Tukey test. For ANOVA, three replications were used in each treatment.

Analyzing Table 3, a statistically significant difference between treatments was observed, because F_{calc} is greater than F_{tab}. Thus, at least one treatment mean was statistically different from the others. To evaluate which means were equal and which were different, the Tukey test was performed, as shown in Table 4. The results showed that the addition of 1 and 2% fiber with 5% NaOH was statistically equal to the reference sample.

The addition of natural fibers at up to 1% was found to be optimal in other papers such as Lazorenko et al. [8], who used fly ash as a precursor and flax fiber as a dispersive phase and by adding 1% fiber, managed to find a value of 10.39 MPa, above the reference that reached 7.60 MPa. Ayeni et al. [9] also had 1% as the main result when adding coconut fiber in a geopolymer matrix. This may be related to the fact that the fibers bridge the cracks, providing an effective transfer between the fiber and the matrix and consequently increasing the resistance, which is low in ceramic materials [9].

Regarding treatments that were performed, the treatment with 5% NaOH was more effective than without treatment and with 10%, because the treatment with sodium hydroxide removes the non-cellulosic amorphous components and consequently improves the anchorage and matrix-fiber adhesion. However, the 10% NaOH

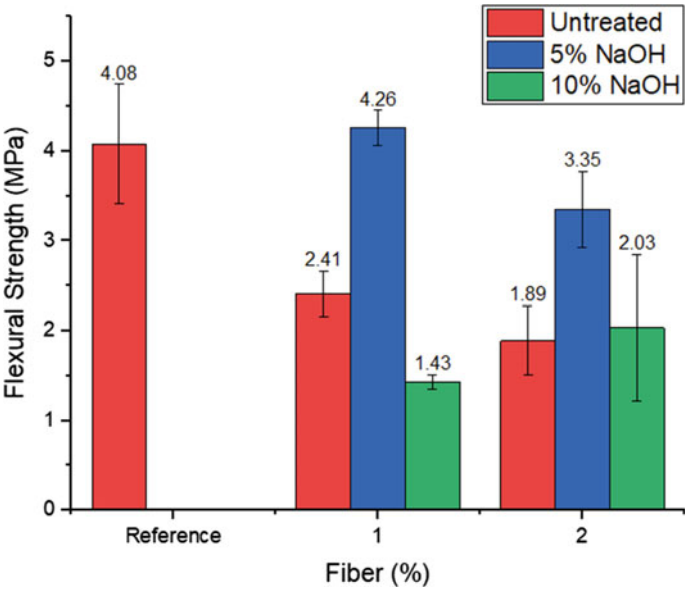

Fig. 2 Flexural strength test results of metakaolin geopolymer mortars with incorporation of açaí fibers after 7 days

Table 3 CRD-ANOVA ($p \leq 0.05$) for flexural strength at 7 days varying according to the dimensions of the specimens

SV	GL	SQ	MQ	F_{calc}	F_{tab}
Treatment	6	46.08	3.75	17.00	2.85
Error	14	1.13	0.22	–	–
Total	20	47.21	–	–	–

Table 4 Tukey test for contrasting mean flexural strength at 7 days

Treatment	Mean (MPa)	Tukey
1%F 5NaOH	4.26	A
Reference	4.08	A
2%F 5NaOH	3.35	AB
1%F	2.41	BC
2%F 10NaOH	2.03	C
2%F	1.89	C
1%F 10NaOH	1.43	C

content added to the alkali activation process of the geopolymer may have led the fibers to have the removal of cellulosic components leading to fiber degradation and consequently decreasing the strength of the composite [10].

Figure 3 shows the result of resistance to compressive strength for metakaolin geopolymeric mortars with the incorporation of treated and untreated açaí fibers after 7 days. Tables 5 and 6 present, respectively, the DIC ANOVA statistical analysis ($p \leq 0.05$) and the Tukey test. For ANOVA, four replications were used in each treatment.

Analyzing Table 5, the statistically significant difference between the treatments is once again observed, because the F_{calc} is greater than the F_{tab}. Thus, at least one treatment mean was statistically different from the other means.

According to the Tukey test, the results showed that the addition of 1 and 2% fibers with NaOH treatment at 5% were statistically equal to the reference sample and with 1% fiber addition. The favorable results with the treatment of 5% NaOH can be explained by the good adherence of the fiber and matrix. Thus, the treatment

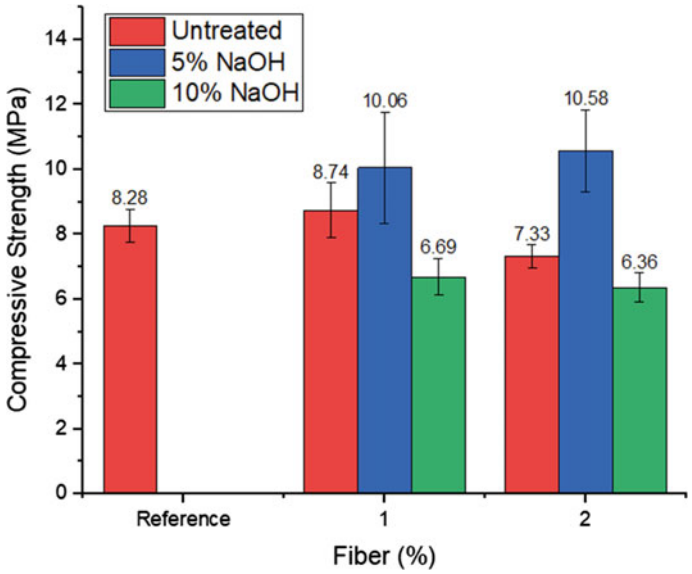

Fig. 3 Compressive strength tests results of metakaolin geopolymeric mortars with incorporation of açaí fibers after 7 days

Table 5 CRD-ANOVA ($p \leq 0.05$) for compressive strength at 7 days varying according to the dimensions of the specimens

SV	GL	SQ	MQ	F_{calc}	F_{tab}
Treatment	6	63.12	10.52	10.28	2.57
Error	21	21.48	1.02	–	–
Total	27	84.60	–	–	–

Table 6 Tukey test for contrasting mean compressive strength at 7 days

Treatment	Mean (MPa)	Tukey
1%F 5NaOH	10.58	A
2%F 5NaOH	10.05	A
1%F	8.74	AB
Reference	8.28	BC
2% F	7.33	BC
1%F 10NaOH	6.69	BC
2%F 10NaOH	6.36	C

with sodium hydroxide proved to be effective due to the possible improvement in fiber properties with the removal of amorphous components and better anchorage [11].

Figure 4 presents dropping-ball penetration index results. It is verified that there was a drop in the penetration index, as the açaí fiber content was increased by 2%. Regarding the treatments, with 10% NaOH, a smaller drop in the penetration index was obtained with 10.36 mm, when compared to the addition without treatment with 9.07 mm.

This happens because the açaí fibers absorb the solution used in the geopolymerization process and consequently increases the viscosity, that is, its ability to flow is reduced. In contrast, the alkaline treatment decreases the hydrophilic nature of the fiber, making the mortar less viscous [10].

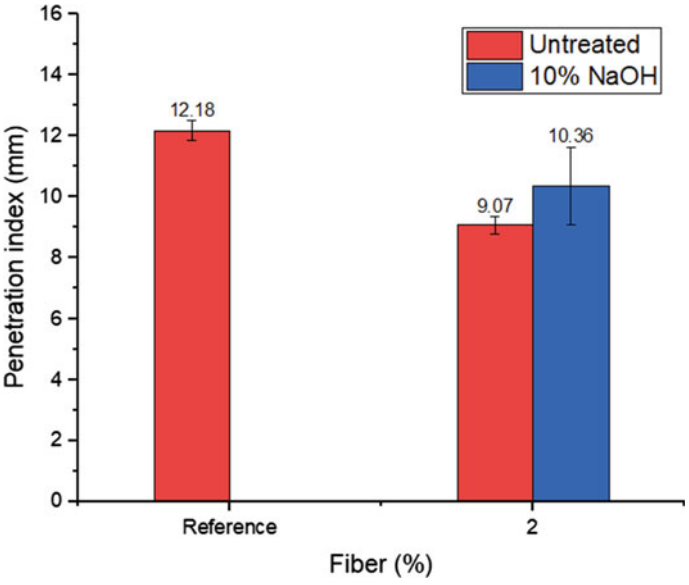

Fig. 4 Dropping ball penetration index results

Conclusion

The objective of this work was to analyze the incorporation of treated and untreated açaí fiber in metakaolin geopolymer mortar with percentages of 1 and 2%. The treatment was performed with NaOH at concentration percentages of 5 and 10%. Thus, it is concluded that:

- The alkaline treatment with 5% NaOH removed some amorphous components, improved the anchoring and adhesion of the fibers and with the addition of 1 and 2% it was possible to obtain the best results in compressive strength and flexural strength, being statistically equal to the mortar of reference.
- Regarding the penetration test by dropping ball, the fibers increase the viscosity of the mortar as expected. However, with the alkaline treatment, the fiber became less viscous because the treatment decreases the hydrophilic nature of the fiber, increasing the penetration index to 10.36 mm with 10% NaOH, while without treatment it had 9.07 mm.

Thus, it is observed that açaí fibers have the potential to be applied in civil construction materials such as mortar by improving mechanical properties such as resistance to flexion and compression and also offer a possibility of circular economy for the management of açaí waste.

Acknowledgements This research was financed by the Universidade Estadual do Norte Fluminense (UENF), partially financed by CAPES (Coordination for the Improvement of Higher Education Personnel—Brazil), CNPq (National Research Coordination), and FAPERJ (Rio State Research Support Foundation). The author A.R.G.A. was funded by FAPERJ through project No. E-26/210.150/2019, E-26/211.194/2021, E-26/211.293/2021, E-26/201.310/2021 and by CNPq through the research grant PQ2 307592/2021-9.

References

1. Oliveira LB, Marvila MT, Fediuk R, Vieira CMF, Azevedo ARG (2023) Development of a complementary precursor based on flue gas desulfurization (FGD) for geopolymeric pastes produced with metakaolin. J Mater Res Technol 22:3489–3501. https://doi.org/10.1016/j.jmrt.2023.01.017
2. Gholampour A, Danish A, Ozbakkaloglu T, Yeon JH, Gencel O (2022) Mechanical and durability properties of natural fiber-reinforced geopolymers containing lead smelter slag and waste glass sand. Constr Build Mater 352:129043. https://doi.org/10.1016/j.conbuildmat.2022.129043/
3. Yasaswini K, Venkateshwara Rao A (2020) Behaviour of geopolymer concrete at elevated temperature. Mater Today Proc 33:239–244. https://doi.org/10.1016/j.matpr.2020.03.833/
4. Farhan KZ, Johari MAM, Demirboğa R (2021) Impact of fiber reinforcements on properties of geopolymer composites: a review. J Build Eng 44:102628. https://doi.org/10.1016/j.jobe.2021.102628/
5. Rahmawati C, Aprilia S, Saidi T, Aulia TB, Hadi AE (2021) The effects of nanosilica on mechanical properties and fracture toughness of geopolymer cement. Polymers 13(13):2178. https://doi.org/10.3390/polym13132178

6. Abbass M, Singh D, Singh G (2021) Properties of hybrid geopolymer concrete prepared using rice husk ash, fly ash and GGBS with coconut fiber. Mater Today Proc 45:4964–4970. https://doi.org/10.1016/j.matpr.2021.01.390/
7. Queiroz, LS, de Souza, LKC, Thomaz, KTC, Leite Lima, ET, da Rocha Filho, GN, do Nascimento, LAS, de Oliveira Pires, LH, Faial, KdoCF, da Costa, CEF (2020) Activated carbon obtained from amazonian biomass tailings (acai seed): modification, characterization, and use for removal of metal ions from water. J Environ Manag 270:110868. https://doi.org/10.1016/j.jenvman.2020.110868
8. Lazorenko G, Kasprzhitskii A, Kruglikov A, Mischinenko V, Yavna V (2020) Sustainable geopolymer composites reinforced with flax tows. Ceram Int 46(8):12870–12875. https://doi.org/10.1016/j.ceramint.2020.01.184/
9. Ayeni, O, Mahamat, AA, Bih, NL, Stanislas, TT, Isah, I, Savastano Junior, H, Boakye, E, Onwualu, AP (2022) Effect of coir fiber reinforcement on properties of metakaolin-based geopolymer composite. Appl Sci 12:5478. https://doi.org/10.3390/app12115478/
10. Santana, HA, Amorim Júnior, NS, Ribeiro, DV, Cilla, MS, Dias, CMR (2021) Vegetable fibers behavior in geopolymers and alkali-activated cement based matrices: a review. J Build Eng 44:103291. https://doi.org/10.1016/j.jobe.2021.103291
11. Wongsa A, Kunthawatwong R, Naenudon S, Sata V, Chindaprasirt P (2020) Natural fiber reinforced high calcium fly ash geopolymer mortar. Constr Build Mater 241:118143. https://doi.org/10.1016/j.conbuildmat.2020.118143/

Evaluation of the Properties of Red Ceramics Prepared with Ornamental Rock

E. B. Zanelato, A. R. G. Azevedo, M. T. Marvila, J. Alexandre, and S. N. Monteiro

Abstract The cutting and processing of rocks in the ornamental rock industry have a significant environmental impact, resulting in the generation of non-reusable solid waste that is either directly discarded in nature or sent to landfills. This study aims to assess the utilization of these residues in ceramic formulations for brick production. Two types of waste from different rocks with distinct chemical and physical characteristics were utilized. Physical and chemical characterization tests were conducted on clays and residues employed in ceramic manufacturing. Ceramic specimens were produced with varying levels of waste incorporation, and tests including water absorption, linear variation and flexural strength were performed. The results demonstrated that the incorporation of both residues, either individually or combined, enhanced the mechanical properties of ceramics, with the most notable improvements observed when the residues were incorporated together.

Keywords Red ceramic · Granite · Marble · Residue

E. B. Zanelato (✉)
IFF—Federal Institute Fluminese, Rua Cel. Valter Kramer, 357—Parque Vera Cruz, Campos Dos Goytacazes, Rio de Janeiro 28080-565, Brazil
e-mail: ebzanelato@gmail.com

A. R. G. Azevedo · J. Alexandre
LECIV—Civil Engineering Laboratory, UENF—State University of the Northern Rio de Janeiro, Av. Alberto Lamego, 2000, Campos Dos Goytacazes, Rio de Janeiro 28013-602, Brazil

M. T. Marvila
DEC—Departament of Civil Engineering, UFV—Federal Viçosa University, Minas Gerais, Rodovia LMG 818, Km 6, Rio Paranaíba 35690-000, Brazil

S. N. Monteiro
Department of Materials Science, IME—Military Institute of Engineering, Square General Tibúrcio, 80, Rio de Janeiro 22290-270, Brazil

Z. Peng et al. (eds.), *Characterization of Minerals, Metals, and Materials 2024*, The Minerals, Metals & Materials Series, https://doi.org/10.1007/978-3-031-50304-7_44

Introduction

According to ABIROCHAS report [1], the estimated Brazilian production of ornamental rocks in 2022 reached 10 million tons (10 Mt). The stone sector not only serves the domestic market, but also plays a significant role in international trade, with exports totaling 2.1 million tons (2.1 Mt) valued at a total of US$1284.9 million in 2022. The products sold both on the national and international markets include unprocessed rocks, in which the raw rock block is sold, or in the form of slabs, once the rock block has been cut and polished. Throughout the rock cutting and polishing process, a substantial amount of waste is generated [2].

This sector presents two main environmental problems, atmospheric pollution and sludge disposal. The rock cutting process generates dust that leads to significant air pollution; however, this pollution can be mitigated through the humidification process [3], a procedure determined by the Ministry of Labor and Employment through Administrative Standard No. 43 of 2008. As a result of the humidification process, the sludge generated by the sector is released directly in bodies of water without prior treatment [4]. It is important to highlight that drying the sludge promotes the dispersion of dust, both through air and water channels [5].

An alternative approach that has been adopted to mitigate the environmental impacts associated with waste is the reuse of part of the water from the humidification process. The sludge is directed to sedimentation tanks where the settled material is transferred to a pool, while the water is recycled for the humidification process [6].

The waste produced during the cutting and polishing processes of ornamental rocks is not biodegradable. Consequently, the substantial amounts of rock dust generated can impact water resources such as rivers and lakes, leading to air pollution, water contamination and soil changes. The volume of rock powder waste generated during the processing phase represents approximately 20–25% of the total rock processed [6].

An alternative for the disposal of this sludge is its use in the civil construction sector. The incorporation of ornamental stone residues into ceramics shows promising results, making its application viable to improve the mechanical properties of ceramics [7]. Marble waste tends to have smaller grains, ensuring better void filling, better packaging and greater mechanical resistance. On the other hand, granite waste, despite having larger particle sizes compared to marble, also has significant potential for use, as its incorporation also increases the mechanical resistance of ceramic products. The objective of this study is to evaluate the combined incorporation of marble and granite waste in the ceramic mass formulation.

Materials and Methods

The clay used in this study was collected directly from the ceramics sector, constituting a material commonly used in the manufacture of ceramic masses in the region. Marble and granite waste were collected in sedimentation tanks from an ornamental stone industry. These residues were collected in the form of sludge, dried initially exposed to the sun and subsequently dried in an oven.

The particle size analysis was conducted following the standards outlined in NBR 7181 [8]. The fraction of the material retained on the 0.074 mm sieve (ABNT #200) was classified through sieving, while the fraction passing through the same sieve was categorized through sedimentation. Hexametaphosphate sodium, a deflocculating agent, was employed for the sedimentation test. Soil classification was performed according to the Casagrande standard (1942)—Unified Soil Classification System, which is also adopted by the U.S. Army Corps of Engineers (for airports) and the U.S. Bureau of Reclamation (for dams).

The material used for the Atterberg limits was disaggregated and passed through a 0.42mm sieve (ABNT #40). The Plastic Limit test was conducted in accordance with NBR 7180 [9], while the Liquid Limit test was performed following NBR 6459 [10].

The determination of grain density was carried out in accordance with NBR 6457 [11] and NBR 6458 [12], using a pycnometer.

The chemical composition was obtained through Energy Dispersive X-ray Spectroscopy (EDX) using the SHIMADZU EDX 700 equipment. This test enabled the identification of the quantities of each of the chemical elements present in the clay.

Six ceramic formulations for production were evaluated, in addition to the reference formulation without incorporation of residues. The levels of incorporation of marble and granite waste are specified in Table 1.

The ceramic formulations were molded by extrusion in the laboratory and fired in an oven at 750 °C. After firing the ceramic, water absorption, linear shrinkage, mass density and flexural strength tests were carried out.

Table 1 Composition of mixtures (in Mass)

	Mixtures (%)		
Mixtures	Clay	Granite	Marble
Ref	100	0	0
90C.10G.0M	90	10	0
80C.20G.0M	80	20	0
90C.0G.10M	90	0	10
80C.0G.20M	80	0	20
90C.5G.5M	90	5	5
80C.10G.10M	80	10	10

Results and Discussion

Figure 1 shows the particle size distribution obtained by the waste and the clay used in the work to make the ceramics.

As illustrated in Fig. 1, the materials have different particle sizes. The soil has smaller grain sizes than the residues. When comparing residues, granite has a larger grain size. The results obtained in the granulometry test are compatible with those found in the literature [6], where the marble residue is finer than the granite residue.

Table 2 presents the results of Atterberg limits and real grain density.

The real grain density of marble and granite waste presents values close to and with a certain similarity to clay. It was not possible to carry out the Atterberg limit test with the residues as they did not present sufficient plasticity for the test.

Table 3 presents the results of the chemical analysis of the residues and clay.

The greater presence of the clay mineral kaulunite ($Al_2O_3 \cdot 2SiO_2 \cdot 2H_2O$) in the North of Rio de Janeiro is compatible with the distribution of chemical elements present in the clay. Marble and granite have a predominance of silica.

The results obtained by the linear variation test are shown in Fig. 2.

The results obtained indicate a reduction in linear variation with increasing waste incorporation. The combinations with 20% residue presented the lowest values while the 10% incorporations presented intermediate values in relation to the reference. Clays present changes in their crystalline structure during burning that promote a decrease in volume and therefore an increase in density. Granite and marble do not show the same tendency, remaining inert [6].

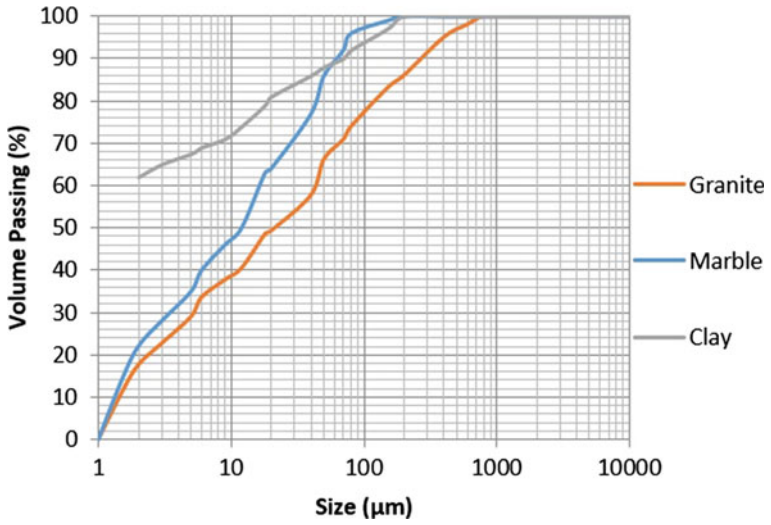

Fig. 1 Granulometry of the used materials

Table 2 Atterberg limits and real grains density

	Clay	Granite	Marble
LL	47.6	-	-
LP	19.6	-	-
IP	28.0	-	-
Yg	2.79	2.68	2.66
USCS	CH	SM	

Table 3 Chemical analysis

Material	Elements (%)								
	SiO_2	Al_2O_3	Fe_2O_3	K_2O	TiO_2	SO_3	CaO	BaO	Others
Clay	43.88	42.55	6.88	1.98	1.65	1.52	1.09	-	0.45
Granite	64.33	16.56	5.21	6.99	0.65	0.99	3.48	0.51	1.28
Marble	83.54	6.12	1.44	1.15	0.51	1.35	4.55	0.38	0.96

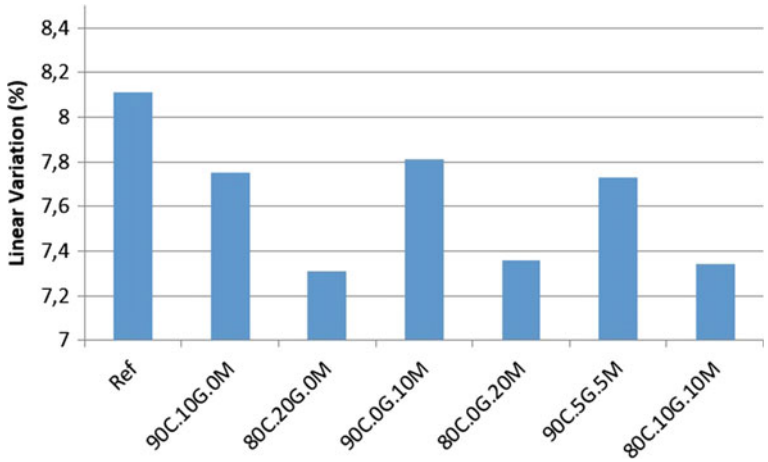

Fig. 2 Linear variation

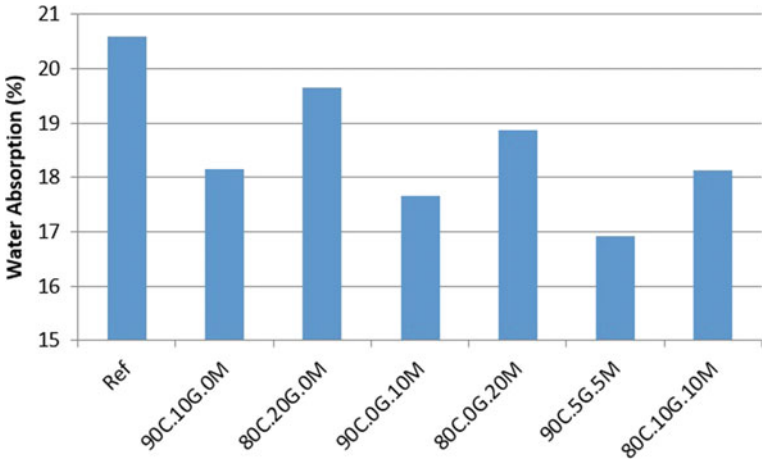

Fig. 3 Immersion absorption

There is no significant difference between the incorporation of granite and marble or their combination, both for incorporation of 10% and for incorporation of 20%, so both granite and marble are inert when fired and reduce the shrinkage of the ceramic.

The results obtained by the ceramic in the immersion absorption test are illustrated in Fig. 3.

It is verified by the test that the presence of residues tends to reduce the water absorption of the ceramic.

Replacing 10% of the clay with waste showed the best results for all waste combinations, whether granite and marble individually or a combination of the two. However, when incorporation increases to 20%, there is an increase in water absorption for all combinations, even if they still present values lower than the reference.

Comparing the addition values of granite and marble waste individually, there is a slightly greater water absorption for granite. Therefore, individually, marble has lower water absorption. Marble has a smaller particle size and greater capacity to fill voids, promoting the filler effect.

The best results were obtained for the combination with 5% marble waste and 5% granite waste, where absorption was the lowest among the combinations evaluated. Even though marble individually has better performance than granite, the combination of waste granulometry improved the packaging of the ceramic. The increase from 5 to 10% of each waste in combination also promotes increased absorption, as seen in the individual addition of waste.

Figure 4 presents the mechanical resistance results.

The mechanical resistance test showed similar trends to those obtained in the immersion water absorption test.

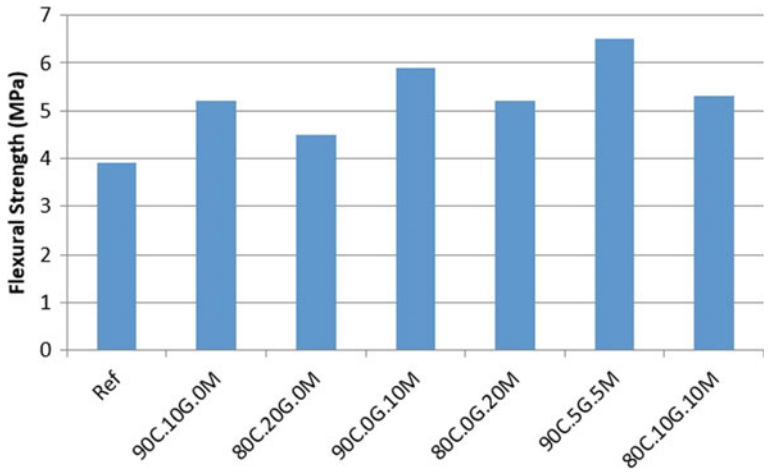

Fig. 4 Mechanical resistance

The 10% incorporation again presents better results than the 20% incorporation, both for combinations with marble and granite waste individually, and for the combination of the two.

In the individual comparison between marble and granite, marble once again presents better results than granite, with the difference in the mechanical resistance test being even more significant. The incorporation of 20% marble presents resistance equivalent to 10% granite. Marble, having a smaller grain size, fills the voids, reducing the porosity of the ceramic. With lower porosity, ceramics tend to have greater mechanical resistance.

The combination of 5% granite and 5% marble continues to stand out as the formulation with the best performance among the combinations evaluated. The increase to 10% granite and 10% marble drastically reduces mechanical resistance compared to incorporating 5% of each, reaching values close to 20% marble.

Conclusion

In this work, the main properties of ceramics with the incorporation of waste were evaluated. The incorporated residues have different physical and chemical characteristics than the clay used in the manufacture of ceramics. The residues have larger grains than clay, with granite having the largest grains. The residues had a lower density than clay and do not have sufficient plasticity for the Atterberg limits. The chemical composition of the waste and clay is compatible with local studies. The properties of the ceramic were directly affected by the incorporation of the residue. In the linear shrinkage test, the greater the presence of residue, the lower the linear shrinkage. Mechanical resistance and water absorption showed similar trends, where

the incorporation of 10% presents better results than the reference and the incorporation of 20%. Individually embedded marble performs better than granite. The incorporation of 5% marble and 5% granite showed the best results in water absorption by immersion and flexural resistance.

Acknowledgements The authors thank the Brazilian agencies CNPq, CAPES, and FAPERJ for the support provided to this investigation.

References

1. Chiodi CF (2023) Balance of Brazilian exports and imports of ornamental rocks in 2022. ABIROCHAS, São Paulo, 35p (Report n.01/2023)
2. Gado RA (2022) The feasibility of recycling marble and granite sludge in the polymer-modified cementitious mortars part A: in polymer-modified cementitious adhesive mortar. Proc Safe Env Prot 159:978–991
3. Alyamaç KE, Aydin AB (2015) Concrete properties containing fine aggregate marble powder. KSCE J Civil Eng 19(7):2208–2216
4. Montani C (2016) XXVII world marble and stones report 2016, Aldus Casa di Edizioni in Carrara
5. Hanieh AA, Abdelall S, Hasan A (2014) Sustainable development of stone and marble sector in Palestine. J Clean Produ 84:581–588
6. Danish A, Mosaberpanah MA, Salim MU, Fediuk R, Rashid MF, Waqas RM (2021) Reusing marble and granite dust as cement replacement in cementitious composites: a review on sustainability benefits and critical challenges. J Build Eng 44:102600
7. Buyuksagis IS, Uygunoglu T, Tatar E (2017) Investigation on the usage of waste marble powder in cement-based adhesive mortar. Cons Build Mat 154:734–742
8. Brazilian Association of Technical Standards (2016) ABNT NBR 7181. Soil—Grain size analysis
9. Brazilian Association of Technical Standards (2016) ABNT NBR 7180. Soil—Plasticity limit determination. Rio de Janeiro
10. Brazilian Association of Technical Standards (2016) ABNT NBR 6459. Soil—liquid limit determination
11. Brazilian Association of Technical Standards (2016) ABNT NBR 6457. Soil samples—preparation for compactation and characterization tests
12. Brazilian Association of Technical Standards (2016) ABNT NBR 6458. Gravel grains retained on the 4, 8 mm mesh sieve—determination of the bulk specific gravity, of the apparent specific gravity and of water absorption

Experimental Investigation of the Factors Affecting Performance of Firefighters' Protective Clothing

J. Lu, M. Ghodrat, and J. P. Escobedo-Diaz

Abstract The role of a firefighter is crucial in safeguarding lives, property, and the environment, as firefighters bravely confront the formidable challenges posed by fires and emergencies. The protective clothing worn serves as a vital barrier, allowing firefighters to operate in extreme conditions while minimizing the risks to their own well-being. This paper characterises a multi-layer material used by NSW Fire and Rescue through cone calorimetry, a powerful fire testing equipment under ISO5660. The multi-layer material was compared with single layer materials used in the 2013 and 2022 Rural Fire Service (RFS) jackets to determine its feasibility to be used by the RFS. Results demonstrated that the time to ignition (TTI) of the multi-layer material, under all heat flux levels, was significantly longer than the two single layer materials. Additionally, it exhibited a lower peak heat release rate (HRR), however, releases greater total thermal energy due to its larger thickness and mass. Both these properties of the material indicate the greater fire resistance of the multi-layer material, but more importantly highlights that this material will allow for an extended time to recognise endangerment and prevent second degree burns.

Keywords Calorimetry · Fire protections · Fabrics

Introduction

Within the perilous and volatile realm of firefighting, the significance of appropriate protective attire cannot be overstated, as it can determine the ultimate outcome between life and death. Consequently, the pursuit of novel materials, textiles, and fabrics for firefighter gear has emerged as a pressing and imperative domain of research. During an interview, acting Inspector James Manuao from New South Wales

J. Lu · M. Ghodrat (✉) · J. P. Escobedo-Diaz (✉)
University of New South Wales at the Australian Defence Force Academy, Canberra, ACT 2600, Australia
e-mail: m.ghodrat@unsw.edu.au

J. P. Escobedo-Diaz
e-mail: j.escobedo-diaz@unsw.edu.au

Z. Peng et al. (eds.), *Characterization of Minerals, Metals, and Materials 2024*, The Minerals, Metals & Materials Series, https://doi.org/10.1007/978-3-031-50304-7_45

Fire and Rescue emphasized the paramount importance of developing protective clothing, affirming that its enhanced safety characteristics "instil greater confidence among firefighters", enabling them to carry out their life-saving duties. Conventionally, firefighter personal protective clothing (FFPC) comprises three distinct layers: the outer shell, moisture membrane, and inner lining. However, the specific composition may vary depending on the firefighting context, such as bushfire fighting or structural firefighting, where certain FFPCs may feature a single layer. Regardless of these variations, each layer assumes a critical role in affording protection and ensuring wearer comfort.

Historically, aramid fibres have dominated the field as the first-choice material for fire resistant clothing. It is highly desired that FFPC is made from materials that have a low thermal conductivity to decrease the rate of heat transferred through the material from the external heat source. Brown and Ennis [1] performed differential scanning calorimetry (DSC) on both Kevlar and Nomex and demonstrated that the fibres have an approximate glass transition temperature (T_g) of 360 °C, which is much greater than the T_g of cotton, 220 °C. Further thermogravimetric analysis (TGA) was conducted and unveiled that both fibres undergo a two-step decomposition process. As temperatures rise, the polymer chains in Nomex begin to break down around 400 °C, whereas in Kevlar, this process commences at 500 °C, highlighting their high melting point temperatures. These excellent thermal resistance qualities can be attributed to the long chains of synthetic polymers linked by strong amide bonds. These bonds are formed between the carboxyl (CO–OH) group of one monomer unit and the amino (NH_2) group of another monomer unit, thus resulting in a repetition of amide links (–CO–NH–) along the polymer chain [2]. Therefore, aramid fibres are currently deemed the first-choice solution for protective clothing against extreme heat conditions.

The moisture membrane plays a crucial role in creating a barrier against external moisture, whilst simultaneously allowing sweat generated from the body to escape. A popular option for this layer is expanded polytetrafluoroethylene (e-PTFE) due to its unique porosity quality that allows water vapour and other gases to pass through it but stops liquids from penetrating through the membrane. This is because in one square centimetre of e-PTFE, there exist 1.4 billion pores. These pores are 20,000 times smaller than water droplets, yet 7000 times larger than a molecule of water vapour [3]. Moreover, e-PTFE possesses a high melting point between 335 and 346 °C, making it more attractive for FFPC [4]. Thermoplastic polyurethane is an alternative option; however, Zhou et al. [5] found its melting point to be 163 °C, which is much lower than the melting point of e-PTFE. Ultimately, e-PTFE is currently the dominating moisture membrane material for protective clothing because of its thermal resistance and porosity quality.

One crucial factor that impacts FFPC is the airgap embedded into or between layers the clothing materials. The thermal conductivity of air is relatively low compared to materials such as Kevlar and Nomex, thus it has the potential to reduce the rate of heat transfer from the external heat source (the fire) to the skin of the wearer. However, the airgap influence is not straightforward and exhibits a more complex nature. Song [6] performed manikin fire testing to identify that the optimal airgap is between 7

and 8 mm for a single layer garment. If the airgap increases beyond 8 mm, natural convection effects begin to occur which do not improve the airgaps insulation value. This is further supported by the work of Benisek and Phillips in their flame exposure experiments, finding that time to second degree burns increased when there was a separation distance between 0 and 8 mm [7]. Ultimately, literature has demonstrated that a small airgap is beneficial to the thermal performance of materials, but the distance needs to be maintained.

The influence of moisture on TPP is complex with a multifaceted behaviour. Firstly, when a material absorbs moisture, it often leads to discomfort and limits movement of the wearer. Additionally, it increases the thermal conductivity, hence promoting heat transfer through the layer. The works of Fu and team [8] identified a decrease in TPP when the tested material had absorbed water against low level radiant heat levels. Conversely, Lee and Baker [9] arrived at dissimilar results, finding that at 50/50 radiant and convective heat, the effect of moisture absorption had a positive influence on TPP. However, for high radiant heat levels, moisture decreases the overall protective performance of the tested material. Therefore, it can be seen that the behaviour of moisture is complicated and for certain types of heat exposure levels, liquid absorption has a negative impact on the TPP.

There is opportunity to enhance protective capabilities through the moisture membrane layer. Fire and Rescue's moisture membrane material, e-PTFE with foamed silicone spacers, is an excellent candidate that can provide an airgap between layers and simultaneously act as a moisture barrier. However, there is a lack of experimental research on e-PTFE with foamed silicone spacers with the adjacent inner lining and outer shell materials, thus limited characterisation of this multi-layered material exists. By conducting experimental analysis on this material and comparing it with the current solutions for Rural Fire Service (RFS) clothing, this research can provide valuable data to future exploration of potential material systems for FFPC to enhance their protective performance, as well as be considered as an option for RFS clothing.

Experimental Methodology

The iCone Classic cone calorimeter is an effective tool due to its powerful capacity to evaluate key thermal characteristics of materials. The system uses radiant heat as the primary source of ignition and heat input to the sample material through a large cone shaped coil that sits above the sample holder. It has a MultiExact 4100 gas analyser and uses the ConeCalc 6 software which allows it to record the time it takes for the material to ignite and the heat release rate when the specimen is exposed to the heat flux. A rigorous calibration and set up process following the ISO5660 standard must be undertaken to ensure that all data readings are accurate and valid. Due to the destructive nature of the experiments and being limited to only four specimens per material, careful consideration was put into the selection of heat flux levels. Heat flux levels of 25, 35 and 50 kW/m^2 were chosen to provide a diverse range of bushfire

Table 1 Heat flux levels and corresponding BAL ratings with short descriptions of the bush fire conditions at these levels

Heat flux level (kW/m^2)	BAL rating	Description
25	29	Increase in ember attacks but no exposure to flames
35	40	Exposure to flames from the fire front with moderate radiant heat levels
50	FZ	Highest attack level where there is direct exposure to flames with extreme radiant heat levels

simulation, as described by Table 1. A heat flux meter was used to achieve the desired levels at a separation distance of 60 mm, as specified in the ISO5660 standard [10]. It is important to note that in real life firefighting practises, it would be highly unlikely for a firefighter to be standing this close to the heat source they are fighting.

After specimen preparation, the mass is recorded into the ConeCalc 6 software along with the surface area, thickness, room temperature and humidity. The specimen was placed under the cone baseline readings were then collected for 60 s before the test to ensure that the initial conditions are stable. Once this is completed, the shutters opened, initiating the start of the test. Time stamps were recorded when the specimen ignited and when it self-extinguished. A spark igniter was available to use which sat between the cone and the specimen. Its purpose was to initiate combustion as without combustion, no heat release rate (HRR) data can be collected.

Materials

The primary material that was tested was a three-layer system from NSW Fire and Rescue which comprises of Nomex/Viscose blend inner lining, an e-PTFE with famed silicone spacers moisture membrane and a Kevlar outer shell (Fig. 1a). In support of this study, the 2013 and 2022 RFS single layer garment material were also tested under the same conditions for a comparative analysis against the multi-layer material (Table 2). The 2013 material is made from 100% PROBAN® treated cotton (Fig. 1b) and the 2022 material is made from KARVIN RS245 which is 65% fire resistant viscose and 35% aramid fibre (Fig. 1c). Specimens were cut to 100 mm × 100 mm, following the ISO5660 standard [10]. In addition, the individual layers of the multi-layer material were tested at 35 kW/m^2 for more detailed characterisation. Each specimen was placed in a homemade aluminium foil tray to stop any loss of mass by dripping if the material melted during the experiment.

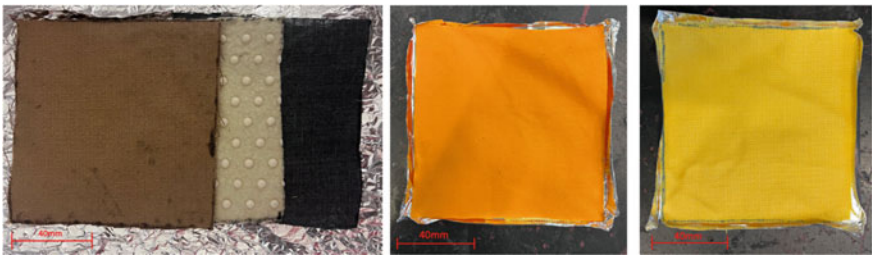

(a) (b) (c)

Fig. 1 **a** Three layers of the multi-layer material: outer shell (Kevlar), moisture membrane (e-PTFE with foamed silicone spacers), inner lining (Nomex/Viscose blend) from left to right respectively. **b** 2013 RFS jacket 100% PROBAN® treated cotton. **c** 2022 RFS jacket 65% fire resistant viscose and 35% aramid fibre

Table 2 Material sample thickness and mass

Material	Thickness (mm) ± 0.005	Mass (g) ± 0.005
2013 RFS cotton garment	0.57	3.4
2022 RFS viscose/aramid garment	0.47	2.6
Multi-layer material	3.5	7

Results

Time to Ignition

Table 3 shows the time it takes for the tested materials to ignite when exposed to the heat flux from the heated cone without the igniter.

As expected, higher heat fluxes resulted in faster ignition times for all materials. The most significant results are displayed by the substantially longer times to ignition for the multi-layer material compared to the 2013 and 2022 garment materials. In fact, at all three heat flux levels, the multi-layer material took three times longer or more than the TTI of the viscose/aramid blend of the 2022 RFS material. In particular, at 25 kW/m^2, the multi-layer material did not ignite until 113 s from the incident heat flux.

Table 3 Time to ignition (±0.5 s) for the three different materials under the three different heat flux levels

Material	Heat flux level (kW/m^2) (no igniter)		
	25	35	50
2013 RFS cotton garment	17 s	12 s	8 s
2022 RFS viscose/aramid garment	16 s	11 s	7 s
Multi-layer material	113 s	35 s	22 s

Table 4 Time to ignition (±0.5 s) for the three different layers of the multi-layer material under the heat flux level of 35 kW/m^2 with and without igniter tool

Material	Time to ignition at 35 kW/m^2	
	Without igniter	With igniter
Nomex/viscose blend—inner lining	5 s	6 s
e-PTFE with foamed silicone spacers—moisture membrane	38 s	22 s
Kevlar—outer shell	Did not ignite	9 s

The individual layers of the multi-layer material were tested under a heat flux level of 35 kW/m^2 to quantify their performance. Table 4 includes the TTI with and without the igniter. Interestingly, the moisture membrane material demonstrated the longest time before ignition, taking 22 s before combustion and flame visualisation with the igniter. This is much longer than the Kevlar outer shell, only taking 9 s. However, as expected, the inner lining was the quickest to ignite, approximately taking the same amount of time with and without the igniter. Moreover, when the Kevlar was tested without the igniter, the specimen did not combust at all, meaning it did not catch on fire within the 160 s total duration of the experiment.

Heat Release Rate

The HRR of a material is an extremely valuable property as it provides critical information about the burning behaviour of a material. The HRR depicts the rate at which a material releases energy as it undergoes combustion where a lower HRR can result in slower fire growth, extended escape time and general firefighter safety.

Table 5 above displays all the peak HRR from the three materials tested under the three different heat flux levels. Under all three heat levels, the multi-layer material demonstrated to have the lowest peak, but furthermore, as shown in the graphs (Figs. 2, 3 and 4), the peak occurs much later than the 2013 and 2022 garments. There is a correlation between the TTI and peak HRR where the peak occurs shortly after the material has ignited. Interestingly, the multi-layer materials TTI was significantly larger when exposed to 25 kW/m^2 compared to the other two heat flux levels, as seen by the peak shifted further on the right side of Fig. 2. However, as depicted by the total area under the graphs and Table 5, the overall thermal heat energy released is greatest for the multi-layer material under all three heat flux levels due to it combusting for longer duration.

Table 5 The peak heat release rate and total heat released of the three different materials under the three different heat flux levels

Material	Peak heat release rate (kW/m^2)			Total heat released (MJ/ m^2)		
	25 kW/m^2	35 kW/m^2	50 kW/m^2	25 kW/m^2	35 kW/m^2	50 kW/m^2
2013 RFS cotton garment	170	610	735	1.2	2.5	1.7
2022 RFS viscose/ aramid garment	220	270	390	0.8	1.3	2.3
Multi-layer material	110	175	220	4.5	6.9	7.8

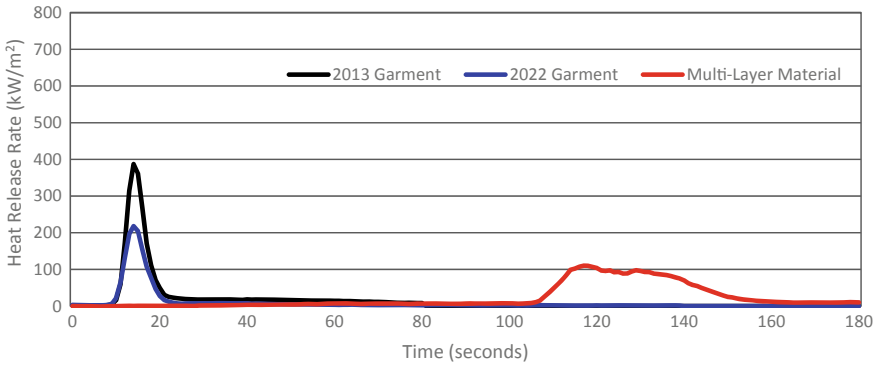

Fig. 2 Heat release rate verse time graph under 25 kW/m^2 for all three materials

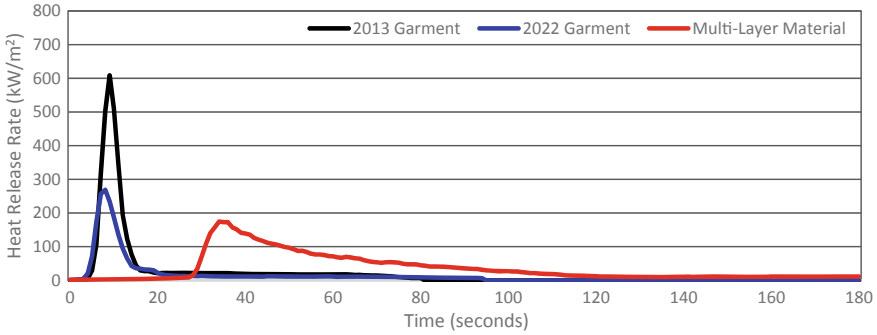

Fig. 3 Heat release rate verse time graph under 35 kW/m^2 for all three materials

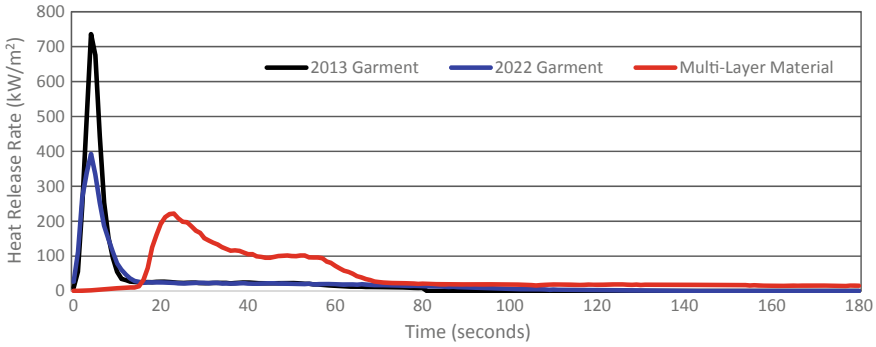

Fig. 4 Heat release rate verse time graph under 50 kW/m^2 for all three materials

Discussion

Experimental testing and analysis of FFPC materials is a pivotal endeavour that unlocks insights into their performance and protective potential. Two characteristics that provide valuable information about materials from the cone calorimeter is the TTI and the HRR.

Although TTI is one of the simplest outputs from the cone calorimeter experiments, it possesses high value for characterising materials for FFPC. It gives an indication of the amount of time a firefighter has to retreat to a safer zone where the heat level is not as intense. As shown in the results, the multi-layer material's TTI performance is drastically greater than the 2013 and 2022 garments which exhibit similar numbers (Table 2). This can be attributed to the HRR and peak HRR as these properties can impact the combustion process, and in turn, lead to a faster flammable reaction of a material. The testing of the 2013 and 2022 garments showed that their peak HRR is more than double that of the multi-layer. As the materials burn, they release higher levels of thermal energy which increases the temperature of surrounding unburned material and oxygen. This ultimately accelerates the combustion process causing the material to ignite quicker.

The cone calorimeter promotes a highly excited exothermic irreversible reaction within the material, thus the fire retardancy can be attributed to the material's chemical reactivity. The PROBAN® treated cotton has limited resistance compared to the more updated RFS jacket Nomex/viscose blend material due to presence of the aramid fibres. These fibres are inherently fire resistant because of the amide linkages with aromatic rings which are less susceptible to chemical and heat attack [11]. In conjunction, the blend of viscose adds to the material by improving upon its comfortability from the smooth fibre's surface finish whilst maintaining the materials' thermal resistance. This is supported by the works of Gu [12] where he identified that a blend ratio of 80/20 (Nomex/Viscose) demonstrated excellent performance in a limiting oxygen index analyser with the shortest damage length. The cone calorimeter test illustrates the greater thermal protection that the Nomex/viscose blend has over

the PROBAN® treated cotton, particularly from the peak HRR which is expected due to the advancement in material technology from 2013 to 2022.

The Kevlar outer shell of the multi-layer is mainly responsible for the low peak heat release rate, withstanding the elevated heat flux from reaching the moisture membrane, inner lining and in reality, the skin of the wearer. Similar to Nomex, Kevlar's high thermal resistance comes from the amide linkages with aromatic rings, however the configuration of the carbon atoms in the rings is the difference in their structure [13]. This chemical structure's properties were demonstrative in the individual layer testing where it did not ignite under 25 kW/m^2 (without spark igniter assistance). The multi-layer material had greater total heat released simply because there was more material to burn and generate more heat, as seen by the thickness and mass in Table 2. Although it does produce more thermal energy, it did have a much lower peak HRR meaning that when ignited, there is a longer time to critically dangerous conditions, lower fire intensity and slower flame spread. The moisture membrane's individual TTI performance under 35 kW/m^2 of heat flux was surprisingly long at 38 s (without spark igniter) and 22 s (with spark igniter). In the system, the foamed silicone spacers add an airgap between the e-PTFE and Kevlar layers which may be why there is a delayed TTI compared to the other materials. The Kevlar and airgaps combined low thermal conductivity impedes the radiant heat, until combustion of the material occurs. The inner lining is the same material as the 2022 RFS jacket, but with a different blend ratio. It is determined that the blend consists of more viscose than Nomex because of the soft surface finish and lighter weight as its purpose is to increase the comfort between skin and clothing. Its individual performance under 35 kW/m^2 of heat flux was very poor, igniting within 5 s of exposure.

Second degree burns (SDB) [10, 14], also described as partial-thickness burns, affect the top outer most layer of the skin (epidermis) and the layer beneath it (dermis). SDB's can be categorised into type types: superficial SDB which are less severe with blistering and swelling, whereas deep SDB are more damaging to the dermis layer and can cause nerve damage with possible infection. Thus, it is crucial to understand the time it takes for the human skin to achieve SDB to give an indication as to the time one has to remove themselves from the hazardous opportunity. The research by Udayraj [15] performed both a numerical and experimental study for second degree burn prediction. By using a bench top test under ISO 6942 [16], Udayraj and team concluded (for case of Fourier conduction for sample 4) that the time to SDB, when exposed to 80 kW/m^2, was 4.9 s for a single layer material. It is important to note that this study does take into consideration thermal relaxation time and a phase lag duration for both heat flux and temperature gradient, and furthermore, uses a higher heat flux than what was used for the cone calorimeter. Nonetheless, it is demonstrative of just how quickly SDB can occur. Ultimately, the time for the skin to develop second degree burns is extremely short as even immediate direct contact with boiling water can cause partial SDBs [17]. The multi-layer demonstrated to have the longest TTI performance under all three heat flux levels compared to the 2013 and 2022 garments, meaning it would provide the longest time for the wearer to retreat to safer conditions before the skin is at risk of second-degree burns.

The disadvantage of the multi-layer material is its mass compared to the 2013 and 2022 RFS materials. Outlined in Table 1, the mass of the multi-layer is much greater, which can be attributed to the number of layers, but mainly the silicone spacers on the moisture membrane. In terms of real-life application, the heavier material may cause more discomfort over a longer period; however, the wearer is better protected, especially for BAL-FZ levels (highest bushfire attack level). Additionally, in cases of flash fire, where the bushfire conditions suddenly change and become more dangerous due to shift in weather conditions or fuel availability, the multi-layer material protective clothing would be more beneficial for the safety of the firefighter.

Conclusion

This reported experimentally characterised a multi-layer material used by the Australian Fire and Rescue using cone calorimetry. Moreover, the material was comparatively analysed against a material used by the Rural Fire Service in 2013 and 2022. The multi-layer consisted of a Nomex/Viscose blend inner lining, an e-PTFE with famed silicone spacers moisture membrane and a Kevlar outer shell and was tested under 25, 35 and 50 kW/m^2 heat flux levels at 60 mm separation distance from the heated cone.

- Results demonstrated that the multi-layer material had a TTI more than double the time of the 2013 and 2022 materials.
- Multi-layer material had the lowest peak HRR meaning that the material does not rapidly release thermal energy when it burns, unlike the other RFS jacket materials. Releasing lower levels of thermal energy ultimately means that the material has better thermal resistance and can withstand longer exposure to extreme heat temperatures, which is valuable for RFS protective clothing.
- Multi-layer material had the largest total heat released across the three heat flux levels compared to the other RFS jacket materials because it was thicker and had greater mass, essentially providing more material to burn and release thermal energy, yet it still performed the best out of the three materials in relation to ignition time.

Therefore, it can be concluded that the multi-layer material offers greater potential for the RFS against radiant heat resistance compared to the materials previously/currently used, however there is a trade-off with the mass of the material.

References

1. Brown JR, Ennis BC (1977) Thermal analysis of nomex® and kevlar® fibers. Text Res J 47(1):62–66

2. Kalantar J, Drzal LT (1990) The bonding mechanism of aramid fibres to epoxy matrices: part 1 a review of the literature. J Mater Sci 25:4186–4193
3. Ebnesajjad S (2017) Properties, characteristics, and applications of expanded PTFE (ePTFE) products. Expanded PTFE Appl Handbook 163–170
4. Choi KJ, Spruiell JE (2010) Structure development in multistage stretching of PTFE films. J Polym Sci Part B Polym Phys 48(21):2248–2256
5. Zhou Z-M, Wang K, Lin K-W, Wang Y-H, Li J-Z (2021) Influence of characteristics of thermoplastic polyurethane on graphene-thermoplastic polyurethane composite film. Micromachines 12(2):129
6. Song G (2007) Clothing air gap layers and thermal protective performance in single layer garment. J Ind Text 36(3):193–205
7. Benisek L, Phillips WA (1981) Protective clothing fabrics: part II. against convective heat (open-flame) hazards1. Text Res J 51(3):191–196
8. Fu M, Weng WG, Yuan HY (2014) Quantitative assessment of the relationship between radiant heat exposure and protective performance of multilayer thermal protective clothing during dry and wet conditions. J Hazard Mater 276:383–392
9. Lee YM, Barker RL (1986) Effect of moisture on the thermal protective performance of heat-resistant fabrics. J Fire Sci 4(5):315–331
10. Second Degree Burns. https://myhealth.alberta.ca/Health/pages/conditions.aspx?hwid=sts14394&lang=en-ca. [Online]
11. Nomex® fiber Technical Guide (2019). [Techreport]. DuPont
12. Gu H (2009) Research on thermal properties of Nomex/Viscose FR fibre blended fabric. Mater Des 30(10):4324–4327
13. KEVLAR® ARAMID FIBER Technical guide (2017). [Techreport]. DuPont
14. The Royal Children's Hosptial Melbourne—Burns Unit. https://www.rch.org.au/burns/clinical_information/#::text=Usually%20a%20Superficial%20Partial%20thickness,untreated%20will%20leave%20scar%20tissue. [Online]
15. Talukdar P, Alagirusamy R, Das A et al (2014) Heat transfer analysis and second degree burn prediction in human skin exposed to flame and radiant heat using dual phase lag phenomenon. Int J Heat Mass Transf 78:1068–1079
16. Protective clothing—protection against heat and fire—method of test: evaluation of materials and material assemblies when exposed to a source of radiant heat. International Organization for Standardization, Geneva, CH, Standard (2002)
17. Mount Nittany Health—Burn, hot water. https://mountnittany.org/wellness-article/burn-hot-water#::text=Hot%20water%20on%20the%20skin,second-degree%20burn%20is%20deeper. [Online]

Experimental Investigation on Electroslag System for C-HRA-3 Heat-Resistant Alloy

Tengchang Lin, Longfei Li, and Yong Yang

Abstract The difference in metallurgical quality of C-HRA-3 alloy smelting using two kinds of slag system was investigated by 10 kg electroslag remelting furnace. The results show that the alloy electroslag ingot smelting by a new-type 50% CaF_2-26% Al_2O_3-20% CaO-3% MgO basic slag system has better surface quality compared to 60% CaF_2-20% Al_2O_3-10% CaO-10% MgO basic slag system. The columnar crystal growth direction of the electroslag ingot, smelting by new-type slag system, has a smaller angle with the centerline, and the depth of the molten pool is greater. The content of Al, Ti, Zr, Si, and B at various positions of two electroslag ingots smelting with the same proportion of TiO_2 and ZrO_2 components can be controlled within the target content range of C-HRA-3 alloy. There are fewer inclusions in the electroslag ingot smelting by new-type slag system, and the proportion of oxide inclusions at four different ingot heights is lower.

Keywords Electroslag remelting · Electroslag system · Refining time · C-HRA-3 alloy · Metallurgical quality

Introduction

C-HRA-3 alloy is a nickel-based heat-resistant alloy material independently designed and developed by the General Institute of Iron and Steel Research, suitable for the manufacturing of large-diameter thick-walled boiler tubes at 700 °C ultra-supercritical power plants [1, 2]. Due to the high content of chromium, cobalt, molybdenum and other alloy elements inside the C-HRA-3 alloy, as well as the high requirements for purity, it needs to be produced through a triple special smelting process of vacuum induction melting-gas shielded electroslag remelting-and vacuum consumable melting [3].

T. Lin (✉) · L. Li · Y. Yang
Metallurgical Technology Research Institute, Central Iron and Steel Research Institute Co., Ltd, Beijing 100081, China
e-mail: Lin_tengchang@163.com

Z. Peng et al. (eds.), *Characterization of Minerals, Metals, and Materials 2024*, The Minerals, Metals & Materials Series, https://doi.org/10.1007/978-3-031-50304-7_46

Electroslag remelting, as an intermediate link in the triple special smelting process, can utilize its advantages in remelting and refining process. By utilizing the interaction between high-temperature slag with metal droplets and controlling crystallizer cooling, electroslag ingots can be obtained with low sulfur content, high cleanliness, good surface quality, and solidification structure [4–6]. In addition to designing a reasonable electrical and cooling system, the selection of the slag system for electroslag remelting is also crucial when smelting specific metal materials. It affects the control of easily burned elements and the effective removal of inclusions in the electroslag ingot [7, 8]. Extensive research on electroslag remelting slag systems' development of nickel-based alloy have been conducted by domestic universities, research institutes, and enterprises. Chen et al. [4], from the General Institute of Iron and Steel Research, studied the effect of electroslag remelting process on the desulfurization effect of nickel based high-temperature alloy GH4169 using the CAF60 slag system (60% CaF_2-20% Al_2O_3-20% CaO). Gao et al. [9], from the Panchang Steel Technology Center, studied the effect of a new pre-melted slag system, 50% CaF_2-22% Al_2O_3-20% CaO-5% MgO-3% TiO_2, on the surface quality of nickel-based alloy GH3128 steel ingots and the burning loss law of easily burned elements. When studying the influence of slag system on the metallurgical quality of high-temperature alloys, Li et al. [7], from Northeastern University, proposed that the slag system for smelting high titanium and low aluminum high-temperature alloys should be 65–70% CaF_2-12–15% Al_2O_3-12–15% CaO-3–8% MgO-2–5% TiO_2, and the slag system for smelting high aluminum and low titanium high temperature alloys should be 60–65% CaF_2-15–20% Al_2O_3-15–20% CaO-0–5% MgO-0–2% TiO_2.

As a new type of nickel-based heat resistant alloy, there have been no reports on the research of the slag system used in electroslag remelting of C-HRA-3 alloy. Utilizing methods such as macrostructure analysis, chemical detection analysis, and automatic inclusion analysis system, this article analyzes the effects of two different slag systems on the surface quality, macrostructure, control of easily burned elements, and differences in the quantity and size characteristics of inclusions in C-HRA-3 nickel based heat-resistant alloy electroslag ingots by 10 kg electroslag remelting experiment, which can provide a theoretical basis for the industrial grade electroslag remelting of C-HRA-3 alloy.

Experimental Materials and Procedures

The 20 kg C-HRA-3 alloy ingot was melted using VIM, and its chemical composition is shown in Table 1. The ingot was forged into a 40 mm diameter rod, and cut into two electroslag remelting electrodes with 10 kg. An inner diameter of φ80 mm water-cooled crystallizer was used for smelting experiments on 10 kg electroslag remelting furnace, and the two slag system components used are shown in Table 2.

During smelting, argon gas was continuously introduced into the crystallizer for protection. Due to the different physical properties of the two slag systems, the voltage of the 1# slag system during smelting was 28 V, the current was 1300–1500 A, and

Table 1 Chemical composition of C-HRA-3 alloy electrode (wt%)

C	Si	Mn	P	S	Cr	Co	Mo	Fe
0.0077	0.041	0.0013	0.001	0.0006	22.08	12.01	8.74	–
Al	Ti	B	Nb	W	Zr	O	N	Ni
0.98	0.42	0.005	0.048	0.66	–	0.0007	0.0017	Bal

Table 2 Chemical composition of two slag systems for electroslag remelting (wt%)

Number	CaF_2	Al_2O_3	CaO	MgO	TiO_2	ZrO_2
1# (Original)	59.4	19.8	9.9	9.9	0.5	0.5
2# (New)	50.4	26.1	19.5	3	0.5	0.5

the melting rate fluctuated in the range of 0.42–0.52 kg/min, while the voltage of the 2# slag system during smelting was 34 V, the current was 1400–1500 A, and the melting rate fluctuated in the range of 0.52–0.62 kg/min.

Comparison of metallurgical quality of electroslag ingots: (1) Observed the surface quality of the electroslag ingot and collected and measured the thickness of the slag skin on the ingot surface. (2) Used acid solution to corrode the longitudinal profile of the electroslag ingot and analyzed the macrostructure characteristics. (3) Taken samples from the tail of the electroslag ingot, 1/4 ingot body, 1/2 ingot body, 3/4 ingot body, and the riser to analyze the content of easily oxidized elements such as Al, Ti, Zr, B, Si, and analyzed their burning loss patterns. (4) Metallographic samples of 8 × 8 × 4 mm were taken at 1/2 radius of four different height positions of the electroslag ingot, as shown in Fig. 1. (5) Analyzed the quantity and size distribution characteristics of inclusions at different heights of electroslag ingots, and compared with the electrode base material.

Results and Analysis

Surface Quality of Electroslag Ingots

The photos of slag skin for smelting C-HRA-3 alloy electroslag ingots with two different slags are shown in Fig. 2. Randomly measuring thickness of 20 fragments, it was found that the average thickness of smelting slag skin of 1# slag was 0.56 mm, and the 2# new slag was 0.42 mm. Compared to the new 2# slag system, the slag skin thickness of 1# slag during electroslag remelting is larger. The photos of surface morphology of C-HRA-3 alloy electroslag ingots produced by two slag systems are shown in Fig. 3. From the figure, it can be seen that there are irregularly distributed pits on the surface of C-HRA-3 alloy ingots smelted with two slag systems, with the surface pits of 1# electroslag ingot that are more severe than 2# electroslag ingot.

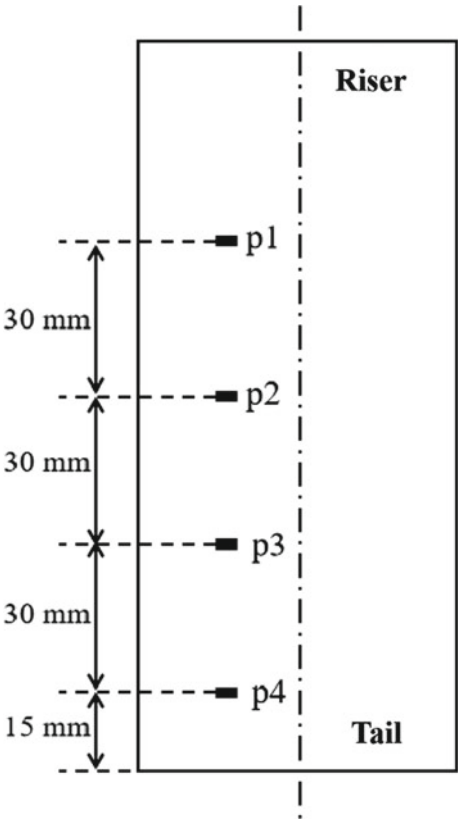

Fig. 1 Schematic diagram of locations for metallographic samples in the longitudinal section of electroslag ingots

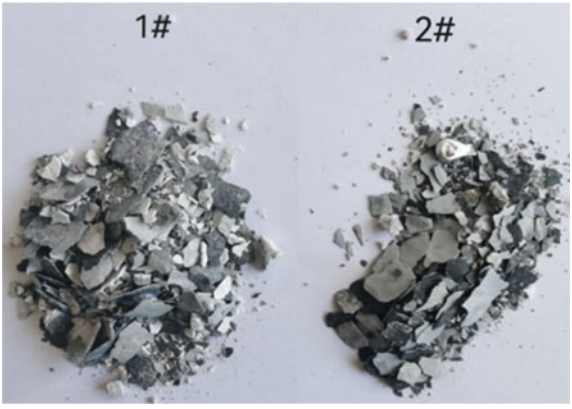

Fig. 2 Morphology of slag skin after smelting by two slag systems

Fig. 3 Surface morphology of two slag systems for smelting electroslag ingots

From the perspectives of slag skin thickness and surface quality, 1# slag has a small slag resistance and low electrical power during smelting, resulting in a small heating capacity of slag and low temperature of slag pool. This leads to large slag skin thickness during smelting of C-HRA-3 alloy in the 1# slag. At the same time, the slag material near the edge of the crystallizer fails to melt well, which can easily cause crusting at the contact between the surface of the slag layer and the inner wall of the crystallizer. As the liquid level of metal melt pool rises to this position, the formation of pits on the surface of the electroslag ingot results in obvious pits on the surface of the electroslag ingot smelted with 1# slag.

Macrostructural Characteristics of Electroslag Ingots

The microstructure morphology of two C-HRA-3 electroslag ingots is shown in Fig. 4, which was obtained by etching with copper sulfate-sulfuric acid-hydrochloric acid solution. It shows that the solidification quality of electroslag ingots produced by two slag systems is stable, with a general porosity of 0.5 grade. The centerline of 1# electroslag ingot is curved, and the solidification direction of columnar crystals on both sides of the centerline changes multiple times. Compared to 1# electroslag ingot, the growth trend of columnar crystals on both sides of the solidification centerline of 2# electroslag ingot is more orderly. Due to the higher melting rate of the 2# slag system during smelting, the angle between the growth direction of columnar crystals above the inclined direction and the centerline is smaller.

In addition, from Fig. 4, it can be seen that the contour of solidification molten pool at riser end of the 2# electroslag ingot is inferred to be about 28.3 mm deep, and its ratio to the diameter of the ingot is about 38.6%. The contour of the solidification

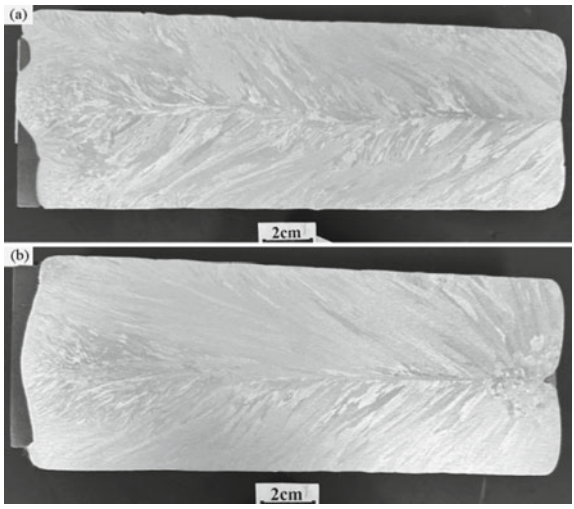

Fig. 4 Macroscopic structures of slag 1 (**a**) and slag 2 (**b**) for smelting electroslag ingots

molten pool at riser end of the 1# electroslag ingot is not obvious. This phenomenon indirectly indicates that the 2# new slag has better insulation properties than the 1# original slag.

Burning Loss Law of Electroslag Ingot Elements

The content changes of Al, Ti, Zr, B, Si at electrode and different positions of two electroslag ingots (ingot tail, 1/4 ingot body, 1/2 ingot body, 3/4 ingot body, riser) are shown in Fig. 5. Except for Al, the upper and lower limits of the content of each element in the vertical axis of the figure are within the content control range of the C-HRA-3 alloy.

The results show that Al content at the tail of 1# electroslag ingot exceeds the target upper limit, while all element contents at other positions are within the control target content range. The excessive content of Al element in the tail of 1# electroslag ingot is mainly due to the melting of aluminum particles added to slag before smelting for deoxidizing. In the early stage of electroslag remelting, alloy droplets pass through the slag pool, and some of the aluminum in the slag pool dissolves in metal droplets, causing the increasing of aluminum content.

In addition, the high content of Zr and Si at the tail of the 1# electroslag ingot is due to small amount of ZrO_2 components and impurity component SiO_2 in slag. During the steel-slag equilibrium process, maybe some ZrO_2 and SiO_2 components in the slag will be reduced by Al, and the resulting Zr and Si elements will enter the C-HRA-3 alloy melt pool. It can be determined that the newly designed 2# slag has less fluctuation of easily oxidizable elements at various height positions of the electroslag ingot.

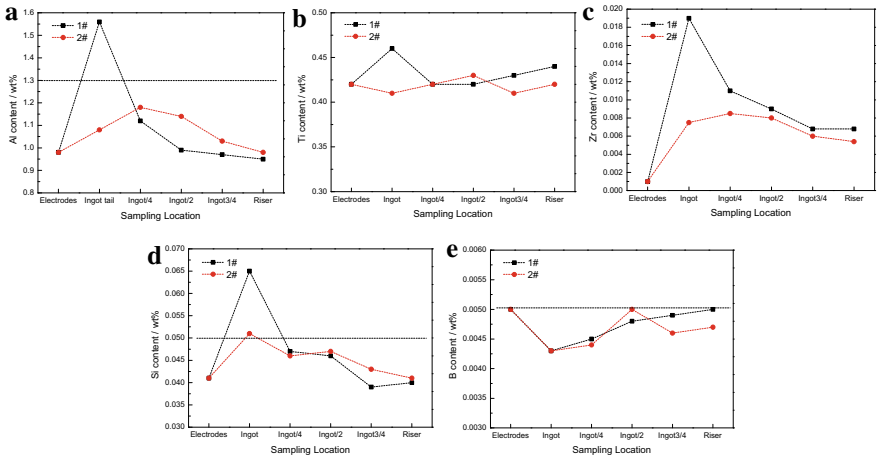

Fig. 5 Contents of various elements at different positions of electroslag ingots smelted by two slag systems and original electrode: **a** Al; **b** Ti; **c** Zr; **d** Si; **e** B

Quantity and Size Characteristics of Inclusions in Electroslag Ingots

By using ZEISS EVO18 + X-MAX80 Automatic Inclusion Analysis System, various types of inclusions, with effective diameters above 1 μm, were statistically analyzed on a 29.8 mm^2 area of each sample of 1# and 2# electroslag ingots in Fig. 1. From the analysis results, it was found that inclusions such as oxides, sulfides, sulfur oxides, carbides, and nitrides exist in each sample, and the oxide inclusions account for more than 50%. The size distribution characteristics of oxide inclusions in each sample are shown in Fig. 6.

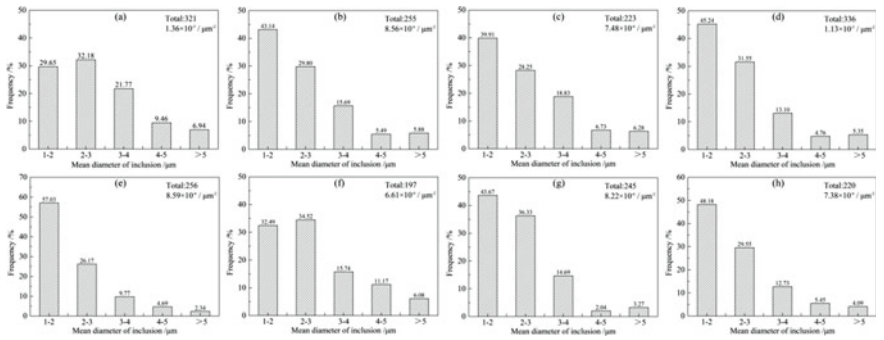

Fig. 6 Statistics on the number and size distribution of oxide inclusions at different positions of electroslag ingots smelted by two slag systems: **a** 1#-p1; **b** 1#-p2; **c** 1#-p3; **d** 1#-p4; **e** 1#-p1; **f** 2#-p2; **g** 2#-p3; **h** 2#-p4

At the same height position, the number of inclusions in each sample of the 1# electroslag ingot, except p3 position, is higher than the 2# electroslag ingot. In addition, the size of inclusions in the 2# electroslag ingot is mainly within the range of 1–3 μm. And inclusions bigger than 5 μm in the 2# electroslag ingot is significantly lower than that of the 1# electroslag ingot. The number of inclusions from tail to body of the ingot (p4 → p1) fluctuates within a small range, but there is no significant upward or downward trend.

Conclusions

(1) Compared with the old 1# slag, C-HRA-3 alloy electroslag ingot, melted with the new 2# slag system, has a thinner slag skin and better surface metallurgical quality; (2) There are no obvious defects in the longitudinal macrostructure of the C-HRA-3 alloy electroslag ingots produced by two different slag systems. Compared with the old 1# slag, the electroslag ingot produced by new 2# slag system has a higher melting rate, a smaller angle between the growth direction of columnar crystals and the centerline, and a clear solidification pool morphology at the riser end of the electroslag ingot; (3) The easily oxidizable elements in electroslag ingots produced by two slag systems meet C-HRA-3 composition requirements, and only Al, Zr, and Si in the tail of 1# electroslag ingot shows significant fluctuations. The number of inclusions in the 2# electroslag ingot is less than that in the 1# electroslag ingot, and the size of inclusions mainly ranges from 1 to 3 μm.

References

1. Chen ZZ, Liu ZD, Dong C, Bao HS, Zhang P, Han K, Gao P (2020) Stress rupture properties and microstructure characteristic of C-HRA-3 heat-resistant alloy at 850 °C. Heat Treat Met 45(01):135–138
2. Chen ZZ, Liu ZD, Bao HS, Gan Y (2017) Kinetics of austenite grain growth in heat-resistant alloy C-HRA-3. Iron Steel 52(07):64–67
3. Liu ZD, Chen ZZ, He XK, Bao HS (2020) Systematical innovation of heat resistant materials used for 630–700 °C advanced ultra-supercritical (A-USC) fossil fired boilers. Acta Metall Sin 56(4):539–548
4. Chen XC, Wang F, Shi CB, Ren H, Feng D (2012) Effect of electroslag remelting process on desulphurization of GH4169. J Iron Steel Res 24(12):11–16
5. Liu FB, Zang XM, Jiang ZH, Geng X (2010) Removal of non-metallic inclusions in current-conductive mould ESR process. China Metall 20(05):5–8
6. Yang BF, Liu JH, Han ZB, Liu HB, He Y, Yao CF (2015) Effect of electroslag remelting on inclusions in FeCrAl stainless steel. J Iron Steel Res 27(10):19–25
7. Li X, Geng X, Jiang ZH, Li HB, Xu FH, Wang LX (2015) Influences of slag system on metallurgical quality for high temperature alloy by electroslag remelting. Iron Steel 50(09):41–46

8. Wu ZH, Guo B, Wang SW, Wang YT, Zhang JW (2023) Effect of electroslag remelting in protective atmosphere on composition and inclusions of DZ2 high-speed axle steel. Spec Steel 44(01):19–24
9. Gao SL (2014) Study on electroslag remelting for GH3128 and GH2132 alloys by new premelted slag. Spec Steel Technol 20(01):50–52

Formation of Solid Solutions of $BaTiO_3$ Doped with Eu^{3+} by Solid-State Reaction

J. P. Hernández-Lara, A. Hernández-Ramírez, J. A. Romero-Serrano, M. Pérez-Labra, F. R. Barrientos-Hernández, R. Martinez-Lopez, and M. I. Valenzuela-Carrillo

Abstract $BaTiO_3$ is generally made by reacting $BaCO_3$ with TiO_2 at a temperature of about 1100 °C. Whatever the technique, the current trend is to produce powders with a strict control of purity, Ba/Ti ratio and particle size, which affects the generation of reproducible microstructures and constant dielectric properties in the sintered product. In this work, the synthesis of solid solutions of $BaTiO_3$ doped with Eu^{3+} was carried out and they were synthesized by the solid-state reaction method. The concentration was varied from $x = 0.003$, 0.05 and 0.10% by weight of Eu^{3+}. The powders were decarbonated at 900 °C and sintered at 1300 °C for 5 h. The experimental results obtained by X-ray diffraction show the consolidation of tetragonal $BaTiO_3$ and the Raman spectroscopy shows the corresponding $BaTiO_3$ spectra that confirm the consolidation in the sintering process. The scanning electron microscopy results mainly showed particles with necks characteristic of the sintering process.

Keywords $BaTiO_3$ formation · Solid solutions · Solid-state reaction

Introduction

$BaTiO_3$ is a ferroelectric compound with a perovskite crystalline structure, which has the ability to accommodate ions of different sizes, so a large number of different dopants can be accommodated in the $BaTiO_3$ lattice, making Barium Titanate a semiconductor. When this material is at a certain temperature, called the Curie temperature (around 120 °C), a phase change called displacement phase transition occurs. Above this temperature, it has a cubic structure and when it cools it changes to a cubic structure. A tetragonal structure with distortion of octahedrons and displacement of

J. P. Hernández-Lara (✉) · A. Hernández-Ramírez · J. A. Romero-Serrano
Higher School of Chemical Engineering and Extractive Industries (ESIQIE)-IPN, 07738 Zacatenco, Mexico City, Mexico
e-mail: juanp_hernandezlara@hotmail.com

M. Pérez-Labra · F. R. Barrientos-Hernández · R. Martinez-Lopez · M. I. Valenzuela-Carrillo
Academic Area of Earth Sciences and Materials, Autonomous University of the State of Hidalgo, Pachuca-Tulancingo Km 4.5 Mineral de la Reforma, 42184 Hidalgo, Mexico

Z. Peng et al. (eds.), *Characterization of Minerals, Metals, and Materials 2024*, The Minerals, Metals & Materials Series, https://doi.org/10.1007/978-3-031-50304-7_47

positive ions away from the central position is formed, causing unit cells to become permanently polarized, leading to spontaneous polarization along the c-axis [1].

$BaTiO_3$ ceramics are widely used in electronic devices as high permittivity capacitors, due to their high dielectric constant and low loss characteristics. It is well known that the ferroelectric and optical properties of ferroelectric ceramics depend on the grain size. Basically, Barium Titanate is prepared by a solid-state reaction between oxides [2–6].

The $BaTiO_3$ structure changes from the cubic paraelectric phase to the tetragonal ferroelectric phase at 120 °C. It has a typical perovskite (ABO3) structure [7]. There are different ceramic processing techniques, some more used than others, but all have the objective of obtaining a solid product with the desired shape from precursor materials, such as a film, fiber or monolith with the required microstructure. Ceramic processing methods can be divided into three groups according to the phase in which the precursor materials are found, whether solid, liquid or gaseous [8].

The incorporation of isovalent impurities has no effect on the defect population; however, anisovalent impurities (of different valence than those it replaces) require the formation of oppositely charged offsetting defects to maintain electrical neutrality. If the replacement cation has a lower valence than the original cation, electron holes could be released, and if the replacement cation has a higher valence than the original cation, electrons could be released. Therefore, conductivity is closely related to the existence of these ionic defects, such as cation and anion vacancies and cation and anion gaps [9–12].

The solid-state reaction technique is the most important and simplest in the preparation of polycrystalline solids, both in the form of powders and densified solids by direct reaction of a mixture of starting materials (reactants). A solid-state reaction, also called a dry mixed oxide reaction, is a chemical reaction in which no solvents are used. It involves the reaction between two solid phases, *A* and *B*, to produce a solid solution *C*. *A* and *B* are commonly metallic elements, while for ceramics they are crystalline compounds [13, 14].

Experimental Methodology

The precursor powders previously calculated were mixed using the $Ba_{1-x}Eu_xTi_{1-x/4}O_3$ mechanism. The grinding was carried out in cylindrical PET containers of 250 mL capacity, and as a grinding medium zirconia balls of 5.05 mm in diameter were used with a material ratio: balls of 1:15 with 2 gr samples. The reactants were wet milled with 100 mL of acetone for 5 h. The mixtures were recovered by filtration, allowing the acetone to evaporate and drying in a muffle oven at 60 °C and heated to 900 °C to decarbonate the samples, subsequently sintering was carried out at a temperature of 1350 °C for 5 h.

Results and Discussion

X-ray Diffraction

Figure 1 shows the X-ray diffraction patterns corresponding to undoped Barium Titanate ($BaTiO_3$) and the sintered samples with $x = 0.003$, $x = 0.05$ and $x = 0.10\%$ by weight of Eu^{3+} at 1350 °C. In the diffractogram you can see the characteristic peaks of undoped $BaTiO_3$ which are found at $2\theta \approx 22.33°$, 31.58°, 39.07°, 45.54°, 51.20°, 56.37°, 65.92°, 70.45°, 75.31°, 79.50°, 83.55° whose highest intensity peak is found at $2\theta \approx 31.58°$. This phase was identified as Tetragonal BaTiO3 (JCPDS 05–0626), for the doped samples $x = 0.003$, $x = 0.05$ and $x = 0.10$ and it can also be seen that as the dopant content increases, the Tetragonal BaTiO3 phase is a consolidated phase.

However, for the samples $x = 0.05$ and $x = 0.10\%$ by weight of Eu^{3+} (Fig. 2) the existence of a deflection can be seen that was identified as a secondary phase [15] Eu_2TiO_5 (JCPDS 22–1100) in the 2θ positions. ≈ 28.59° and 33.20°, as well as the presence of a remnant of Eu_2O_3 precursor powder (JCPDS 340,392) at position $2\theta \approx 30.10°$.

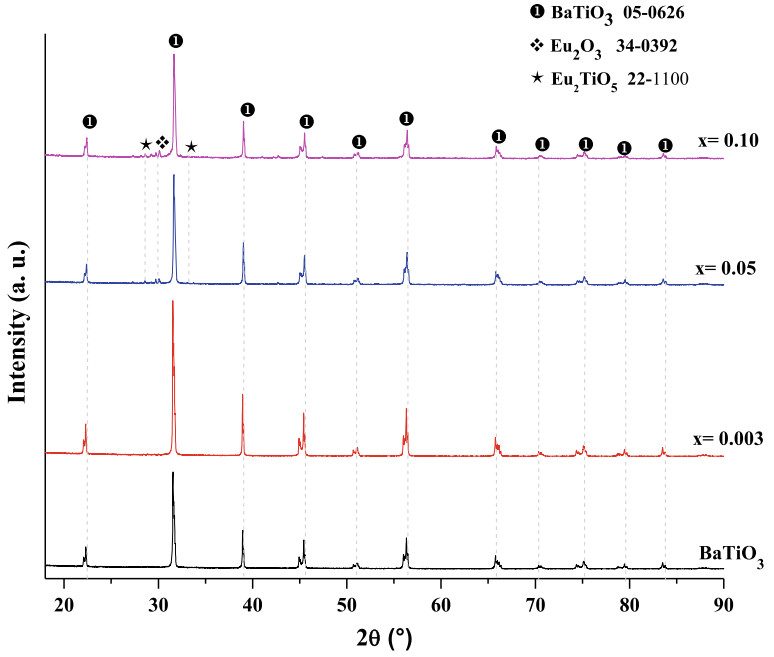

Fig. 1 Diffraction patterns of undoped $BaTiO_3$ samples, $x = 0.003$, $x = 0.05$, and $x = 0.10\%$ by weight Eu^{3+}

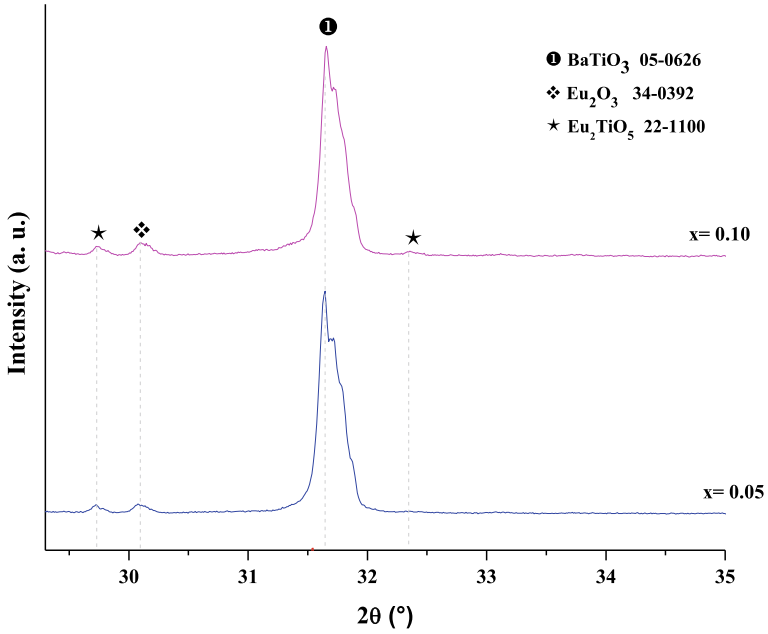

Fig. 2 Diffraction patterns of the Eu_2TiO_5 secondary phase in the samples $x = 0.05$, $x = 0.10\%$ by weight of Eu^{3+}

It is worth mentioning that this secondary phase has a tendency to increase with the increase of the dopant as observed in the X-ray diffraction patterns. Mrazek et al., and Orihashi et al., found that lanthanide titanium oxides that crystallize in a pyrochlorine-type structure with general formula Re_2TiO_5 and $Re_2Ti_2O_7$ (Re = Rare Earths) have been extensively investigated in recent years for their interesting photoluminescence properties [16, 17].

Raman Spectroscopy

Figure 3 shows the Raman spectra for undoped $BaTiO_3$ and the samples $x = 0.003$, 0.05, 0.01, Eu^{3+} % by weight prepared by the solid-state reaction. The frequency coverage area is from 150 to 1200 cm^{-1}. Results reported by Gardiner et al. [18] are consistent with what was reported in this research, the characteristic bands are located at 205 cm^{-1}, (E (TO + LO), A1 (LO)), 265 cm^{-1} (A1 (TO)), 304 cm^{-1} (B1, E (TO + LO)), 513 cm^{-1} (A1(TO), E (TO)) and 717 cm^{-1} (A1 (LO), E (LO)). These bands were also observed in studies by Matsuoka et al., and Ikushima et al., [19, 20].

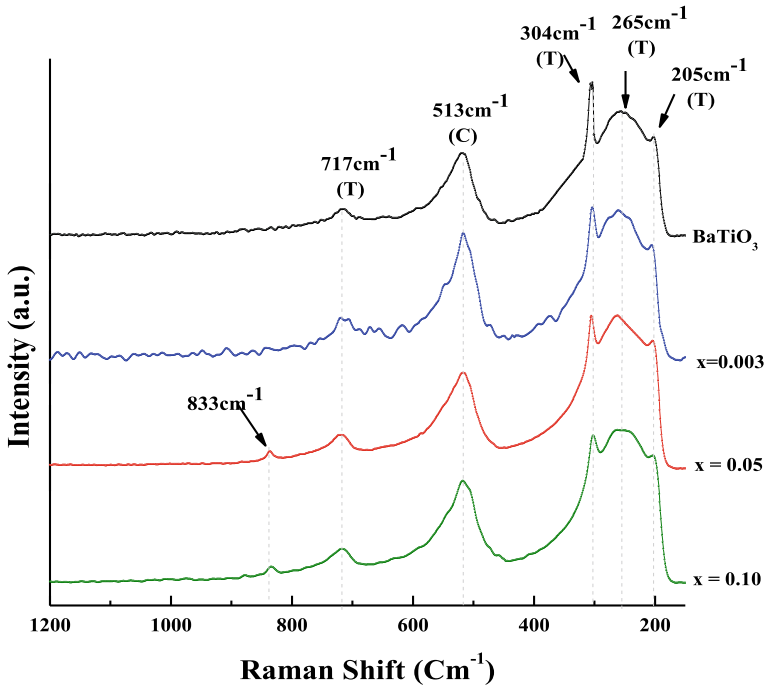

Fig. 3 Raman spectra of undoped $BaTiO_3$, $x = 0.003$, $x = 0.05$, $x = 0.10\%$ by weight Eu^{3+}

Scanning Electron Microscopy (SEM)—Energy Dispersed Spectroscopy (EDS)

Figure 4 shows the morphology of the sintered powders at 1350 °C of the sample $x = 0.003\%$ by weight using a 5.0 kV acceleration voltage and a magnification of X5000. Powders consist of individual particles and aggregates with various sizes, have a random orientation with porosity, mostly grains tending to sphericity. It can also be noted that the microstructure is partially homogeneous.

Figure 5 shows the EDS results for the sample $x = 0.003\%$ by weight of the powders sintered at 1350 °C where the results of the semiquantitative analysis are shown. The presence of the elements of the doped ceramic powders can be observed, and for this sample there is no presence of the dopant and it can be noted in Table 1 since it is one of the low compositions.

Figure 6 shows the micrograph of the sintered powders at 1350 °C of the sample $x = 0.05\%$ by weight using a 5.0 kV acceleration voltage and a magnification of X5000. In this micrograph we can see formations of necks of the particles with a random orientation and of different sizes as reported by Hernandez-Lara et al. and Barrientos Hernandez et al. [13, 14].

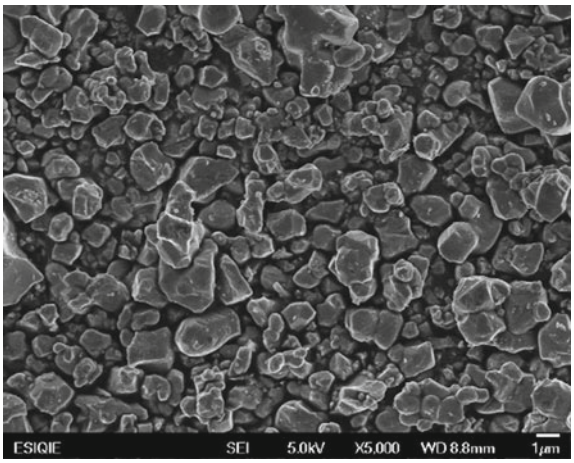

Fig. 4 Micrograph of the sample $x = 0.003\%$ by weight Eu^{3+}

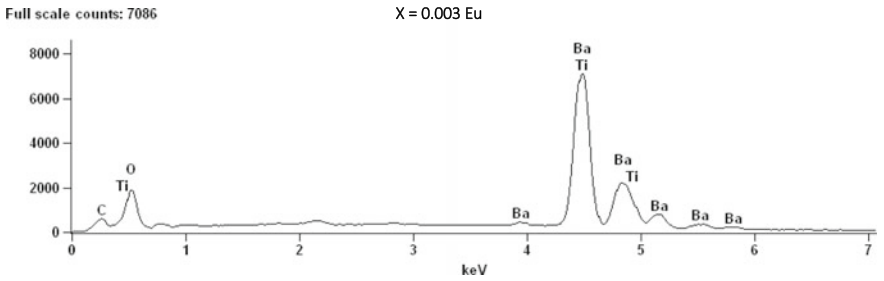

Fig. 5 EDS of the sample $x = 0.003\%$ by weight of the sintered powders at 1350 °C

Table 1 Elements of the sample $x = 0.003\%$ by weight of the powders sintered at 1350 °C

Element line	Weight (%)	Atom (%)
O K	15.23	50.78
Ti K	22.45	25.01
Ba L	62.32	24.21
Total	100.00	100.00

Figure 7 shows the EDS results for the sample $x = 0.05\%$ by weight of the sintered powders at 1350 °C where the presence of the elements of the sintered doped powders can be observed, in this sample there is the presence of the dopant and the increase of the dopant is more evident and this can be corroborated in Table 2.

Figure 8 shows the morphology of the sintered powders at 1200 °C of the sample $x = 0.10\%$ by weight using a 5.0 kV acceleration voltage and a magnification of

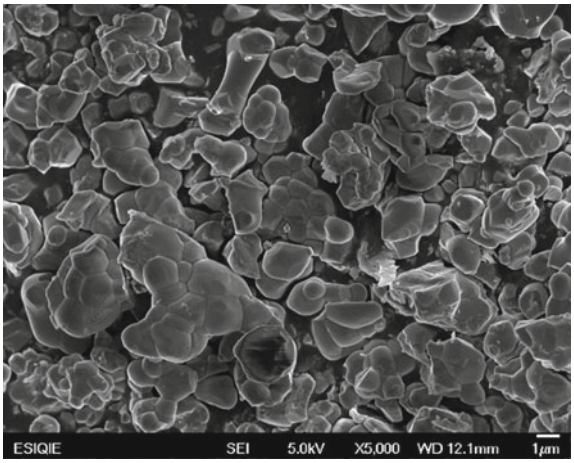

Fig. 6 Micrograph of the sample $x = 0.05\%$ by weight Eu^{3+}

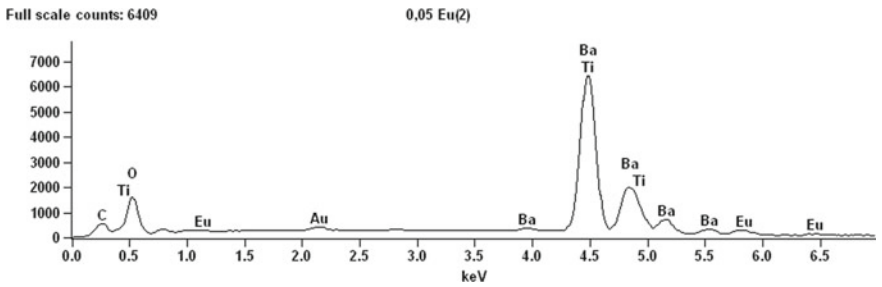

Fig. 7 EDS of the sample $x = 0.05\%$ by weight of the sintered powders at 1350 °C

Table 2 Sample elements $x = 0.05\%$ by weight of the powders sintered at 1350 °C

Element line	Weight (%)	Atom (%)
O K	13.79	48.06
Ti K	22.54	26.23
Ba L	60.12	24.41
Eu L	3.54	1.30
Total	100.00	100.00

X5000. The powders consist of particles with the formation of necks characteristic of a sintering process with various sizes, and they have a random orientation with porosity in some areas. It can also be noted that the microstructure is partially homogeneous and agglomerates are formed in some areas.

Figure 9 shows the EDS results for the sample $x = 0.10\%$ by weight of the powders sintered at 1350 °C where the presence of the elements of the doped ceramic

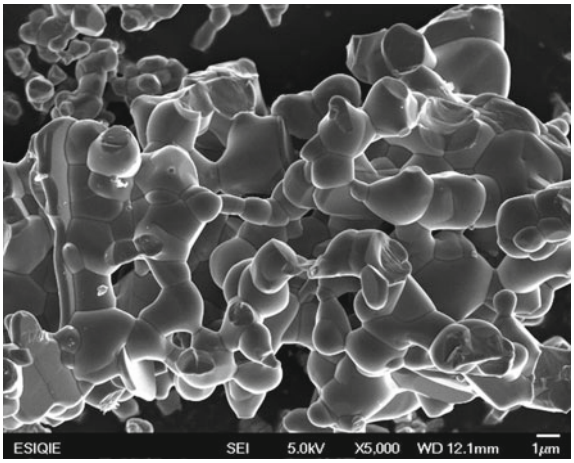

Fig. 8 Micrograph of the sample $x = 0.10\%$ by weight Eu^{3+}

powders can be observed, for this sample the dopant is already evident because the concentration is higher and the other elements decrease due to the increase in dopant, and this can be corroborated in Table 3.

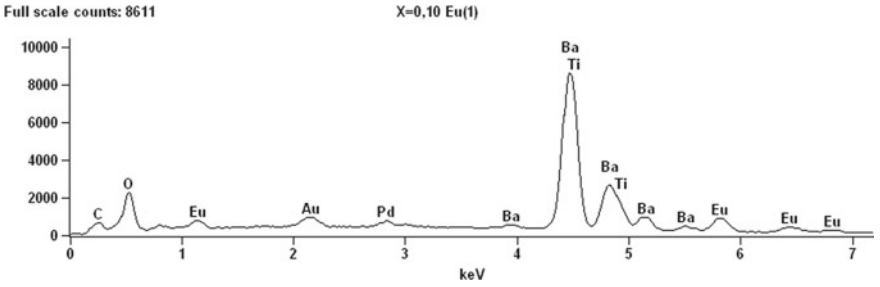

Fig. 9 EDS of the sample $x = 0.10\%$ by weight of the sintered powders at 1350 °C

Table 3 Sample elements $x = 0.10\%$ by weight of the powders sintered at 1350 °C

Element line	Weight (%)	Atom (%)
O K	15.73	52.83
Ti K	20.13	22.58
Ba L	50.60	19.80
Eu L	13.54	4.79
Total	100.00	100.00

Conclusion

X-ray diffraction patterns confirmed the consolidation of tetragonal $BaTiO_3$ according to the identification chart (JCPDS 05–0626) at positions $2\theta \approx 22.33°$, 31.58°, 39.07°, 45.54°, 51.20°, 56.37°, 65.92°, 70.45°, 75.31°, 79.50°, 83.55° as well as the highest intensity peak is found at $2\theta \approx 31.58°$ however there is a secondary phase Eu_2TiO_5 (JCPDS 22-1100) at positions $2\theta \approx 28.59°$ and 33.20° and a remnant of the precursor powder, Eu_2O_3 (JCPDS 340,392) at position $2\theta \approx 30.10°$. The Raman spectra show the characteristic bands of $BaTiO_3$ at room temperature, located at 205 cm^{-1}, (E (TO + LO), A1 (LO)), 265 cm^{-1} (A1 (TO)), 304 cm^{-1} (B1, E (TO + LO)), 513 cm^{-1} (A1 (TO), E (TO)) and 717 cm^{-1} (A1 (LO), E (LO)), and this agrees with what has been reported in the literature. The Scanning Electron Microscopy analyzes show particles of different sizes which present the characteristic necks of a sintering process and by Energy Dispersed Spectroscopy (EDS) it can be confirmed that in the semiquantitative analysis the increase in dopant in the samples is more abundant.

Acknowledgements This work has been carried out thanks to the support of IPN-ESIQIE, the Autonomous University of the State of Hidalgo and Conahcyt.

References

1. He J (2012) Growth mechanism and interface effects on microstructure of perovskite-type barium titanate-based epitaxial films
2. Hreniak D, Łukowiak E, Maruszewski K, Pązik R, Stręk W (2002) Structure, spectroscopy and dielectric properties of $BaTiO_3$: Eu^{3+} nanocrystallites prepared by the sol–gel method. Mater Sci 20(1):43–50
3. Sakabe Y, Minai K, Wakino K (1981) High-dielectric constant ceramics for base metal monolithic capacitors. Jpn J Appl Phys Suppl 20–4:147–150
4. Simon-Seveyrat L, Hajjaji A, Emziane Y, Guiffard B, Guyomar D (2007) Re-investigation of synthesis of $BaTiO_3$ by conventional solid-state reaction and oxalate coprecipitation route for piezoelectric applications. Ceram Int 33:35–40
5. West AR, Adams TB, Morrison FD, Sinclair DC (2004) Novel high capacitance materials: $BaTiO_3$: La and $CaCu_3Ti_4O_{12}$. J Euro Ceram Soc 24:1439–1448
6. Nalwa HS (1999) Handbook of low and high dielectric constant materials and their applications. Academic Press, USA
7. Carter CB, Norton MG (2007) Ceramics materials—science and engineering. Springer
8. Rahaman MN (2003) Ceramic processing and sintering, 2nd edn. CRC Press
9. Yanagida H (1996) The chemistry of ceramics. Wiley, Tokyo
10. Levinson LM (1988) Electronic ceramics. Marcel Dekker Inc., New York
11. Buchanan RC (1998) Ceramic materials for electronics; processing, properties and applications, 2nd edn. Urbana, IL, pp 47–49
12. Smyth DM (2000) The defect chemistry of metal oxides. Oxford University Press
13. Hernández-Lara JP, Pérez-Labra M, Gutierrez-Hernández CC, Barrientos-Hernández FR, Romero-Serrano JA, Hernández-Ramírez A, Reyes-Pérez M, Juárez-Tapia JC, Reyes-Cruz V (2019) Structural analysis of sintered products of $BaTiO_3$ doped with Sm^{3+}. In: Characterization of minerals, metals and materials 2019, pp 765–772

14. Barrientos-Hernández FR, Arenas-Flores A, Cardoso-Legorreta E (2010) Síntesis y caracterización de $BaTiO_3$ dopado con Nb^{5+} mediante el mecanismo $BaTi_{1-5x}Nb_{4x}O_3$. Superficies y Vacío 23(3):10–14
15. Brzozowski E (2002) Secondary phases in Nb-doped $BaTiO_3$ ceramics. Ceram Int 28:773–777
16. Mrázek J, Surýnek M, Bakardjieva S, Buršík J, Kašík I (2014) Synthesis and crystallization mechanism of europium-titanate $Eu_2Ti_2O_7$. J Cryst Growth 391(1):25–32
17. Orihashi T, Nakamura T, Adachi S (2016) Synthesis and unique photoluminescence properties of $Eu_2Ti_2O_7$ and Eu_2TiO_5. J Am Ceram Soc 1–8
18. Graves PR, Gardiner D (1989) Practical Raman spectroscopy. Springer, Berlin
19. Matsuoka T, Fujimura M, Matsuo Y (1972) PTCR behavior of $BaTiO_3$ with Nb_2O_5 and MnO_2 additives. J Am Ceram Soc 55:108–116
20. Ikushima H, Hayakawa S (1967) National technical reports, vol 13, pp 209–216

Homogenizing Treatment of AISI 420 Stainless and AISI 8620 Steels

Victor M. Lopez-Hirata, Maribel L. Saucedo-Muñoz, Karina Rodríguez-Rodríguez, and Héctor J. Dorantes-Rosales

Abstract In the present work, rocker arm low AISI 8620 and needle-nose pliers martensitic stainless AISI 420 steels, obtained from melting and gravity casting processes, were analyzed during the homogenizing treatment. The as-cast steel specimens were microstructural and mechanically characterized by optical microscope, scanning electron microscope, and hardness test. In the case of AISI 8620 steel, the observed microstructure was ferrite and carbides with a hardness of 26 HRC. In contrast, the observed microstructure was ferrite and two types of carbides with a hardness of 52 HRC for the AISI 420 steel. Both steel specimens were homogenized in the austenite region. The homogenizing temperature was determined using the Thermo-Calc calculated equilibrium pseudobinary phase diagrams. The homogenizing time was obtained by Dictra software. The homogenizing temperature and time were 900 °C and 8×10^4 s (22 h), respectively, for the AISI 8620 steel, and 1040 °C and 7×10^4 s (19 h), respectively, for the AISI 420 steel. The results showed that the homogenized microstructure was ferrite, cementite (pearlite), and $M_{23}C_6$ carbides with a hardness of 88 HRB for AISI 8620 steel, and ferrite and $M_{23}C_6$ carbides with a hardness of 43 HRC for AISI 420 steel.

Keywords AISI 420 steel · AISI 8620 steel · As-cast steel homogenizing · Thermo-Calc · Microstructure evolution · Mechanical properties

Introduction

The low-alloy AISI 8620 steel and AISI 420 martensitic stainless steels are widely used in the automotive and metal-mechanic industries to fabricate different tools and automobile parts [1, 2]. Some of the components are produced using melting and

V. M. Lopez-Hirata (✉) · M. L. Saucedo-Muñoz · K. Rodríguez-Rodríguez · H. J. Dorantes-Rosales
Instituto Politécnico Nacional (ESIQIE), UPALM Edif. 7, 07300 Ciudad de México CDMX, Mexico
e-mail: vlopezhi@prodigy.net.mx

Z. Peng et al. (eds.), *Characterization of Minerals, Metals, and Materials 2024*, The Minerals, Metals & Materials Series, https://doi.org/10.1007/978-3-031-50304-7_48

casting processes. The as-cast steel presents the dendrite formation and microsegregation related to low mechanical properties mainly attributed to the non-uniform chemical composition [3]. To improve the mechanical properties, a homogenizing treatment is recommendable for eliminating the dendrites and microsegregation. The homogenizing treatment is usually carried out at high temperatures in the austenite phase field, which permits the atomic diffusion process, and thus the composition fluctuations are reduced [4]. To conduct this heat treatment, the austenizing temperature is selected from an equilibrium phase diagram, while the processing time can be obtained by a solution of the second Fick's law [5, 6].

Thermo-Calc TC software is a CALPHAD-based software, which enables us to calculate the equilibrium phases and the equilibrium phases diagram for a multicomponent alloy [5]. Besides, the TC-Dictra software enables us to determine the time for a homogenizing heat treatment time by solving numerically the diffusion problems using a finite volume method and atomic mobility data, which considers the atomic interaction among the alloying elements [6].

Thus, the present work aims to carry out experimental and numerical analyses of the homogenizing treatment for the as-cast rocker arm low AISI 8620 steel, and needle-nose pliers martensitic stainless AISI 420 steel AISI microstructure to determine the optimum parameters of heat treatment.

Experimental Procedure

The chemical composition of the as-cast AISI 8620 and AISI 420 steel is shown in Table 1. These steels were obtained by a gravity casting process. Steel specimens of about 1 cm × 1 cm × 1 cm were obtained by a diamond-disc cutting machine. The homogenizing treatment was carried out at an austenizing temperature of 900 and 1040 °C, and subsequently furnace cooling. The heat-treated specimens were metallographically prepared, etched with Nital etchant, and then observed with optical (OM) and scanning electron (SEM) microscopes. EDX-SEM analyses was also conducted in the as-cast steels. According to the standard procedure, either the Rockwell "*B*" or "*C*" hardness was determined, following ASTM E-12 standard [7]. Ten hardness measurements were determined.

Table 1 Chemical composition in wt.% for the steels

Steel	C %	Mn %	Si %	Cr %	Ni %	Mo %
AISI 8620	0.22	0.88	0.58	0.48	0.55	0.21
AISI 420	0.32	0.81	0.63	13.41	0.36	0.17

Numerical Procedure

Thermo-Calc, TC, software was used to analyze the stability of phases in the steels and to calculate the pseudo binary Fe–C phase diagram. The kinetic and thermodynamic data was determined from the Thermo-Calc databases for steels, TCFe11 [8]. TC-Dictra was used to calculate the homogenizing time during the austenizing treatment using TCFe11 and MOBFe6 data bases [9].

Results and Discussion

Microstructure of the As-Cast Steels and Their Analysis by Scheil Module

Figure 1a, b show the OM micrographs for the as-cast AISI 8620 and 420 steels, respectively. A non-homogeneous microstructure is noted for both cases because of the non-equilibrium solidification process [x]. The SEM micrographs corresponding to Fig. 1a, b are shown in Fig. 2a, b, respectively. These figure indicate that α ferrite, cementite Fe_3C, and alloyed carbides are present in the microstructure of both steels.

The results for the EDX line scanning analysis are shown in Figs. 3 and 4 for the as-cast AISI 8620 and 420 steels, respectively. It can be noted that the highest composition fluctuation corresponds to the Mn concentration profile for the as-cast AISI 8620 (Fig. 3b). Thus, this composition variation was used for the TC-Dictra calculations. In contrast, the highest composition fluctuation corresponds to the Cr concentration profile for the as-cast AISI 420 steel (Fig. 4b). Therefore, this element variation was used for the TC-Dictra calculations.

Figure 5a, b present the results of the Thermo-Calc Scheil analysis, a plot of temperature versus mol fraction of solid phases, for the as-cast AISI 8620 and 420 steels, respectively. In the case of AISI 8620 steel, the first solid phase is the δ ferrite.

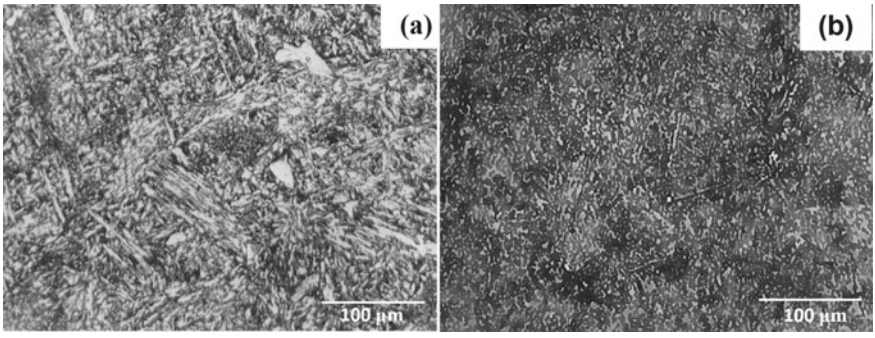

Fig. 1 OM micrographs for the as-cast **a** AISI 8620, and **b** AISI 420 steels

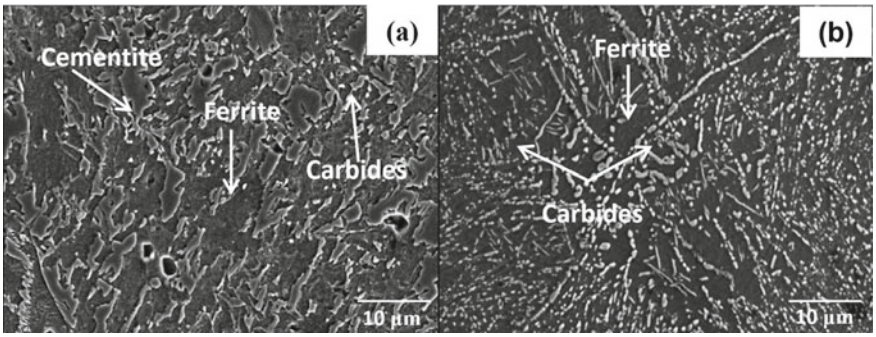

Fig. 2 SEM micrographs for the as-cast **a** AISI 8620, and **b** AISI 420 steels

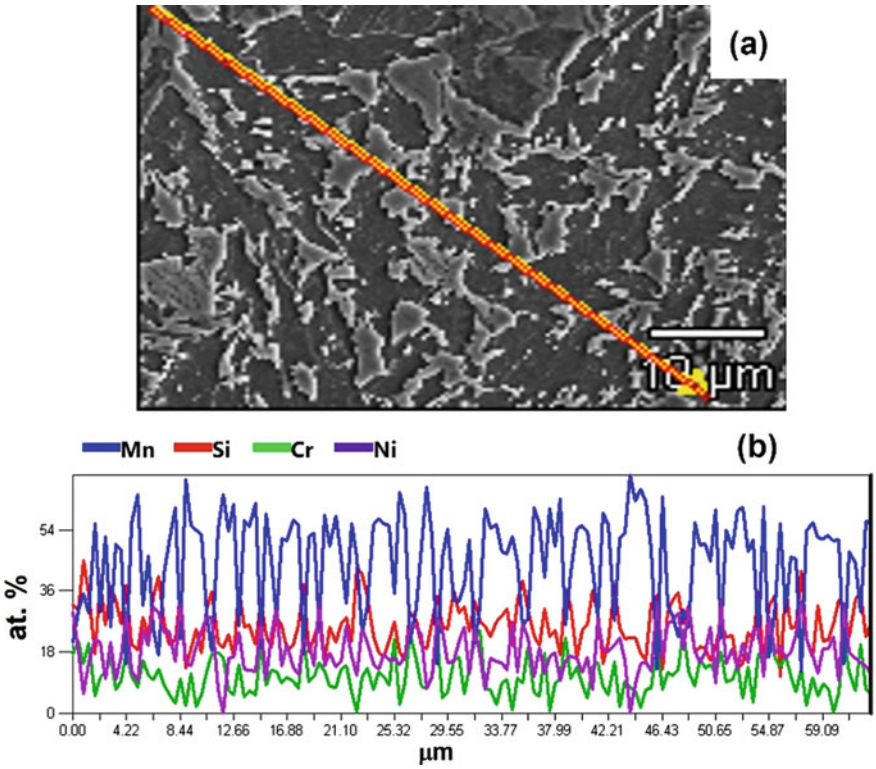

Fig. 3 **a** SEM micrograph and **b** EDX scanning analysis for the as-cast AISI 8620 steel

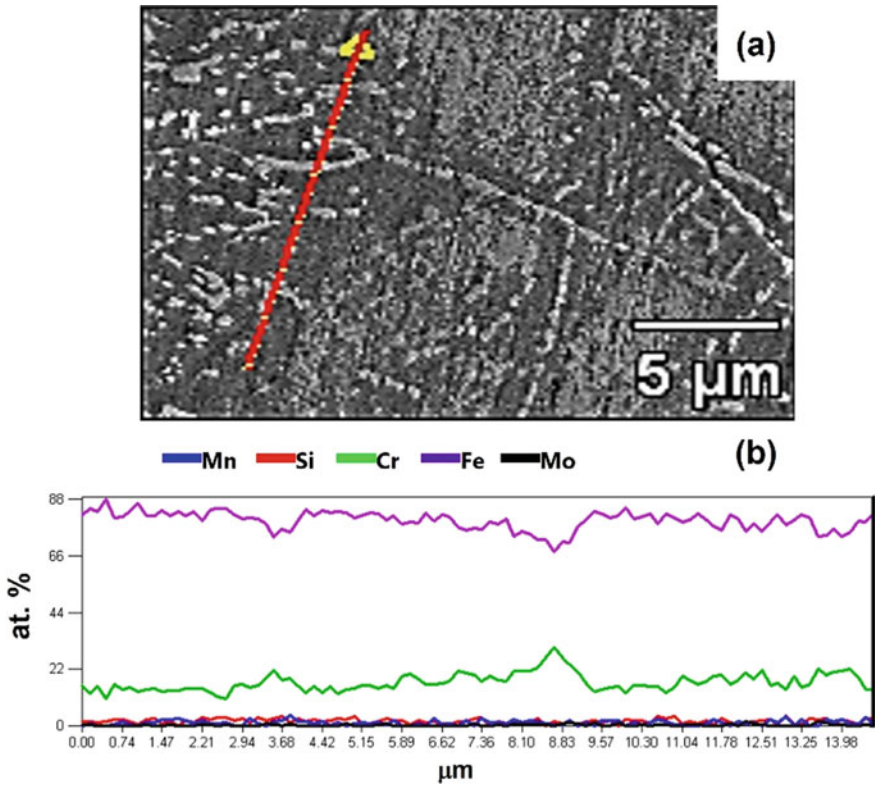

Fig. 4 **a** SEM micrograph and **b** EDX scanning analysis for the as-cast AISI 420 steel

The γ austenite phase is the second solidified one, and the last solidified phase was the cementite Fe_3C at about 1125 °C. In contrast, the solidification process of AISI 420 steel is very similar to the previously shown; however, the Cr-rich M_7C_3 carbide is formed at approximately 1275 °C instead of the cementite. The Thermo-Calc Scheil analysis also indicates that the microsegregation corresponds to a partition coefficient *k* less than 1 [3]. That is, the first formed solid, dendrites, presented a lower content of solutes than those corresponding to the last formed solid, interdendritic regions, for both as-cast steels [10].

Homogenizing Treatment

Thermo-Calc calculated results indicate that the austenizing temperature for the homogenizing treatments is approximately 900 and 1040 °C for the (a) AISI 8620 and (b) 420 steels. These temperatures are in a single-phase region, austenite, and they are suitable for the homogenizing treatment of steels.

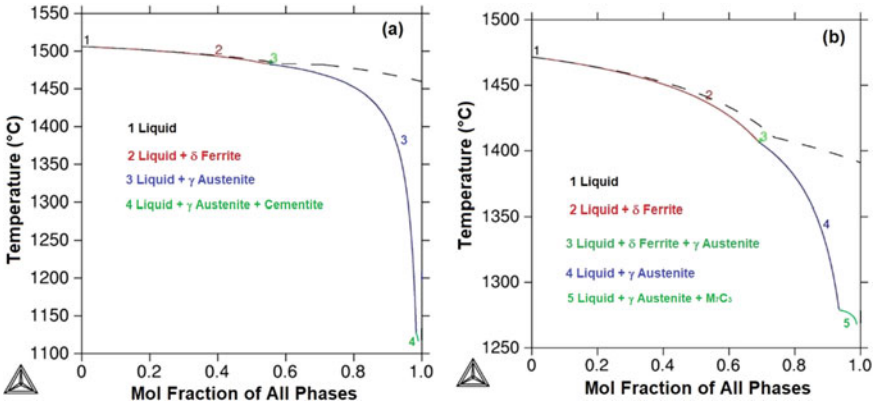

Fig. 5 Thermo-Calc Scheil analysis for the **a** AISI 8620 and **b** 420 steels

The TC-Dictra results for the simulation of the homogenizing treatment are shown in Fig. 6a, b for the as-cast (a) AISI 8620, and (b) AISI 420 steels. The distance between the interdendritic zone and the center of dendrite was approximately 10 μm. The concentration profiles become flat with the aging time. The homogenizing time to obtain a uniform chemical composition was 8×10^4 s at 9000 °C for the as-cast AISI 8620. In contrast, a time of 7×10^4 s was enough for homogenizing at 1040 °C the chemical composition of the as-cast AISI 420 steel.

Figure 7a, b show the OM micrographs of the homogenized AISI 8620 and 420 steels. The microstructure is uniform for both steels compared to that of Fig. 1a, b. The principal microconstituent is ferrite with different carbides for both steels. This fact agrees well with the Thermo-Calc results, which show the presence of ferrite,

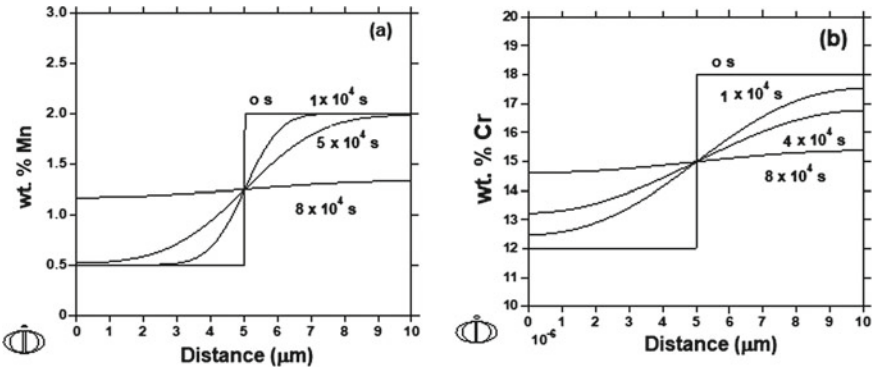

Fig. 6 TC-Dictra simulation of the homogenizing treatment for different times of **a** AISI 8620 and **b** AISI 420 steels

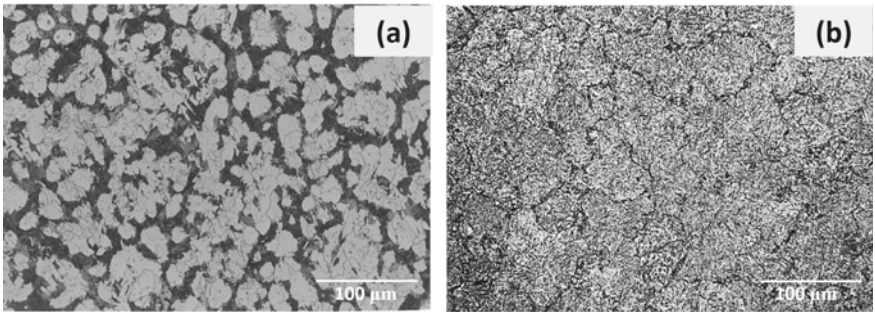

Fig. 7 OM micrographs of the homogenized **a** AISI 8620 and **b** AISI 420 steels

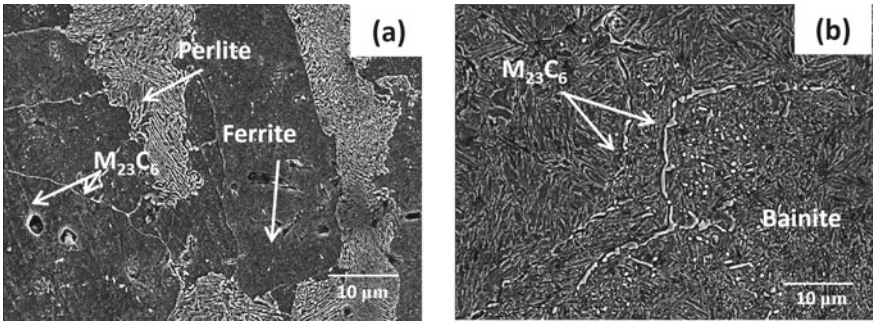

Fig. 8 SEM micrographs of the homogenized **a** AISI 8620 and **b** AISI 420 steels

cementite, and Cr-rich $M_{23}C_6$ carbide in equilibrium conditions. The SEM micrographs corresponding to Fig. 7a, b are shown in Fig. 8a, b, respectively. Figure 8a shows the presence of ferrite, pearlite, and $M_{23}C_6$ carbides, while Fig. 8b indicates the existence of bainite, ferrite + cementite, and Cr-rich $M_{23}C_6$ carbides.

Mechanical Properties

The homogenizing treatment causes a homogeneous chemical composition, and the steel hardness is expected to decrease. In the case of the AISI 8620, the as-cast condition presented 26 ± 2 HRC. In contrast, the homogenized steel has a hardness of 88 ± 2 HRB, approximately equal to 10 HRC. On the other hand, the hardness for the as-cast AISI 420 steel was 52 ± 2 HRC, and it decreased to 45 ± 2 HRC after homogenizing. This softening of the homogenized steels is promoted by more

uniform chemical composition and distribution of the microconstituents. The homogenizing treatment is expected to contribute obtaining better mechanical properties in the subsequent heat treatment, carburizing process for the AISI 8620 steel, and quenching and tempering for the AISI 420 steel [1, 2].

Conclusions

A study of the homogenizing treatment of the AISI 8620 and 420 steel was conducted, and the conclusions are summarized as follows:

1. The microstructure evolution developed during the heat treatment of these steels is consistent with the Thermo-Calc calculation.
2. TC-Dictra enables us to establish the parameters for the homogenizing treatment, 900 °C and 8×10^4 s for the as-cast AISI 8620 steel and, 1140 °C and 7×10^4 for the as-cast AISI 420 steel.
3. The microconstituent of the as-cast steels were ferrite, cementite, and Cr-rich carbides for both steels. On the other hand, the homogenized AISI 8620 steel shows the presence of ferrite, pearlite, and $M_{23}C_6$ carbides. In contrast, bainite (ferrite + cementite), and $M_{23}C_6$ carbides are present for the other as-cast steel.
4. The homogenizing treatment, as expected, promoted the decrease in hardness for the as-cast steels because of the microstructure and chemical composition homogenization.

Acknowledgements The authors wish to thank the financial support from SIP-COFAA-IPN and CONACYT A1-S-9682.

References

1. Erdogan M (2003) The effect of martensite volume fraction and particle size on the tensile properties of a surface-carburized AISI 8620 steel with a dual-phase core microstructure. Mater Charact 49:445–454
2. Barlow L, Toit M (2012) Effect of austenitizing heat treatment on the microstructure and hardness of martensitic stainless steel AISI 420. J Mater Eng Perform 2:1327–1328
3. Porter DA, Easterling KE (1992) Phase transformations in metals and alloys. Chapman and Hall, UK
4. Totten GE (2006) Steel heat treatment handbook: metallurgy and technologies. Taylor & Francis, USA
5. Andersson JO, Helande T, Höglund L, Shi P, Sundman B (2002) Thermo-Calc and DICTRA, computational tools for materials science. Calphad 26:276–300
6. Borgentam A, Engstrom A, Hoglund AJ (2012) DICTRA, a tool for simulation of diffusional transformations in alloys. J Phase Equilib 21:269–271
7. ASTM (2016) ASTM E18/E18M-16a, standard test methods for Rockwell hardness of metallic materials

8. Thermo-Calc software 2022b/tcfe11 data
9. Thermo-Calc Dictra software 2022b/mobfe6 data
10. Lippard HE, Campbell CE, Björklind T, Borggren U, Kellgren P, Dravid VP, Olson GB (1998) Microsegregation behavior during solidification and homogenization of AerMet100 steel. Metall Mater Trans B 29:205–207

Improving the Reduction Swelling Behavior of Fired Hematite Pellets by Increasing Basicity

Deqing Zhu, Bohua Li, Jian Pan, Zhengqi Guo, Congcong Yang, and Siwei Li

Abstract Oxide pellets are widely regarded as high-quality raw materials for BF ironmaking and direct reduction iron processes due to their excellent strength, performance and environmental properties. The decrease in the availability of magnetite resources has made the steel industry increasingly relying on hematite pellets. Therefore, understanding the reduction behavior, especially the swelling mechanism, and improving the reduction behavior of hematite pellets in coal-based reduction processes is of paramount importance. In this study, high grade hematite pellets were selected as the raw material, and the basicity was adjusted for the evaluation of coal-based reduction behavior. The results showed that natural basicity hematite pellets could achieve a maximum reduction expansion of 55.20%. Increasing the pellet basicity significantly improved the post-reduction swelling, ultimately leading to normal swelling, with a metallization rate exceeding 94%. Through mineral analysis and microscopic morphology analysis, it was found that an increase in basicity leads to a denser grain structure, reducing the reaction rate and thus decreasing the strain forces generated during reduction. Additionally, the growth of iron grains results in the formation of a denser iron layer after reduction, further lowering the RSI (Reduced Swelling Index).

Keywords Basicity · High grade hematite · Direct reduction · Reduction swelling index

Introduction

Fired oxidized pellets, as an essential raw material for BF iron making with high grade and excellent reducibility, play a crucial role in optimizing the furnace burden composition. Additionally, they enhance productivity and reduce production cost by reducing the amount of coke required and slag volume [1]. In recent years, due to the

D. Zhu · B. Li (✉) · J. Pan · Z. Guo · C. Yang · S. Li
School of Minerals Processing and Bioengineering, Central South University, Changsha 410083, China
e-mail: lbh205601052@csu.edu.cn

Z. Peng et al. (eds.), *Characterization of Minerals, Metals, and Materials 2024*, The Minerals, Metals & Materials Series, https://doi.org/10.1007/978-3-031-50304-7_49

decreasing availability of high-quality magnetite and rising prices, there has been a growing trend of utilizing more hematite as raw material for pellet production [2]. The limited application of hematite pellets can be attributed to the poor inherent characteristics of hematite raw materials, such as high roasting temperature requirements and tendencies for adhesion and high reduction swelling rate [3]. The direct reduction iron (DRI) is a high-quality raw material for steelmaking. With abundant coal resources in China, coal-based reduction process has huge application potention [4]. In this study high-grade hematite pellets were used as raw materials and a comparative analysis of the metallization rate and reduction swelling rate of the pellets were conducted. The reduction bahavior of the fired pellets was improved by adjusting the basicity and optimizing process parameters, and the mechanism was revealed.

Raw Materials and Experiment

Materials

In this study, two types of fired pellets were prepared from high grade hematite concentrate, they exhibited a compressive strength of approximately 2500 N per pellet and size ranging from 10 to 13 mm.

The primary chemical compositions of these fired pellets with two different basicity levels are presented in Table 1, Pellets P0 has natural basicity(0.037), while P0.2 possesses 0.20 basicicty.

As observed from Table 1, both types of fired oxidized pellets with different basicity levels exhibit iron grades exceeding 67%. With increasing basicity, the calcium oxide content gradually rises, leading to a slight decrease in iron grade, while other chemical components show minimal differences. The alkali metals (K_2O, Na_2O) in the two types of oxidized fired pellets have low contents, with the highest levels not exceeding 0.009 and 0.073%. The ferrous content remains below 0.56%. This indicates complete oxidation. Furthermore, the impurity content, including gangue minerals, is low, making them high-grade hematite pellets suitable for coal-based reduction. The increase in basicity results in a decrease in porosity.

The selected reducing agent is Shenfu coal, and its industrial analysis is presented in Table 2.

Table 1 The primary chemical compositions and porosity of fired oxidized pellets with different basicity levels/wt%

Pellets types	Fe_{total}	FeO	SiO_2	Al_2O_3	CaO	MgO	S	P	K_2O	Na_2O	Porosity
P0	67.26	0.56	1.62	1.17	0.06	0.083	0.0024	0.0530	0.0090	0.073	27.37
P0.2	67.19	0.53	1.30	1.27	0.26	0.080	0.0021	0.0050	0.0081	0.068	22.96

Table 2 Proximate analysis of reductant coal/wt%

Index	FC_{ad}	V_{ad}	A_{ad}	M_{ad}	St_{ad}
Content	58.12	30.81	5.39	5.68	0.34

FC_{ad}—Air dry base fixed carbon; V_{ad}—Air-dried base volatiles; A_{ad}—Air dry basis ash; *Mad*—Air dry basis moisture; St_{ad}—Air dry base total sulfur

The study [5] indicates that for direct reduction, coal is generally required to have a fixed carbon content exceeding 50%, a volatile matter content of around 30%, ash content below 10%, and total sulfur content not exceeding 1%. As indicated in Table 2, Shenfu coal meets all these requirements. Therefore, Shenfu coal is found to be suitable as a reducing agent in this research.

Experimental

Reduction of Fired Pellets

The coal-based reduction roasting experiments were conducted in a muffle furnace. To prepare 100 g of the required fired oxidized pellets, uniform and crack-free pellets were carefully selected. The experiment involved weighing the necessary Shenfu coal and the prepared oxidized fired pellets, loading them together in a crucible. Approximately one-third of the required Shenfu coal was placed in the lower part of the crucible, followed by the placement of the fired pellets on top of the coal, and then the remaining Shenfu coal was load to completely cover the fired pellets. After reaching the roasting time, the hot samples were removed and placed in a nitrogen gas chamber to coal and preventing oxidation. They were then cooled down to room temperature and retrieved to obtain the reduced products. The metallization rate and reduction swelling index (RSI) were measured.

The metallization rate of the reduced pellets is calculated by sampling and analyzing the mass fractions of total iron and metallic iron within the reduced pellets, using Formula (1):

$$\eta\mathrm{Fe} = \mathrm{Fe_{metal}}/\mathrm{Fe_{total}} \times 100\% \tag{1}$$

where ηFe is the metallization rate of the reduced pellets, %; $\mathrm{Fe_{metal}}$ is the mass fraction of metallic iron in the reduction product, %; $\mathrm{Fe_{total}}$ is the mass fraction of total iron in the reduced pellets, %.

The reduction swelling rate is measured using the wax sealing method to determine the volume of pellets before and after reduction. Firstly, before reduction, the volume of fired oxidized pellets is determined using the drainage method. After drying, the reduction experiment is conducted, and the resulting reduced pellets are coated with

wax. Then, the volume is measured again using the drainage method. The reduction swelling is calculated using the Formula (2):

$$\mathrm{RSI} = (V_0 - V_1)/V_0 \tag{2}$$

where RSI is reduction swelling index, %; V_0 is the initial volume of the oxidized pellets, cm^3; V_1 is the volume after reduction of the pellets, cm^3.

Mechanism of the Direct Reduction of Fired Pellets

The mechanism of the direction reduction of fired pellets was demonstrated by using optical microscopy, XRD, optical microscopy and EDS.

Observing and analyzing the mineral phase of fired pellets by using optical microscopy (Leica DMLP).

X-ray powder diffraction analysis (XRD) was employed for phase analysis of the reduction products and similar materials. The scanning range was set between 10° and 80°/2θ, with a scanning rate of 2° per minute, using a Cu anode target with a wavelength of 1.54056 Å.

The scanning electron microscope model used was Zeiss Sigma 300, and the energy-dispersive spectrometer model was Oxford XMAX20.

Results

The Influence of the C/Fe Mass Ratio on the Direct Reduction Behavior of Fired Pellets

From Fig. 1, it can be observed that an increase in the C/Fe mass ratio leads to a gradual improvement in the metallization rate of the fired oxidized pellets. Notably, when C/Fe increases from 0.4 to 0.8, the increase in metallization rate is most significant, and then maintains a slow upward trend. Taking the P0 pellets as an example, when C/Fe increases from 0.4 to 0.8, the metallization rate increases from 90.27 to 93.26%, a substantial improvement of 2.99% was observed. When it continues to increase to 2.0, the metallization rate is 95.71%. The RSI of the fired oxidized pellets decreases significantly with the increase in the C/Fe mass ratio. For instance, in the case of P0 pellets, as C/Fe increases from 0.4 to 2.0, the expansion rate decreases from 45.50% to 26.23%, indicating a decline of 19.27%. Similarly, P0.2 pellets show a decrease in swelling rate by 20.00%. This suggests that appropriately increasing the C/Fe mass ratio is beneficial for improving the metallization rate of the fired pellets and reducing the swelling rate.

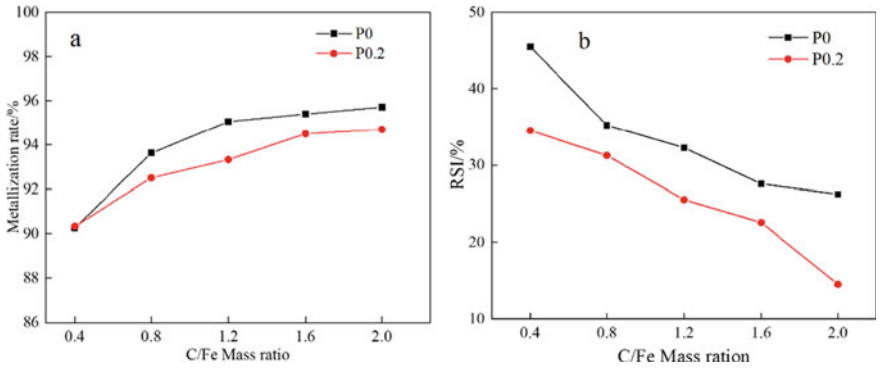

Fig. 1 The effect of C/Fe mass ratio on direct reduction performance at 1050 °C for 120 min (**a** metallization rate, **b** RSI)

The Impact of Reduction Temperature on the Direct Reduction Performance

Under the conditions of a fixed coal-to-ore mass ratio of 2:1 and a reduction time of 120 min, using bulk addition of coal and pellets in an isothermal reduction process, the influence of the reduction temperature on the metallization rate and swelling rate of the reduced pellets was investigated.

From Fig. 2, it can be seen that the metallization rate of the two different basicity pellets increases significantly with the rise in temperature. At 950 °C, both types of pellets exhibit metallization rates exceeding 90%, and as the temperature increases to 1050 °C, the metallization rate surpasses 94%. The temperature increase not only enhances the concentration of CO in the system but also promotes the progress of iron oxide reduction reactions, leading to an increase in the metallization rate of the pellets.

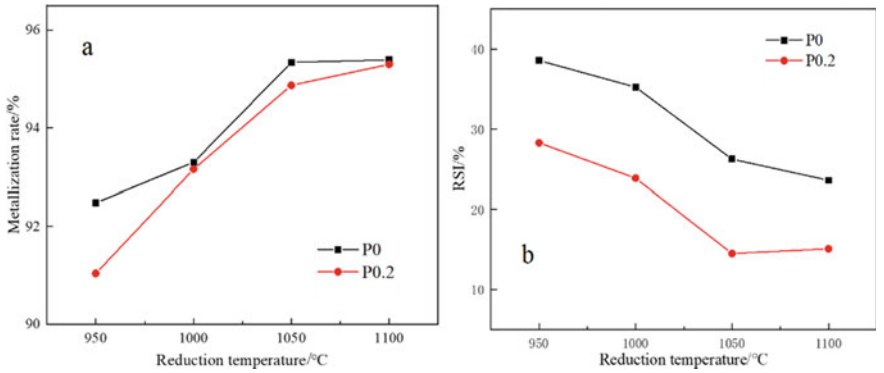

Fig. 2 The impact of reduction temperature on pellet performance (**a** Metallization rate, **b** RSI)

The reduction swelling index (RSI) of the two different basicity pellets exhibits a slight increase followed by a decrease trend with the rise in temperature. At a reduction temperature of 1050 °C, the pellet's RSI notably decreases. Specifically, the RSI for P0.2 pellets reaches the valley at 14.52%, indicating normal expansion. Further increasing the reduction temperature to 1100 °C results in a decrease in the swelling rate for P0 pellets to 23.60%, while the expansion rate for P0.2 pellets slightly increases to 15.11%. Therefore, an increase in basicity of fired pellets can depress the reduction swelling rate.

Discussion

Optical Microstructure Analysis

Figure 3 illustrates the microstructure of fired hematite pellets with various basicitylevels. As has been established in many researches, the consolidation mechanism of fired hematite pellets with natural basicity ($R = 0.037$) is mainly the solid diffusion and recrystallization of Fe_2O_3 [6, 7]. The Fe_2O_3 particles within the P0 pellets are observed to be well-dispersed and fine, while simultaneously exhibiting a higher pore density with relatively large pores. The increase in pore density is beneficial for accelerating the reduction rate but can impede control over pellet swelling. With an increase in the basicity of P0.2 pellets, a small amount of liquid phase is generated, thereby enhancing solid mass diffusion and promoting the growth of Fe_2O_3 grains [8]. Consequently, iron particles become more agglomerated and the pore density decreases. The dense iron grains help to reduce the RSI of the pellets.

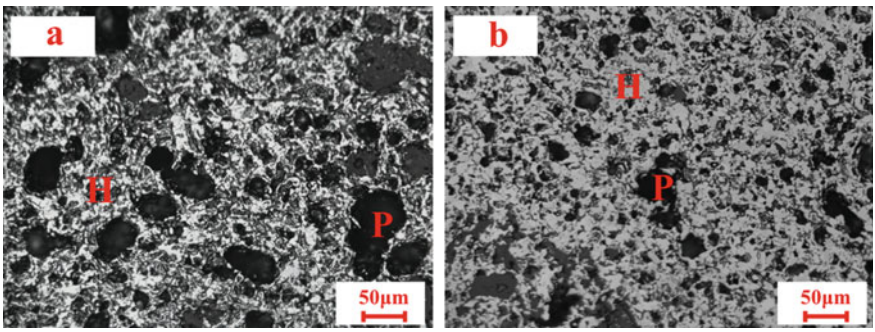

Fig. 3 Optical microstructure of P0 and P0.2 fired pellets (H—Hematite, P—Pore, **a** P0, **b** P0.2)

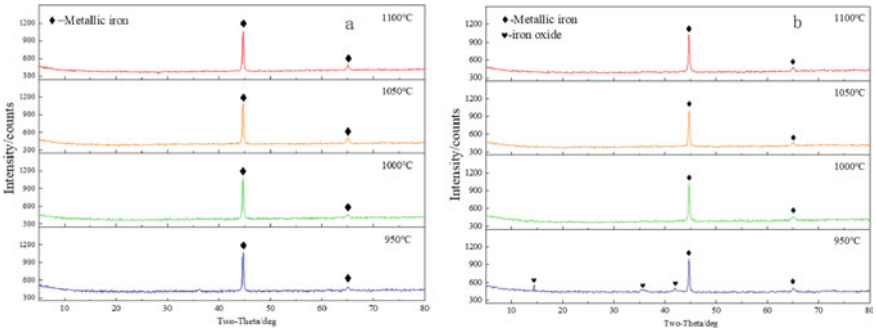

Fig. 4 X-ray diffraction analysis of the two types of basicity-reduced pellets at different reduction temperatures (120 min, C/Fe = 2, **a** P0, **b** P0.2)

The Phase Compositions

From Fig. 4, it can be observed that at a reduction temperature of 950 °C, P0.2 pellets still contain some unreacted iron oxides at the end of the reduction process. In the case of P0 pellets, only metallic iron is present after reduction. This indicates that P0.2 basicity pellets require a higher reaction temperature or reaction time for complete reduction. As the reduction temperature is further increased to 1000–1100 °C, after reduction at these temperatures, the main product for all two types of high-grade pellets is metallic iron. The diffraction peak of P0 pellet metal iron is slightly higher than that of P0.2 pellet, indicating that P0 pellet reduction is more thorough, which is consistent with the results in Fig. 2a.

Microstructure and Minerals Compositions of Reduced Pellets

As shown in the EDS analysis of P0 pellets in Fig. 5a, after reduction, the metallic iron phase formed inside the fired pellets is highly pure, with virtually no other impurity components. However, there are still other slag phases present inside the pellets, as indicated by point 2 in the image. The outermost slag phase of the pellets consists primarily of ferrous orthosilicate (Fe_2SiO_4), followed by components such as aluminosilicates, as shown in point 3. The impurity composition in the innermost part of the pellets is mainly composed of vein minerals, with silicon dioxide as the primary component.

After reduction of P0.2 pellets, as shown in Fig. 5b, a highly pure metallic iron phase is present with almost no other impurity components, indicating a relatively high degree of reduction. However, other slag phases are still distributed within the pellets, as indicated by point 4 in Fig. 5b. After reduction of P0.2 pellets, the composition of the slag phase in both the inner and outer layers is similar, primarily composed of ferrous orthosilicate (Fe_2SiO_4). Due to the addition of Ca^{2+}, as shown in

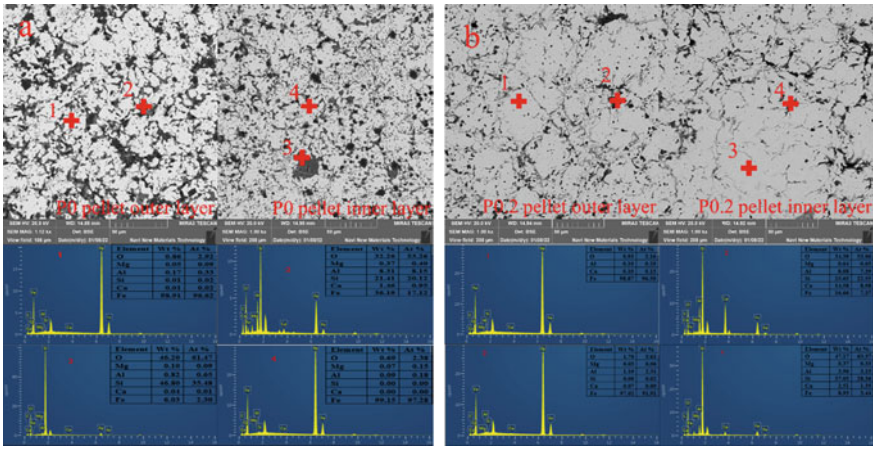

Fig. 5 SEM and EDS analysis of the two types of pellets with different basicity levels after reduction at 1050 °C for 120 min (**a** P0, **b** P0.2, Magnification: 1000×)

point 2 in Fig. 5b, the presence of calcium ferrites and calcium aluminosilicates can be observed. At the same time, it can be observed from the graph that an increase in basicity leads to a tighter connection between the metallic iron grains in the oxidized pellets after reduction, ultimately softening and forming a metallic iron layer, thereby reducing the reduction swelling rate [9, 10], having better anti-expansion ability. The formation of a metallic iron layer reduces porosity, leading to a decrease in reduction rate and, consequently, a reduction in internal stress during the reduction process [11]. All of these factors create favorable conditions for reducing expansion.

Conclusion

(1) Increasing the C/Fe ratio and raising the reduction temperature both contribute to improving the metallization rate and reducing the swelling rate of high-grade hematite pellets during coal-based reduction. Among these factors, a C/Fe mass ratio of 2 and a reduction temperature of 1050 °C appear to be most suitable.

(2) The reduction rate of calcium ferrite is lower than that of iron oxide, and an increase in basicity leads to a reduction in the reduction rate of P0.2 pellets. At a reduction temperature of 950 °C, the reaction is incomplete, and iron oxide persists. However, upon raising the reduction temperature, the same reduction product as that of P0 pellets is FeO.

(3) Mineralogical and microscopic analysis has revealed that an increase in basicity leads to a reduction in the porosity of fired pellets, which is conducive to the connection and growth of iron grains after reduction. This tighter connection

of reduced sintered iron grains reduces internal stress. Phase analysis indicates that the increase in basicity does not alter the reaction products after reduction.

References

1. Wang XD, Jin YL (2021) Strategy analysis and testing study of high ratio of pellet utilized in blast furnace. Iron Steel 56(05):7–16 (in Chinese). https://doi.org/10.13228/j.boyuan.issn0449-749x.20210081
2. Sha YZ, Maarten G, Song YS (2019) Technical and economic analysis of blast furnace operation with high pellet ratio in China. Ironmaking 38(06):1–5 (in Chinese)
3. Tian JQ, Qing GL, Liu CJ, Li YX (2018) Production experiment of low silica alkaline pellet by limestone. China Metall 28(04):13–16. https://doi.org/10.13228/j.boyuan.issn1006-9356.20170272. (in Chinese)
4. Xun HJ, Shi XF, Zhang YY, Wan XY, Cao XE (2015) Experiment of coal-based direct reduction of high phosphorus oolitic hematite. J Iron Steel Res 27(12):30–35. https://doi.org/10.13228/j.boyuan.issn1001-0963.20140294. (in Chinese)
5. Chen J (2007) Non coking coal metallurgical technology. Chemical Industry Press. ISBN:9787502593223 (in Chinese)
6. Wu H, Chun TJ, Wang P, Zhou S, Zhou TB (2022) Consolidation mechanism of fluxed hematite pellets. J Iron Steel Res Int 29(10):9. https://doi.org/10.1007/s42243-022-00744-0
7. Sarkar A, Sinha O P, Mandal A K (2016) Utilization of lime fines as an effective binder as well as fluxing agent for making fluxed iron ore pellets. J Inst Eng (India), Ser D. Metallur Mater Eng Mining Eng. https://doi.org/10.1007/s40033-015-0079-3
8. Dwarapudi S, Ranjan M (2010) Influence of oxide and silicate melt phases on the RDI of Iron ore pellets suitable for shaft furnace of direct reduction process. ISIJ Int 50(11):1581–1589. https://doi.org/10.2355/isijinternational.50.1581
9. Guo YF, Liu K, Chen, F, Wang S, Zheng FQ, Yang LZ, Liu YZ (2021) Effect of basicity on the reduction swelling behavior and mechanism of limestone fluxed iron ore pellets. Powder Technol Int J Sci Technol Wet Dry Particulate Syst 393291-300. https://doi.org/10.1016/j.powtec.2021.07.057
10. Qing GL, Wang CD, Hou EJ, Liu HS, Ma L, Wu K (2014) Compressive strength and metallurgical property of low silicon magnesium pellet. J Iron Steel Res 26(04):7–12. https://doi.org/10.13228/j.boyuan.issn1001-0963.2014.04.010. (in Chinese)
11. Shi Y, Zhu DQ, Pan J, Guo ZQ, Lu SH, Xu MJ (2022) Improving hydrogen-rich gas-based shaft furnace direct reduction of fired hematite pellets by modifying basicity. Powder Technol 408. https://doi.org/10.1016/J.POWTEC.2022.117782

Influence of Ordinary Portland Cement (OPC) During Collectorless Flotation of Galena

Martín Reyes Pérez, Saúl García Pérez, Ramiro Escudero García, Iván A. Reyes Domínguez, Miguel Pérez Labra, Francisco Raúl Barrientos Hernández, Julio Cesar Juárez Tapia, Gustavo Urbano Reyes, and Mizraim U. Flores Guerrero

Abstract Worldwide, galena PbS is the most abundant mineral sulfide for obtaining metallic lead; however, mineral deposits are frequently associated with impurities that contaminate the concentrate obtained during flotation, such as pyrite or arsenopyrite. These minerals can be depressed efficiently with the addition of ordinary Portland cement (OCP); however its effect in collectorless flotation galena is unknown. In this work, the depressant action of OPC on galena flotation as a function of pH was analyzed. Under highly alkaline conditions pH 12, a % w/w cumulative flotation of galena of 71.5 is obtained with a pulp potential of − 44.2 mV, with an electrical conductivity (k) of 1246 μS/cm, the decrease in the alkaline pH of the pulp by adding sulfuric acid depresses the flotation of galena, thus, at pH 9 a separation of around 10.81% w/w was obtained, with an oxidizing potential of + 352.2 mV.

Keywords Galena · Ordinary Portland cement · Depressant · Collectorless · Flotation

M. R. Pérez (✉) · S. G. Pérez · M. P. Labra · F. R. B. Hernández · J. C. J. Tapia · G. U. Reyes
Academic Area of Earth Sciences and Materials, Autonomous University of the State of Hidalgo, Road Pachuca-Tulancingo Kilometer 4.5 Mineral de la Reforma, Hidalgo 42180, México
e-mail: mreyes@uaeh.edu.mx

R. E. García
University Michoacana of San Nicolas Hidalgo, Institute of Research in Metallurgy and Materials C.P, 45000 Morelia, Michoacán, México

I. A. R. Domínguez · M. U. F. Guerrero
Institute of Metallurgy, Autonomous University of San Luis Potosí, San Luis Potosí (SLP) 78210, México

M. R. Pérez · S. G. Pérez · R. E. García · I. A. R. Domínguez · M. P. Labra · F. R. B. Hernández · J. C. J. Tapia · G. U. Reyes · M. U. F. Guerrero
Industrial Electromechanics Area, Technological University of Tulancingo, 43642 Hidalgo, México

Z. Peng et al. (eds.), *Characterization of Minerals, Metals, and Materials 2024*, The Minerals, Metals & Materials Series, https://doi.org/10.1007/978-3-031-50304-7_50

Introduction

Galena is also known as lead glance; it is a natural lead sulfide mineral; this species of lead is the most abundant in the world; it can contain around 1–2% of silver which makes it an important source. Practically all metallic lead produced from concentrates is by the pyrometallurgical method [1]. The galena mineral (PbS) is generally associated with both metallic sulfides of economic value [2–4] and sulfide-type impurities such as pyrite [5] or arsenopyrite [6] and non-sulfide impurities such as silica, calcite, fluorite, among others. [7]. For the separation by flotation and the concentration of this mineral from the minerals that accompany it, the use of organic and inorganic chemical reagents is necessary for its activation and/or depression of the impurities [4].

Some of these inorganic depressant reagents are, for example, chromate, potassium dichromate or cyanide [8, 9]. However, they are harmful to humans and pollutants of the environment. On the other hand, organic reagents have been used for the depression of galena flotation, organic species show some advantages compared to inorganic depressants such as the fact that they are biodegradable and environmentally friendly, but they are more expensive compared to inorganic ones [3].

Galena depressant organic species such as sodium polyacrylate, humic acid, Dextrin [10], carboxyl methyl cellulose, alginate, and poly aspartate have been widely studied. These are some of the most used reagents for galena depression. Besides it requires the surface oxidation of galena to carry out an efficient depression in the presence of these reagents [11].

For the depression of sulfides without economic value, ordinary Portland cement (OPC) has been tested, and this is a material composed of different phases: tricalcium silicate, dicalcium silicate, tricalcium aluminate, and tetra calcium aluminum ferrite, which hydrate quickly, the species ettringite ($3Ca_6Al_2\,(SO_4)_3(OH)_{12}{\cdot}26H_2O$), formed in a shorter time may be responsible for the depression of gangue minerals [12]. It has been mentioned that, due to the crystalline characteristics of this phase, it can incorporate anionic or cationic ions into its structure through sorption or substitution of ions such as Ca^{2+}, Al^{3+}, y OH^- y $SO4^{2-}$, and the latter (the sulfate ion), which can be a substitute in the structure of ettringite, exchanged its place for metal oxides such as $AsO4^{3-}$, in sulfurous species such as arsenopyrite, and depressed it [13].

It has been seen that the use of Portland cement can depress gangue metal sulfides such as arsenopyrite, the presence of 400 mg/L of OPC depresses the flotation of FeAsS by up to 54% (w/w) this at a pH 12, and a potential + 78 mV pulp. The addition of OPC releases ions anions and other charged entities that modify the electrical conductivity that reached a value of 225 μS/cm [14]. OPC acts well as a depressant of gangue mineral sulfides, but how it affects mineral sulfides of interest such as galena, among other valuable mineral sulfides, as a function of pH and pulp potential remains uninvestigated. Therefore, this research focuses on evaluating the effect of added ordinary Portland cement OPC to the flotation pulp of a single galena

mineral on a wide variety of pH values, to measure the flotation of PbS under these conditions.

Experimental Methodology

To evaluate the effect of ordinary Portland cement (OPC) on the collectorless flotation of a single galena mineral as a function of pH, a mineral in physical appearance of a single majority phase of galena was used, the mineral prior to the tests. Flotation was characterized by X-ray diffraction (XRD) in a Bruker model D8 equipment with the following characteristics: Cu radiation kα $\lambda = 1.5406$ Å, voltage 30 kV, intensity: 20 mA, Scanning speed in 2° (2 Theta), Scintillation counter with scanning beam from 10° to 90°, Passage size and time: 0.02, 0.65 respectively.

The semi-quantitative chemical characterization and morphological analysis of the galena mineral particles was carried out in a JEOL brand JSM 5900 LV scanning electron microscope (SEM), with magnifications of up to 500,000X, equipped with a back-dispersive energy detector OXFORD brand.

The mineral was pulverized in an agate mortar, the particle size was analyzed in a Beckman Coulter laser diffraction particle size analyzer (ATP), Model LS I3320. The OPC used for the collectorless flotation tests was a commercial one from Mineral de la Reforma, Hidalgo, Mexico. Methyl isobutyl carbinol (MIBC) was used as frother agent at a concentration of 60 mg/L; no collector was used. To vary the pH of the pulp, concentrated sulfuric acid (H2SO4) or a 0.1 M solution and, 0.1 M sodium hydroxide, was used as needed. The pH values evaluated were the natural pH that resulted from the addition of OPC pH 11, 12, 9 and 8 in all tests where deionized water was used.

For the flotation tests, a stainless steel Denver laboratory celd of 1 L capacity was used, equipped with a diffuser and an impeller attached to the bottom of the cell, as well as 720 mg/L of OPC, the values of the pH and the oxide reduction potential (ORP) mV were measured used a thermo Scientific Orion 3 Star potentiometer equipped with a Ross ultra triode platinum pH electrode provided with a temperature sensor. In addition, electrical conductivity was measured using a hatch brand conductivity meter. The ORP values were expressed and graphed in reference to the standard hydrogen electrode (SHE) by adding + 242 mV to the measured ORP value in each flotation test using 8 g of finely pulverized ore.

The conditioned flotation pulp was carried out inside the flotation cell, 1 L of water, the frother agent, the OPC and the mineral were added, in this sequence, and the pH values evaluated were 12, 11, 9 and 8. During each chemical modification of the pulp, the pH value, ORP and electrical conductivity were recorded. Once the conditioned stage was completed, the flotation test began. The collection times of the concentrate were 0.5, 1, 2, 4, 6, 8 and 10 min of flotation. Figure 1 shows the flow chart of the experimental procedure.

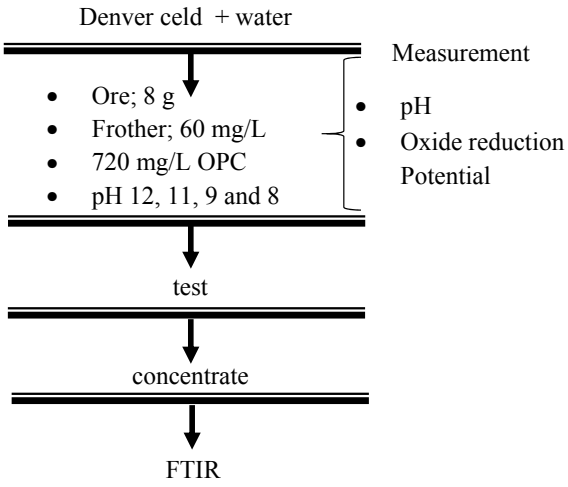

Fig. 1 Flow sheet of the experimental procedure

The floated pulp contained the galena particles was received in previously weighed plastic containers, the wet concentrate was dried at room temperature and by difference in the weight obtained, the quantity in grams of floated mineral was obtained at each proposed time, and the percentage value in flotation weight % F (w/w) relative to the feed ore was added, where the concentrates were weighed used a precision analytical balance.

Results and Discussion

Galena mineral was characterized by XRD, SEM–EDS and ATP. Figure 2 shows the diffraction pattern obtained from the galena that is observed as the only major crystalline phase, the diffraction data obtained were identified using the Match 1.1 software along with the diffraction pattern that fits with the characterized mineral sample, the reference being 96–900–8695.

Figure 3a shows a general SEM image at 1500× of the unseized galena particles, which have an irregular morphology made up of smooth surfaces and straight edges. When the mineral is pulverized, it tends to fractionate into small cubic prisms, with sizes less than 15 μm. Figure 3b presents a detailed SEM micrograph of a cubic galena particle with a magnification of 10,000X. The surface appears to have a regular morphology with adhered microparticles.

Figure 4a shows in detail a galena particle and (b) the semiquantitative microanalysis by energy dispersion and the EDS spectrum. The analysis did not detect any other metallic element, except for the characteristic elements of galena, lead 87.49%, and sulfur 12.51%. The mineral is stoichiometrically rich in metal and poor in sulfur.

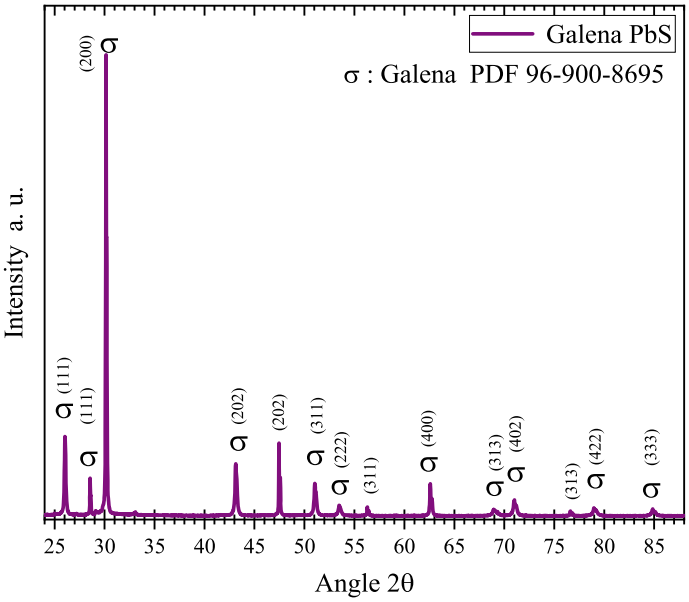

Fig. 2 X-ray diffraction pattern of galena mineral

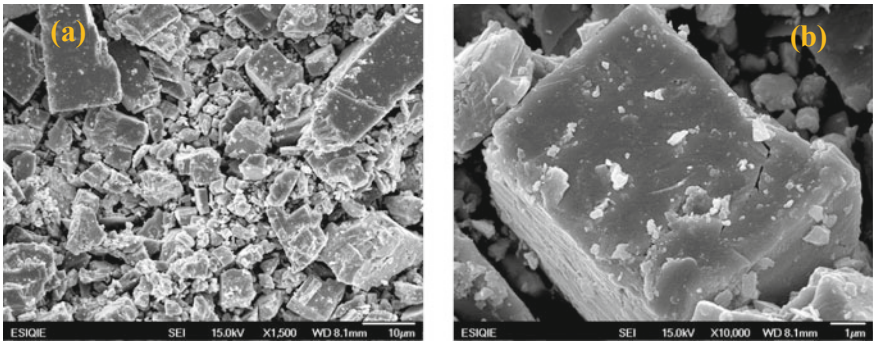

Fig. 3 SEM micrograph **a** of the unseized galena particles general image and **b** detailed image of a mineral particle

The pulverized particles were analyzed by laser diffraction in an ATP equipment. The statistical analysis obtained in the measurement presents a mean of 5.9 μm, a median of 4.7 μm and a mode of 6.4 μm. 10% are particles smaller than 1.4 μm, 25% are smaller than 2.4 μm, 50% are smaller than 4.7 μm, 75% are smaller than 8.0 μm and 90% are particles < 12.0 μm. In other words, 90% of the particles have a size between 1.4 and 12.0 μm.

Figure 5 shows the % (w/w) of cumulative flotation of galena in the presence of 720 mg/L of ordinary Portland cement at several pH values. It is observed that the

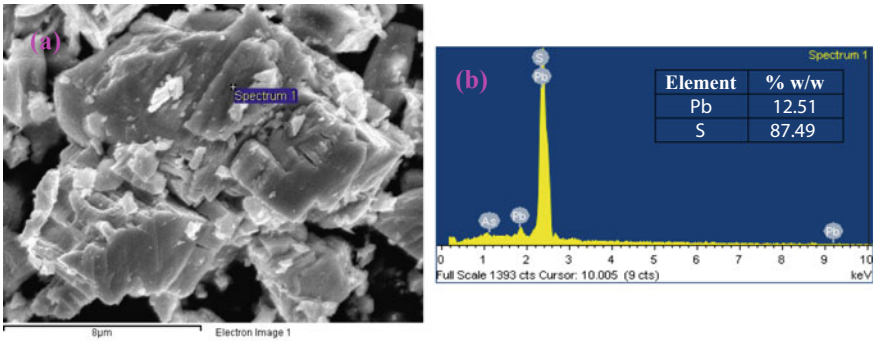

Fig. 4 **a** SEM micrograph of a galena particle in detail **b** EDS spectrum and semiquantitative chemical analysis

flotation of galena is similar whether with Portland cement or not when the pH of pulp is 9.5. I achieved separation efficiencies of 70% (w/w), while when flotation is carried out at pH 8 and 9 the galena is substantially depressed and, the % (w/w) of flotation is less than 15%.

A similar effect was previously reported where the presence of ordinary Portland cement at pH 11.7 leads to galena depression [12] however the authors do not consider the potential of the pulp. Figure 6 shows the pH record during the conditioning of the

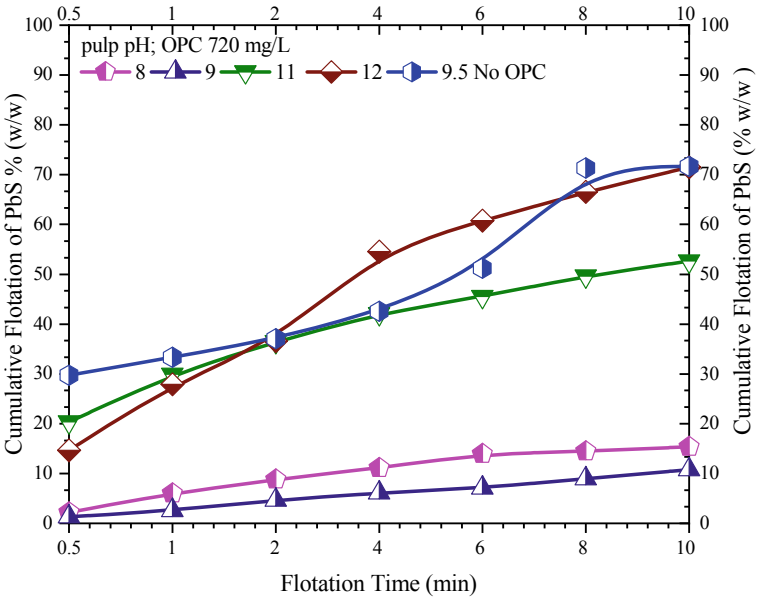

Fig. 5 % w/w cumulative flotation of galena versus time (min). In the presence of 720 mg/L OPC at several pH values

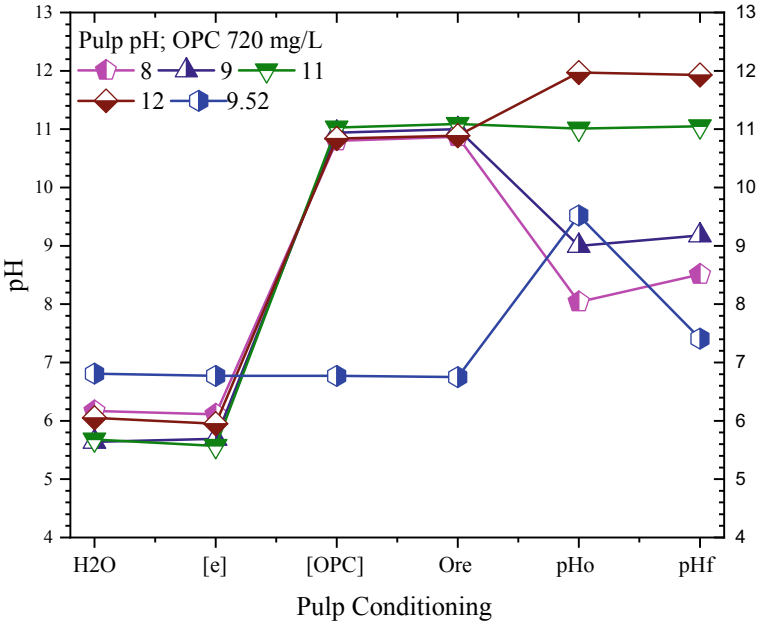

Fig. 6 Flotation pH behavior during conditioning. In the presence of OPC

flotation pulp in the presence of 720 mg/L of OPC. This gives an alkaline character to the pulp pH of 11.0, subsequently when the mineral is added, the pH does not change. Then the pH is adjusted with sulfuric acid or sodium hydroxide as appropriate.

As presented in Fig. 5, a minor pH causes the flotation of galena to decrease drastically and this is due to the variations that occur in the oxide reduction potential of the pulp, changing its condition from a reduced state, that is, from negative potentials. which have at pH 11 and 12 to oxidant potentials of up to + 352.2 mV as shown Fig. 5 at these pH values where the flotation of galena is considerably large.

Meanwhile, a change from pH 11 or 12 to pH 8 and 9 using sulfuric acid generates an oxidizing potential as seen in Fig. 7 and the galena surface is depressed, achieving flotation efficiencies of less than 15% w/w. As presented in Fig. 5, OPC can act as a surface activating agent for galena at pH 11 and 12 or a surface depressant for lead sulfide at pH 8 and 9.

This dual behavior that OPC presents is undoubtedly due to the variation in pH and this is because of the structural changes that occur to the cement particles when the pH decreases, causing their decomposition. In previous works it has been reported that the flotation of galena in the absence of OPC and at pH between 5 and 6, good flotation efficiencies of 75% are obtained [15], however, the presence of OPC and the decrease in pH causes the depression of galena. The electrical conductivity of the pulp with the addition of cement increases considerably, obtaining values of around 700 μS/cm, where the change in pH at 12, 9 and 8 increases the electrical conductivity of the flotation pulp. Figure 8 presents the behavior of the electrical

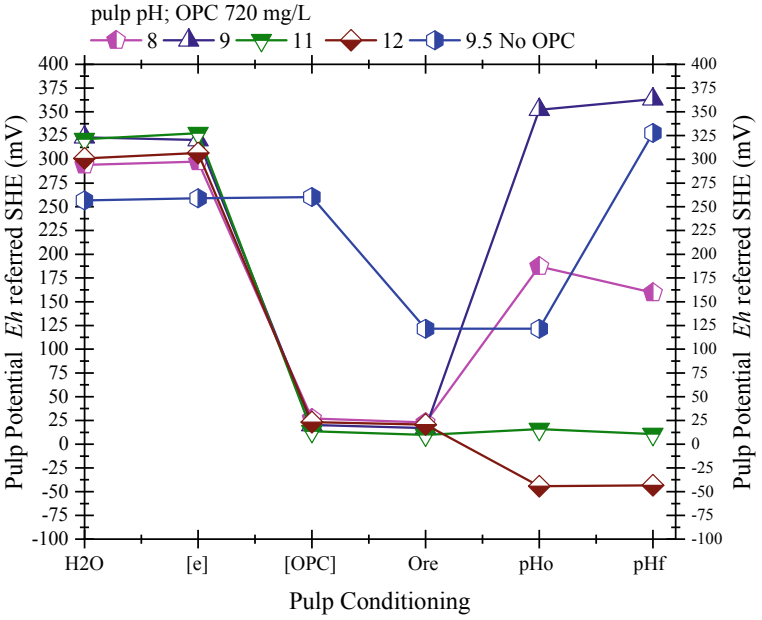

Fig. 7 Behavior of pulp potential during conditioning in the presence of OPC

conductivity K (μS/cm) of the pulp during conditioning when OPC is not used and the electrical conductivity of the pulp is substantially lower.

Conclusions

The galena flotation/depression study was carried out in the presence of ordinary Portland cement at pH 12, 11, 9 and 8. The galena mineral used for these experimental tests consisted of a single majority crystalline phase composed of lead sulfide with a semiquantitative chemical concentration of 87.49% (w/w) lead and 12.51% (w/w) sulfur. Galena is depressed in the presence of OPC if the pH of the flotation pulp is 8 and 9, lowering the alkaline pH of the pulp with sulfuric acid that causes decomposition of OPC and this causes surface depression of galena. The decrease in pH changes the oxidizing conditions of the pulp and the potential reaches values between + 352.2 and + 187.2 mV, oxidative potentials; on the other hand, alkaline pH values are generated by the addition of OPC give negative pulp potentials, that is, reducing potentials of around – 44.2 mV.

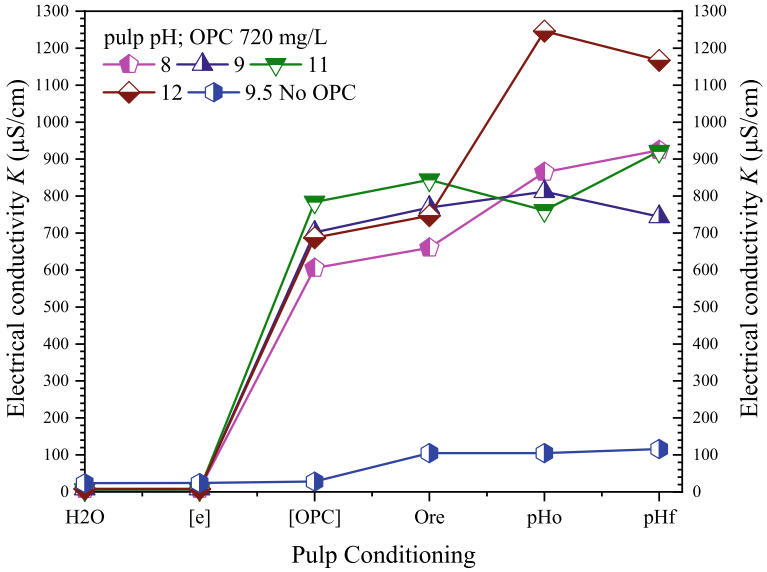

Fig. 8 Variation of electrical conductivity K (µS/cm) during pulp conditioning

References

1. Zhou Z, Wang C, Ma B, Zhang B, Liu D, Xiong H, Xu B (2023) Separation of lead sulfide from galena concentrate via two-step vacuum distillation. Vacuum 213:112155
2. Li J, Song K, Liu D, Zhang X, Lan Z, Sun Y, Wen S (2017) Hydrolyzation and adsorption behaviors of SPH and SCT used as combined depressants in the selective flotation of galena from sphalerite. J Mol Liq 231:485–490
3. Wang X, Qin W, Jiao F, Wang D (2023) The galvanic interaction enhanced the flotation separation of chalcopyrite and galena with humic acid as galena depressant. Miner Eng 201:108197
4. Bulatovic S, Wysouzil DM, Bermejo FC (2001) Development and introduction of a new copper/lead separation method in the Raura plant (Peru). Miner Eng 14(11):1483–1491
5. Jing G, Jian S, Chen J, Xu S, Sun W, Lin S, Gao Z (2023) Selective depression of pyrite with a novel thiocarbonate in a pyrite-galena flotation system. Miner Eng 202:108271
6. Wang C, Zhai Q, Liu R, Luo Y, Xie Z, Cao Z, Sun W (2023) Surface modification with hydroxyl calcium ions strengthen CMC selectively depress arsenopyrite: bridging adsorption mechanism and application in Cu-As separation. Appl Surf Sci 618:156642
7. Nowosielska AM, Nikoloski AN, Parsons DF (2022) Interactions between coarse and fine galena and quartz particles and their implications for flotation in NaCl solutions. Miner Eng 183:107591
8. Hu Y, Wu M, Liu R, Sun W (2020) A review on the electrochemistry of galena flotation. Miner Eng 150:106272
9. Prestidge CA, Ralston J, Smart SC (1993) The role of cyanide in the interaction of ethyl xanthate with galena. Colloids Surf A 81:103–119
10. Zhang J, Zhang XG, Wei XX, Cheng SY, Hu XQ, Luo YC, Xu PF (2022) Selective depression of galena by sodium polyaspartate in chalcopyrite flotation. Miner Eng 180:107464
11. Bolin NJ, Laskowski JS (1991) Polysaccharides in flotation of sulphides. Part II. Copper/lead separation with dextrin and sodium hydroxide. Int J Mineral Process 3(1–4): 235–241

12. Oh JH, Yu TS, Min JH, Yim MY, Min BH (1977) The effect of Portland cement of flotation of copper–lead bulk concentrate. J Korean Inst Min 14:207–211
13. Kumarathasan P, McCarthy GJ, Hassett DJ, Pflughoeft-Hassett DF (1989) Oxyanion substituted ettringites: synthesis and characterization; and their potential role in immobilization of As, B, Cr, Se and V. MRS Online Proc Libr (OPL) 178:83
14. Reyes M, Martínez Rojo E, Escudero R, Patiño F, Reyes IA, Flores MU, Barrientos FR (2023) Depression of arsenopyrite during collectorless flotation in presence of aqueous metal ions and inorganic compounds. Minerals 13(9): 1200
15. Reyes M (2020) El Papel depresor del pH durante la flotación sin colector de mineral de galena conteniendo esfalerita. Tópicos de Investigación en Ciencias de la Tierra y Materiales Publicación anual 7(7):1–7

Intensifying Acid Leaching Behaviors of Fe, Ni, and Cr from Stainless-Steel Scraps via Ultrasonic Treatment

Yifei Zhang, Qianqian Chu, Bingbing Liu, Guihong Han, and Yanfang Huang

Abstract Stainless steel has a broad application in various areas of the national economy, while a mass of stainless-steel scraps is generated during the abrasive machining process. These scraps are rich in metallic ingredients such as Fe, Ni, and Cr, which shows an extremely comprehensive recovery value. Due to good plasticity and ductility, the stainless-steel scraps are hard to grind to fine particles. The low dissolution efficiency of coarse particles limits the efficient utilization of stainless-steel scraps. This work provides a clean and intensifying acid leaching method of Fe, Ni, and Cr from stainless-steel scraps via ultrasonic treatment. Under the conditions of ultrasound power of 540W, H_2SO_4 concentration of 3 mol/L, leaching time of 15 min, temperature of 30 °C, and liquid-to-solid ratio of 20:1, the leaching efficiencies of Fe, Ni, and Cr are 99.93, 99.91, and 99.92%, which are much higher than those with the conventional leaching process.

Keywords Stainless-steel scraps · Metals recovery · Acid leaching · Ultrasound-assisted · Intensifying

Introduction

Stainless steel, which has the advantages of good corrosion resistance, high ductility, and strong plasticity, is widely used in various fields such as petrochemical, aerospace, medical equipment, and so on. However, during the abrasive machining process of stainless steel, a mass of stainless steel waste is generated due to the wear of equipment and alloy workpieces. According to relevant literature reports, the content of metallic ingredients, including Fe, Mo, Cu, Ni, and Cr in stainless-steel scraps is as high as 70 wt%, identifying its great value for recovery [1].

Y. Zhang · Q. Chu · B. Liu (✉) · G. Han · Y. Huang
School of Chemical Engineering, Zhengzhou University, Zhengzhou 450001, Henan, China
e-mail: liubingbing@zzu.edu.cn

B. Liu · G. Han · Y. Huang
Zhongyuan Critical Metals Laboratory, Zhengzhou 450001, Henan, China

Z. Peng et al. (eds.), *Characterization of Minerals, Metals, and Materials 2024*, The Minerals, Metals & Materials Series, https://doi.org/10.1007/978-3-031-50304-7_51

China is not richly endowed with mineral resources and some strategic resources such as nickel and chromium are heavily dependent on imports. Recycling and utilizing stainless-steel scraps can effectively alleviate the tense supply–demand relationship of nickel and chromium resources in China [2]. However, these stainless-steel scraps are stacked in factories and cannot be effectively utilized which is not only a waste of resources, but also a potential pollution risk to the environment. Therefore, a green and feasible method is urgently needed to retrieve the abundant stainless-steel scraps.

Because mineral oil is required to be added as a coolant during the abrasive machining process, some stainless-steel scraps may contain grease which is detrimental to the recycling process and will produce harmful gas to the environment [3]. After removing the grease and other impurities such as corundum and silicon carbide, the stainless-steel scraps can be recycled by the pyrometallurgy method, and the products can be used as raw materials for metallurgy [4, 5]. Zhang [6] removed mineral oil by ethanol soaking and pure water washing, and changed the original slag system by adding CaO, then obtained Fe–Mo–Cu crude alloy after smelting. Chen [7] proposed a new process with pre-reducing and smelting to comprehensively utilize stainless steel pickling sludge, dedusting ash, and iron oxide scale. The obtained ferrochrome alloy material after smelting can be applied in stainless steel smelting charges.

Ultrasound which has high energy is an elastic mechanical vibration wave with a frequency ranging from 20 kHz to 50 MHz. Many researchers have found that introducing ultrasound during the leaching process can increase the leaching efficiencies. The improvement of leaching efficiencies by ultrasound is mainly due to its unique ultrasonic cavitation effect. During the ultrasound-assisted leaching process, the physical effect of ultrasonic cavitation enables to make an intense collision between the solid and the leaching solution and accelerates the diffusion of the leaching solution into the interior of the solid [8]. The chemical effect of ultrasonic cavitation can promote the production of hydroxyl radicals in the solution system, which can enhance the potential of the leaching system and promote the oxidation reaction of the system [9]. Therefore, ultrasonic-assisted leaching has been widely applied in many fields such as industrial waste residue treatment, mineral resource smelting, and waste battery recycling [10–13].

Grinding can greatly accelerate the diffusion rate of the leaching process. Due to the excellent plasticity and ductility, it is difficult to reduce the particle size of stainless steel powders by grinding. The low dissolution efficiency of coarse particles limits the efficient utilization of stainless-steel scraps. Liu's [14] study showed that the particle size of copper cadmium slag could be decreased from 30 to 1 μm after ultrasonic treatment. It can be expected that ultrasonic treatment can also effectively reduce the particle size of stainless-steel powder and improve leaching efficiencies. The main purpose of this study was to provide a clean and intensifying acid leaching method of Fe, Ni, and Cr from stainless-steel scraps via ultrasonic treatment, and the influence of ultrasound and other parameters on leaching efficiencies was studied.

Experimental

Experimental Materials

The stainless-steel powder used in this experiment is obtained from a stainless-steel factory. 2.5 g of stainless-steel powder was put into a reaction vessel and 40 mL of aqua regia (HNO_3: HCl 1:3 v/v) was added, then kept heating until the metal components of the sample were completely dissolved. The solution is filtered and put into a 250 mL volumetric flask to a constant volume. The testing result of the chemical composition of raw samples using ICP-OES is shown in Table 1. The Cr, Ni, and Fe contents in this stainless-steel scrap are 18.2%, 12.1%, and 60.3%, respectively.

Conventional Leaching

Stainless-steel scraps were placed in a reaction vessel, and sulfuric acid, hydrochloric acid, and nitric acid solutions with different concentrations (0.5–3 mol/L) under the liquid–solid ratio (5–20 mL/mg) were added as leaching agents respectively. The reaction temperature (30–80 °C) was maintained by a constant thermostat water bath, the stirring speed was controlled by a magnetic stirrer, and the leaching time was 0–90 min. The effects of different leaching agents and other leaching parameters on the leaching efficiencies of Fe, Cr, and Ni were studied.

Ultrasound-Assisted Leaching

In ultrasound-assisted leaching, the raw materials and experimental procedures were the same as used in conventional leaching, but an ultrasonic generator was instead of the magnetic stirrer to enhance the leaching of stainless-steel scraps. The leaching time of ultrasonic-assisted leaching experiments was in the range of 0–30 min, and ultrasonic power was 40–90%.

After the leaching reaction, the solution was filtered to remove the leaching residue. The filtrate was diluted to a constant volume and metal ion content was detected with ICP-OES. The leaching efficiencies are calculated according to the following:

Table 1 Chemical composition of the raw material

Elements	Si	B	Cr	Ni	Fe
Content (%)	2.0	4.2	18.2	12.1	60.3

$$x = \frac{m_1}{m_2} = \frac{c_1 V}{\alpha m_0} \tag{1}$$

where x refers to the leaching efficiency, %; m_1 is the mass of metal content in the leachate, g; c_1 is the concentration of metal content in the leachate, g/L; V is the leachate volume, L; m_2 is the mass of metal ion content in the raw materials before leaching, g; α is the metal grade in the stainless-steel scraps, %; m_0 the mass of the stainless-steel scraps used in each leaching experiment, g.

Results and Discussion

Effect of Leaching Agents

The leaching efficiencies of stainless-steel scraps in different leaching agents were determined under an acid concentration of 3 mol/L, and liquid–solid ratio of 20:1 at 80 °C for 60 min. The experimental results are shown in Fig. 1. Under this experimental condition, the leaching efficiencies of Fe, Ni, and Cr in stainless-steel scraps with nitric acid were less than 1%, while both hydrochloric acid and sulfuric acid could achieve high leaching efficiencies. The possible reason is that the chromium-rich oxide passivation on the surface of stainless steel could remain stable in oxidizing acids, prevent corrosion, and provide good resistance to nitric acid corrosion [15]. Therefore, nitric acid is not a suitable leaching agent for stainless-steel scraps. The other conventional leaching experiments are using hydrochloric acid or sulfuric acid.

Effect of Leaching Parameters

The effect of temperature on the leaching efficiencies of Fe, Ni, and Cr in stainless-steel scraps was determined under an acid concentration of 3 mol/L, with liquid–solid ratio of 20 mL/g for 30 min. As presented in Fig. 2a, the leaching efficiencies of Fe, Ni, and Cr with sulfuric acid instantly increase from 84.28% (Fe), 87.59% (Ni), and 88.67% (Cr) to 97.93% (Fe), 94.9% (Ni) and 97.87% (Cr) as the temperature increases from 30 to 80 °C. The leaching efficiencies with hydrochloric acid also increase significantly from 80.12% (Fe), 80.04% (Ni), and 82.53% (Cr) to 96.71% (Fe), 94.48% (Ni) and 97.59% (Cr). As the temperature increased, the viscosity of the solution declined, and the thermal motion of molecules in the solution was enhanced, which could promote mass diffusion and accelerate the reaction.

The acid concentration is a crucial factor in increasing the rate of leaching. The relationship between initial acid concentration and leaching efficiencies is shown in Fig. 2b. When initial concentrations were at a low level, the leaching efficiencies of sulfuric acid and hydrochloric acid were both unsatisfactory. One possible

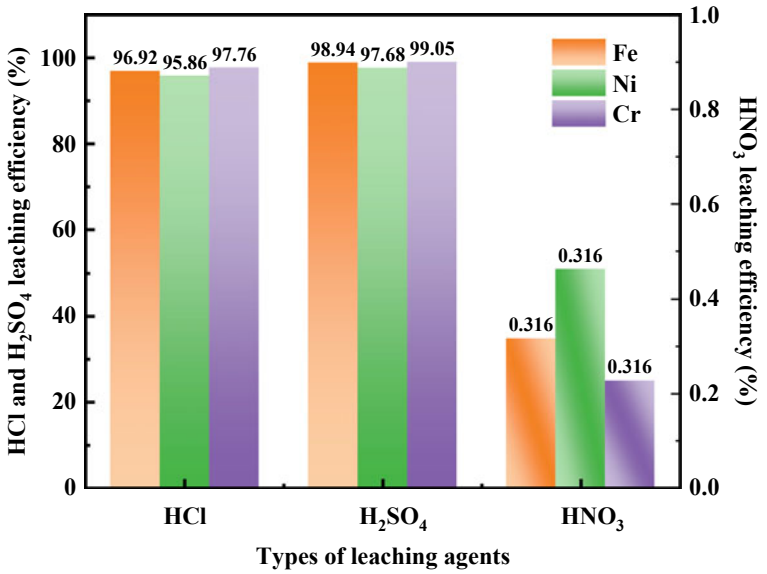

Fig. 1 The leaching efficiencies of Fe, Ni, and Cr from stainless-steel scraps by different acid solutions

reason is that total acid was insufficient to react with stainless-steel scraps fully. With the increasing acid concentration, the leaching efficiencies of Fe, Ni, and Cr was increased rapidly. The preferred leaching efficiencies were obtained when the acid concentration was increased to 3 mol/L, and under this condition, the leaching efficiencies in sulfuric acid were 97.93% (Fe), 94.90% (Ni), 97.87% (Cr), and in hydrochloric acid were 96.71% (Fe), 94.48% (Ni), 97.59% (Cr), respectively.

To determine a suitable leaching time, the effect of time on the leaching efficiencies was studied and the result is illustrated in Fig. 2c. At the beginning of leaching, due to the high initial concentrations of acid and stainless-steel scraps in the solution, the solid–liquid mass diffusion was rapid, and the reaction efficiencies of Fe, Ni, and Cr were at a high level. As the reaction continued, the reactants in the solution were gradually consumed, and the platform of leaching efficiencies appeared after 45 min. Therefore, a leaching time of 45 min is recommended in this experiment.

The liquid–solid ratio is also an important factor in changing the leaching rate. According to Fig. 2d, it can be observed that with a low liquid–solid ratio, the leaching efficiencies were inadequate. One reason is similar to the condition under low initial acid concentration, and the low liquid–solid ratio can also cause an increase in slurry density, which is not conducive to mass diffusion. However, a higher liquid–solid ratio means more consumption of acid solution and a lower concentration of metal ions in the leaching solution, which will adversely affect subsequent treatment. The leaching efficiencies tended to stabilize after the liquid–solid ratio reached 20 mL/g, so the optimal liquid–solid ratio condition for this experiment is 20 mL/g.

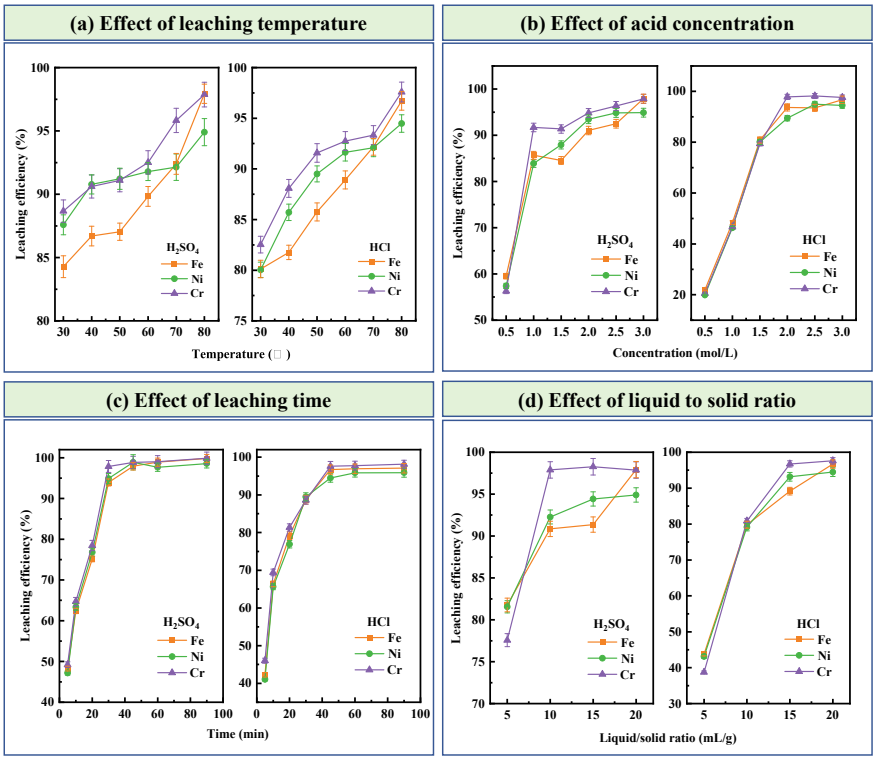

Fig. 2 Effect of leaching parameters on metal leaching efficiencies in conventional leaching. **a** The effect of temperature; **b** The effect of initial acid concentration; **c** The effect of leaching time; **d** The effect of liquid–solid ratio

Based on the experimental data, it can be found that the leaching laws of Fe, Ni, and Cr in sulfuric acid and hydrochloric acid are identical. Under the condition of insufficient acid, the leaching performance of sulfuric acid is slightly better than that of hydrochloric acid. As the concentration and liquid–solid ratio increase, the leaching performances are gradually approached. The optimal leaching conditions obtained through single-factor experiments are at a temperature of 80 °C, an initial acid concentration of 3 mol/L, a leaching time of 45 min, and a liquid–solid ratio of 20 mL/g. At these conditions, the difference between them is not significant, the leaching performance of sulfuric acid is slightly better than that of hydrochloric acid. Therefore, in subsequent ultrasound-assisted leaching experiments, sulfuric acid was used as the leaching agent.

Ultrasound-Assisted Leaching

The enhancement of ultrasound on hydrometallurgy leaching is mainly attributed to its unique "cavitation effect" [16]. When ultrasonic waves propagate in a liquid medium in alternating positive and negative forms, a large number of cavitation bubbles are generated. These bubbles grow and annihilate in a very short time, forming high temperature and pressure environments and strong turbulence locally, which can promote mass diffusion and strengthen chemical reactions [17].

The effect of leaching time was studied under the conditions of concentration of 3 mol/L, temperature of 30 °C, liquid–solid ratio of 20:1, and ultrasonic power of 80%. According to Fig. 3a, it is concluded that the leaching efficiencies of Fe, Ni, and Cr increased rapidly before 15 min. Further extending time had no apparent influence on the leaching efficiencies, indicating that the optimal leaching time is 15 min. Comparing the magnetic stirring experimental data with sulfuric acid in Fig. 2c, it can be found that the leaching rate of ultrasonic-assisted leaching is higher than that of conventional leaching before 20 min. It indicates that ultrasound-assisted leaching greatly enhances the leaching efficiencies of stainless-steel scraps. After 30 min, the leaching efficiencies were exceeded by conventional leaching, possibly due to the influence of temperature. The ultrasound-assisted leaching is at 30 °C, while conventional leaching is at 80 °C. As is well known, temperature can affect the equilibrium of the reaction. Although ultrasound-assisted leaching at 30 °C has a faster leaching velocity, the leaching efficiencies at 80 °C in the equilibrium state are higher.

The leaching efficiencies of Fe, Ni, and Cr elements in stainless-steel scraps by ultrasonic power are shown in Fig. 3b. When the ultrasonic power was at 40% (intensity of about 240 W), the leaching efficiencies of metal ions were less than 60%. With the increase of ultrasonic power, the leaching efficiencies of Fe, Ni, and Cr increased rapidly. At the ultrasonic power of 90%, the leaching efficiencies of the three elements were close to 100%. Therefore, 90% was chosen as the optimal ultrasonic intensity. Comparing the data of sulfuric acid at 30 °C in Fig. 2a, it can be found that the leaching efficiencies of ultrasonic-assisted leaching were significantly better than that of conventional leaching during a shorter time.

To further explore the advantages of ultrasonic-assisted leaching compared to mechanical stirring leaching, sulfuric acid was used as a leaching agent to leach stainless-steel scraps with different particle sizes. Under the conditions of acid concentration of 3 mol/L, liquid–solid ratio of 20 mL/g, and ultrasonic power of 50%, at 80 °C for 45 min (conventional leaching) or 30 min (ultrasonic-assisted leaching), the experimental results are shown in Fig. 3c. It can be seen that with a larger particle size, the leaching efficiencies of ultrasonic-assisted leaching were significantly higher than that of mechanical stirring leaching, and the leaching efficiencies were about 5% higher under the same conditions. As the particle size gradually declined, the gap between the two methods also decreased. When the particle size range was between 0.075 and 0.27 mm, the leaching efficiencies of ultrasonic leaching and conventional leaching were already close. Reducing the particle size

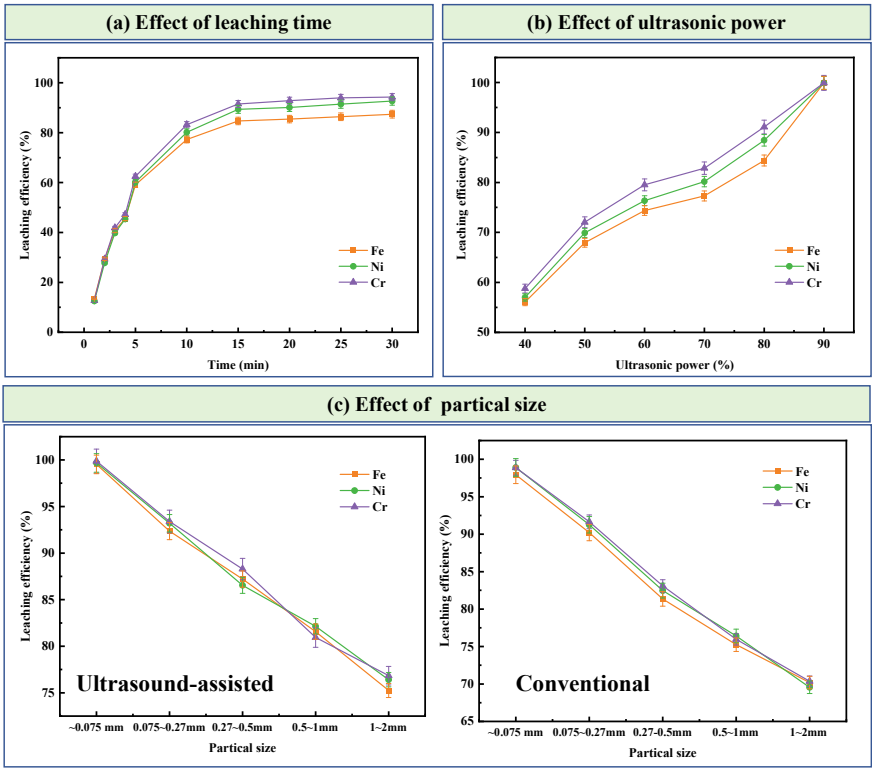

Fig. 3 Effect of leaching parameters on leaching efficiencies in the ultrasound-assisted leaching. **a** The effect of leaching time; **b** the effect of ultrasonic power; **c** the comparison of the leaching efficiencies of Fe, Ni, and Cr by ultrasound-assisted and magnetic stirring leaching experiments with different particle sizes

can increase the surface area of solid–liquid contact, reduce diffusion resistance, and improve the diffusion rate. It indicates that ultrasonic-assisted leaching has a significant advantage over mechanical stirring leaching in improving the diffusion rate. When the particle size is small, the diffusion rate is fast enough, so the improvement brought by the ultrasonic is no longer significant.

Conclusions

1. Due to the passive film of rich chromium oxide on the surface of stainless steel in HNO_3 solution, it is difficult for nitric acid to leach Fe, Ni, and Cr from stainless-steel scraps. However, sulfuric acid and hydrochloric acid have better leaching effects. Their leaching patterns are similar, and sulfuric acid is slightly better than hydrochloric acid in terms of leaching efficiencies.

2. The optimal leaching conditions for conventional leaching are a temperature of 80 °C, a leaching agent concentration of 3 mol/L, a leaching time of 45 min, and a liquid–solid ratio of 20 ml/g. Under these conditions, the leaching efficiencies of Fe, Ni, and Cr with sulfuric acid are 97.93%, 98.90%, and 98.87% respectively.
3. Compared to conventional leaching, ultrasonic-assisted leaching can significantly improve the diffusion rate of the solution, increase the leaching rate, and reduce the leaching time. This improvement effect is more significant when the particle size of stainless-steel scraps is larger. The optimal experimental conditions for ultrasonic-assisted leaching are at a concentration of 3 mol/L, leaching time of 15 min, temperature of 30 °C, liquid–solid ratio of 20:1, and ultrasonic intensity of 90% (about 540 W). At this point, the leaching rate of Fe, Ni, and Cr from stainless-steel scraps by sulfuric acid is 99.93, 99.91, and 99.92%.

Acknowledgements The authors wish to express their thanks to the National Natural Science Foundation of China (No. 52174263), Natural Science Foundation of Henan Province (No. 222300420075, 222301420030), the Innovative Talents Supporting Plan in Universities of Henan Province (No. 23HASTIT004) for the financial support, and the Project of Zhongyuan Critical Metals Laboratory (No. GJJSGGYQ202323).

References

1. Kim ES, Kim SM, Lee YZ (2021) The effect of plateau honing on the friction and wear of cylinder liners. Wear 400:207–212
2. Luo LB (2012) Low-carbon economy to encourage scrap stainless steel recycling industry. Resour Recycl 06:46–47
3. Nie Q, Zhang HP, Li YJ et al (2022) Technical study on comprehensive recycling utilization of grinding wheel ash of one stainless steel. Yunnan Metall 51(06):57–61
4. Xia M, Yan QZ, Ge CC et al (2010) Recovery technology and performance of stainless steel swarf. Foundry Technol 31(02):172–175
5. Li AZ (2017) Research of using electrostatic separation technique to recycle stainless steel powder. Special Cast Nonferrous Alloys. 37(09):990–992
6. Zhang L, Su S, Liu B et al (2021) Sustainable and high-efficiency recycling of valuable metals from oily honing ferroalloy scrap via de-oiling and smelting separation. J Hazard Mater 413:125399
7. Chen QY, Pan J, Zhu DQ et al (2022) Recovery of valuable metals from stainless steel dust and sludge pellets by pre-reduction-smelting. Chin J Nonferrous Metals 32(9):2726–2740
8. Yang J, He L, Liu X et al (2018) Comparative kinetic analysis of conventional and ultrasound-assisted leaching of scheelite by sodium carbonate. Trans Nonferrous Metals Soc China 28(4):775–782
9. Long W, Yuan SUN, Wang S et al (2023) Leaching mechanism of strategic metals from superalloy scrap under ultrasonic cavitation. Trans Nonferrous Metals Soc China 33(1):304–314
10. Jin YG, Mei GJ, Li SY (2006) Ultrasonic assisted leaching of cobalt from waste lithium-ion battery $LiCoO_2$ electrode. Hydrometall China 02:97–99
11. Xin W (2013) Study on microwave carbon-thermal reduction ultrasonic enhanced leaching of indium rich zinc slag. Kunming University of Science and Technology
12. Zhu P, Zhang X, Li K et al (2012) Kinetics of leaching refractory gold ores by ultrasonic-assisted electro-chlorination. Int J Miner Metall Mater 19(6):473–477

13. Yao JH, Qiu XP, Chen X, Zhang H, Li YW (2017) Ultrasonic-assisted leaching of indium and zinc from jarosite slag. Hydrometall China 36(04):262–266
14. Liu H, Wang S, Fu L et al (2022) Mechanism and kinetics analysis of valuable metals leaching from copper-cadmium slag assisted by ultrasound cavitation. J Clean Prod 379:134775
15. Xu YH, Kong LZ, Lu W, Xu GY et al (2015) Electrochemical corrosion behavior of AISI type 304 stainless steel in nitric acid media. Corrosion Protect 36(10):905–909
16. Wang S, Cui W, Zhang G et al (2017) Ultra fast ultrasound-assisted decopperization from copper anode slime. Ultrason Sonochem 36:20–26
17. Nazerian M, Bahaloo-Horeh N, Mousavi SM (2023) Enhanced bioleaching of valuable metals from spent lithium-ion batteries using ultrasonic treatment. Korean J Chem Eng 1–10

Modelling and Simulation of the Scrap Melting in the Consteel EAF

Hongjin Zhang, Guangsheng Wei, Afan Xu, Chunyang Wang, and Rong Zhu

Abstract A modelling study was carried out on the melting process of scrap in the Consteel electric arc furnace. By establishing a dynamic melting model based on energy input efficiency and energy balance, combined with the energy input and scrap transport process in the furnace, the melting process and temperature changes of scrap in the furnace were simulated. The accuracy of the model was verified by actual production measurement results. This model shows the effects of scrap transport temperature and speed on the scrap melting rate and furnace temperature during the operation of the steel electric arc furnace, which helps to develop a reasonable operating system for the melting process.

Keywords Consteel EAF · Scrap melting · Energy efficiency · Continuous charging

Introduction

The Consteel electric arc furnace (EAF) is a special type of EAF consisting of the EAF body, scrap charging section, scrap preheating section and dust removal system. The Consteel EAF has the characteristics of continuous charging, continuous preheating, continuous melting and continuous smelting. Compared with traditional top-charging EAFs, the Consteel EAF has the advantages of short melting time, lower power consumption, lower noise and lower power grid pollution [1] In the melting operation of the Consteel EAF, the charging speed and preheating temperature of the scrap are important control parameters related to whether the melting in the furnace

H. Zhang · A. Xu · C. Wang · R. Zhu
Institute for Carbon Neutrality, University of Science and Technology, Beijing 100083, China
e-mail: zhj8544297@163.com

H. Zhang · G. Wei (✉) · A. Xu · C. Wang · R. Zhu
Beijing Key Laboratory of Research Center of Special Melting and Preparation of High-End Metal Materials, University of Science and Technology Beijing, Beijing 100083, China
e-mail: wguangsheng10@163.com

Z. Peng et al. (eds.), *Characterization of Minerals, Metals, and Materials 2024*, The Minerals, Metals & Materials Series, https://doi.org/10.1007/978-3-031-50304-7_52

is stable. In order to establish an appropriate charging system, it is necessary to study the melting process of scrap in the Consteel EAF.

A large number of scholars have conducted research on the melting process of scrap in EAFs. Some scholars have studied the melting mechanism of scrap in molten steel through experimental methods [2] or numerical simulation methods [3], while Logar [4] has studied the overall melting of scrap through a melting mechanism model. However, most of the current research objects are traditional top charging EAFs with multiple charging, and there is little research on the melting process of scrap in Consteel EAFs with scrap preheating and continuous charging. This paper combines the EAF energy efficiency model with the scrap melting and heating model to simulate the scrap melting process in the Consteel EAF. Based on this, the temperature inside the furnace and the changes in scrap quantity during the melting process are studied, providing a reference for formulating a reasonable charging operation system.

Materials and Methods

Assumption

The following assumptions are made in this model:

(1) During the calculation process, it is believed that all phases are in thermodynamic equilibrium;
(2) The fuel gas injected by the burner is completely burned;
(3) Maintain consistent temperature between slag and molten steel;
(4) The physical heat brought by preheating scrap completely enters the molten pool.

Energy Efficiency Model of EAF

Electrical and chemical energy are the main energy sources of EAFs, and for Consteel EAFs the physical heat provided by scrap preheating is also an important energy component. During the melting process, the power supply system supplies electrical energy to the furnace through electrodes, the oxygen supply system supplies chemical energy to the furnace through oxygen lances, and the burner also supplies combustion energy to the furnace. Once in the furnace, only part of this energy can be used to melt the scrap and heat the molten steel, while the rest is lost through channels such as off-gas, dust, cooling water and circulation losses. Following the work of Pfeifer and Kirschen [5], we define a symbol η to describe the actual proportion of the input energy used for scrap melting and molten steel heating, as calculated by Eq. (1).

$$\eta_i = \frac{\text{useful energy}}{\text{input energy}} = \frac{Q_{\text{use}}}{Q_{\text{all}}} \tag{1}$$

According to the definition of energy balance and energy efficiency in the smelting process, the energy distribution during the smelting process can be written as follows Eq. (2).

$$\eta_{\text{el}}\eta_{\text{arc}} \int_{\text{Charging}}^{\text{Tapping}} P_{\text{El}}\mathrm{d}t + \eta_{\text{Ch}} Q_{\text{Ch}} + \eta_{\text{Bu}} Q_{\text{Bu}} = Q_{\text{st}} + Q_{\text{sc}} \tag{2}$$

In Eq. (2), $\eta_{\text{el}}\eta_{\text{arc}}$ is the circuit efficiency and thermal efficiency of the power system, %, which is closely related to the foaming situation of the melt pool; P_{El} is the power supply, kW; η_{Ch} is the efficiency of chemical energy, %; Q_{Ch} is the input amount of chemical energy, kWh, which includes the heat of oxidation reaction, carbon powder reaction, slag formation, and secondary combustion; η_{Bu} is the thermal efficiency of burner combustion,%; Q_{bu} is the heat released by the burner combustion, kWh; Q_{sc} is the heat received by scrap, kWh; Q_{st} is the heat received by molten steel, kWh.

In the calculation of this model, P_{El} is obtained from the power supply curve derived from the secondary system of the EAF, the input amount of chemical energy Q_{Ch} is determined by the temperature, quality, and chemical composition changes of the steel slag during the smelting process, and the input amount of burner energy Q_{bu} is determined by the gas consumption of the burner. The physical heat brought into the furnace by the preheating scrap is taken as the enthalpy $\sum h_{\text{sci}}$ (kWh) of scrap in the model, which is the initial condition of the model and is not included in energy efficiency.

Heat Transfer and Melting Model of Scrap

Energy Distribution

The melting process of the scrap is a very important part of the smelting process in EAF. Because the Consteel EAF uses a continuous charging mode, the mass of steel in the molten pool remains greater than the mass of scrap for most of the smelting time. This state is also known as “flat bath” smelting. In this state, the electric arc and burner flame are applied directly to the slag layer and the surface of the molten steel, and the arc energy Q_{el} (kWh) and burner energy Q_{bu} (kWh) are fed into the molten steel. The oxygen jet supplied by the oxygen lance will react unimpeded with the molten pool, so that the chemical energy Q_{ch} (kWh) enters the molten steel, and this part of the energy also contains the heat of the secondary combustion and the carbon powder reaction. The energy received by the molten steel is defined as Q_{st} (kWh), and its composition is shown in Eq. (3). Since there is a temperature

difference between the scrap entering the furnace and the molten steel, the energy required for the melting of the scrap will be transferred from the molten steel to the scrap, and the amount of the transfer is defined as Q_{ms} (kWh), which is a physical quantity related to the total surface area of the scrap and the difference between the temperature of the scrap and that of the molten steel. The energy received by the scrap in Q_{sc} (kWh) is calculated as in Eq. (4) since it is obtained from the heat transfer from the molten steel to the scrap.

$$Q_{st} = \eta_{el} Q_{el} + \eta_{ch} Q_{ch} + \eta_{bu} Q_{bu} - Q_{ms} \tag{3}$$

$$Q_{sc} = Q_{ms} \tag{4}$$

When the charging is finished and all the scrap in the furnace has been melted, only molten steel exists at this point, and all the energy input will go to the molten steel, as in Eq. (5).

$$Q_{st} = \eta_{el} Q_{el} + \eta_{ch} Q_{ch} + \eta_{bu} Q_{bu} \tag{5}$$

Heat Transfer Between Scrap and Steel

In the melting process, due to the existence of a long period of time in the state of simultaneous existence of scrap and molten steel, the temperature of the molten steel is higher than that of the scrap, and heat will be transferred to the scrap, which is not only related to the temperature difference, but also related to the surface area of the scrap and the immersion of the scrap in the molten steel. The resulting change in temperature of the scrap and the molten steel is not negligible. This heat transfer is calculated with reference to the work of Van [6] using the following Eq. (6).

$$Q_{ms} = h K_{sc} A (T_{st} - T_{stm}) \Delta t \tag{6}$$

h is the heat transfer coefficient of heat transfer from steel to scrap, W/(m^2·K); K_{sc} is the correction coefficient introduced on behalf of the degree of immersion of scrap by steel. A is the total surface area of scrap in the furnace, m^2, which can be converted according to the mass, shape and density of scrap in the furnace. T_{st} is the current temperature of molten steel in the furnace, K. T_{stm} is the temperature of molten steel in the furnace at the liquid-phase line, K, which is re-accounted according to the composition at each calculation step, taking into account the change in the composition of molten steel. Δt is the calculation interval, min.

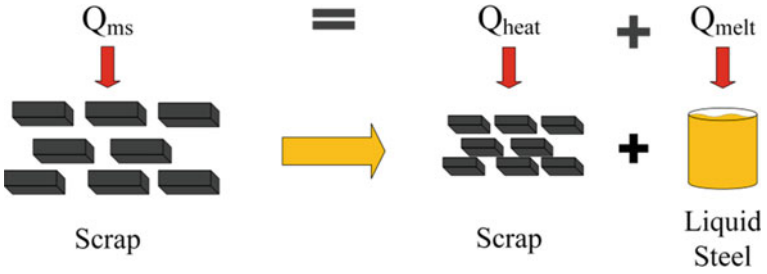

Fig. 1 Energy distribution for melting and warming of scrap

Scrap Melting Process

The melting part of the model for the steel scrap refers to the work of Bekker [7]. In the scrap melting process, the melting and heating of the scrap are synchronised, and the energy received by the scrap Q_{sc} is decomposed into the energy Q_{heat} (kWh) for heating the scrap and the energy Q_{melt} (kWh) for melting the scrap according to the ratio of the current temperature of the scrap T_{sc} (K) to the melting point of the scrap T_{scm} (K), which will be accounted for based on the initial composition of the scrap. The distribution model is shown in Fig. 1, where the further the scrap temperature is from the melting point, the greater the proportion of energy used to heat the scrap, and conversely, the greater the proportion of energy used to melt the scrap.

$$Q_{melt} = Q_{sc}\left(\frac{T_{sc}}{T_{scm}}\right) \tag{7}$$

$$Q_{heat} = Q_{sc}\left(1 - \frac{T_{sc}}{T_{scm}}\right) \tag{8}$$

For the melted scrap, using the initial temperature T_{sci} (K), specific heat capacity C_{sc} (kWh/kg K) and enthalpy of melting H_{scm} (kWh/kg) of the scrap, it is possible to calculate the weight m_{scm} (kg) of the scrap melted in the step, updating the current mass of molten steel m_{st} (kg) and the mass of scrap m_{sc} (kg). The enthalpy held by the melted scrap, $Q_{scm} + Q_{melt}$ (kWh), will all go into the total enthalpy of the molten steel h_{st} (kWh), and then the current average molten steel temperature T_{st} can be accounted for based on the initial molten steel enthalpy $\sum h_{sti}$ (kWh), the current molten steel mass m_{st}, and the specific heat capacity of the molten steel C_{st} (kWh/kg K). In the Consteel EAF, since the scrap is added to the furnace in a continuous manner, the amount of scrap in the furnace m_{sc} will be affected by the melting volume m_{scm}, but also by the addition amount of scrap to the furnace. It will also be affected by the charging rate V_{sc} (kg/min), as in Eq. (10).

For the warmed up scrap, taking 0 °C (273 K) as the starting point of enthalpy calculation, the total enthalpy of scrap at this temperature is defined as $h_{sc} = 0$. Calculating the enthalpy change of scrap from the beginning of smelting $\sum \Delta h_{sc}$ (kWh),

and the initial enthalpy of scrap due to the preheating $\sum h_{sci}$ (kWh), combining with the mass of scrap in the furnace at this time m_{sc}, and the specific heat capacity of scrap C_{sc}, the average temperature of scrap T_{sc} at this time can be calculated, as in Eq. (12).

$$m_{scm} = \frac{Q_{melt}}{C_{sc}(T_{scm} - T_{sci}) + H_{scm}} \tag{9}$$

$$\Delta m_{sc} = m_{scm} + V_{sc}\Delta t \tag{10}$$

$$T_{st} = \frac{\sum \Delta h_{st} + \sum h_{sti}}{C_{st} \cdot m_{st}} + 273 \tag{11}$$

$$T_{sc} = \frac{\sum \Delta h_{sc} + \sum h_{sci}}{C_{sc} \cdot m_{sc}} + 273 \tag{12}$$

Model Validation

Production data and samples were collected from a 60t Consteel EAF operating in Guizhou, China. A comparison of the model predictions and actual measurements of the molten steel temperature in the furnace for specific oxygen and power supply operations is shown in Fig. 2. In the 35th-37th minute, there is a drop in the furnace temperature, which is due to the fact that a large amount of scrap is in the transition phase of melting at this time in the final melting stage of the scrap, and the phase transition process absorbs more heat, resulting in a brief drop in temperature in the furnace. After the 37th minute, as predicted by the model, the scrap was completely melted and the liquid steel began to heat up rapidly. According to the on-site observation, the complete melting time of the scrap is also the 37th minute. It can be seen that the model is basically accurate in predicting the temperature change in the furnace and the melting of the scrap. It can be used to study the temperature change and melting of scrap in the furnace.

Simulation Results and Discussion

Parameter Settings for Simulation

The basic model parameters used in the simulation are shown in Tables 1, 2, 3 and are largely derived from the actual furnace. In the simulation, the operating conditions were kept constant, except that the conditions for preheating and charging

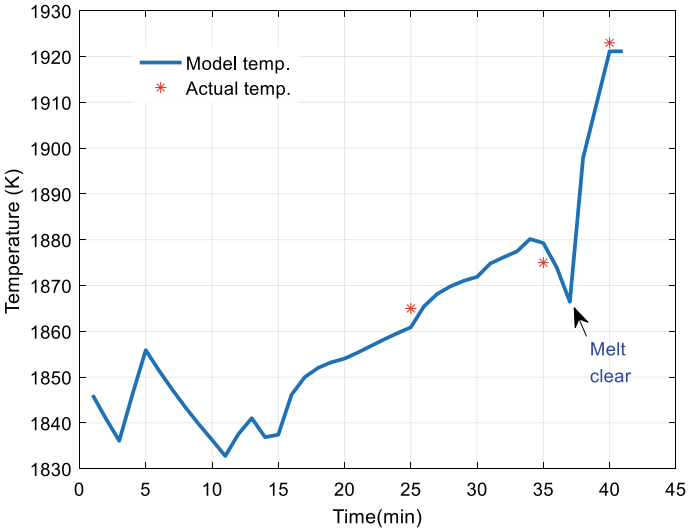

Fig. 2 Simulation results and actual measurements of the temperature in the furnace

Table 1 Scrap information

Component (wt%)	Fe	C	Si	Mn	P	Size (m)
Scrap	97.85	0.18	0.25	0.55	0.03	$0.4 \times 0.15 \times 0.15$

Table 2 Auxiliary material information

Component (wt%)	CaO	MgO	SiO_2	C	Al_2O_3
Dolomite	64.5	32	3	–	0.45
Lime	98.5	–	2.5	–	–
C powder	–	–	–	100	–

the scrap were changed. Figure 3 shows the operating and charging curves used in the simulation; the operating curve includes the input power of electrical energy, the intensity of oxygen supply and the fuel flow rate consumed by the burner. The charging curve includes the supply curves of carbon powder, lime, dolomite and the velocity curve of the slag from the melting process.

Effect of Charging Time

In the smelting operation of a Consteel EAF, the charging time accounts for about 80% of the total smelting time. Here, different charging time scenarios are simulated

Table 3 Values of other key parameters

Model parameter	Value	Units
Power supply efficiency $\eta_{el}\eta_{arc}$	80	%
Chemical energy efficiencyη_{Ch}	80 (for oxygen injection) 100 (for oxidation reaction) [8] 30(for post combustion)	%
Burner efficiency η_{Bu}	50	%
Heat transfer coefficient in liquid metal h	10,000 [9]	W/(m^2 K)
Scrap charging amount	70,000	kg
Hot heel	50,000	kg
Hot heel temperature	1853	K
Submersion correction factor K_{sc}	1	–

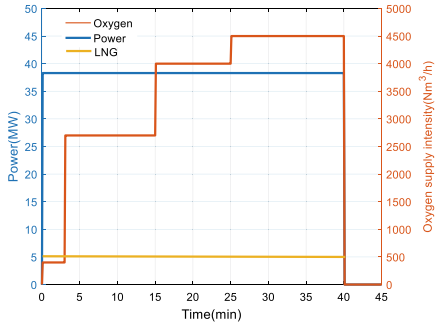

(a) Power,Oxygen supply and burner operating curves

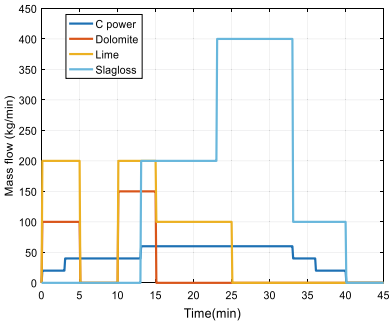

(b) Auxiliary and slagging operating curves

Fig. 3 Operating curves used for the simulation process

for a total charge of 70 t. The preheating temperature is set to 573 K, and the charging times are 30 min, 33 min and 35 min, corresponding to an average charging rate of 2.33 t/min, 2.12 t/min and 2 t/min, respectively.

The comparison between the temperature in the furnace and the amount of scrap is shown in Fig. 4. The charging speed will obviously affect the accumulation rate of scrap in the furnace, 30 min charging mode, the accumulation of scrap in the furnace for a long time of more than 30t, too fast charging speed, the stability of the flat melting pool is broken, resulting in a continuous decline in the temperature of the furnace, until the stopping of the charging, the amount of scrap to stop the accumulation of the temperature began to rise significantly. Under the charging rate of 33 and 35 min, the accumulated amount of scrap is not enough to destroy the smelting condition of the flat bath, so the temperature in the furnace maintains a relatively stable state.In the pre-smelting stage, the temperature in the furnace is 30 min > 33 min > 35 min. It is worth noting that the overall melt-clearing time of the scrap was basically the same at all three charging speeds, which was the 38th

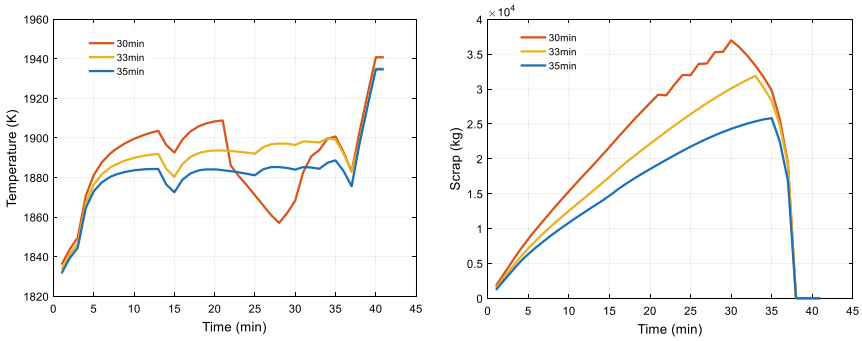

(a) Furnace temperature profile (b) The amount of scrap in the furnace

Fig. 4 Effect of charging time on furnace temperature and scrap amount

min, indicating that there is little correlation between the melt-clearing time and the charging speed under a certain charging amount.

Effect of Preheating Temperature

Consteel EAF through the high temperature off-gas on the Consteel preheating section of the scrap preheating, in general, the preheating temperature can reach about 573 K, if the sealing and the scrap heat transfer conditions are better, it can reach more than 673 K. Here under the condition of charging 33 min, charging speed 2.12 t/min, change the preheating temperature to 473–773 K, simulate the change of temperature in the furnace and the change of the accumulated amount of scrap and the result is shown in Fig. 5. It can be seen that the influence of the preheating temperature of scrap on the temperature in the furnace and the accumulated amount of scrap is significant.

In the pre-smelting period (before 15 min), the trend of the temperature inside the furnace is more consistent, but it is worth noting that the higher the preheating temperature, the lower the increase in the temperature of the molten steel inside the furnace. In particular, at the 773 K preheat temperature, the temperature inside the furnace actually decreases in the late stage. This is because the higher the preheating temperature, the faster the melting speed of the scrap, the lower the apparent expression of the accumulation of scrap. The large amount of molten scrap causes a large expenditure of enthalpy heat of phase change and also increases the total amount of molten steel at that moment. Since the operation of the energy input is the same for each preheating temperature, a larger amount of steel will also make the average temperature of the steel at that moment lower for the same energy input, so the temperature in the furnace will be lower instead of higher at the preheating temperature. However, if the preheat temperature is too low, e.g. 473 K, the accumulated scrap will be more than 30 t for a long time, which will destabilise the melting of the

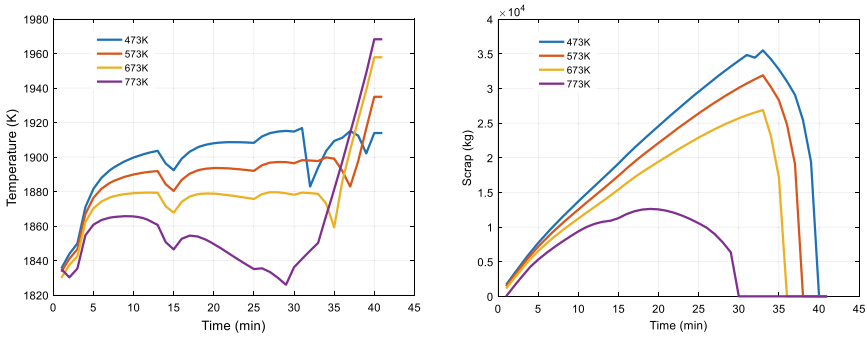

(a) Furnace temperature profile (b) The amount of scrap in the furnace

Fig. 5 Effect of preheating temperature on furnace temperature and scrap amount

flat melt pool and the temperature will fluctuate greatly. Higher preheat temperatures and faster melting rates are also detrimental to maintaining a stable temperature in the furnace. The preheat temperature also has a significant effect on the melt clearing time; the higher the preheat temperature, the shorter the melt clearing time and, at the same time, the higher the end point temperature due to the large amount of physical heat generated by the high preheat temperature.

Conclusion

In the modelling and simulation in this paper, the temperature in the furnace of the consteel EAF during the melting process of the scrap will first increase and then remain stable until the end of the melting process, and then rise to the discharge specification. During the charging process, the melting and heating of the scrap are simultaneous, and if not all of the scrap can be melted immediately, the remaining scrap will accumulate and heat up, and eventually all of it will be melted quickly after reaching the melting point. The charging rate of the scrap does not affect the final melting time, but significantly affects the temperature in the furnace. The faster the charging rate, the higher the temperature in the furnace. Too fast charging will destroy the flat bath condition. The preheating temperature of the scrap affects the temperature in the furnace by influencing the melting rate. With a high preheating temperature, the melt pool mass grows faster and the melt pool temperature is lower for the same energy input due to the fast melting rate and low scrap accumulation.

References

1. Memoli F, Grasselli A, Giavani C (2010) Consteel© EAF and conventional EAF: a comparison in maintenance practices. Metall Ital 102:7
2. Li J, Provatas N, Brooks G (2005) Kinetics of scrap melting in liquid steel. Metall Mater Trans B 36:293–302. https://doi.org/10.1007/s11663-005-0031-2
3. Yao CL, Zhu HC, Jiang ZH (2022) Numerical investigation on melting characteristics of scrap with heat and mass transfers in molten steel. J Iron Steel Res Int 30(6):1090–1100. https://doi.org/10.1007/s42243-022-00864-7
4. Meier T, Logar V, Echterhof T (2016) Modelling and simulation of the melting process in electric arc furnaces-influence of numerical solution methods. Steel Res Int 87(5):581–588. https://doi.org/10.1002/srin.201500141
5. Pfeifer H, Kirschen M, Simoes JP (2005) Thermodynamic analysis of electrical energy demand. Paper presented at the 8th European Electric Steelmaking Conference, Birmingham, May 2005
6. Van Ende M-A (2022) Development of an electric arc furnace simulation model using the effective equilibrium reaction zone (EERZ) Approach. JOM 74(4):1610–1623. https://doi.org/10.1007/s11837-022-05186-3
7. Bekker JG, Craig IK, Pistorius PC (1999) Modeling and simulation of an electric arc furnace process. ISIJ Int 39(1):23–32. https://doi.org/10.2355/isijinternational.39.23
8. Kirschen M, Badr K, Pfeifer H (2011) Influence of direct reduced iron on the energy balance of the electric arc furnace in steel industry. Energy 36(10):6146–6155. https://doi.org/10.1016/j.energy.2011.07.050
9. Opitz F, Treffinger P (2016) Physics-based modeling of electric operation, heat transfer, and scrap melting in an AC electric arc furnace. Metall Mater Trans B 47:1489–1503. https://doi.org/10.1007/s11663-015-0573-x

Mortar Rheology with Partial Replacement of Lime with Dredging Residue

I. D. Batista, M. T. Marvila, J. Freitas, E. B. Zanelato, S. N. Monteiro, J. C. Carneiro, G. C. Xavier, L. G. C. H. Silva, J. Alexandre, and A. R. G. Azevedo

Abstract The dredging of harbors is an extremely necessary activity, which is associated with the problem of the disposal of the dredged material, which, even if properly disposed of, affects the environment, not to mention the logistics and disposal costs. Therefore, the present work aims at reducing the extraction of raw materials and reusing the dredging slurry by incorporating the residue into the mortar as a partial substitute for the lime binder. The substitutions were made on a mass base in the mixing ratio of 0, 10, 20, and 30%. The consistency of the mortar was determined using the flow table and checked with the ball test. The squeeze flow test was

I. D. Batista · J. Freitas · G. C. Xavier · J. Alexandre · A. R. G. Azevedo (✉)
LAMAV—Advanced Materials Laboratory, UENF—State University of the Northern Rio de Janeiro, Av. Alberto Lamego, 2000, Campos dos Goytacazes, Rio De Janeiro 28013-602, Brazil
e-mail: afonso@uenf.br

G. C. Xavier
e-mail: gxavier@uenf.br

J. Alexandre
e-mail: jonas@uenf.br

M. T. Marvila
UFV—Federal University of Viçosa, CRP—Rio Paranaíba Campus, Rodovia BR 230 KM 7, Rio Paranaíba, MG 38810-000, Brazil
e-mail: markssuel.marvila@ufv.br

E. B. Zanelato
IFF—Fluminense Federal Institute, Rua Dr. Siqueira, 273, Parque Dom Bosco, Campos Dos Goytacazes, RJ 28030-130, Brazil

S. N. Monteiro
Department of Materials Science, IME—Military Institute of Engineering, Square General Tibúrcio, 80, Rio de Janeiro 22290-270, Brazil

J. C. Carneiro · L. G. C. H. Silva
PORTO DO AÇU—Porto do Açu Operações S.A, Rua do Russel, 804, Flamengo, Rio de Janeiro, RJ 22210-030, Brazil
e-mail: juliane.carneiro@portodoacu.com.br

L. G. C. H. Silva
e-mail: gustavo.cruz@portodoacu.com.br

Z. Peng et al. (eds.), *Characterization of Minerals, Metals, and Materials 2024*, The Minerals, Metals & Materials Series, https://doi.org/10.1007/978-3-031-50304-7_53

performed to determine the rheological properties of the mortar. The results were satisfactory, since the binder lime and the dredged slurry have similar granulometry, indicating adequate rheological properties of the material.

Keywords Sustainability · Ecological mortar · Characterization · Dredging residue

Introduction

Population growth requires an increasing number of new buildings, consequently with the consumption of cement and aggregates, and thus the production and extraction of raw materials, increase significantly [1]. At the same time, population growth has led to a greater amount and a variety of solid waste [2]. This waste is often inappropriately disposed, which can cause environmental damage [3]. Deforestation, which is often a consequence of urbanization and leads to increasing siltation of the bottom of water bodies [4], making dredging extremely necessary to maintain the existing depth in navigation channels [5], an activity that must be carried out regularly [6, 7].

Dredge spoils are increasingly valued [8], and several studies have been conducted on this subject to find viable uses [9]. Some of these uses investigated so far are the admixture of residues in the production of cement [10], bricks [11], paving stones [12], and mortar [13].

This waste is a potential source of construction materials to reduce the extraction of raw materials and the disposal of solid waste [14]. Like lime, dredging residues improve the workability of mortar [15]. Mortars made from dredging residues must be tested for environmental compatibility and must always meet regulatory criteria [16]. In addition, environmental tests must be carried out. Therefore, the present study aims to produce mortar by partially replacing lime with the dredged material to extract a smaller amount of raw materials from the environment and, at the same time, to reuse material that would otherwise be discarded, evaluating the properties in the fresh state about the rheology of the material.

Materials and Methods

Portland cement type CP II F-32, hydrated lime CH III, and port dredged sediment provided by Porto do Açu (RPA), located in the north of the state of Rio de Janeiro, were used to conduct this study. The natural quartz sand from the Paraíba do Sul riverbed, located in Campos dos Goytacazes, Brazil, and distilled water for the final composition of the mortar.

The mortar was prepared according to ABNT NBR 16541:2016 [17], which describes the procedures for the preparation of mortar mixtures for wall and ceiling

Fig. 1 Mortar production

claddings with a mixing ratio of 1:1:6 (cement: lime: sand) in a mass of materials and with mixtures with partial replacement of lime by residues in percentages of 10, 20 and 30% in addition to the reference mortar, which has a replacement of 0%. Figure 1 shows the method of mortar preparation.

The consistency index was determined according to the recommendations of ABNT NBR 13276:2016 [18], where a setting table is used to determine the consistency index, a truncated cone form, a metal sleeve, a metal ruler, and a caliper gauge. The mortar was prepared according to ABNT NBR 16541:2016 [17] and then poured into the frustoconical mold in three different layers, positioning itself in the middle area of the setting table. While the layers were poured, the mortar was compacted with fifteen, ten, and five strokes, respectively, using the standard sleeve. When the mold was full, the mortar was leveled with a metal ruler. Subsequently the mold was removed and a total of 30 drop blows were applied to the drop table in 30 s. After the last drop, the spread mortar was measured using a caliper, requiring three diametrical measurements evenly distributed in the mortar. The water/cement ratio was determined for each mortar according to the standard spread of the technical standard of 260 $\pm$ 5 mm [18]. Figure 2 shows the mold production sequence for the consistency test.

The ball drop test was performed by BS 4551:Part 1:1998 [19], using a mold made of a rigid material with an inner diameter of 100 mm and an inner depth of 25 mm, a metal ruler, a methacrylate ball and methyl with a diameter of 25 mm and a mass of 9.8 g and a fully polished surface, a ball drop mechanism, and a caliper to measure the penetration depth of the ball. The test consists of shaping the mortar in the mold, leveling the mortar in the mold, attaching the ball to the drop mechanism and dropping it onto the mortar, and then measuring how far the ball has penetrated

(a) (b) (c)

Fig. 2 Consistency index test: **a** Mold filled with mortar; **b** trunk without the mold; **c** mortar after spreading

the mortar, ideally, it should be according to the standard penetrated (10 ± 0.5) mm. The device for this test is shown in Fig. 3.

The squeeze flow rheology test was performed according to ABNT NBR 15839:2010 [20]. To perform the test, you need a compression testing machine, a lower plate with a surface area of at least 160 mm in diameter, an upper plate with a diameter of (101 ± 0.5) mm, a mold for making the test specimen with an inner diameter of (101 ± 0.5) mm and a height of (10 ± 0.1) mm, and a spatula. The test consists of filling the mold, picking up the mortar using a spatula and, leveling the mold on the lower plate, then the upper plate must move until it touches the specimen. The load and displacement must be set to zero before starting the test. The test was performed 10 min after the completion of the mortar preparation and at a speed of 3 mm/s and after 15 min of molding at a speed of 0.1 mm/s on different specimens, as recommended in the literature on this subject [20]. The test ends when the maximum displacement of 9 mm or the maximum load of 1 kN is reached, generating stress/displacement curves. Figure 4 shows the test being carried out.

Results and Discussion

The consistency index allows to determine the water/cement ratio of each of the studied proportions, and it can be seen in Fig. 5 that the higher the percentage of replacement of lime by residue, more water was necessary to achieve the same standard workability of the mortar, which is reported in the literature to be 260 ± 5 mm [18]. The presented characteristics of the residue could indicate some possibilities for lower cement demand in compositions with a larger amount of residue, such as the possibility of a greater demand for hydration of the hardened cement paste depending on the standard composition of the mortars [21]. There is also the possibility that this phenomenon is related to the fineness of the residue, which visually

Fig. 3 Dropping ball test equipment

(a) (b)

Fig. 4 Squeeze flow test apparatus: **a** before the test; **b** after the test

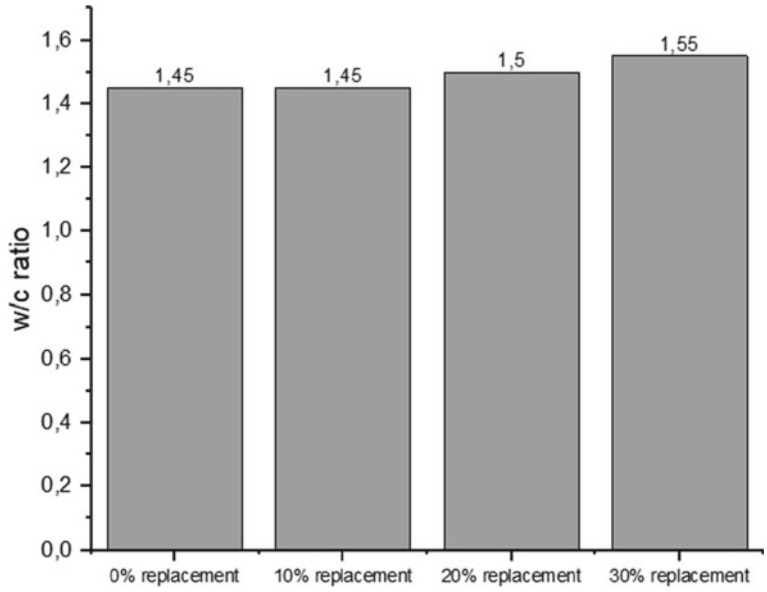

Fig. 5 Consistency index results—water/cement ratio

shows greater compatibility with the other components of the mortar, suggesting the need for cement in the mixture [22]. However, it should be noted that the amount added to the cement may be relatively small if each mixture is evaluated individually.

Another issue that can be correlated with the water-cement ratio of a mortar mix relates to the mechanical properties, is the compressive strength, which can affect the usability of the composite, but this was not the objective of this study.

Below, in Fig. 6, you can see the results of the ball drop test, which can be used as a complementary method to analyze the consistency and workability of the mortar. However, the results were not satisfactory, since the standard suggests values of (10 $\pm$ 0.5) mm, which did not occur in any of the proportions [19]. One of the probable reasons why this analysis was not met by either the standard or the reference mix is that to the use of lime in the composition, which can affect the workability of the mortar and which, is not common in some countries that use this standard that is widely used in Brazil, although.

Nevertheless, considering that the reference composition (0%) meets the normative conditions for the Brazilian reality, it can be said that the addition (additions without the "the") of higher concentrations of the residue caused a lower measured penetration, which could indicate that the mortar hardening process is affected by the addition of larger amounts of waste, with a composition of 20% being the closest to the standard results as acceptable [19].

The rheological squeeze flow test in Fig. 7 shows that the reference curves (0%) exhibit similar behavior at both times points and loading rates, suggesting that these variations have no significant effect on the reference composition. At addition rates

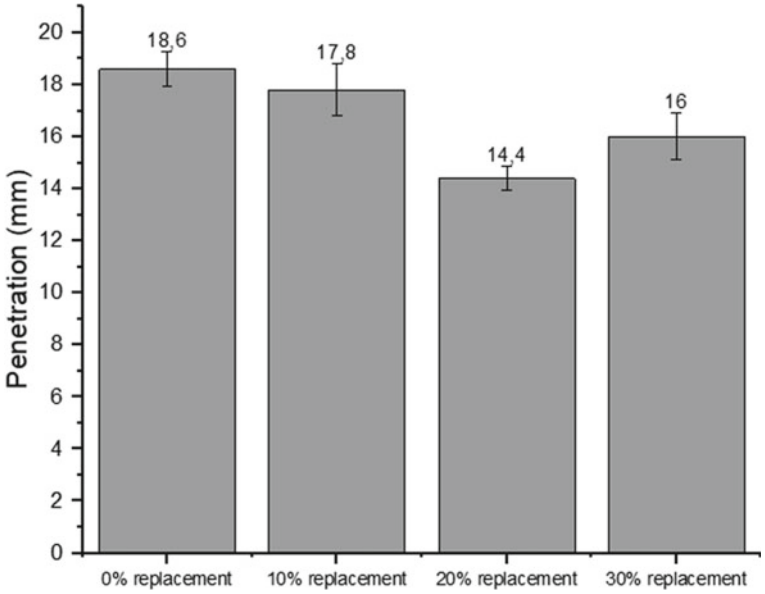

Fig. 6 Dropping ball results

of 10% of residue, we can observe a decrease in displacement at the same maximum loading. This can be advantageous when applying mortar to walls to be faced, as it reduces the work of the processing team. However, the behavior is not stable at higher additions. It can be observed that at 20%, at a the time of 15 min and the corresponding load, the displacement decreases more than in the previous mixtures, which is certainly more positive, but the behavior after 10 min was very different, showing that this property had a significant influence in this composition. At values of 30%, the mortars show a high displacement and a lower maximum shear rate, which can be a major problem in terms of general application in buildings. However, this analysis requires further additions [23].

In general, it is observed in the squeeze flow test that are mixed with a lower percentage of residue have a better tendency to have smaller displacements at a constant loading rate, which may be advantageous for the desired application. However, the need for more specific and complementary studies in this segment must be emphasized.

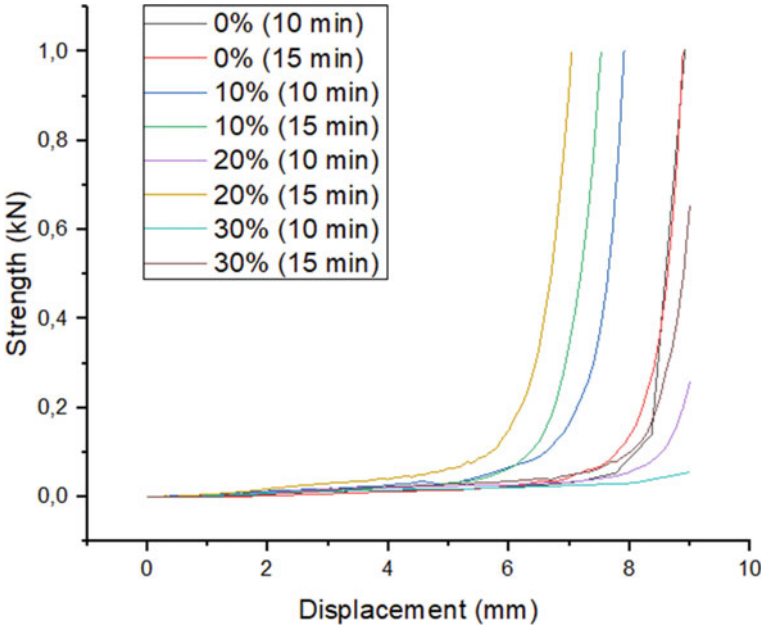

Fig. 7 Strength × displacement curve by squeeze flow test

Conclusion

Based on the results presented, it can be concluded that port waste influences the water/cement ratio of mortars when used to replace hydrated lime, which can directly impact its workability, measured through the consistency index. The use of the technique for determining consistency using the dropping ball still requires greater depth and studies into the reality of materials and compositions typically from Brazil, which could also be a contribution to future research in this area. The Squeeze Flow rheology test shows that compositions with lower incorporation percentages, such as 10%, presented a smaller displacement for the same loading range, which may be acceptable for the desired application. It is also noteworthy that for larger incorporations the results are not adequate. It is still necessary to conclude that there is a need for further studies related to rheological characterization techniques in the fresh state of these mixtures, with greater refinement of techniques and studies in this thematic area.

Acknowledgements This research was financed by the Universidade Estadual do Norte Fluminense (UENF), partially financed by CAPES (Coordination for the Improvement of Higher Education Personnel—Brazil), CNPq (National Research Coordination) and FAPERJ (Rio State Research Support Foundation). of January). The author A.R.G.A. was funded by FAPERJ through project No. E-26/210.150/2019, E-26/211.194/2021, E-26/211.293/2021, E-26/201.310/2021 and by CNPq through the research grant PQ2 307592/2021-9. This project also has support from CNPQ through

process no. 424539/2021-7—Call CNPq/SEMPI/MCTI no. 021/2021—RHAE Program—Line 1—Innovative Companies and Cais Açu Lab, Research, Development and Innovation at Porto do Açu Operações S.A.

References

1. Oliveira PS, Antunes MLP, Cruz NC, Rangel EC, Azevedo ARG, Durrant SF (2020) Use of waste collected from wind turbine blade production as an eco-friendly ingredient in mortars for civil construction. J Clean Prod 274:122948. https://doi.org/10.1016/j.jclepro.2020.122948
2. Chen YC (2018) Effects of urbanization on municipal solid waste composition. Waste Manag 79:828–836. https://doi.org/10.1016/j.wasman.2018.04.017
3. Mrkajic V, Stanisavljevic N, Wang X, Tomas L, Haro P (2018) Efficiency of packaging waste management in a European Union candidate country. Resour Conserv Recycl 136:130–141. https://doi.org/10.1016/j.resconrec.2018.04.008
4. Dang TA, Bernard SK, Prince WA (2013) Design of new blended cement based on marine dredged sediment. Construct Build Mater 41:602–611. https://doi.org/10.1016/j.conbuildmat.2012.11.088
5. Tang C-S, Cheng Q, Wang P, Wang H-S, Wang Y, Inyang HI (2020) Hydro-mechanical behavior of fiber reinforced dredged sludge. Eng Geol 276:105779. https://doi.org/10.1016/j.enggeo.2020.105779
6. Chen M, Ding S, Gao S, Fu Z, Tang W, Wu Y et al (2019) Efficacy of dredging engineering as a means to remove heavy metals from lake sediments. Sci Total Environ 665:181–190. https://doi.org/10.1016/j.scitotenv.2019.02.057
7. Norén A, Fedje KK, Stromvall A-M, Rauch S, Skold YA (2020) Integrated assessment of management strategies for metal-contaminated dredged sediments—what are the best approaches for ports, marinas and waterways? Sci Total Environ 716:135510. https://doi.org/10.1016/j.scitotenv.2019.135510
8. Laoufi L, Senhadji Y, Benazzouk A (2016) Valorization of mud from Fergoug dam in manufacturing mortars. Case Stud Constr Mater 5:26–38. https://doi.org/10.1016/j.cscm.2016.06.002
9. Loudini A, Ibnoussina M, Witam O, Limam A, Turchanina O (2020) Valorisation of dredged marine sediments for use as road material. Case Stud Constr Mater 13:e00455. https://doi.org/10.1016/j.cscm.2020.e00455
10. Chu DC, Kleib J, Amar M, Benzerzour M, Abriak N-E (2022) Recycling of dredged sediment as a raw material for the manufacture of Portland cement—numerical modeling of the hydration of synthesized cement using the CEMHYD3D code. J Build Eng 48:103871. https://doi.org/10.1016/j.jobe.2021.103871
11. Gillot T, Cojan I, Haurine F, Poirier C, Bruneaux M-E (2021) Demonstrating the influence of sediment source in dredged sediment recovery for brick and tile production. Resour Conserv Recycl 171:105653. https://doi.org/10.1016/j.resconrec.2021.105653
12. Kamali S, Bernard F, Abriak N-E, Degrugilliers P (2008) Marine dredged sediments as new materials resource for road construction. Waste Manag 28(5):919–928. https://doi.org/10.1016/j.wasman.2007.03.027
13. Safhi AM, Benzerzour M, Rivard P, Abriak N-E, Ennahal I (2019) Development of self-compacting mortars based on treated marine sediments. J Build Eng 22:252–261. https://doi.org/10.1016/j.jobe.2018.12.024
14. Bortali M, Rabouli M, Yessari M, Errouhi AA, Zejli D, Hajjaji A (2022) Regulatory framework for the beneficial reuse of dredged sediments as construction materials: a case study in Marocco. Mater Today Proc 66(1):441–446. https://doi.org/10.1016/j.matpr.2022.06.316

15. Botelho LCG, Xavier GC, Paes ALC, Azevedo ARG (2023) Lime replacement by finely ground clay from the north fluminense region of RJ in mortar for coating walls and ceilings. J Mater Res Technol 23:5105–5114. https://doi.org/10.1016/j.jmrt.2023.02.058
16. BRAZIL. CONAMA Resolution No. 454, of November 1, 2012. Establishes the general guidelines and reference procedures for the management of material to be dredged in waters under national jurisdiction
17. NBR 16541 (2016) Mortar for laying and coating walls and ceilings—Preparation of the mixture for carrying out tests
18. NBR 13276 (2016) Mortar for laying and coating walls and ceilings—Determination of the consistency index
19. BS 4551:Part 1 (1998) Methods of testing mortars, screeds and plasters.
20. NBR 15839 (2010) Mortar for laying and coating walls and ceilings—Rheological characterization by the squeeze-flow method.
21. Nazari A (2012) Experimental study and computer-aided prediction of percentage of water absorption of geopolymers produced by waste fly ash and rice husk bark ash. Int J Miner Process 110–111:74–81. https://doi.org/10.1016/j.minpro.2012.04.007
22. Oliveira LB, Marvila MT, Fediuk R, Vieira CMF, Azevedo ARG (2023) Development of a complementary precursor based on flue gas desulfurization (FGD) for geopolymeric pastes produced with metakaolin. J Mater Res Technol 22:3489–3501. https://doi.org/10.1016/j.jmrt.2023.01.017
23. Azevedo ARG, Alexandre J, Marvila MT, Xavier GC, Monteiro SN, Pedroti LG (2020) Technological and environmental comparative of the processing of primary sludge waste from paper industry for mortar. J Clean Prod 249:119336. https://doi.org/10.1016/j.jclepro.2019.119336

Nucleation of One Single Sn Droplet on Al Thin Film Explored by Nanocalorimetry

Bingjia Wu, Chenhui Wang, Jiayi Zhou, Kai Ding, Bingge Zhao, and Yulai Gao

Abstract In order to investigate the nucleation process of micro-nano scale droplet in non-equilibrium state, it is necessary to obtain the thermodynamic parameters of rapid phase transition during the solidification process. In addition, the matrix can play a significant role in the solidification nucleation of the metals. In this paper, the nucleation process of one single Sn droplet on the surface of Al film was studied by nanocalorimetry. The results showed that the surface roughness of Al thin film prepared by magnetron sputtering was about 11.9 nm. With the cooling rate increasing from 5 to 10,000 K/s, the undercooling enlarges from 96 to 104 K. However, the undercooling kept nearly unchanged irrespective of the overheating extending from 5 to 120 K. In this case, the nucleation of the Sn droplet is triggered by Sn/Al interface structure, which is nearly independent on the overheating.

Keywords Nanocalorimetry · Nucleation · Al thin film · Cooling rate · Undercooling · Overheating

Introduction

The nucleation undercooling and growth process of grains during the solidification of metal melts can highly affect the microstructure of subsequent metal components, consequently influencing the properties of the material [1, 2]. The nucleation techniques employed in metal solidification can be categorized into two types: homogeneous nucleation and heterogeneous nucleation. In the case of bulk metal

B. Wu · C. Wang · J. Zhou · K. Ding · B. Zhao · Y. Gao (✉)
State Key Laboratory of Advanced Special Steel, School of Materials Science and Engineering, Shanghai University, Shanghai 200444, China
e-mail: ylgao@shu.edu.cn

B. Zhao
e-mail: binggezhao@shu.edu.cn

Y. Gao
Shanghai Engineering Research Center for Metal Parts Green Remanufacture, Shanghai 200444, China

Z. Peng et al. (eds.), *Characterization of Minerals, Metals, and Materials 2024*, The Minerals, Metals & Materials Series, https://doi.org/10.1007/978-3-031-50304-7_54

melts, heterogeneous nucleation is typically observed due to the inevitable existence of impurities [3]. A notable reduction of impurities can be realized by dispersing the large metal melt into micro- and nano-sized metal droplets accompanied with the increase in specific surface area and surface curvature. The solidification of these metal droplets exhibits a "size effect", enabling rapid solidification under high undercooling condition and refinement of the microstructure grain [4, 5], which presents a novel approach to investigate metal solidification. Furthermore, with the development of 3D printing technology, the solidification process of micro- and nano-sized metal droplets can produce a significant impact on the mechanical property of subsequent products. The gas atomization method [6], plasma method [7], and consumable-electrode direct current arc technique (CDCA) [8] are commonly employed for the preparation of metal droplets. However, obtaining the thermodynamic parameters during the solidification process of these metal droplets proves to be difficult. On the one hand, the conventional differential scanning calorimeter (DSC) has been employed to investigate the heterogeneous nucleation behavior of micro-sized droplets with an Al matrix, including Bi [9], Pb [10], Sn [11], and In [12] etc. Nevertheless, the restricted cooling rate (DSC solely attaining 500 K/min [13]) and inadequate sensitivity of conventional calorimeters still keep a challenge in attaining rapid solidification of metal droplets and obtaining precise undercooling, thereby impeding further exploration of their nucleation behavior.

In the 1990s, with the rapid development of nanotechnology and microelectromechanical systems (MEMS), Allen et al. first designed a nanocalorimetry [14, 15]. Compared to traditional calorimeters, nanocalorimetry possesses extremely high heating cooling rates, reaching 10^6 K/s [16–18]. Due to the use of thin film heaters and thermocouples in the nanocalorimetry, the addenda heat capacity is significantly reduced [15, 19], greatly improving the sensitivity of the nanocalorimetry to the level of nJ/K. Consequently, the utilization of nanocalorimetry enables the precise determination of thermodynamic parameters for micro and nano-sized metal droplets during rapid solidification, which provides crucial empirical support for investigating the nucleation mechanism of metal droplets. In 2009, Gao et al. [20] employed a fast scanning calorimeter to study the changes in undercooling of SnAgCu droplet at six orders of magnitude of cooling rates. Yang et al. [21] observed a substantial rise in the undercooling of one single Sn droplet in size of 10 μm, ranging from 300 to 1000 K/s, revealing two distinct nucleation mechanisms during its solidification process. Li et al. [22] used a nanocalorimetry to study the effect of nucleation undercooling of Sn droplet on Si thin films with different roughness, and found that the larger the interface roughness, the more conductivity occurred to promote heat transfer and reduce the undercooling of the Sn droplet.

In this work, the nucleation of one single Sn droplet on the Al thin film prepared by magnetron sputtering technique was studied using a nanocalorimetry. The results indicated that as the cooling rate increasing from 5 to 10,000 K/s, the undercooling also increases. However, the change of the undercooling at various levels of overheating was not substantial, primarily due to the impact of the nucleation substrate.

Table 1 Parameters of Al films prepared by magnetron sputtering technique

Film	Sputtering power, W	Sputtering time, min	Argon flow rate, sccm	Sputtering pressure, Pa
Al	60	30	60	0.8

Experimental Procedures

The rod-shaped Sn ingot was melted and dispersed to small droplets in a liquid medium using CDCA technique [8]. Due to the surface tension of Sn and the hydrostatic pressure of the liquid medium, the Sn droplets solidified into spherical shapes, resulting in the formation of Sn droplets to be used in the experiment. An Al thin film was deposited onto an SiO_2 slide using a magnetron sputtering equipment (JGP-560, SKY Technology Development) and an Al target (99.99 wt.%). The surface and cross section morphology of the Al thin film were examined using a scanning electron microscope (SEM, JSM-6700F), and its thickness was measured. The surface morphology of the Al thin film was examined using atomic force microscopy (AFM, Nanonavi SPA-400). To obtain a suitable size of Al thin film for the test area, the film was detached from the SiO_2 slide by means of a knife and subsequently fragmented into multiple flakes. The detailed preparation parameters for the Al thin film are listed in Table 1.

The Al thin film was transferred to the test zone of the nanocalorimetric sensor (Xensor Integration, XI 39395) through a copper wire (with the diameter of 30 μm) under an optical microscope (OM, Olympus SZ61), and then one single Sn droplet was selected and positioned on the Al thin film. The lower position of Sn droplet corresponds to the position of the thermopiles. In order to study the nucleation of the Sn droplet on the Al thin film, a nanocalorimetry (DFSC, Spark III, Functional Materials Rostock e.V.) was employed under a pure Ar atmosphere to melt Sn droplet at a heating rate of 100 K/s to the maximum temperature between 510 and 625 K. Subsequently, the solidification of Sn droplet was carried out at different cooling rates of 5–10,000 K/s to obtain typical nanocalorimetric curves. Statistical analysis was then conducted to determine the undercooling of the Sn droplet under different experimental conditions.

Results and Discussion

The image of SiO_2 slide is presented in Fig. 1a, and the appearance of Al thin film deposited on SiO_2 slide is shown in Fig. 1b. Obviously, the Al thin film exhibits a satisfactory surface finish at a sputtering power of 60 W, indicating the successful preparation of the Al thin film.

The surface of the Al thin film was observed through SEM, as shown in Fig. 2a, b. The prepared the Al thin film surface was relatively flat, clean, and free from

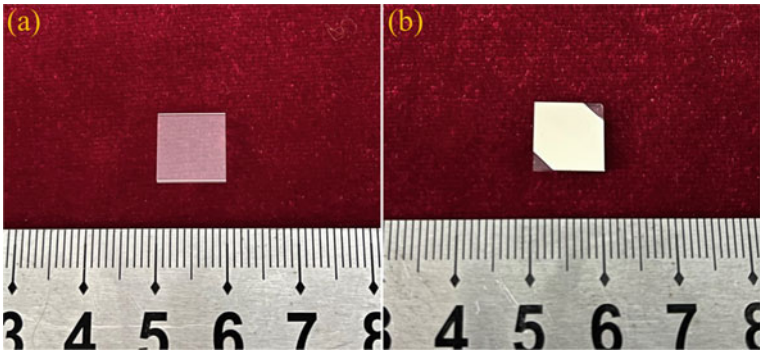

Fig. 1 Appearance of SiO_2 slide and Al film: **a** before deposition; **b** after deposition

contamination by other impurities. In order to observe the cross-section of Al thin film under SEM, the conductive adhesive was applied onto the Al thin film, which was subsequently detached from the SiO_2 slide. The Al thin film was then clipped with a tweezer to form small fragments. The cross-sectional morphology of the small fragmented Al thin film, as observed through SEM, is depicted in the bright region of Fig. 2c, d, with an approximate thickness of 280 nm. Consequently, the deposition rate of the Al thin film is estimated to be around 9.3 nm/min.

The thermodynamic energy theory suggests that in order to minimize the total energy, a thin film should have the smallest surface area, which means that the film should become an ideal planar state. However, it is unattainable to achieve this ideal state. In the growth process of the actual thin films, the gas phase incident on the substrate surface is irregular, leading to the presence of a certain roughness in the resulting thin films. To gain a more comprehensive understanding of the surface states of the Al thin film, AFM was employed to characterize its surface structure. Figure 3a, b reveal the two-dimensional and three-dimensional AFM images of the Al thin film respectively. This analysis result exhibits that the surface roughness of the Al thin film measures 11.9 nm, indicating a relatively uniform surface structure.

The positional relationship between one single Sn droplet with a diameter of about 11 μm and an Al thin film on the sensor before and after the nanocalorimetric test is displayed in Fig. 4, indicating that the Sn droplet position during the test is always located on the Al thin film and the heating area of the sensor. It should be noted that before testing, due to differences in test conditions (Ar atmosphere, surrounding temperature, etc.), the sensor temperature needs to be calibrated [23].

In the nanocalorimetric test, the Sn droplet was heated at a heating rate of 100 K/s to different maximum temperatures of 510, 515, 520, 535, 565, and 625 K (the melting point of Sn is 505.1 K, which means the overheating temperatures are about 5, 10, 15, 30, 60, and 120 K respectively). After holding for 0.1 s, the Sn droplet solidified at different cooling rates between 5 and 10,000 K/s. Ten identical cycles were conducted under each test condition with the same single droplet. The typical nanocalorimetric curves with cooling rates of 5, 50, 1000, and 10,000 K/s are shown

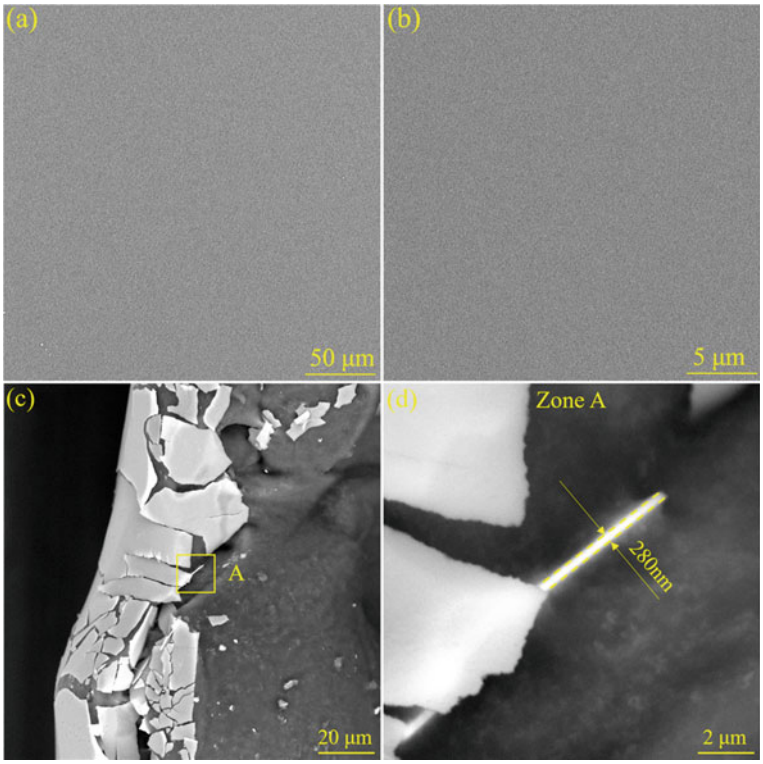

Fig. 2 Scanning electron microscope images of Al thin film: **a**, **b** surface of the Al thin film; **c**, **d** cross section of the Al thin film

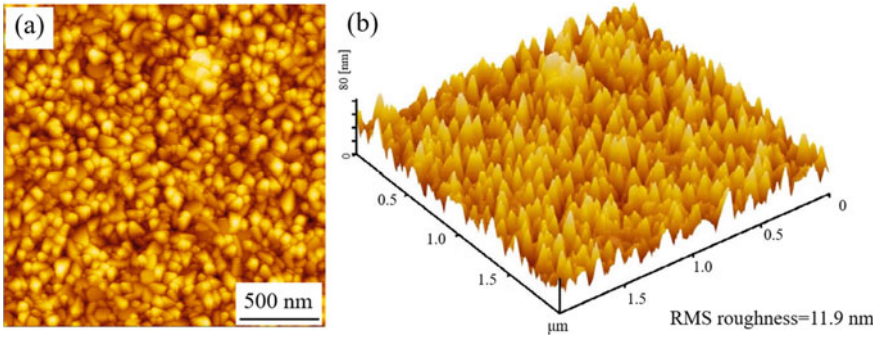

Fig. 3 Atomic force microscope images of Al thin film: **a** 2D image of the surface morphology, **b** 3D image of the surface morphology

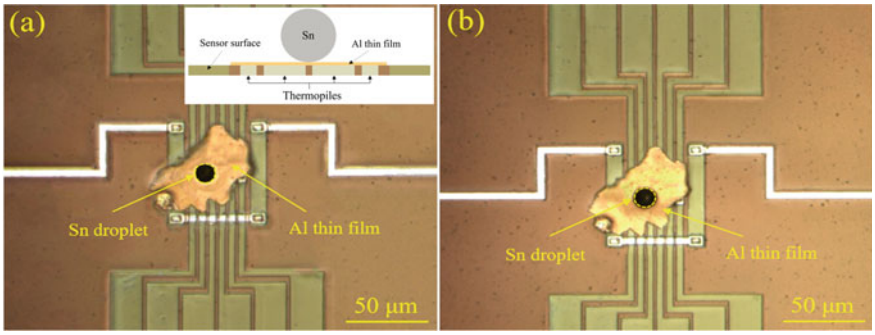

Fig. 4 The location of the Al thin film and one single Sn droplet on the heating area of the sensor: **a** before testing, **b** after testing. The illustration of the cross section of one single Sn droplet and the Al film on the sensor is shown in the inset of (**a**)

in Fig. 5. The melting peaks in these curves overlap with each other, and the starting temperature of these melting peaks is defined as the melting temperature T_m, whose values remain consistent at different cooling rates, indicating good repeatability of nanocalorimetric testing.

Despite the thinness of the Al film and its surface oxide layer, the thermal lag resulting from the rapid heating and cooling of the Sn droplet during nanocalorimetric testing will still affect the obtained results [20]. In this study, we employed a fitting approach to determine the thermal lag by analyzing the apparent melting temperatures of Sn on the Al film under various scanning rates. This correction allowed for accurate determination of the melting and solidification temperatures. The undercooling obtained under identical nanocalorimetric test conditions may vary within a specific range due to the random nature of nucleation [24]. Figure 6 illustrates the correlation between undercooling and cooling rate of a Sn droplet at six distinct levels of overheating. The undercooling value of Sn represents the mean value derived from ten cycles. It is observed that the average undercooling value increases from 94 to 104 K with the cooling rate increases. Among them, at the overheating of 5 K, the average change of undercooling is the largest, from about 96–104 K. In the study of Fan et al., the undercooling of metal Ti also increases with the increase of cooling rate before the formation of amorphous structure.

Figure 7 illustrates the impact of Sn droplet overheating at the Sn/Al interface on undercooling at varying cooling rates. The undercooling remains relatively unaffected between overheating temperatures of 5–120 K. This indicates that the nucleation of the Sn droplet is triggered by the Sn/Al interface, and the Al film provides the same heterogeneous nucleation sites. So, the undercooling of the Sn droplet was determined by the structure of the Sn/Al interface at a given cooling rate, irrespective of the degree of overheating.

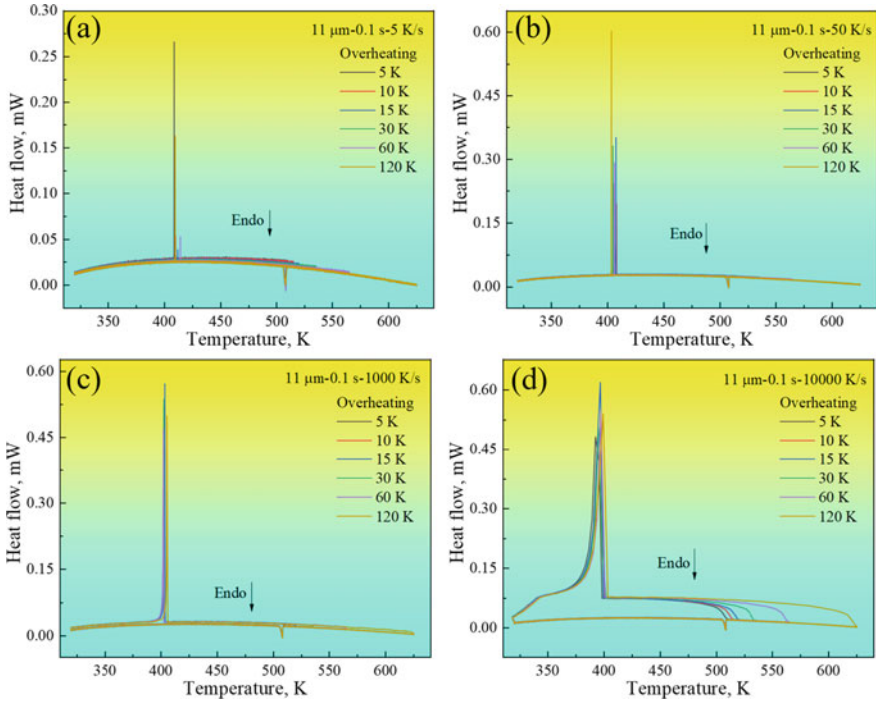

Fig. 5 Nanocalorimetry curves of nucleation of one single Sn droplet on Al thin film at different cooling rates: **a** 5 K/s, **b** 50 K/s, **c** 1,000 K/s, **d** 10,000 K/s

Conclusions

(1) An Al film with the thickness about 280 nm was successfully deposited on SiO_2 slide using magnetron sputtering technique. The deposition rate was measured to be approximately 9.3 nm/min, and the surface roughness was around 11.9 nm.

(2) The nucleation process of one single Sn droplet with a diameter of about 11 μm on the Al film was tested by a nanocalorimetry. The undercooling of Sn droplet on the Al film substrate increased with the increase of cooling rate within the range of 5–10,000 K/s.

(3) Within the overheating range of 5–120 K, the influence of overheating on the nucleation undercooling of the Sn droplet was slight due to the dominant role of the Sn/Al interface structure in the heterogeneous nucleation process of Sn.

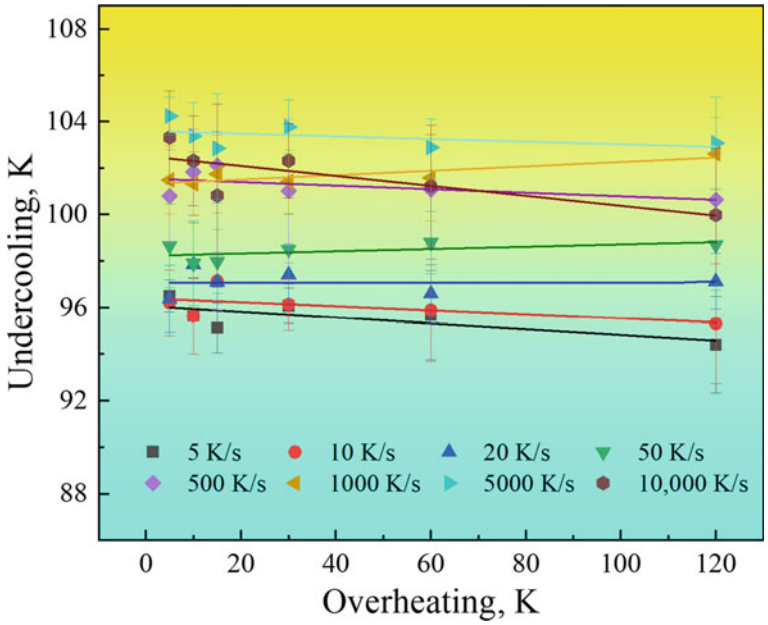

Fig. 6 The relationship between undercooling and cooling rate of one single Sn droplet at different overheating temperatures

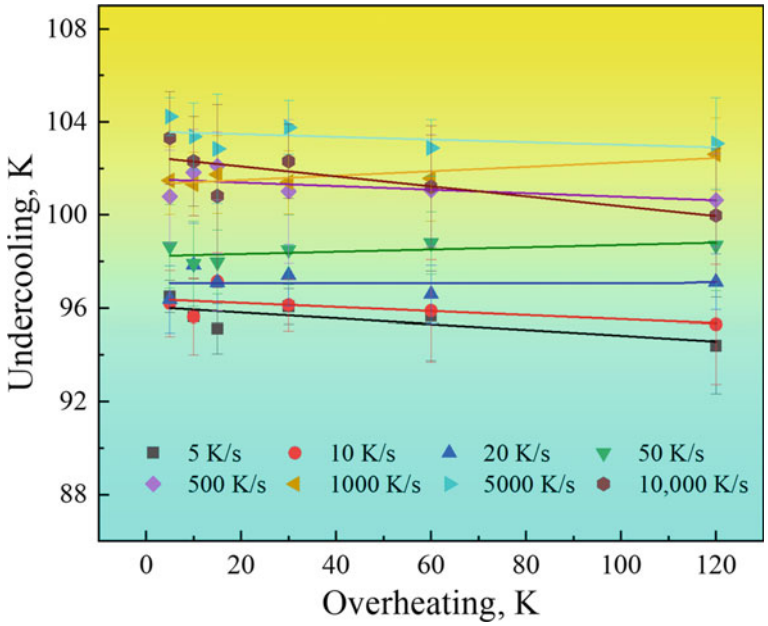

Fig. 7 The relationship between undercooling and overheating temperature of one single Sn droplet at different cooling rates

Acknowledgements This work was supported by the National Natural Science Foundation of China (Grant nos. 52071193 and 51671123).

References

1. Li JF, Jie WQ, Yang GC, Zhou YH (2002) Solidification structure formation in undercooled Fe–Ni alloy. Acta Mater 50(7):1797–1807
2. Algoso PR, Hofmeister WH, Bayuzick RJ (2003) Solidification velocity of undercooled Ni–Cu alloys. Acta Mater 51(14):4307–4318
3. Oxtoby DW (1990) New perspectives on freezing and melting. Nature 347(6295):725–730
4. Ma K, Zhao Y, Xu X, Hou H (2019) The effect of undercooling on growth velocity and microstructure of $Ni_{95}Cu_5$ alloys. J Cryst Growth 513:30–37
5. Xu XL, Zhao YH, Hou H (2019) Observation of dendrite growth velocity and microstructure transition in highly undercooled single phase alloys. Maters Charact 155:109793
6. Prather CA, Craig CD, Baumann JM, Morgan MM (2023) Experimental and theoretical investigation of rotary atomization dynamics for control of microparticle size during spray congealing process. Powder Technol 418:118278
7. Xu JL, Khor KA, Gu YW, Kumar R, Cheng P (2005) Radio frequency (rf) plasma spheroidized HA powders: powder characterization and spark plasma sintering behavior. Biomaterials 26(15):2197–2207
8. Zhao J, Gao YL, Zhang WP, Song TT (2012) Observation of the solidification microstructure of Sn3.5Ag droplets prepared by CDCA technique. J Mater Sci Mater Electron 23(12):2221–2228
9. Goswami R, Chattopadhyay K (1996) The solidification behaviour of Bi particles embedded in an Al matrix. Acta Mater 44(6):2421–2429
10. Moore KI, Zhang DL, Cantor B (1990) Solidification of Pb particles embedded in Al. Acta Metall Mater 38(7):1327–1342
11. Kim WT, Zhang DL, Cantor B (1991) Microstructure of rapidly solidified aluminium-based immiscible alloys. Mater Sci Eng A 134:1133–1138
12. Liu Y, Guo JJ, Su YQ, Ding HS, Jia Y (2001) Microstructures of rapidly solidified Al–In immiscible alloy. Trans Nonferrous Met Soc China 11(1):84–89
13. Mathot VBF, Goderis B, Scherrenberg RL, Van VEW (2002) High-speed calorimetry for the study of the kinetics of (De) vitrification, crystallization, and melting of macromolecules. Macromolecules 35(9):3601–3613
14. Allen LH, Ramanath G, Lai SL, Ma Z, Lee S, Allman DDJ, Fuchs KP (1994) 1,000,000 °C/s thin film electrical heater: In situ resistivity measurements of Al and Ti/Si thin films during ultra rapid thermal annealing. Appl Phys Lett 64(4):417–419
15. Lai SL, Ramanath G, Allen LH, Infante P, Ma Z (1995) High-speed (10^4 °C/s) scanning microcalorimetry with monolayer sensitivity (J/m^2). Appl Phys Lett 67(9):1229–1231
16. Minakov AA, Herwaarden AW, Wien W, Wurm A, Schick C (2007) Advanced nonadiabatic ultrafast nanocalorimetry and superheating phenomenon in linear polymers. Thermochim Acta 461(1–2):96–106
17. Lai SL, Carlsson JRA, Allen LH (1998) Melting point depression of Al clusters generated during the early stages of film growth: nanocalorimetry measurements. Appl Phys Lett 72(9):1098–1100
18. Gao YL, Zhao BG, Vlassak JJ, Schick C (2019) Nanocalorimetry: door opened for in situ material characterization under extreme non-equilibrium conditions. Prog Mater Sci 104:53–137
19. Denlinger DW, Abarra EN, Allen K, Rooney PW, Messer MT, Watson SK, Hellman F (1994) Thin film microcalorimeter for heat capacity measurements from 1.5 to 800 K. Rev Sci Instrum 65(4):946–959

20. Gao YL, Zhuravlev E, Zou CD, Yang B, Zhai QJ, Schick C (2009) Calorimetric measurements of undercooling in single micron sized SnAgCu particles in a wide range of cooling rates. Thermochim Acta 482(1–2):1–7
21. Yang B, Gao YL, Zou CD, Zhai QJ, Abyzov AS, Zhuravlev E, Schmelzer JWP, Schick C (2011) Cooling rate dependence of undercooling of pure Sn single drop by fast scanning calorimetry. Appl Phys A 104(1):189–196
22. Li S, Zhang L, Zhao BG, Ding K, Gao YL (2022) Cooling rate and roughness dependence of the undercooling for one single Sn droplet with Si thin film substrate by nanocalorimetry. Paper presented at the 151st TMS annual meeting, Anaheim, California, 27 Feb–03 Mar 2022, pp 305–314
23. Minakov AA, Schick C (2007) Ultrafast thermal processing and nanocalorimetry at heating and cooling rates up to 1 MK/s. Rev Sci Instrum 78(7):2335–2364
24. Yang B, Gao YL, Zou CD, Zhai QJ, Zhuravlev E, Schick C (2009) Repeated nucleation in an undercooled tin droplet by fast scanning calorimetry. Mater Lett 63(28):2476–2478

Numerical Simulation of Scrap Preheating with Flue Gas in EAF Steelmaking Process

Hang Hu, Lingzhi Yang, Guangsheng Wei, Yuchi Zou, Botao Xue, Feng Chen, Shuai Wang, and Yufeng Guo

Abstract EAF steelmaking process is served as energy intensive fields, which releases massive high-temperature flue gas with consumption of extensive raw materials and energies. The effective utilization of waste heat is essential for energy conservation and emission reduction in the iron and steel industry. Scrap preheating with flue gas is a high-efficiency method for direct waste heat recovery and utilization. In this paper, the influence of scrap size and arrangement on preheating effectiveness was researched and simulated by ANSYS Fluent 18.2 software. The temperature distribution characteristics and quantitative values of scrap were further calculated and analyzed. The results indicated that the average temperature of the scrap was higher than 500 °C after continuously being preheated for 15 min by flue gas at 1200 °C. This study is beneficial for evaluating scrap temperature before charging to the EAF, and expected to facilitate green, low-carbon, and environmentally friendly development of efficient waste heat utilization in the EAF steelmaking process.

Keywords EAF steelmaking · Numerical simulation · Scrap preheating · Flue gas · Temperature distribution

Introduction

Electric arc furnace (EAF) steelmaking process is the main method for steel production both in China and world [1]. It mainly takes scrap as raw metallurgical charges, thereby realizing the reuse and recycling of scrap steel resources. EAF steelmaking process is characterized by energy-intensive and high-cost, especially large-scale electricity and other fossil fuels consumption [2]. In the EAF smelting process, the

H. Hu · L. Yang (✉) · Y. Zou · F. Chen · S. Wang · Y. Guo
School of Minerals Processing and Bioengineering, Central South University, Changsha 410083, China
e-mail: yanglingzhi@csu.edu.cn

G. Wei · B. Xue
School of Metallurgical and Ecological Engineering, University of Science and Technology Beijing, Beijing 100083, China

Z. Peng et al. (eds.), *Characterization of Minerals, Metals, and Materials 2024*, The Minerals, Metals & Materials Series, https://doi.org/10.1007/978-3-031-50304-7_55

temperature of the flue gas discharged from the fourth-hole is as high as 1200 °C. Direct emission of this flue gas would undoubtedly result in extensive energy wasting. It is of great significance to recover the waste heat of flue gas for improving energy efficiency [3].

Many researchers are committed to the studies of the recovery and utilization of flue gas waste heat in the EAF steelmaking process. Brandt et al. [4] designed a tube bundle heat exchanger driven by heat transfer oil for recovering the waste gas heat, and simulated the designed device with ANSYS CFX software. Tian et al. [5] evaluated the exergy loss of the off-gas heat recovery system integrated with the EAF steelmaking process, and compared the carbon reduction effect before and after adopting the heat recovery strategy. Ramirez et al. [6] developed a large organic Rankine cycle and waste heat recovery unit and used it in a steel plant to recover waste heat from the electric arc furnace flue gas and produce steam as a heating source. Pili et al. [7] also researched the organic Rankine cycle heat recovery system, but he focused on the power generation technology by high-temperature off-gas. Yang et al. [3] compared four off-gas waste heat utilization methods: scrap preheating, waste heat power generation, steam production, and low-grade gas production, the results indicated that the best plan for waste heat utilization was to combine scrap preheating with low-grade gas production. Lee et al. [8] discussed the preheating effect of a vertical shaft preheater and horizontal double-shell flue gas preheater for preheating scrap. Li et al. [9] proposed a vertical high temperature flue gas preheating charge and circulation technology, and found that high temperature flue gas can increase the temperature of the charges above 600 °C.

From the above description, it is concluded that preheating scrap by flue gas is the optimal solution for direct utilization of waste heat. This scheme has the advantages of higher heat transfer rate, finer energy efficiency, lower electricity consumption, and shorter tap-to-tap time. Therefore, in this paper, a two-dimensional model of the flue gas preheating scrap system (FG-PSS) was established according to a steelwork. Based on the numerical simulation of ANSYS Fluent 18.2 and theoretical calculation, the influence of scrap size and arrangement on preheating effectiveness was researched and analyzed. Besides, the temperature distribution characteristics and quantitative values of scrap and flue gas were further investigated. The results revealed that the average temperature of the scrap was higher than 500 °C after continuously preheated for 15 min by flue gas at 1200 °C. This research is expected to provide a basis for high-efficiency utilization of waste heat in the EAF steelmaking process.

Mathematical Modeling and Numerical Simulation

Governing Equations and Sub-Models

In the scrap storage bin, the accumulational scrap is continuously heated by the bottom-top high-temperature flue gas with the temperature of 1200 °C. The convection and radiation heat transfer are carried out between scrap and flue gas. The basic governing equations and sub models of the heat transfer simulation process are shown below.

(1) Mass-momentum-energy conservation equations

In a typical transportation and chemical reaction process, the total amount of materials and energy sources of the system are conserved. The mass, momentum, and energy conservation equations are displayed in Eqs. (1)–(5).

$$\partial\rho/\partial t + \nabla \cdot \left(\rho \overrightarrow{\upsilon}\right) = S_m \tag{1}$$

$$\begin{aligned}\rho\frac{\mathrm{d}\upsilon_x}{\mathrm{d}t} &= \rho F_x - \frac{\partial p}{\partial x} + \frac{\partial}{\partial x}\left(\mu\frac{\partial \upsilon_x}{\partial x}\right) + \frac{\partial}{\partial y}\left(\mu\frac{\partial \upsilon_x}{\partial y}\right) \\ &\quad + \frac{\partial}{\partial z}\left(\mu\frac{\partial \upsilon_x}{\partial z}\right) + \frac{\partial}{\partial x}\left[\frac{\mu}{3}\left(\frac{\partial \upsilon_x}{\partial x} + \frac{\partial \upsilon_y}{\partial y} + \frac{\partial \upsilon_z}{\partial z}\right)\right]\end{aligned} \tag{2}$$

$$\begin{aligned}\rho\frac{\mathrm{d}\upsilon_y}{\mathrm{d}t} &= \rho F_y - \frac{\partial p}{\partial y} + \frac{\partial}{\partial x}\left(\mu\frac{\partial \upsilon_y}{\partial x}\right) + \frac{\partial}{\partial y}\left(\mu\frac{\partial \upsilon_y}{\partial y}\right) \\ &\quad + \frac{\partial}{\partial z}\left(\mu\frac{\partial \upsilon_y}{\partial z}\right) + \frac{\partial}{\partial y}\left[\frac{\mu}{3}\left(\frac{\partial \upsilon_x}{\partial x} + \frac{\partial \upsilon_y}{\partial y} + \frac{\partial \upsilon_z}{\partial z}\right)\right]\end{aligned} \tag{3}$$

$$\begin{aligned}\rho\frac{\mathrm{d}\upsilon_z}{\mathrm{d}t} &= \rho F_z - \frac{\partial p}{\partial z} + \frac{\partial}{\partial x}\left(\mu\frac{\partial \upsilon_z}{\partial x}\right) + \frac{\partial}{\partial y}\left(\mu\frac{\partial \upsilon_z}{\partial y}\right) \\ &\quad + \frac{\partial}{\partial z}\left(\mu\frac{\partial \upsilon_z}{\partial z}\right) + \frac{\partial}{\partial z}\left[\frac{\mu}{3}\left(\frac{\partial \upsilon_x}{\partial x} + \frac{\partial \upsilon_y}{\partial y} + \frac{\partial \upsilon_z}{\partial z}\right)\right]\end{aligned} \tag{4}$$

$$\partial(\rho T)/\partial t + \mathrm{div}(\rho \upsilon T) = \mathrm{div}(\lambda \mathrm{grad} T/c_p) + S_m \tag{5}$$

where υ_x, υ_y, and υ_z denote the velocity of fluid in the directions of x, y, and z, m/s; ρF_x, ρF_y, and ρF_z, denote the mass force per unit volume, N; μ denotes the viscosity of fluid, Pa s; T denotes the temperature of fluid, K; div denotes the velocity divergence; S_m denotes the energy source term.

(2) Radiation heat transfer equation

The simulation of radiation heat transfer between scrap and flue gas should meet the requirement of Eq. (6).

$$\frac{\mathrm{d}I(\vec{r},\vec{s})}{\mathrm{d}s}+(\alpha+\sigma_s)I(\vec{r},\vec{s})=\alpha n^2\frac{\sigma T^4}{\pi}+\frac{\sigma_s}{4\pi}\int_0^{4\pi}I(\vec{r},\vec{s})\Phi(\vec{s},\vec{s}\prime)\mathrm{d}\Omega\prime \quad (6)$$

where $I\left(\overrightarrow{r},\overrightarrow{s}\right)$ denotes the radiation intensity of different direction vector ($\overrightarrow{r}$) and locations ($\overrightarrow{s}$), W/m^2. s denotes the travel length of the ray, m. α, n, and σ_s denotes the absorption coefficient, refraction coefficient, and scattering coefficient, respectively. T denotes the temperature of the radiator, K. Φ denotes the phase function. $\Omega\prime$ denotes the space angle, rad.

(3) Simulation controlling models

The simulation controlling models mainly include the DO radiation model and the standard $k-\varepsilon$ turbulence model, which are displayed in Eq. (7) and Eqs. (8)–(9). The turbulent viscosity is determined by Eq. (10).

$$\nabla\cdot(I(\vec{r},\vec{s})\vec{s})+(\alpha+\sigma_s)I(\vec{r},\vec{s})=\alpha n^2\frac{\sigma T^4}{\pi}+\frac{\sigma_s}{4\pi}\int_0^{4\pi}I(\vec{r},\vec{s})\Phi(\vec{s},\vec{s}\prime)\mathrm{d}\Omega\prime \quad (7)$$

$$\frac{\partial}{\partial t}(\rho k)+\frac{\partial}{\partial x_i}\left(\rho k\mu_i\right)=\frac{\partial}{\partial x_j}\left[\left(\mu+\frac{\mu_t}{\sigma_k}\right)\frac{\partial k}{\partial x_j}\right]+G_k+G_b-\rho\varepsilon-Y_M+S_k \quad (8)$$

$$\frac{\partial}{\partial t}(\rho\varepsilon)+\frac{\partial}{\partial x_i}(\rho\varepsilon\mu_i)=\frac{\partial}{\partial x_j}\left[\left(\mu+\frac{\mu_t}{\sigma_\varepsilon}\right)\frac{\partial\varepsilon}{\partial x_j}\right]+C_{1\varepsilon}\frac{\varepsilon}{k}(G_k+C_{3\varepsilon}G_b)-C_{2\varepsilon}\rho\frac{\varepsilon^2}{k}+S_\varepsilon \quad (9)$$

$$\mu_t=\rho C_\mu\frac{k^2}{\varepsilon} \quad (10)$$

The specific meanings, numerical values and derivation processes of the relevant parameters in the correlation sub-models and governing equations are referred to reference [10, 11].

Basic Assumptions and Boundary Conditions of Model Building

The research object of this paper is a flue gas preheating scrap system of a 100t EAF. The relevant parameters of the FG-PSS are shown in Table 1. The accumulation form of scrap in the scrap storage bin is chaotic and disordered. Besides, the scrap geometry is also different. These make it difficult to obtain the temperature distribution character of scrap during preheating. Thus, the physical field of actual FG-PSS is simplified to meet the requirement of numerical simulation. A 1:10 calculation

Table 1 Relevant parameters of flue gas preheating scrap system

Object	Parameters	Value
Scrap	Bulk density	0.6 t/m^3
	Maximum block size	1500 mm
	Total mass	30 ton
	Initial temperature	25 °C
Flue gas	Initial temperature	1200 °C
	Volume flow	2000 Nm^3/min
	Dust content	1.5%
Scrap storage bin	Height	5 m
	Length	4 m
	Width	2 m

model is established based on the bulk density of scrap and geometric parameter of the scrap storage bin, as shown in Fig. 1.

In the preheating process of the long strip scrap, due to the non-uniformity of the radiation heat transfer process of high temperature flue gas, the ability of the bottom scrap to receive radiation heat energy is obviously stronger than that of the upper scrap, resulting in a great non-uniformity of the temperature distribution of local overheating and undercooling phenomenon. Considering that the scrap does not show obvious continuous distribution, and there will be a hot flue gas flow channel

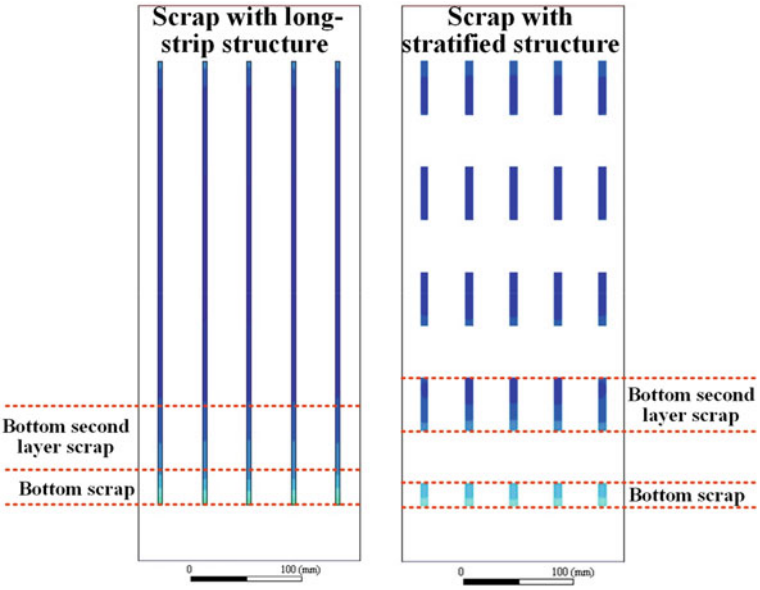

Fig. 1 Geometric model and zone division of scrap

between the adjacent scrap, forming a large area of high temperature flue gas and scrap full convection heat exchange, and the radiation heat exchange between the adjacent scrap will also be significantly strengthened. Thus, except for long strip scrap, the five-layer structure of the scrap was also simulated under the condition that the overall scrap area remains unchanged. The temperature distribution of two different scrap arrangements were simulated and compared.

Results and Discussion

The simulation results are displayed in Fig. 2. The flue gas heated the scrap from bottom to top in the scrap storage bin, and its temperature gradually decreases. With the increase of heating time, the temperature of the scrap gradually increases from outside to inside. The scrap located in the bottom possesses great preheating effect, while that at the top is worse.

When the scrap was arranged in a long-strip structure (Scheme 1), the flue gas flow suffered less resistance, which led to the short residence time, incomplete utilization of waste heat, and poor heat transfer coefficient. In contrast, adopting the stratified structure (Scheme 2) was beneficial for increasing airflow aisle, frictional resistance and heat transfer area, strengthening flow disturbance and convection heat transfer. Furthermore, more scrap was involved in the radiant heat transfer system. Therefore, the scrap with stratified structure enjoyed better preheating effect, and the temperature of the scrap was higher, and the temperature field distribution was more uniform in FG-PSS. In light of the situation that the scrap in the scrap storage bin was continuously charged into the EAF, and the heating surface of the scrap constantly changed. We concentrated on the bottom scrap, and obtained the average temperature by the face-averaging method. The detailed values were displayed in Table 2.

In scheme1, the scrap was continuously preheated by the flue gas at 1200 °C for 15 min, the average temperature of the scrap at the bottom layer and bottom second layer had reached 599.09 and 432.15 °C, respectively. In scheme 2, under the same conditions, the average temperatures were 607.30 and 467.18 °C, respectively. Both two schemes could meet the corresponding index of the preheating temperature of the scrap higher than 500 °C. However, scheme 2 had significant advantages in higher preheating temperature and utilization efficiency of waste heat. In the actual production practice, the average temperature of the scrap after being preheated by the flue gas can reach more than 500 °C, and this optimization method achieves better benefits on reducing energy consumption, improving production efficiency, and maintaining effective waste heat recovery.

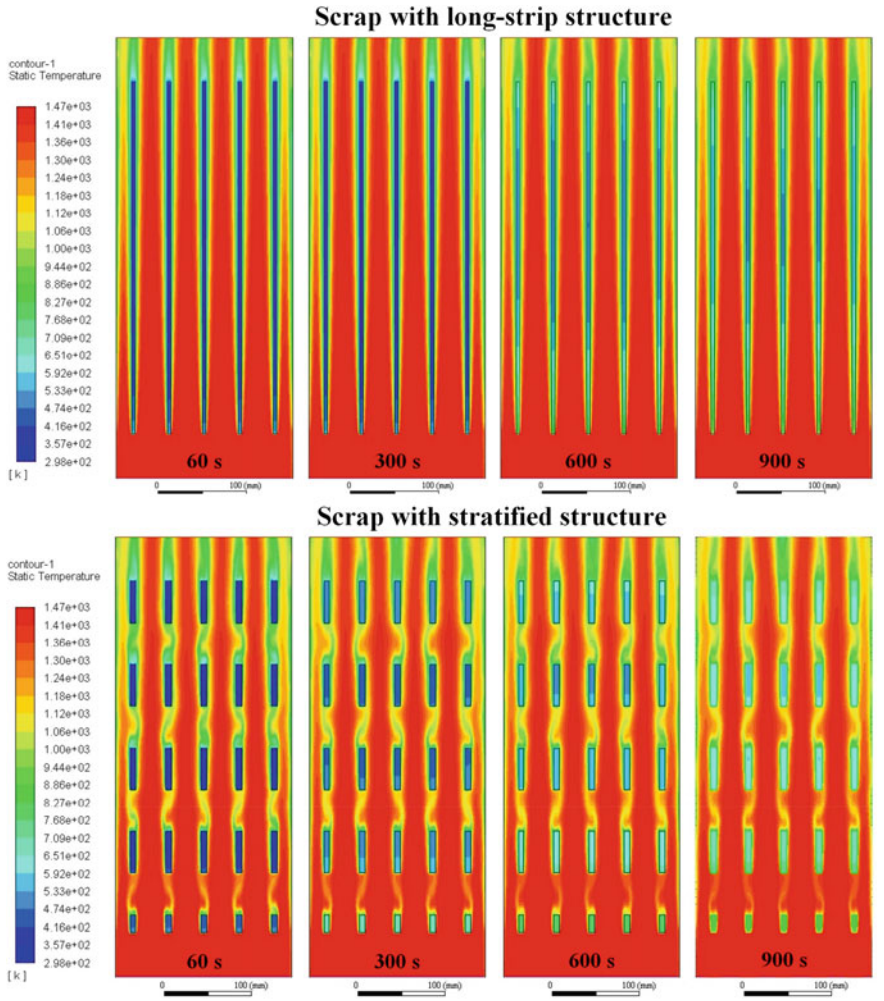

Fig. 2 Temperature contours of FG-PSS under different scrap arrangement

Table 2 Average temperature of bottom scrap under different heating times

Scheme	Preheating time	Average temperature (°C)				
		0 s	60 s	300 s	600 s	900 s
Scheme 1	Bottom second layer scrap	25 °C	127.25 °C	277.80 °C	367.55 °C	432.15 °C
	Bottom scrap	25 °C	191.81 °C	404.11 °C	522.91 °C	599.09 °C
Scheme 2	Bottom second layer scrap	25 °C	142.55 °C	297.60 °C	402.35 °C	467.18 °C
	Bottom scrap	25 °C	235.45 °C	424.65 °C	534.24 °C	607.30 °C

Conclusion

Preheating scrap by high-temperature flue gas is an efficient way to recover and utilize waste heat in EAF steelmaking process, which increases the charged temperature of the scrap and reduce energy consumption. In this paper, a two-dimensional model of FG-PSS was developed to investigated the preheating effect and temperature distribution. Two scrap arrangements were researched and compared from perspectives of temperature contours and average temperature of the bottom scrap under different preheating times. The relevant conclusions are summarized as follows:

(1) When the scrap was arranged at the long-strip structure, the average temperature of the scrap at the bottom layer and bottom second layer had reached 599.09 and 432.15 °C, respectively, with the preheating time of 15 min. This scheme could meet the corresponding index of the preheating temperature of scrap higher than 500 °C. However, it also existed the phenomenon of local supercooling and overheating, and uniform temperature field distribution of scrap.
(2) Under the condition that the stratified structure of scrap arrangement was adopted, the average temperatures of the scrap at the bottom layer and the bottom second layer were 607.30 and 467.18 °C, respectively. This scheme could not only meet the requirement, but also enhanced the heat transfer coefficient and utilization efficiency of waste heat.
(3) In the course of practical industrial applications, considering the disorganized distribution of scrap, abundant flue gas aisle, the convective heat transfer effect under turbulent viscous heating is significantly improved, and scrap can be preheated to the higher temperature.

Acknowledgements The authors are grateful for financial support from the National Natural Science Foundation of China (No. 52174328).

References

1. Yang LZ, Hu H, Yang ZS, Xue BT, Guo YF, Wang S (2021) A review on bath fluid flow stirring technologies in EAF steelmaking. J Iron Steel Res Int 28(11):1341–1351
2. Brandt C, Schüler N, Gaderer M, Kuckelkorn JM (2014) Development of a thermal oil operated waste heat exchanger within the off-gas of an electric arc furnace at steel mills. Appl Therm Eng 66(1–2):335–345
3. Tian BH, Wei GS, Hu H, Zhu R, Bai H, Wang ZM, Yang LZ (2023) Effects of fuel injection and energy efficiency on the production and environmental parameters of electric arc furnace-heat recovery systems. J Clean Prod 405:136909
4. Ramirez M, Epelde M, Arteche MG, Panizza A, Hammerschmid A, Baresi M, Monti N (2017) Performance evaluation of an ORC unit integrated to a waste heat recovery system in a steel mill. Energy Proced 129:535–542
5. Pili R, Martínez LG, Wieland C, Spliethoff H (2020) Techno-economic potential of waste heat recovery from German energy-intensive industry with organic rankine cycle technology. Renew Sust Energ Rev 134:110324

6. Yang LZ, Jiang T, Li GH, Guo YF, Chen F (2018) Present situation and prospect of EAF gas waste heat utilization technology. High Temp Mat Pr-ISR 37(4):1–7
7. Chen LG, Yang B, Shen X, Xie ZH, Sun FR (2015) Thermodynamic optimization opportunities for the recovery and utilization of residual energy and heat in China's iron and steel industry: a case study. Appl Therm Eng 86:151–160
8. Lee B, Sohn I (2014) Review of innovative energy savings technology for the electric arc furnace. JOM 66(9):1581–1594
9. Li QS, Zhao CZ, Xie GW (2021) Study on the technology of vertical preheating and recycling of fully enclosed submerged arc furnace. Energy Metall Ind 40(04):21–23
10. Mombeni AG, Hajidavalloo E, Nejad MB (2016) Transient simulation of conjugate heat transfer in the roof cooling panel of an electric arc furnace. Appl Therm Eng 98:80–87
11. Khodabandeh E, Rahbari A, Rosen MA, Ashrafi ZN, Akbari OA, Anvari AM (2017) Experimental and numerical investigations on heat transfer of a water-cooled lance for blowing oxidizing gas in an electrical arc furnace. Energy Convers Manage 148:43–56

Obtaining Ferroelectric Tetragonal Phase Type $Ba_{1-3x}La_{2x}Ti_{1-3x}Bi_{4x}O_3$ ($0 < x < 0.0075$) Using the Mechanical Grinding Method

María Inés Valenzuela Carrillo, Miguel Pérez Labra, Francisco Raúl Barrientos Hernández, Ricardo Martínez López, and Martín Reyes Pérez

Abstract Pure and doped barium titanate powders were prepared by the ball milling method starting from Barium Carbonate ($BaCO_3$, 99.0%), Titanium Oxide (TiO_2, 99.0%), Lanthanum Oxide (La_2O_3, 99.9%), and Bismuth Oxide (Bi_2O_3, 99.999%). The stoichiometric calculations were made using the $Ba_{1-3x}La_{2x}Ti_{1-3x}Bi_{4x}O_3$ mechanism with the concentrations $x = 0.000$, 0.0025, 0.005, and 0.0075 (wt.%). The powders were mixed in a ball mill with zirconia oxide balls of three different diameter sizes (2.95, 5.05, and 6.48 mm) for 6 h and dried. The powders were sintered at 1200 °C for 5 h; the heating rate was 4 °C/min. The structural evolution of the samples was characterized by X-ray diffraction (XRD) and Rietveld refinement. The analysis of XRD patterns revealed the formation of a well-crystallized tetragonal phase of $BaTiO_3$ (JCPDS 961525438) for the compositions $x = 0.0$, 0.0025, and 0.005 and the beginning of a tetragonal to cubic phase transition was observed for the composition $x = 0.0075$.

Keywords Ceramics · Characterization · Powder materials · $BaTiO_3$ · Lanthanum · Bismuth

M. I. V. Carrillo (✉) · M. P. Labra · F. R. B. Hernández · R. M. López · M. R. Pérez
Academic Area of Earth Sciences and Materials, Autonomous University of Hidalgo State, Road Pachuca- Tulancingo km 4.5 Mineral de La Reforma, 42184 Hidalgo, Mexico
e-mail: inesvalenzuelac10@gmail.com

Z. Peng et al. (eds.), *Characterization of Minerals, Metals, and Materials 2024*, The Minerals, Metals & Materials Series, https://doi.org/10.1007/978-3-031-50304-7_56

Introduction

Since its discovery, Barium Titanate ($BaTiO_3$) has caught researchers' attention because of its applications in capacitors, multilayer capacitors (MLCs), and energy storage devices. $BaTiO_3$ has a Perovskite structure with tetragonal symmetry at room temperature and a high dielectric constant [1]. Dielectric materials have some inherent properties, such as ferroelectricity, piezoelectricity, and pyroelectricity. Because of these electrical properties, $BaTiO_3$ has multiple electronic applications [2].

The electrical and structural properties of $BaTiO_3$ depend on a series of composition and processing parameters, such as the dopant ions involved, the conditions, and the method of ceramic processing, especially temperature, time, pressure, and sintering atmosphere [2]. Different types of dopants are used to study the effects of their improvement on $BaTiO_3$, mainly on the electrical properties of the ceramic [3]. The present work reports the synthesis and characterization of $Ba_{1-3x}La_{2x}Ti_{1-3x}Bi_{4x}O_3$ ceramics, where x represents the concentration of dopant ions (wt.%); these ions have been selected because there is evidence of an improvement in the dielectric properties of $BaTiO_3$ individually doped with La^{3+} or Bi^{3+} [4, 5]. It is considered that the valence state and the radius of La^{3+} (1.06 Å) and Bi^{3+} (1.20 Å) ions are intermediate between those of Ba^{2+} ion (1.42 Å) and Ti^{4+} ion (0.61 Å). It is then expected that La^{3+} and Bi^{3+} can occupy either barium or titanium sites, depending on the Ba/Ti mole ratio [6, 7].

The synthesis method can also be varied to obtain different characteristics in the material. The ceramic could be obtained by conventional solid-state reaction or by non-conventional methods, such as the Pechini process, the sol–gel procedure, or special mechanical treatment of initial powders [8]. In the present work, the ball milling method was used; this process is part of the solid-state synthesis methods and has been successfully used to synthesize nano-crystalline oxide powders, such as perovskite ferroelectrics [9]. The ball charge was distributed by three sizes of zirconia balls considering the Gaudin-Schuman distribution [10]. The zirconia material was chosen to avoid contamination in the milling process.

Materials and Methods

The doped barium titanate ceramics were prepared by the ball milling method starting from Barium Carbonate ($BaCO_3$, 99.0% CAS: 513-77-9), Titanium Oxide (TiO_2, 99.0% CAS: 13463-67-7), Lanthanum Oxide (La_2O_3, 99.9% CAS: 1312-81-8) and Bismuth Oxide (Bi_2O_3, 99.999% CAS: 1312-81-8). These powders have a mean particle size of 7.69 μm for $BaCO_3$, 0.76 μm for TiO_2, 5.67 μm for La_2O_3, and 15.05 μm for Bi_2O_3. The stoichiometric calculations were made using the $Ba_{1-3x}La_{2x}Ti_{1-3x}Bi_{4x}O_3$ mechanism with the concentrations $x = 0.0$, 0.0025, 0.005, and 0.0075 (wt.%). The powders were mixed in a cylindrical PET container with

zirconia oxide balls of three different diameter sizes (2.95, 5.05, and 6.48 mm) in acetone as a control medium for 6 h and dried. The ball charge distribution for ball milling was calculated by the Gaudin-Schumann equation [10]:

$$Y = 100 \times \left(\frac{d}{d_{\max}}\right)^{3.8}$$

where,

- Y—cumulative contribution of a ball of smaller diameter d
- d—ball diameter
- $d_{\max}$—diameter of the largest ball.

The powders were sintered in air at 1200 °C for 5 h; the heating rate was 4 °C/min. The crystalline evolution was identified by an X-ray diffractometer (XRD, Inel Equinox 2000) with $K_{\alpha 1}$ radiation.

Results and Discussion

The X-ray diffraction patterns (XRD) obtained for the $BaTiO_3$-based sintered powders are shown in Fig. 1, corresponding to the compositions $x = 0.0$, 0.0025, 0.005, and 0.0075. XRD diffractogram analysis was performed using Match!3 software, where the phases present in each composition were determined. All the peaks observed in the diffractograms for the compositions $x = 0.000$, 0.002, 0.005, and 0.0075 of La^{3+} and Bi^{3+} (wt%) are comparable with those present in the diffraction pattern for pure $BaTiO_3$ in the tetragonal phase at room temperature JCPDS 961525438 (at positions $2\theta \approx 26.12°$, 37.06°, 45.80°, 53.49°, 60.30°, 66.67°, 78.56°, 84.42°, 89.56°, 90.44°).

In Fig. 1, slight width and position differences in the peaks can be observed, which is attributed to a lattice parameter change in the ceramic structure as an effect of the addition of the dopant ions La^{3+} and Bi^{3+}. However, the general form coincides with what is expected for $BaTiO_3$ in the tetragonal phase, and no other phase is observed. Therefore, at the concentration $x = 0.0075$, the solubility limit of the dopants in the $BaTiO_3$ structure is not yet exceeded.

Figure 2 compares the XRD results for concentrations $x = 0.0$, 0.0025, 0.005, and 0.0075, between the positions $2\theta = 86°$ and $2\theta = 95°$. It can be observed how the peak located at $2\theta \approx 89.56°$ decreases in intensity from $x = 0.0$ until almost disappearing at the concentration $x = 0.0075$, which demonstrates a transformation from tetragonal to cubic phase as the amount of dopant increases.

The structural evolution of solid solutions was studied through changes in the volume of the unit cell and its lattice parameters (a and c). To calculate the lattice parameters, the results obtained from the XRD diffractograms were used and the Rietveld refinement method was performed using the FullProf software. Table 1

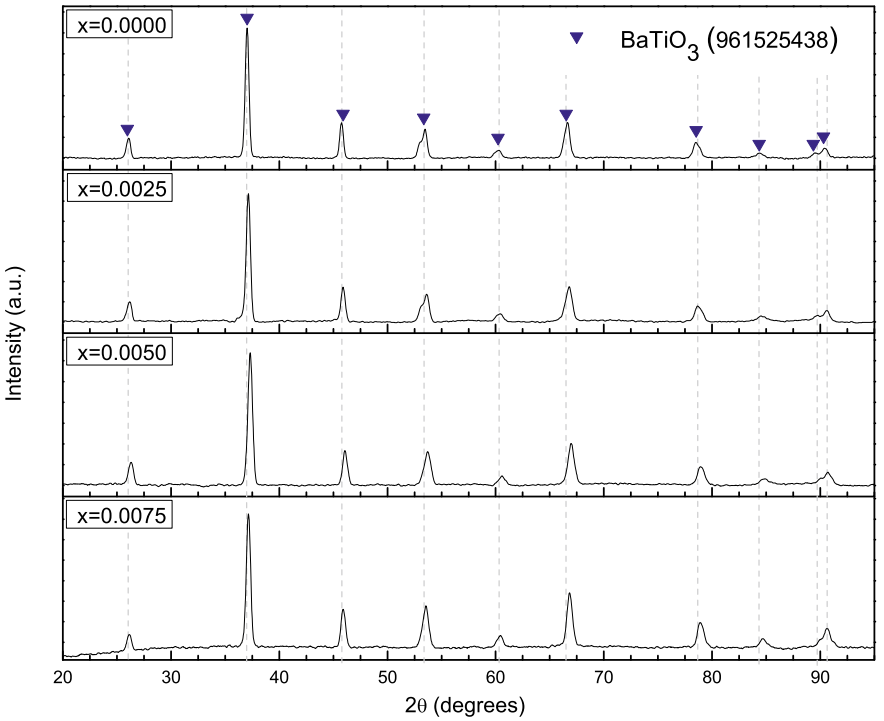

Fig. 1 XDR patterns for the compositions $x = 0.0$, 0.0025, 0.005, and 0.0075 of La^{3+} and Bi^{3+} (wt.%)

represents the evolution of lattice parameters, *a* and *c*, as a function of the concentration *x* for the tetragonal unit cell, and it was observed that these parameters generally experience a slight contraction compared to the parameters for the undoped $BaTiO_3$ ($x = 0.0$). This decrease in the lattice parameters is attributed to the partial substitution of La^{3+} and Bi^{3+} ions at the Ba^{2+} and Ti^{4+} sites. From the change in lattice parameters, we can assume a greater substitution in the Ba^{2+} ion, since the results indicate the substitution of a smaller ion that results in the decrease of the lattice parameters, and Ba^{2+} presents a larger ionic radius (1.42 Å) than the ionic radius of the dopants La^{3+} (1.06 Å) and Bi^{3+} (1.20 Å).

In the fourth column, we can see how the tetragonality ratio of the system evolves, which is related to the ferroelectricity of the ceramic. When the tetragonality is 1 it means that the system is in cubic phase and no longer has the ferroelectricity property of a tetragonal structure. It can be seen that from the concentration $x = 0.0$ to $x = 0.0025$ there is an increase in tetragonality, which decreases at the concentrations $x = 0.005$ and $x = 0.0075$. The tetragonality closest to 1 is found at $x = 0.0075$ (1.0038), that is, it is closest to a cubic phase. This result agrees with the XRD results in Fig. 2

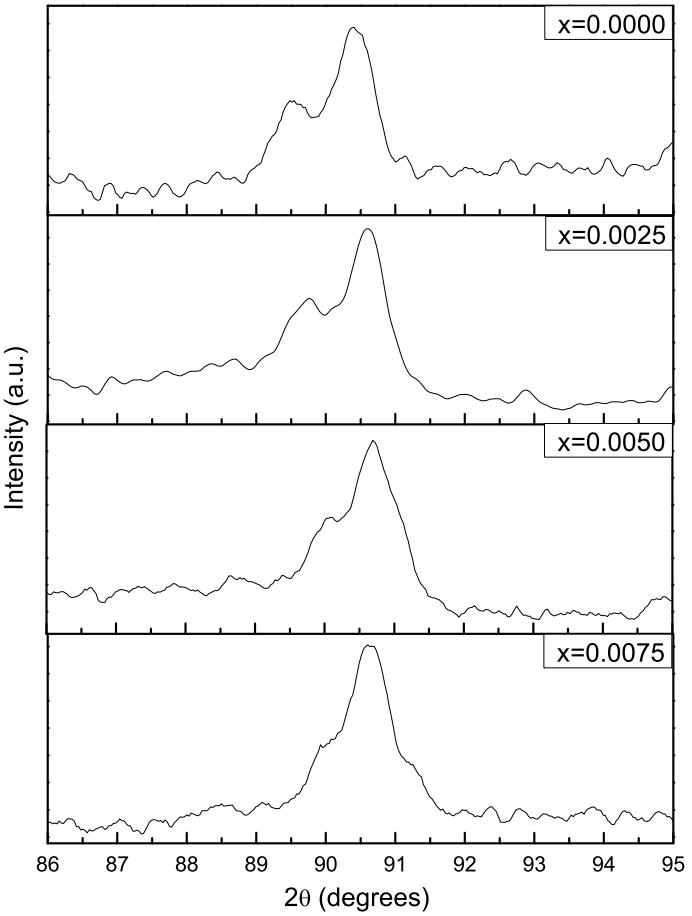

Fig. 2 XDR patterns for the compositions $x = 0.0$, 0.0025, 0.005, and 0.0075 of La^{3+} and Bi^{3+} (wt.%) between the positions $2\theta = 86°$ and $2\theta = 95°$

Table 1 Lattice parameters calculations for each concentration x

x	Parameters		Tetragonality (c/a)	Volume (Å^3)
	a (Å)	c (Å)		
0.0000	3.9915	4.0250	1.0084	64.1266
0.0025	3.9697	4.0048	1.0088	63.1097
0.0050	3.9582	3.9865	1.0071	62.4579
0.0075	3.9728	3.9878	1.0038	62.9400

where the beginning of a transition to cubic phase is observed at the concentration $x = 0.0075$, since one of the characteristic peaks of $BaTiO_3$ in the tetragonal phase begins to decrease.

In addition, Table 1 shows the unit cell volume evolution for each composition. In this case, it is observed that all the compositions present a contraction in the cell volume compared to the composition $x = 0.0$, which represents the pure $BaTiO_3$.

Conclusions

The XRD patterns obtained correspond to the diffraction pattern of pure $BaTiO_3$ in the tetragonal phase at room temperature (JCPDS 961525438). No secondary phase is identified; therefore, the solubility limit of La^{3+} and Bi^{3+} ions in $BaTiO_3$ has not yet reached for $x = 0.0075$. It was determined that the concentration of La^{3+} and Bi^{3+} in solid solutions of the type $Ba_{1-3x}La_{2x}Ti_{1-3x}Bi_{4x}O_3$ have significant effects on the a and c lattice parameters, which decrease compared to pure $BaTiO_3$ in the tetragonal phase. The evolution of the tetragonality, as well as the XRD results, indicate a transformation from tetragonal to cubic phase as the amount of dopant increases, which is evident due to the decrease of the peak located at $2\theta \approx 89.56°$ in the diffractograms, which is almost imperceptible in the concentration $x = 0.0075$.

References

1. Vijatović MM, Bobić JD, Stojanović BD (2008) History and challenges of barium titanate: Part I. Sci Sinter 40:155–165. https://doi.org/10.2298/SOS0802155V
2. Vijatović MM, Bobić JD, Stojanović BD (2008) History and challenges of barium titanate: Part II. Sci Sinter 40:235–244. https://doi.org/10.2298/SOS0803235V
3. Buscaglia M, Buscaglia V, Viviani M, Nanni P, Hanuskova M (2000) Influence of foreign ions on the crystal structure of batio3. J Eur Ceram Soc 20:1997–2007. https://doi.org/10.1016/S0955-2219(00)00076-5
4. Vijatovic M, Stojanovic B, Bobic J, Ramoska T, Bowen P (2010) Properties of lanthanum doped batio3 produced from nanopowders. Ceram Int 26(1817):1824. https://doi.org/10.1016/j.ceramint.2010.03.010
5. Wu S, Wei X, Wang X, Yang H, Gao S (2010) Effect of Bi_2O_3 additive on the microstructure and dielectric properties of batio3-based ceramics sintered at lower temperature. J Mater Sci Technol 26:472–476. https://doi.org/10.1016/S1005-0302(10)60075-8
6. Dunbar TD, Warren WL, Tuttle BA, Randall CA, Tsur Y (2004) Electron paramagnetic resonance investigations of lanthanide-doped barium titanate: dopant site occupancy. J Phys Chem 108:908–917. https://doi.org/10.1021/jp036542v
7. Hennings DF (2001) Dielectric materials for sintering in reducing atmospheres. J Eur Ceram Soc 21:1637–1642. https://doi.org/10.1016/S0955-2219(01)00082-6
8. Stojanovic BD, Jovalekic C, Vukotic V, Simoes AZ, Varela JA (2005) Ferroelectric properties of mechanically synthesized nanosized barium titanate. Ferroelectrics 319:65–73. https://doi.org/10.1080/00150190590965424

9. Stojanovic B, Simoes A, Paiva-Santos C, Jovalekic C, Mitic V, Varela J (2005) Mechanochemical synthesis of barium titanate. J Eur Ceram Soc 25:1985–1989. https://doi.org/10.1016/j.jeurceramsoc.2005.03.003
10. Magdalinovic N, Trumic M, Trumuc M, Andric L (2012) The optimal ball diameter in a mill. Physicochem Probl Min Process 48:329–339. https://doi.org/10.5277/ppmp120201

Performance Evaluation of Açaí Fiber as Reinforcement in Coating Mortars

J. F. Natalli, I. S. A. Pereira, E. R. G. Júnior, S. A. A. Malafaia, I. D. Batista, M. V. Barbosa, M. T. Marvila, F. M. Margem, T. E. S. Lima, S. N. Monteiro, and A. R. G. Azevedo

Abstract The Amazon region faces a major obstacle caused by the high production of several natural fibers, such as açaí (*Euterpe oleracea*). There is still no specific and consolidated destination for agro-industrial waste generated in the different stages of processing Amazonian fibers, causing environmental changes in the region. Furthermore, it is known that the use of these fibers can promote an increase in ductile behavior and tensile strength in cementitious composites. With the objective of contributing to the creation of new strategies that guarantee the improvement of mortar properties and, at the same time, collaborate for an efficient disposal of the waste in question, this work aimed to evaluate properties of mortars in the fresh state with the addition of acai fibers. Three types of mortar were developed: (1) reference (without the use of fibers); (2) with the addition of fibers without surface treatment; and (3) with the addition of material with surface treatment based on tannic acid with a concentration of 5% by volume. The fibers were added in the proportions of 0.5,

J. F. Natalli · I. S. A. Pereira · E. R. G. Júnior · S. A. A. Malafaia · I. D. Batista · M. V. Barbosa · T. E. S. Lima
LAMAV—Advanced Materials Laboratory, UENF—State University of the Northern Rio de Janeiro, Av. Alberto Lamego, 2000, Campos Dos Goytacazes, Rio De Janeiro 28013-602, Brazil
e-mail: 202111100131@pq.uenf.br

M. T. Marvila
UFV—Federal University of Viçosa, CRP—Rio Paranaíba campus; Rodovia BR 230 KM 7, Rio Paranaíba, Minas Gerais 38810-000, Brazil
e-mail: markssuel.marvila@ufv.br

S. N. Monteiro
Department of Materials Science, IME—Military Institute of Engineering, Square General Tibúrcio, 80, Rio De Janeiro 22290-270, Brazil

A. R. G. Azevedo (✉)
LECIV—Civil Engineering Laboratory, UENF—State University of the Northern Rio de Janeiro, Av. Alberto Lamego, 2000, Campos Dos Goytacazes, Rio De Janeiro 28013-602, Brazil
e-mail: afonso@uenf.br

F. M. Margem
LEPROD—Production Engineering Laboratory, UENF—State University of the Northern Rio de Janeiro, Av. Alberto Lamego, 2000, Campos dos Goytacazes, Rio De Janeiro 28013-602, Brazil
e-mail: fmargem@uenf.br

Z. Peng et al. (eds.), *Characterization of Minerals, Metals, and Materials 2024*, The Minerals, Metals & Materials Series, https://doi.org/10.1007/978-3-031-50304-7_57

1.0 and 3.0% in relation to the Portland cement mass. From the results, it was verified that there was a reduction in the consistency index and mass density and an increase in the content of air incorporated in the mortars according to the addition of fibers. Thus, based on these results, the present study seeks to present the alterations of some properties in the fresh state caused by the addition of this natural reinforcement.

Keywords Açaí fibers · Reinforcement · Mortars

Introduction

The increasing demand for "green" products is related to a greater diffusion of sustainable development and circular economy concepts and understanding of their global positive impacts [1]. The usage of these products in civil construction is a promising strategy, since the sector is related to a large global share of CO_2 emissions, large consumption of natural resources and intense need for materials, such as steel, which require a lot of energy in its manufacturing process [2–4].

In this scenario, the growing interest of companies and researchers in composites with natural fibers is observed, boosting the development of less costly products that contribute to sustainable practices in civil construction [5–8]. The great availability of this type of fiber in the Brazilian Amazon region, derived from açaí agro-industrial residues, stands out (*Euterpe oleracea Mart*). According to data provided by the most recent statistical yearbook in Brazil [9], the production of açaí in the country in 2021, largely concentrated in the regions of Amazonas and Pará, reached 1.5 million tons, of which part is consumed by national industries and the great remainder destined for the global market. According to Domingues et al. [10], every 100 tons of fruit generate 80 tons of waste, which correspond to seeds and fibers. There is still no specific destination for all this material, most of which are discarded in landfills or even accumulated in the streets, sewage networks and rivers of the region, causing risks to the health of the population due to environmental contamination or the proliferation of transmission agents of illnesses [11].

Plant fibers incorporation into cementitious materials has already proven to be an effective method for improving several parameters, such as tensile strength, ductility, fracture toughness and relatively low density [12–14]. However, two issues that have been extensively studied related to these natural materials are its hydrophilicity and durability in alkaline environments [15–17]. Treatments carried out on the surface of the fibers tend to reduce these disadvantages and are the subject of current research studies [18, 19].

Tannic acid is a natural polyphenol that occurs in various plants and fruits [1]. It is characterized as a promising substance that modifies polymeric biocomposites that combines antioxidant and antibacterial properties and presents advantages such as biodegradability, high adhesion, non-toxicity, low cost and high availability [1]. Despite these benefits, this acid is still poorly studied as a type of surface treatment for plant fibers [1].

This paper aims to evaluate the performance of mortars in the fresh state with the addition of açaí fibers without and with surface treatment based on tannic acid. In this way, this research contributes to the development of new sustainable products for civil construction, also helping to reduce environmental problems related to fruit production in the Amazon region.

Materials and Methods

The açaí fibers were collected from the seed of the fruit, a by-product of the pulping of an agroindustry located in the municipality of Alto Rio Novo (Espírito Santo, Brazil). The açaí produced in this region is similar to that processed in the Amazon region, previously proven by Azevedo et al. [6]. The fibers were obtained manually and, after processing, the material was washed in running water and dried in an oven at 60 °C for a period of 24 h. After drying, part of the amount of fibers was subjected to surface treatment based on tannic acid [1].

Portland cement composed of blast furnace slag specified in Brazil as CP II-E-32 (equivalent to ASTM Type I SM) was used. The fine aggregate used was quartz sand from the Paraíba do Sul river, located in Campos dos Goytacazes, state of Rio de Janeiro, Brazil. This sand was homogenized and prepared to enable its application in mortars.

Seven types of mortar were produced in the proportion of 1:1:6:1.35 (cement: lime: sand: water/cement factor) with addition of fibers in relation to Portland cement mass (Table 1). The preparation of each mix followed the Brazilian normative procedure of NBR 16541 [20] for mixing, homogenizing and preparing mortars. The addition of açaí fibers occurred at the time of introducing the other components of the mixture, in order to avoid agglomeration of this material.

Mortars were characterized in the fresh state regarding consistency index—NBR 13276 [21], incorporated air content determined by the pressiometric method and mass density according to NBR 13278 [22]. It is very important to mention that all fresh state tests were with instantaneous measurements (without repetitions), as recommended by the Brazilian technical standard. Thus, the results must be expressed

Table 1 Mortars mixing ratio

Mortars	Content
Ref	Reference (0%)
1.5UT	1.5% untreated fibers
3UT	3.0% untreated fibers
5UT	5.0% untreated fibers
1.5TA	1.5% treated fibers
3TA	3.0% treated fibers
5TA	5.0% treated fibers

by the values obtained in a single repetition, without the need for a statistical evaluation. The analysis of these studies must consider the values of the reference mixtures as a direct comparison.

The flow table tests designated here in this study as a consistency index NBR 13276 [21], involves filling the standard conical mold ($d1$ ¼80 mm, $d2$ ¼ 125 mm, h ¼ 65 mm) in three layers compacted with 15, 10 and 5 punches of the standard hammer for the first, second and third layer, respectively. Then the mold is lifted, and 30 falls are applied (1 cm height, one fall per second). The spread of the mixture is defined based on the average of three diameters measured using a caliper. The ideal spreading diameter for laying and coating mortars, according to the regulations, is equivalent to 260 ± 5 mm [21]. The water content for the reference mortar was adjusted to present spread within the established range. After this adjustment, the water cement factor was fixed for the other mortars mixing ratio.

Results and Discussion

The horizontal spreading of mortars is closely related to the fluidity of the mixtures, and consequently to the workability, a property that favors its application as a coating for walls and ceilings. According to Fig. 1, it appears that there was a reduction in this scattering with the addition of a natural fiber, as well as with the increase in its percentages. The greater amount of fibers present in the matrix causes an increase in mass stability, providing greater internal cohesion of the system [23]. It is also observed that the surface treatment provided an even more pronounced reduction in the consistency index, with the exception of the 1.5%TA treatment.

According to Pawlowska et al. [1], tannic acid creates a coating on the surface of the fibers capable of increasing the durability of this material in an alkaline environment and reducing its hydrophilicity. However, from the results presented in Fig. 1, it is assumed that this layer created on the açaí fibers can cause an increase in chemical adhesion between the fiber and the matrix and, consequently, a reduction in the fluidity of the mixtures.

Thus, as expected, for the use of açaí fibers in the composition of coating mortars, it is essential to use plasticizing additives that will have the function of improving the workability of these matrices, without compromising their applicability.

Based on the results of Fig. 2, it appears that all mixtures had incorporated air levels within the range established by the literature, between 7 and 17% [24]. This limit indicates an acceptable zone of values that will not compromise properties in the hardened state of the mortar. It is observed that the incorporation of fibers caused an increase in the incorporated air content of the mixtures, since it is propitious that in the region of the interface between the surface of the fiber and the mortar the formation of voids occurs [25].

Void content of the mixtures with the addition of treated fibers was lower than that of the matrices with the presence of untreated fibers, remaining, however, above the reference value. It is inferred that the cement grains in the paste approached the

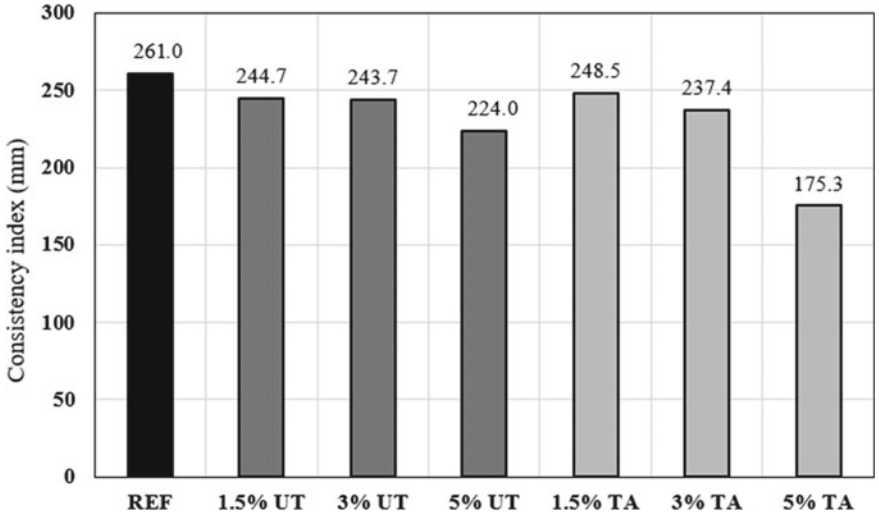

Fig. 1 Consistency index results of each mortar mixing ratio

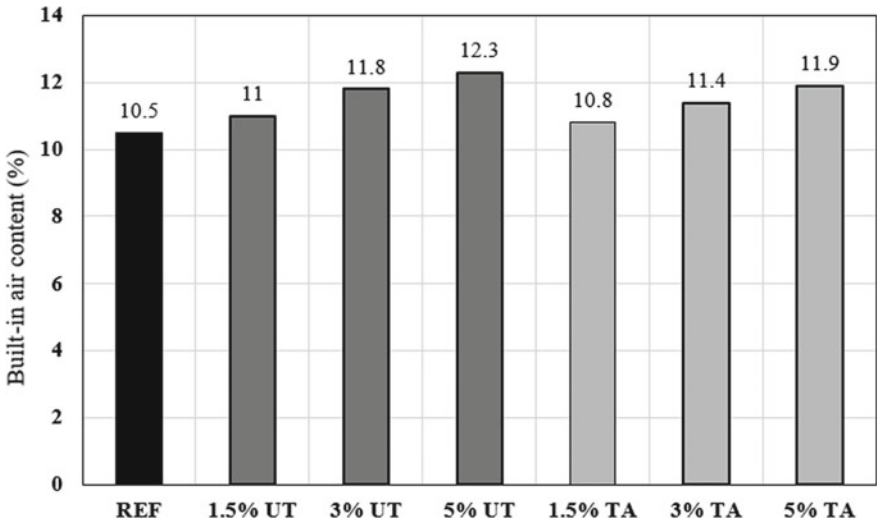

Fig. 2 Incorporated air content index results of each mortar mixing ratio

fibers, reducing the interfacial transition zone. Unlike the treatment with NaOH, in which there is an interfibrillar increase that causes the cement to migrate into the empty spaces between the fibrils, the tannic acid creates a layer that surrounds the fiber (insert reference). Thus, it is suggested that this coating created chemically attracts the cement grains from the paste, reducing the air content.

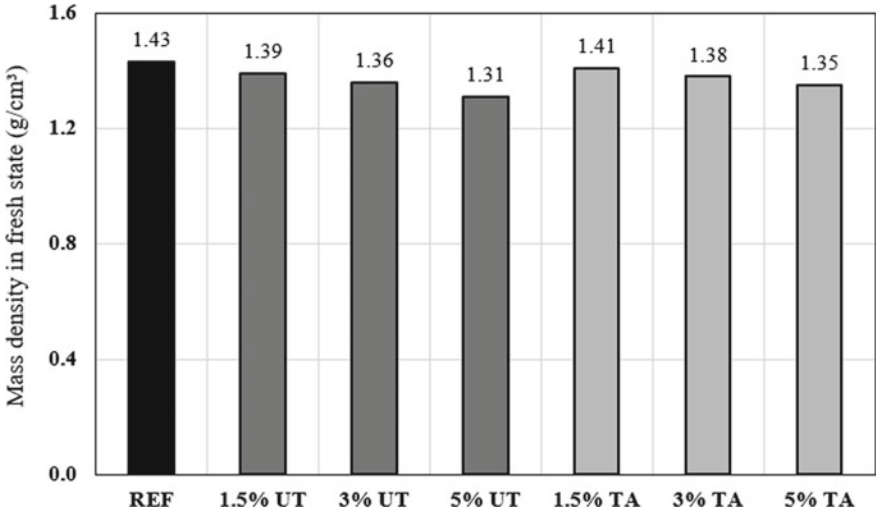

Fig. 3 Incorporated air content mass density index results of each mortar mixing ratio

Mass density results are shown in Fig. 3. It is verified that there is a reduction of this property in the fresh state for all the mixes with fiber addition, making the application of these mixtures contribute to the reduction of the specific weight of the building. This is due to the fact that the density of the açaí fiber is relatively lower compared to Portland cement [26]. It is also observed the effect that occurs after the surface treatment of the fibers with tannic acid, which led to an increase in the individual specific mass of the material.

Conclusion

This paper aimed to evaluate the performance of mortars in the fresh state with the addition of açaí fibers without and with surface treatment based on tannic acid. Tannic acid has shown to be useful to promote chemical adhesion between fiber/matrix, affecting results obtained by the analyses carried out.

It was verified that treated fibers incorporation caused a reduction in consistency index and mass density and an increase in the content of air incorporated in the mortars, validating its use and its consequent positive effects. Thus, based on these results, the present study presented changes in some properties in the fresh state caused by the addition of this natural reinforcement.

Acknowledgements This research was funded by the State University of the Northern Fluminense (UENF), partially financed by CAPES (Coordenação de Aperfeiçoamento de Pessoal de Nível Superior—Brazil), CNPq (Coordenação Nacional de Pesquisa) and FAPERJ (Fundação de Apoio à Pesquisa do Estado do Rio de Janeiro). The participation of A.R.G.A. was sponsored by FAPERJ

through the research fellowships proc.no: E-26/210.150/2019, E-26/211.194/2021, E-26/211.293/2021, E-26/201.310/2021 and by CNPq PQ2 307592/2021-9.

References

1. Pawłowska A, Stepczynska M, Walczak M (2022) Industrial crops and products. In: Flax Fibres modified with a natural plant agent used as a reinforcement for the polylactide-based biocomposites, vol 184, p 115061
2. Pacheco-Torgal F, Jalali S (2011) Cementitious building materials reinforced with vegetable fibres: a review. Constr Build Mater 25:575–581
3. ANEPAC (2015) Associação nacional de entidades de produtos de agregados para construção civil. http://www.anepac.org.br/
4. Santos TA, Cilla MS, Ribeiro DV (2022) Use of asbestos cement tile waste (ACW) as mineralizer in the production of Portland cement with low CO_2 emission and lower energy consumption. J Clean Prod 335:130061
5. Marvila MT, Azevedo ARG, Cecchin D, Costa JM, Xavier GC, Carmo DF, Monteiro SN (2020) Durability of coating mortars containing açaí fibers. Case Stud Constr Mater 13:e00406
6. Azevedo ARG, Marvila MT, Tayeh BA, Cecchin D, Pereira AC, Monteiro SN (2021) Technological performance of açaí natural fibre reinforced cement-based mortars. J Build Eng 33:101675
7. Azevedo ARG, Lima TES, Reis RHM, Oliveira MS, Candido VS, Monteiro SN (2022) Guaruman fiber: a promising reinforcement for cement-based mortars. Case Stud Constr Mater 16:e01029
8. Ahmad J, Zhou Z (2022) Mechanical properties of natural as well as synthetic fiber reinforced concrete: a review. Constr Build Mater 333:127353
9. IBGE (2020) Anuário estatístico do Brasil. https://biblioteca.ibge.gov.br/biblioteca-catalogo?id=720&view=detalhes
10. Domingues AFN, Mattietto RA, Oliveira M (2017) Teor de lipídeos em caroços de Euterpe oleracea. Mart Embrapa Amazônia Oriental, Pará
11. Sato MK, Lima HV, Costa AN, Rodrigues S, Mooney SJ, Clarke M, Pedroso AJS, Maia CMB (2020) Biochar as a sustainable alternative to ac¸ aí waste disposal in Amazon, Brazil. Process Saf Environ Protect 139:36–46
12. Huang H, Gao X, Teng L (2021) Fiber alignment and its effect on mechanical properties of UHPC: an overview. Constr Build Mater 296:123741
13. Wen X, Zhang P, Wang J, Hu S (2022) Influence of fibers on the mechanical properties and durability of ultra-high-performance concrete: a review. J Build Eng 52:104370
14. Liang S, Du H, Liu Y, Chen Y, Liu J, Wei Y (2023) Experimental study and mesoscale finite element modeling of elastic modulus and flexural creep of steel fiber-reinforced mortar. Constr Build Mater 12:129875
15. Mohr BJ, Biernacki JJ, Kurtis KE (2006) Microstructural and chemical effects of wet/dry cycling on pulp fiber–cement composites. Cem Concr Res 36:1240–1251
16. Tonoli GHD, Belgacem MN, Siqueira G, Bras J, Savastano H, Lahr FAR (2013) Processing and dimensional changes of cement based composites reinforced with surface-treated cellulose fibres. Cem Concr Comp 37:68–75
17. Teixeira RS, Santos SF, Christoforo AL, Payá J, Savastano H, Lahr FAR (2019) Impact of content and length of curauá fibers on mechanical behavior of extruded cementitious composites: analysis of variance. Cem Concr Comp 102:134–144
18. Laverde V, Marin A, Benjumea JM, Ortiz MR (2022) Use of vegetable fibers as reinforcements in cement-matrix composite materials: a review. Constr Build Mater 340:127729

19. Nayak JR, Bochen J, Golaszewska M (2022) Experimental studies on the effect of natural and synthetic fibers on properties of fresh and hardened mortar. Constr Build Mater 347:128550
20. ABNT (2016) NBR 16541: argamassa para assentamento e revestimento de paredes e tetos—Preparo da mistura para a realização de ensaios. ABNT, Rio de Janeiro
21. ABNT (2016) NBR 13276: argamassa para assentamento e revestimento de paredes e tetos—Determinação do índice de consistência. Associação Brasileira de Normas Técnicas, Rio de Janeiro
22. ABNT (2005) NBR 13278: argamassa para assentamento e revestimento de paredes e tetos—determinação da densidade de massa e do teor de ar incorporado. Associação Brasileira de Normas Técnicas, Rio de Janeiro
23. Zukowski B, Silva FA, Filho RDT (2018) Design of strain hardening cement-based composites with alkali treated natural curauá fiber. Cem Concr Comp 89:150–159
24. Azevedo ARG, Alexandre J, Marvila MT, Xavier GC, Monteiro SN, Pedroti LG (2020) Technological and environmental comparative of the processing of primary sludge waste from paper industry for mortar. J Clean Product 249:119336
25. Lertwattanaruk P, Suntijitto A (2015) Properties of natural fiber cement materials containing coconut coir and oil palm fibers for residential building applications. Constr Build Mater 94(30):664–669
26. Okada K, Ooyama A, Isobe T, Kameshima Y, Nakajima A, MacKenzie KJD (2009) Water retention properties of porous geopolymers for use in cooling applications. J Eur Ceram Soc 29(10):1917–1923

Phase Equilibrium in Solid Solutions of $BaTiO_3$ Doped with Eu^{3+} and Gd^{3+}

R. Martínez López, M. Pérez Labra, F. R. Barrientos Hernández, M. I. Valenzuela Carrillo, M. Reyes Pérez, J. A. Romero Serrano, A. Hernández Ramírez, and J. P. Hernández Lara

Abstract Barium titanate is an ABO_3 type perovskite of great interest due to its magnetic, dielectric, piezoelectric, and thermal properties, among others. At room temperature $BaTiO_3$ presents a stable tetragonal crystalline structure. In this work, solid solutions of the $Ba_{1-3x}Gd_{2x}Ti_{1-3x}Eu_{4x}O_3$ type were sintered by the solid state reaction method in air at 1300 °C for 6 h with steps of 4 °C per minute with $x =$ 0, 0.001, 0.002 and 0.003. The tetragonal (JCPDS 96-150-7757) and cubic (JCPDS 96-155-9964) phase of $BaTiO_3$ was determined by X-ray diffraction and Rietveld refinement when $BaTiO_3$ was doped. The evolution of the equilibrium of the phases was analyzed according to the increase of the dopants Eu^{3+} and Gd^{3+} and the increase in the stability of the cubic phase of $BaTiO_3$ was determined.

Keywords Characterization · Ceramics · Powder materials · Dopants

R. Martínez López (✉) · M. Pérez Labra · F. R. Barrientos Hernández · M. I. Valenzuela Carrillo · M. Reyes Pérez
Academic Area of Earth Sciences and Materials, Autonomous University of the State of Hidalgo, Pachuca-Tulancingo Km 4.5, Mineral de La Reforma, 42184 Hidalgo, México
e-mail: richi_3489@hotmail.com

J. A. Romero Serrano · A. Hernández Ramírez · J. P. Hernández Lara
Higher School of Chemical Engineering and Extractive Industries (ESIQIE)-IPN, 07738 Zacatenco, México

Z. Peng et al. (eds.), *Characterization of Minerals, Metals, and Materials 2024*, The Minerals, Metals & Materials Series, https://doi.org/10.1007/978-3-031-50304-7_58

Introduction

Barium titanate is an ABO_3 type perovskite, of great interest due to its magnetic, dielectric, piezoelectric, and thermal properties, among others. At room temperature $BaTiO_3$ presents a stable tetragonal crystalline structure. $BaTiO_3$ properties can be improved by modifying the sintering process variables, including temperature, pressure, sintering atmosphere, sintering time, heating and cooling rate, composition doping, etc. By modifying the sintering variables, not only the properties of the material are modified, but also its structure and chemical composition. Anisovalent doping is a technique that directly modifies the chemical composition and microstructure of the material, this change also has important effects on its properties. Anisovalent doping modifies the crystalline structure by contracting or expanding the lattice according to the ionic radius of the dopant, the chemical composition changes when doping and the creation of possible second phases by exceeding the solubility limit of the structure [1–3, 5, 6].

There are various techniques for synthesis of $BaTiO_3$ ceramics, among them we can mention Sol–Gel, chemical vapor deposition, molten salts, solid state reaction method, etc. In the same way, there are various sintering techniques, among them we can mention sintering without pressure, with hot isostatic pressure, cold, microwave, etc. each method of synthesis and sintering with its advantages and disadvantages, of which the choice of the most adequate is essential for obtaining ceramics with adequate chemical and microstructural properties for the application for which they are intended [1, 4, 7].

In this work, $BaTiO_3$ ceramics were synthesized by means of the solid state reaction method, which has proven to be suitable for obtaining ceramics with controlled chemical composition and microstructure. In addition, it is an economical and simple method. The sintering process is carried out in an uncontrolled air atmosphere. To obtain $BaTiO_3$-based ceramics with desired dielectric properties such as high relative permittivity and low dielectric loss, the crystalline structure is doped with the rare earth elements Gd^{3+} and Eu^{3+} using the $Ba_{1-3X}Gd_{2X}\ Ti_{1-3X}Eu_{4X}O_3$ mechanism in the compositions $x = 0$, 0.001, 0.002 and 0.003 of Gd^{3+} y Eu^{3+} [1, 6, 7].

Experimental Development

The precursor powders, $BaCO_3$ (CAS 513-77-9), TiO_2 (CAS 13463-67-7), Eu_2O_3 (CAS 1308-96-9), and Gd_2O_3 (CAS 12064-62-9) with 99.9% purity of the Sigma Aldrich brand, were mixed. The stoichiometric formula used was $Ba_{1-3X}Gd_{2X}Ti_{1-3X}Eu_{4X}O_3$. In which x is equal to 0, 0.001, 0.002 y 0.003. The mixtures were synthesized at 1300 °C for 6 h with a heating ramp of 4 °C per minute in a Thermolyne oven. The synthesized powders were pressed in a hydraulic press at 100 MPa in a 10 mm diameter stainless steel die and the resulting green

pellets were sintered at 1300 °C for 6 h with a heating ramp of 4 °C in an oven. Thermolyne brand in an air atmosphere. The equilibrium of the phases was determined by X-ray diffraction in an Equinox 2000 diffractometer with Cobalt K_{a1} radiation and Rietveld Refinement with the software Match! 3 and FullProf with the Pseudo-Voigt profile shape function.

Results and Discussion

Figure 1 shows the composition $x = 0$, in which a single phase was identified, tetragonal $BaTiO_3$ (JCPDS 96-150-7757), the structural parameters were determined by Rietveld Refinement, $a = 3.9782$ A°, $c = 4.0094$ A°, a tetragonality ratio of 1.0078, a volume of 63.4542 $A^{\circ 3}$. Figure 2 shows the composition $x = 0.001$ in which two phases were identified, tetragonal $BaTiO_3$ (JCPDS 96-150-7757) with $a = 3.9927$ A°, $c = 4.0094$ A°, tetragonality ratio of 1.0089, volume of 64.2224 $A^{\circ 3}$ and is present in 99.2%, the second phase identified was cubic $BaTiO_3$ (JCPDS 96-155-9964) with structural parameters $a = 4.0356$ A°, volume of 65.7221 $A^{\circ 3}$ and is present in 0.8%. Figure 3 shows the composition 0.002 in which, like the previous composition, there is tetragonal $BaTiO_3$ (JCPDS 96-150-7757) with $a = 3.9934$ A°, $c = 4.0276$ A°, tetragonality ratio of 1.0085, volume of 64.2310 $A^{\circ 3}$ and is present in 81.5%, and the second phase, cubic $BaTiO_3$ (JCPDS 96-155-9964) with structural parameters $a = 4.0337$A°, volume of 65.6298 $A^{\circ 3}$ and is present in 18.5%. Finally, Fig. 4 shows the composition 0.004, where the tetragonal $BaTiO_3$ phase (JCPDS 96-150-7757) is present with $a = 4.0018$ A°, $c = 4.0477$ A°, tetragonality ratio of 1.0085, volume of 64.6333 $A^{\circ 3}$ and is present in 97.8%, the second phase, cubic $BaTiO_3$ (JCPDS 96-155-9964) with structural parameters $a = 4.0477$ A°, volume of 66.3185 $A^{\circ 3}$ and is present in 2.2%.

As mentioned above and as observed in Table 1, the composition $x = 0$ only presents the stable phase at room temperature tetragonal $BaTiO_3$ (JCPDS 96-150-7757), in the doped compositions, $x = 0.001$, 0.002 and 0.004 maintains the tetragonal $BaTiO_3$ phase (JCPDS 96-150-7757) but presents an increase in the structural parameters, a increases from 3.9782 to 3.9927 A° then to 3.9934 A° and finally to 4.0018 A°, c increases from 4.0094 to 4.0286 A° then to 4.0276 A° and finally to 4.0359 A°, the tetragonality ratio increases from 1.0078 to 1.0089 and subsequently decreases to 1.0085, the volume presents an increase from 63.4542 to 64.2224 $A^{\circ 3}$, then to 64.2310 $A^{\circ 3}$ and finally to 64.6333 $A^{\circ 3}$. With respect to the cubic $BaTiO_3$ phase (JCPDS 96-155-9964), increasing the dopant concentration from $x = 0.001$ to $x = 0.002$ increases its presence from 0.8 to 18.5%, subsequently the presence of the phase decreases to 2.2% as the dopant concentration increases from $x = 0.002$ to $x = 0.003$. The structural parameter a and the volume decrease from 4.0356 to 4.0337 A° and from 65.7221 to 65.6298 $A^{\circ 3}$, later increasing to 4.0477 and 66.3185 $A^{\circ 3}$.

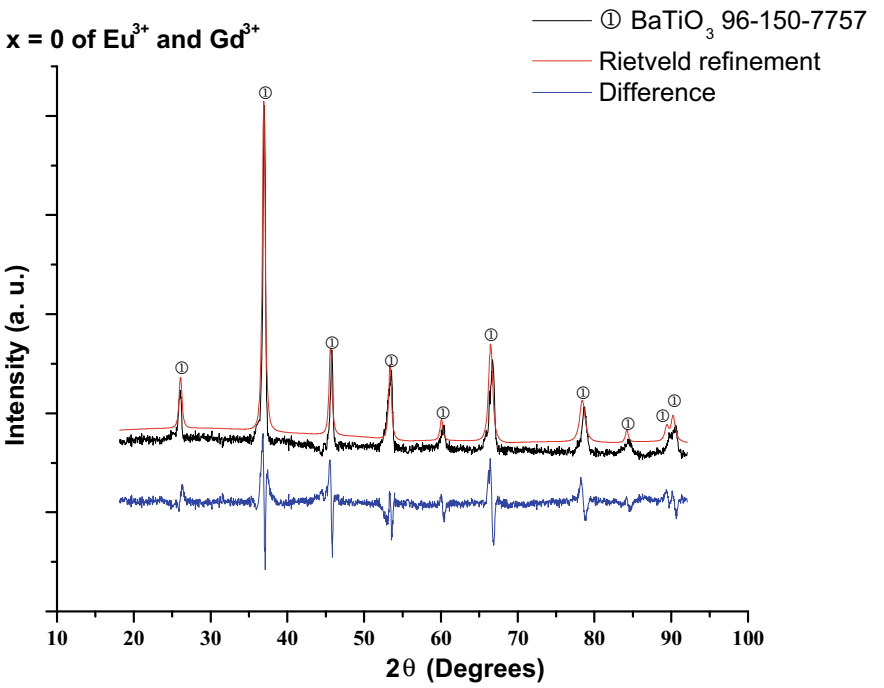

Fig. 1 Diffractogram of the $x = 0$ composition of Eu^{3+} and Gd^{3+}, calculated profile and difference

Conclusions

The increase in the structural parameters a, c and volume in the tetragonal $BaTiO_3$ phase (JCPDS 96-150-7757), are clear evidence that there is an incorporation of the doping elements Gd^{3+} and Eu^{3+} in the crystalline structure of $BaTiO_3$ at the titanium site due to the difference in the ionic radius between titanium ($r(Ti^{4+}) = 0.68$ A°) and the ionic radius of the dopants [$r(Gd^{3+}) = 1.02$ A° and $r(Eu^{3+}) = 1.12$A°]. Furthermore, the tetragonality ratio of the doped samples is greater than the value in the undoped composition. The cubic $BaTiO_3$ phase (JCPDS 96-155-9964) appeared in composition $x = 0.001$ with a 0.8%, when increasing the composition to $x = 0.002$ the cubic $BaTiO_3$ phase increases to 18.5% but subsequently decreases to 2.2% when increasing the composition to $x = 0.003$, the stability of the cubic $BaTiO_3$ phase, the increase in the structural parameter a and the increase in the volume of the crystalline structure were related to a substitution of the dopant elements (Gd^{3+} and Eu^{3+}) in the titanium site as in the tetragonal $BaTiO_3$ phase.

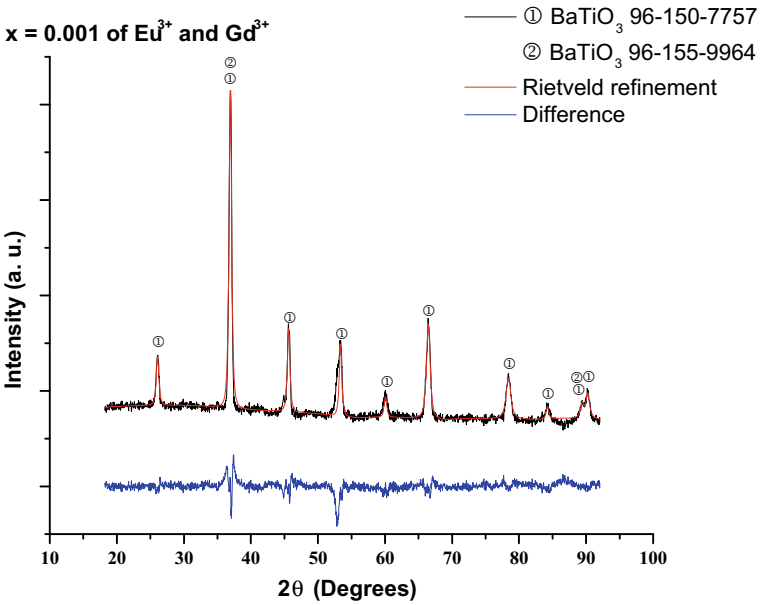

Fig. 2 Diffractogram of the $x = 0.001$ composition of Eu^{3+} and Gd^{3+}, calculated profile and difference

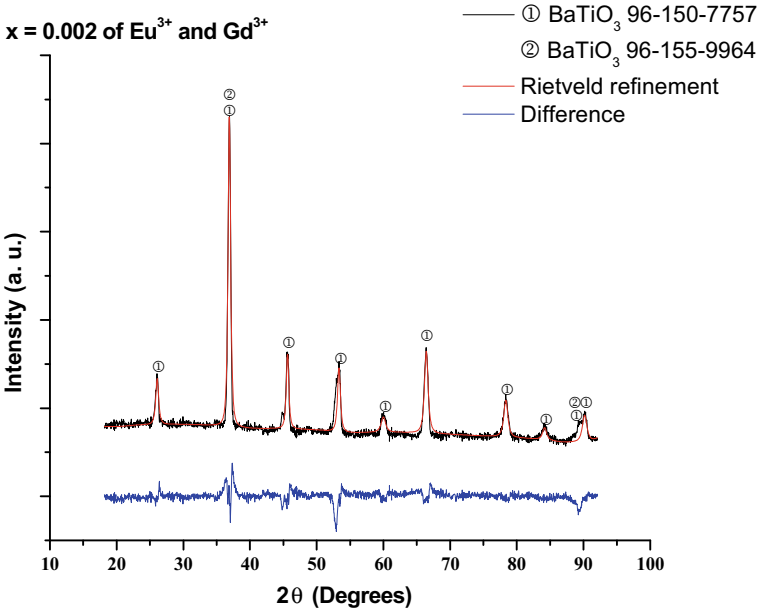

Fig. 3 Diffractogram of the $x = 0.0002$ composition of Eu^{3+} and Gd^{3+}, calculated profile and difference

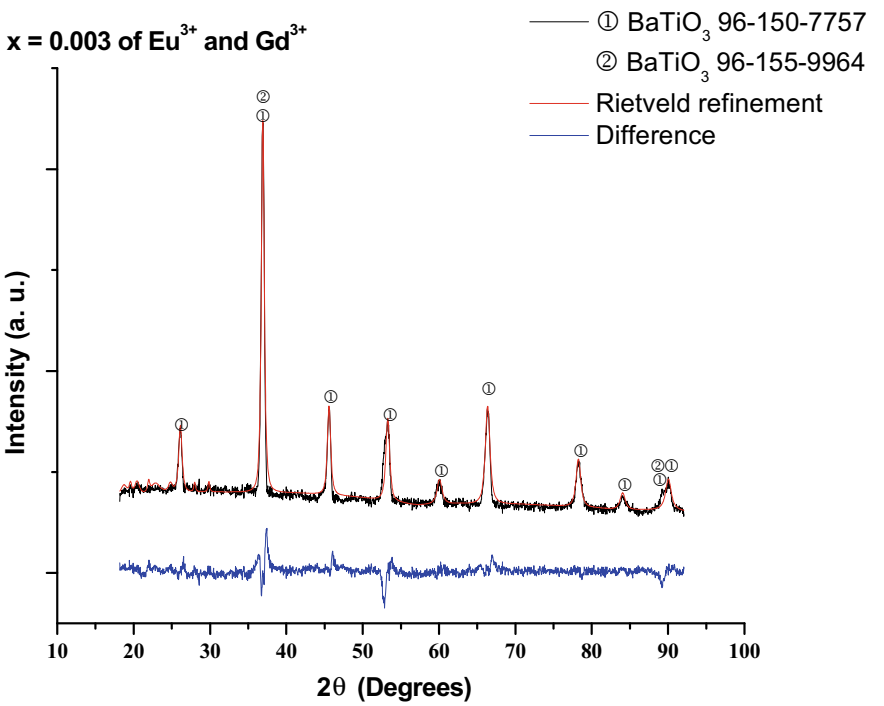

Fig. 4 Diffractogram of the $x = 0.003$ composition of Eu^{3+} and Gd^{3+}, calculated profile and difference

Table 1 Data obtained by Rietveld refinement

x/parameter	Phase	*a* (A°)	*c* (A°)	c/a	Volume ($A^{\circ 3}$)	Phase fraction (%)	x^2
0	$BaTiO_3$ tetragonal	3.9782	4.0094	1.0078	63.4542	100	1.3
0.001	$BaTiO_3$ tetragonal	3.9927	4.0286	1.0089	64.2224	99.2	1
	$BaTiO_3$ cubic	4.0356	–	–	65.7221	0.8	
0.002	$BaTiO_3$ tetragonal	3.9934	4.0276	1.0085	64.2310	81.5	1.1
	$BaTiO_3$ cubic	4.0337	–	–	65.6298	18.5	
0.003	$BaTiO_3$ tetragonal	4.0018	4.0359	1.0085	64.6333	97.8	1.2
	$BaTiO_3$ cubic	4.0477	–	–	66.3185	2.2	

References

1. Liu Q, Liu J, Lu D, Zheng W, Hu C (2018) Structural evolution and dielectric properties of Nd and Mn co-doped $BaTiO_3$ ceramics. J Alloys Compd 760:31–41
2. Hayashi H, Kakamura T, Ebina T (2013) In-situ Raman spectroscopy of $BaTiO_3$ particles for tetragonal-cubic transformation. J Phys Chem Solids 74:957
3. Ran J, Liu H, Dong H, Gao P, Cheng H, Xu J, Wang H, Wang Z, Fu Q, Yan J, Liu J (2022) Accurate quantification of TiO_2(B)'s phase purity via Raman spectroscopy. GEE 8:1371–1379
4. Xue K et al (2023) Composition-driven morphological evolution of $BaTiO_3$ nanowires for efficient piezocatalytic hydrogen production. Chemosphere 338:139337
5. Lengyel A et al (2022) Synergy effect of temperature, electric and magnetic field on the depth structure of the FeRh/$BaTiO_3$ composite multiferroic. MSEB 285:115939
6. Lukacs V et al (2022) Phase coexistence and grain size effects on the functional properties of $BaTiO_3$ ceramics. J Eur Ceramt 42:2230–2247
7. Padurariu L (2021) Modifications of structural, dielectric and ferroelectric properties induced by porosity in $BaTiO_3$ ceramics with phase coexistence. J Alloys Compd 889:161699

Development of Artificial Granite with Epoxy Resin Matrix Mixed with Cashew Nut Shell Liquid

Pablo Barbosa Jacintho, Maria Luiza Pessanha Menezes Gomes, José Lucas Decotê de Carvalho Lírio, Elaine Aparecida Santos Carvalho, Afonso Rangel Garcez de Azredo, Sérgio Neves Monteiro, and Carlos Maurício Fontes Vieira

Abstract The demand for environmentally friendly products with good performance has grown a lot in recent years. The construction industry generates a large amount of waste, favoring the production of artificial stones with properties superior to natural ornamental stones without compromising aesthetics. The objective of this work is to develop and characterize an artificial stone made with granite waste, from the cutting stages of a quarry, in an epoxy resin matrix mixed with cashew oil, ASG-EC. Tests were carried out to evaluate the physical, mechanical, and chemical properties of the stone, in addition to analyzing the microstructure. The ASG-EC presented density (2.21 g/cm^3) within the expected range, high values of water absorption (1.02%) and apparent porosity (2.25%), and it is considered of very high resistance with flexural strength of 23.18 MPa. Furthermore, it proved to be resistant to chemical attacks, showing a change in color only when exposed to $C_6H_8O_7$, CH_3COOH and KOH.

Keywords Artificial stone · Granite waste · Epoxy · Cashew nut shell

P. B. Jacintho · M. L. P. M. Gomes (✉) · J. L. D. de Carvalho Lírio · E. A. S. Carvalho · A. R. G. de Azredo · C. M. F. Vieira
Advanced Materials Laboratory—LAMAV, State University of the Northern Rio de Janeiro—UENF, Av. Alberto Lamego, 2000, Campos dos Goytacazes 28013-602, Brazil
e-mail: malu_pmg@hotmail.com

A. R. G. de Azredo
e-mail: afonso@uenf.br

C. M. F. Vieira
e-mail: vieira@uenf.br

S. N. Monteiro
Department of Materials Science, Military Engineering Institute—IME, Praça General Tibúrcio, 80, Praia Vermelha, Urca, Rio de Janeiro 22290-270, Brazil

Z. Peng et al. (eds.), *Characterization of Minerals, Metals, and Materials 2024*, The Minerals, Metals & Materials Series, https://doi.org/10.1007/978-3-031-50304-7_59

Introduction

Waste generation has been growing a lot and has been causing global concern because its improper disposal is harmful to the environment in several aspects, provoking pollution, garbage accumulation, and even climate change [1]. Employing waste in the production process and reducing environmental impacts is something of paramount importance and beneficial to society, their application in composite materials is an alternative to reduce their excess. Some examples are the application of industrial, agricultural and urban waste being used as reinforcement, examples of this are EPDM (ethylene propylene diene monomer rubber) waste being embedded in an epoxy matrix, marble dust and tamarind bark particles being applied in reinforced biocomposites, development of reinforced epoxy composites with fine granite particles [2–5].

Focusing on the construction industry, responsible for generating large amounts of waste, the improper disposal of them has generated a great concern worldwide, that being the case, bringing utility to these wastes is of paramount importance to mitigate environmental impacts. The use of quarry waste in the manufacture of an artificial ornamental stone is one alternative [6]. Construction and demolition waste when reintroduced into the industry, in addition to reducing the impacts subsequently caused, leads to an economic incentive for the ornamental stone market and reduces the environmental impacts caused by it [7].

In 2019, around 154.4 million tons of ornamental stones were produced worldwide, with Brazil being responsible for 8.2 million tons, it has thus occupied a prominent position among the five largest producers of ornamental stones, participating globally with 5.3% of production. Consequently, huge amounts of waste are generated that are deposited in landfills or reserved areas in companies for disposal [8].

According to Singh et al. it is estimated that about 30% of rocks become waste and unfortunately they are discarded incorrectly in the environment, it is estimated that about 2–2.4 million tons of waste are produced in the ornamental stone sector [8]. Waste from the cutting and polishing of granite blocks is in the form of pebbles and sludge. Several studies have sought scientific and technical solutions for the use of this type of waste [9–12]. The main focus is simply to remove these wastes from the environment in a profitable and cost-effective manner, we have, in a special way, a destination for them as composites that simulate natural stones and are marketed as artificial stones [6].

Using artificial stone instead of natural stone has technical advantages, such as its lightness due to the lower density of the polymeric material used as matrix. In addition, artificial stones generally have a lower porosity and lower number of defects. While natural stones have a higher number of voids and defects, making them more susceptible to contamination and fractures [6].

Epoxy-based thermosetting polymeric resins have chemical resistance, electrical insulation, high adhesive strength and high thermomechanical properties. The most significant materials for the industrial sectors are mainly based on Bisphenol A

diglycidyl ether (BADGE), and the curing process happens with the use of amines. The synthetic polymeric substances, however, have the capacity to cause impacts on the environment and complications to human health. For this reason, resins derived from biological sources or resins capable of incorporating vegetable oils appear as an option to replace conventional products in a more sustainable way [13–16].

Epoxy resins produced from vegetable oils bring improvements in characteristics like in impact strength, resistance and fracture toughness, qualities that are normally limited to BADGE-based resins. This particularity is associated with the densely reticulated network that is formed [17, 18].

Cashew nut shell liquid (CNSL) is a by-product not suitable for consumption from the agricultural industry, a resource fully available in nature, one of its main components is cardanol, a compound used as a modifying agent for epoxy resins [19].

Many types of artificial stones are produced, however, these researches vary in relation to the production methods, the employed matrix (epoxy resin, polyester, polyurethane, natural resins, cement matrices, etc.), to the types of aggregates used (marble, granite, bottle glass, eggshell, chamotte, glass powder from lamination, quartz, etc.) and the proportions of the components used [20–24]. Each research presents in its results unique characteristics of each stone produced, which are most often produced from solid waste and polymeric resins [23]. These rocks are often produced containing a high content of residues (between 85 and 90%) and low content of binding material, between 5 and 15% of resin, using the vacuum vibro-compression process for its production [23].

In order to minimize the growing generation of waste especially in the ornamental stone industry and encouraging the development of sustainable materials in the civil construction industry sector. The present work aims to make artificial stone slabs with the vacuum vibro-compression method using granite residues in an epoxy resin matrix with the addition of cashew nut oil.

Materials and Methods

In the present study, granite waste from the cutting stage was used, provided by the company Brumagran headquartered in Cachoeiro de Itapemirim, Brazil.

As a polymeric binder, 70% by weight of epoxy resin Bisphenol A diglycidyl ether (BADGE) mixed with 10% by weight of the curing agent Triethylenetetramine (TETA) was used, as specified by the supplier, mixed with 30% cashew nut shell liquid (CNSL). The epoxy resin was supplied by Epoxy fiber with a density of 1.15 g/cm^3, while the CNSL, originating in Fortaleza, Brazil, and supplied by Resibras, has a density of 0.97 g/cm^3, according to the supplier.

The residue particles were categorized into two granulometric ranges: big (2.000–1.190 mm) and medium (1.190–0.149 mm), for this the pebbles needed to be fragmented and had to pass through a jaw crusher to then be sieved into the mentioned sizes.

For the production of the slabs and artificial stone, the granite particles were first put in an oven at 100 °C for 24 h to remove moisture. Subsequently, the granite, resin and cashew oil were placed in an automatic cylindrical mixer to homogenize the mixture. The homogenized mass was then added into a mold with 100 mm length, 100 mm width and 10 mm height, the mold was placed on a vibrating table, from the Productest, for 2 min to promote the spreading of the material on the surface of the mold and allow a better accommodation of the particles for pressing in addition to contributing to the removal of air bubbles that could be present.

After the vibration time, the mold was placed in a hydraulic press at a compaction pressure of 10 tons, at 90 °C, where it remained for 25 min maintaining pressure in the mold. After pressing, the mold was cooled at room temperature to remove the artificial stone slab and subsequently, the produced slabs were placed in a post-curing process at 90 °C for a period of 24 h.

Density, apparent porosity and water absorption were determined by the method described in Annex B of the NBR 15845-2 (2015). For the test, 10 samples of each type of stone were used, measuring 50 mm length, 50 mm width and 10 mm height [25].

The surface of the sample was sanded and polished and the microstructure was observed in an Olympus Confocal microscope (LEXT OLS4000) in order to assess the presence of voids that may be present in the material, and to determine the homogeneity of particles dispersion in the matrix.

The three-point bending strength test was performed on the samples to determine the maximum breaking strength. The test was conducted in an INSTRON universal testing machine, model 5582, according to ABNT/NBR 15845-6 [26]. Six samples, with dimensions of 100 mm length, 25 mm width and 10 mm height, were tested under loading rates of 0.25 mm/min, using 100 kN load cells and a distance of 80 mm between the two points.

A test was carried out to determine the resistance to chemical attacks of the artificial stones, according to the recommendations of ABNT/NBR 16596/17 [27]. The reagents were used, in the concentrations and exposure times described in Table 1.

Table 1 Chemical reagents, concentrations and exposure time used in chemical attack tests

Code	Reagents	Concentrations	Time (h)
1	Ammonium chloride	100 g/L	24
2	Sodium hypochlorite	20 mg/L	24
3	Citric acid	100 g/L	24
4	Lactic acid	100 g/L	24
5	Acetic acid	3% v/v	24
6	Hydrochloric acid	3% v/v	96
7	Hydrochloric acid	18% v/v	96
8	Potassium hydroxide	30 g/L	96
9	Potassium hydroxide	100 g/L	96
10	Deionized water	–	96

Results and Discussion

Physical Index Characterization

The data presented in Table 2 shows the results regarding the density, water absorption capacity and apparent porosity of the artificial rock produced, where density reveals the mass per unit of volume of a given rock, where lower values indicate a higher amount of unfilled space. Both water absorption rates and apparent porosity are expressed in percentage form, denoting the proportion of voids with external connection and the total percentage of voids present in a material, respectively [28].

The matrix used to make the stone is a factor that must be taken into account because it will directly influence the density of the final product, in this work, epoxy resin was used, which has a density of 1.15 g/cm^3, mixed with cashew oil, density 0.97 g/cm^3, while natural granite has a density of approximately 2.4 g/cm^3.

The use of resin to make the artificial stone ends up provoking a reduction in the weight of the stone, this is due to the fact that resin and CNSL residue have a much lower density than pure granite and with the amount of resin used, the density of ASG-EC was lower in comparison. The main function of the resin is to permeate the pores and cracks of the rock, filling these empty spaces.

The discovered water absorption and apparent porosity of ASG-EC were 1.02% and 2.25% respectively. It is important for artificial stones to have low levels of water absorption and an impermeable surface since depending on the place where it will be used, the stones will be in constant contact with water. According to Chiodi and Rodrigues, an artificial stone with low water absorption should have values between 0.1 and 0.4% [28]. The value obtained is 2.55 times higher than that recommended by the researchers.

The apparent porosity value was also considered high compared to what is recommended in the literature. Chiodi and Rodrigues classify high quality artificial stones as having an apparent porosity below 0.5%, so the porosity content of ASG-EC is approximately 4.5 times higher than that recommended [28]. Waterproofing the surface of the artificial stone can be an alternative to improving the high levels of water absorption and apparent porosity of the material, allowing it to be used in places with a constant presence of liquids.

Lee et al. made synthetic stone materials with waste glass and PET. For the same compaction pressure (9.8 MPa) and vibration frequency of 50 Hz, they obtained a stone with a density of 2.114 g/cm and water absorption of 0.203%, values lower than those presented in this work [29].

Table 2 Result of the physical indices of the artificial rock

Density (g/cm^3)	Water absorption (%)	Apparent porosity (%)
2.21 ± 0.07	1.02 ± 0.11	2.25 ± 0.22

Barani and Esmaili created synthetic stone materials using 16% polyester resin and granite, quartz and glass waste, obtaining stones with higher specific density (2.65 g/cm^3), and lower water absorption values (0.68%), than the stones produced in the present work with epoxy resin with the addition of CNSL [30].

The authors [29, 30] attribute the lower values of water absorption and porosity of the stones as a result of the action of the vacuum. Here the vacuum acts by removing air bubbles trapped inside the stones, reducing the number of pores and consequently the absorption of water of the material. The vibration to which all the stones were subjected for manufacture, together with the action of the vacuum, allows the movement of the particles inside the material to facilitate the removal of bubbles trapped in the interstices. It is possible that the lack of use of vacuum during the production of ASG-EC stones limited the removal of bubbles inside the material resulting in the obtained values of porosity and water absorption of the plates.

Flexural Strength

As guided by the "Stone Application Guide as Coating", artificial stones used for tiling are categorized as high-strength materials when their flexural strength is in the range of 16–20 MPa and are considered of very high strength when this value exceeds 20 MPa [28]. The stone produced in this work presented resistance of 23.19 ± 3.48 MPa, therefore, it is considered to have very high resistance. Figure 1 shows the flexural stress–strain graph of the studied stone.

According to the Brazilian standard NBR 15844 (2015) which determines the requirements for granite to be used for tiling, the value of maximum flexural strength must be greater than 10 MPa, demonstrating the superiority of artificial granite when compared to a natural stone [31].

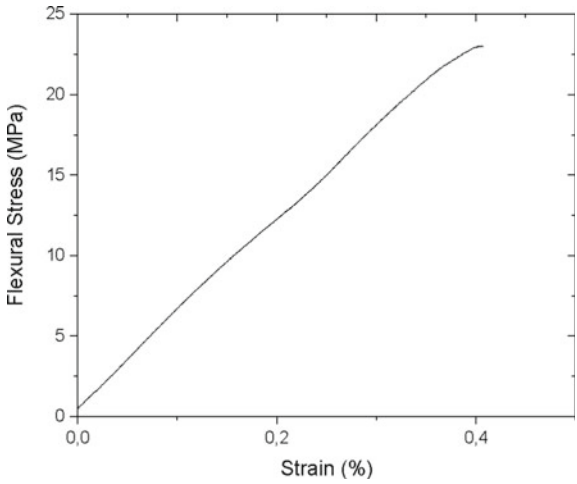

Fig. 1 Flexural stress–strain graph of studied artificial stone

A research carried out by Agrizzi et al. used polyurethane derived from castor oil, a resin that totally originated from a natural source, together with quartz particles to produce an artificial stone named AS-PU, which achieved a flexural strength of 10.77 ± 0.64 MPa [32]. The present work also made use of a natural source to compose the matrix, using oil derived from the cashew shell, in which a value of 23.19 MPa was achieved, a value higher than that found by the author.

Agrizzi et al. also developed another type of stone with epoxy resin BADGE and quartz, AS-PE and achieved 27.96 ± 1.86 MPa of flexural strength. The observed difference in rock strength was mainly due to the higher strength of the epoxy resin (93.6 MPa) compared to the polyurethane resin (23.0 MPa). When comparing the ASG-EC of the present work to the AS-PE [32], it is possible to observe that the stones do not present significant variations to their standard deviations. Thus, the addition of CNSL did not significantly change the properties of the epoxy matrix.

Another factor that influences the resistance of materials is its porosity, bearing in mind that pores act as stress concentrators, thus decreasing their resistance. The porosity amount of ASG-EC was considered high, which may have limited the mechanical strength performance of the stone.

Confocal Microscopy

Figure 2a, b show the stones produced for this work after the cutting and sanding process, the marks observed on the granite grains are due to the high hardness of the quartz present and the low efficiency of polishing with alumina to remove them. The images respectively present captures through the infrared capture mode and the visible light capture mode of the confocal device.

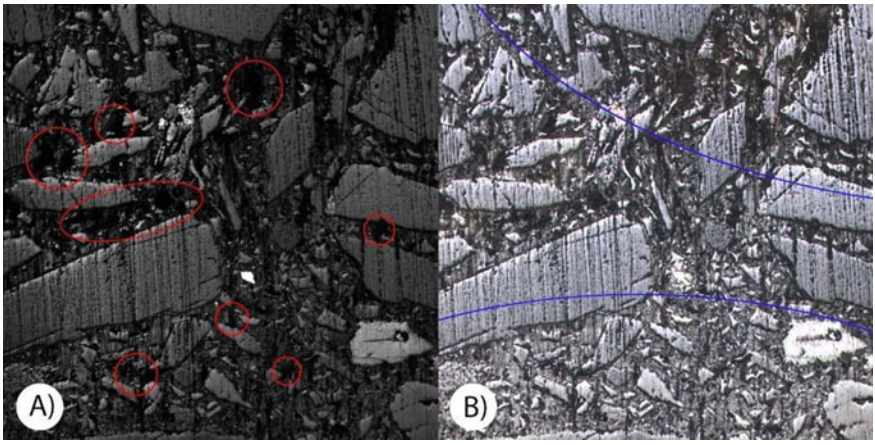

Fig. 2 Micrographs obtained through confocal microscope with a magnification increase of 108 times

When performing the analysis of the images obtained by confocal microscopy, it was possible to observe two regions within the stones, a lighter region and a darker region. The clearest region can be described as a line that divides the plates in half, the lines were observed inside more than one specimen and are perceptible to the naked eye.

The location of the observed lines suggests that it is a region of greater densification, where there was a higher concentration of granite particles and there is less presence of resin that would have been displaced towards the interstices. Friedrich relates an increase in densification of polymer matrix composite materials and a better adhesion to the reinforcing particles to an increase in compaction of the material in response to pressure and pressing time [33].

Such considerations can be based on the observation of smaller diameter pores in the lower region of the image and a smaller number of pores than those observed and highlighted in the upper region of the images.

Resistance to Chemical Attacks

The test to evaluate resistance to chemical reactions, analyzes changes in the color of the artificial stones produced according to the standard guidelines, in addition to observing whether there was dissolution of the material and mineral detachment after exposure to compounds from cleaning products, foods and atmospheric acids [27]. These substances may be in contact with the surface of the stones used for tiling, and the test evaluates the possible damage that could be caused by this exposure.

After carrying out the test, the surfaces are visually inspected for mineral dissolution and detachment, in addition to observing any changes in color. The results indicate that there was no dissolution or mineral detachment in any of the materials examined, however, a change in the chromatic tone of the analyzed stones was evident.

Figure 3 shows the specimens after being exposed to reagents 1–10.

Based on the results illustrated in Fig. 3, although the color of the rocks was not homogeneous, it was possible to verify that the samples examined did not show any change in color when exposed to reagents 1, 2, 4, 6 and 10. However, when subjected to reagents 3, 5, 7, 8 and 9, the material revealed changes in color, with a more pronounced color change, especially in response to reagent 3-citric acid ($C_6H_8O_7$), 5-acetic acid (CH_3COOH) and 8-potassium hydroxide (KOH), therefore, you should avoid using products that especially contain such reagents in their composition, in order not to alter the aesthetics of the stone.

The chemical resistance of ASG-EC to most reagents tested can be associated with the remarkable chemical resistance of the epoxy resin matrix used to make the stone, since epoxy resin is known for its high resistance to chemical substances, especially those of an alkaline nature [29].

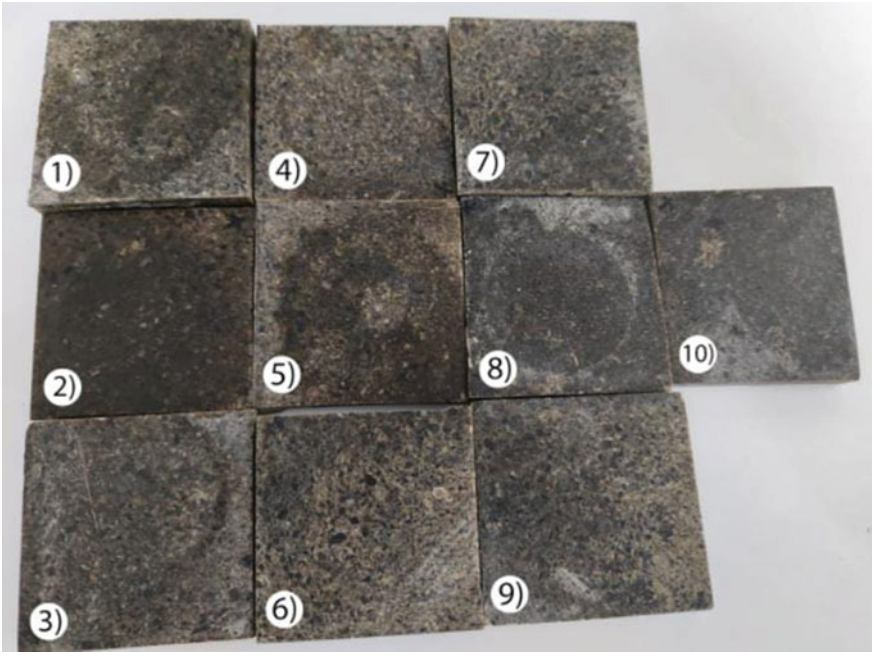

Fig. 3 ASG-EC specimens after exposure to chemical agents 1–10

Conclusions

The present study enabled the development of a new type of artificial stone from granite waste in an epoxy resin mixed with cashew oil matrix. The material had a lower apparent density than natural granite due to the presence of polymer in its composition, apparent porosity and water absorption with values higher than those stipulated for use in tiling, however, it is possible to waterproof it with resin to improve its physical properties. Regarding mechanical resistance, the stone can be considered as having high flexural resistance, in addition to being considered highly resistant to chemical attack, without showing material dissolution and mineral detachment after exposure to the reagents, showing only chromatic changes after exposure to $C_6H_8O_7$, CH_3COOH, KOH.

Acknowledgements The authors thank FAPERJ (process E-26/200.139/20220) for funding the research and UENF for its support.

References

1. Gomes MLPM, Carvalho EAS, Sobrinho LN, Monteiro SN, Rodriguez RJS, Vieira CMF (2018) Production and characterization of a novel artificial stone using brick residue and quarry dust in epoxy matrix. J Mater Res Technol 7(4):492–498. https://doi.org/10.1016/j.jmrt.2018.08.012
2. Bo Ren B, Zhao Y, Bai H, Kang S, Zhang T, Song S (2021) Eco-friendly geopolymer prepared from solid wastes: a critical review. Chemosphere 267:128900. https://doi.org/10.1016/j.chemosphere.2020.128900
3. Temiz M, Kocaman S, Ahmetli G (2023) Evaluation of EPDM waste in environmentally friendly epoxy hybrid composites. J Ind Eng Chem 126:224–238. https://doi.org/10.1016/j.jiec.2023.06.012
4. Karthikeyan JR, Girimurugan R, Sahoo G, Maheskumar P, Ramesh A (2022) Experimental investigations on tensile and flexural properties of epoxy resin matrix waste marble dust and tamarind shell particles reinforced bio-composites. Mater Today Proc 68(6):2215–2219. https://doi.org/10.1016/j.matpr.2022.08.435
5. Arumugam H, Mohamed IM, Ahn C-H, Rimdusit S, Muthukaruppan A (2023) Development of high performance granite fine fly dust particle reinforced epoxy composites: structure, thermal, mechanical, surface and high voltage breakdown strength properties. J Mater Res Technol 24:2795–2811. https://doi.org/10.1016/j.jmrt.2023.03.199
6. Carvalho ES, Marcos AF (2018) Tele-media-art—web-based inclusive teaching of body expression. In: 17th international conference on information technology based higher education and training (ITHET), Olhao, Portugal, pp 1–6. https://doi.org/10.1109/ITHET.2018.8424803
7. Bao Z (2023) Developing circularity of construction waste for a sustainable built environment in emerging economies: new insights from China. Dev Built Environ 13. https://doi.org/10.1016/j.dibe.2022.100107
8. Gencel O, Ozel C, Koksal F, Erdogmus E, Martínez-Barrera G, Brostow W (2021) Properties of concrete paving blocks made with waste marble. J Clean Prod 21(1):62–70. https://doi.org/10.1016/j.jclepro.2011.08.023
9. Chajec A (2023) The use of granite powder waste in cementitious composites. J Mater Res Technol 25:4761–4783. https://doi.org/10.1016/j.jmrt.2023.06.253
10. Lohar J, Shrivastava N, Sharma A (2023) Feasibility of granite processing waste as a fill material in geotechnical applications. Mater Today Proc. https://doi.org/10.1016/j.matpr.2023.04.655
11. Nuaklong P, Hamcumpai K, Keawsawasvong S, Pethrung S, Jongvivatsakul P, Tangaramvong S, Pothisiri T, Likitlersuang S (2023) Strength and post-fire performance of fiber-reinforced alkali-activated fly ash concrete containing granite industry waste. Constr Build Mater 392. https://doi.org/10.1016/j.conbuildmat.2023.131984
12. Ahmadi SF, Reisi M, Amiri MC (2022) Reusing granite waste in eco-friendly foamed concrete as aggregate. J Build Eng 46. https://doi.org/10.1016/j.jobe.2021.103566
13. Sogancioglu M, Ahmetli G, Yel E (2017) Comparative study on waste plastics pyrolysis liquid products quantity and energy recovery potential. Energy Procedia 118:221–226. https://doi.org/10.1016/j.egypro.2017.07.020
14. Cai X, Li C, Qiao C, Peng D (2019) Renewable coumarin-derived network as a toughening structure for petroleum-based epoxy resins. ACS Omega 4(14):16080–16087
15. Cai X, Li C, Qiao C, Peng D, Pascault JP (2014) Renewable coumarin-derived network as a toughening structure for petroleum-based epoxy resins. Chem Rev 114(2):1082–1115
16. Park S-J, Jin F-L, Lee J-R (2004) Synthesis and thermal properties of epoxidized vegetable oil. Macromol Rapid Commun 25(6):724–727
17. Kumar S, Krishnan S, Mohanty S, Nayak SK (2018) Synthesis and characterization of petroleum and biobased epoxy resins: a review. Polym Int 67(7):815–839
18. Roudsari GM, Mohanty AK, Misra M (2017) Green approaches to engineer tough biobased epoxies: a review. ACS Sustain Chem Eng 5(11):9528–9541
19. Lima CADA, Pastore GM, Lima EDPDA (2000) Study of the antibacterial activity of anacardic acids from the cashew *Anacardium occidentale* nut shell oil of the clone of cashew-midget-precocious CCP-76 and CCP-09 in five stages of maturation on oral microorganisms. Food Sci Technol 20(3):358–362. https://doi.org/10.1590/S0101-20612000000300013

20. Demartini TJC, Rodríguez RJS, Silva FS (2018) Physical and mechanical evaluation of artificial marble produced with dolomitic marble residue processed by diamond-plated bladed gang-saws. J Mater Res Technol 7(3):308–313
21. Silva TLC, Carvalho EAS, Barreto GNS, Silva TBP, Demartini TJC, Vieira CMF (2023) Characterization of artificial stone developed with granite waste and glass waste in epoxy matrix. J Mater Res Technol. https://doi.org/10.1016/j.jmrt.2023.08.045
22. Barreto GNS, Carvalho EAS, Souza VdSd, Gomes MLPM, de Azevedo ARG, Monteiro SN, Vieira CMF (2022) Engineered stone produced with glass packaging waste, quartz powder and epoxy resin. Sustainability 2022:14. https://doi.org/10.3390/su1412722
23. Cunha TP, Siqueira FB, Holanda JNF (2019) Development of sustainable eggshell waste-polyester resin composite material for using as artificial rock. Mater Res 22
24. Peixoto J, Carvalho EAS, Gomes MLPM, Guimarães RS, Monteiro SN, de Azevedo ARG, Vieira CMF (2022) Incorporation of industrial glass waste into polymeric resin to develop artificial stones for civil construction. Arab J Sci Eng 47(3):4313–4322
25. Brazilian Association of Technical Norms—ABNT NBR 15845-2 (2015) Rocks for cladding—part 2: determination of bulk density, apparent porosity and water absorption. ABNT, Rio de Janeiro (in Portuguese)
26. Brazilian Association of Technical Norms—ABNT NBR 15.845-6 (2015) Rocks for classing—part 6: determination of modulus of rupture (three point bending). ABNT, Rio de Janeiro (in Portuguese)
27. Brazilian Association of Technical Norms—ABNT NBR 16596 (2017) Rocks for cladding—chemical attack resistance—test method. ABNT, Rio de Janeiro (in Portuguese)
28. Chiodi Filho C, Rodrigues EP (2020) Guia de Aplicação de Rochas em Revestimentos, 2nd edn. Abirochas, São Paulo, 119 pp (in Portuguese)
29. Lee M-Y, Ko C-H, Chang F-C, Lo S-L, Lin J-D, Shan M-Y et al (2008) Artificial stone slab production using waste glass, stone fragments and vacuum vibratory compaction. Cem Concr Compos 30:583–587
30. Barani K, Esmaili H (2016) Production of artificial stone slabs using waste granite and marble stone sludge samples. J Min Environ 7(1):135–141
31. Brazilian Association of Technical Standards—ABNT NBR 15844 (2015) Rocks for coating—requirements for granite. ABNT, Rio de Janeiro (in Portuguese)
32. Agrizzi CP, Carvalho EAS, Borlini MCG, Barreto GNS, de Azevedo ARG, Monteiro SN, Vieira CMF (2022) Comparison between synthetic and biodegradable polymer matrices on the development of quartzite waste-based artificial stone. Sustainability 14(11):6388. https://doi.org/10.3390/su14116388
33. Friedrich D (2021) Thermoplastic moulding of wood-polymer composites (WPC): a review on physical and mechanical behaviour under hot-pressing technique. Compos Struct 262:113649. https://doi.org/10.1016/j.compstruct.2021.113649

Preparation and Characterization of 3D Printed Biobased Composites from a PBAT/PLA Blend with Lignin and Titanium Dioxide

Gustavo F. Souza, Rene R. Oliveira, Janetty J. P. Barros, Deepa Kodali, Vijaya Rangari, and Esperidiana A. B. Moura

Abstract Biobased composites produced from biopolymers reinforced with suitable fillers are an attractive route for producing sustainable materials with improved and diversified properties for a wider range of applications. In this study, biobased composites based on PBAT/PLA blend (Ecovio®), kraft lignin, and titanium dioxide (TiO_2) were prepared. First, using gamma-irradiation at 30 kGy, pristine kraft lignin was modified. Then, the pristine lignin, irradiated lignin, and TiO_2 were successfully incorporated into a PBAT/PLA blend matrix using a typical melt-mixing process with a twin-screw extruder. Filaments produced by the extrusion process from neat PBAT/PLA and its biobased composites were used to obtain parts by FDM 3D printing. Non-irradiated and irradiated lignin were characterized by ATR-FTIR and XRD analysis. The biobased composite samples were characterized by tensile tests, SEM, and XRD analysis. According to results the incorporation of a small amount of lignin and TiO_2 into PBAT/PLA blend and FDM 3D printing led to obtaining of biobased composites with suitable properties for a wider range of applications.

Keywords Kraft lignin · PBAT/PLA · TiO_2 · 3D printing · Tensile tests · SEM · DRX

G. F. Souza · J. J. P. Barros · E. A. B. Moura (✉)
Centro de Química e Meio Ambiente, Instituto de Pesquisas Energéticas e Nucleares, Av. Prof. Lineu Prestes, 2242, São Paulo, SP 05508-000, Brazil
e-mail: eabmoura@ipen.br

R. R. Oliveira
Centro de Ciências e Tecnologia de Materiais, Instituto de Pesquisas Energéticas e Nucleares, Av. Prof. Lineu Prestes, 2242, São Paulo, SP 05508-000, Brazil

D. Kodali
Department of Materials Science and Engineering, Tuskegee University, Tuskegee, AL 36088, USA

V. Rangari
Christian Brothers University, Memphis, TN 38104, USA

Z. Peng et al. (eds.), *Characterization of Minerals, Metals, and Materials 2024*, The Minerals, Metals & Materials Series, https://doi.org/10.1007/978-3-031-50304-7_60

Introduction

The significant impact of conventional polymers (petroleum-based polymers), most of which are non-biodegradable, on the environment has driven both academia and industry to explore innovative strategies for reducing the extensive use of these highly polluting materials. This involves recycling and developing biobased composites from bio-based polymers, aligning with bioeconomy and circular economy principles [1, 2]. Bio-based polymers are defined as polymers made from biological sources. These polymers can be synthesized directly in their polymeric form within living organisms, such as microorganisms, algae, or plants. Alternatively, they can be derived from biomass or engineered through biotechnological processes. As a result, these polymers are derived from renewable resources and are biodegradable and eco-friendly. Notable examples include the well-known and widely used cellulose, lignin, and starch, Notable examples include cellulose, lignin, and starch, alongside industrially produced polymers in the past few decades, thanks to advances in chemical processing and biotechnology, like polylactic acid and polyhydroxyalkanoate, which have gained significant attention from the industry [3, 4].

Biobased composites, made from bio-based polymeric matrices with suitable micro/nanofillers offer a sustainable pathway for producing greener and more versatile materials with high potential to replace conventional polymers in various traditional applications. Among the frequently used micro/nanofillers are natural fibers and nanofillers derived from biomass, as well as inorganic reinforcements like silver nanoparticles, carbon nanotubes, reduced graphene oxide, calcium carbonate ($CaCO_3$) alumina (Al_2O_3), silica (SiO_2), and titanium dioxide (TiO_2).

The addition of micro/nanofillers to bio-based polymers enhances their specific characteristics, rendering them eco-friendly and cost-effective alternatives capable of yielding products with properties similar to or even superior to those made from conventional polymers. This not only acts as a substitute but also curbs the use of non-biodegradable and environmentally harmful fossil polymers [4–6].

TiO_2, a metal oxide material with unique characteristics such as simple control, low cost, inherent non-toxicity, biocompatibility, environmental sustainability, and great resistance to chemical erosion, has been shown as a strengthening agent to biobased polymeric matrices for developing biobased composite materials. These materials exhibit notable improvements in physicochemical, mechanical, UV blocking, gas barrier, water resistance properties, and antibacterial activity [2, 6].

Commercial biodegradable polymers, such as poly(butylene adipate-co-terephthalate) (PBAT) and polylactide (PLA) are available, with PBAT offering flexibility and PLA providing strength. However, PLA's rigidity leads to brittleness. The combination of flexible PBAT with rigid PLA through melt blending enhances properties while preserving biodegradability. Blending PBAT with PLA emerges as a highly promising and environmentally sustainable method for enhancing the mechanical properties of PLA, especially addressing its inherent brittleness while ensuring adequate ductility [6–8]. PBAT/PLA blends exhibit good mechanical properties and excellent biodegradability facilitated by specific microorganisms and enzymes.

Nonetheless, due to the significant difference in solubility parameters between PBAT (22.95 cal/cm^3) and PLA (10.1 cal/cm^3), the resulting blends are only partially miscible and exhibit weak interfacial adhesion. As a result, the effective transfer of interphase stress, crucial for toughening PLA with PBAT, becomes limited. Therefore, enhancing compatibility between the two components becomes essential. Experimental evidence indicates that the addition of compatibilizers significantly improves the blend's miscibility and structural homogeneity. Common types of compatibilizers include various peroxides, free radical crosslinking agents (DCP), isocyanates (MDI), and epoxy-functionalized compounds [6–8].

Lignin, the planet's second most abundant natural polymer after cellulose, possesses eco-friendly, biodegradable characteristics, along with antioxidant properties and antimicrobial activity. It is a complex macromolecule composed of aromatic polymers with similar structures, finding diverse applications. Kraft Lignin, a by-product of the kraft paper process, is notably produced in substantial amounts, accounting for about 35% of the dry mass output of black liquor. Currently, it is used as fuel within the chemical recovery cycle due to its thermal energy capacity. However, excessive production has led to black liquor surpluses that surpass the boiler's burning capacity, creating an industry bottleneck and waste. Extracting lignin from black liquor for commercial additives offers a potential solution, finding use in pellets, resins, surfactants, and adhesives [8–10].

Recent studies reveal that incorporating irradiated lignin enhances compatibility in polymeric composites, improving UV absorption, strength, and antibacterial activity. Ionizing radiation emerges as an alternative to facilitate functional group formation, enhancing interaction efficiency with other polymers. Our earlier studies demonstrate that irradiated lignin (30–90 kGy gamma radiation) significantly enhances compatibility with PBAT/PLA blends, unlike non-irradiated lignin [8, 9].

The application of 3D FDM printing technology, an additive manufacturing (AM) technique, to bio-based composite provides superior advantages over conventional methods such as injection molding. 3D FDM printing is cost-effective, easy to maintain, and enables the production of intricate geometries. This technology allows the creation of intricate objects with diverse materials, minimizing design cycles, costs, and waste. It has attracted the interest of various industry segments due to its capacity to produce lightweight yet robust structures for aerospace, automotive, military, art, education, and architecture, and beyond. 3D printing allows for the rapid production of objects with various configurations that benefit the physical and mechanical aspects of the parts. This technology enables the quick and efficient production of test specimens and samples with properties different from other manufacturing methods [2, 7, 11–13].

The present study investigates the mechanical and morphological properties of biobased composite materials based on PBAT/PLA blends (Ecovio®), irradiated and non-irradiated kraft lignin, and titanium dioxide (TiO_2). These materials are prepared using a combination of melting extrusion and FDM 3D printing.

Materials and Methods

Materials

PBAT/PLA Blend (Ecovio® T2308, "BASF SE"), MFI: 9.5 cm^3/10 min (ISO 1133), density: 1.4 g cm^{-3} (ISO 1183); titanium dioxide (TiO_2), and kraft lignin obtained from agro-industry residues, such as eucalyptus, supplied by Suzano S/A (Sao Paulo, Brazil); (pH: 3.8; solids content: 95%; ash content: 2%), were used in this study.

Methods

Kraft Lignin Preparation and Irradiation

Kraft lignin was previously washed with deionized water to remove residual impurities. Next, 20 g of lignin was mixed with an aqueous solution of 200 mL of H_2O/HCl (0.01 mol/L of HCl), and the mixture was stirred magnetically for 30 min. Subsequently, the lignin was rinsed repeatedly with deionized water using a centrifuge until it reached a neutral pH of approximately 7.0. Following this, the lignin was dried in an oven with air circulation at 60 °C for 24 h. Part of the prepared lignin was subjected to irradiation using the Cobalt-60 Multipurpose Gamma irradiator at room temperature, in the presence of air, dose rate of 5 kGy/h, total radiation dose of 30 kGy.

Titanium Dioxide (TiO_2) Preparation

Titanium Dioxide (TiO_2) was previously dried in an oven with air circulation at 60 °C for 24 h.

Composite Preparation

The PBAT/PLA blend was firstly dried in an oven with an air circulation system, at 80 °C for 24 h to reduce the blend's moisture content to below 2%. The biobased composites were prepared with PBAT/PLA blend, TiO_2, irradiated and non-irradiated lignin, according to composition presented in Table 1. The compositions (PBAT/PLA/Lignin/TiO_2) were hand premixed and then processed in a Thermo Scientific HAAKE twin-screw co-rotating extruder, model Rheomex 332p, with 16 mm screw diameter and a length-diameter-ratio of 25. The biobased composites were processed in a two-step to better dispersion of lignin and TiO_2 into the PBAT/PLA matrix. The

Table 1 PBAT/PLA/lignin/TiO_2 biobased composites composition

Composition	PBAT/PLA (wt.%)	TiO_2 (wt.%)	N-irradiated[a] lignin (wt.%)	Irradiated lignin (wt.%)
Neat PBAT/PLA	100	0	0	0
PBAT/PLA/TiO_2/ n-iLignin[a] 0.5/1.0 (wt.%)	98.5	0.5	1.0	0
PBAT/PLA/TiO_2/ i-lignin[b] 0.5/1.0 (wt.%)	98.5	0.5	0	1.0

[a] Non-irradiated lignin
[b] Irradiated lignin

compositions were processed in the temperature profile of 150/165/175/175/165/150 °C, and screw speed at 30 rpm. The extruded biobased composites were cooled down, pelletized, and dried again in an oven with an air circulation system at 80 °C for 4 h.

Filaments Preparation

The biobased composites with different amount of TiO_2, irradiated and non-irradiated lignin were fed at Thermo Scientific HAAKE twin-screw co-rotating extruder to produce the filaments for 3D FDM. The temperature profile was 145/160/175/175/165/145 °C, screw speed set at 30 rpm, temperature of cooling water of the filaments was 35 °C, and filament diameter was 1.75 ± 0.01 mm. The main processing steps of the biobased composites and filaments are depicted schematically presented in Fig. 1.

Fused Deposition (FDM) 3D Printing

The specimens for tensile and water absorption tests were manufactured using the Fused Deposition Modeling (FDM) technique on a 3D printer, and they were pre-sliced using the Cura3D software, employing the following settings: 100% infill density, printed with a 0.4 mm nozzle, at a speed of 80 mm/s. The printing temperatures for all blends were set at 180 °C for the nozzle and 70 °C for the build platform to ensure adequate adhesion of the printed components. The components were produced using an Artillery Sidewinder X1 3D printer.

Characterization

Attenuated Total Reflectance-Fourier Transform Infrared Spectroscopy (ATR-FTIR)

ATR-FTIR analyses of the non-irradiated and irradiated lignin were recorded with a Perkin Elmer—Frontier. Tests carried out in the medium infrared range with wavenumber ranging from 4000 to 650 cm^{-1}, with 16 scans and resolution of 4 cm^{-1}.

X-ray Diffraction (XRD)

XRD patterns of non-irradiated and irradiated lignin, PBAT/PLA blend and its biobased composites were recorded on a siemens-d5000 diffractometer operated at 40 kV and 40 mA, with cu k_α radiation ($\lambda = 15.4$ Å), over the 2θ range from 5 to 40°.

Scanning Electron Microscopy (SEM) Analysis

SEM analyses were conducted in a Model LX-30 Philips instrument operated at an electron acceleration voltage of 12 kV. The samples' cryofractured surfaces under liquid nitrogen were sputtered with a gold layer before SEM analyses of the morphology of the samples' surfaces.

Water Absorbency Measurements

Water absorbency measurements of the biobased composite samples were performed in triplicates to ensure accuracy, and the average values were recorded. The biobased composite's water absorbency was assessed through swelling tests. Each sample was sectioned into 2 × 2 cm^2 piece, dried at 45 ± 2 °C for 24 h in a circulating air oven, pre-weighed, and then placed in 20 mL of deionized water in petri dishes. After 24 h at room temperature, the samples were removed from deionized water, quickly wiped with filter paper to remove droplets on the surface, and then weighed. This process was repeated at specific time intervals until equilibrium swelling was reached. The swelling ratio was calculated using Eq. 1. This systematic approach provided insights into the water absorbency and swelling behavior of the biobased composites.

$$\text{Swelling Ratio (\%)} = \left(\frac{\text{Ws} - \text{Wd}}{\text{Wd}}\right) \times 100 \tag{1}$$

where Ws = weight of the swollen samples, Wd = weight of the dry samples. All three replicates.

Tensile Tests

Printed specimens from the neat PLA/PBAT and its biobased composites were submitted to tensile tests on Instron model 5564, according to ASTM D 638-99, at room temperature at a cross-head speed of 50 mm/min. For each composition, five specimens were tested, and the average value of five specimens with the standard deviation was recorded.

Results and Discussion

Attenuated Total Reflectance-Fourier Transform Infrared Spectroscopy (ATR-FTIR)

Figure 1 shows ATR-FTIR spectra of non-irradiated and irradiated lignin at absorbed doses of 30 kGy. The difference between non-irradiated and irradiated lignin lies in the intensification of absorption bands, along with the displacement of the characteristic hydroxyl group band from 3385 cm^{-1} to a lower value, specifically 3262 cm^{-1}. These changes can be attributed to the influence of irradiation, which causes the cleavage of certain functional groups while simultaneously leading to an increase in OH groups. Furthermore, some of these groups with higher bond energies are shifted to lower wavenumbers. An increase in the concentrations of C=O and C=C in the lignin structure is also observed, as documented in previous studies [14, 15]. When lignin is exposed to gamma radiation, the radiant energy absorbed by the substance directly impacts its molecular electronic structure, resulting in valence electron transitions. This, in turn, triggers various physical and chemical processes in the material, as mentioned in previous research [16–18].

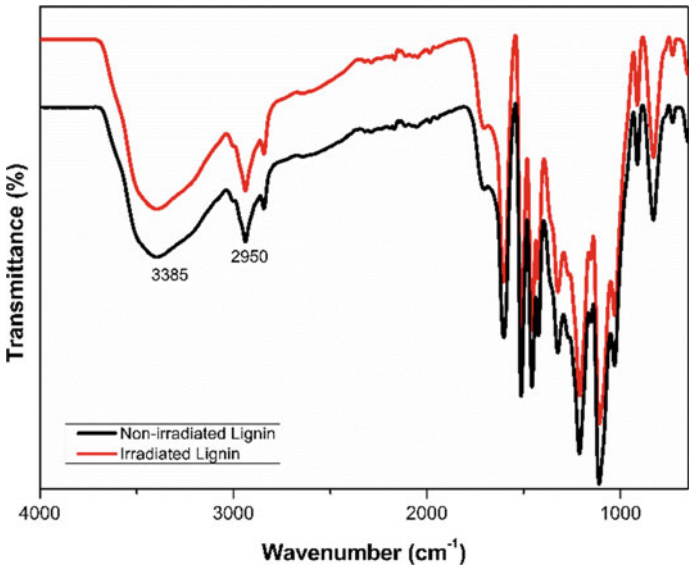

Fig. 1 ATR-FTIR spectra of non-irradiated lignin and irradiated lignin at 30 kGy

XRD Analysis Results

The XRD patterns of neat PBAT/PLA and its biobased composites are shown in Fig. 2. In the neat PBAT/PLA, PBAT is found in higher concentration, leading to the prevalence of characteristic diffraction peaks associated with PBAT in the X-ray diffraction (XRD) pattern. These peaks, identified at 16, 17, 21, and 24°, correspond to the crystalline planes of PBAT. PLA, conversely, exhibits a prominent diffraction peak at 16°, as demonstrated in previous studies such as those conducted by Li et al. and Liu et al. [19, 20]. It is noteworthy that the relative intensity of these peaks diminishes while their width increases in compositions containing lignin, whether it be PBAT/PLA/TiO_2/n-iLignin or PBAT/PLA/TiO_2/i-lignin at 30 kGy. This observation suggests that the addition of lignin may promote a more heterogeneous nucleation within the PBAT/PLA, consequently increasing crystallinity when lignin is subjected to irradiation. Substantiating this effect, other research has also showed to its occurrence in the sample, as elucidated by the XRD results of irradiated lignin-biobased composites [21].

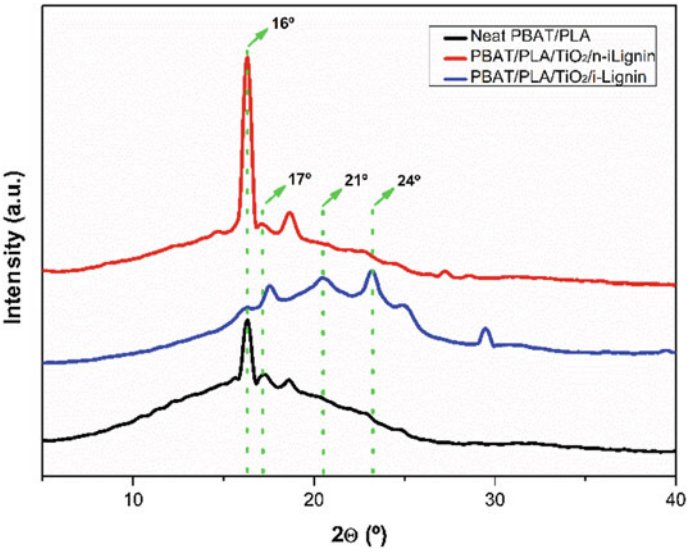

Fig. 2 XRD patterns of neat PBAT/PLA and its biobased composites

SEM Analysis Results

The SEM images of cryogenic fracture surfaces of neat PBAT/PLA and its biobased composites are depicted in Fig. 3. It can be observed from Fig. 3a that neat PBAT/PLA exhibits a biphasic morphology characteristic of immiscible systems. In this morphology, PLA spheroidal domains are intricately dispersed within the PBAT matrix. Upon the addition of non-irradiated lignin and TiO_2 the image exhibits irregular particles embedded in the PBAT/PLA matrix, indicating a low compatibility between PBAT/PLA, non-irradiated lignin, and TiO_2 [22, 23]. On the other hand, the incorporation of irradiated lignin at 30 kGy and TiO_2 into the PBAT/PLA blend displayed improved polymer interface, i.e., reduced phase segregation between PBAT and PLA, suggesting that irradiated lignin presented better interaction with the blend and also influenced the blend's compatibility. Similar findings were reported by Xiong et al. [24], who observed that lignin methylation promoted enhanced interaction between PBAT and lignin.

Water Absorbency Measurements

The swelling ratio for water absorbency measurements of the neat PBAT/PLA and its biobased composites is presented in Table 2. Upon the addition of non-irradiated lignin and TiO_2, the swelling ratio increased from 1.2 to 1.3%, that is, the water absorbency growth about 8% compared to neat blend. Otherwise, when irradiated

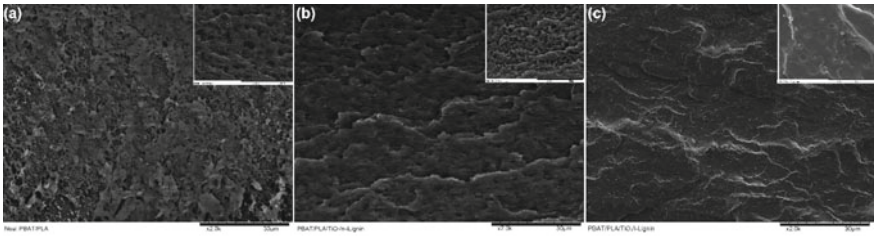

Fig. 3 SEM images of cryogenic fracture surfaces at 2000 and 5000× of magnification: **a** PBAT/PLA; **b** PBAT/PLA/TiO_2/n-iLignin; **c** PBAT/PLA/TiO_2/i-lignin

Table 2 Swelling ratio of the neat PBAT/PLA blend and its biobased composites

Samples	Swelling ratio (wt.%)	Water absorbency (%)
Neat PBAT/PLA	1.2	
PBAT/PLA/TiO_2/n-iLignin[a]	1.3	+ 8.0
PBAT/PLA/TiO_2/i-lignin[b]	1.0	− 16.7

[a] Non-irradiated lignin
[b] Irradiated lignin

lignin was added, a reduction of approximately 17% in water absorbency was noticed. This indicates that the incorporation of irradiated lignin increased the hydrophobicity of the samples, an important characteristic to expanding the application field of PBAT/PLA.

Tensile Test Results

Table 3 presents the dependence of tensile strength at break, elongation at break, and Young's modulus on the content of irradiated and non-irradiated lignin and TiO_2 in the PBAT/PLA composites. As shown in Table 3, the tensile strength and Young's modulus of the non-irradiated lignin-based composites decreased. This declining trend in tensile strength and Young's modulus likely results from poor dispersibility and low compatibility between the non-irradiated lignin domains and PBAT/PLA matrix, as shown in the SEM images of cryogenic fracture surfaces in Fig. 3b. Meanwhile, when irradiated lignin was incorporated into the PBAT/PLA matrix, a gain of about 10% in tensile strength, Young's modulus and elongation at break was observed. This indicates a better wetting effect of irradiated lignin with the PBAT/PLA blend matrix, and also influenced the blend's compatibility, as can be seen in SEM (Fig. 3c).

Table 3 Tensile test results of neat PBAT/PLA and its biobased composites

Samples	Tensile strength at break (MPa)	Elongation at break (%)	Young's modulus (MPa)
Neat PBAT/PLA	72.8 ± 2.6	17.4 ± 1.1	626.9 ± 24.6
PBAT/PLA/TiO_2/ n-iLignin[a]	62.9 ± 5.3	17.2 ± 0.3	593.6 ± 64.4
PBAT/PLA/TiO_2/ i-lignin[b]	80.1 ± 6.4	19.1 ± 0.8	689.6 ± 56.5

[a] Non-irradiated lignin
[b] Irradiated lignin

Conclusion

The present study investigated the mechanical and morphological properties of biobased composite materials based on PBAT/PLA blends (Ecovio®), irradiated and non-irradiated kraft lignin, and titanium dioxide (TiO_2), prepared from a combination of melting extrusion and FDM 3D printing. ATR-FTIR analysis results showed that the gamma irradiation of lignin caused changes in physical and chemical properties of lignin. According to SEM results the incorporation of irradiated lignin at 30 kGy and TiO_2 into the PBAT/PLA blend displayed improved polymer interface and also influenced the blend's compatibility. Tensile test results shown a gain of about 10% in tensile strength, Young's modulus and elongation at break to irradiated lignin-biobased composites instead of non-irradiated lignin. In conclusion, the incorporation of a small amount of lignin and TiO_2 into a PBAT/PLA blend has been shown to yield biobased composites with improved mechanical and morphological properties. These enhanced properties make these composites suitable for a wider range of applications, including but not limited to packaging materials, automotive components, and various consumer products. In addition, this study highlights the potential of biobased composites as sustainable alternatives to traditional plastics. Future research should investigate how to optimize filler concentrations and processing parameters more effectively, in order to adjust the properties of these biocomposites to meet specific application requirements.

Acknowledgements The authors wish to thank FAPESP, CAPES and CNPq for providing support for this work.

Funding Sources The authors would like to thank the funding from FAPESP/Process Number 2019/00862.

References

1. Qiu S, Zhou Y, Waterhouse GIN, Gong R, Xie J, Zhang K, Xu J (2021) Optimizing interfacial adhesion in PBAT/PLA nanocomposite for biodegradable packaging films. Food Chem 334:127487. https://doi.org/10.1016/j.foodchem.2020.127487
2. Sciancalepore C, Togliatti E, Marozzi M, Rizzi FMA, Pugliese D, Cavazza A, Pitirollo O, Grimaldi M, Milanese D (2022) Flexible PBAT-based composite filaments for tunable FDM 3D printing. ACS Appl Bio Mater 5:3219–3229. https://doi.org/10.1021/acsabm.2c00203
3. Meraldo A (2016) Introduction to bio-based polymers. In: Multilayer flexible packaging, 2nd edn, pp 47–52. https://doi.org/10.1016/B978-0-323-37100-1.00004-1
4. George V, Sanjay MR, Srisuk R, Parameswaranpillai J, Siengchin S (2020) A comprehensive review on chemical properties and applications of biopolymers and their composites. Int J Biol Macromol 154(2020):329–338. https://doi.org/10.1016/j.ijbiomac.2020.03.120
5. Irshad MA, Nawaz R, Rehman MZ, Adrees M, Rizwan M, Ali S, Ahmad S, Tasleem S (2021) Synthesis, characterization and advanced sustainable applications of titanium dioxide nanoparticles: a review. Ecotoxicol Environ Saf 212:111978
6. Urquijo J, Aranburu N, Dagréou S, Guerrica-Echevarría G, Eguiazábala JI (2017) CNT-induced morphology and its effect on properties in PLA/PBAT-based nanocomposites. Eur Polym J. https://doi.org/10.1016/j.eurpolymj.2017.06.035
7. Yang J, Li W, Mu B, Xu H, Hou X, Yang Y (2022) 3D printing of toughened enantiomeric PLA/PBAT/PMMA quaternary system with complete stereo-complexation: compatibilizer architecture effects. Polymer 242:124590. https://doi.org/10.1016/j.polymer.2022.124590
8. Barros JJP, Soares CP, Moura EAB, Wellen RMR (2022) Enhanced miscibility of PBAT/PLA/lignin upon γ-irradiation and effects on the non-isothermal crystallization. J Appl Polym Sci e53124
9. Kumar A, Tumu VR, Chowdhury SR, Ramana Reddy SVS (2019) A green physical approach to compatibilize a bio-based poly (lactic acid)/lignin blend for better mechanical, thermal and degradation properties. Int J Biol Macromol 121:588
10. Kun D, Pukánszky B (2017) Polymer/lignin blends: interactions, properties, applications. Eur Polym J 93:618–641. https://doi.org/10.1016/j.eurpolymj.2017.04.035
11. Hong S-H, Park JH, Kim OY, Hwang S-H (2021) Preparation of chemically modified lignin-reinforced PLA biocomposites and their 3D printing performance. Polymers 13:667. https://doi.org/10.3390/polym13040667
12. Oliveira C, Rocha J, Ribeiro JE (2022) Mechanical and physical characterization of parts manufactured by 3D printing. In: Da Silva LFM (ed) Advanced structured materials. Springer, Cham, pp 77–88. https://doi.org/10.1007/978-3-031-18130-6_6
13. Sun C, Wang X, Liu Y (2022) A critical review of 3D printing in construction: benefits, challenges, and risks. In: Da Silva LFM (ed) Advanced structured materials. Springer, Cham
14. Cheng Y-F, Shen Q (2018) Quantitatively evaluation of the effects of γ-irradiation dose and time on the structure and properties of lignin. Int Wood Prod J 9(4):186–193. https://doi.org/10.1080/20426445.2018.1481142
15. Wu X, Chen L, Chen J, Su X, Liu Y, Wang K, Qin W, Qi H, Deng M (2019) The effect of ^{60}Co γ-irradiation on the structure and thermostability of alkaline lignin and its irradiation derived degradation products. Waste Biomass Valor 10(10):3025–3035. https://doi.org/10.1007/s12649-018-0271-3
16. Ayoub A, Venditti RA, Jameel H, Chang HM (2014) Effect of irradiation on the composition and thermal properties of softwood kraft lignin and styrene grafted lignin. J Appl Polym Sci 131(1)
17. Rajeswara Rao N, Venkatappa Rao T, Ramana Reddy S, Sanjeeva Rao B (2015) Effect of electron beam on thermal, morphological and antioxidant properties of kraft lignin. Adv Mater Lett 6(6):560–565
18. Nakamura K, Katayama K, Amano T (1973) Some aspects of nonisothermal crystallization of polymers. II. Consideration of the isokinetic condition. J Appl Polym Sci 17(4):1031–1041

19. Li M, Jia Y, Shen X, Shen T, Tan Z, Zhuang W, Zhao G, Zhu C, Ying H (2021) Investigation into lignin modified PBAT/thermoplastic starch composites: thermal, mechanical, rheological and water absorption properties. Ind Crops Prod 171:113916
20. Liu Y, Liu S, Liu Z, Lei Y, Jiang S, Zhang K, Yan W, Qin J, He M, Qin S (2021) Enhanced mechanical and biodegradable properties of PBAT/lignin composites via silane grafting and reactive extrusion. Compos Part B Eng 220:108980
21. Ye H, Zhang Y, Yu Z (2017) Effect of desulfonation of lignosulfonate on the properties of poly(lactic acid)/lignin composites. BioResources 12(3):4810–4829
22. Anwer MA, Naguib HE, Celzard A, Fierro V (2015) Comparison of the thermal, dynamic mechanical and morphological properties of PLA-Lignin & PLA-Tannin particulate green composites. Compos Part B Eng 82:92–99
23. Guo J, Chen X, Wang J, He Y, Xie H, Zheng Q (2019) The influence of compatibility on the structure and properties of PLA/lignin biocomposites by chemical modification. Polymers 12(1):56
24. Xiong SJ, Pang B, Zhou SJ, Li MK, Yang S, Wang YY, Shi Q, Wang SF, Yuan TQ, Sun RC (2020) Economically competitive biodegradable PBAT/lignin composites: effect of lignin methylation and compatibilizer. ACS Sustain Chem Eng 8:5338

Process Mineralogical Analysis of a Typical Vanadium Titano-magnetite Concentrate

Jian Pan, Xin Wang, Deqing Zhu, Zhengqi Guo, Congcong Yang, and Siwei Li

Abstract This study is focused on the detailed investigation of the process mineralogy of a typical Vanadium titano-magnetite concentrate (VTM) to efficiently utilize its valuable elements like iron, vanadium, and titanium. The investigation covers mineral phase composition, phase-embedding properties, and the distribution behavior of the main elements of VTM. The phase composition of VTM consists of 84.11% titanomagnetite, 6.52% hematite-limonite, 1.41% ilmenite, 3.87% olivine, and 3.31% alumina. The ore of VTM consists of individual metallic mineral grains and intergrowth grains with diverse structures and particle sizes. Titanomagnetite is predominantly found in self-formed grain structures. Hematite-limonite is mainly present in crystalline structures. It also coexists with titanomagnetite or can be cemented in olivine with a sponge meteorite structure. Ilmenite and magnesium spinel exist as exogenous crystals within the titanomagnetite. Pyroxene, olivine, silicate, and clay minerals occur in different forms and intergrowths with metallic minerals. Iron and titanium elements in VTM exist mainly in the forms of ilmenite and titanomagnetite, while vanadium elements occur in isomorphism forms within these mineral phases.

Keywords Vanadium titano-magnetite concentrate · Process mineralogy · Phase composition · Phase embedding characteristics · Elements distribution behavior

J. Pan · X. Wang (✉) · D. Zhu · Z. Guo · C. Yang · S. Li
School of Minerals Processing and Bioengineering, Central South University, Changsha 410083, China
e-mail: gangtiexiwangxin@csu.edu.cn

J. Pan · D. Zhu · Z. Guo · C. Yang · S. Li
Low-Carbon and Hydrogen Metallurgy Research Center, Central South University, Changsha 410083, China

Z. Peng et al. (eds.), *Characterization of Minerals, Metals, and Materials 2024*, The Minerals, Metals & Materials Series, https://doi.org/10.1007/978-3-031-50304-7_61

Introduction

Vanadium titano-magnetite concentrate (VTM) is a widely occurring multi-metal associated iron ore. The main components of VTM are iron, titanium, and vanadium, which make it a crucial resource for the global titanium and vanadium industries. Additionally, VTM also contains trace amounts of associated metal elements such as chromium, scandium, cobalt, nickel, and platinum, further enhancing its potential value [1–5].

Compared to conventional iron ore, VTM has a more complex mineral composition. Research indicates that VTM is primarily composed of titanomagnetite, ilmenite, sulfide minerals, and silicate minerals [6, 7]. Titanium and iron elements are closely interconnected in VTM, with titanium primarily existing in titanomagnetite and ilmenite, while only a small amount is found in gangue minerals [8–12]. As of yet, no independent vanadium minerals have been identified in VTM. Instead, vanadium is present through isomorphic substitution for iron, with approximately 80–95% of vanadium concentrated in titanomagnetite [13–16].

Moreover, the chemical and mineral composition of VTM can vary across different regions due to varying ore geological conditions [17]. For instance, VTM found in Chengde, China, comprises coarser mineral grains and looser ore structure. In terms of chemical composition, VTM in Chengde consists mainly of iron, vanadium, and titanium elements, usually lacking other rare elements. Conversely, VTM from the Panzhihua-Xichang region is characterized by finer mineral grains and a more compact ore structure [18]. Additionally, VTM in this region contains several beneficial associated minerals such as chromium, gallium, cobalt, nickel, scandium, copper, manganese, selenium, tellurium, and platinum group elements, in addition to iron, vanadium, and titanium [19–21]. Therefore, a comprehensive process mineralogical analysis is required to efficiently exploit the valuable iron, vanadium, and titanium elements present in VTM. However, much of the current research in this field lacks systematic and in-depth analysis.

This study utilized a typical VTM sample obtained from South Africa as the raw material. Through chemical composition analysis, chemical phase analysis, X-ray diffraction (XRD) analysis, optical microscopy analysis, and scanning electron microscope-energy dispersion spectrum (SEM-EDS) analysis, the process mineralogy of this VTM sample was thoroughly investigated. The goal was to reveal the mineral phase composition, phase embedding characteristics, and distribution behavior of the main elements. The findings of this investigation can significantly contribute to the subsequent development and utilization of VTM.

Table 1 Chemical compositions of VTM/wt.%

Fe_{total}	FeO	TiO_2	V_2O_5	SiO_2	Al_2O_3	MgO	CaO
51.64	16.80	12.96	1.52	4.44	4.37	1.20	0.17
K_2O	Na_2O	Cu	Zn	Pb	P	S	LOI[a]
0.18	0.051	0.022	0.042	0.017	0.0071	0.13	2.88

[a] *LOI* loss on ignition

Table 2 Size distribution of VTM/wt.%

+ 0.5 mm	0.15 ~ 0.5 mm	0.074 ~ 0.15 mm	0.043 ~ 0.074 mm	− 0.043 mm
0	0.23	1.63	27.40	70.74

Materials and Methods

Materials

Tables 1 and 2 present the chemical composition and particle size distribution of VTM obtained from South Africa, respectively. The concentrate is classified as high-vanadium vanadium titano-magnetite concentrate, containing 51.64% iron, 12.96% titanium, and 1.52% vanadium. The extraction of vanadium from this type of VTM typically involves wet metallurgical processes to extract vanadium first, followed by pyrometallurgical processes to recover molten iron and high-titanium content slag. The high-titanium slag can then be further processed to recover the titanium element. Alternatively, the ore can be directly smelted, resulting in ferrotitanium alloy and vanadium-containing slag, which can be used to recover iron, titanium, and vanadium. However, it is important to note that the concentrate also contains adverse elements, such as 4.44% SiO_2, 4.37% Al_2O_3, and 1.2% MgO, which can impact direct vanadium extraction or pyrometallurgical processes. Harmful metal elements such as alkali metals, P, and S are present in relatively low concentrations. From Table 2, it is evident that the concentrate has fine particle size, with over 98% of particles being less than 0.074 mm, necessitating pre-pelleting for smelting.

Experimental Methods

To investigate the mineral phase composition, phase embedding characteristics, and distribution behavior of the main elements in a typical vanadium titano-magnetite concentrate, the VTM sample was mixed, divided, and sampled for XRD analysis, chemical phase analysis, optical microscopy analysis, and SEM-EDS analysis. The research methods employed are as follows:

1. XRD analysis: The XRD phase analysis of VTM was conducted using a SIEMENS D500 X-ray diffractometer. MDI Jade 6.0 software was employed for mineral composition analysis. The instrument scanned the range of 10–80° 2θ with a step size of 0.02°, using a Cu anode target with a wavelength of 1.54056 Å.
2. Chemical phase analysis: A selective dissolution method was applied to determine the content of iron, vanadium, and titanium elements in different mineral forms in VTM samples based on their solubility and dissolution rate in chemical solvents.
3. Optical microscopy analysis: Microscopic analysis of VTM was performed using a Leica DM RXP optical microscope. A mixture of resin and curing agent was poured into a fixture with the VTM sample for solidification. After solidification, the sample was sliced, polished, and air-dried to produce a thin section for observation under the microscope.
4. SEM-EDS analysis: The FEI QUANTA 200 scanning electron microscope and EDAX-Mahwah-NJ model EDS spectrometer were utilized to analyze thin sections of VTM to detect the distribution behavior of major elements. By employing these research methods, a comprehensive understanding of the mineralogical characteristics of VTM can be obtained, providing valuable insights for the subsequent development and utilization of this resource.

Results and Discussion

Phase Composition

Figure 1 displays the XRD analytical outcomes of the VTM, with Tables 3, 4 and 5 unveiling the results from chemical phase examinations. Primary iron-forming minerals in this context encompass ilmenite, hematite, and titanomagnetite. Still, the gangue minerals primarily comprise titanite, pyroxene, garnet, olivine, diaspore, and alumina. As per the information from Fig. 1 and Table 3, the distinct phase composition of VTM includes 84.11% titanomagnetite, 6.52% hematite-limonite, 1.41% ilmenite, 3.87% olivine, and 3.31% alumina.

Iron in the VTM ore primarily exists in the form of titanomagnetite, accounting for 89.04% of the total iron content, while the iron element in the form of hematite-limonite, ferrosilite and ilmenite respectively accounting for 7.74%, 2.09% and 0.95%. Titanium exists in the ore mainly as ilmenite, accounting for 95.35% of the total titanium content, with the remaining titanium present in the form of titanomagnetite and sillimanite. In addition, vanadium is not only present in isomorphous association with ilmenite and titanomagnetite but also exists in small amounts in the form of silicates (Table 6).

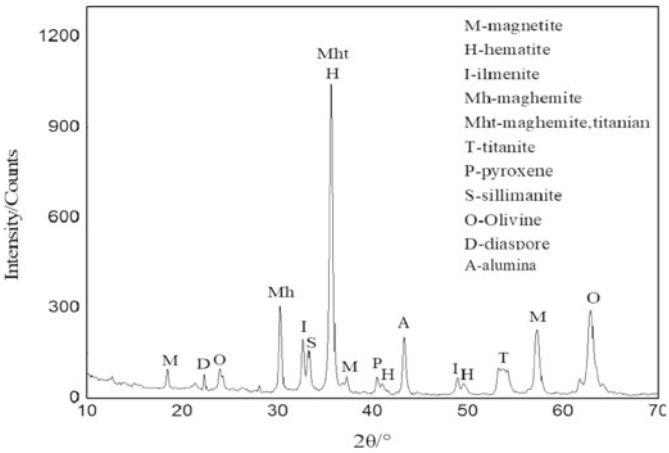

Fig. 1 XRD analysis of VTM. M-magnetite: Fe_3O_4; H-hematite: Fe_2O_3; I-ilmenite: $FeTiO_3$; Mh-maghemite: $Fe_{21.333}O_{32}$; Mht-maghemite, titanium: $Fe_{0.23}(Fe_{1.95}Ti_{0.42})O_4$; T-titanite: $CaTiSiO_5$; P-pyroxene: $Mg_2FeAl_2(SiO_4)_3$; S-sillimanite: Al_2SiO_5; O-olivine: $(Mg,Fe)_2SiO_4$; D-diaspore: AlO(OH); A-alumina: Al_2O_3

Table 3 Chemical phase composition of VTM/wt.%

Titanomagnetite	Hematite-limonite	Ilmenite	Olivine	Alumina	Others
84.11	6.52	1.41	3.87	3.32	0.77

Table 4 Chemical phase analysis of iron in VTM/wt.%

Occurrence state	Titanomagnetite	Hematite-limonite	Ferrosilite	Ilmenite	Iron carbonate
Fe contents	48.65	4.23	1.14	0.52	0.10
Percentage	89.04	7.74	2.09	0.95	0.18

Table 5 Chemical phase analysis of titanium in VTM/wt.%

Occurrence state	Titanomagnetite	Ilmenite	Sphene
TiO_2 contents	12.51	0.558	0.052
Percentage	95.35	4.25	0.40

Table 6 Chemical phase analysis of vanadium in VTM/wt.%

Occurrence state	Titanomagnetite	Silicate	Ilmenite
V_2O_5 contents	1.57	0.093	0.015
Percentage	93.56	5.55	0.89

Phase Embedding Characteristics

Figures 2, 3, 4, 5 and 6 present the results of optical microscopy analysis of VTM. The natural ore of VTM exhibits various structures such as dense granular, plate-like, and flake-like forms, all of which possess a distinct metallic sheen on fresh surfaces. Under microscopic examination, VTM displays a diverse array of ore structures, primarily comprising crystalline formations and solid solution separation structures.

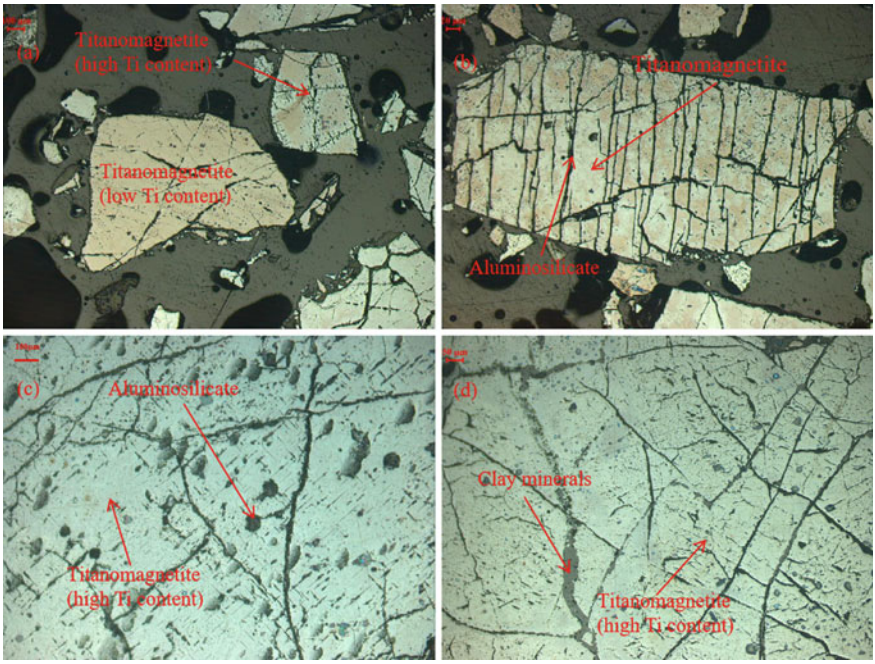

Fig. 2 Characteristics of phase embedding between titanomagnetite and other minerals

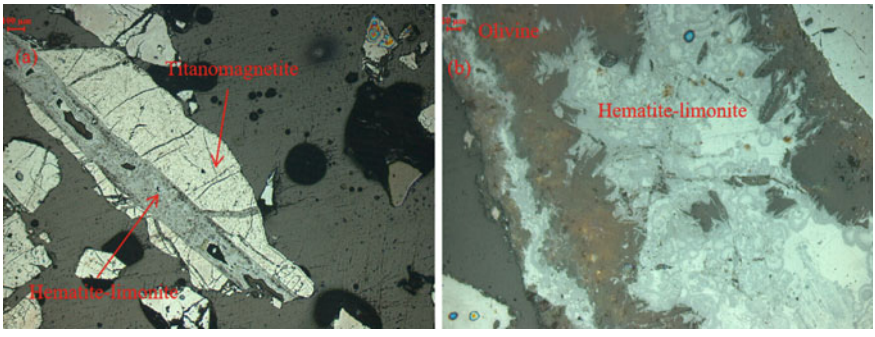

Fig. 3 Characteristics of phase embedding between hematite-limonite and other minerals

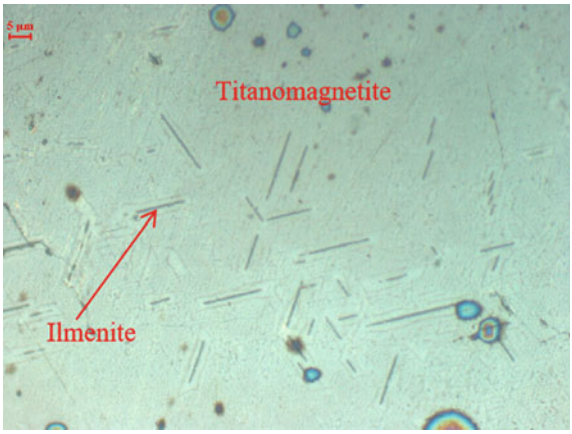

Fig. 4 Characteristics of phase embedding between ilmenite and titanomagnetite

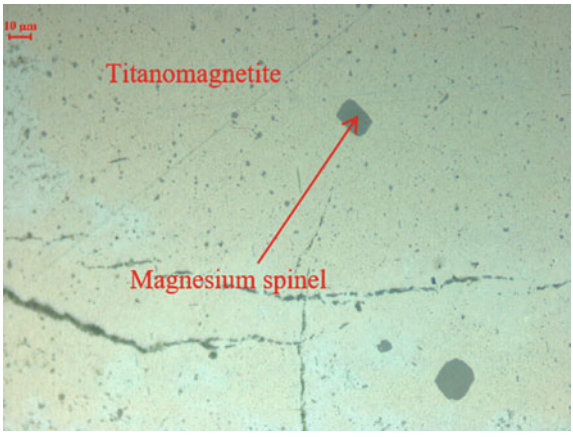

Fig. 5 Characteristics of phase embedding between magnesium spinel and titanomagnetite

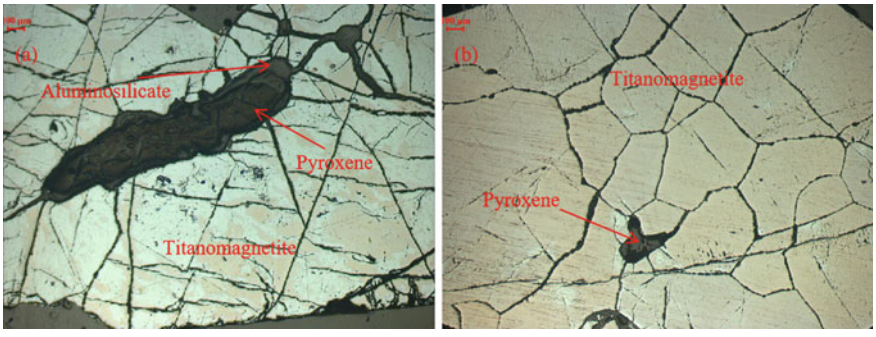

Fig. 6 Characteristics of phase embedding between pyroxene and titanomagnetite

The ore primarily consists of individual metallic mineral grains and intergrowth grains, exhibiting a wide range of particle sizes and diverse structural patterns. Titanomagnetite is predominantly present within self-formed grain structures, spanning from coarse grains measuring 0.1–4 mm, to medium grains, occasionally accompanied by fine grains. In Fig. 2a, titanomagnetite appears as a grayish-blue hue with a subtle brown interference color under reflected light. This coloration varies with changes in the chemical formula $Fe_{1-x}Fe_{2-2x}Ti_xO_4$, specifically the value of 'x'. Along the cleavage fractures of titanomagnetite, intergrowth minerals such as aluminosilicates are observed (Fig. 2b). Furthermore, high titanium content titanomagnetite with a spotted structure is found distributed within an aluminosilicate matrix (Fig. 2c), and these high titanium content titanomagnetite grains exhibit a crushed structure reminiscent of granite, with clay minerals filling crevices (Fig. 2d).

Hematite-limonite predominantly exists in crystalline structures, with intergrowth bodies ranging in diameter from 0.2 to 1 mm. In addition to fine self-formed granular structures (Fig. 3a), hematite-limonite grains also manifest plate-like structures and coexist with titanomagnetite grains. Furthermore, these grains can be observed cemented within olivine, forming a sponge meteorite-like structure (Fig. 3b). Figures 4 and 5 respectively depict ilmenite and magnesium spinel as exogenous crystals existing in the form of solid solutions within the titanomagnetite.

While independent gangue minerals are scarce in the ore, minerals such as pyroxene, olivine, silicate, and clay minerals are present in various forms and often intergrown with metallic minerals. For example, as demonstrated in Fig. 6, pyroxene forms a ring structure, with aluminosilicate minerals encapsulated within the ilmenite, or directly fills cracks within the titanomagnetite grains.

Elements Distribution Behavior

Figure 7 show the SEM-EDS analysis results of VTM by map scan patterns, respectively. The elements of iron, titanium and vanadium in vanadium-titanium magnetite are mostly distributed in the titanomagnetite and ilmenite phases. The main elements of gangue minerals are calcium, aluminum, silicon and oxygen, and basically no iron, vanadium and titanium are detected. Combining the results from Tables 2, 3, 4 and 5, iron and titanium elements in VTM exist mainly in the forms of ilmenite and titanomagnetite, while vanadium elements occur in isomorphism forms within these mineral phases.

Conclusions

In this manuscript, process mineralogical analysis of a typical vanadium titanomagnetite concentrate was investigated thoroughly. The specific phase composition of VTM is 84.11% titanomagnetite, 6.52% hematite-limonite, 1.41% ilmenite, 3.87%

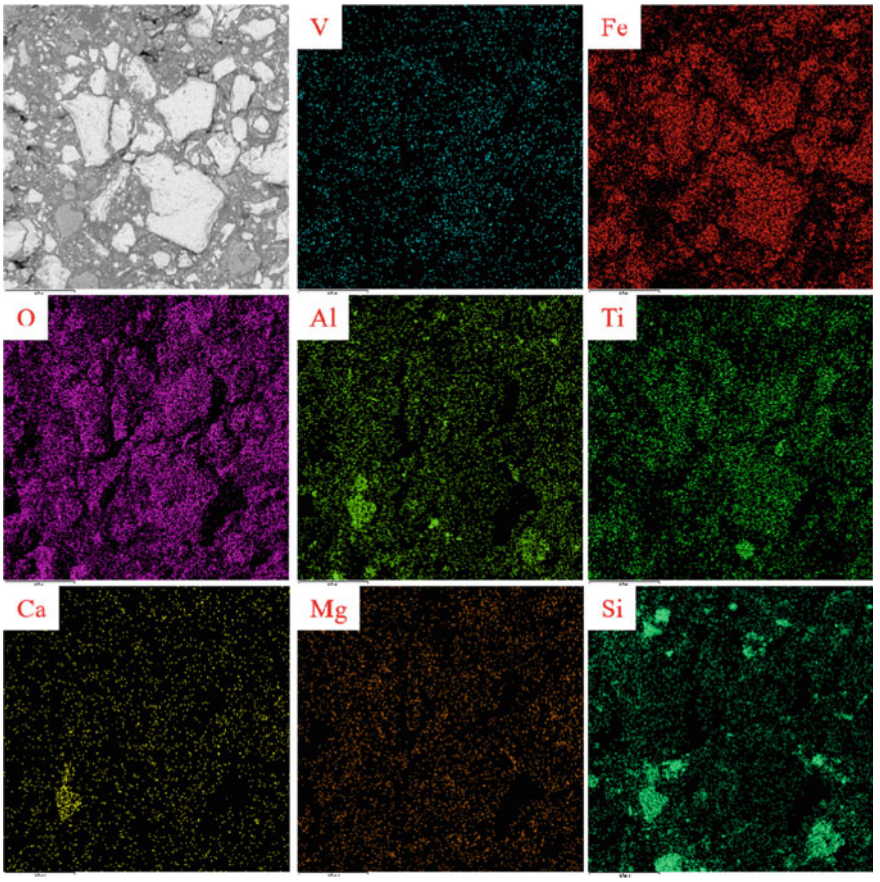

Fig. 7 SEM-EDS analysis of VTM by map scan pattern

olivine and 3.31% alumina. Iron in the VTM ore primarily exists in the form of titanomagnetite, hematite-limonite, ferrosilite and ilmenite, accounting for 89.04%, 7.74%, 2.09%, and 0.95% of the total iron content, respectively. Titanium exists in the ore mainly as ilmenite, accounting for 95.35% of the total titanium content, with the remaining titanium present in the form of titanomagnetite and sillimanite. In addition, vanadium is not only present in isomorphous association with ilmenite and titanomagnetite but also exists in small amounts in the form of silicates. The ore of VTM consists of individual metallic mineral grains and intergrowth grains with diverse structures and particle sizes. Titanomagnetite is predominantly found in self-formed grain structures. Hematite-limonite is mainly present in crystalline structures. It also coexists with titanomagnetite or can be cemented in olivine with a sponge meteorite structure. Ilmenite and magnesium spinel exist as exogenous crystals within the titanomagnetite. Pyroxene, olivine, silicate, and clay minerals occur in different forms and intergrowths with metallic minerals.

References

1. Yang SL (2012) Non-blast furnace smelting technology of vanadium titano-magnetite. Metallurgy Industry Press, Beijing
2. Shi Y, Zhu DQ, Pan J, Guo ZQ, Lu SH, Xue YX (2022) Investigation into the coal-based direct reduction behaviors of various vanadium titanomagnetite pellets. J Mater Res Technol 19:243–262. https://doi.org/10.1016/j.jmrt.2022.04.146
3. Zhang JL, Xing XD, Cao MM, Jiap KX, Wang CL, Ren S (2013) Reduction kinetics of vanadium titano-magnetite carbon composite pellets adding catalysts under high temperature. J Iron Steel Res Int 20(2):1–7. https://doi.org/10.1016/S1006-706X(13)60048-5
4. Chen SY, Fu XJ, Chu MS, Liu ZG, Tang J (2015) Life cycle assessment of the comprehensive utilisation of vanadium titano-magnetite. J Clean Prod 101:122–128. https://doi.org/10.1016/j.jclepro.2015.03.076
5. Gao JJ, Li SN, Wang F, Yang S, Zhang YY (2023) Performance calculation of slag from vanadium titano-magnetite by full oxygen bath smelting process. Energy Rep 9(7):1235–1243. https://doi.org/10.1016/j.egyr.2023.04.191
6. Shi Y, Guo ZQ, Zhu DQ, Pan J, Lu SH (2023) Isothermal reduction kinetics and microstructure evolution of various vanadium titanomagnetite pellets in direct reduction. J Alloy Compd 953:170126. https://doi.org/10.1016/j.jallcom.2023.170126
7. Liu BB, Chu QQ, Huang YF, Han GH, Sun H, Zhang L (2023) Preparation and characterization of electromagnetic wave absorbing material from polymetallic vanadium titano-magnetite (VTM): oriented phase transformation underlying formation mechanism. Ceram Int 49(7):10914–10927. https://doi.org/10.1016/j.ceramint.2022.11.285
8. Safdar F, Zhang Y, Zheng SL, Chen X, Sun P, Zhang Y, Li P (2020) Recovery of TiO_2-enriched material from vanadium titano-magnetite concentrates by partial carbon reduction and mild acid leaching. Hydrometallurgy 193:105324. https://doi.org/10.1016/j.hydromet.2020.105324
9. Yan ZP, Zhang Y, Zheng SL, Zhang Y, Sun P, Song ZW, Safdar F, Qi T (2022) Preparation of titanium mineral from vanadium titanomagnetite concentrates by hydrogen reduction and acid leaching. Trans Nonferrous Metal Soc 32(9):3099–3109. https://doi.org/10.1016/S1003-6326(22)66006-0
10. Li X, Lin J, Zhang D, Xiong ZH, He XQ, Yuan M, Wang MX (2020) Material flow analysis of titanium dioxide and sustainable policy suggestion in China. Resour Policy 67:0301–4207. https://doi.org/10.1016/j.resourpol.2020.101685
11. Filippou D, Hudon G (2020) Extractive metallurgy of titanium. Elsevier, Amsterdam
12. Sui YL, Guo YF, Jiang T, Qiu GZ (2019) Separation and recovery of iron and titanium from oxidized vanadium titano-magnetite by gas-based reduction roasting and magnetic separation. J Mater Res Technol 8(3):3036–3043. https://doi.org/10.1016/j.jmrt.2018.05.031
13. Boni M, Bouabdellah M, Boukirou W, Putzolu F, Mondillo N (2023) Vanadium ore resources of the African continent: state of the art. Ore Geol Rev 157:105423. https://doi.org/10.1016/j.oregeorev.2023.105423
14. Guo XF, Dai SJ, Wang QQ (2020) Influence of different comminution flowsheets on the separation of vanadium titano-magnetite. Miner Eng 149:106268. https://doi.org/10.1016/j.mineng.2020.106268
15. Gilligan R, Nikoloski AN (2020) The extraction of vanadium from titanomagnetites and other sources. Miner Eng 146:106106. https://doi.org/10.1016/j.mineng.2019.106106
16. Zhu XB, Li W, Guan XM (2016) Vanadium extraction from titano-magnetite by hydrofluoric acid. Int J Miner Process 157:55–59. https://doi.org/10.1016/j.minpro.2016.09.012
17. Haldar SK, Tišljar J (2014) Introduction to mineralogy and petrology. Elsevier, Amsterdam
18. Li C (2014) Study on sintering ore-forming mechanism of vanadium-titanium magnetite in Chengde. Master thesis, Hebei United University
19. Zhu L (2017) Metallogenic element enrichment status and metallogenic significance of vanadium titano-magnetite in Panzhihua, Sichuan Province. Master thesis, Sichuan Petroleum University

20. Li Y, Liu YS, Liu JW, Wang MX, Hao JB (2017) Panzhihua vanadium titanium magnetite mineralization geological characteristics and metallogenic regularity. World Nonferrous Met 01:95–97 (Chinese)
21. Institute of Comprehensive Utilization of Minerals, Chinese Academy of Geological Sciences, Key Laboratory of Comprehensive Utilization of Vanadium Titanium Magnetite, Ministry of Land and Resources (2015) Resources and comprehensive utilization technology of vanadium titano-magnetite in Panzhihua-Xichang. Metallurgy Industry Press, Beijing

Production and Characterization of Artificial Stone for the Making of Permeable Pavement

Rafael Bittencourt Miranda, Elaine A. S. Carvalho, Afonso Rangel Garces de Azevedo, Sergio N. Monteiro, and Carlos Maurício F. Vieira

Abstract In addition to the generation of industrial waste, especially in the ornamental stones sector, another problem caused by modernization which affects urban lifestyle and the environment is soil sealing. The loss of permeability leads in the surface to an increase in water runoff leading to floods, and through channels, to the transferring of these volumes to nearby water bodies leading to problems like silting up of rivers. The present work has the objective of producing permeable pavement using gravel waste in an epoxy resin matrix, and analyzing the feasibility of its use with the characterization of its properties. The slabs of permeable artificial stone were developed with the granite gravel waste having a granulometry between 10 and 20 mm. The characterization was made for porosity evaluation through water immersion, determination of the permeability coefficient and mechanical property. The results were of an (11 ± 1.7)% void ratio of the artificial stone, which indicates low porosity, and with a permeability coefficient of 2 mm/s the material can be utilized as a permeable pavement. The maximum flexural strength value of 4.26 ± 0.08 MPa, above the 2 MPa determined by the standard minimum, this parameter shows that this permeable pavement made with artificial stone has potential to be applied as tiling.

Keywords Artificial stone · Coating · Permeable pavement · Residue

R. B. Miranda · E. A. S. Carvalho (✉) · C. M. F. Vieira
Advanced Materials Laboratory—LAMAV-CCT, State University of the Northern Rio de Janeiro—UENF, Av. Alberto Lamego, 2000, Campos dos Goytacazes 28013-602, Brazil
e-mail: elainesanttos@yahoo.com.br

A. R. G. de Azevedo
Civil Engineering Laboratory—LECIV, State University of the Northern Rio de Janeiro—UENF, Av. Alberto Lamego, 2000, Campos dos Goytacazes 28013-602, Brazil

S. N. Monteiro
Materials Science Department, Military Institute of Engineering—IME, Praça General Tibúrcio, 80, Urca, Rio de Janeiro, RJ 22290-270, Brazil

Z. Peng et al. (eds.), *Characterization of Minerals, Metals, and Materials 2024*, The Minerals, Metals & Materials Series, https://doi.org/10.1007/978-3-031-50304-7_62

Introduction

With the industrial revolution beginning in the 18th century, society not only had improvements in quality of life, but also began producing enormous quantities of waste that are improperly discarded, provoking innumerous environmental problems. Because of that, there has been a search for self-sustainable solutions to the final destination of these materials [1, 2].

The destination of 75% of the production from the ornamental stone sector goes to the construction industry, and Brazil is between the top 4 biggest producers of this sector, and that production is accompanied by just as big, volume of waste, between 2.0 and 2.5 million tones [3, 4].

The generation of industrial waste, especially in the ornamental stone sector, requires care because of the nature of the materials. Together with the care of the waste produced, there is also a concern with the high exploitation of natural resources needed for this sector [5, 6].

That way, the concept of Circular Economy is an adequate model of management for this sector. The reintroduction of waste in the industry's production chain is one of the methodologies adopted in this model, maintaining quality standards, reducing the consumption of resources and decreasing the impacts caused by the production systems [7, 8].

Another problem caused by modernization which affects urban lifestyle and the environment is soil sealing. With the development of urban areas there was also an increase in paving, thus removing the natural drainage capacity of the soil, and that can bring about from flooding to the lowering of the water table [9, 10].

Soil sealing, one of the problems caused by the advancements that can be seen in urban environments, may lead to reduced infiltration of rainwater for water bodies, leading to a reduction of availability of water in periods of drought [11, 12].

The loss of permeability leads, in the surface, to an increase in water runoff leading to floods, and through channels, to the transferring of these volumes to nearby water bodies leading to problems like silting up of rivers [12].

The development of permeable pavement is presented as a solution of this problem in addition to allowing a greater appreciation of these materials. They are capable of allowing intense drainage of water, therefore increasing soil permeabilization, and these permeable pavements can be produced using industrial waste that would otherwise be discarded inappropriately [13, 14].

Permeable pavements are used as technological tools and implemented in places intended for low vehicle traffic or sidewalks, squares and parks [14]. The present work aims to develop permeable pavement using particles of granite gravel in an epoxy resin matrix, and analyze the feasibility of its use.

Materials and Methods

Materials

The residue of granite waste (gravel) were collected as waste of the sieving process in the Itereré Quarry located in the mountain region of Serra da Bela Vista, a 17 km of Campos dos Goytacazes city, north of the Rio de Janeiro state. The granite gravel waste has a granulometry between 10 and 20 mm [15].

The epoxy matrix used is the epoxy resin Bisphenol A diglycidyl ether (DGEBA); commercial name: MC130, together with the curing agent Triethylenetetramine (TETA). Both are provided by company EPOXYFIBER.

Water Immersion Test to Determine the Void Ratio and Water Absorption

The Brazilian Association of Technical Standards (NBR 9778) was used to determine the void ratio and water absorption [16]. It started with the preparation of 5 specimens (Fig. 1). Then the sample drying process was started in an oven at a temperature of 105 °C ± 5 °C, for about 72 h, and soon after, the dried specimens were weighed.

After drying, and as recommended by the standard, the saturation of specimens in a container with water was started at a temperature of 23 °C ± 2 °C for 72 h, being the first 24 h with a third of any specimen immersed, the next 24 h with two thirds of the specimens immersed and the last 24 h with the specimens completely submerged.

Fig. 1 Specimen for the water immersion test

And after this period, the specimens were weighed: their submerged mass and their saturated mass. Given all these steps, calculations were performed to determine the void ratio and water absorption. Equation (1) was used to determine water absorption and Eq. (2) was used for void ratio.

$$W_a = \left(\frac{M_{sat} - M_o}{M_o} \right) \times 100\% \tag{1}$$

$$V_r = \left(\frac{M_{sat} - M_o}{M_{sat} - M_i} \right) \times 100\% \tag{2}$$

where

V_r Void index (%)
W_a Water absorption by immersion (%)
M_o Oven-dried test specimen mass (g)
M_i Mass of the specimen, immersed in water (g)
M_{sat} Mass of the specimen saturated in water at a temperature of 23 °C (g).

Test to Determine the Permeability Coefficient

The specimens were cleaned so as not to have sediments or other materials adhered to the stone, right after, a polyvinyl chloride (PVC) ring was positioned in contact with the specimens and sealed in this contact area, to prevent side leaks. Figures 2 and 3 show the way of assembly for the test.

The permeability coefficient determination test was carried out according to standard Brazilian National Standards Organization (NBR 16416) and American Society for Testing and Materials (ASTM C1701) [17, 18].

(1) Pre-wetting of the plate was carried out and then the test started after 30 s or less;
(2) An 18 kg mass of water began to be poured into the PVC ring with enough speed to maintain the water level between the inner marks of 10 and 15 mm as shown in Fig. 3;
(3) The time interval was marked on a stopwatch, beginning as soon as the water reached the surface of the specimen and finishing when there was no more free water on the surface. The time was recorded with an accuracy of 0.1 s.
(4) The test was repeated two more times within a 5-min interval, which eliminated the need for pre-wetting for the second and third tests.

The permeability coefficient was calculated using Eq. (3).

$$K = \frac{C \cdot m}{\left(d^2 \cdot t\right)} \tag{3}$$

Fig. 2 Assembly of the test to determine the permeability coefficient (a)

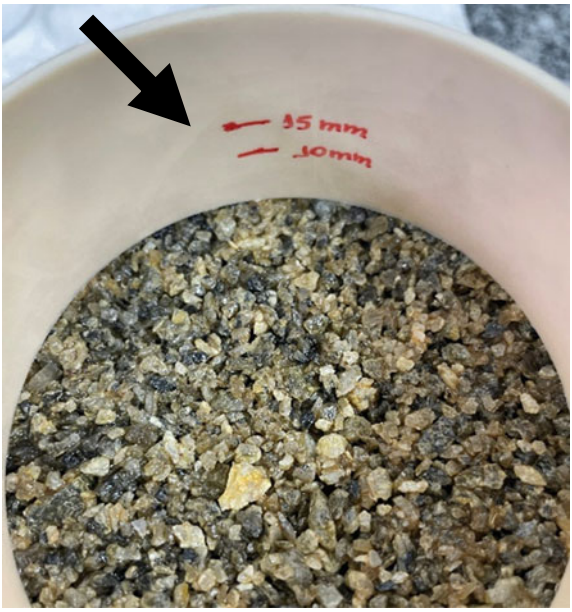

Fig. 3 Assembly of the test to determine the permeability coefficient (b)

where

K is the permeability coefficient expressed in millimeters per hour (mm/h);
m is the mass of infiltrated water expressed in kilograms (kg);
d is the inner diameter of the infiltration cylinder expressed in millimeters (mm);
t is the time required for water to percolate expressed in seconds (s);
C is the SI unit conversion factor, with a value equals to 4,583,666,000.

Three Point Flexural Test

The prismatic specimens were manufactured and tested for flexural strength based on the standard Brazilian National Standards Organization (ABNT NBR 15.805) [19], in the dimensions of 200 mm length, 50 mm width and 50 mm height. Applying the load progressively, with a loading rate of (100 ± 10) N/s, until the slab ruptures. Flexural strength is obtained according to Eq. (4).

$$f_t = \frac{1.5 \times P \times L}{B \times t^2} \tag{4}$$

where

f_t is the flexural strength, expressed in megapascals (MPa);
P is the load applied to the center of the plate, expressed in Newtons (N);
L is the distance between the supports, expressed in millimeters (mm);
B is the width of the plate along the fracture line, expressed in millimeters (mm);
t is the thickness of the plate, expressed in millimeters (mm).

Results and Discussion

Table 1 presents the results found in the water immersion test, where the use of big particle aggregates implies larger pores and considerable permeability.

Table 1 Result of the water immersion test of the permeable artificial stone produced with granite powder waste and epoxy resin

Sample	Water absorption (%)	Void index (%)
1	4.69	9.09
2	6.87	13.04
3	6.25	11.59
4	5.88	11.86
5	4.96	9.38
Medium	5.73 ± 0.9	11 ± 1.7

The analyzed specimens obtained results within the pre-established limit by Neville [20], where it was established that water absorption analysis cannot be used as a measure in order to determine quality, however, this author reports that pavements considered to be of good quality present absorption results of less than 10%, a rate that the specimens analyzed were well below, at (5.73 ± 0.9)%.

The void ratio of the permeable concrete mainly depends on the size of the aggregates and generally ranges from 15 to 30% [15]. Tennis et al. [21], in his study, points out that void rates of around 20% guarantee good characteristics in terms of resistance and also permeability.

Concrete considered permeable is considered to have low porosity when it has a percentage of voids below 15%, and with high porosity if these rates are greater than 30% [22]. The results were (11 ± 1.7)% of voids index of the permeable stone with granite dust, which demonstrates low porosity.

Concrete becomes permeable through the interconnection between the voids, which is an important property considering the granulometry. The amount of voids has influence on strength and permeability, which are the most important properties that impact the performance of the permeable pavement.

Faria et al. [23] in his research, determine that the aggregate with a characteristic maximum diameter of 19 mm produces a hydrological advantage for having larger pores and greater permeability. The granulometry of the permeable stones produced varies from 10 to 20 mm, which may have interfered in the results of this variation of aggregates.

The values organized in Table 2 were obtained in the test for the permeability coefficient, also known as hydraulic conductivity of the concrete. Permeability occurs because the composition contains minimal or no proportion of small aggregate particles, which allows percolation between the pores [24], being defined by NBR 16416 [17] as the process in which water travels through the voids in the pavement.

For the newly constructed pavement to be considered permeable, the permeability coefficient obtained must be greater than 0.1 cm/s, 2 mm/s according to NBR 16416 [17]. However, the study by Kia et al. [25] shows a wide variation from 0.003 to 3.3 cm/s, while in the research by Bhutta et al. [26] permeability values ranged between 0.25 and 3.3 cm/s and Ibrahim et al. [27] obtained a range of 1.5–2.82 cm/

Table 2 Results of the determination of the permeability coefficient of the permeable artificial stone with granite powder residue and epoxy resin

Sample	Mass of water (kg)	Diameter of the inner filtration cylinder (mm)	Time required for water to percolate (s)	Permeability coefficient (mm/h)/(cm/s)/(mm/s)
1	18	75	2100	6984.63
2	18	75	1860	7885.87
3	18	75	2160	6790.62
Medium				7220.37 ± 584/0.201/2

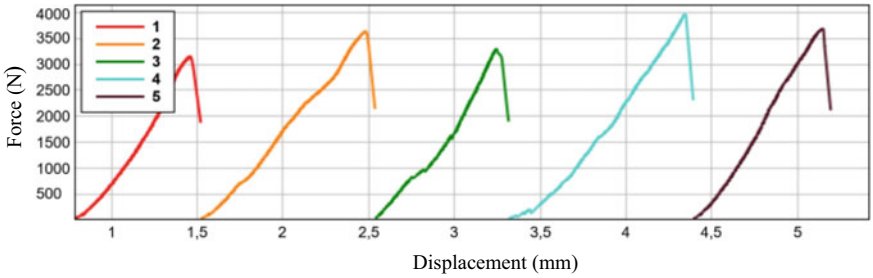

Fig. 4 Graph of force versus displacement of permeable stone using gravel and epoxy resin

s. According to American Society for Testing and Materials (ASTM C1701), the minimum permeability coefficient that guarantees permeability to water is 1.5 mm/s, and it is necessary to reach a value higher than this criterion [18].

These parameters refer to permeable pavement based on concrete, not having specific norms for tiles or artificial stones with the use of resin as a binder in place of cement. Through this parameter, it shows that the preliminary tests of the artificial stone with gravel powder waste and epoxy resin, is within the parameters that researches indicate for a floor to be considered permeable.

With an average permeability coefficient of 0.014 m/s, those studies recommend the use of permeable concrete in areas with light vehicles and sidewalks, as well as, its mechanical characteristics avoid pathologies related to the tightness and permeability of the pavement where the material is used.

Figure 4 refers to the force–displacement graph of the permeable stone with gravel waste and epoxy resin; a break in rigidity between 3000 and 3500 N of force can be observed.

Table 3 shows the maximum flexural strength results for the permeable artificial stone specimens. It was obtained as 4.26 MPa with low dispersion of values, a value that is represents 100% increase relative to the ABNT NBR 15805 standard, which suggested a minimum value of 2 MPa [19]. It is believed that the low viscosity of the resin used had a positive effect on flexural strength because the polymer chains evenly distributed within the samples helped to resist fractures caused by flexion [28]. It is also above the Brazilian technical specifications (because they are greater than 1 MPa) [29].

The particle aggregate size distribution and polymer viscosity affect the internal pore size and therefore the mechanical properties. Given the result presented, the permeable stone can be used in light vehicle traffic and pedestrian traffic, according to NBR 12412 (2012). Even with this paradigm of high voids and not being able to reach high resistances, the permeable concrete pavement can reach, when properly executed, flexural strength > 3.5 MPa.

Table 3 Maximum force and maximum flexural strength at 3 points bending test of the permeable artificial stone

Samples	Force (N)	Maximum flexural strength (MPa)
1	3153.17	3.78
2	3636.75	4.36
3	3308.48	3.97
4	3956	4.75
5	3682.22	4.42
Average	3547.42 ± 2.39	4.26 ± 0.08

Conclusion

It was verified that the permeable pavement is an efficient alternative in combating surface runoff, thus making it possible to minimize the constant accumulation of water in our traffic routes during the rainy months.

- Water absorption was (5.73 ± 0.9)%, below 10%;
- The results were (11 ± 1.7)% of voids index of the permeable stones made with gravel waste, which demonstrates low porosity;
- The test for permeability, a relevant factor, obtained expressive results, requested by the norm;
- The permeable artificial stone obtained a maximum flexural strength of 4.26 MPa, twice the value specified in the standard.

The initial study with the development of a permeable artificial stone using gravel waste, demonstrates an alternative to minimize problems of water accumulation while also giving a correct destination for the disposal of waste.

The literature recognizes the benefits of using permeable concrete as instruments that seek to increase infiltration to reduce surface runoff, and also as a sustainable strategy for the country. Though continuous monitoring is recommended, with the aim of evaluating changes in performance over time, because this topic still needs a lot of specific studies for adverse situations.

Acknowledgements The authors acknowledge UENF for the physical space and the funding agencies FAPERJ, CAPES, and CNPq for supporting this research.

References

1. Araújo DC, Silva PO, Curi WF, Cabral JJSP (2017) Multicriteria analysis applied to the management of urban pluvial waters. Braz J Water Resour 22:1–11
2. Costa J, Barbassa LL (2006) Design parameters for microreservoirs, permeable pavements and urban flood forecasting. Sanit Environ Eng 11(1):46–54

3. Barreto LSS, Ghisi E, Godoi C, Oliveira FJS (2020) Reuse of ornamental rock solid waste for stabilization and solidification of galvanic solid waste: optimization for sustainable waste management strategy. J Clean Prod. https://doi.org/10.1016/j.jclepro.2020.122996
4. Bahiense AV, Alexandre J, Xavier GC, Azevedo ARG, Monteiro SN (2021) Dosage of interlocking paving with ornamental rock waste: an experimental design approach, particle packing and polluting potential. Case Stud Constr Mater. https://doi.org/10.1016/j.cscm.2021.e00596
5. Faut L, Soyeur F, Haezendonck E, Dooms M, Langen PW (2023) Ensuring circular strategy implementation: the development of circular economy indicators for ports. Marit Transp Res
6. Alfaia RGSM, Costa AM, Campos JC (2017) Municipal solid waste in Brazil: a review. Waste Manag Res 35(12):1195–1209. https://doi.org/10.1177/0734242X17735375
7. Zhu J, Ren ZJ (2023) The evolution of research in resources, conservation & recycling revealed by Word2vec-enhanced data mining. Resour Conserv Recycl. https://doi.org/10.1016/j.resconrec.2023.106876
8. Soares LBFS, Barraqui NSG, Gomes TC (2022) Principles of circular economy for the use of solid waste from ornamental rocks in the development of draining floors. South Am Dev Soc J 8(22):286
9. Muthukumar S, Saravanan AJ, Raman A, Sundaram MS, Angamuthu SS (2021) Investigation on the mechanical properties of eco-friendly pervious concrete. Mater Today Proc 46(Part 10):4909–4914. https://doi.org/10.1016/j.matpr.2020.10.333
10. Ferguson BK (2005) Porous pavements. In: Integrative studies in water management and land development. CRC Press, Boca Raton
11. Sansalone JJ, Xuheng K, Ranieri V (2008) Permeable pavement as a hydraulic and filtration interface for urban drainage. J Irrig Drain Eng ASCE 134:666–674. https://doi.org/10.1061/(ASCE)0733-9437(2008)134:5(666)
12. Rahangdale S, Maran S, Lakhmanil S, Gidde M (2017) Study of pervious concrete. Int Res J Eng Technol 04(06):2563–2566
13. Modani PO, Vyawahare MR (2013) Utilization of bagasse ash as a partial replacement of fine aggregate in concrete. Procedia Eng 51:25–29. https://doi.org/10.1016/j.proeng.2013.01.007
14. Parra GG, Teixeira BA (2015) Permeability analysis and permeable pavement installation methods contained in scientific articles and technical catalogues. Natl Mag City Manage 3(15):142–157
15. Muthukumar S, Saravanan AJ, Raman A, Sundaram MS, Angamuthu SS (2021) Investigation on the mechanical properties of eco-friendly pervious concrete. Mater Today Proc 46:4909–4914
16. ABNT Brazilian Association of Technical Standards. NBR 9778 (2009) Water absorption by void index. Rio de Janeiro
17. ABNT Brazilian Association of Technical Standards. NBR 16416 (2015) Permeable concrete pavements—requirements and procedures. Rio de Janeiro
18. American Society for Testing and Materials. ASTM 1701/C 1701 M-09 (2009) Standard test method for infiltration rate of in place pervious concrete. ASTM
19. ABNT Brazilian Association of Technical Standards. NBR 15805 (2015) Raised concrete slab floors—requirements and procedures. Rio de Janeiro
20. Neville AM (ed) (1997) Propriedades do Concreto. Editora Pini, São Paulo
21. Tennis PD, Leming ML, Akers DJ (2004) Pervious concrete pavements, EB302. Portland Cement Association, Skokie, Illinois
22. Batezini R (2013) Preliminary study of permeable concrete as a pavement coating for light vehicle areas. Dissertation, University of São Paulo
23. Faria AC, Santana JG, Barbosa JM, Donato M (2019) Draining concrete pavement: study of the granulometry that favors drainage and that affects the minimum resistance. In: 33° ANPET transport research and education congress, Balneário Camboriú, Santa Catarina, 10–15 Nov 2019
24. Caetano MO, Selbach JBO, Gomes LP (2016) Gravimetric composition of CDW for the finishing stage in horizontal residential works. Built Environ 16(2):51–67

25. Kia A, Wong HS, Cheeseman CR (2017) Clogging in permeable concrete: a review. J Environ Manage 15(193):221–233. https://doi.org/10.1016/j.jenvman.2017.02.018
26. Bhutta MAR, Tsuruta K, Mirza J (2012) Evaluation of high-performance porous concrete properties. Constr Build Mater 31:67–73. https://doi.org/10.1016/j.conbuildmat.2011.12.024
27. Ibrahim A, Mahmoud E, Yamin M, Patibandla VL (2014) Experimental study on Portland cement pervious concrete mechanical and hydrological properties. Constr Build Mater 50:524–529
28. Shin Y, Hyeong P, Jinha P, Cho H, Oh S, Chung S, Yang B (2022) Effect of polymer binder on the mechanical and microstructural properties of pervious pavement materials. Constr Build Mater. https://doi.org/10.1016/j.conbuildmat.2021.126209
29. Bittencourta SV, Magalhães MS, Tavares MEN (2021) Mechanical behavior and water infiltration of pervious concrete incorporating recycled asphalt pavement aggregate. Case Stud Constr Mater. https://doi.org/10.1016/j.cscm.2020.e00473

Reducing MgO Content of Blast Furnace Slag

Jie Liu, Dongming Zhao, Qiang Zhong, Hui Zhang, Libing Xv, and Jin Xun

Abstract In order to improve technical and economic indexes of ironmaking (BF), metallurgical properties of blast furnace slag with low (MgO) were studied systematically based on the laboratorial and industrial tests. The results showed the melting temperature of blast furnace slag with 4–7% MgO was lower than 1350 °C under the condition of low Al_2O_3 content. The viscosity of the slag met the requirement of blast furnace smelting when the temperature of slag was 1500 °C and the MgO content was higher than 3%. The best basicity of the slag was about 1.245. In the industrial test, the MgO content and the viscosity of the blast furnace slag were maintained in the ranges of 4.5–5.0% and 0.16–0.2 Pa s, respectively. The slag with low MgO had good desulfurization capacity by regulating slag basicity.

Keywords Blast furnace slag · Viscosity · MgO content · Basicity · Metallurgical property

Introduction

In blast furnace (BF) production, the properties of the BF slag strongly affect the production system and the safety of BF. During the slag smelting which controls the cost and efficiency of BF production, MgO as an important component in the slag, impacts the production process by various complex physical and chemical reactions. It either decomposes silicon oxygen complex anions into simple silicon oxide tetrahedron or creates low melting point compounds through its reactions with other components, such as SiO_2 and $A1_2O_3$. These reactions enable reduction of the viscosity and melting temperature of BF slag to maintain successive BF production.

J. Liu · D. Zhao · H. Zhang · L. Xv · J. Xun
Iron and Steel Research Institute of Angang Group, Anshan 114009, China

J. Liu · Q. Zhong (✉)
School of Minerals Processing and Bioengineering, Central South University, Changsha 410083, China
e-mail: zhongqiang@csu.edu.cn

Z. Peng et al. (eds.), *Characterization of Minerals, Metals, and Materials 2024*, The Minerals, Metals & Materials Series, https://doi.org/10.1007/978-3-031-50304-7_63

Table 1 Chemical composition of BF slag

$w(SiO_2)$ (%)	$w(CaO)$ (%)	$w(MgO)$ (%)	$w(Al_2O_3)$ (%)	$w(TiO_2)$ (%)	R
35.35	40.80	7.42	10.75	0.70	1.15

A lot of experimental studies and industrial practice [1–3] have proved that low MgO content in the BF burden will help to improve the iron grade of sinter and to reduce fuel consumption and slag output, thereby improving the technical and economic indexes of BF. Prior to 2015, the MgO content of slag produced by BFs in Ansteel exceeded 7%, and the ratio of $w(MgO)/w(Al_2O_3)$ was above 0.6, which did not conform to the development trend of BF production. Therefore, it is necessary to determine the suitable $w(MgO)$ of slag under the raw material conditions in Ansteel.

Experimental

The Al_2O_3 content in BF burden was from 10 to 13%, which was far below 15% in most BFs. The low Al_2O_3 content and high ratio of $w(MgO)/w(Al_2O_3)$ created a good condition for reducing the MgO content of the slag in the BF. The BF slag in Ansteel was used as the sample, and several chemical reagents were used to adjust the composition of the slag. The chemical composition of the BF slag is shown in Table 1.

The properties of BF slag were measured by a GTW-08 slag viscometer (Fig. 1) whose working temperature was 1600 °C, and its highest heating temperature was 1700 °C. The measurement range of viscosity was 0.05–20 Pa s. The size of the graphite crucible used in the test was Φ40 mm × 150 mm (inner diameter × height). The schematic diagram of the experiment apparatus is shown in Fig. 1. The influence of MgO, Al_2O_3 content and basicity ($CaO + MgO/Al_2O_3 + SiO_2$) on metallurgical properties of blast furnace slag was studied by adjusting the slag sample with an analytical and pure chemical reagent. The viscosity of the slag was measured by inner cylinder rotating viscometer.

Results and Discussion

Effect of MgO Content on Slag Melting Temperature

The variation of melting temperature of slag with basicity and $w(MgO)$ in the laboratory is shown in Fig. 2.

The variation of melting temperature of the slag showed that it declined with the increase of the $w(MgO)$ from 4 to 8%. When the basicity of the slag was 0.8 or 1.2 and the $w(MgO)$ was 6%, the melting temperature of the slag was the lowest.

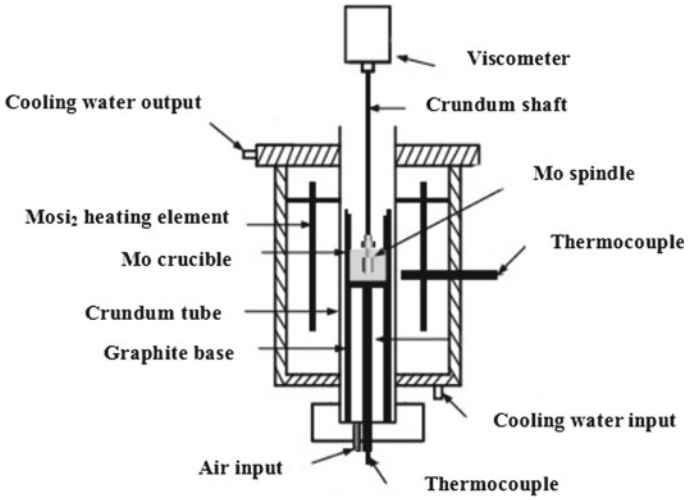

Fig. 1 Apparatus for viscosity measurements

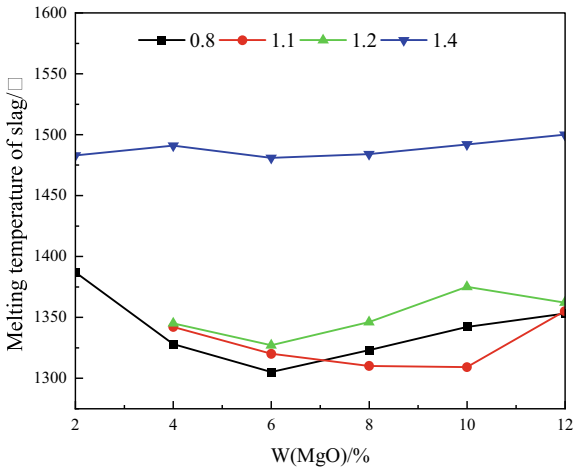

Fig. 2 Variation of melting temperature of slag with basicity and *w*(MgO)

At the slag basicity of 1.1 and *w*(MgO) of 7%, the melting temperature of the slag also had the lowest value. When the basicity of the slag increased to 1.4, the melting temperature of the slag rose significantly, reaching 1475 °C, which cannot meet the production requirements of BF. Based the theory of the phase diagram, the low melting temperature and low viscosity regions of the BF slag are a result of the formation of melilite and merwinite [4] with the *w*(MgO) of 10%. In the area where the basicity of the slag is in the range of 0.7–1.3 and *w*(MgO) is in the range of 4–7%, the melting temperature of the slag is the lowest [5], and the melting temperature of the slag will rise when the basicity of the slag is out of the area.

So, when the MgO content of the slag is 4% and the basicity of the slag is from 0.8 to 1.2, the melting temperature of the slag is lower than 1350 °C, meeting the production requirements of BF. Therefore, reducing the MgO content of the slag in Ansteel is feasible.

Effect of MgO Content on Slag Viscosity

According to the statistical results of 8 BFs in Ansteel in 2015, the average temperature of molten iron temperature was above 1500 °C. Because the temperature of the slag was about 20–30 °C higher than that of molten iron which would fluctuate, the lowest temperature of the slag was above 1520 °C and the average temperature should be around 1550 °C. At the slag temperature of 1500 °C or 1550 °C, the viscosity of the slag was measured at different MgO contents of the slag. The results are shown in Fig. 3.

At 1500 °C, the viscosity of the slag dropped slowly when *w*(MgO) was up to 2.5%. The viscosity of the slag decreased sharply when *w*(MgO) increased from 2.5 to 5%. When the MgO content of the slag exceeded 5%, the downward trend became unapparent. When the temperature of the BF slag increased to 1550 °C, the viscosity of the slag was around 0.33 Pa s even without MgO. If the viscosity of the slag in large BFs (0.4 Pa s) was used as the benchmark [6, 7], the viscosity level could meet the requirement of BF production when the *w*(MgO) was more than 3%. When the *w*(MgO) was varied from 2 to 5%, the viscosity had large fluctuations (around 0.2 Pa s). Meanwhile, the viscosity became unstable [8]. Considering the melting property of the slag and the production cost, the MgO content of the slag could be reduced to 4%. Therefore, the BFs in Ansteel still can reduce the magnesium content.

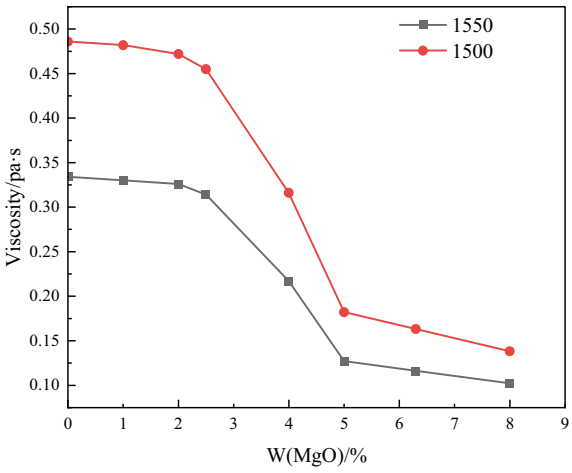

Fig. 3 Variation of slag viscosity with *w*(MgO)

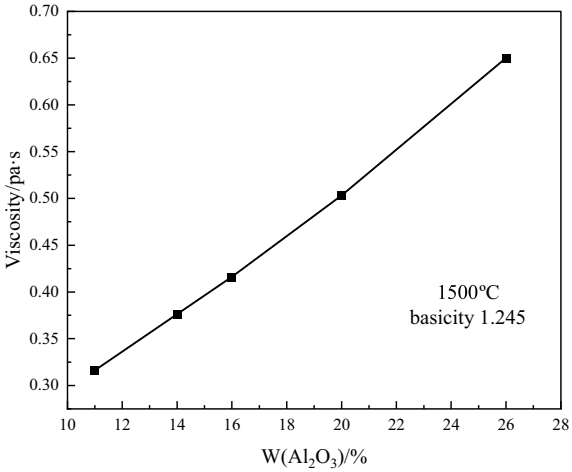

Fig. 4 Variation of slag viscosity with $w(Al_2O_3)$

Effect of Al_2O_3 Content on Slag Viscosity

According to the above study, the variation of the viscosity with $w(Al_2O_3)$ could be determined with 4% w(MgO) as the critical value at a constant basicity. The results are shown in Fig. 4.

At 1500 °C, the viscosity increased nearly linearly with the increase of the Al_2O_3 content of slag. The Al_2O_3 content of slag was about 15% when the viscosity of slag was 0.4 Pa s. At present, the Al_2O_3 load of BF in Ansteel varies from 10 to 13%, which creates favorable conditions for reducing the MgO content of the slag.

Effect of Basicity on Slag Viscosity

Figure 5 presents the effect of basicity on the slag viscosity at the slag temperature of 1500 °C or 1550 °C with the w(MgO) of 4%. When the basicity increased from 1.17 to 1.25, the viscosity of the slag dropped sharply. However, the viscosity increased slowly after the basicity exceeded 1.245. Therefore, as long as the temperature was no less than 1500 °C and the critical value of w(MgO) was 4% [9–13], the viscosity of the slag could meet the requirements of BF production, and the optimal basicity should be around 1.245.

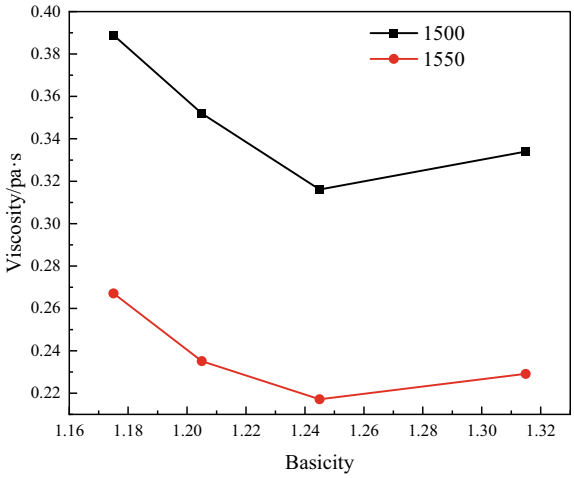

Fig. 5 Viscosity with different basicity

Desulfurization Capacity of Slag

In view of the effect of molten iron desulphurization, slag with $w(\mathrm{MgO}) = 4\%$, $w(\mathrm{Al_2O_3}) = 11\%$, and basicity of 1.245 was used. The variations of desulfurization distribution coefficient (L_S) with $w(\mathrm{MgO})$, $w(\mathrm{Al_2O_3})$ and basicity are shown in Fig. 6.

From Fig. 6, the relations between $w(\mathrm{MgO})$ and L_S, between $w(\mathrm{Al_2O_3})$ and L_S, and between basicity and L_S were given by $Y = 15.84 + 1.141X$, $Y = 71.64 - 3.26X$, $Y = -103 + 103.6X$, respectively. These factors affected L_S to different extents, following the order: $w(\mathrm{MgO}) < w(\mathrm{Al_2O_3}) <$ slag basicity [14, 15].

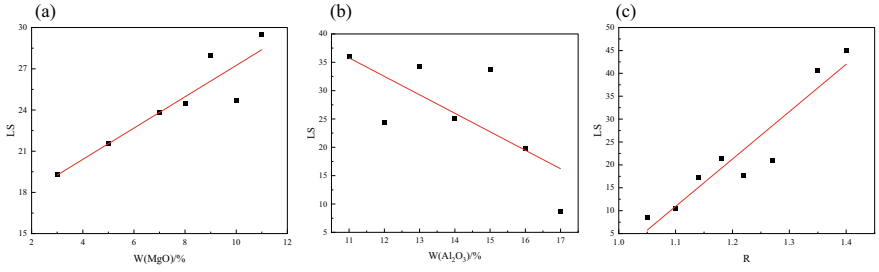

Fig. 6 Variation of L_S with different parameters: **a** $w(\mathrm{MgO})$, **b** $w(\mathrm{Al_2O_3})$ and **c** R

Industrial Application

From 2015 to 2016, industrial applications of reducing the MgO content of the slag in Ansteel were carried out. Several BF slags were sampled and analyzed during this period. The main chemical compositions of the slags are shown in Table 2. The values of slag viscosity at 1500 °C in different BFs are given in Fig. 7.

After reducing w(MgO) in the BF slag, the w(MgO) was generally around 4.9% and the w(MgO) of each BF reached 4–4.5% at the minimum. The analysis showed that the ratio of w(MgO)/w(Al_2O_3) was 0.56 in blast furnace B, and the rest of the BF was about 0.45. By measuring the viscosity of the actual slag in the BF production, Fig. 7 shows the viscosity of the BF slag within the range of 0.16–0.20 Pa s. Based

Table 2 Chemical compositions of different slags

Item	Blast furnace A	Blast furnace B	Blast furnace C	Blast furnace D	Blast furnace E
w(SiO_2) (%)	35.44	35.65	34.92	35.70	35.62
w(CaO) (%)	44.06	43.24	43.00	44.47	46.41
w(MgO) (%)	4.88	4.75	5.03	4.91	4.95
w(Al_2O_3) (%)	10.95	10.78	11.32	10.76	11.36
w(S) (%)	1.20	1.17	1.31	1.24	1.20
w(MgO)/w(Al_2O_3)	0.45	0.44	0.44	0.46	0.44
Basicity	1.243	1.213	1.231	1.245	1.303
Temperature of molten iron (°C)	1522	1546	1516	1506	1505

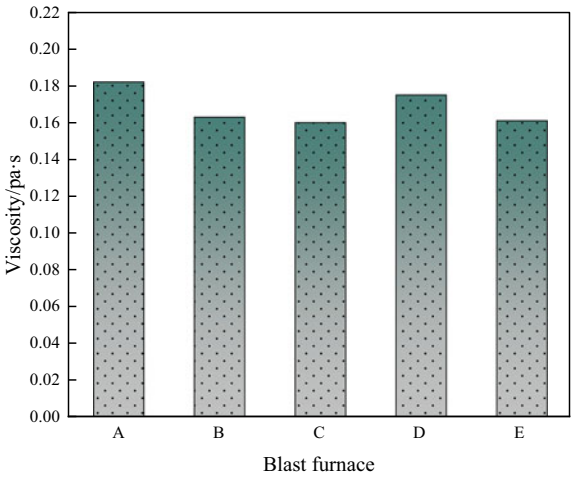

Fig. 7 Viscosity of different BF slags

Table 3 L_S in blast furnace D

	MgO content of slag (%)	S content of molten iron (%)	S content of slag (%)	L_S	R
Blast furnace D	7.10	0.0208	1.087	52.26	1.178
	6.00	0.0200	1.010	50.50	1.175
	5.07	0.0200	1.110	55.50	1.245

on the analysis of slag viscosity in actual production, after reducing the ratio of $w(MgO)/w(Al_2O_3)$, the viscosity of the BF slag in Ansteel was still low. The values of L_S in blast furnace D under different conditions are shown in Table 3.

When the basicity of the slag was in the range of 1.178–1.175 and the MgO content of the slag decreased from 7.1 to 6%, the S content of molten iron dropped and the L_S decreased from 52.26 to 50.50. When the basicity of the slag reached 1.245, the MgO content of the slag decreased to 5.07, while the S content of the slag increased to 1.110 and the L_S increased to 55.50. Therefore, reducing the MgO content of the slag will increase the desulfurization capacity at a reasonable basicity of the slag.

By reducing the MgO content of the slag preliminarily, the output of the BF slag was reduced by nearly 17 kg/t Fe on average. Furthermore, the test created an economic benefit of nearly 60 million RMB and realized a good combination of the technical index and the economic-technical index.

Conclusion

(1) The Al_2O_3 content in burden for BF in Ansteel was generally 10–13%. When the MgO content of the slag reduced to about 4%, the basicity was 0.8–1.2 and the melting temperature of slag was less than 1350 °C, which met the production requirements of BF.

(2) When the basicity was 1.24 and $w(Al_2O_3)$ was 11%, the viscosity of the slag at 1500 °C dropped slowly with the $w(MgO)$ up to 2.5%. The viscosity of the slag dropped sharply when the $w(MgO)$ was varied in the range of 2.5–5%. The downward trend became unapparent when the $w(MgO)$ exceeded 5%. The viscosity of the slag was less than 0.5 Pa s.

(3) The $w(MgO)$, $w(Al_2O_3)$, slag basicity affected L_S to different extents, following the order: $w(MgO) < w(Al_2O_3) <$ slag basicity. By reducing $w(MgO)$, the slag basicity could be properly optimized for improved desulphurization capacity of the slag.

(4) The industrial production showed that the MgO content of the slag in Ansteel was about 4.9% when the temperature of molten iron was 1500–1550 °C. When the ratio of $w(MgO)/w(Al_2O_3)$ was about 0.45, the viscosity of the slag was 0.16–0.2 Pa s. The BFs still have a lot of room for improvement in the economic index and in reducing slag output.

References

1. Deng M, Han X, Liu L et al (2016) Influence of MgO on mineral structure and metallurgical properties of blast furnace slag with medium titanium. Iron Steel 51(4):14
2. Li F, Lu Q, Hu B et al (2006) Metallurgical properties of BF slag and slagging regime. Iron Steel 41(1):19
3. Xu R, Zhang H, Zhang J et al (2016) Evaluation of Jingtang blast furnace slag properties and analysis of low MgO slag performance. China Metall 26(11):16
4. Tang D, Wang Y, Wang Y et al (2015) Low MgO smelting practice of Laiwu steel's 3200 m^3 BF. Ironmaking 34(2):31
5. Guo J, Cheng S, Zhao H (2013) Modeling research for estimating viscosity of SiO_2–CaO–MgO–$A1_2O_3$ system molten slag based on slag structure theory. J Iron Steel Res 25(8):6
6. He H, Wang Q, Zeng X (2006) Effect of MgO content on BF slag viscosity. J Iron Steel Res 18(6):11
7. Shen F, Zheng H, Jiang X et al (2014) Influence of Al_2O_3 in blast furnace smelting and discussions on proper $w(MgO)/w(Al_2O_3)$ ratio. Iron Steel 49(1):1
8. Sun Z (2014) Effect of MgO on high aluminous slag stability. Iron Steel 49(4):18
9. Shen F, Jiang X, Wu G et al (2006) Proper MgO addition in blast furnace operation. ISIJ Int 46(1):65
10. Sunahara K, Nakano K, Hoshi M et al (2008) Effect of high Al_2O_3 slag on the blast furnace operations. ISIJ Int 48:420
11. Kim H, Matsuura H, Tsukihashi F et al (2012) Effect of Al_2O_3 and CaO/SiO_2 on the viscosity of calcium silicate-based slags containing 10 mass Pct MgO. Metall Mater Trans B 44:5
12. Shankar A, Görnerup M, Lahiri AK et al (2007) Experimental investigation of the viscosities in CaO–SiO_2–MgO–Al_2O_3 and CaO–SiO_2–MgO–Al_2O_3–TiO_2 slags. Metall Mater Trans B 38:911
13. Zhang J (2002) Applicability of mass action law to sulphur distribution between slag melts and liquid iron. J Univ Sci Technol Beijing 9(2):90
14. Guo D, Zhang J, Lu D et al (2014) Effect of R on viscosity of CaO–SiO_2–Al_2O_3–MgO–TiO_2 in blast furnace slags. Iron Steel 49(10):13
15. Zhang X, Lü Q, Liu X et al (2015) Optimal proportion of Ti, Mg and Al in BF slag. Iron Steel 50(6):8

Reaction Mechanism in EAF Steelmaking Process Based on Selective Oxidation, Bath Stirring and Furnace Body Heat Transfer

Lingzhi Yang, Zeng Feng, Yinghui Zhao, Yang Peng, Hang Hu, Yuchi Zou, Shuai Wang, Feng Chen, and Yufeng Guo

Abstract EAF steelmaking is characterized by complex charge structure, vigorous chemical reaction, and intensive energy source. The existed disadvantages lead to the big difference of temperature and chemical composition in molten bath, and finally make it difficult for end point controlling. There is still a lack of research on reaction regularity and smelting mechanism in the EAF steelmaking process. In this paper, the EAF was divided into "furnace body area" and "molten bath area". The characteristics of bath fluid flow, elements selective oxidation, heat transfer behavior in EAF steelmaking process based on bath stirring and multiple input energy were explored and determined through thermodynamic calculation and thermal experiments. The results revealed the reaction mechanism in the EAF steelmaking process based on selective oxidation, bath stirring, and furnace body heat transfer. This research is expected to provide theoretical basis for energy saving and optimization, emission reduction, and green development of the EAF steelmaking process.

Keywords EAF steelmaking · Reaction mechanism · Selective oxidation · Bath stirring · Furnace body heat transfer

L. Yang · Z. Feng · H. Hu (✉) · Y. Zou · S. Wang · F. Chen · Y. Guo
School of Minerals Processing and Bioengineering, Central South University, Changsha 410083, China
e-mail: CSU-huhang@csu.edu.cn

Y. Zhao · Y. Peng
Hengyang Valin Steel Tube Co. Ltd., Hengyang 421000, China

Z. Peng et al. (eds.), *Characterization of Minerals, Metals, and Materials 2024*, The Minerals, Metals & Materials Series, https://doi.org/10.1007/978-3-031-50304-7_64

Introduction

Electric arc furnace (EAF) steelmaking process is the main method for steel production in the contemporary world, which satisfies the requirements of smelting of varies of clean special steel products [1, 2]. However, due to the flat molten pool, irregular structure of the furnace body, and slow velocity of fluid flow, the momentum, heat and mass transfer between gas and liquids are reduced, and the dynamic conditions of molten steel (MS) flow are restricted. The above weak conditions lead to the difficulties of separation between the slag and MS, poor removal effect of impurity elements, and lower smelting efficiency in the EAF steelmaking process [3–5]. In addition, the EAF steelmaking process is characterized by complicated charge structure, insufficiently initial carbon content, unbalanced chemical reaction in bath area, and considerable discrepancy of chemical composition and temperature of MS. Thus, it is very difficult to predict and control the end-point state, and understand the fluid flow law of MS under of multiple stirring conditions. Matching the relationship between fluid flow with chemical reactions, and predicting the metallurgical reaction intensity and smelting process in the EAF is significant [6–8]. Furthermore, the temperature and chemical composition of MS are influenced by the interactions from multi-energy inputs, such as electrode radiation, carbon powder and natural gas injections, physical heat of high-temperature hot metal, and heat transfer by thermal effect of the chemical reaction in the molten bath. The heat losses, in the form of "metal-slag-gas-water-furnace": flue dust and flue gas, slag flowing out the furnace door, splashing metal, radiation and convection heat transfer of furnace body, and indirect heat transfer of cooling water directly affect the energy utilization efficiency, energy saving effect and emission reduction benefit in the EAF steelmaking process [9–12]. In general, this still lacks quantitative description of the materials-energies variation characteristics, and theoretical supports of high-efficient utilization of energy in the EAF steelmaking process. It is extremely urgent to further investigate the reaction law and smelting mechanism in the current EAF steelmaking process [13, 14].

Based on the above description, in this paper, the EAF is divided into "furnace body area" and "molten bath area" to solve the present problems in the current EAF steelmaking process. Through theoretical calculation, dynamics numerical simulation, thermodynamics analysis, the characteristics of bath fluid flow and selective oxidation of MS elements under stirring technologies were determined. Besides, the heat transfer behavior of furnace body area and heat losses under actions of multi-energy inputs were described quantitatively. Finally, the reaction mechanism, as well as the control models in the EAF steelmaking process based on selective oxidation, bath stirring and furnace body heat transfer were proved and developed. This research is expected to provide theoretical foundation for high-efficiency smelting and intelligent control in the EAF steelmaking process.

Mathematical Modeling and Theoretical Analysis

In this section, a new method for area division based the EAF steelmaking characteristics was clarified. The EAF was divided into two areas: furnace body area (FBA) and molten bath area (MBA), as shown in Fig. 1. The operations of oxygen injection and electricity supply directly affect the MBA. Under the action of violent chemical reactions, the energy of MBA changes at each stage. The direct influence area of oxygen injection in MBA is called as "Intensive reaction area", where violent oxidation reactions between MS elements occur. The outside area of the intensive reaction area is called as "Fluid flow area", where the chemical composition of MS changes based on the mass transfer of fluid flow under bath stirring. The whole furnace body outside the MBA is the FBA. The energy changes of FBA are dependent on heat transfer with the high-temperature MBA and external heat dissipation. The temperature and composition variation of MS is caused by the synergistic actions of two areas.

Thermodynamic Characteristics of Element Selective Oxidation in Intensive Reaction Area

According to thermodynamic software FactSage 8.1, the Gibbs free energy change, activity coefficient, and interaction coefficient of each element during the oxidation reaction in the EAF steelmaking process were calculated and summarized which are helpful for determining behavior, sequence and reaction heat effect of each element during the oxidation in the intensive reaction area. The specific calculation process was shown in Fig. 2. Based on the initial smelting data collected in real time, such as composition and temperature OF MS, the activities of elements C, Si, Mn, P and Fe

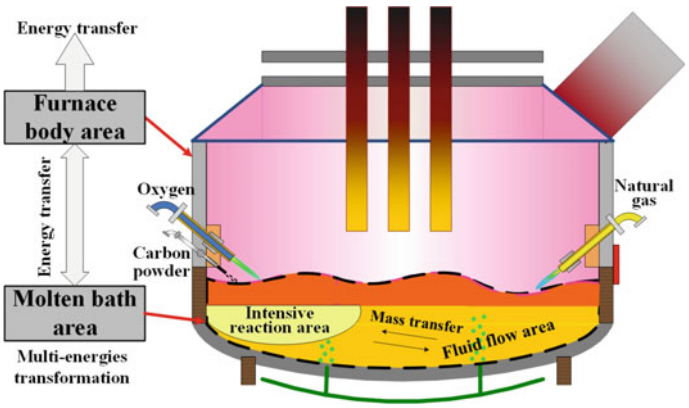

Fig. 1 Area deviation of EAF

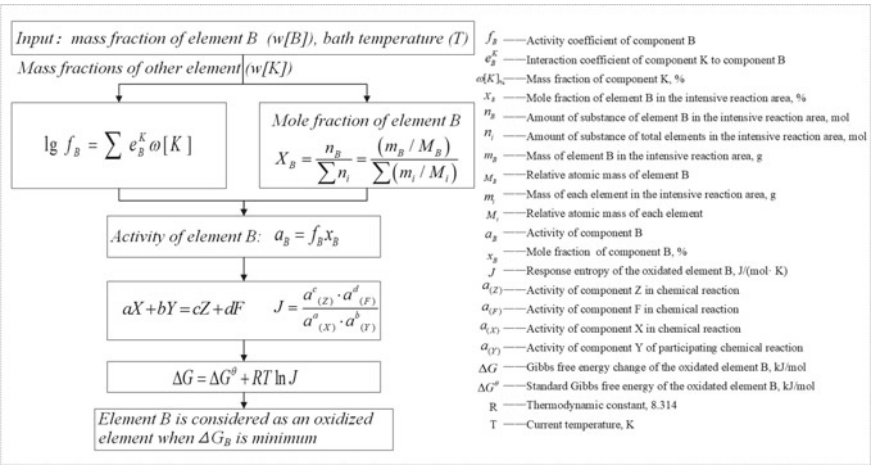

Fig. 2 Flow diagram of element selective oxidized

were calculated by thermodynamic theory of metallurgical physiochemistry. Under the inputting condition, the Gibbs free energy change of each element reacting with oxygen was obtained by van Hough isothermal equation. The principle of lowest Gibbs free energy change was selected as the current oxidation element.

Dynamic Characteristics of Fluid Flow and Mass Transfer in Molten Bath Area

The influences of bottom-blowing (bottom-blow flow, hole arrangement, gas species, bottom-blow patterns), oxygen injection (oxygen flow, oxygen parameters), and electromagnetic stirring on bath fluid flow and mass transfer were systematically investigated by numerical simulation software ANSYS Fluent, physical model cold-state experiments, 50 kVA semi-industrial EAF and field industrial experiments. It was found that the bottom-blow flow distribution, oxygen flow and preheat temperature played an important role in improving the exchange efficiency of kinetic energy between gas and liquid, slowing down the recession of jet velocity and temperature, and increasing the length of the jet core section. The kinetic mass transfer between the intensive reaction area and fluid flow area is related to the average flow velocity of MS and the size of the reaction zone. The size of the reaction zone (the pit volume) was related to factors including the average flow rate of MS and oxygen, oxygen temperature and height of oxygen lance. Considering various factors of the coupling relationship between the pit volume and the average velocity of MS the quantitative calculating equation for the pit volume in the intensive reaction area and the average velocity of MS in the fluid flow area were obtained, which were displayed in Eqs. (1)–(2).

$$v = 10^{-5} \times [1.723Q + 7.852T - 8.04H - 9.216\theta + 506.5 f_{CO} + 1.472 \cdot (N_1 + N_2 + N_3)] \quad (1)$$

$$v = 10^{-3} \times (2.502N_1 + 2.173N_2 + 3.602N_3 + 161.3 f_{lf} + 0.671Q) \quad (2)$$

where V denotes the pit body of intense reaction area, m^3; v denotes the average velocity of MS in fluid flow area, m/s. Q, T, and H, θ denotes the flow rate, temperature of oxygen and the height and angle of oxygen lance; f_{CO} denotes the coupling condition of the decarbonization reaction. N_1, N_2, N_3 denotes the gas flow of the bottom blow hole of 1#, 2#, and 3#, NL/min; f_{lf} denotes the Lorentz force, N.

Convection-Radiation Heat Transfer Behavior of Furnace Body Area

Through theoretical calculation, numerical simulation analysis, field investigation and detecting verification, the main methods of heat losses in EAF steelmaking, covering heat transfer of cooling water, convection of ambient air, radiation of high-temperature furnace body were clarified. The temperature distribution characteristics and heat loss under the influence of different air velocities, air temperatures, smelting stage parameters and wall surface emissivities were determined. Based on the numerical heat transfer simulation results, the quantifying heat loss equation was obtained by mathematical fitting, single factor analysis and multi-factor coupling analysis, as displayed in Eq. (3).

$$Q_{EAF} = -22.683v_{EAF}^2 + 62.162v_{EAF} - 0.678t_{air}^{EAF} + 205.858\varepsilon_{wall}^{EAF} + 0.153t_{roof} + 0.068t_{up}^{EAF} + 0.595t_{down}^{EAF} + 0.820t_{bottom} + 191.130 \quad (3)$$

where Q_{EAF} denotes the heat loss, kWh; v_{EAF} denotes air velocity, m/s; t_{air}^{EAF} denotes the air temperature, °C; ε_{wall}^{EAF} denotes the surface emissivity of furnace body; t_{roof}, t_{up}^{EAF}, t_{down}^{EAF}, and t_{bottom} denotes the temperature of roof, upper shell, lower shell, and furnace bottom, °C.

Model Interface and Function Description

Based on the above description, several tools covering TCP/IP communication, Visual studio 2013 software, and SQL2012 database tool were applied to develop three models, which include "Element selective oxidation model of intensive reaction area in EAF steelmaking process (ESO-EAF)", "Dynamic model of molten steel flow and mass transfer in molten bath area in EAF steelmaking process (DFM-EAF)", and

"Convection-radiation heat transfer model of furnace body area in EAF steelmaking process (CRM-EAF)".

Element Selective Oxidation Model of Intensive Reaction Area in EAF Steelmaking Process

The main interface of "Element selective oxidation model of intensive reaction area in EAF steelmaking process" is shown in Fig. 3, which is composed of MS composition module, selective oxidation module, parameter design, main interface module and basic smelting information. The model is applicable to dynamically judge and analyze the material-energy variation characters covering limitation and thermal effect of element selective oxidation. The application of this model is beneficial for prediction of process parameters and end-point element content in the EAF steelmaking process.

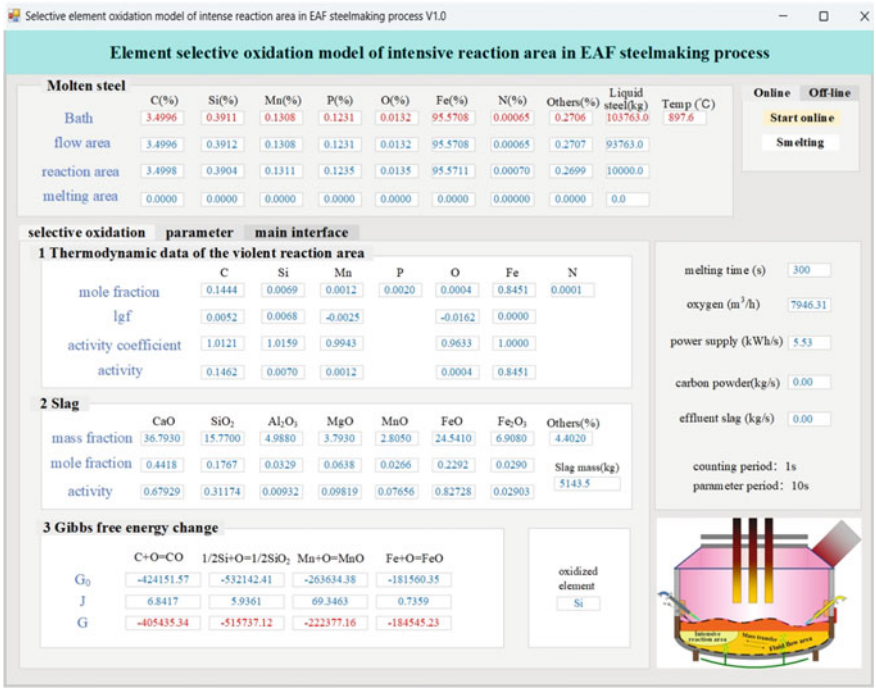

Fig. 3 Model interface and function description of ESO-EAF

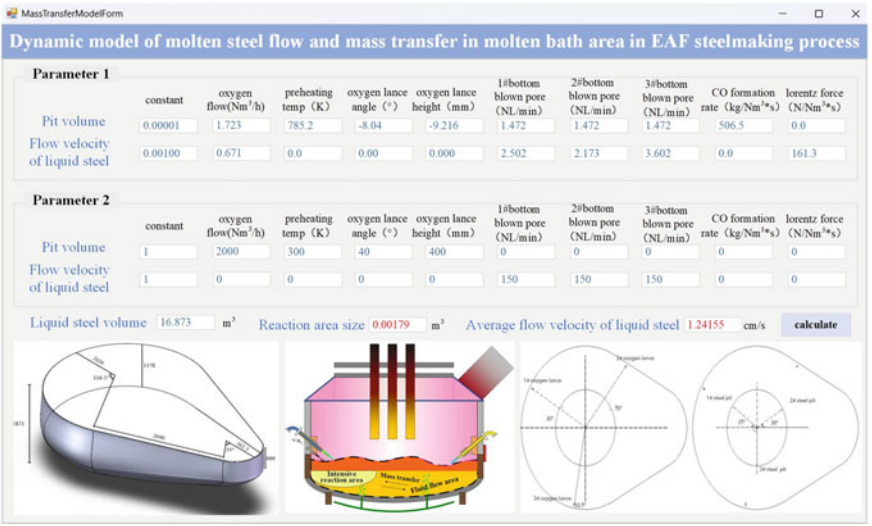

Fig. 4 Model interface and function description of DFM-EAF

Dynamic Model of Molten Steel Flow and Mass Transfer in Molten Bath Area in EAF Steelmaking Process

The main interface of "Dynamic model of molten steel flow and mass transfer in molten bath area in EAF steelmaking process" is shown in Fig. 4, which is composed of parameter-1 coefficient module of quantitative evaluation expression, and parameter-2 process module of actual steelmaking stirring and calculation module. The model is applicable to quantitatively evaluate the dynamic physical property parameters covering MS flow velocity under different stirring conditions. The application of this model is expected to provide dynamic theory and technical support for improving energies-materials utilization efficiency in the EAF steelmaking process.

Convection-Radiation Heat Transfer Model of Furnace Body Area in EAF Steelmaking Process

The main interface of "Convection-radiation heat transfer model of furnace body area in EAF steelmaking process" is shown in Fig. 5, which is composed of the heat loss related parameter module in the hot metal distribution process and EAF steelmaking process. The model is applicable to quantitatively calculate and systematically evaluate the heat losses and influencing factors. The application of this model

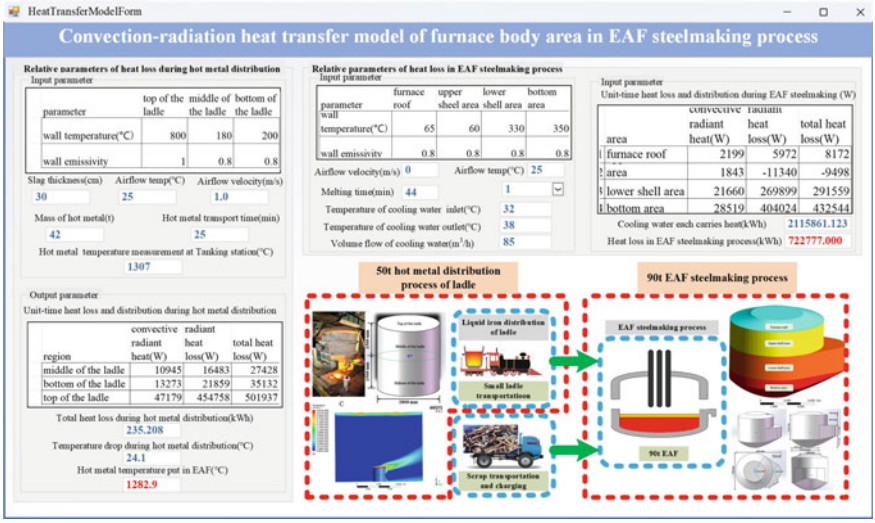

Fig. 5 Model interface and function description of CRM-EAF

is beneficial for exploring ways of further reducing energy loss and efficient waste heat utilization in the EAF steelmaking process.

Conclusions

In this paper, we introduced three control models based on the EAF steelmaking mechanism covering selective oxidation, bath stirring, and furnace body heat transfer. The main conclusions are summarized as follows: The EAF was divided into "furnace body area" and "molten bath area" to investigate the reaction law and smelting mechanism in the current EAF steelmaking process. The element selective oxidation model of intensive reaction area in the EAF steelmaking process was developed for dynamically judging and analyzing the material-energy variation characters, and providing the basis for prediction of end-point element content. The dynamic model of molten steel flow and mass transfer in the molten bath area in the EAF steelmaking process was developed for quantitatively evaluating the dynamic physical property parameters, and helping to improve energies-materials utilization efficiency. The convection-radiation heat transfer model of furnace body area in EAF steelmaking process was developed for quantitatively calculating and systematically evaluating the heat losses and influencing factors, and expecting to guide the development of further energy loss reduction and efficient waste heat utilization.

Acknowledgements The authors are grateful for financial support from the National Natural Science Foundation of China (No. 52174328).

References

1. Yang LZ, Hu H, Yang S, Wang S, Chen F, Guo YF (2023) Life cycle carbon footprint of electric arc furnace steelmaking processes under different smelting modes in China. Sustain Mater Technol 35:e00564
2. Tian BH, Wei GS, Hu H, Zhu R, Bai H, Wang ZM, Yang LZ (2023) Effects of fuel injection and energy efficiency on the production and environmental parameters of electric arc furnace-heat recovery systems. J Clean Prod 405:136909
3. Yang LZ, Hu H, Yang ZS, Xue BT, Guo YF, Wang S (2021) A review on bath fluid flow stirring technologies in EAF steelmaking. J Iron Steel Res Int 28(11):1341–1351
4. Lv M, Zhu R, Yang LZ (2019) High efficiency dephosphorization by mixed injection during steelmaking process. Steel Res Int 90(3):1800454
5. Hu H, Yang LZ, Guo YF, Chen F, Wang S, Zheng FQ, Li B (2021) Numerical simulation of bottom-blowing stirring in different smelting stages of electric arc furnace steelmaking. Metals 11(5):799
6. Yang LZ, Yang ZS, Wei GS, Guo YF, Chen F, Zheng FQ (2019) Influence of ambient and oxygen temperatures on fluid flow characteristics considering swirl-type supersonic oxygen jets. ISIJ Int 59(12):2272–2282
7. Wei GS, Peng YH, Zhu R, Yang LZ, Wu XT (2020) Fluid dynamics analysis of O_2–CaO jet with a shrouding flame for EAF steelmaking. ISIJ Int 60(3):481–491
8. Yang ZS, Yang LZ, Cheng T, Chen F, Zheng FQ, Wang S, Guo YF (2020) Fluid flow characteristic of EAF molten steel with different bottom-blowing gas flow rate distributions. ISIJ Int 60(9):1957–1967
9. Zhao F, Sun DB, Zhu R, Yang LZ (2017) Effect of shrouding gas parameters on characteristics of supersonic coherent jet. Metall Mater Trans B 48(3):1807–1816
10. Yang LZ, Xue BT, Song JL, Wei GS, Guo YF, Xie X, Liu QS (2020) Real-time prediction model of slag composition in electric arc furnace steelmaking. Chin J Eng 42(01):39–46
11. Yang LZ, Li B, Guo YF, Wang S, Xue BT, Hu SY (2022) Influence factor analysis and prediction model of end-point carbon content based on artificial neural network in electric arc furnace steelmaking process. Coatings 12(10):1508
12. Yang LZ, Jiang T, Li GH, Guo YF, Chen F (2018) Present situation and prospect of EAF gas waste heat utilization technology. High Temp Mater Process 37(4):1–7
13. Yang LZ, Jiang T, Li GH, Guo YF (2017) Discussion of carbon emissions for charging hot metal in EAF steelmaking process. High Temp Mater Process 36(6):615–621
14. Li ZH, Yang LZ, Guo YF, Wang S, Hu H (2022) Calculation of heat loss of furnace body in electric arc furnace steelmaking. Paper presented at the 12th international symposium on high-temperature metallurgical processing, Anaheim, California, 27 Feb–3 Mar 2022

Surface Activation and Directional Modification in the Technological Properties of Natural Perovskite Under the Action of High-Power Electromagnetic Pulses

Igor Zh. Bunin, Irina A. Khabarova, and Maria V. Ryazantseva

Abstract One of the main complexities of production of a high-quality perovskite concentrate at its high recovery (perovskite flotation, as a result of which a perovskite concentrate with a content of 49–50% TiO_2 released) is connected with the similar physicochemical and technological (namely, flotation) properties of perovskite, calcite and olivine. Application of high-energy (pulsed-power) technologies in processing of refractory ores enables efficient softening and selective disintegration of finely disseminated mineral complexes, and enhances contrast between the physicochemical and flotation properties. In this paper, we report the results of experimental studies on nonthermal effect of high-power nanosecond electromagnetic pulses on the surface morphology, structural, physicochemical and flotation properties of natural perovskite from one of the Russia deposit. Using the methods of analytical electron microscopy (SEM–EDX) and microhardness (Vickers test), we observed the formation of deep parallel microcracks, and the subparallel pyramidal protrusions on the perovskite surface. The morphological changes caused a monotonic decrease in the microhardness of the mineral with an increase of the high-voltage treatment times; the relative change of the microhardness changed from 20 to 33%. The Fourier-transform infrared spectroscopy (FTIR) data showed that short pulsed treatment times lead to the partial hydration of damaged mineral surface. The electromagnetic pulses perovskite pretreatment caused the following changes in the physicochemical properties of the perovskite: we made a shift in the electrokinetic potential towards positive values, an increase in the contact angle, as well as the improved adsorption of the collector and the higher flotation activity of perovskite by 10–15%.

Keywords Perovskite · High-power electromagnetic pulses · Surface modification · Microhardness · Hydrophobicity · Sorption · Flotation

I. Zh. Bunin (✉) · I. A. Khabarova · M. V. Ryazantseva
N.V. Melnikov's Institute of Comprehensive Exploitation of Mineral Resources, Russian Academy of Science (ICEMR RAS), Moscow 111020, Russia
e-mail: bunin_i@mail.ru

Z. Peng et al. (eds.), *Characterization of Minerals, Metals, and Materials 2024*, The Minerals, Metals & Materials Series, https://doi.org/10.1007/978-3-031-50304-7_65

Introduction

The Russian share in the world production of TiO_2 concentrate is only 0.4% (for 2018–2020). At the same time, the Russian Federation accounts for 15% of the world's titanium reserves. Only in the Murmansk region, three deposits of titanium–magnetite ores (namely, Kolvitskoye, Pudozhgorskoye and Afrikanda) are located. These deposits contain significant reserves of titanium, rare (Nb, Ta) and rare earth metals [1].

In Russia, the Afrikanda deposit is the largest in terms of titanium reserves (the total amount of TiO_2 in the ores of the deposit is ~ 52 million tons (Mt), and the average content is ~ 9%); this deposit is considered as a promising source of both titanium and rare (rare earth) elements [1, 2]. Titanium is the main useful component in ores, and it is found in perovskite and titanium–magnetite; perovskite contains (wt., %): 50.8–56.8 TiO_2, 0.64–2.50 $(Nb, Ta)_2O_5$, 0.12–1.93 SiO_2, 0.15–1.30 Al_2O_3, 0.43–2.00 Fe_2O_3, up to 1.44 FeO, 2.18–10.7 Ln_2O_3 (total REM oxides), and other minor components [2, 3].

Perovskite (calcium titanium oxide, perfect formula $CaTiO_3$, chemical composition (Ca, REE, Na)(Ti, Nb)O_3 [4]) is a mineral from a large family of perovskites that share a generic formula ABX_3 (where the X position can be taken by such anions as O^{2-}, F^-, Cl^-, Br^-, I^-, OH^--groups etc.). Minerals of perovskite group are a group of accessory minerals that share a formula ABO_3 where the A position is taken by the main cations Ca, Sr, Pb, Ce, La, Nd, Pr, Na, K, Th, U; the B position can be taken by Ti, Nb, Fe, Ta, Zr, with possible isomorphic impurities Al, Si, Mg and Mn [4–6]. At present, natural perovskite belongs to the space symmetry group *Pbnm* [5]; the correct choice of this symmetry group was confirmed by the discovery of natural perovskite crystals with a small number of twins [5, 6]. The crystal structure of the mineral is distorted relative to the ideal cubic structure as a result of a combination of two antiphase rotations of the TiO_6 octahedra around the a and b axes and a rotation about the c axis. In such a structure, the TiO_6 octahedra are slightly distorted, while the coordination polyhedron of calcium cations is strongly distorted due to the rotation of the octahedra and the displacement of calcium from the A position by 0.29 Å [6]. Perovskite possesses semiconducting properties, the band gap $E_g = \sim 1.2$–4 eV [7], the conductivity type is n, the electric conductivity is ~ 10^{-7} $(\text{Ohm cm})^{-1}$, the thermoelectric coefficient is 7, the carrier concentration is ~ 4×10^{11} cm^{-3} [8]; the mineral is paramagnetic, the density is ~ 4–4.2 g cm^{-3}, and the Mohs hardness is 5.5–6 [3].

One of the main complexity of production of a high-quality perovskite concentrate at its high recovery (namely, perovskite flotation, as a result of which a perovskite concentrate with a content of 49–50% TiO_2 released) is connected with the similar physicochemical and technological (process, namely, flotation) properties of perovskite, calcite and olivine [2, 3]. Application of high-energy (pulsed-power) technologies [8–17] in the processing of refractory ores enables efficient softening and selective disintegrating of finely disseminated mineral complexes, enhances contrast between the physicochemical and flotation properties of minerals,

and improves the further separation; thanks to the formation of hydrophobic and hydrophilic micro- and nanophases on the minerals surface. In [18, 19] we experimentally established that the rational pretreatment with high-power electromagnetic pulses of rare metal minerals provided higher selectivity of rare metal minerals (columbite and zircon) flotation separation, without any appreciable boost in flotation activity of rock-forming minerals (feldspar and quartz).

This study aims to analyze the *nonthermal* effects produced by the high-power nanosecond electromagnetic pulses (HPEMP [20, 21]) at standard conditions of atmospheric pressure in the air on the surface structure and morphology, microhardness, electrokinetic potential, contact angle, adsorbability and floatability of Afrikanda perovskite with a view to enhancing flotation of complex perovskite-titanomagnetite ores.

Experimental

Mineral Samples and Conditions of Electromagnetic Pulse Treatment

We performed our studies using monomineral fractions of perovskite in the form of grains extracted from hand specimens of Afrikanda perovskite (Kola Peninsula, Russia; the museum of the Geological Institute of the Kola Science Center of the RAS) and specially manufactured polished plates are 4.5 mm thick. The chemical composition and the content of impurities of the samples was determined by the X-ray fluorescence analysis using spectrometer ARL Advant'X (Thermo Fisher Scientific Inc.), mass percentage: 48.0 TiO_2, 35.5 CaO, 5.41 SiO_2, 2.15 CeO_2, 1.87 Al_2O_3, 1.62 Fe_2O_3, 0.88 Nb, 1.01 F, 0.65 Nd, 0.55 Na_2O, 0.39 MgO, 0.33 La_2O_3, 0.26 Sr, 0.10 V_2O_5, 0.09 K_2O, 0.08 ZrO_2, 0.05 Sm_2O_3, 0.05, Ta_2O_5, 0.04 BaO, 0.03 Y_2O_3, 0.03 Cs_2O, 0.01 Ni, 0.01 Pb, Pr—not detected, Th—not detected.

The details of the electrophysical parameters of high-voltage electromagnetic effect and the pretreatment conditions of perovskite samples are given in [19, 22]; the treatment duration range is $t_{treat} = 10–150$ s. The front, duration and amplitude of out voltage pulse were ~ 3–8 ns, 30–50 ns and 70 kV, respectively; the electromagnetic field strength in the electrode gap 7 mm long were 10^7 V m^{-1}, the frequency repetition rate of nanosecond pulses was 375 Hz. Figure 1 shows the structural scheme of the experimental modular unit for continuous treatment of dry and moist (S:L from 10:1 to 5:1) mineral feeds with nanosecond HPEMP developed at ICEMR RAS in cooperation with the Scientific-Production Enterprise FON, Ryazan.

For enhancing efficiency of the electromagnetic pulses effect, we moistened the milled perovskite samples with distilled water at an S:L ratio of 5:1. Then, the samples were placed on a thin dielectric base surface on the side of the grounded electrode. The presence of a gap between the surface of the top mineral layer and the surface of the active electrode (~ 0.1–0.2 mm) inevitably initiated periodic high-voltage spark

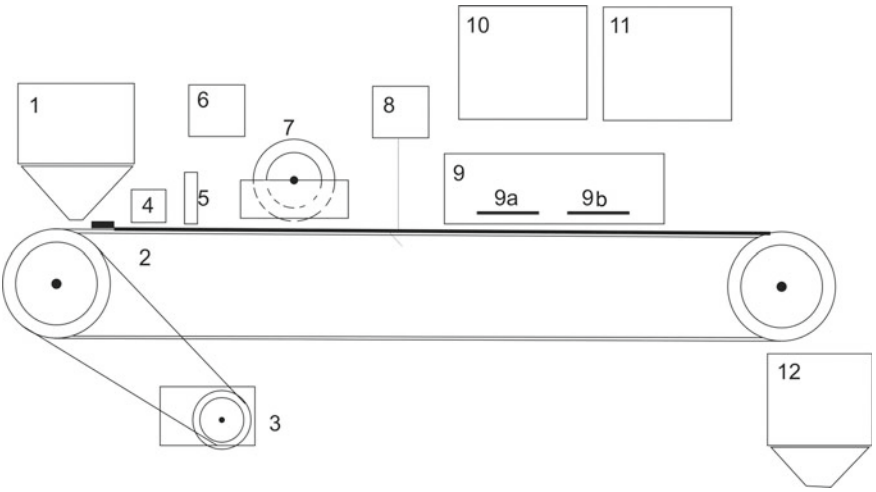

Fig. 1 Structural scheme of the experimental unit for the treatment of mineral products by high-power nanosecond electromagnetic pulses with a capacity of 20 kg/h: *1* hopper for loading and dosing material, *2* transport system with a movable electrode, *3* electric drive; technological blocks, *4* and *5* pre-forming the material flow in width and height, *6* rock moistening, *7* final formation of the rock flow, *8* changes in the level of material flow, *9* block of electrodes and HPEMP former, *10* control pulse generator, *11* voltage converter, *12* storage hopper for processed mineral material

discharges. After HPEMP treatment, the samples were dried in the air and were kept in the rare atmosphere up to the analysis and flotation tests.

Analysis Methods

The change in the surface structure and morphology of perovskite after treatment by electromagnetic pulses was analyzed using the analytical scanning electron microscopy SEM–EDX (scanning electron microscope LEO 1420 VP with energy-dispersive micro analyzer INCA Energy 350), and Fourier-transform infrared spectroscopy (FTIR, spectrometer Nicolet-380 (USA) with Smart Diffuse Reflectance). We registered the IR spectra of perovskite in a range from 4000 to 400 cm^{-1} (spectral resolution 4–6 cm^{-1}, 100 scans); the intensity of the characteristic lines in the IR spectra varied from spectrum to spectrum, for this reason, the estimate of the relative intensity of the spectrum lines used the ratio of the optical density of each line to the optical density D of IR line 442–494 cm^{-1}.

The microhardness of the mineral was determined using the Vickers test (*HV*, MPa) [22]: microhardness tester PMT-3M; the load on the indenter was 100 g, and the loading time was 10–15 s. The flow potential (ζ-potential, mV) of mineral particles in size 50 μm was determined on Microtrac ZETA-Check Zeta Potential Analyzer. The surface contact angle ($\theta°$) of the polished sections before and after energy effects

was measured using the drop technique, with distilled water drop of diameter of 2–3 mm lying on the flat surface [19, 22], with the help of a digital optical microscope and image analysis program ImageJ with DropSnake and LB-ADSA plugins [23].

The procedure of estimating adsorption of a complexing flotation agent (capryl hydroxamic acid [24]) at the surface of perovskite before and after treatment by HPEMP included agitation of a mineral sample with the agent solutions, filtration of the solid phase, washing, drying of the filtrate and analysis of the mineral surface by the diffuse reflectance FTIR (spectrometer IRAffinity, Shimadzy with diffuse reflection accessory DiffuzIR, Pike Technologies). Flotation of the test samples (1.0 g, particle size $-80 + 40$ μm) was carried out in a flotation cell of 20 ml: the samples were agitated in water for 1 min, then the collector was fed (capryl hydroxamic acid, 200 g/t); the mineral and the agent contact time was 1 min; pH of the medium was brought to 5.5 by adding the aqueous solution of H_2SO_4; after that frother MIBK was added as a frother to interact with the mineral for 0.5 min; the froth product was separated for 2 min.

Results and Discussion

In the initial state (before effect of HPEMP), microstructural defects in perovskite surface represent mostly the complex curved interfaces of mineral phases formed by noncrystallographic planes and the slot-like cavities and flaws in perovskite matrix. Optically uniform grains of perovskite are nonuniform in the SEM–BSE images and are composed of two phases (Fig. 2a–c): a more bright-grey phase having the composition of $(Ca_{0.92}Na_{0.05}(Ce_{0.03}Nd_{0.01})_{0.04})_{1.00}(Ti_{0.95}Fe_{0.03}Nb_{0.02})_{1.00}O_{3.00}$ and a dark-grey phase having the composition of $(Ca_{0.96}Na_{0.02}(Ce_{0.02}Nd_{0.01})_{0.03})_{1.01}(Ti_{0.97}Fe_{0.02}Nb_{0.01})_{1.00}O_{3.01}$.

The interfaces of these phases are complex, curved, noncrystallographic, probably epigenetic, connected with the redistribution of the components in metasomatic recrystallization, as a result of which perovskite undergoes accumulation of loparite $NaCe(Ti,Nb)_2O_6$, increase in the contents of Na and REE, and redistribution of Th and Nb. The slot-like cavities between the zonal grains of perovskite are filled with calcite and silicates (maize-yellow titanite Tit-$CaTiSiO_5$ with impurities of Al and Fe, and with britholite-(Ce) (Brt)—silicophosphate of rare earths $Ca_2(Ce, Ca)_3[(OH, F)|(SiO_4, PO_4)_3]$) (Fig. 2c). Moreover, the cavities contain coarse grains of pyrite, completely replaced by micro cryptocrystallitic aggregates of iron hydroxides (limonite $FeOOH \cdot (Fe_2O_3 \cdot nH_2O)$). Rare earth carbonates from ancylite group fill the finest flaws which grow through the whole volume of perovskite: these are ancylite-(Ce) having the composition of $(Sr_{0.53}Ca_{0.47})_{1.00}(Ce_{0.50}La_{0.32}Nd_{0.12}Pr_{0.06})_{1.00}[CO_{3.00}]_{2.00}(OH) \times H_2O$ and calcioancylite-(Ce) having the composition of $(Ca_{0.70}Sr_{0.30})_{1.00}(Ce_{0.52}La_{0.28}Nd_{0.15}Pr_{0.05})_{1.00}[CO_{3.00}]_{2.00}(OH) \times H_2O$.

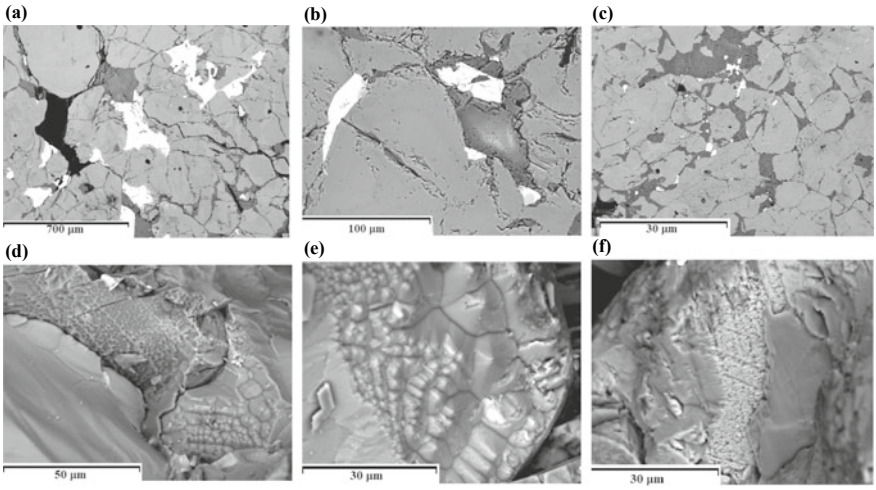

Fig. 2 SEM micrographs of perovskite surface **a**, **b**, **c** before and **d**, **e**, **f** after exposure to high-power nanosecond electromagnetic pulses ($t_{treat} = 50$ s). **c** Bright (in BSE) britholite inclusions in cavities filled with dark titanite among a perovskite aggregate. Scale: **a** 700, **b** 100, **d** 50, **c**, **e**, and **f** 30 μm

According to SEM data, the electromagnetic pulse treatment of perovskite particles ($t_{treat} = 50$ s) caused the damages of perovskite structure and modify the surface in some areas of the test samples (Fig. 2d–f). The morphological changes of the mineral surface represent by characteristic pyramidal spikes (Fig. 2e) produced by the crystal surface exposed (cleaning), as well as parallel microcracks (Fig. 2f) which appear as a consequence of polysynthetic twinning typical of perovskite crystals. The structure of minerals of the perovskite group consists of frameworks, layers, or square grids of vertex-connected BX_6 octahedra [5]. In this regard, when exposed to high-voltage electric fields, the migratory (interlayer) and/or electron-relaxation polarization of the mineral [25] are very possible mechanisms of microdamages formation and softening of crystals. Nonthermal HPEMP treatment softens the mineral surface; microhardness of perovskite decreases with longer time of treatment from 930 MPa in the initial state to 620 MPa at $t_{treat} = 150$ s, i.e. $\Delta HV_{max} = 33\%$. It should be specially noted that under short-term pulses ($t_{treat} = 30$ s), microhardness also decreases ($HV = 750$ MPa; $\Delta HV = 19\%$).

The infrared spectrum (FTIR) of perovskite (without treatment by HPEMP) included lines in the range of 400–800 cm^{-1}, conditioned by variation of structural groups in the crystal lattice of the mineral, and lines in the range of 900–4000 cm^{-1}, connected with the presence of the impurities C–O, O–H, and metal (Me)–O groups localized on the mineral surface [3, 4, 26]. To analyze the changes of the perovskite surface under the impact of HPEMP, four characteristic lines were selected in the infrared spectra of the mineral (Fig. 3): at 442–494 cm^{-1} (ν Ti–O–Ti), 632–659 cm^{-1} (ν Me–O), 916–950 cm^{-1} (peroxo-groups –O–O–) and at 1435–1444 cm^{-1} (ν C–O).

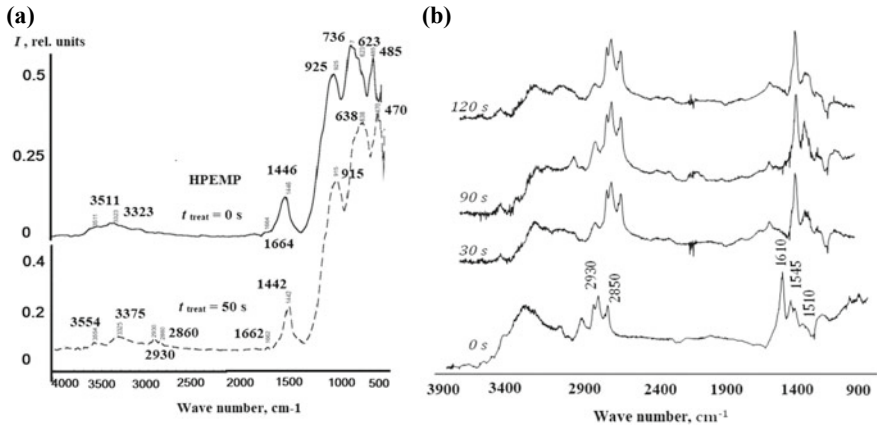

Fig. 3 **a** Characteristic FTIR spectra of perovskite before (0 s, solid top line) and after (t_{treat} = 50 s, dashed bottom line) treatment with high-power electromagnetic pulses. **b** Effect of HPEMP on adsorption activity of perovskite surface relative to collecting agent (capryl hydroxamic acid)

As a result of perovskite treatment by HPEMP for t_{treat} = 10–30 s, the relative intensity increased in the lines at 632–659 cm^{-1}, 916–950 cm^{-1} and 1435–1444 cm^{-1}, governed by the vibrations of Me–O, –O–O–, and C–O, respectively. Probably, these changes in the IR-spectrum mean partial oxidation of the surface of pre-moistened perovskite particles under the action of spark discharge plasma produced by the effect of periodic nanosecond high-voltage pulses in the air. Simultaneously with oxidation, hydration of perovskite surface takes place, which is identified by the increased intensity in the line at 1616–1693 cm^{-1}, due to the presence of mineral-adsorbed molecules of H_2O (δ O–H in H_2O). Increasing of the pulsed electromagnetic treatment duration to $t_{treat} = 50 \div 150$ s apparently causes a local rise in the temperature and, as a consequence, deoxidizing (dehydration) of perovskite surface, which is specified by the decrease in the relative intensity in the lines at 632–659, 916–950 and 1435–1444 cm^{-1} (Fig. 3a).

It should be specially noted that the experiments with nanosecond electromagnetic pulsed treatment of natural and artificial (man-made) materials are classified as the so-called nonthermal effects, since the energy of a single pulse (~ 0.1 J) and of the whole series of pulses is low and is not capable of substantially elevating the temperature of the sample as a whole [20, 21]. However, for a time much shorter than the characteristic measurement time of the thermophysical properties of mineral components making up the sample, the local temperature during the electromagnetic pulsed treatment can be very high [27].

The electrokinetic potential of perovskite changes nonlinearly (non-monotonous) subject to time of the pulsed electromagnetic treatment. As a result of short-term (t_{treat} = 10–50 s) impact of HPEMP, the negative values of the electrokinetic potential decrease from − 85.5 mV (t_{treat} = 0 s) to − 84 mV and − 77 mV at t_{treat} = 10 and 50 s, respectively. With an increase in the treatment time to 150 s, ζ-potential increased in the region of negative values up to − 82 mV.

With increasing duration of the pulsed electromagnetic treatment, the contact angle ($\theta°$) of perovskite surface changes nongradually (Fig. 3): it increases from 75° (t_{treat} = 0 s) to 80.5° at t_{treat} = 30 s. The increase in exposure time led to a monotonous decrease in the contact angle to ~ 60°. The inserts in Fig. 4 represent snapshots of the water droplets on the perovskite surface during the contact angle tests; the electromagnetic pulses pre-treatment time t_{treat} = 0, 30 and 150 s. Probably, the found effects of the increased hydrophobic behavior and decreased negative values of the electrokinetic potential the mineral as a result of the short-term (t_{treat} = 30 s) energy deposition can improve the adsorption and flotation properties of perovskite.

Figure 3b is a graphic representation of IR-curves of the initial and treated by HPEMP samples (t_{treat} = 30–120 s) of perovskite in the presence of a collecting agent (capryl hydroxamic acid). The spectral analysis reveals the following characteristic features in the profiles of diffusive reflectance IR-spectra of micropowdered perovskite, which characterize the mechanism of the agent adsorption at the mineral surface. In the spectrum of the initial sample (t_{treat} = 0 s) there is a series of bands which describe attachment of capryl hydroxamic acid at perovskite surface: absorption at 2850 and 2930 cm^{-1}—valence vibrations in the bond C–H of saturated hydrocarbons; the bonds at 1510 and 1550 cm^{-1} characterize complexing with titanium, and the bond at 1610 cm^{-1} is reflective of physical sorption of hydroxamic acid.

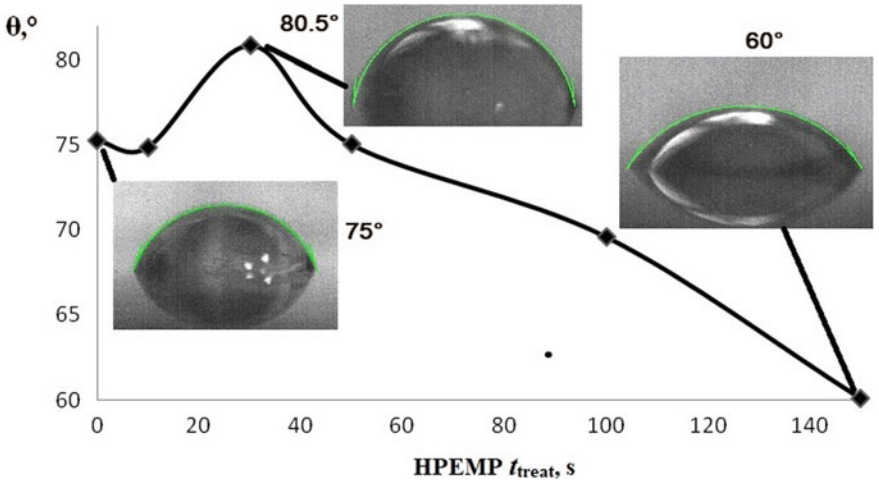

Fig. 4 The change in contact angle of perovskite as a result of exposure to HPEMP

The spectral curves of the HPEMP-treated samples have a similar set of characteristic IR-spectra peaks but the integral intensities of the bands related to the adsorbed collector increase by 1.2 times as compared with the initial sample (Fig. 3b).

Considering the test data on modifying effect exerted by the high-power electromagnetic pulses on the physicochemical properties of perovskite, we decided to analyze the influence of HPEMP on the floatability of the mineral with capryl hydroxamic acid. After preliminary electromagnetic pulsed treatment, owing to the change in the structural and physicochemical properties of the mineral surface, enhanced hydrophobic behavior and improved adsorbability, the total flotation recovery (ε, %) of monomineral fraction of perovskite grows by ~ 10–15%. From the initial values of mineral flotation recovery in the froth $\varepsilon \cong 80\%$ ($t_{\text{treat}} = 0$ s), at $t_{\text{treat}} = 60$ s, the recovery of perovskite was 90% and at $t_{\text{treat}} = 120$ s, $\varepsilon \sim 95\%$.

Conclusions

The analysis of the data on SEM and FTIR has proved the efficiency of the impulse (HPEMP) treatment for the surface morphology, microhardness, physicochemical and flotation properties modification of Afrikanda perovskite. The morphological changes of the mineral surface represent characteristic pyramidal spikes produced by the crystal surface exposed (cleaning), and parallel microcracks which appear as a consequence of polysynthetic twinning typical of perovskite crystals. These defects induce softening of the mineral surface and monotonous decrease in its microhardness with longer time of the HPEMP treatment on the whole by $\Delta HV_{\max} = 20$–33% at $t_{\text{treat}} = 30$–150 s. Under short-term electromagnetic impact ($t_{\text{treat}} = 10$–30 s), the structural surface modification and changes of the mineral technological properties are conditioned by oxidation (hydration) of the surface and, at $t_{\text{treat}} = 50$–150 s, the dehydration process occurred. The modifying effect exerted by HPEMP on the physicochemical and technological properties of the mineral, is expressed by the shift of the electrokinetic potential towards the positive values, by the increase in the contact angle at $t_{\text{treat}} = 30$ s and by the improved adsorption of the collecting (flotation) agent, which enhances floatability and total extraction of monomineral fraction of perovskite in flotation froth by ~ 10–15%. Our technological results, the determined parameters of energy effects and the reagent regime of perovskite flotation demonstrate the actual feasibility to apply the nonthermal high-power nanosecond electromagnetic pulses effects to improve flotation efficiency of perovskite ores.

Acknowledgements This work supported in part by the President of the Russian Federation under contract number NSh 7608.2016.5 (Academician V. A. Chanturiya's Scientific School). The authors are grateful to Ph.D. (geological and mineralogical sciences) E. V. Koporulina, and to the Ph.D. (technical sciences) N. E. Anashkina for their help in the experimental studies.

References

1. Sokolov SV (2020) Perovskite and titanite—potential nonconventional sources of titanium: a case-study of Afrikanda deposit. Paper presented at the Plaksin's scientific readings-2020, Apatity, Russia, 21–26 Sept 2020
2. Nikolaev AI, Larichkin FD, Luhton MM (2003) Problems of integrated re-appraisal and mining of Afrikanda perovskite-titanomagnetite ore deposit. Min Mag (Gorn Zh) 11:10–14
3. Naifhonov TB, Beloborodov VI, Zakharova IB (1994) Flotation of complex titanium and zirconium ores. KNC RAN, Apatity
4. Mitchell RH, Welch MD, Chakhmouradian AR (2017) Nomenclature of the perovskite supergroup: a hierarchical system of classification based on crystal structure and composition. Miner Mag 81(3):411–461. https://doi.org/10.1180/minmag.2016.080.156
5. Popova EA (2018) Crystal chemistry and physical properties of minerals and synthetic compounds having perovskite-type structure. Ph.D. thesis, Saint-Petersburg State University
6. Mitchell RH (2002) Perovskites: modern and ancient. Almaz Press Inc., Ontario
7. Xiao Z, Zhou Y, Hosono H (2018) Bandgap optimization of perovskite semiconductors for photovoltaic applications. Chem A Eur J 24:2305–2316. https://doi.org/10.1002/chem.201705031
8. Shafeev RS, Chanturiya VA, Yakushkin VP (1971) Ionizing radiation effect on flotation. Nauka, Moscow
9. Mesyats GA (2004) Pulse power engineering and electronics. Nauka, Moscow
10. Lehr J, Pralhad R (2018) Foundations of pulsed power technology. Wiley-IEEE Press, Piscataway. https://doi.org/10.1002/9781118886502
11. Avtaeva SV (2011) Barrier discharge: research and application. Lambert Academic Publishing, Saarbrücken
12. Chanturiya VA, Bunin IZh, Ryazantseva MV, Filippov LO (2011) Theory and application of high-power nanosecond pulses to processing of mineral complexes. Miner Process Extract Metall Rev 32(2):105–136. https://doi.org/10.1080/08827508.2010.530722
13. Kurets VI, Solovyov MA, Zhuchkov AI, Barskaya AV (2012) Electrodischarge technologies for processing and destruction of materials. Publishing House of TPU, Tomsk
14. Bunin IZh, Ryazantseva MV, Samusev AL, Khabarova IA (2017) Composite physicochemical and energy action on geomaterials and aqueous slurries: theory and practice. Min Mag (Gorn Zh) 11:77−83. https://doi.org/10.17580/gzh.2017.11.14
15. May F, Hamann S, Quade A, Bruser V (2017) Froth flotation improvement by plasma pretreatment of sulfide minerals. Miner Eng 113(11):95–101. https://doi.org/10.1016/j.mineng.2017.08.009
16. Rostovtsev VI, Bryazgin AA, Korobeinikov MV (2020) Improvement of milling selectivity and utilization completeness through radiation modification of mineral properties. J Min Sci 56(6):1000–1009. https://doi.org/10.1134/S1062739120060125
17. Huang W, Chen Y (2021) The application of high voltage pulses in the mineral processing industry. Powder Technol 393(11):116–130. https://doi.org/10.1016/j.powtec.2021.07.003
18. Chanturiya VA, Bunin IZh, Ryazantseva MV (2017) Modifying the physicochemical and electrical properties of tantalite and columbite surfaces under conditions of electrochemical treatment and high-voltage nanosecond pulses. Bull Russ Acad Sci Phys 81(3):269−274. https://doi.org/10.3103/S1062873817030066
19. Bunin IZh, Anashkina NE, Khabarova IA, Ryazantseva MV (2023) Effect of high-power nanosecond electromagnetic pulses on the microhardness, physicochemical and flotation properties of rare metal minerals. In: Zhang M (ed) Characterization of minerals, metals, and materials 2023. The Minerals, Metals & Materials Society, Pittsburgh; Springer, Cham, pp 369–378. https://doi.org/10.1007/978-3-031-22576-5_36
20. Bunin IZh, Bunina NA, Vdovin VA, Voronov PS, Gulyaev YuV, Korzhenevsskii AV, Lunin VD, Chanturiya VA, Cherepenin VA (2001) Experimental studies of non-thermal effect of high-power electromagnetic pulses on rebellious gold-bearing raw materials. Bull Russ Acad Sci Phys 65(12):1788–1792

21. Cherepenin VA (2006) Relativistic multiwave oscillators and their possible applications. Phys Usp 49(10):1097–1102. https://doi.org/10.1070/PU2006v049n10ABEH006109
22. Bunin IZh, Chanturiya VA, Anashkina NE (2015) Experimental validation of mechanism for pulsed energy effect on structure, chemical properties and microhardness of rock-forming minerals of kimberlites. J Min Sci 51(4):799−810. https://doi.org/10.1134/S1062739115040177
23. Stalder AF, Melchior T, Muller M (2010) Low-bond axisymmetric drop shape analysis for surface tension and contact angle measurements of sessile drops. Colloids Surf A 364(1−3):72–81. https://doi.org/10.1016/j.colsurfa.2010.04.040
24. Wang W, Zhu Y, Zhang S (2017) Flotation behaviors of perovskite, titanaugite, and magnesium aluminate spinel using octyl hydroxamic acid as the collector. Minerals 7(8):134. https://doi.org/10.3390/MIN7080134
25. Poplavko YuM, Pereverzeva LP, Raevsky IP (2009) Physics of active dielectrics. Publishing House of the SFU, Rostov
26. Nakamoto K (2008) Infrared and Raman spectra of inorganic and coordination compounds. Part A: theory and applications in inorganic chemistry. Wiley. https://doi.org/10.1002/9780470405840
27. Chanturiya VA, Bunin IZh, Kovalev AT (2005) Selective disintegration of finely disseminated mineral complexes under exposure to high-power pulses. Bull Russ Acad Sci Phys 69(7):1186–1190

Synthesis and Characterization of TiO_2 Nanoparticles by Green Chemistry, Using Aloe Vera

R. H. Olcay, I. A. Reyes, E. G. Palacios, L. García, P. A. Ramírez, L. Guzmán, and M. U. Flores

Abstract Titanium oxide nanoparticles were synthesized by green chemistry technique, using aloe vera extract, titanium chloride (2 M, $TiCl_4$) in 1000 mL of ultra-pure water, where aloe vera extract was added drop by drop and kept with constant agitation of 400 rpm, having a pH ~ 7 with HCl or NaOH. The synthesis product was recovered by centrifugation (10,000 rpm) and washed repeatedly with absolute ethanol. The nanoparticles were washed again with ultra-pure water and dried at 100 °C for 7 h, at the end of drying, a fine white powder was obtained which was characterized by X-ray diffraction, where it was determined that the anatase phase (TiO_2) was obtained, so it has a tetragonal structure, with cell parameters of $a = 3.79$ Å, $c = 9.51$ Å. From the synthesis product nanoparticles of sizes ranging from 2 to 30 nm have been obtained, this was confirmed by transmission electron microscopy.

Keywords Green chemistry · TiO_2 nanoparticles · Aloe vera extract · Characterization

R. H. Olcay
Universidad Arturo Prat, Departamento de Ingeniería Metalúrgica, Facultad de Ingeniería y Arquitectura, Iquique, Chile

I. A. Reyes
Instituto de Metalurgia, Universidad Autónoma de San Luis Potosí, San Luis Potosí 78210, San Luis Potosí, México

Catedrático CONACYT, Consejo Nacional de Ciencia y Tecnología, Benito Juárez 03940, Ciudad de México, México

E. G. Palacios · M. U. Flores (✉)
Escuela Superior de Ingeniería Química e Industrias Extractivas-IPN, Unidad Profesional Adolfo López Mateos, Zacatenco, Ciudad de México 07738, México
e-mail: mflores@utectulancingo.edu.mx

L. García · P. A. Ramírez · L. Guzmán · M. U. Flores
Área de Electromecánica Industrial, Universidad Tecnológica de Tulancingo, Camino a Ahuehuetitla, #301 Col. Las Presas, Tulancingo, Hidalgo 43642, México

L. Guzmán
Universidad Vizcaya de Las Américas, Carretera Mexico-Tuxpan, km 139, # 200, Fraccionamiento Santa Ana, Tulancingo, Hidalgo 43642, México

Z. Peng et al. (eds.), *Characterization of Minerals, Metals, and Materials 2024*, The Minerals, Metals & Materials Series, https://doi.org/10.1007/978-3-031-50304-7_66

Introduction

At the nanoscale, which pertains to the atomic or molecular level, materials are purposefully designed and engineered in the realm of nanotechnology. This field allows for the development of innovative materials, tools, and systems that exhibit enhanced capabilities due to their manipulation of structures and particles at an extremely minute scale. Nanotechnology has recently made significant advancements in various fields of study and technological developments. The development of new material at the nanoscale ranges between 1 and 100 nm, which is what a nanoparticle entails [1, 2]. Especially metal nanoparticles have recently attracted a lot of attention due to their unique properties like large surface area, high stability, facile chemical modification, efficacy as a filler for enhanced permeability, and synthesis flexibility [3]. The advent of nanotechnology with the fascinating physicochemical properties of nanoparticles (NPs) has ignited explosive interest in its applications in various fields. In particular, the unique size (1–100 nm) of NPs, their morphology, and other properties impart enhanced capabilities that allow them to find revolutionary utilities in numerous fields, including medicine, electronics, pharmaceutical industry, agriculture, and many others [4–6]. Titanium dioxide (TiO_2), usually called titania, is a semiconducting metal oxide that has received a great attention since the discovery of the photocatalytic water splitting on a TiO_2 electrode under ultraviolet (UV) light in 1972 [4]. Among them, TiO_2 NPs are a well-known semiconductor with a wide bandgap of 3.2 eV for anatase and 3.0 eV for rutile phase [7], but the brookite phase is rare to obtain [8]. The anatase and rutile phase of TiO_2 exhibits a tetragonal crystal structure, but the brookite phase is an orthorhombic structure [9]. The transition metal oxide, mainly TiO_2, is widely used in cosmetics, photocatalysts, medicines, sensors, and solar cell applications because of its peculiar properties like interconnected pores and large surface area [10]. Therefore, the preparation of nanoparticulate TiO_2 with tailored specific surface area and high porosity for specific applications is of interest due to the new properties expected. Biological methods have thus been explored as alternative greener routes involving application of natural plant extractor microbes in the reduction of Ti^{4+} and stabilizing the oxide titanium nanoparticles formed [8]. Use of plant extract is more favorable than using microbes because it does not require isolation and culturing of the bacteria or fungi. The challenge with this route for titanium and other transition metals like niobium, tantalum, silicon and bismuth is the absence of readily and stable water soluble salts precursors that can easily provide cations for bioreduction [5]. Therefore, in this work the synthesis of titanium oxide nanoparticles (TiO_2 NP's) was performed using a methodology of green chemistry, in which nanoparticles of TiO_2 in the form of anatase with a size of 5–35 nm were favorably obtained with a spherical morphology with agglomeration. By means of X-ray diffraction it was possible to determine that there is a crystalline phase of TiO_2, which has been confirmed as anatase and by FTIR-ATR which confirmed the presence of metal oxide. Aloe vera extract had previously been used for the synthesis of silver nanoparticles, but never for titania nanoparticles. The synthesis of titanium oxide using aloe vera extract is a novel, economical and environmentally friendly

technique. In the present study, *Aloe vera* extract was used for the green synthesis of TiO_2 expecting the polysaccharide acemannan in the inner gel to act as a suitable reductant and stabilizing agent for titania synthesis.

Materials and Methods

Titanium oxide nanoparticles were synthesized by green chemistry technique, using aloe vera extract, titanium chloride (2 M, $TiCl_4$) in 1000 mL of ultra-pure water, where aloe vera extract was added drop by drop and kept with constant agitation of 400 rpm, having a pH ~ 7 with HCl or NaOH. The synthesis product was recovered by centrifugation (10,000 rpm) and washed repeatedly with absolute ethanol. The nanoparticles were washed again with ultra-pure water and dried at 100 °C for 7 h, at the end of drying, a fine white powder was obtained. (This whole process is shown in Fig. 1.) For X-ray diffraction characterization, TiO_2 powder was placed on a flat glass and a brand diffractometer was used as a Bruker. The XRD analysis was performed using a Bruker D8 powder diffractometer (Bruker Corporation, Billerica, MA, USA), with Ni filtered radiation from a Cu anode (kα1 = 1.5406 Å; 40 kV and 35 mA). Diffraction patterns were recorded in the angular range 2θ of 10–90°, with a step size = 0.01° and a step time = 3 s. Transmission Electron Microscopy analyses were performed to determine the size, morphology, crystalline nature, and dispersal of the synthesized iron and silver nanoparticles. The analyses were conducted using a JEOL JEM 2100 TEM operated at 120 kV. The titanium oxide was confirmed by FTIR-ATR y in a PerkinElmer Spectrum Two with Universal ATR (PerkinElmer Inc. Waltham, MA, USA) 2500–450 cm^{-1}.

The titanium oxide was synthesized by the chemical reduction method of titanium chloride ($TiCl_4$), using aqueous aloe vera extracts as reducing, stabilizing, and size control agent. In this nucleation process aloe vera extract plays an important role to regulate size and shape of the AgNP. The chemistry involved in the formation of TiO_2 nanoparticles is displayed in Fig. 2.

Results and Discussion

The presence of titanium dioxide was confirmed by X-ray diffraction, as the peaks match with the crystallographic chart of the International Centre for Diffraction Data-Powder Diffraction File (ICDD-PDF) 00-021-1272, which belongs to the anatase (TiO_2). For the pure TiO_2 XRD spectra, well defined peaks are observed at 25.54°, 35.02°, 37.93°, 40.13°, 48.31°, 54.13°, 55.37°, 62.99°, 69.07°, 70.69°, 74.82°, 75.01°, 77.73°, 80.98°, and 82.63° related to planes (101—predominant), (103), (004), (112), (200), (105), (211), (213), (204), (116), (220), (107), (215), (301), (303) respectively. All the diffraction peaks correspond to the tetragonal anatase phase of TiO_2, with lattice parameters are $a = b = 3.7852$ Å, $c = 9.5139$ Å. Figure 3

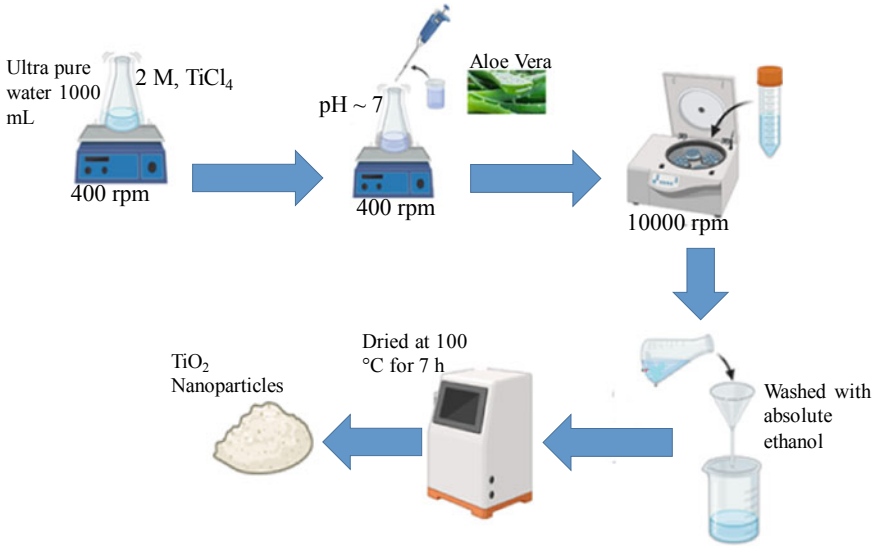

Fig. 1 Schematic methodology for synthesis of titanium oxide nanoparticles

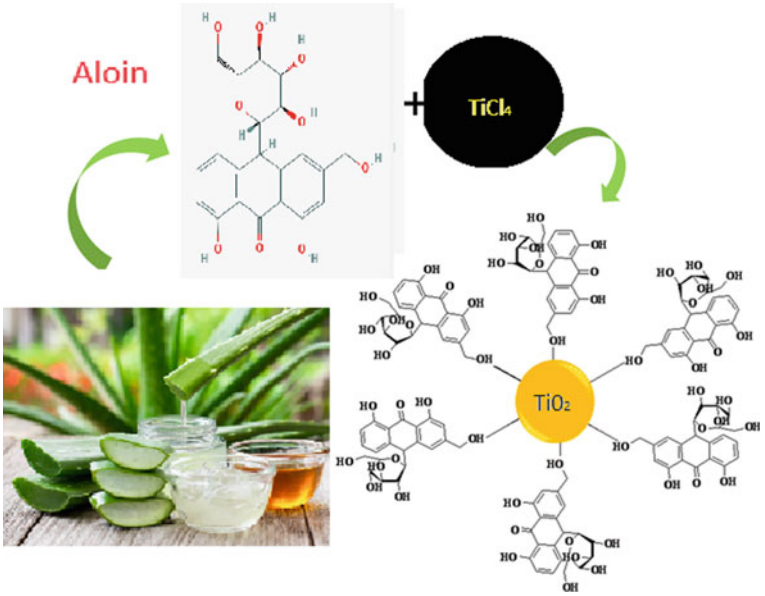

Fig. 2 The chemistry involved in the synthesis of TiO_2 nanoparticles using aloe vera extract

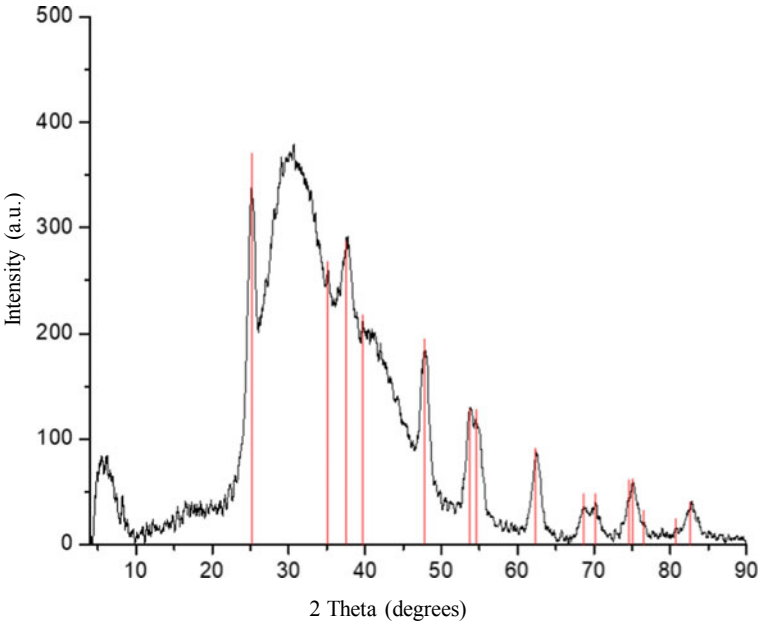

Fig. 3 XRD spectrum of titanium oxide synthesized using aloe vera

shows the diffractogram where it is observed that the crystallographic planes match with those of the anatase, however, noise is shown, which is attributed to the aloe vera extract that was used. There is no any spurious diffraction peak found in the sample. The 2θ peaks at 25.54 and 48.31° confirm its anatase structure. The intensity of XRD peaks of the sample reflects that the formed nanoparticles are crystalline and broad diffraction peaks indicate very small size crystallite. These results suggested that the titanium oxide powder is composed of irregular polycrystalline.

Transmission electron microscopy (TEM) analysis was used to investigate the morphology of the synthesized titanium oxide nanoparticles, as shown in Fig. 4. The TEM micrographs showed that the green-synthesized titanium oxide nanoparticles were spherical in shape, with an average measure of 20 nm. The TEM image of titanium oxide nanoparticles revealed that the nanoparticles were spherical in shape, with a size of ~ 5–35 nm. Many nanoparticles appeared to be somewhat big and amorphous with larger particles which possibly resulted from agglomeration during the synthesis process.

Figure 5 shows the spectrum of energy dispersive X-ray spectroscopy, where titanium, and oxygen are observed; titanium and oxygen check the presence of nanoparticles of TiO_2, the presence of carbon is due to the sample preparation to the analysis by EDS.

Figure 6 shows the spectrum of FTIR-ATR made to the nanoparticles of TiO_2, which shows the presence of organic compounds even after washing the sample, these organic compounds belong to aloe vera. However, the absorption bands at 856

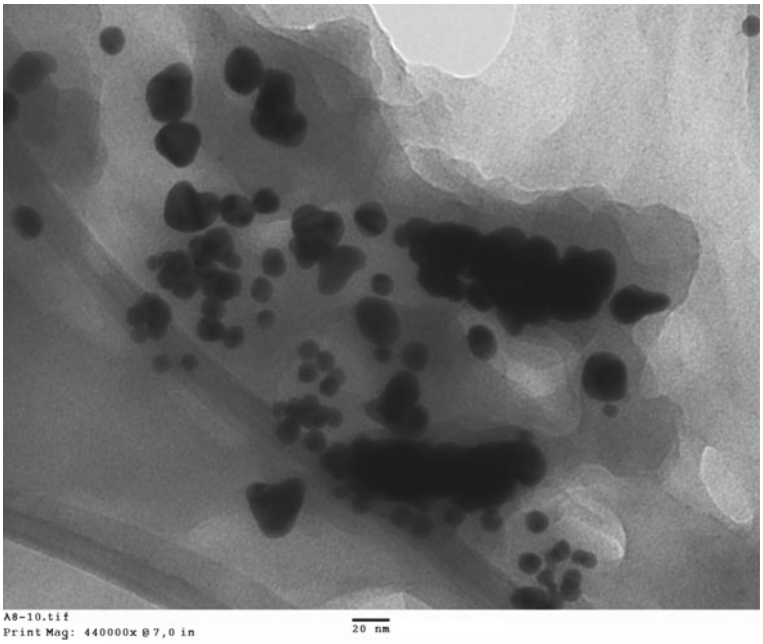

Fig. 4 TEM micrographs of TiO_2 nanoparticles

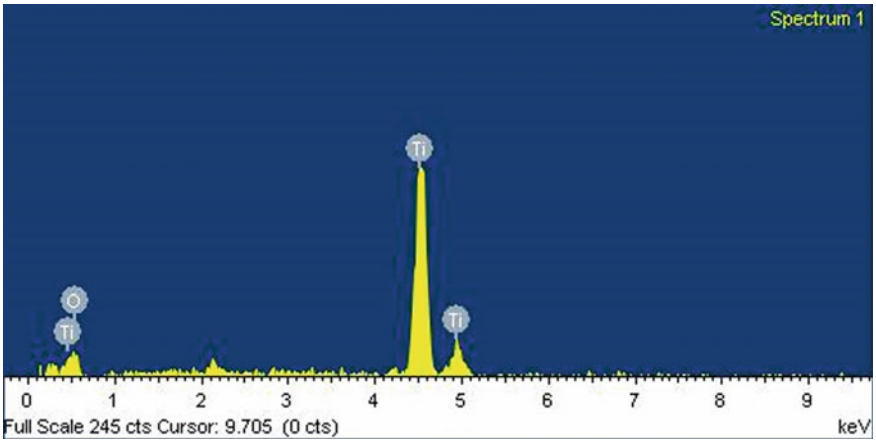

Fig. 5 EDS spectrum of titanium oxide nanoparticles

and 667 cm^{-1} belong to the Ti=O bond with which the presence of metal oxide is confirmed and suggests that it should be washed with some solvent to remove the excess of organic material.

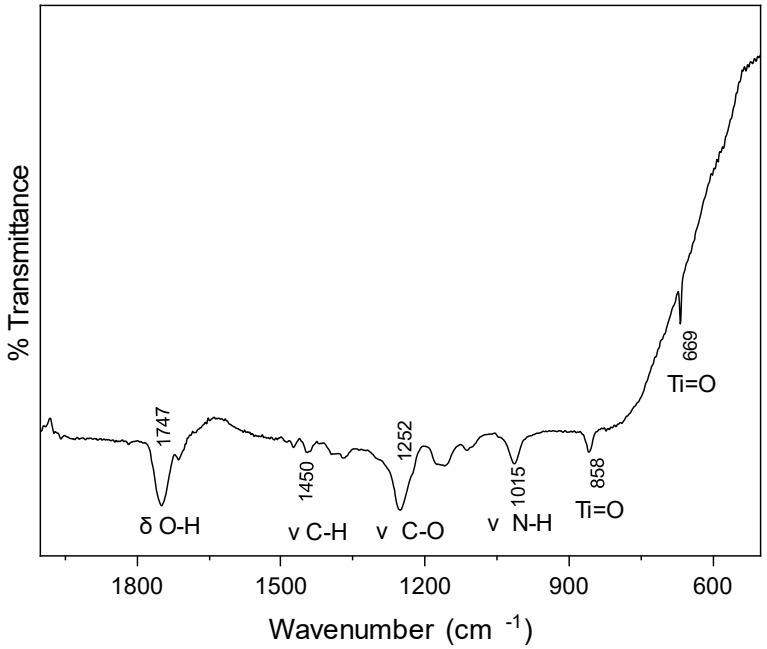

Fig. 6 FTIR-ATR spectrum of titanium oxide nanoparticles

Conclusions

The titanium oxide nanoparticles were synthesized using aloe vera extract. The sample was characterized by XRD showing that there is titania the form of tetragonal anatase, and its unit cell parameters are $a = b = 3.78$ Å, $c = 9.51$ Å. The nanoparticles of titania were characterized by SEM and nanoparticles of TiO_2 in size were obtained between 5 and 35 nm. Nanoparticles have agglomeration because they were not subjected to ultrasound before being analyzed by TEM The samples were characterized by FTIR-ATR to confirm the presence of the titanium oxide bond, whose metallic bond is located in the region of 858 and 669 cm^{-1}, however presents more bands of transmittance due to the aloe vera extract. The elemental analysis performed by EDS confirms the presence of Ti and O in the sample showing carbon contamination due to graphite tape.

References

1. Mbenga Y, Adeyemi JO, Mthiyane DMN, Singh M, Onwudiwe DC (2023) Green synthesis, antioxidant and anticancer activities of TiO_2 nanoparticles using aqueous extract of *Tulbaghia violacea*. Results Chem 6:101007. https://doi.org/10.1016/j.rechem.2023.101007

2. Begum SJ, Pratibha S, Rawat JM, Venugopal D, Sahu P, Gowda A, Qureshi KA, Jaremko M (2022) Recent advances in green synthesis, characterization, and applications of bioactive metallic nanoparticles. Pharmaceuticals 15:455. https://doi.org/10.3390/ph15040455
3. Hussain R, Hasan M, Iqbal KJ, Zafar A, Tariq T, Saif MS, Hassan SG, Shu X, Caprioli G, Anjum SI (2023) Nano-managing silver and zinc as bio-conservational approach against pathogens of the honey bee. J Biotechnol 365:1–10. https://doi.org/10.1016/j.jbiotec.2023.01.009
4. Gebre SH, Sendeku MG (2019) New frontiers in the biosynthesis of metal oxide nanoparticles and their environmental applications: an overview. SN Appl Sci 1(8):928
5. Hemalatha K, Madhumitha G, Kajbafvala A, Anupama N, Sompalle R, MohanaRoopan S (2013) Function of nanocatalyst in chemistry of organic compounds revolution: an overview. J Nanomater 2013:341015. https://doi.org/10.1155/2013/341015
6. Roopan SM, Kumar SHS, Madhumitha G, Suthindhiran K (2015) Biogenic-production of SnO_2 nanoparticles and its cytotoxic effect against hepatocellular carcinoma cell line (HepG2). Appl Biochem Biotechnol 175(3):1567–1575
7. TaghaviFardood S, Ramazani A, Moradnia F, Afshari Z, Ganjkhanlu S, YekkeZare F (2019) Green synthesis of ZnO nanoparticles via sol-gel method and investigation of its application in solvent-free synthesis of 12-aryl-tetrahydrobenzo[α]xanthene-11-one derivatives under microwave irradiation. Chem Methodol 3(6):696–706
8. Ruddaraju LK, Pammi SVN, Guntuku GS, Padavala VS, Kolapalli VRM (2020) A review on anti-bacterials to combat resistance: from ancient era of plants and metals to present and future perspectives of green nano technological combinations. Asian J Pharm Sci 15(1):42–59
9. Arularasu MV (2019) Effect of organic capping agents on the optical and photocatalytic activity of mesoporous TiO_2 nanoparticles by sol–gel method. SN Appl Sci 1(5):393
10. Abisharani JM, Devikala S, Kumar RD, Arthanareeswari M, Kamaraj P (2019) Green synthesis of TiO_2 nanoparticles using *Cucurbita pepo* seeds extract. Mater Today Proc 14:302–307

Use of Red Mud in Soil Stabilization for Pavement Through Alkali Activation

Sarah Souza Silva, Beatryz Cardoso Mendes, Taciano Oliveira da Silva, Emerson Cordeiro Lopes, Flávio Antônio Ferreira, and Leonardo Gonçalves Pedroti

Abstract The concern about the amount of solid waste generated in aluminum production has led to studies on the reuse of this waste in various types of construction materials. This research investigated the use of red mud in soil stabilization for pavement through alkali activation. Experiments with tropical soil and red mud activated with NaOH (6, 8, and 10 mol) aimed to optimize the soil properties. The mixture was evaluated for mechanical performance, and ideal proportions of mud (10, 20, 30, and 40%) were determined. Compaction curves were performed for different proportions of the residue, obtaining values for optimum moisture content and maximum density. There was an improvement in the strength of the samples with the replacement of up to 20% of red mud, and it showed a significant improvement, with results exceeding 300%, when compared to compaction without additives.

Keywords Geopolymer · Sustainability · Red mud · Soil stabilization

Introduction

The mining sector plays a strategic role on the global economy, exerting significant influence on wealth creation and job opportunities in various nations. Mining encompasses the extraction of a wide range of essential minerals, such as iron, copper, gold, silver, aluminum, coal, diamonds, lead, zinc, nickel, and uranium, which play vital roles in various economic sectors, including construction, automotive industry, energy, electronics, and others. However, this economic activity comes with a considerable challenge: the continuous generation of waste from mining operations [1–3].

S. S. Silva (✉) · B. C. Mendes · T. O. da Silva · E. C. Lopes · F. A. Ferreira · L. G. Pedroti
DEC—Civil Engineering Department, UFV—Federal University of Viçosa, Av. Peter Rolfs, s/n, Campus Universitário, Viçosa 36570-000, Brazil
e-mail: sarah.s.souza@ufv.br

Z. Peng et al. (eds.), *Characterization of Minerals, Metals, and Materials 2024*, The Minerals, Metals & Materials Series, https://doi.org/10.1007/978-3-031-50304-7_67

The significant accumulation of mining waste represents an environmental and safety challenge [2]. To mitigate this problem, it is imperative to explore viable and sustainable alternatives [4]. One solution under study is the use of these waste materials in other sectors, such as construction and transportation. In this context, research focuses on the production of geopolymers through alkaline activation as a promising approach. This study is dedicated to the treatment of bauxite residue, which is known to be rich in silicon and aluminum oxides [5–7].

Geopolymers offer a wide range of applications, and this research focuses on soil stabilization for use in roads [8], aiming to enhance the performance of these infrastructures. By exploring this alternative, the goal is to contribute to the addressing of challenges related to mineral industry waste management and promote more sustainable practices in the construction and infrastructure sectors. This research seeks a direct connection between innovation in construction materials and solutions for pressing environmental issues, pointing towards a more efficient and environmentally responsible future.

Materials and Methods

The materials used in this research were bauxite residue (RM), tropical soil, sodium hydroxide, and distilled water. The RM was obtained from the Bom Jardim dam located in the city of Miraí, MG. The soil collection was conducted in the vicinity of Viçosa, MG, near BR 120. The alkaline solutions were produced with commercial sodium hydroxide pellets (NaOH P.A., 99%, CRQ) and distilled water at varying molar concentrations [9].

The solid materials (red mud and soil) underwent physical, chemical, and mineralogical characterization tests. The particle size distribution of the red mud was determined using the Laser Particle Size Analysis technique, following NBR NM ISO 13320 [10]. Regarding the soil, the particle size distribution curve was determined according to the specifications of NBR 7181 [11], following the steps of fine sieving and sedimentation of particles smaller than 2 mm; the density of the grains was determined in accordance with NBR 6508 [12].

Regarding chemical and morphological characterization, both materials were analyzed comprehensively. Chemical characterization was performed using the X-ray fluorescence (XRF) technique with the Shimadzu EDS-720 equipment. The constituent oxides of the samples were obtained using this technique. To determine the mineralogical composition of the clay, silt, and sand fractions of each material, X-ray Diffraction (XRD) was performed for mineralogical characterization, using the D8 Discover diffractometer (Bruker), with CuKα radiation (1.5418 Å), 2θ ranging from 3 to 70°, 0.05° 2θ step-scan and 1.0 s/step [13].

Before producing the test specimens, a compaction test was conducted to establish certain parameters such as maximum bulk density and optimum moisture content. This test was performed using modified energy compaction [14, 15]. For the production of the test specimens, three NaOH solutions were prepared, each with different molar concentrations (6, 8, and 10 M). Additionally, distilled water was also used as part of the study, representing a zero concentration of NaOH. Regarding the solid material, mixtures were created in five different proportions: pure soil (0% RM), 10, 20, 30, and 40% NaOH. Taking these two factors into consideration, a total of 20 mixtures were formulated and 5 test specimens were molded for each mixture. The dimensions of the molded test specimens were 3.05 cm in height with a 3.05 cm diameter, and the proportion of the solution added to the mixtures corresponded to the optimum moisture content. Compaction was carried out with a force of two tons, resulting in a maximum density ranging from 1.995 to 2.039 g/cm^3. It is important to note that each mixture was prepared individually before molding. To preserve moisture, the molded test specimens were covered with plastic film and stored in a humid chamber for seven days, following the guidelines of NBR 12655:2015—Preparation of the Mixture and Curing of Concrete Test Specimens [16], considering the similarity between geopolymers and concrete under these conditions.

After the established curing period, a compression strength test was immediately conducted using a universal testing machine. Following the completion of the mechanical tests, a sample of the tested material from each mixture was immersed in acetone for 24 h to halt the reactions. Subsequently, these samples were subjected to microstructural analysis using the X-ray diffraction (XRD) technique.

Results and Discussion

Characterization of Raw Materials

From the results of the particle size distribution of the particles in the red mud, it is possible to classify the type of material. The mean diameter ($D50$) of the material is 8.0 μm, indicating that the residue already has a finer particle size. It can be classified as a silty material, with approximately 20% clay fraction in its composition.

Regarding the soil's particle size distribution curve, it predominantly exhibits clay-like characteristics. Over 60% of its particles have diameters smaller than 5 μm, while approximately 30% fall within the range of 0.005–0.05 mm, which characterizes a silt fraction.

Table 1 presents the chemical composition of both the soil and the red mud. It is possible to observe that both materials analyzed have a high concentration of both SiO_2 and Al_2O_3 and a relatively high content of Fe_2O_3. SiO_2 is the main component for the formation of a geopolymeric matrix that is based on the three-dimensional organization and arrangement in which silicon (Si) atoms alternate with aluminum atoms in tetrahedral coordination, sharing oxygen atoms [17]. However, studies have

Table 1 Chemical composition of RM and soil

Raw material	Chemical composition (%)									L.O.I. (%)
	SiO_2	Al_2O_3	Fe_2O_3	P_2O_5	K_2O	SO_3	Ti_2O	Na_2O	Other	
Soil	28.76	39.75	21.56	0.36	0.21	0.72	1.44	7.01	0.19	2.31
RM	44.41	32.39	15.56	0.34	0.09	0.9	2.50	3.62	0.19	19.73

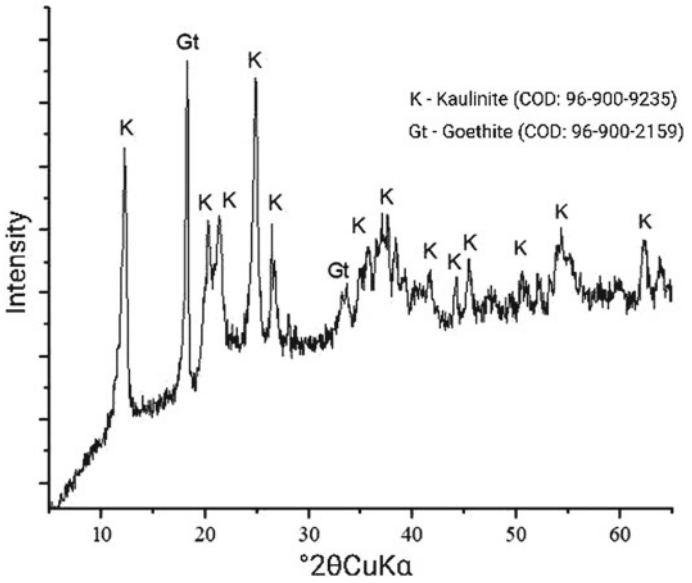

Fig. 1 Red mud XRD patterns (K—kaolinite; G—goethite)

indicated that the presence of iron oxide (Fe_2O_3) can inhibit geopolymerization reactions by substituting Al^{3+} ions with Fe^{3+} ions [18].

Figure 1 depicts the X-ray diffraction (XRD) patterns of the red mud. The red mud exhibits the following crystalline phases: kaolinite and goethite, which suggest that the silica and alumina present are not in their reactive form, making their dissolution in an alkaline medium more challenging. Kaya and Soyer-Uzun [19] found that the presence of iron in goethite (FeO(OH)) in red mud negatively affected the compression strength of the samples.

Proctor Compaction Test

In Fig. 2, the results of modified Proctor compaction tests conducted on soil and red mud mixtures at the five different studied addition ratios (0, 10, 20, 30, and 40%) are presented. The analysis reveals that the optimum moisture content remained

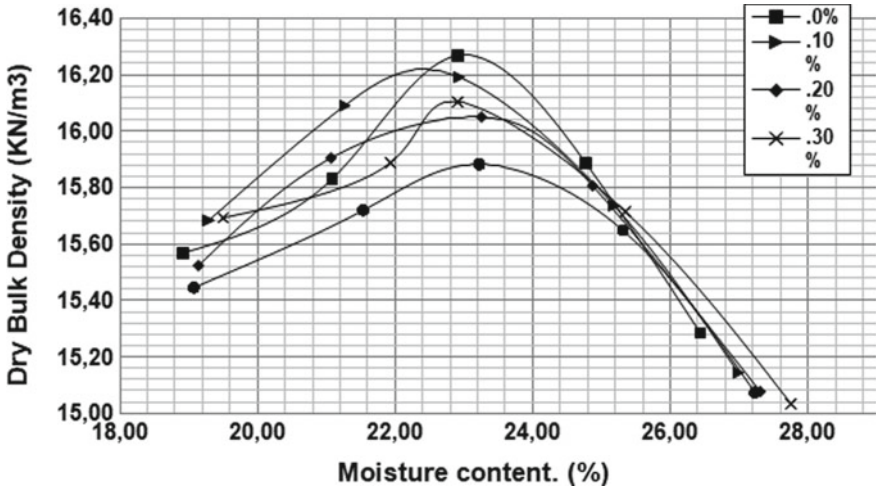

Fig. 2 Proctor compaction test

relatively constant, around 23%, considering possible experimental variations. As for the dry unit weights, they ranged from 16.27 to 15.88 kN/m^3. Furthermore, it is possible to observe a slight decrease in the density value as the proportion of residue increases in the mixtures.

Characterization of Geopolymeric

Figure 3 displays the compressive strength results of the 20 mixtures after seven days of curing. It is noticeable that the increase in mechanical strength concerning the increase in the proportion of red mud in the mixture was not significant. However, it is important to highlight that the increase in the concentration of the NaOH solution resulted in a considerable increase in strength (approximately 300%). This analysis is presented in more detail in Figs. 4 and 5, which show an analysis of variance (ANOVA) with a confidence level of 85.6% and the application of the Tukey test. Despite the relatively insignificant influence of the proportion of red mud in the mixtures, its combined effect with the variation in the concentration of the NaOH solution resulted in significant outcomes.

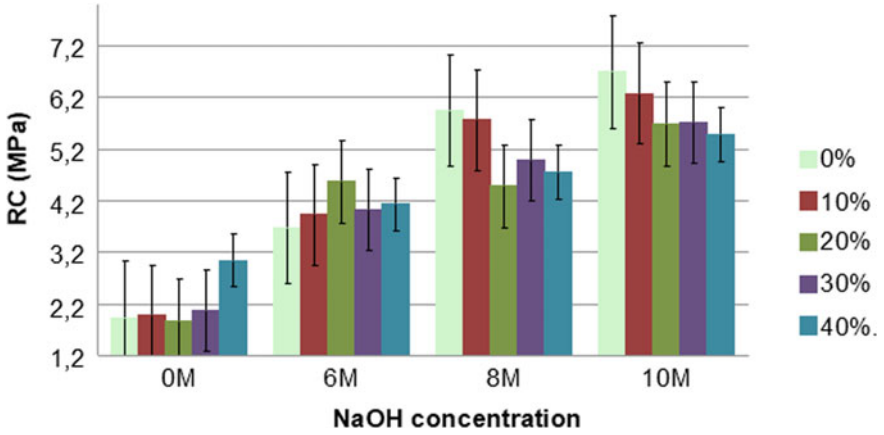

Fig. 3 Compression strength values for each mixture made, varying RM and NaOH concentrations

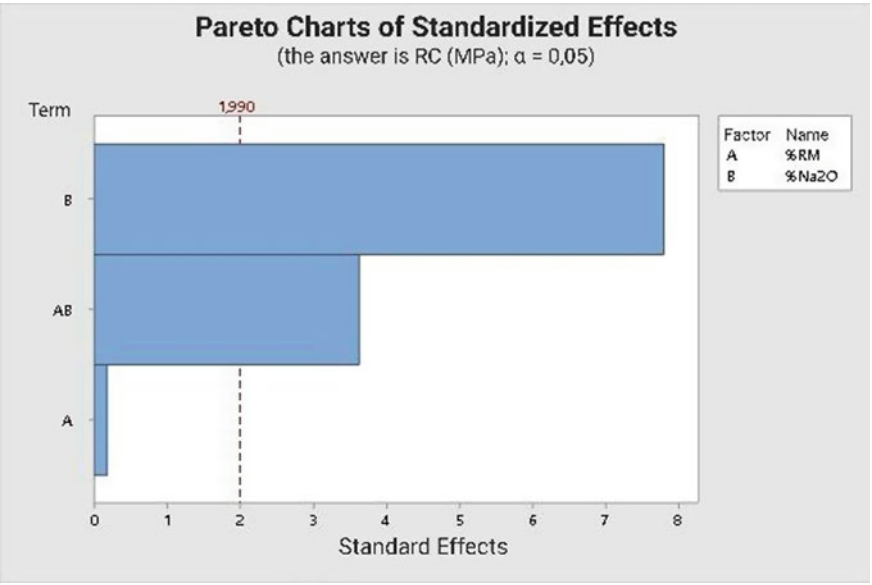

Fig. 4 Significance level of individual study factors and their interaction on compressive strength

Conclusions

The present research aimed to analyze the mechanical behavior and microstructure of geopolymers produced from mixtures of soil and bauxite residue, reacting with an alkaline solution of NaOH. Based on the results obtained and the statistical analyses

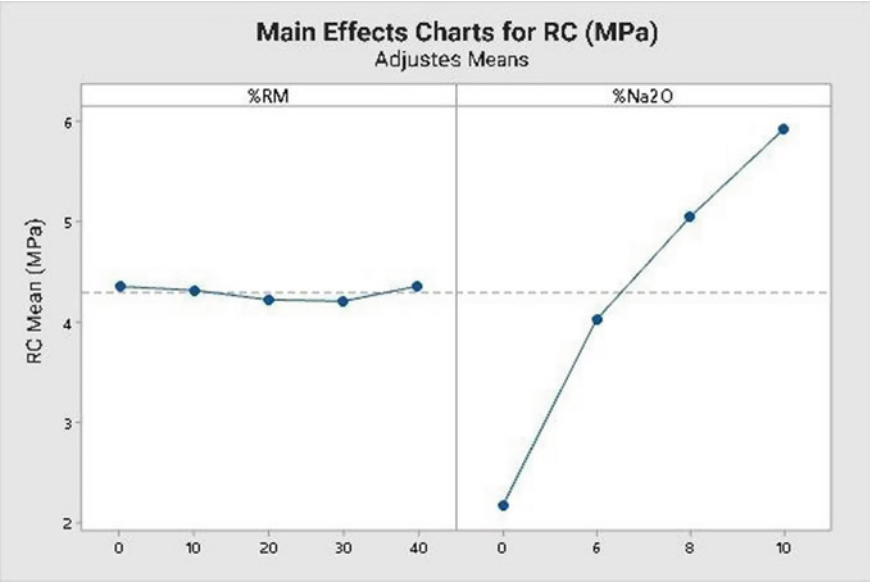

Fig. 5 Main effects on compressive strength: comparing the relevance of RM concentration and NaOH concentration

conducted through ANOVA and Tukey's test ($\alpha = 0.05$), the following conclusions can be highlighted.

The formation of geopolymers for the purpose of soil stabilization and increased strength has proven to be a viable and effective approach within the limits of this research. However, the use of bauxite residue did not show significant relevance in this context, and it may or may not be incorporated. Given the environmental concerns related to the use of this residue, further studies will be necessary to assess its application in construction in a broader sense.

The soil itself used in this study demonstrated suitable properties to react with the alkaline solution and develop strength. Therefore, future studies should consider soils with more challenging and unsuitable characteristics for pavement applications to further evaluate the potential of geopolymers usage in these circumstances.

Acknowledgements The authors would like to thank the FAPEMIG agency for the financial support provided and the Sustainable and Innovative Construction Research Group (SICon) for the technical assistance.

References

1. The importance of mining for global development, 6 Mar 2023. https://www.correiasmercurio.com.br/a-importancia-da-mineracao/

2. Antos RCdVd (2021) Contribution of the mineral sector to the Brazilian gross domestic product
3. Bruschi GJ et al (2022) Evaluation of leaching from cemented bauxite residues through wetting and drying cycles of durability test. Environ Sci Pollut Res 29(39):59247–59262
4. Ou X et al (2022) Analysis of engineering characteristics and microscopic mechanism of red mud–bauxite tailings mud foam light soil. Materials 15(5):1782
5. Grillo F, Matoski A, Alberti ME (2021) Characterization of geopolymers made with glass residues and anodizing sludge. Braz J Dev 7(6):60707–60725
6. Andrade IKR (2022) Development of one-part geopolymer based on metakaolin and red mud
7. Krivenko P (2017) Why alkaline activation—60 years of the theory and practice of alkali-activated materials. J Ceram Sci Technol 8(3):323–333
8. Rios S, da Fonseca AV (2016) Soil stabilization with geopolymers for roadbed layers. In: 15CNG: 15th national congress of geotechnics and 8th Luso-Brazilian geotechnical congress
9. Mendes BC et al (2023) Application of mixture design of experiments to the development of alkali-activated composites based on chamotte and waste glass. Constr Build Mater 379:131–139
10. ABNT (2011) NBR NM ISO 13320:2011. Nanotecnologia—Partículas—Determinação do tamanho de partículas por análise de imagem de microscopia eletrônica de transmissão. ABNT, Rio de Janeiro
11. Associação Brasileira de Normas Técnicas (2016) NBR 7181:2016. Solo—Análise granulométrica. ABNT, Rio de Janeiro
12. Associação Brasileira de Normas Técnicas (1986) NBR 6508: Grãos de Solos Que Passam Na Peneira de 4,8 mm. Rio de Janeiro
13. Antunes MLP, da Conceição FT, Navarro GRB (2011) Characterization of Brazilian red mud (bauxite refining waste) and assessment of its properties for future applications. In: International workshop advances in cleaner production
14. Associação Brasileira de Normas Técnicas (1986) NBR 7185: Solo—Ensaio de compactação utilizando energia modificada. Rio de Janeiro
15. Bruschi GJ, dos Santos CP, Levandoski WMK et al (2022) Leaching assessment of cemented bauxite tailings through wetting and drying cycles of durability test. Environ Sci Pollut Res 29:59247–59262. https://doi.org/10.1007/s11356-022-20031-5
16. Associação Brasileira de Normas Técnicas (2017) NBR 16605: Cimento Portland e outros materiais em pó—Determinação de massa específica. Rio de Janeiro
17. Vassalo EAS (2013) Obtaining geopolymer from activated metakaolin. Master's thesis in civil engineering, Federal University of Minas Gerais, 104 pp
18. Kaze RC et al (2018) Microstructure and engineering properties of $Fe_2O_3(FeO)$–Al_2O_3–SiO_2 based geopolymer composites. J Clean Prod 199:849–859
19. Kaya K, Soyer-Uzun S (2016) Evolution of structural characteristics and compressive strength in red mud-metakaolin based geopolymer systems. Ceram Int 42(6):7406–7413

Author Index

Z. Peng et al. (eds.), *Characterization of Minerals, Metals, and Materials 2024*, The Minerals, Metals & Materials Series, https://doi.org/10.1007/978-3-031-50304-7

Subject Index

Z. Peng et al. (eds.), *Characterization of Minerals, Metals, and Materials 2024*, The Minerals, Metals & Materials Series, https://doi.org/10.1007/978-3-031-50304-7